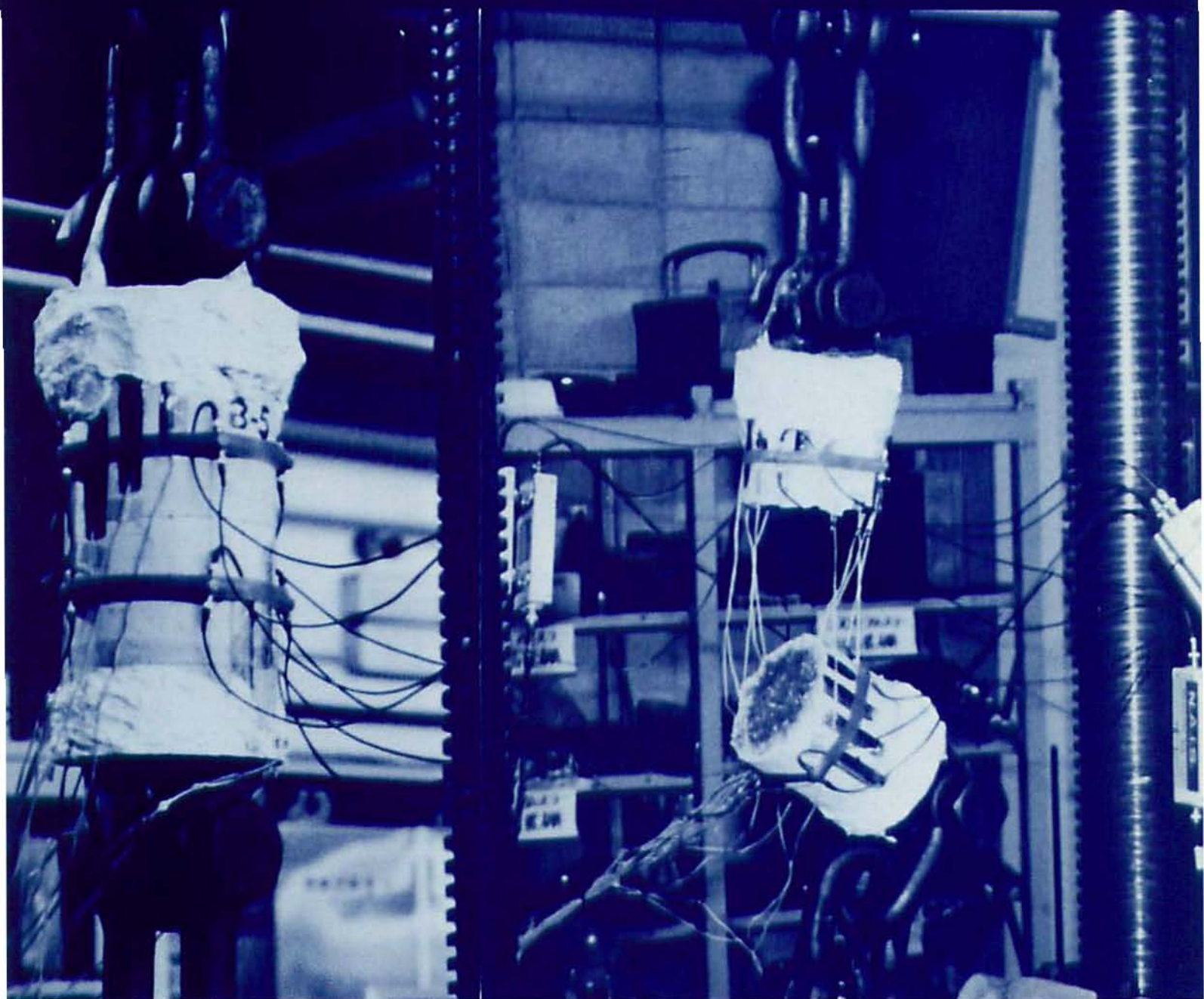


An International
Forum For
The AE Science
and Technology

JOURNAL OF ACOUSTIC EMISSION

Vol.10,Nos.1-2, 1991/92



AE TESTING OF CONCRETE JOINT AT HAZAMA

Endorsed by
AEWG, AEWGI
CARP and
EWGAE

Published by
Acoustic Emission Group
Los Angeles, CA

JOURNAL OF ACOUSTIC EMISSION

Editor: Kanji Ono

Associate Editors: A. G. Beattie, T. F. Drouillard, R. Hill and S. L. McBride

1. Aims and Scope of the Journal

Journal of Acoustic Emission is an international journal designed to be of broad interest and use to both researcher and practitioner of acoustic emission. It will publish original contributions of all aspects of research and significant engineering advances in the sciences and applications of acoustic emission. The journal will also publish reviews, the abstracts of papers presented at meetings, technical notes, communications and summaries of reports. Current news of interest to the acoustic emission communities, announcements of future conferences and working group meetings and new products will also be included.

Journal of Acoustic Emission includes the following classes of subject matters;

A. Research Articles: Manuscripts should represent completed original work embodying the results of extensive investigation. These will be judged for scientific and technical merit.

B. Engineering Applications: Articles must present significant advances in the engineering applications of acoustic emission. Material will be subject to reviews for adequate description of procedures, substantial database and objective interpretation.

C. Technical Notes: This class provides publications of works of current interest, and new or improved experimental techniques and procedures.

D. Communications: Short items of current interest, discussions of published articles and relevant applications.

E. AE Literature: This section will collect the titles and abstracts of papers published elsewhere and those presented at meetings and conferences. Reports of conferences and symposia will also be presented, together with meeting schedules.

F. Reviews, Tutorial Articles and Special Contributions: This class of articles will cover the subjects of general interest.

Nontechnical Section: This part will cover book reviews, significant personal and technical accomplishments, current news and new products.

2. Endorsement

Acoustic Emission Working Group (AEWG), European Working Group on Acoustic Emission (EWGAE), Committee on Acoustic Emission from Reinforced Composites (CARP), and Acoustic Emission Working Group of India have endorsed the publication of Journal of Acoustic Emission. This Journal gratefully acknowledges financial contributions from EWGAE and AEWG.

3. Governing Body

The Editor and Associate Editors will implement the editorial policies described above. The Editorial Board will advise the editors on any major change. The Editor, Professor Kanji Ono, has the general responsibility for all the matters. Associate Editors, Dr. S.L. McBride and Dr. A.G. Beattie, assist the review processes as lead reviewers and Associate Editor, Dr. R. Hill coordinates the regional review processes for Europe. Mr. T.F. Drouillard is responsible for the AE Literature section.

The members of the Editorial Board will advise and assist the editors on the publication policies and other aspects. They will promptly review the manuscript assigned and will contribute actively to the Journal. The Board presently includes the following members:

John Baron	(Canada)
F. Beall	(USA)
L. Bolin	(Sweden)
F.R. Breckenridge	(USA)
S.H. Carpenter	(USA)
H. Crostack	(FRG)
D.M. Egle	(USA)
P. Fleischmann	(France)
T.J. Fowler	(USA)
L. Golaski	(Poland)
M.A. Hamstad	(USA)
H.R. Hardy, Jr.	(USA)
T. Holroyd	(UK)
I.V. Ivanov	(USSR)
P. Jax	(FRG)
T. Kishi	(Japan)
A.E. Lord, Jr.	(USA)
K. Mogi	(Japan)
W. Morgner	(DDR)
C.R.L. Murthy	(India)
A. Nielsen	(Denmark)
M. Ohtsu	(Japan)
A.A. Pollock	(USA)
J. Rogot	(France)
I. Roman	(Israel)
C. Scruby	(UK)
C. Thaulow	(Norway)
E. Waschkies	(FRG)
K. Yamaguchi	(Japan)

4. Publication

Journal of Acoustic Emission is published quarterly in March, June, September and December by Acoustic Emission Group, 308 Westwood Blvd. - Box 364, Los Angeles, CA 90024-1647. It may also be reached at 6532 Boelter Hall, University of California, Los Angeles, California 90024 (USA) telephone 213-825-5233.

5. Subscription

Subscription should be sent to Acoustic Emission Group. Annual rate for 1990 and 1991 is US \$90.00. For surface delivery, add \$6 in the U.S. and \$8 for Canada and elsewhere. For air mail delivery to US and Canada, add \$15, South America and Western Europe, add \$23 and add \$28 elsewhere. Add \$5.00 for orders not prepaid and requiring invoices. Overseas orders must be paid in US currencies with a check drawn on a US bank. Inquire for individual and bookseller discounts.

6. Advertisement

Advertisement only for products and services related to acoustic emission will be accepted. Send a camera ready copy one month before scheduled publication date. Inquire for rates. Announcements for books, training courses and future meetings will be included without charge.

**The International Joint Meeting, 1st Workshop on Acoustic
Emission in Civil Engineering and 2nd Workshop on AE
and Rock Fracture Mechanics,
Kumamoto, Japan, October 29 - 31, 1990**

**Current Research and Future Trend of AE Applications to Civil
Engineering and Geological Technology**

**Masayasu Ohtsu
Topical Editor**

Introduction

The International Joint Meeting, 1st Workshop on Acoustic Emission in Civil Engineering and 2nd Workshop on AE and Rock Fracture Mechanics, was held at the city of Kumamoto, October 29 - 31, 1990. This Meeting was sponsored by Acoustic Emission Working Group of the Kyushu Association for Bridges and Structural Engineering. In all, 29 papers related to the application of AE to civil engineering and geological technology were presented. This was the first international activity on AE applications to these fields. Fifteen of the papers presented are included in this special issue of Journal of Acoustic Emission.

The conference was organized into sessions on source characterization, civil engineering materials, structural integrity, mechanical behavior and Kaiser effect of rock, and concrete engineering. In the session on civil engineering materials, the majority of the papers were concerned with geological materials and concrete. In the area of structural integrity, the stability of rock cavern, tunnel, and landslide were reported. The application of Kaiser effect to the evaluation of geostress was also presented.

As indicated by these reports, AE applications in these areas are growing rapidly at present. Actually, the research activities in geo-technology first boomed some twenty years ago, but no sustained efforts had been conducted at the major companies and institutes. Renewed interests in recent years have arisen from the need of inspection technologies in construction fields related with three R's for infrastructures, namely, repair, restoration and rehabilitation.

Code and Standardization

In the fields related to geological materials and concrete, AE techniques are inherently applicable to monitor the construction process and to maintain existing structures. With respect to the geological materials and structures, AE application to the process monitoring is well known. Because the construction processes are highly dependent on site conditions, however, the inspection procedure is not unique to the site. The in-process monitoring of industrial products is not readily transferrable to geological materials. Still, the need for the monitoring of construction processes is increasing. The safety monitoring of existing geologic structures is also in demand. A number of concrete structures are approaching their service-life limit due to deterioration. This is why techniques for three R's are needed, AE applications for the evaluation of concrete deterioration in particular.

Practical geological and concrete applications require the standardization, because the construction works are normally under governmental supervision. Consequently, to advance AE technology further, the establishment of the codes is essential. The Japanese Society for Nondestructive Inspection (JSNDI), the Japan Concrete Institute (JCI), and the Japan Society of Civil Engineers (JSCE) are all working on this aspect currently.

Concluding Remarks

Geologic materials and concrete cover a variety of engineering fields, such as mineral science, mining, petroleum engineering, resource engineering, and civil engineering. Structures related with these technologies are of large scale and AE applications are useful in various phases. However, a new technology devel

Professor Masayasu Ohtsu is affiliated with Department of Civil and Environmental Engineering, Kumamoto University, Kumamoto 860, Japan.

oped may be either unknown or inapplicable in other fields. This is the biggest obstacle to AE applications in these fields. Researchers publish results in only their own field and people in other fields often unaware of other's success. Consequently, mutual communications are critically important and international conferences such as this one should be held often around the world.

I hope that reports from this International Joint Meeting stimulate further developments and result in wider uses of acoustic emission technology.

CONTENTS

Variety of Acoustic Emission Waveforms Produced by Discrete Crack Growth in Rock Steven D. Glaser and Priscilla P. Nelson	S1-S12
Estimation of Maximum Stress in Old Railway Riveted I-Girder Bridges using Acoustic Emission Signals Hisanori Otsuka, Hiroshi Hikosaka, Hiroyuki Miyatake and Syouzou Nakamura	S13-S17
Another Look at Booming Sand Marcel F. Leach and Gottfried A. Rubin	S18-S21
Expected Acoustic Emission from Around a Shaft in Intact Rock B.J.S. Wilkins and G.L. Rigby	S22-S28
Acoustic Emission Monitoring during Microseismic Activity Caused by Mine Subsidence Brian R. A. Wood and Robert W. Harris	S29-S34
Acoustic Emission/Microseismic Activity Monitoring of Salt Crystallization for Stone Conservation M. Montoto, R.M. Esbert, L.M. Suárez del Río, V.G. Ruiz de Argandoña and C.M. Grossi	S35-S41
Acoustic Emission Monitoring during In-situ Heater Test of Granite T. Ishida, K. Kitano, N. Kinoshita and N. Wakabayashi	S42-S48
Using Acoustic Emission Testing in Seepage Investigations Andrew R. Blystra	S49-S54
Acoustic Emission of Penetration Experiments to Judge Soil Condition S. Naemura, M. Tanaka, S. Nishikawa, M. Nakamura, K. Jo and T. Kishishita	S55-S58
A Laboratory Investigation of AE from Coal R. W. Harris, B. R. A. Wood and T. Flynn	S59-S62
Determination of the Initial Stresses on Rock Mass using Acoustic Emission Method K. Michihiro, K. Hata, H. Yoshioka and T. Fujiwara	S63-S76
U.S. Bureau of Mines Research on the Kaiser Effect for Determining Stress in Rock Michael J. Friedel and Richard E. Thill	S77-S89
Evaluation of Joint Properties of Anti-washout Underwater Concrete by Acoustic Emission Measurement Kazuya Miyano, Tatsuo Kita, Yuji Murakami and Takako Inaba	S90-S96
Automated Determination of First P-Wave Arrival and Acoustic Emission Source Location E. Landis, C. Ouyang and S. P. Shah	S97-S103
Application of Acoustic Emission Techniques in the Evaluation of Frost Damage in Mortar Hisatoshi Shimada and Koji Sakai	S104-S109

Variety of Acoustic Emission Waveforms Produced by Discrete Crack Growth in Rock

Steven D. Glaser and Priscilla P. Nelson

The authors are affiliated with Department of Civil Engineering, The University of Texas, Austin, Texas 79712. S.D. Glaser is now with National Institute of Standards and Technology, Gaithersburg, MD 20899.

Abstract

An experimental program was undertaken to investigate high-fidelity acoustic emission (AE) waveforms produced during discrete fracture propagation in rock. Large chevron-notched specimens were loaded in controlled conditions, and characteristic acoustic emissions associated with Mode I and Mode II fracture were isolated. Tested rock included medium-grained granite and micritic dolostone. The entire test system, including surface-mounted NIST type piezoelectric transducers, was calibrated for each experiment to establish the system response function.

The AE waveforms belonged to five characteristic classes. By far the most common three classes are related to basic step impulses. Prominent subclasses of several classes are identified and discussed in detail. The variety of AE event classes was the same in Mode I and Mode II loadings for both rock types. The mechanism for crack propagation in rock is thought to be due to localized tensile failure for both tensile and shear loadings.

1. Introduction

For the last few years, a program has been underway at the University of Texas at Austin to carefully record and decode calibrated AE waveforms from discrete fracture propagation in rock. The goal was to sort these waveforms into characteristic shape groups and correlate these groups with a known and controlled mode of fracture propagation. The recorded signals clearly divided into five main classes (Glaser, 1990; Glaser and Nelson, 1992a). However, within these classes there were tight subgroupings of signals that obviously were due to very similar source mechanisms. These subtle differences within waveform classes hold additional information about the fracture process, much of which is not readily understood. This paper presents the range of waveform shapes recorded during our experimental program. The explanations of the possible causal mechanisms given in this paper are deduced from the experimental results.

2. Summary of the Experiment

2.1 Experimental Plan

This experimental program was undertaken to decode the displacement record of stress waves produced during discrete fracture propagation in rock. The testing conditions were carefully controlled so that characteristic waveform shapes could be correlated with the mode of crack propagation. The specimens used for this series of tests were loaded such that the stress regime causing crack growth was known, at least on a macroscopic scale. The specimens were loaded first in four-point bending to insure that crack growth would be in Mode I, then in four-point shear (Ingraffea, 1981; Jeng and Shah, 1989) to promote crack growth in Mode II. The specimens had a chevron notch cut perpendicular to the long axis so that the plane of fracture would be known, and to improve control over the rate of crack growth. The crack front traveled through 257 mm of the material, with a maximum crack front length of 295 mm after the crack front propagated past the chevron notch. Two different rocks, San Saba dolostone and Elberton granite were used as specimens so that it could be determined whether the associated fracture mechanisms would be a function of rock type.

The samples used for this experimental program were quite large (0.3 m x 0.3 m x 1 m) so that a suitable length of signal was recorded before reflections from specimen boundaries and sample resonance would contaminate the signal. Waveforms were accepted as AE events only if the initial arrival of energy was unambiguously present in the record. Only the initial part of each event waveform was used for analysis; from the initial arrival of the P-wave to the arrival of the S-wave. Thus, the signals analyzed were effectively from an infinite half-space.

The effect of each specimen on the waveforms traveling from the crack to the transducer was accounted for by calibrating the test system at the beginning of each loading. The impulse response function for the entire test setup—the load frame, specimen, transducer, electronics, and digitizer—was derived and an inverse filter calculated so that the system bias could be removed from the recorded signals. In fact, the effect of the system was very slight. Almost all signal energy was below 350 kHz.

NIST-type high-fidelity piezoelectric transducers were built to insure that the output of the transducer was proportional to vertical surface displacement only and had a virtually flat frequency response to well over 1 MHz, and a small amount of phase shift to the signal. Similar care was taken with the unity gain matching preamplifier and 20 dB amplifier.

In addition to the AE waveforms collected, the load, load point displacement, crack mouth opening or sliding displacement and trigger time were continuously logged throughout the test for each event. This allowed correlation between individual AE event waveforms and specimen condition at that time.

2.2 Method of Pattern Recognition

It was initially planned to use a commercial pattern recognition program, ICEPAK from Tektrend International, to choose and sort the waveforms into characteristic classes (Glaser and Nelson, 1989). However, after much work it became apparent that ICEPAK was not designed for, and was unsuited for, this task (Glaser, 1990; Glaser and Nelson, 1992b). Instead, a straightforward heuristic method was chosen by directly observing waveforms recorded.

All the waves for the dolostone test were printed out on separate sheets of paper. The waveforms were then sorted into as many different stacks as appeared to be needed to define characterizable groups. After several days the process was repeated. An archetypal shape for each group was formed for each stack, or class.

After sustained exposure to the data, it became evident that the events could be divided into eight main classes, with many subgroupings. The result of this methodology was verified when the signals from the granite tests were sorted. The waveforms fell into the same groupings found for the dolostone, with no forcing of decisions.

3. Characteristic Waveform Shapes

3.1 Waveform Notation

Careful systematic sorting of the AE waveforms detected during the dolostone and granite testing resulted in five classes (and three subclasses) of events: Classes A (and A1), B (and B1), C (and C1), D, and E. Archetypal waveforms representing characteristics of each class are presented and described in the following sections. Archetypal waveforms from prominent subgroupings within the classes are also presented.

For clarity, a shorthand notation for the material test and cycle being discussed was developed. The first letter in the notation gives the material being tested - d for dolostone and g for granite. The second letter, C, stands for cycle. This is immediately followed by the number of the cycle (a total of three cycles for dolostone and four for granite testing). After the cycle number is given, the letter M is given which stands for Mode. This is followed by 1 for Mode I and 2 for Mode II. If an individual waveform is being identified, a number will follow which will give the relative position of that waveform in relation to all the signals analyzed for that loading cycle. This counter is reset for each loading cycle. For the dolostone test, there were two Mode I and one Mode II loading cycles. The granite test was comprised of one Mode I and three Mode II loading cycles. This nomenclature system is summarized by: iCjMk:m, where i = {d,g} dolostone or gran-

ite, $j = (1,2,3)$ loading cycle, $k = \{1,2\}$ loading Mode, $m =$ the m -th event in the loading cycle. As an example, the 143rd event of the second dolostone loading cycle, which was loaded in Mode I geometry would be labeled dC2M1:143. This system will be used to refer to loading cycles as well as to label waveforms in figures to provide an indication of where in the test the event occurred.

3.2 Class A Signals

The Class A event is the most common waveform shape. This class was by far the most prevalent type in the Mode I tests as well as appearing frequently in the Mode II tests. The dolostone Class A archetype is shown in Fig. 1, and is characterized by a sharp initial displacement rise on the order of 2 to 8 μs , followed by a fairly constant displacement in the same direction as the initial motion. This type of event can be characterized as approaching a "boxcar wave" for the initial P-wave displacement. The S-wave energy arrives very suddenly in a sense of motion opposite to that of the initial displacement. There often is an increase in displacement, of varying relative amplitude, several μs before the actual displacement reversal caused by arrival of the shear component.

Figure 2 shows a waveform that results from breaking a glass capillary tube at the central area of the dolostone failure surface. Since the location of this source event was known, the time of arrival of the first reflection (side), refraction (SP-wave), and S-wave can be calculated. These arrivals are labeled in Fig. 2 as SIDE, SP, and S respectively. It is interesting to note the close similarity between the Class A event and the signal shown in Fig. 2. This similarity in signal shape leads to the conclusion that the Class A waveforms are caused by a step-force kinematic.

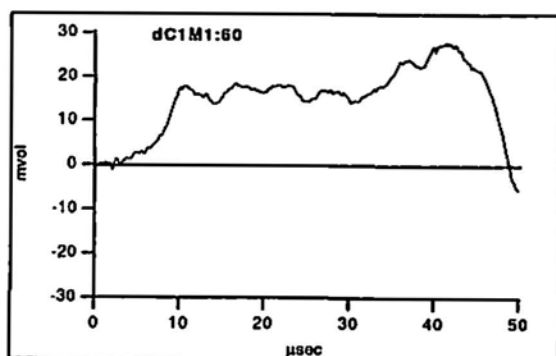


Fig. 1 The dolostone Class A archetype.

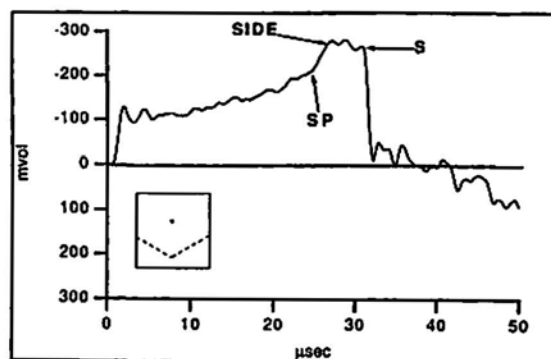


Fig. 2 Typical waveform resulting from step force input on failure plane.

An exemplary granite Class A signal is shown in Fig. 3. Many of the granite Class A events, which often had a low signal amplitude, exhibited a large oscillatory displacement after the initial rise. These superimposed oscillations have a "typical" frequency of about 330 kHz (ranging from 220 to 480 kHz). Such higher frequency information "riding" on the constant table-like displacement was also noticed for the dolostone. However, for the granite, the amplitude of this oscillation can be on the scale of the P-wave displacement. Therefore, the heuristic technique developed for pattern recognition of dolostone signals was slightly extended to sort the granite waveforms.

Given the lithology of the granite, the modulation present among all classes of signals from the granite test is not surprising. The initial portions (0 to 20 μs) of most of the granite signals have a maximum amplitude of less than 5 mV, compared to more than 10 mV for the dolostone signals. Because of the low signal amplitude, the influence of background noise on the granite waveforms is more significant. In addition, the individual crack growth increments for the granite are very small and on the order of grain size (0.1 to 2.5 mm), so that the displacements are much smaller temporally and spatially than for the dolostone. This leads to a less "drawn out," more oscillatory waveform. Another contribution to the modulation comes

from crack surface damage which developed in the granite. The granite crack surface was covered with small loose "flakes" which can serve as small vibrators superimposing the higher frequency oscillation on the general archetypal macro-shape.

The increments of macrocrack growth did not occur as single, isolated, and large discrete events in the granite. Neighboring grains could fracture *almost* simultaneously, the signals of the many small micro-events interacting both constructively and destructively, leading to an apparently oscillatory waveform. Signals from multiple crack growth increments, with a second distinct waveform arriving microseconds after the arrival of the trigger event, were represented among the granite waveforms but were absent from the dolostone signal ensemble.

Among the dolostone Class A waveforms, there is also variability in the relative amplitude of the short displacement rise, or "precursor", before the sudden arrival of the S-wave. This "precursor" was also present in the waveforms generated by capillary breaks, and is in some part due to the arrival of the critically refracted S-wave, or SP-wave. The "precursor" was not very apparent in the granite Class A signals. The relative importance of this "precursor" for the dolostone and the granite events can be seen in Fig. 1 and Fig. 3.

Class A waveforms with a strong "precursor" are placed in a subgroup of Class A, Subclass A1. The dolostone archetype for Subclass A1 is illustrated in Fig. 4. This subclass is virtually the same as Class A, except the precursor before the S-wave arrival is so dominating as to be an obvious sorting criterion.

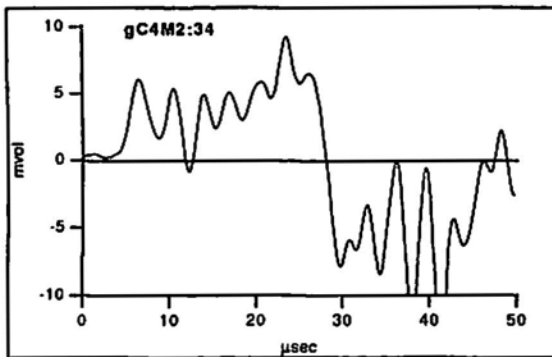


Fig. 3 The granite Class A archetype.

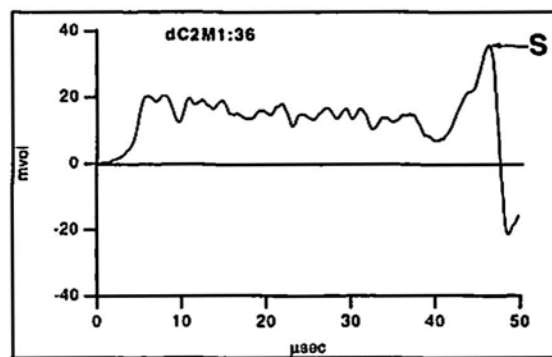


Fig. 4 The dolostone Subclass A1 archetype.

3.3 Class B Signals

The dolostone Class B archetype is shown in Fig. 5, and is characterized by a gradual ramp-like initial arrival of P-wave energy followed by a sudden arrival of S-wave. In this class, too, there may be higher frequency oscillation riding on the main displacement, and a varying amplitude "precursor" displacement jump shortly before the S-wave arrival. It has been shown experimentally (Glaser, 1990; Nelson and Glaser, 1992) and implied theoretically (Ohtsu and Ono, 1986; Hayashi and Nishimura, 1986) that the ramp-like Class B event is caused by the same step-like source mechanism as the Class A waveform. For the Class B signal, this center of motion is oriented so that some component of the step force is directed away from the surface being monitored by the transducer.

An exemplary granite Class B waveform is shown in Fig. 6. Class B events were fairly common among the granite signals, although at a much smaller occurrence rate than for the dolostone. For both the granite and the dolostone, the Class B signals were associated with Mode II propagation for which the failure surface was more uneven than for Mode I crack growth. The granite fracture surface was certainly smooth compared to the numerous large and inclined fracture planes on the dolostone failure surface. The inclined fracture increment surfaces occurred much less frequently for the granite than for the dolostone, so the far fewer number of Class B signals is not unexpected. Among the Class B events there is a group of signals which shows a small initial displacement dip for 5 to 10 μ s preceding the main positive displace

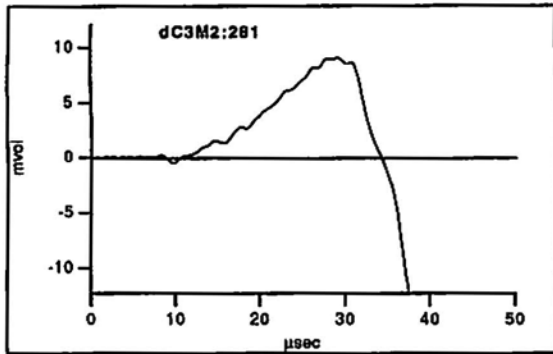


Fig. 5 The dolostone Class B archetype.

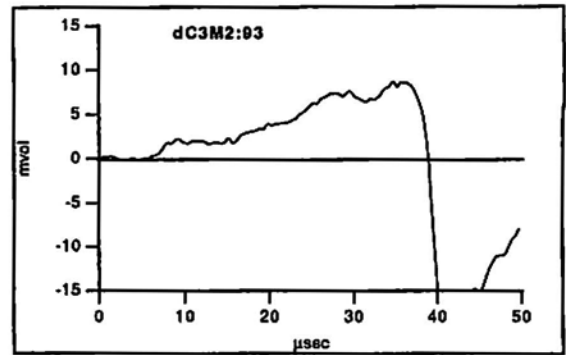


Fig. 8 A dolostone Class B waveform transitional to Class A.

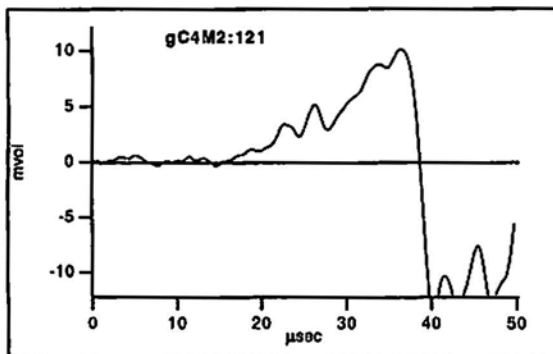


Fig. 6 The granite Class B archetype.

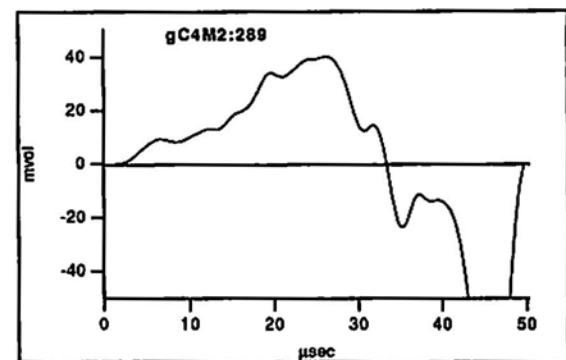


Fig. 9 The granite Subclass B1 archetype.

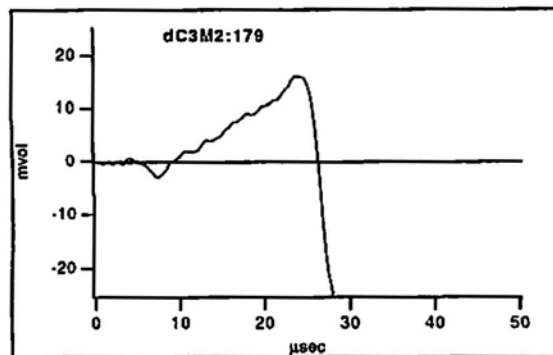


Fig. 7 Example of dolostone Class B subclass signal variety.

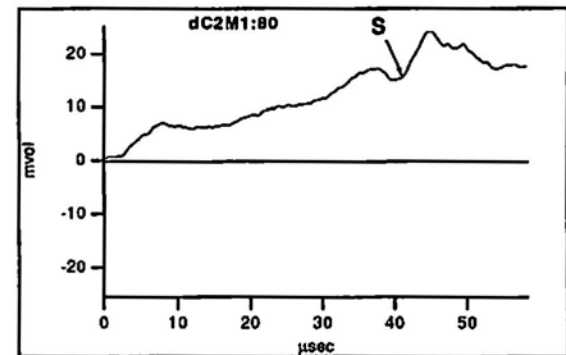


Fig. 10 The dolostone Class C archetype.

ment ramp. An example of this group is shown in Fig. 7. The cause of this substantial sharp displacement couple is not known at this time. An example of the organic nature of the actual waveform shapes is given in Fig. 8, where the wave shown has a sharp initial small-displacement rise. This type of event is classified as Class B since the step, which is the Class A criteria, is of small magnitude in comparison to the subsequent ramp increase in displacement.

A distinct subclass of the Class B is the granite Subclass B1 archetype shown in Fig. 9. A typical Subclass B1 waveform can be characterized as a Class B except there is no discernible distinct arrival point of S-wave, SP-wave, or reflected wave energy. The Subclass B1 events occur almost exclusively among the later Mode II events for both rock types, and occur quite rarely in the Mode I loadings.

3.4 Class C Signals

The dolostone Class C archetype is given in Fig. 10. This waveform is characterized by a sudden sharp arrival of P-wave energy followed by a relatively constant displacement reminiscent of a square wave pulse or the Class A archetype. The arrival of the shear energy is sudden and sharply defined as for the Class A signal, but the S-wave displacement appears to be in the same direction as the P-wave energy arrival. The downwards motion of the Class C waveform arrives long after the expected S-wave arrival. For the period corresponding exclusively to the P-wave displacement, there is no difference between the Class C signal and the Class A archetype.

The difference between the shape of the Class C and Subclass A1 signals is that the "precursor" of the Subclass A1 event blends into, and actually contains, the S-wave arrival. If the signals were truncated at the time of first reflection, about 12 to 15 μs after the initial arrival, the Class A, A1, and C signals would be indistinguishable.

Like the Class B signal, the Class C signal is thought to be caused by the same step-like source kinematic as the Class A signal. For the Class C signal, the step-like source motion occurs at an orientation such that some major portion of the energy is directed towards the surface being monitored by the transducer. While the experimental connection is not as solid as for the Class B signal, the Pekeris solution (Pekeris and Lifson, 1957) leads to this conclusion. Extending this logic, because the granite failure surface was much smoother than the dolostone failure plane, there were few Class C events among the granite signals compared to the dolostone ensemble.

Among the dolostone signals a Subclass C1 archetype shown in Fig. 11 was identified. Subclass C1 starts with a smooth ramp or slight steep rise, gradually reaching a maximum before the shear energy arrival, which is not as distinct and sharp as for the Class C events. Our understanding of the C1 signal source is limited. There is an interesting and possibly important group within Subclass C1, in which there is a large change in the direction of the surface displacement (Fig. 12). This group of subclass C1 events occurs predominantly quite late in the Mode II loading of both rocks, and the shapes of these events are remarkably constant. This group could possibly be related to the Class B signal, with a large initial displacement.

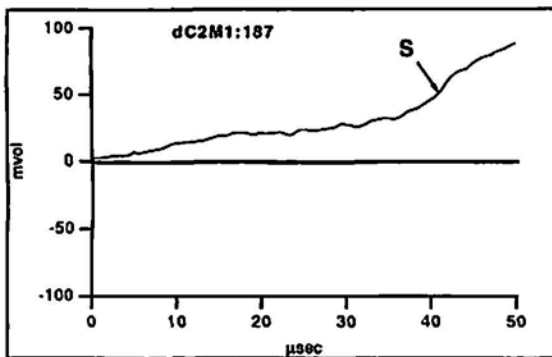


Fig. 11 The dolostone Subclass C1 archetype.

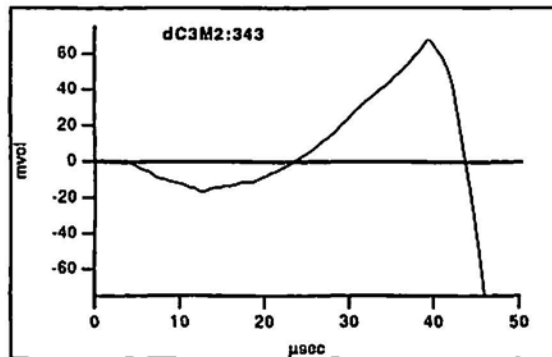


Fig. 12 Example of dolostone Subclass C1 group common towards the end of the test.

3.5 Class D Signals

The Class D archetype is shown in Fig. 13. This may be characterized as a boxcar that is initially displaced. The initial negative displacement is followed by positive displacement recovery and a subsequent nearly constant displacement. This shape is somewhat reminiscent of the waveforms reported for

the pencil lead break calibration at different radial distances from the transducer (Michaels et al., 1981). The Class D archetype often shows a sudden, sharp, positive displacement immediately before the S-wave arrival and always exhibits a sudden shear energy arrival in a direction opposite to the main P-wave energy. The Class

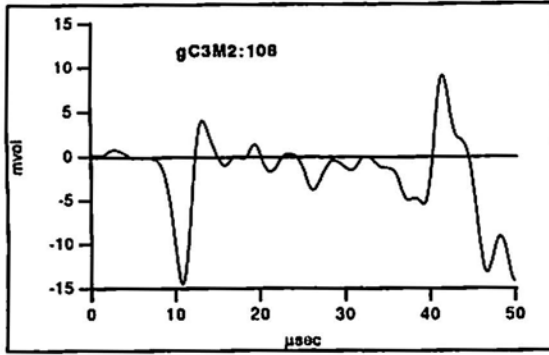


Fig. 13 The granite Class D archetype.

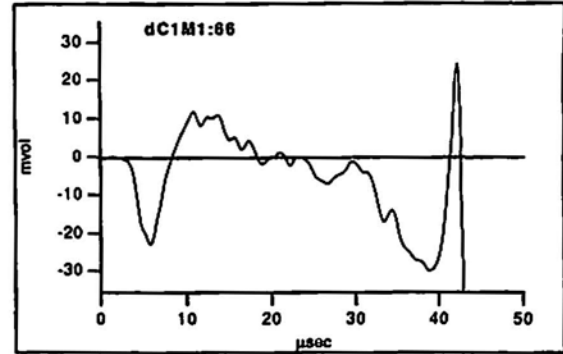


Fig. 14 The dolostone Class D archetype.

D dolostone archetype is shown in Fig. 14. Class D events contain complex displacement patterns indicating a much more complicated source kinematic than is adequate for other events. The dolostone and granite Class D events generally have a relatively low amplitude, averaging 10 mV. For the dolostone, considering the initial 25 μ s of the signal (before S-wave arrival), only 30 % of the Mode II Class D waveforms had an amplitude above 10 mV.

3.6 Class E Signals

A characteristic dolostone and granite Class E waveforms are shown in Fig. 15a and 15b. However, a clear representative archetype was unavailable for the Class E events. These events are with rounded initial arrival and no discernible shear energy arrival within the usual first 50 μ s. Discernible wave mode arrival is absent in this class. In fact, most of the Class E events, especially for the granite, were later discarded when their source was shown to have been located outside of the possible fracture zone. However, with only two transducers, not all Class E events could be so discarded. The fact that the difference in initial arrival times for the two transducer channels is within the allowable location window for a sizable percentage of the Class E events might mean that some of these signals are real AE events which should be understood in the context of the applicable loading. Another possibility is that the "valid" Class E signals might be caused by some form of crack face interaction.

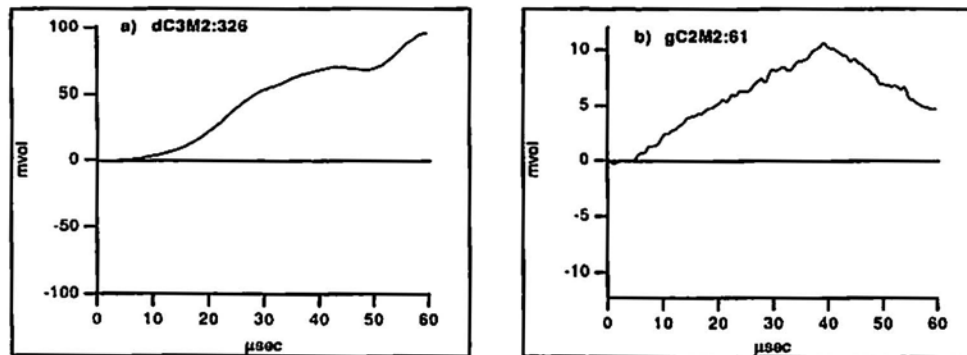


Fig. 15 The dolostone (a), and granite (b) Class E archetypes.

3.7 Waveforms with "Pre-arrival" Energy

For all but a handful of events, the P-wave arrival rose directly out of the background noise. A troublesome ambiguity concerning wave arrival arose. This problem is identified in reference to Fig. 16, with the perceived arrival of the P-wave is labeled 'P'. For a few events, there is a long, gradual precursor to the commonly seen P-wave arrival. This precursor occurs over the order of 10 to 20 μ s and, given the arrival time for the shear wave and other reflections, this precursor cannot be part of the conventional P-wave

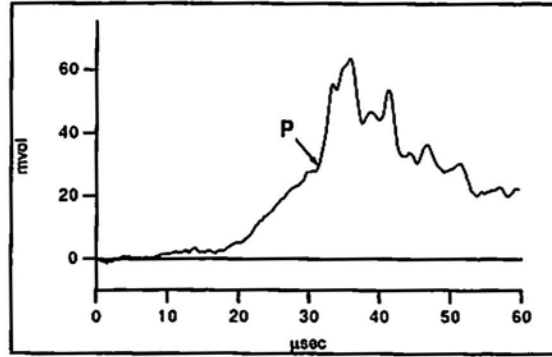


Fig. 16 A signal showing a long, gradual pre-arrival to the actual wave arrival.

arrival. The near-field energy can never arrive before the P-wave (Aki and Richards, 1980, p. 45) and therefore cannot be the cause of this precursor. A possible explanation is that the actual causal event is not a single, sharp, step function but might be characterized by some crack surface rubbing or localized displacement before a sudden release of energy due to crack growth.

3.8 Summary

This research indicates that there are five characteristic signal shapes (and three subclass shapes) that are present in the data. To clarify the important differences among the five classes, Table 1 highlights the major features of each class. These group selections are not necessarily a unique classification, but extreme attention was given to avoid bias and introduction of preconceived notions. The fact that the same archetypical classes are applicable for such different rocks as granite and dolostone reinforces the conclusion that these groupings reflect a commonality in causal mechanisms. The existence of the same classes of waveforms from both tensile and shear loadings of the specimen indicates that the same mechanisms are at work in both materials during both Mode I and Mode II loadings.

Table 1 The major classification features associated with the arrival of the P- and S-wave.

Class	P-Wave		S-Wave Direction with respect to the P-wave
	Direction	Abruptness	
A	up	jump	opposite
B	up	jump	opposite
C	up	jump	same
D	down	jump	opposite
E	up	rolling	same

4. Waveform Shapes Unique to the Granite Test

4.1 Oscillatory Granite Signals

The granite AE events show a great deal of oscillatory behavior. In fact, a group of events from the Mode II loadings can be seen as undifferentiated oscillating waveforms, comprising about 10 % of all Mode II events. Two such events are shown in Fig. 17. Comparison with other events, and experimental work using sources on a variety of facet orientations (Glaser, 1990; Nelson and Glaser, 1992; Glaser and Nelson, 1990), lead to the conclusion that these waveforms could not be caused by a step-like displacement. In the tensile Mode I load cycle of the granite test, only five events (1.7 %) were oscillatory. In this loading geometry, the two crack faces are being pulled apart, causing a direct cleavage of the rock with few if any chances for bifurcation or surface damage creating flakes. Thus, few flakes can serve as resonators and the sense of movement makes it hard to excite the loose grains and flakes that might exist.

The oscillation cannot be caused by the detection system since this behavior was not present during any of the dolostone test runs using the same equipment. Neither are these oscillations universally present in all the granite events. What is more likely is that these oscillations are caused by either discrete mineral grains or the fractured "flakes" which could act as small oscillators. In an attempt to isolate the source of the oscillations, capillary breaks were made at several locations on a saw-cut vertical surface of a granite specimen. If the oscillations are due to crystal vibration or wave scattering, then this behavior should manifest itself when capillaries are broken on the saw-cut face. No oscillatory behavior manifested. This indicates that discrete mineral grain vibrations or grain-induced wave scattering are not the cause of this behavior.

In the Mode II geometry, the two crack faces are displaced past each other. This sliding action can easily excite loose particles. The heterogeneous formation of localized fracture throughout the process zone, as evidenced by the numerous bifurcations and multi-sized detritus, creates many good oscillators of appropriate size (length = $n/2 * \text{wavelength}$, where $n = \text{integer}$; Bueche, 1980).

In an attempt to isolate the flake resonating mechanism, the actual failure surface of the granite specimen was used. Both capillary breaks and loose material crushing were used as sources. This source model is appropriate because, immediately behind the AE event/crack tip, the crack surfaces are disengaged, acting like free surfaces. Figure 18a shows a typical waveform resulting from breaking a capillary on the saw-cut surface. In comparison, Fig. 18b shows an example waveform from the breaking of a capillary at a loose, shattered area on the actual failure surface. Rather than the typical sharp rise and following steady table-like displacement that was obtained from the saw-cut surface, the wave in Fig. 18b strongly resembles the oscillatory waveforms under discussion. Very similar waveforms were produced when loose grains which make up part of the process zone on the failure surface are crushed or "popped" off the surface. Clearly, the oscillations are associated with the fracture surface and process zone "flakes" that were so prevalent on the granite failure surface.

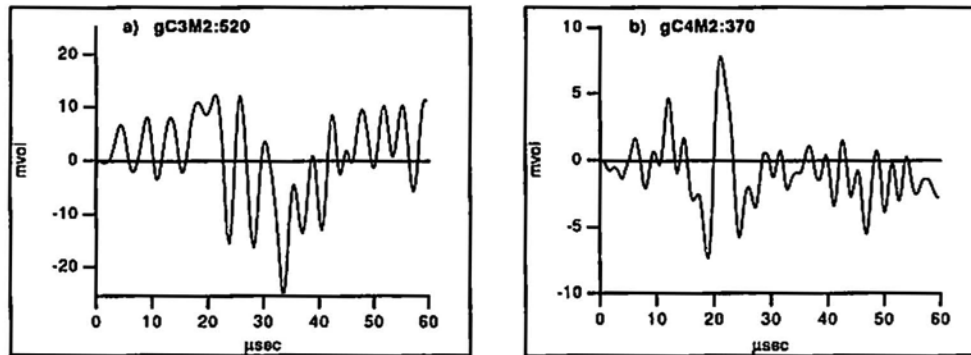


Fig. 17 Examples of undifferentiated oscillatory granite signals.

4.2 Very Low Amplitude Granite Signals

A total of 8 % of the granite signals were of very low amplitude and could not be classified. Figure 19 shows such a Mode II signal, with defined characteristic features that could be due to either the P-wave or S-wave arrival or specimen resonances. In all cases, the pretrigger length used by the digitizer insured that the P-wave arrival would be digitized if the digitizer was triggered by the S-wave arrival, ruling out the possibility that the start of the signal was missed. It should be noted that Mode II granite signals had a relatively low amplitude and often had a P-wave arrival amplitude larger than the early S-wave displacements. This is most likely due to an orientation effect, where the amplitude of the S-wave propagation pattern is approaching zero, while the P-wave amplitude never disappears. Another possibility is subtractive interference from a "doppleganger" or multiple event "cascades".

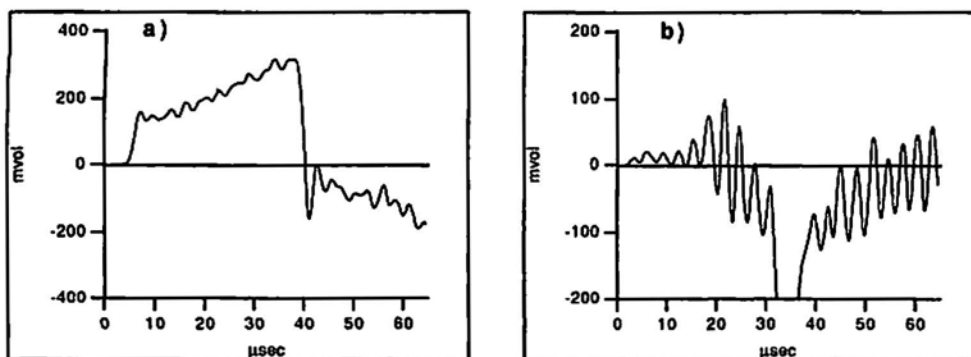


Fig. 18 Example of the results of breaking a capillary on a saw-cut surface (a) and on a loose flake of granite on the failed surface (b).

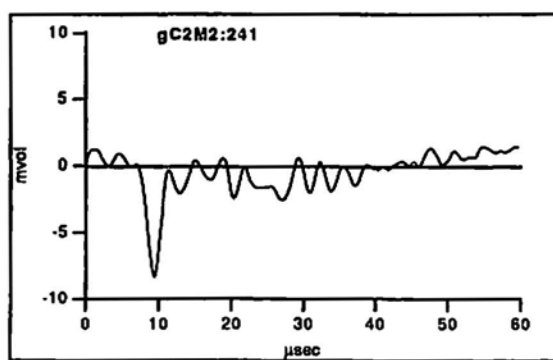


Fig. 19 An exemplary granite very low amplitude signal.

We attempted to develop a heuristic approach for classifying these very low amplitude events by examining the immediately preceding and subsequent events. This yielded results as ambiguous as the direct classification attempt. The amplitudes are so low that there is not enough information present to make an informed decision. This "class" is repeated but is only a significant portion (18 %) of the first granite Mode II cycle and is rare in the rest of the test (0 to 4 %). We suggest that these Very Low Amplitude events are otherwise classifiable signals lost in noise rather than distinct enough to warrant a new classification. Any remaining questions can be answered by newer, more expensive, instrumentation that would facilitate lowering the system background noise level. Simply boosting gain will just make the ambiguous signal, and the noise, proportionally larger.

5. Conclusions

In summary, the same classes of AE waveforms were recorded for the granite test as were for the dolostone test. The same events were present in Mode I and Mode II loadings, implying that the same mechanisms are at work. The waveforms recorded during the granite test were generally low amplitude signals compared to the events from the dolostone test. This is associated with the granite fracture growth increments being on the scale of the small individual grains rather than the fingernail-sized facets of the dolostone. The granite signals also displayed some high frequency oscillation believed to be caused by resonance of loose rock flakes and grains in the fracture zone.

While the analysis of data from this experimental program allowed many interesting and important conclusions to be reached, the experiment seemed to raise as many questions as it answered. Many of the ambiguities about event validity and shape could be answered in tests using a three dimensional array of

least six transducers. This would allow the accurate location of where the event took place, and the calculation of the event Green's function, of particular interest for Class D events so that the relevant source kinematic could be determined. Since this was the only class of signal from fracture that is not believed caused by a step-like source related to tensile crack growth, the Class D signal is believed to hold the answer about what processes besides tensile cracking exist in the process zone. Accurate source location would also answer questions concerning the validity of Class E events, and would increase the understanding of how the spatially-distributed crack tip process zone develops in the Mode II geometry. This experimental program is seen as productive and rewarding, but is also seen as the starting point for many more studies and discoveries. It is hoped that enough researchers take this as a signpost on the road to decoding the natural information given us by nature.

Acknowledgement

This project is currently being funded by the State of Texas Advanced Research Program, FICE code 003658-512. Previous support was also provided by the National Science Foundation, Contract MSM-8600567. This support is greatly appreciated.

References

- K. Aki and P.G. Richards (1980), *Quantitative Seismology*, W.H. Freeman, San Francisco, p. 45.
- F.J. Bueche (1980), *Introduction to Physics for Scientists and Engineers*, McGraw-Hill, New York, pp. 712.
- S.D. Glaser (1990), "Acoustic Emission Waveforms Produced by Discrete Crack Propagation in Rock," Doctoral Dissertation, The University of Texas at Austin, Austin, Texas, p. 368.
- S.D. Glaser and P.P. Nelson (1992a), "Acoustic Emissions Produced by Discrete Fracture in Rock: Part 2: Kinematics of crack growth during controlled Mode I and Mode II loading of rock," *International Journal of Rock Mechanics*, in press.
- S.D. Glaser and P.P. Nelson (1992b), "High-Fidelity Waveform Detection for Acoustic Emissions From Rock," *Materials Evaluation*, 50(3), 354-366.
- S.D. Glaser and P.P. Nelson (1990), "Correlation of Quantitative AE Waveforms with Discrete Fracture Mechanisms in Rock", *Progress in Acoustic Emission V*, JSNDI, Tokyo, pp. 414-421.
- S.D. Glaser and P.P. Nelson (1989), "Quantitative Characterization of Acoustic Emission Waveforms Produced by Discrete Mode I Crack Propagation", *Proc. International Conference on Recent Developments in the Fracture of Concrete and Rock*, Wales, Great Britain. Elsevier, London, pp. 111-120.
- K. Hayashi and H. Nishimura (1986), "Considerations on Field AE Data Based on Theoretical Studies of Elastic Waves Due to Sudden Movement of a Subsurface Reservoir Crack," *Progress in Acoustic Emission III*, JSNDI, Tokyo, pp. 742-749.
- Y.S. Jenq and S.P. Shah (1989), "Trajectory and Stability of Cracks in Concrete Subjected to Mixed Mode Loading," *Proceedings of the 1989 SEM Spring Conference on Experimental Mechanics*, Society for Experimental Mechanics, Bethel, CT, pp. 43.

T. Kishi (1985), "Acoustic Emission Source Characterization and Its Application to Micro-Cracking," *Zeitschrift Fur Metallkunde*, 76(7), 512-51.

A.R. Ingraffea (1981), "Mixed-Mode Fracture Initiation in Indiana Limestone and Westerly Granite," *Proceedings, 22nd U.S. Symposium on Rock Mechanics*, pp. 186-191.

J.E. Michaels, T.E. Michaels, and W. Sachse (1981), "Applications of Deconvolution to Acoustic Emission Signal Analysis," *Materials Evaluation*, 39(10), 1032-1036.

P.P. Nelson and S.D. Glaser (1992), "Acoustic Emissions Produced by Discrete Fracture in Rock: Part 1: Effects of system: source location and orientation effects," *International Journal of Rock Mechanics*, in press.

M. Ohtsu and K. Ono (1986), "The Generalized theory and Source Representations of Acoustic Emission," *Journal of Acoustic Emission*, 5(4), 124-133.

C.L. Pekeris and H. Lifson (1957), "Motion of the Surface of a Uniform Elastic Half-Space Produced by a Buried Pulse," *Journal of the Acoustic Society of America*, 29, 1233-1238.

M. Shibata (1984), "A Theoretical Evaluation of Acoustic Emission Signals, the Rise Time Effect of Dynamic Forces," *Materials Evaluation*, 42(1), 107-120.

Estimation of Maximum Stress in Old Railway Riveted I-Girder Bridges using Acoustic Emission Signals

Hisanori Otsuka, Hiroshi Hikosaka, Hiroyuki Miyatake
and Syouzou Nakamura

Hisanori Otsuka is affiliated with Public Works Research Institute, Ministry of Construction, Takehara, Tsukuba 305, Japan, Hiroshi Hikosaka is with Kyushu University, Hiroyuki Miyatake is with JR Kyushu Corp. and Syouzou Nakamura is with Kawasaki Steel Company.

Abstract

The applicability of acoustic emission tests for the estimation of the maximum stresses in old riveted girder bridges was investigated. A good agreement between experimental and theoretical values was found.

1. Introduction

Acoustic emission is a type of nondestructive testing methods which could monitor the stress variation, the yielding of materials and initiation and propagation of cracks. An early application to steel structures was reported by Pollock (1972) on the performance of a portable military bridge. In the test, AE sources were attributed to locations where plastic deformation had occurred. In the United States, successive research programs have been conducted to develop AE monitoring systems for bridges (ASNT, 1987).

It is well known that AE signals are seldom detected at stress levels less than the maximum stress previously experienced in the materials (Kaiser, 1953). Significant AE signals can be observed once stress exceeds the previous maximum level. The phenomenon is called Kaiser effect.

The maximum stress is needed for predicting the residual fatigue life of structures, because fatigue damage may be evaluated from this information. From this viewpoint, we investigated the possibility of the application of AE to the maximum stress estimation in old riveted girder bridges. In addition, we studied AE signals during tensile tests in specimens of various ages.

2. Experimental

The measurement of AE signals in our experiment was conducted using the 9502U-PLOT (NF Circuit Design Block Co.) The equipment consists of two transducers, two pre-amplifiers, a main analyzer, an X-Y plotter and an oscilloscope. Using the analyzer, hit time, source location, maximum amplitude of AE signals, and external data (strain and load, etc.) can be recorded in real time, and then analyzed results are obtained by an X-Y plotter.

Old railway girder bridges used for this experiment are a 95-year-old bridge with a 6.7 m span length (in service for 92 years) and a 60-year-old bridge with 5.99 m span length (in service for 54 years). The bridges consist of single-span-deck girders. The 95-year-old girders were separated into a single plate girder at the site. Rust and paint on these girders were removed by shot-blasting.

Both girders have doubly symmetric cross sections. Flanges of the girder consist of two angles and one cover plate. Figure 1(a) shows the cross section of the 95-year-old girder. The 60-year-old girders have the same cross sectional configuration except for the dimension of 747 mm height and 223 mm width. Figure 1(b) shows the cross section of the girder tested under fatigue loading. These girders (named as test girders) were prepared for testing by cutting off from the original girder and welding a compression flange to the web. AE tests were conducted for the original girder and the test girder for the 95-year-old girders and the

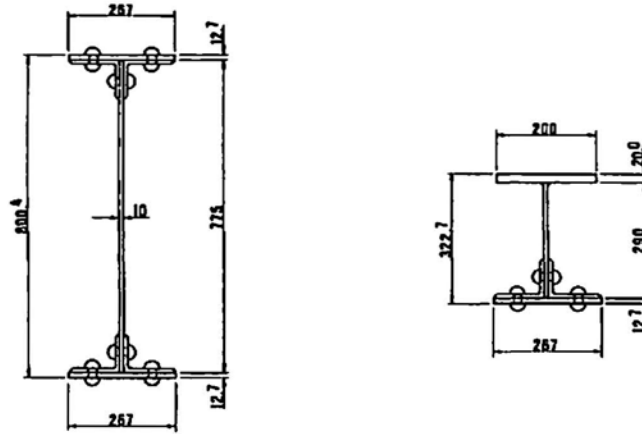


Fig. 1 Cross section of a 95-year-old girder. (a: left) Original shape. (b: right) Shape for fatigue test.

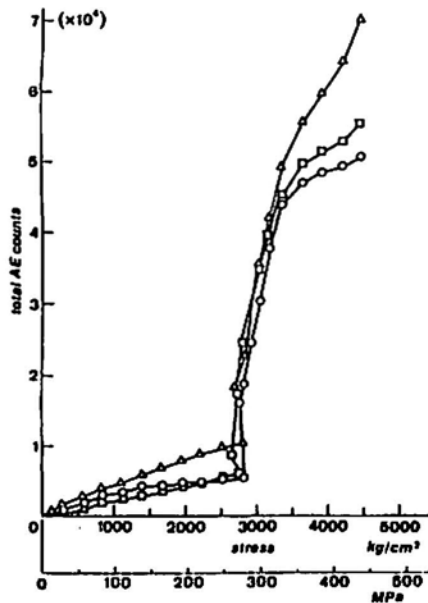


Fig. 2 Total AE counts vs. stress (new material, SS400).

SS400, 60- and 95-year-old steels. A threshold level was set at 60 dB in these experiments. It is found that the occurrence of AE signals are different before and after yielding. The number of AE events is clearly discriminated into two stages of pre- and post-yielding. Prior to yielding, AE event rate is smaller than that of post-yielding. After yielding, curves of cumulative AE counts are varied, depending upon material. In the case of new SS400 steel, the occurrence of AE signals decreases as stresses approach the ultimate strength. In contrast, AE generation of the 95-year-old steel increases close to the ultimate strength. The 60-year-old steel exhibits an intermediate trend.

Figure 5 shows an example of Kaiser effect, conducted using the 60-year-old steel specimen. The specimens were machined from the neutral axis of the girder. Thus, the specimens were not significantly stressed during service. It is clearly observed that AE signals at the cycle 2 begin to occur from about 70 % level of the maximum stress at the cycle 1, and the occurrence of AE signals is less active than those of cycle 1. The slope of the curve at the beginning stage in cycle 2 is approximately equal to the slope near the maximum stress of cycle 1. Considering the results of all specimen, AE signals in cycle 2 begin to

two test girders for the 60-year-old girders. AE signals were measured at lower flanges, because these flanges were in service mainly as tension members until the girders were removed. Sample specimens for tensile tests were cut off from web steel near the neutral axis.

Table 1 shows the chemical composition of the 95- and 60-year-old steels. Values of phosphorus and sulfur in both steels are slightly higher than those values of an ordinary mild steel, JIS-SS400. However, both steels could be comparable to SS400. The mechanical properties of both materials are also shown in Table 1. The yield and the ultimate strength of the 60-year-old steels are lower than those of comparable steels and the elongation of the 95-year-old steel is the lowest of all steels.

3. AE Signals During Tensile Tests

Figures 2, 3 and 4 show the relationship between total AE counts and nominal stress for

Table 1 The chemical composition and mechanical properties of the 95- and 60-year-old steels.

Test girder	Location	C	Si	Mn	P	S	Al
95 year old	web	0.14	0.017	0.57	0.057	0.066	0.001
	stiffener	0.12	0.018	0.61	0.055	0.043	0.005
60 year old	web	0.204	0.01	0.50	0.015	0.037	0.001

Test girder	Yield stress (MPa)	Ultimate strength (MPa)	Young's modulus (MPa)	Elongation (%)
95 year old	289	433	20.6×10^4	24.1
60 year old	265	403	20.7×10^4	29.7
new	284	444	20.6×10^4	29.3

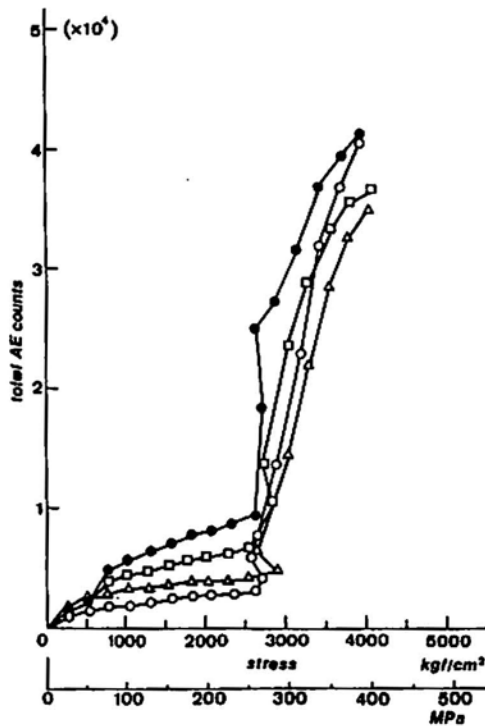


Fig. 3 Total AE counts vs. stress (a 60-year-old girder).

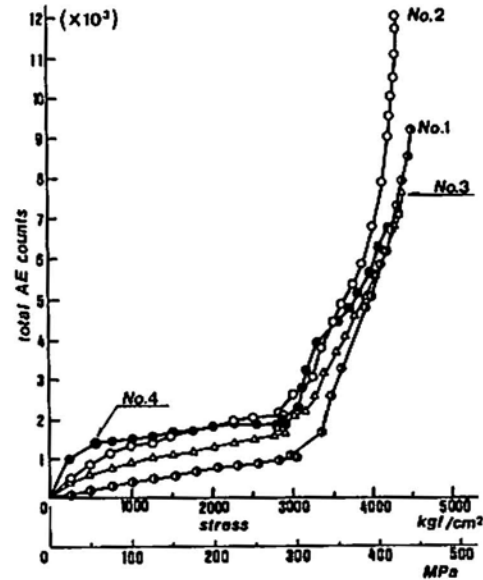


Fig. 4 Total AE counts vs. stress (a 95-year-old girder).

actively occur at about 70% of the maximum stress in cycle 1. Eventually, the rapid increase on the slope of the cumulative curves is observed above the previous maximum stress. It is noted that AE activity during the unloading is almost zero.

4. Estimation of Maximum Stress from AE Signals in Old Girders

AE signals were measured for the 95- and 60-year-old girders during two loading-unloading cycles. Two AE sensors were installed on the top surface of the tension-side flange near midspan for the 95-year-old girder and on the bottom surface for the 60-year-old girder. Two sensors face each other across the rivet. Strain gauges are attached on the flange outside of the rivet. Therefore, strains over the so-called net area cross section were measured. During the experiment, strains were also recorded onto the AE analyzer.

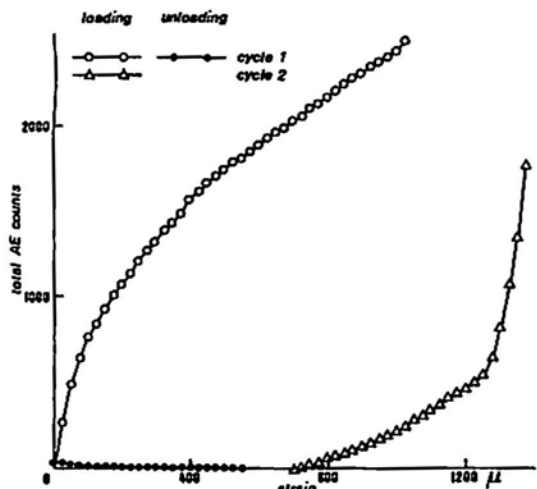


Fig. 5 The confirmation of Kaiser effect.

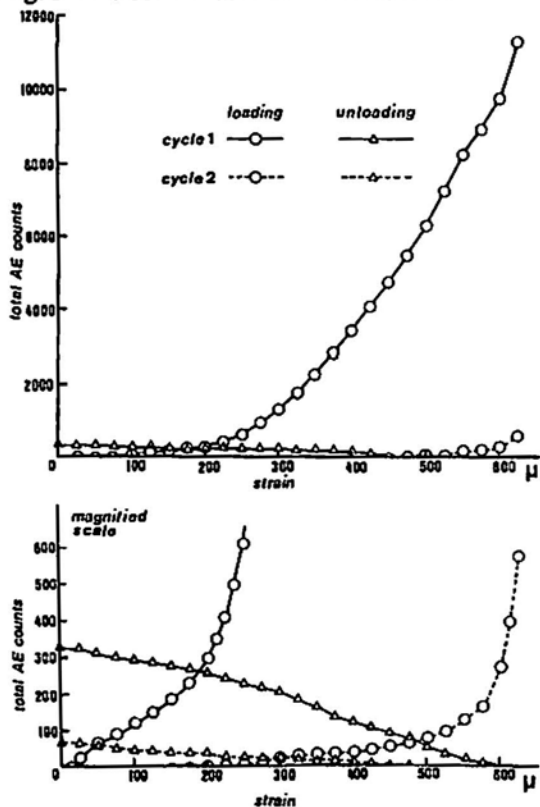


Fig. 6 Total AE counts during cyclic loads.

definite and the maximum stress was calculated for both directions. The section moduli of the girders were calculated from the initial cross section because the degree of the corrosion was not known. Impact coefficients were calculated from the formula in the specifications, assuming that the maximum speed of the locomotive is 60 km/h. Based on these assumptions, the theoretical maximum stresses were computed as shown in Table 2. These values are considered to be a little higher than actual values, because the continuity and the stiffness of the rail are not taken into calculation.

When comparing these values with the estimated values from the AE tests, a clear agreement is observed. Therefore, it is concluded that by using the AE tests, the estimation of the maximum stress of old girders is possible with the sufficient accuracy.

Figure 6 shows the relationship between the cumulative AE counts and strains of the 95-year-old girder. AE signals increase beyond the strain of 200×10^{-6} of the first cycle. This may be associated with Kaiser effect. A cause of AE signals during the unloading could be due to the noise of friction between the components of flange.

To estimate the maximum stress for both girders, Figs. 7 and 8 are drawn in the magnified scale for cumulative AE counts. It is rather difficult to identify the point of changing slope, because the slopes change gradually in the graphs. Consequently, the transition points were determined as the intersection of two extrapolated lines. The strain of this intersection is considered to correspond to the maximum strain. Multiplying Young's modulus to the maximum strain, the maximum stress based on Kaiser effect was determined. The maximum stresses for the 95- and 60-year-old girders were estimated to be 43.2 and 32.4 MPa, respectively.

In estimating the maximum strain of the first loading from the second loading curves, only 6.5% and 3.3% errors were encountered for 95- and 60-years-old girders, respectively. This means that when time elapsed is short, the accuracy of the maximum stress estimation from the AE cumulative curve is fairly good because of the existence of clear slope change.

5. Estimation of Maximum Stress Caused by Locomotive Loading

According to the traffic records on the maximum loading applied to the girders, D51-locomotive (KS equivalent value = 142 kN) and C11-locomotive (KS = 105 kN) were the heaviest locomotives for the 95- and 60-years-old girders, respectively. The maximum stresses were calculated from the design information on the wheel arrangements. Loading direction on the test girders was not

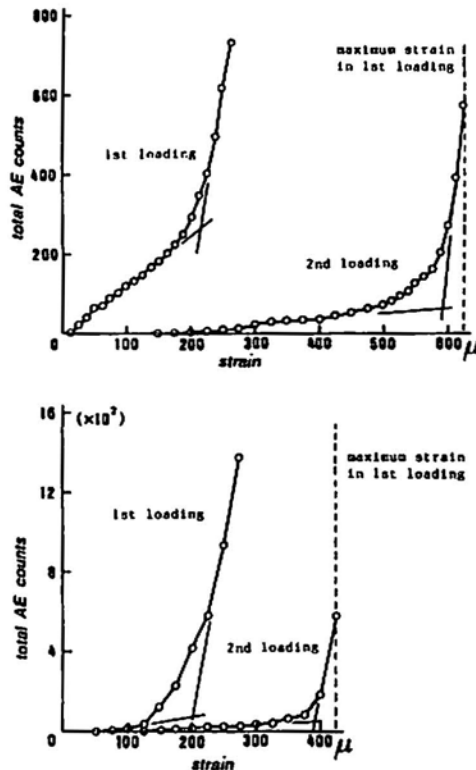


Fig. 7 Estimation of maximum stress (95-year-old girder).

6. Conclusion

Since the maximum stress is one of the most important information to predict the residual fatigue life of structures, the applicability of AE tests for the estimation of the maximum stresses in old riveted girder bridges was investigated. A good agreement between experimental and theoretical values was found. Thus, it may be concluded that AE tests are successfully applied to the estimation of the maximum stress of steel girders.

References

ASNT (1987), *Nondestructive Testing Handbook*,

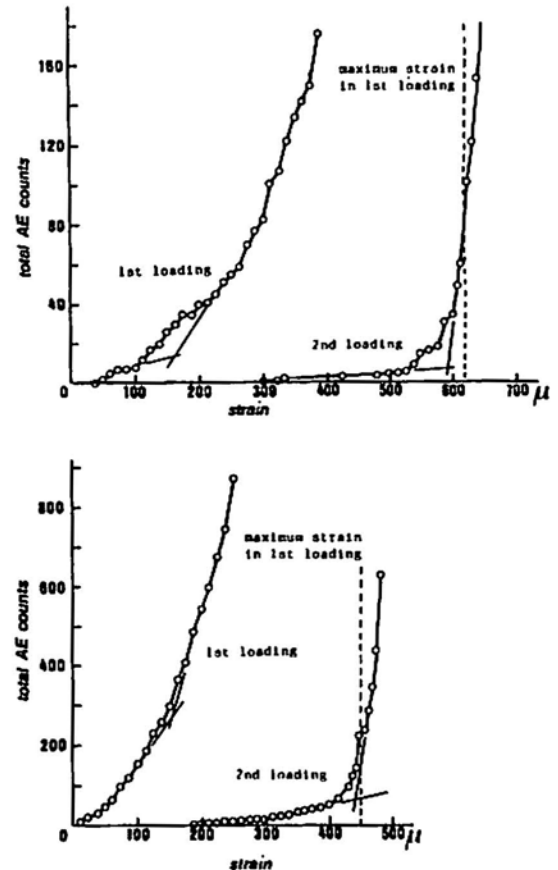


Fig. 8 Estimation of maximum stress (60-year-old girder).

Vol. 5, AE Testing, ASNT, Columbus, OH, pp. 333-339.

J. Kaiser (1953), "Erkenntnisse und Folgerungen aus der Messung von Gerauschen bei Zugbeanspruchung von Metallische Werkstoffen, Archiv fur das Eisenhütten Wesen, 24(1-2), 43-45.

A.A. Pollock and B. Smith (1972), "Stress-Wave Emission Monitoring of a Military Bridge", *Non-destructive Testing*, pp. 348-353.

Table 2 Maximum stresses.

Test girder	Absolute maximum mo. (kN)	Maximum mo. at measuring points (kN)	Section modulus (mm ³)	Impact coefficient	Calculated maxi. stress (MPa)	Maxi. stress by AE tests (MPa)
95 year old	270	239 or 247	6.74x10 ⁶	1.30	46.2 or 47.6	43.2
60 year old	158	153 or 156	5.45x10 ⁶	1.31	36.6 or 37.5	32.4

Another Look at Booming Sand

Marcel F. Leach and Gottfried A. Rubin

The authors are affiliated with Dept. of Physics & Astronomy, Laurentian University, Sudbury, Ontario P3E 2C6, Canada.

Abstract

This is a comparative study of a relatively rare phenomenon which occurs in some desert regions. Analysis of the acoustic emissions of booming sand reveals an intense and very distinct beat pattern; to the best of our knowledge, this is the first published report on this feature obtained in the laboratory for airborne signals produced by relatively small samples of booming sand. In-situ samples of the sand have been sectioned into small size ranges in an attempt to determine whether any size fraction has a monopoly on booming. The period of the carrier wave within the beat patterns denotes low frequency emissions having peaks which seem proportional to the inverse of the particle diameter. The length of the beat envelope, which characterizes the beat period, appears to vary with the number of sand particles; this suggests that the motion of the sand can be represented by a cell model with varying mean free path. These observations should help in the investigation of the sounding mechanism of the booming phenomenon.

1. Introduction

These are typical descriptive accounts of the booming phenomenon which occurs in some desert regions:

- a) In the field: R.A. Bagnold (1954): "On two occasions it happened on a still night, suddenly - a vibrant booming so loud I had to shout to be heard by my companion. Soon other sources, set going by the disturbance, joined their music to the first, with so close a note that a slow beat was clearly recognized. This weird chorus went on for more than five minutes continuously before silence returned and the ground ceased to tremble"
- b) In the lab: A rhythmic thrum of a few hundred Hz like the rubbing of fingers on a washboard, producing noticeable vibrations in the hand.

Several theories have been suggested to explain the sounding mechanism, classified generally:

- 1) with respect to the *sources*, i.e. the particles of sand or the interstitial air, into friction or cushion theories and 2) with respect to their *physical characteristics* such as grain shape, texture, degree of sorting, moisture content and number of adhered solid contaminants and other properties which form the basis of the coherence theories which postulate that all grains vibrate in phase and move in large masses, as proposed by Reynolds (1885) and Poynting and Thomson (1909).

It seems however that no individual theory can explain the phenomenon adequately and there exists, to our knowledge, only one report (qualitative) by Lewis (1936) of what may have been successful reproduction of booming in the laboratory, where the vocal quality was quickly lost unless kept in airtight containers and which could only be restored after special heat treatment. AE was not recorded nor is there any mention of a discernible beat.

The following is a report on a quantitative study of AE from two closely matched sands, in an attempt to help formulate a comprehensive theory of the booming mechanism.

2. Procedures

1) Microscopic examination of the sand grains has revealed that: a) Booming sand is reasonably spherical, rounded, with a smooth polished surface and b) Ottawa sand is also spherical, rounded, with a rougher textured surface. But booming sand is no more spherical and rounded than other sands or than ordinary glass beads, and no smoother than the latter.

2) Numerical size analysis by image splitting analysis shows that:

a) booming sand has a uniform Gaussian distribution over a size range of 120 - 560 μm with an average diameter and standard deviation of $321 \pm 84 \mu\text{m}$, typical of other dune sands. This agrees with results obtained by conversion of a weight size distribution obtained by sieving where between 60 to 69% of a sample of booming sand was retained within the 50 to 70 sieve range. (See Fig. 1.)

b) Ottawa sand extends over a size range 160 - 640 μm with an average diameter and standard deviation of $358 \pm 115 \mu\text{m}$, deviates slightly from a uniform Gaussian distribution by having a higher proportion of small sizes. (See Fig. 2.)

Thus this sample of Ottawa sand is slightly coarser than the booming sand, not quite as uniformly distributed and has a slightly higher standard deviation. These results agree with those obtained by sieving analysis. However, the size distribution of booming sand is no more uniform and narrow than many ordinary sands, and considerably less so than many samples of ordinary glass spheres.

3) Large samples of each sand (approximately 375 - 740 g) were inserted into glass 675 ml coffee jars. Shaking by hand produced very different audible signals, the Ottawa sand generating a low intensity swishing sound while the booming sand produced a much louder thrum and generated vibrations in the hand. These sounds were picked up by a small microphone secured through a hole in the jar covers and fed into the input of a storage oscilloscope to produce the following records, at same sensitivity level (20 mV/div.) and same sweep rate (20 ms/div.): Ottawa sand emitted low intensity, typical random noise patterns as seen in Fig. 3 and booming sand emitted high intensity beat patterns, which are believed to be the first recorded in the laboratory from air-borne signals produced by relatively small samples of booming sand. Carrier and beat periods are shown in Fig. 4.

4) Each sand sample was then sieved into 8 narrow fractions ranging in size from particles retained on sieve 35 to those passing sieve 80. Each subsample was hand shaken and the emitted signals captured on the storage oscilloscope as before.

5) Each of the subsamples of booming sand was fractioned successively into 1/2, 1/4, 1/8 ... of its original size and its emission examined and recorded.

3. Results and Discussion

The beat signal shown in Fig. 4 is typical of the AE recorded for those fractions of booming sand which contained approximately one million particles or more, which occurred for 5 of the 8 fractions. Among these five fractions which produced beats, there appeared variations of the carrier period and, much more noticeably, very large variations in the beat period depending on the grade of the fraction. Carrier and beat periods were then averaged over 60 signals for each of the booming samples.

Figure 5 summarizes results for the average carrier period (t_c) versus nominal sieve opening size, where nominal sieve size has been used to represent particle size (D). The dots refer to the five booming fractions. The range of variation of t_c is its standard deviation over 60 measurements while that of D has been extended over the nominal size of grids neighbouring those of each retained sample. The open circle is for data given by an unfractioned sample of booming sand, where the variation in D is the measured standard deviation.

There appears to be a linear relationship between these variables, in agreement with similar results which we have obtained for glass and steel spheres. Projections onto the y-axis and conversion into the frequency domain indicate that the carrier frequencies of these booming samples range from 172.4 to 294 Hz.

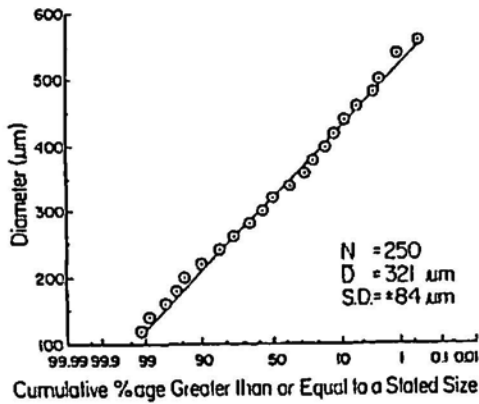


Fig. 1 Numerical size distribution of booming sand.

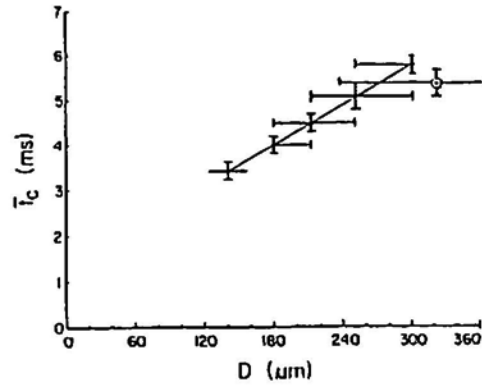


Fig. 5 Average carrier wave period vs. particle size.

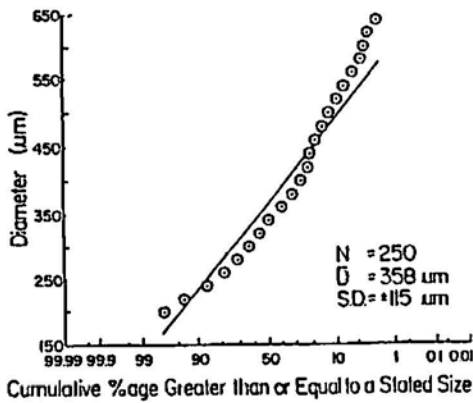


Fig. 2 Numerical size distribution of Ottawa sand.

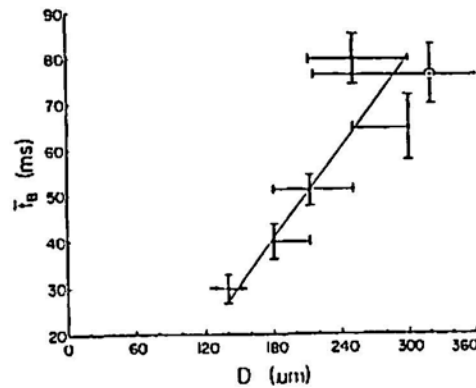


Fig. 6 Average beat period vs. particle size.

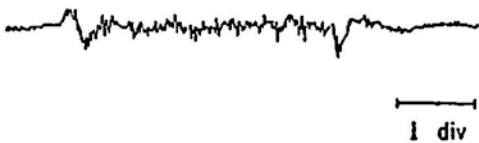


Fig. 3 Typical signal emitted by Ottawa sand.

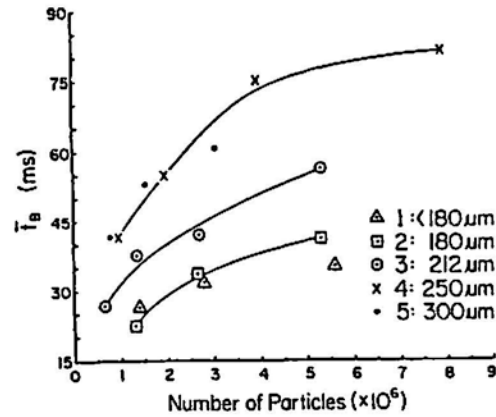


Fig. 7 Average beat period vs. number of particles for each subsample.

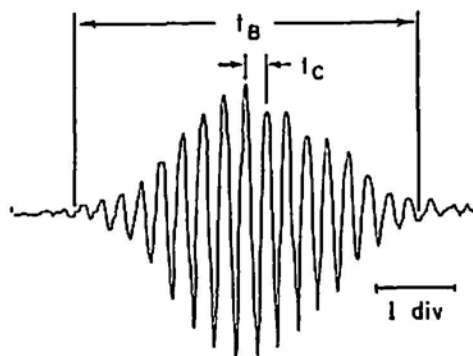


Fig. 4 Typical signal emitted by booming sand.

Figure 6 shows results for the average beat period (t_B) versus particle size. Again there is a reasonably linear relationship between these two variables. Projections onto the y-axis yield beat frequencies for these samples ranging from 12.5 to 33.7 Hz, which all exceed the limit of perception by the human ear.

The result obtained for the unfractionated sample seems to indicate that, while no size fraction with a sufficient number of particles has a monopoly on booming, the fractions of largest sized particles and/or the most populated fraction are probably most active. It also seems that booming is not critically dependent on the narrowness of the size distribution.

Deviations of the two coarsest samples from the straight line was believed to be attributable to the number of particles in each of these fractions, the coarsest fraction having many fewer particles than the three finest while the second coarsest contained many more particles than any other fraction. In order to test this assumption, each booming subsample was further fractionated as outlined in Procedure 5. Results for these fractions are plotted in Fig. 7; they show 1) a very strong dependence of the beat period on sample size and provide a reasonable explanation for the fact that sands which produce audible beats in the field do not necessarily generate beats which are discernible by the human ear when operating on small laboratory samples, and 2) a dearth of particles beyond the 1/8th fraction also explains the eventual disappearance of the beat patterns.

4. Conclusion

From the experiments reported above, it seems that several agents are responsible for the booming sands. It is likely that booming is mediated by factors such as grain shape, texture, degree of sorting, moisture content and number of adhered solid contaminants. The present study suggests for the first time that knowledge of the number of sand particles may also be necessary, if not sufficient, in order to understand booming dunes and to identify the booming mechanism. It is hoped that the experiments reported here do not muddy the water but rather encourage further inquiry aimed at solving the basic query into how booming sands work and suggest new lines of thought for others who might be similarly intrigued with the phenomenon.

References

- R.A. Bagnold (1954), "The Physics of Blown Sand and Desert Dunes", Chap. 17, Chapman Hall, pp. 247-256.
- D. Reynolds (1885), "On the Dilatancy of Media Composed of Rigid Particles in Contact", Philos. Mag., Fifth Series, 469-481.
- J.H. Poynting and J.J. Thomson (1909), "Textbook of Physics, Sound", Chap. IX, Charles Griffin and Co., pp. 134-145.
- A.D. Lewis (1936), "Roaring Sands of the Kalahari Desert", South Afr. Geog. J., 19, 33-49.

Expected Acoustic Emission from Around a Shaft in Intact Rock

B.J.S. Wilkins and G.L. Rigby

The authors are affiliated with Materials and Mechanics Branch, AECL Research, Whiteshell Laboratories, Pinawa, Manitoba R0E 1L0 Canada.

Abstract

We are examining the possible disposal of nuclear fuel waste, in a vault, deep in plutonic rock. The most probable way in which components of this waste could escape to the biosphere is by water transport through cracks in the rock. Therefore, there is interest in the possibility of time-dependent changes occurring in the crack population. Below 100°C, the dominant mechanism of deformation in intact rock is microcracking. Hence, a model (Micro-Crack Driven Intact Rock Creep) has been developed, from which can be estimated time-dependent displacements (creep) and acoustic emissions around openings in rock, in response to stress-state perturbations. In this model, the stress-state safety factor (SF) around openings is estimated. SF is the ratio of the maximum principal stress at failure (σ_{1f}) to the applied maximum principal stress (σ_1). Slow crack-growth data are used to estimate time-dependent changes in SF, from which displacements and the distribution of acoustic emissions are estimated. The model has been applied to a vertical shaft at the Canadian Underground Research Laboratory. The predicted displacements and acoustic emissions compare favorably with those observed, around the shaft.

1. Introduction

An opening introduced into a rock mass perturbs the in situ stress state. As a result stress is concentrated around the opening. The stress concentration is expressed as a disturbance in the strength safety factor. Strength safety factor (SF) is defined as the ratio of the maximum principal stress at failure (σ_{1f}) to the applied maximum principal stress (σ_1); that is σ_{1f}/σ_1 . A Micro-Crack Driven Intact Rock Creep (MCDIRC) model has been developed to estimate the decline in both the uniaxial compressive strength of the rock (α_c) and SF, produced by time-dependent microcracking (Wilkins and Rigby, 1989). The model assumes that radial strain (ϵ_r) results from rock dilation caused by the creation, extension and dilation of microcracks. Microcracking has the additional effect of reducing the rock stiffness.

At the Canadian Underground Research Laboratory (URL), AECL Research is studying the post-excavation response of rock (granite) around openings by a variety of techniques. These techniques include recording acoustic emission (AE), measuring strain (using extensometers) and recording the velocities of compressional and shear (P and S) waves in the frequency range of 10 to 15 kHz. In this paper, the spatial distribution and the time scale of the post-excavation response predicted by MCDIRC are compared to those measured around the shaft, and at other openings, at the URL.

2. Input to MCDIRC

The model requires as input the following: the in situ stress state (the stress state prior to excavation), that is the vertical (σ_z) and horizontal stress components (σ_x , σ_y); the compressive strength of the rock (α_c); the values of certain constants (m, n, and s); and the original radius of the shaft. From this information can be estimated: the time required for any small wall movement postulated and the corresponding radial-strain (ϵ_r) distribution (alternatively, wall movement and ϵ_r can be calculated for any desired time), and changes everywhere of both SF and σ_z .

The constants m and s are those required to estimate the maximum principal stress at failure. (σ_{1f}) is given by (Hoek and Brown, 1980),

$$\sigma_{1f} = |\sigma_3| + \sigma_c [m(\sigma_3/\sigma_c) + s]^{1/2} \quad (1)$$

where σ_3 is the minimum principal stress.

Essentially, as slow crack-growth proceeds (in compression it is the cooperative growth of many microcracks), the strength of the rock decreases and SF falls to unity, at which time the rock fails. The derivative of SF with respect to time is given by

$$d(SF) / dt = [(SF)^{(3-n)}] / (n-2) \quad (2)$$

where t is in seconds. The constant n depends on the rock type and the environment (Anderson and Grew, 1977; Atkinson, 1987; Wilkins et al., 1984). The procedures to obtain $d(SF)/dt$ and n experimentally are discussed elsewhere (Wilkins and Rigby, 1989).

3. How MCDIRC Works

The distribution of SF around the opening is estimated. A ray, out from the opening, is chosen in the direction of interest. For a vertical shaft, it is most useful to choose a ray out from the center-line in a horizontal plane. Then SF is determined along the ray. This is illustrated in Fig. 1, where at $t = 0$ and $t > 0$, SF is shown as a function of the radial distance (r), normalized by the original radius of the shaft (r_0). At $t = 0$ (immediately after excavation), $SF = g(r/r_0)$ and for $t > 0$, $SF = f(r/r_0)$. The function $f(r/r_0)$ comes directly from $d(SF)/dt$, and is given in terms of $g(r/r_0)$ by

$$f(r/r_0)^{(n-2)} = g(r/r_0)^{(n-2)} - g(a)^{(n-2)} + b^{(n-2)} \quad (3)$$

where (a,b) are the coordinates of a point that lies on $f(r/r_0)$. Figure 1 indicates that at $t > 0$, SF has decreased to unity on the shaft wall, and the shaft wall has moved inward to $(r/r_0) = \xi$ (ξ is just less than 1). Strain rates in the radial direction (de_r/dt) are estimated from $d(SF)/dt$, $g(r/r_0)$ and $f(r/r_0)$. This is discussed elsewhere (Wilkins and Rigby, 1989).

4. Post-Excavation Rock Response Around Openings at the URL

The source location of the acoustic emission (from microseismic events) at the URL has been studied (Tabeli and Young, 1989). The main shaft was excavated incrementally using a series of full-face blasts. AE was recorded for several hours after most of these blasts. Figure 2 shows some of the data. Figure 2(i) shows the number of events versus time for a typical blast (#65, depth 348 m, 1988 February 28, 23:29h). Figure 2(ii) is a summary of all events from several blasts between the 324 and 443 m depths. It shows AE versus r/r_0 for a given time period. In both figures, the abscissa is normalized by the maximum value.

At the 352 m depth, time-dependent radial strain has been measured with three Bof-ex extensometers⁴ with a repeatability of $\pm 1 \mu\text{m}$ (Martin, 1988; Thompson and Lang, 1987). The excavation to the 352 m depth was completed on 1987 February 4. The extensometers were put in place and tested by February 8. Immediately after further blasting (~10 minutes) the output from the extensometers were recorded continuously until February 26 (February 28 for extensometer 1). In Fig. 3 are reproduced the results from extensometer 2 (the results from extensometers 1 and 3 are similar). These results showed that the radial strain rate (de_r/dt), over any radial gauge-length for a given extensometer, decreased to a constant value after about 6 days. In Table 1, the constant values, measured for the three radial gauge-lengths (which were 0.1 to 0.45, 0.45 to 0.8 and 0.8 to 5.0 m), are given along with the de_r/dt values predicted by MCDIRC.

The shaft at the 352 m depth is circular in cross-section with a radius of 2.5 m. The in situ stress state, the uniaxial compressive strength of the rock, m and s are estimated to be $\sigma_z \approx 15$, $\sigma_x \approx \sigma_y \approx 35$ MPa; $\sigma_c \approx 200$ MPa everywhere; $m \approx 28$, and $s \approx 1$, respectively (Martin, 1990). The MCDIRC predictions in Table 1 were based on this input with selected values of $n = 17, 18, 19, 20, 22$ and 24 .

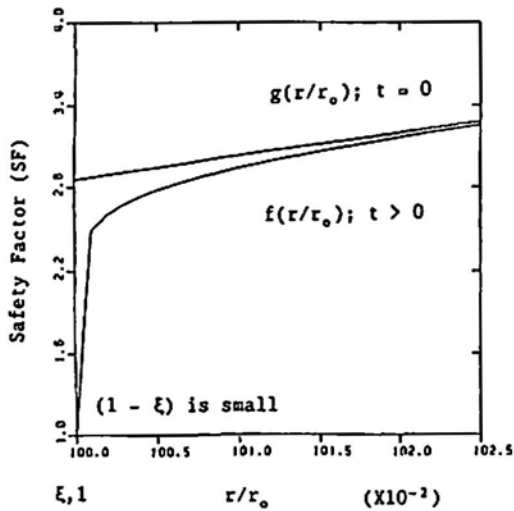


Fig. 1 Safety factor versus normalized radical distance (r/r_0), for $t = 0$ and $t > 0$.

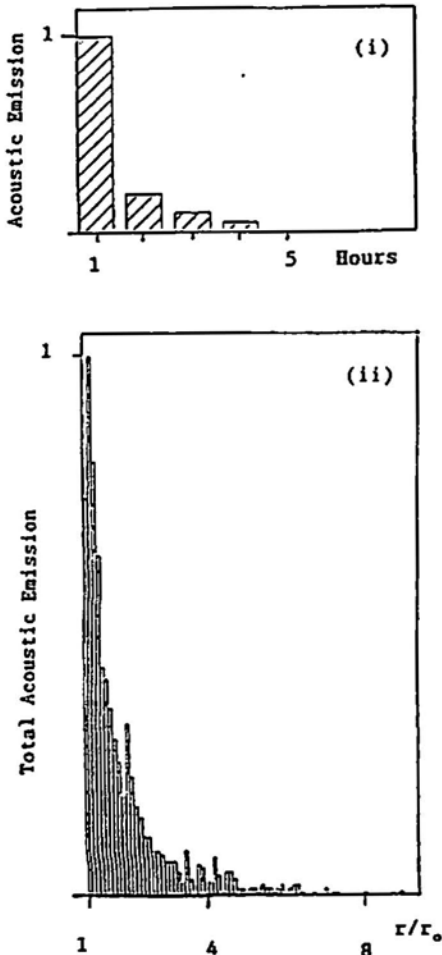


Fig. 2 (i) Normalized acoustic emission versus time after blasting; (ii) normalized total acoustic emission after blasting versus normalized radial distance (r/r_0).

In Fig. 1 are shown the SF distributions from MCDIRC, for when SF has decreased to unity at the wall ($t > 0$) and for the original SF distribution ($t = 0$), both for $n = 18$. In Fig. 4, normalized ϵ_r and normalized α_c are plotted against r/r_0 , when SF has reached 1 at the wall. The normalized ϵ_r plots are for $n = 17$ and 24, and the normalized α_c plot is for $n = 18$. In these examples, for small wall movements (up to a few mm), the normalized strain plots are independent of time. This is because the value of $d\epsilon_r/dt$, at any r/r_0 , is constant for small wall movements. When $\xi = 0.9988$, the wall has moved inward by 3 mm, and $\epsilon_r = 0.10$ and 0.16 at the wall for $n = 17$ and 24, respectively (MCDIRC).

At the URL, well after excavation (1 year) in room 205 (depth 240 m), P and S wave (10 to 15 kHz) velocities were measured at various distances into the rock (Hayles, 1990). Typical results are shown in Figs. 5(i) and (ii), where normalized wave-velocities are plotted against distance into the room wall.

P and S wave velocities offer a measure of rock integrity because more attenuation is expected with more cracks. The velocities of the recorded P waves appeared less in the first metre into the wall, which is consistent with the rock there containing more cracks. The S wave results showed no particular trend, which is not surprising because their arrival times are less certain.

5. Discussion and Conclusions

At the URL, all the measurements indicate a similar pattern of post-excavation response, with time and with distance into the rock around openings. The main features of the pattern are, a rapid decrease in response with distance into the rock, away from the opening wall, and a rapid decrease in response with time everywhere. However, there are large differences in scale for both the distance into the rock and the time. The AE decays to small values in just a few hours after blasting and originates from as far out as (r/r_0) = 5. In contrast, the radial strain, as the extensometers indicate, took several days to decrease to small values, and was hardly detectable at $r/r_0 > 2$.

Most probably, the initial high strain rates (measured by extensometers) and the AE indicate mainly the settling-in immediately after the blast.

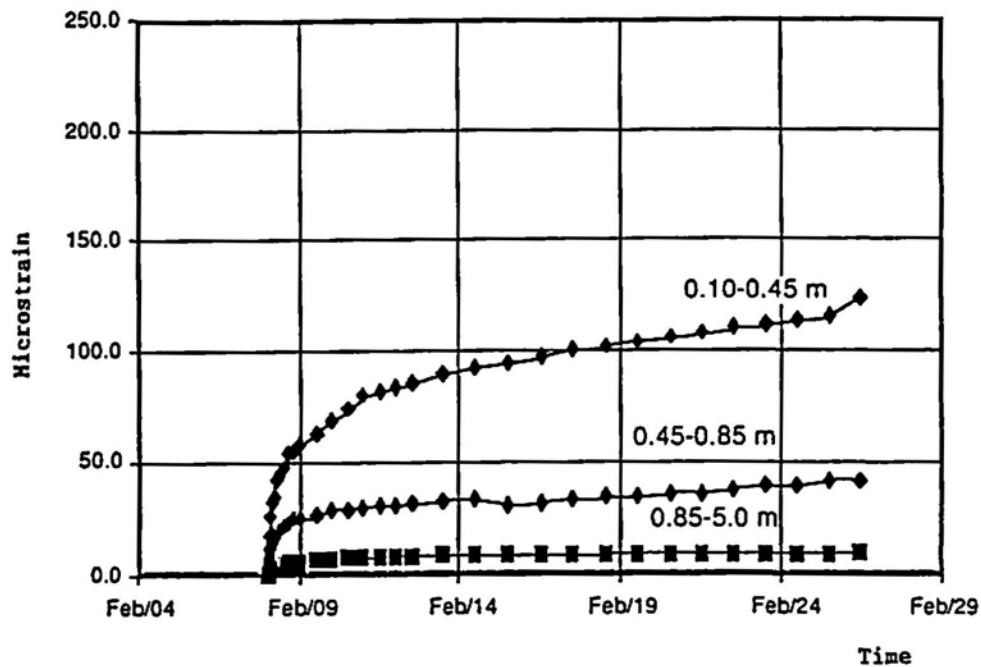


Fig. 3 Microstrain (radial direction) (ϵ_r) versus time (reading date) for extensometer 2.

Table 1 Data of $d\epsilon_r/dt$ from URL at 352 m depth; Measured by extensometers and predicted by MCDIRC.

	Radial Gauge-Lengths		
	0.10 to 0.45 m ($r_0/r = 1.04$ to 1.18)	0.45 to 0.85 m 1.18 to 1.34	0.85 to 5.0 m 1.34 to 3.0)
	Constant $d\epsilon_r/dt$ (h^{-1}) from Extensometers		
Extensometer 1.	1.24×10^{-7}	9.80×10^{-9}	5.56×10^{-9}
Extensometer 2.	1.07×10^{-7}	2.62×10^{-8}	2.80×10^{-9}
Extensometer 3.	1.48×10^{-7}	1.22×10^{-8}	3.50×10^{-10}
	$d\epsilon_r/dt$ (h^{-1}) from MCDIRC		
n = 17	2.6×10^{-6}	9.7×10^{-9}	9.6×10^{-11}
n = 18	6.9×10^{-7}	1.7×10^{-9}	1.4×10^{-11}
n = 19	1.8×10^{-7}	3.1×10^{-10}	1.9×10^{-12}
n = 20	4.9×10^{-8}	5.6×10^{-11}	2.7×10^{-13}
n = 22	3.6×10^{-8}	1.8×10^{-11}	5.4×10^{-14}
n = 24	2.7×10^{-8}	5.9×10^{-12}	1.1×10^{-14}

However, the decreases in the strain rates that occurred over a much longer time period were probably due to time-dependent strain produced by ongoing microcracking and were not associated with the blasting directly. Presumably, AE also was occurring over the longer time period, but at a lower level than the installed system was capable of recording.

MCDIRC predicts the rapid decrease in the response with distance into the rock. However, it does not directly predict the rapid decrease in the response with time. This is because stress relaxation (produced by closure of the opening and by stiffness reduction through microcracking) and blast damage are excluded from the model.

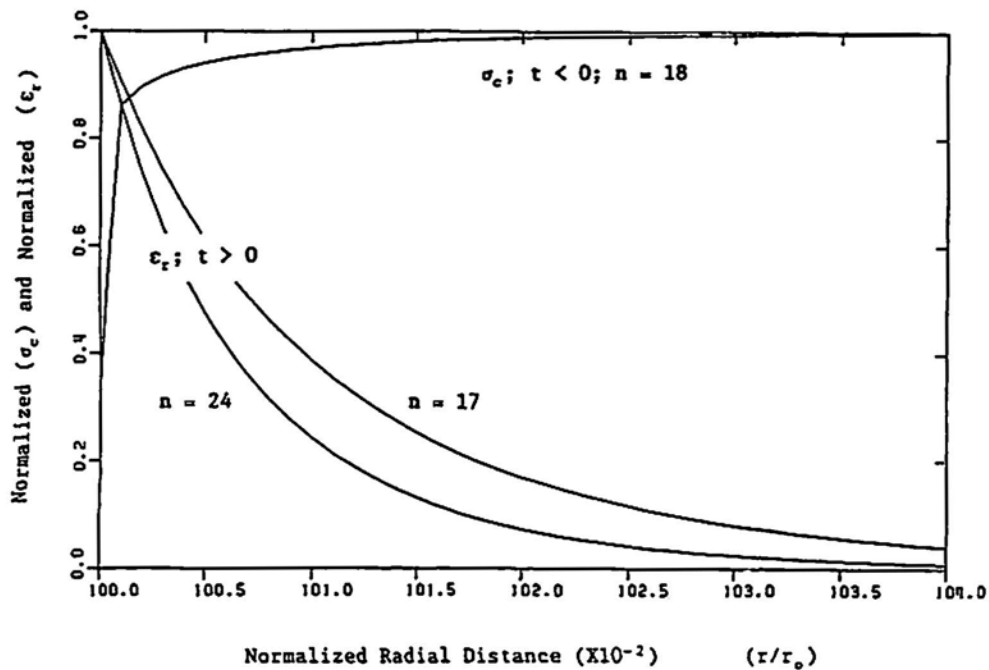


Fig. 4 Normalized uniaxial compressive strength (σ_c) and normalized radial strain (ϵ_r) versus normalized radial distance (r/r_0), where SF(wall) = 1 and $t > 0$.

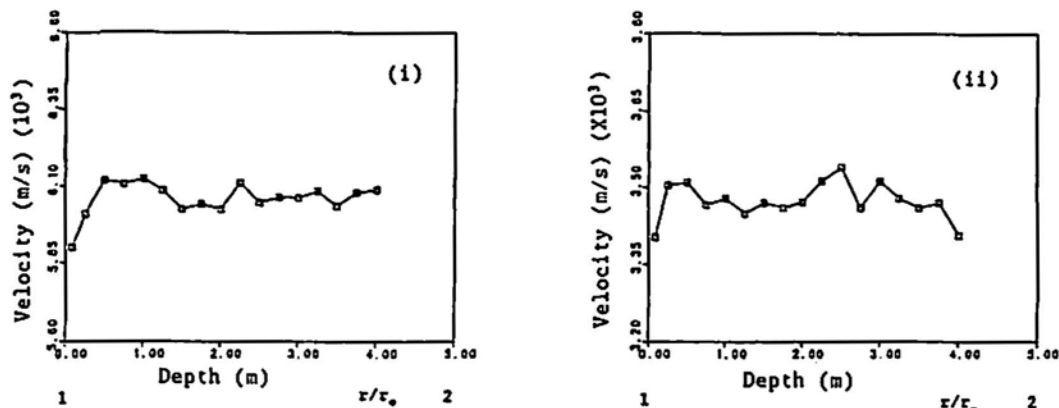


Fig. 5 (i) P-wave velocity versus normalized radial distance (r/r_0); (ii) S-wave velocity versus normalized radial distance (r/r_0).

The normalized ϵ_r versus r/r_0 plots shown for $n = 17$ and 24 are similar. They both indicate a rapid decrease in normalized ϵ_r (1 to $\sim 10^{-4}$) in the first ~ 15 cm of the wall. The actual amount of wall movement and the strain everywhere for a given time depends on the value of n assumed. For example, when the wall has moved in by 3 mm, and at $n = 17$ and 24 , the strain at the wall is 0.10 and 0.16 , respectively. Hence, some decrepitation at the shaft wall is bound to happen, no matter how carefully the shaft is excavated.

The major influence of n is on the strain rate. As n increases the predicted $d\epsilon_r/dt$ decreases. If $17 \leq n \leq 20$, for the parameters assumed for the 352 m depth at the URL, MCDIRC predicts $d\epsilon_r/dt$ values similar to that measured by the extensometers (for the 0.1 to 0.45 m gauge-length). Judging from the literature, this range of n values is plausible for the rock at the URL (Atkinson, 1987; Wilkins et al., 1984).

In intact rock at $< 100^{\circ}\text{C}$, the response to blasting and to the SF disturbance around an opening should be both immediate and time-dependent microcracking. All of the post-excavation responses are consistent with this idea. The P/S wave and the AE results, and the agreement between MCDIRC and the final extensometer readings (last 12 days), suggest that the extensometers did provide eventually a measure of the time-dependent strain, produced by the stress concentration around the shaft, rather than simply a measure of the energy transferred to the rock by the blasting.

The extensometers did not measure ϵ_r for the first 10 cm into the shaft wall. However, the MCDIRC prediction can be used to position the normalized ϵ_r (measured) versus r/r_0 plot to allow a comparison with the normalized AE versus r/r_0 plot (normalized by the reading at the wall). The long-term extensometer data and the predictions of MCDIRC can be compared on a quantitative basis. It seems improbable that AE and ϵ_r can be equated for a given volume of rock on a general basis. However, on a site-specific basis it may be possible.

Acknowledgements

The work reported here was funded by the CANDU Owners Group (COG).

References

- O.L. Anderson and P.C. Grew (1977), "Stress Corrosion Theory of Crack Propagation with Applications to Geophysics", *Rev. Geophys. Space Phys.*, 15, 77.
- B.K. Atkinson (1987), *Fracture Mechanics of Rock*, Academic Press, New York.
- J.G. Hayles (1990), private communication.
- E. Hoek and E.T. Brown (1980), *Underground Excavations in Rock*, Inst. Min. Metall., London.
- C.D. Martin (1988), "Shaft Excavation Response in a Highly Stressed Rock Mass", *Proc. NEA Workshop on Excavation Response in Geological Repositories for Radioactive Waste*, OECD, Paris, France, Winnipeg, Canada.
- C.D. Martin (1990), "Characterizing In Situ Stress Domains at the AECL Underground Research Laboratory", *Can. Geotech. J.*, 27, 631-646.
- S. Talebi and R.P. Young (1989), "Failure Mechanism of Crack Propagations Induced by Shaft Excavations at The Underground Research Laboratory", *Proc. Int. Symp., Rock Physics at Great Depth*, Pau, France, A.A. Balkema, Rotterdam, Netherlands.
- S. Talebi and R.P. Young (1989), "Final Report on Source Locations of Microseismic Events Induced by Shaft Excavation at The Underground Research Laboratory", Contract Rept. to AECL Research, Pinawa, Canada.
- P.M. Thompson and P.A. Lang (1987), "Geomechanical Instrumentation Applications at the Canadian Underground Research Laboratory", *Proc. 2nd Int. Symp. Field Measurements and Geomechanics*, Kobe, Japan, A.A. Balkema, Rotterdam, Netherlands.
- B.J.S. Wilkins, A.R. Reich and W.R. Wallace (1984), "Slow Microcracking in Plutonic Rocks", Atomic Energy of Canada Limited Tech. Rec., TR-264. Unrestricted, unpublished report available from SDDO, Atomic Energy of Canada Research Company, Chalk River, Ontario, K0J 1L0, Canada.

B.J.S. Wilkins and G.L. Rigby (1989), "MCDIRC - A Model to Estimate The Creep of Intact Rock Around a Shaft", *Proc. Int. Symp. on Rock Physics at Great Depth*, Pau, France, A.A. Balkema, Rotterdam, Netherlands.

B.J.S. Wilkins and G.L. Rigby (1989), "MCDIRC - A Model to Estimate Creep Produced by Microcracking Around a Shaft in Intact Rock", Atomic Energy of Canada Limited Rept., AECL-10068, Pinawa, Canada.

Acoustic Emission Monitoring during Microseismic Activity Caused by Mine Subsidence

Brian R. A. Wood and Robert W. Harris

The authors are affiliated with CSIRO Division of Geomechanics, Lucas Heights Research Laboratories, PMB 7, Menai 2234, Australia

Abstract

An underground coal mine was operational until 1979 and was then closed and the entry sealed. Some seven years later a residential subdivision was developed in the area above the previous mine. The development included a major shopping area and many hundreds of homes. On December 7, 1988, rumbling noises were heard in the night by residents, and the following morning it was observed that in selected areas cracks had appeared in lawns, gardens and roadways. An acoustic emission study of the area was commenced on December 13, 1988 using two monitoring locations, and continued until the end of February 1989. The detected signals were in some cases probably associated with primary defect activity, while others were thought to be secondary as they were consequential to the initiating defect activity. A range of signal analysis techniques applied to the captured waveforms indicated that a number of different source mechanisms (about 4 or 5) were operating. Activity from a nearby fault line was also detected which in a few instances was seen to be activated by surface loading. Core samples taken from a number of drill holes into the mine area 155 m below the surface confirmed that there had been some pillar collapse in some selected areas and some rock movement in the 145 m of rock between the mined area and the surface.

1. Introduction

Subsidence of the ground in a residential subdivision had occurred which caused damage to property and was therefore of considerable concern to local homeowners. The subdivision was constructed over an underground coal mine which was operational until 1979 when it ceased operations and the entry was sealed. After a period of approximately seven years a residential subdivision was developed in the area above this previous mine and included a major shopping area and many hundreds of homes. On December 7, 1988, rumbling noises were heard in the night by residents, and the following morning it was observed that in specific areas cracks had appeared in lawns, gardens and roadways. The type of surface deformation occurring is shown in Fig. 1 which shows the cracking along the roadway and Fig. 2 which shows damage to a house in the area.

An acoustic emission study of the area was commenced on December 13, 1988 using two monitoring locations, and continued until the end of February 1989. Initially a simple long term monitoring project was carried out and at a later time there was also an intensive monitoring phase for a period of one week. The mine layout and the subdivision roadway is shown in Fig. 3.

2. Instrumentation.

Since it was not possible to place transducers directly onto bedrock, waveguides constructed of 25 mm steel rod were employed. Holes were bored so as to reach bedrock at depths of 9 to 12 m and then each waveguide was then anchored into the bedrock by grouting with cement. Three monitoring locations were prepared by drilling holes and grouting steel waveguides into these holes, however due to local conditions and traffic movements only two monitoring locations were used which were about 200 m apart. One location which was in the grounds of a church was referred to as "Church" and the other located in a nearby



Fig. 1 Surface deformation on roadway.

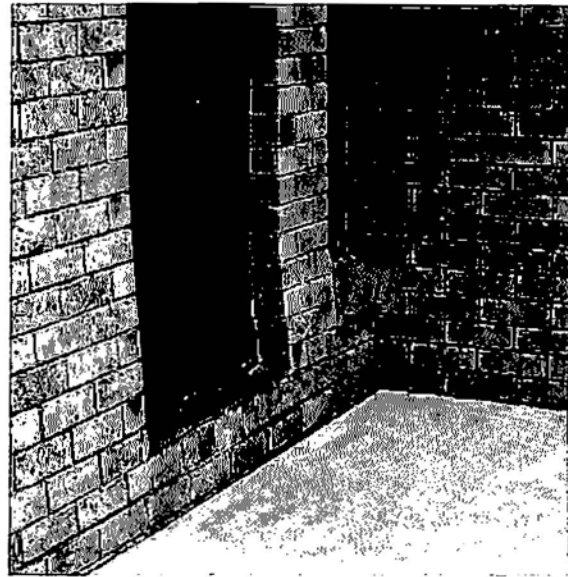


Fig. 2 Damage to a house.

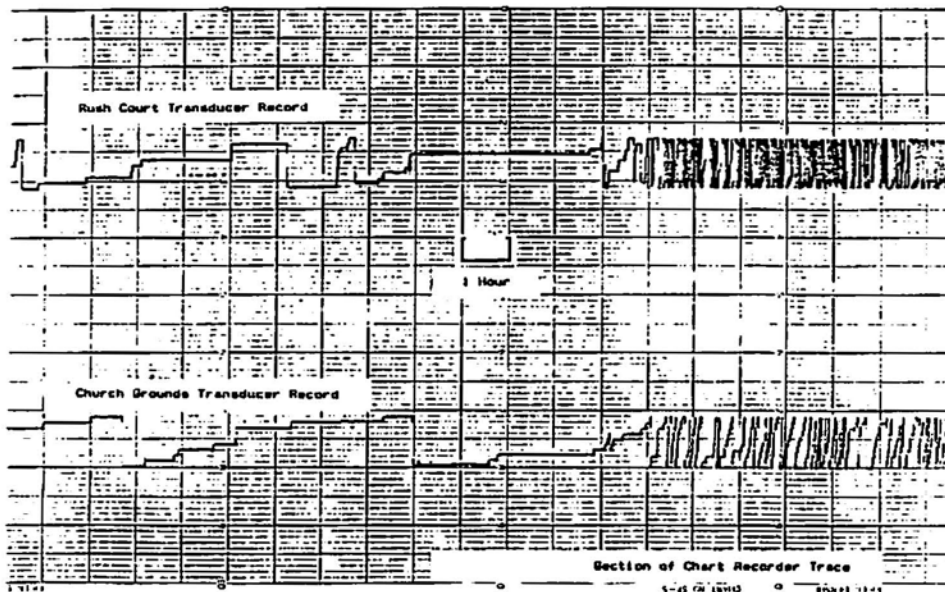


Fig. 3 Section of long term monitoring record.

street referred to as "Rush Court". Bruel and Kjaer model 4335 accelerometers were then attached to the ends of the waveguides with silicon cement and the above ground assembly contained so as to be made waterproof and protected from the weather and environmental interference.

The signals detected by the transducers were amplified 40 dB by a preamplifier situated adjacent to the transducer, and then this amplified signal was passed along a co-axial cable to the central monitoring location where the signal was boosted a further 30 dB. The amplified signal was routed to a digital oscilloscope so that complete waveforms could be captured and stored on computer disk (intensive monitoring phase) and envelope detected for analysis by the CSIRO-EAR equipment (Wood and Harris, 1984) (intensive monitoring phase) and/or a counter/chart recorder combination (long term monitoring).

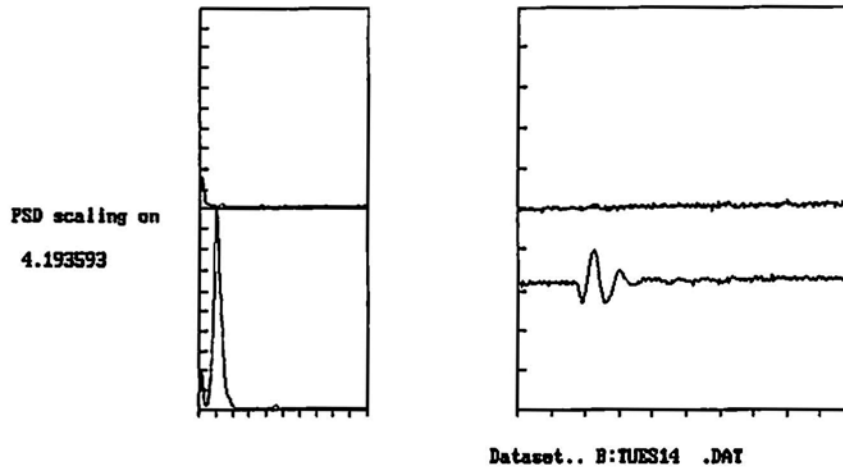


Fig. 4 One typical low amplitude event.

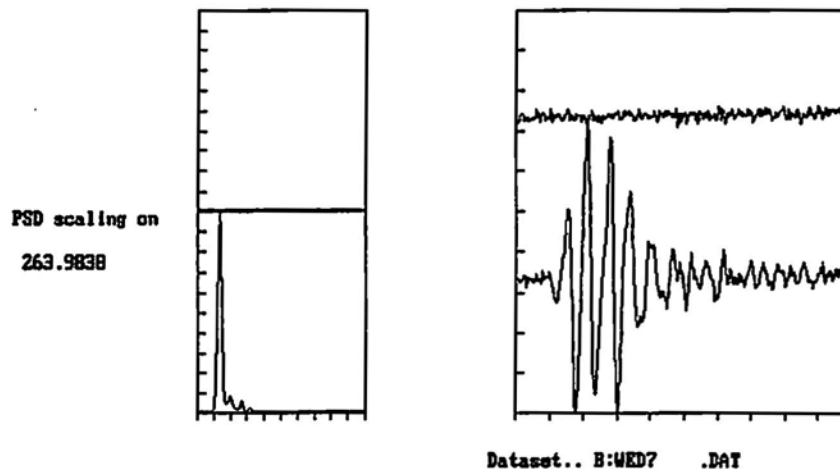


Fig. 5 A typical high amplitude event.

3. Results and Discussion

The monitoring program was divided into two sections, one being a 10 week period where data was recorded automatically, and the other being a 7 day period where data was observed as it was recorded and some on-line analysis carried out.

The simple long term monitoring program indicated that activity was sporadic and when activity commenced there was generally a pattern exemplified by a series of low amplitude events which increased in frequency of occurrence until there was a higher amplitude pulse and then there was little activity until the sequence commenced again. A section of the recorded data which shows the spasmodic acoustic emission activity from both the monitoring locations as a function of time is shown in Fig. 3. This type of activity could be considered to be indicative of some sort of 'stick-slip' phenomenon where activity increased until there is an avalanche when a much larger energy release occurs and then there is a quiescent state until the process recommences.

Unfortunately very little of the avalanche effect was observed during the intensive monitoring program however a variety of different waveforms were observed together with some waveforms which were similar to the low and high amplitude signals observed visually during the long term monitoring when an observer was present. These waveforms were typified by Fig. 4 for the low amplitude events (0.5 to 1 V peak ampli-

tude) and Fig. 5 for the higher amplitude events (2 to 5 V peak amplitude). The right hand side of the figures show the waveforms from the two locations with the upper trace associated with the location designated "Church" and the lower one associated with the location designated "Rush Court". The left hand side of the figures provides the power spectral densities of the signals for the range 0 to 50 kHz, and alongside the spectra are the frequencies of the first two dominant spectral peaks.

An examination of Fig. 4 showed that the first excursion is sometimes positive and sometimes negative so that the sources producing the acoustic emission will sometimes start off as a compression and sometimes as a tension (the identification between the sign of the excursion and the tension/compression nature of the source requires an accurate determination of the phase characteristics of the system which could not be carried out at the time).

Figure 6 shows a higher frequency transient with a 4 V peak amplitude which may arise as a result of the excitation of the higher order vibration modes in the steel waveguide as a consequence of the deformation of the waveguide and grout composite due to bedrock motion resulting from the higher level of energy released by the active source. An idea of the range of lower frequency transients that were observed is shown in Fig. 7. These again show different polarities for the first excursion. The slow ringdown and 'erratic' nature of the pulses given in Fig. 7 would be consistent with larger source to transducer separations associated with deeper or more distant rock deformation/movement.

The well defined envelope of Fig. 8 indicates that the signal originated at some distance from the monitoring location and there were no major discontinuities or boundaries in the propagation path to distort the final signal.

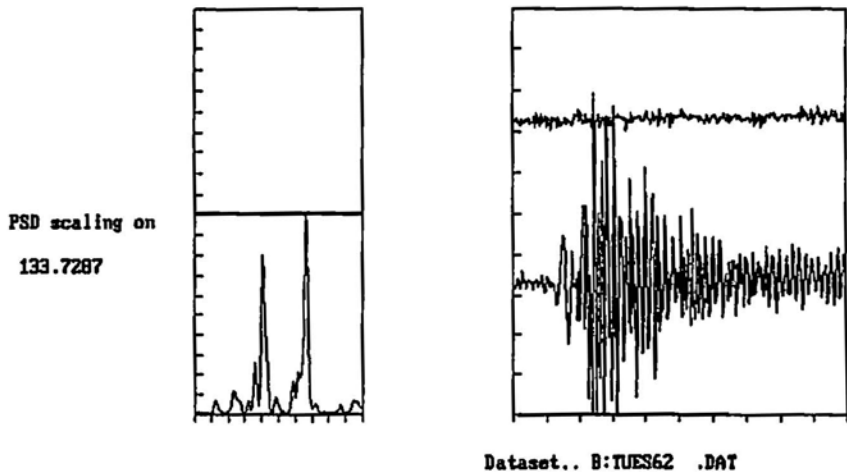


Fig. 6 High frequency transient.

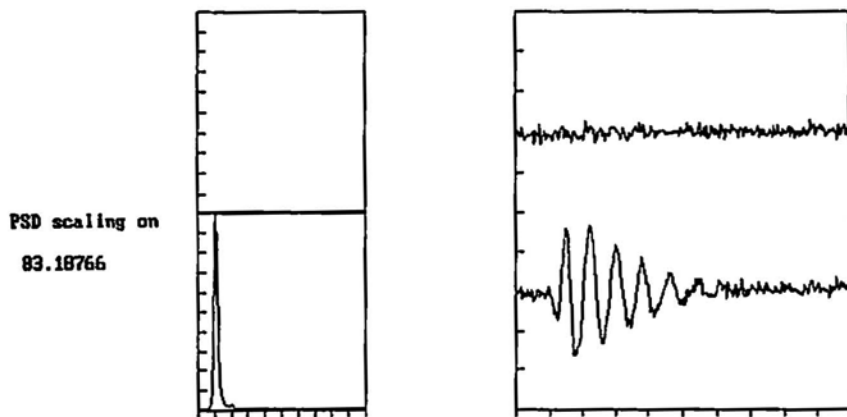


Fig. 7 Typical low frequency events.

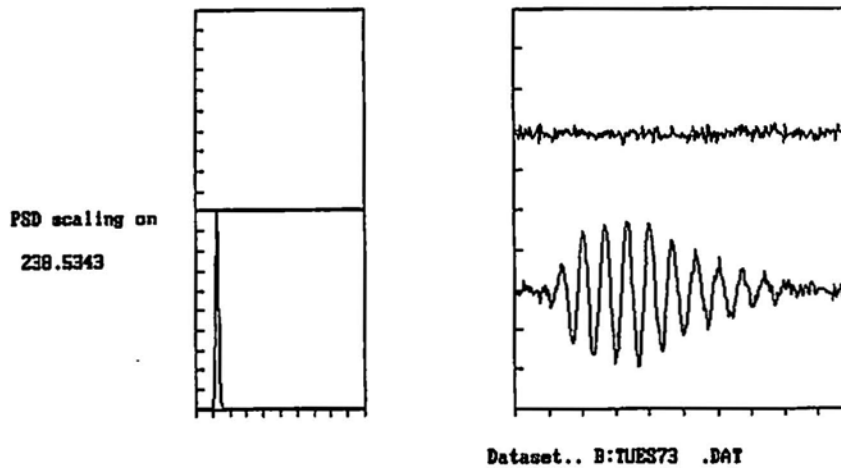


Fig. 8 Transient with well defined envelope.

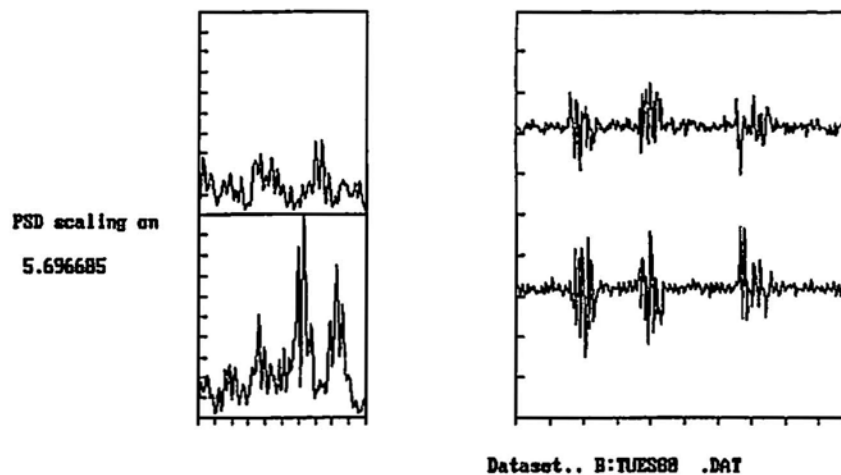


Fig. 9 Unusual transient.

The unusual waveforms typified by Fig. 9 were often detected and considered a mystery until it was observed that pulses similar to those in Fig. 9 occurred when a heavy truck was driven along the road and passed over the location where the known fault crossed the road. The pulse velocity and attenuation measurements indicated that there was a significant attenuation for any propagating signal. Thus, the similar peak amplitude and arrival time of the signal at the two separated monitoring locations indicate that there was a plane or zone of movement along a significant length of the fault line rather than only localised deformation under the truck. This effect was observed for several positions of the truck indicating that while the trigger location may be different, the actual fault movement or weakest points of contact on the fault faces was the same.

The locations of the surface movement varied, and while in some cases adjoining buildings and structures were affected, it was more usual for the surface deformation to be completely random. This was evidenced in a number of cases where subdivision drains were severely damaged (Fig. 1), and houses 10 m away were free of any damage (Fig. 2). In another case where a row of houses existed, only one home was severely damaged.

A series of bore holes were put down to the mine area about 155 m below the surface at locations where solid pillars of coal were known to exist. Thick continuous sandstone was found with some faulting and an aquifer was found in one area at a depth of 30 m. At a depth of 155 m, solid black coal was found,

and the fragments had bright surfaces, while another nearby borehole indicated broken, oxidised and fragmented pieces of coal.

4. Conclusions

The results of the investigations showed that there were a number of different deformation mechanisms operating in the monitored region which were mirrored in the variety of AE signals detected.

The earlier investigations indicated that a stick-slip type of mechanism could be operating in some circumstances and associated with this mechanism is an avalanche effect where a larger increase of energy was preceded by a series of lower amplitude events having an increasing frequency of occurrence. This is thought to be particularly relevant to the fault area.

Any further investigations need to be extended so that there is available a means of calibrating the systems to distinguish between tension/compression at the source initiation and also data should be available from a basic laboratory investigation on the behaviour of the typical bedrock material. Artificial signals need to be injected into the bedrock using a technique such as the 'buffalo gun' used in a borehole so that the signals detected by a transducer array would provide data on elastic wave propagation.

Acknowledgements

The authors wish to acknowledge the assistance and participation of the Queensland Mines Department in funding this project, and the co-operation given by the Collingwood Park Anglican Church, whose property was used as a base. The assistance of Hollingsworth Consultants and the valued discussions are appreciated. The support and assistance of the CSIRO Acoustic Emission Team who provided the necessary back-up is acknowledged.

Reference

B.R.A. Wood and R.W. Harris (1984), "Acoustic emission event counting using an Apple microcomputer", *Progress in Acoustic Emission II*, eds. K. Yamaguchi et al., JSNDI, Tokyo, pp. 351-358.

Acoustic Emission/Microseismic Activity Monitoring of Salt Crystallization for Stone Conservation

M. Montoto, R.M. Esbert, L.M. Suárez del Río,
V.G. Ruiz de Argandoña and C.M. Grossi

The authors are affiliated with University of Oviedo, Dept. of Geology, Group of Petrophysics, 33005 Oviedo, Spain.

Abstract

The spontaneous crystallization of salts in the void spaces of building stones creates stresses which can exceed the local rock strength and contribute to mechanical deterioration of the stone mass. This phenomenon constitutes one of the most severe and worldwide deterioration process affecting relevant historic buildings of the world cultural heritage. Thus, better knowledge of the stresses inside the stone must be gained in order to apply appropriate conservation procedures. Future objective of this research is in-situ AE/MS monitoring of treated and non-treated stones to assess the effectiveness of the applied conservation techniques.

Stones selected for this study belong to the Murcia Cathedral (Murcia, Spain), which is a Gothic-Baroque XIV-XV century monument. Some of the sculptures, which are composed of high porosity ($n_0 = 30\%$) limestone, are highly deteriorated by salt crystallization. To evaluate this mechanical deterioration process, episodes of salt crystallization in samples of the above mentioned limestone have been carried out in the laboratory. The AE/MS was monitored in the 100-300 kHz range. The preliminary results show the effectiveness of AE/MS to follow the evolution of the internal stresses in the stone during the hydration process suffered by the Na_2SO_4 crystals.

1. Introduction

Salt crystallization phenomena can be observed on the surface or in the external layer of many building stones. These salts are observed in the form of efflorescences or whitish crusts which contribute to an ugly appearance of the original surface of the stone. They are soluble salts formed by a partial solution of the stone and the mortars by circulating water; later they precipitate into the pore space of the stone due to changes in the thermohydric conditions and water evaporation (Arnold and Zehnder, 1989; Zehnder and Arnold, 1989). This deterioration is important in historic buildings and sculptures made of stone and is the result of a physico-chemical mechanism.

Very often the new salts so formed are hydrated and during their crystallization they stress the walls of the pore system. Such stresses are large enough to develop microcracks into the stone contributing to its deterioration. (Fig. 1).

Acoustic emission has been selected as the most appropriate NDT technique to monitor those internal stresses, as part of the Stone Conservation Program at the University of Oviedo (Spain). To evaluate the mechanical deterioration process, episodes of salt crystallization in samples of the Murcia Cathedral limestone have been carried out in the laboratory. The AE/MS was monitored in the 100-300 kHz range. The preliminary results show the effectiveness of AE/MS technique to follow the evolution of the internal stresses in the stone during the hydration process suffered by the Na_2SO_4 crystals.

The Murcia Cathedral stone (Murcia, Spain) has been selected for the following reasons:

- It is made of a calcareous stone with a low degree of cohesion; it is poorly cemented and has an elevated porosity ($n_0=30\%$). Therefore it tends to disaggregate. Consequently, it is very sensitive to stresses and AE/MS signals are easily developed.

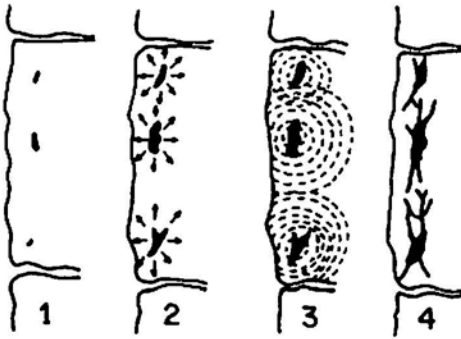


Fig. 1 Sketch of damaging effects due to salt crystallization inside monumental stones. (1) Salt crystallization starts inside the pore space of stone. (2) Local stress fields start to develop associated to the mechanical stresses. (3) Microseismic activity (acoustic emission) is generated. (4) Depending on the local stress and the local strength of the stone, cracks are formed and grow.

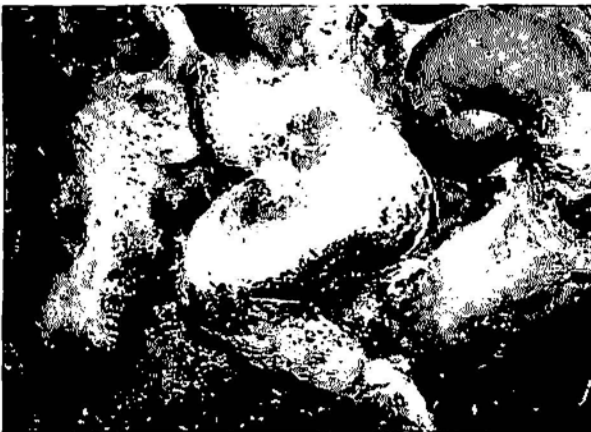


Fig. 2 Salt crystallization phenomenon developed in the limestone of the Cathedral of Murcia (Spain).

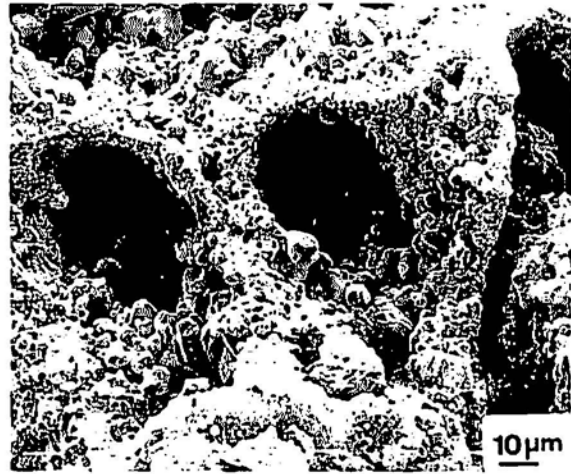


Fig. 3 Some textural aspects of the Murcia Cathedral limestone (SEM).

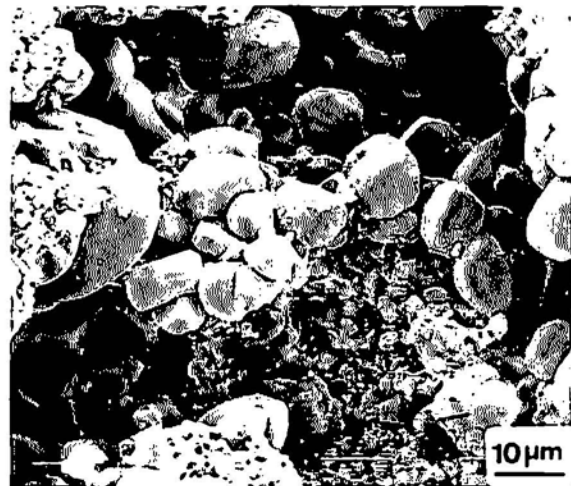


Fig. 4 Some textural aspects of the Murcia Cathedral limestone (SEM).

- In the Murcia Cathedral this kind of deterioration is frequently found.
- The Cathedral is placed in downtown Murcia, a city having mild and relatively humid climate (60% R.H.) with sea-influence as well, implying the presence of sea-salts in the air - mainly chlorines - and atmospheric pollutants (SO_2 , CO_2 , dust, smoke, fumes, etc). As a consequence salt crystallization is one of the most frequent deterioration mechanisms developed in the Cathedral's calcareous stone as shown in Fig. 2 (Esbert et al., 1990).

2. Petrophysics

Limestone from the Murcia Cathedral has a poorly-cemented detrital texture. Main physical properties controlling its weatherability are: high open porosity ($n_o = 30\%$), low density ($\rho_d = 1,813 \text{ kg/m}^3$), high water imbibition capacity (C.I. = 11.7 %) and very high capillary suction (C.A. = $1.73 \times 10^{-1} \text{ kg/m}^2\text{s}^{1/2}$) (Esbert et al., 1990). The mean grain size is about $150 \mu\text{m}$. Its uniaxial compressive strength is 3 MPa.

Its composition, deduced from the x-ray diffraction analysis, is: calcite (89.5%), quartz (7.5%), dolomite (1%) and accessories (tourmaline, iron oxides and micas) (2%). Fossils (mainly algae, foraminifers and echinoderms), peloids and older rock fragments can be observed in the stone (Figs. 3 and 4). Eventually argillaceous minerals (smectite group) are present as well. It is light-colored stone, varying from nearly white to light yellow (10 YR/2 and 8/3) (Goddard et al., 1979), and showing a fine grained and quite uniform aspect.

3. Experimental

The deterioration process due to the crystallization of salts into the pore space of building stones, has been reproduced in laboratory by a well known ageing test: salt crystallization. Different test conditions of salt crystallization have been proposed by different authors (Alonso et al., 1987); the final results being clearly dependent on the experimental procedure. In our experiment one complete cycle includes: immersion for 4 hours in an aqueous solution of 14% decahydrated sodium sulfate, renewed each three cycles; drying for 14 hours, at 60°C in an oven and cooling for 6 hours at 18°C and 75% relative humidity (Fig. 5). Eleven cycles of the salt crystallization were performed on cubic specimens having 5 cm edge of the Murcia Cathedral limestone. The weight loss was 5.5% at the end of the ageing test.

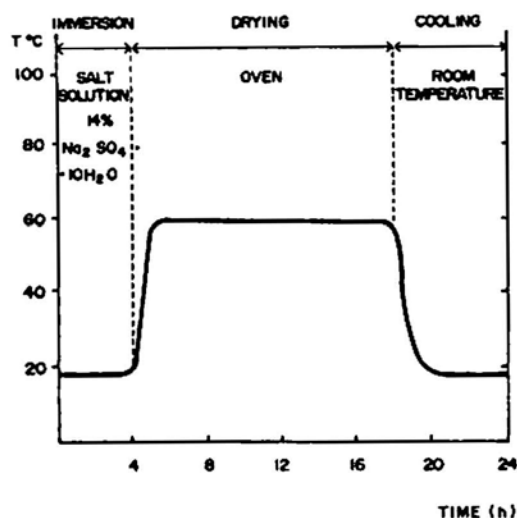


Fig. 5 Salt crystallization cycle for the Murcia limestone.

4. Acoustic Emission Monitoring

This technique has not been very often applied to stone conservation programs; only some papers (Caneva and Maravelli, 1983; Accardo et al., 1983) deal with in-situ applications, while others (Fukuda, 1985; Faria Santos and Bieniawski, 1986; Ruiz de Argandona et al., 1986; Calleja et al., 1986; Esbert et al., 1988; Faria Santos and Mrugala, 1989) considered AE/MS monitoring in laboratory tests. Faria Santos and Mrugala (1989) related the degree of experimental deterioration to AE/MS activities for a sandstone.

During our experiments the AE/MS activities were continuously monitored, using counts per second, with a Spartan 3000 instrument (Physical Acoustic Corporation, NJ, USA) using a 150 kHz transducer and 100-300 kHz filter; gain was 80 dB.

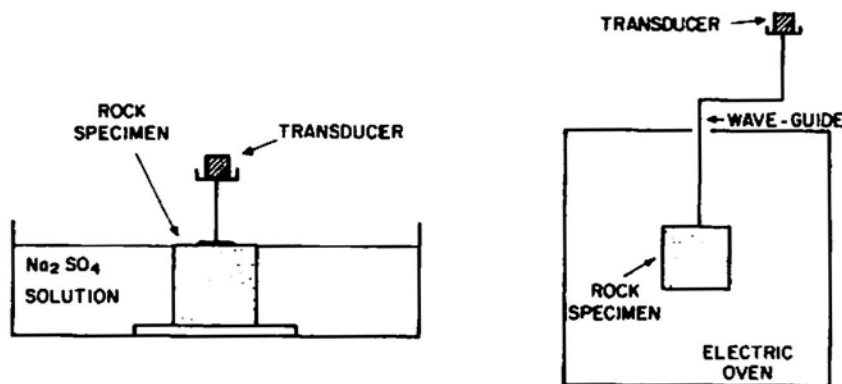


Fig. 6 Experimental setup of transducers attached to the specimens.

In order to avoid the heating and wetting of the transducer during the tests, it was placed outside the oven (during drying and cooling) and outside the salt solution (during

immersion) and it was connected to the rock surface through a glass waveguide to pick up the AE/MS signals as shown in Fig. 6. This glass waveguide was attached to the specimen surface using an Ag-glyce interface during the drying and cooling steps, and with vacuum grease during the immersion step. In order to avoid AE/MS signals due to the emission of air bubbles, the salt solution reached up to about 1 mm from the upper surface of the cube during immersion.

The AE/MS proved again to be useful for monitoring stressed porous rocks. When subjected to uniaxial compressive stress, the highly porous (30%) Murcia limestone exhibited immediate AE/MS at the very moment of starting the loading cycle; that is, at very low stresses. This arises from textural rearrangement inside the rock, followed by a stage of more or less constant AE rate and that of a gradual increase due to the initiation and growth of microfissures. Then, a fast increment of the AE/MS occurs as failure approaches (Fig. 7); a similar behavior has been observed in an altered granite (Montoto et al., 1984).

5. Results and Petrophysical Interpretation

During the salt crystallization cycles, the acoustic emission generated by the specimens mainly appears during the cooling stage, and minor and irrelevant acoustic emission is monitored in the immersion and drying stages.

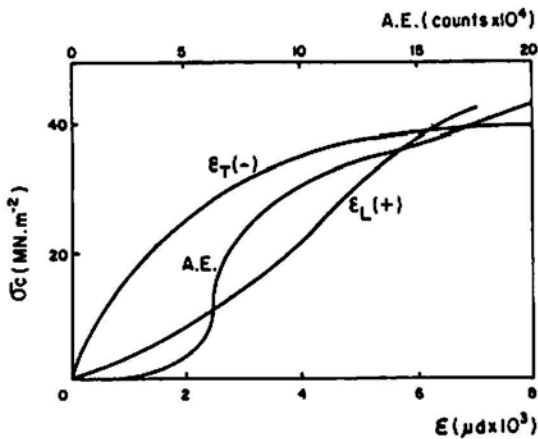


Fig. 7. AE/MS behavior of an altered granite under uniaxial compressive stresses.

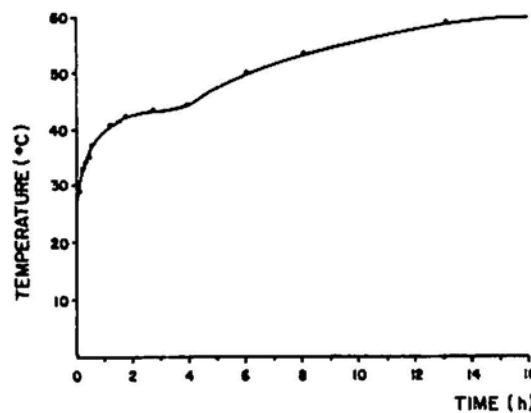


Fig. 9. Variation of the temperature at the center of the specimen during drying.

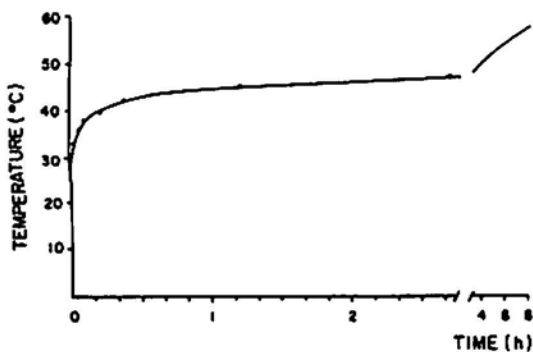


Fig. 8. Variation of the temperature at the surface of the specimen during drying.

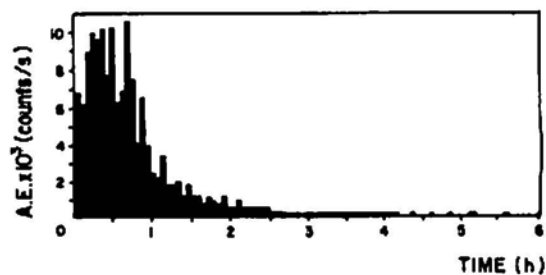


Fig. 10 AE rate vs. time in the 4th cycle during cooling.

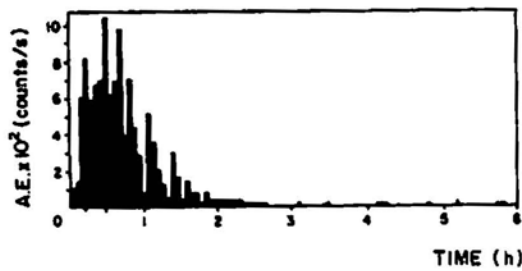


Fig. 11 AE rate vs. time in the 10th cycle during cooling.

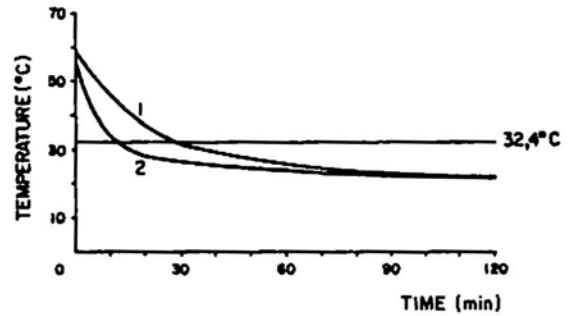


Fig. 12 Variation of the temperature of the specimen during cooling: (1) center, (2) surface.

a. Immersion

During immersion in the salt solution, the monitored AE/MS is irrelevant, with few AE peaks, smaller than 10 counts/s. From this, it can be deduced that, at this stage, no salt hydration is produced or, at least, even if some hydration exists, stresses are not high enough to produce AE/MS. This hydration seems to be completed before the immersion in the cooling stage. The few AE signals could be due to other phenomena; e.g., the expansion of clayey minerals due to uptake of water is able to produce local stress concentrations and cannot be neglected.

In some cycles (not included in the present study), in which the specimen and the lower part of the waveguide were covered by the solution, a higher AE/MS rate was monitored during the first moments of absorption of the salt solution. These initial AE registers are due to air ejection from the sample interior, in the form of air bubbles that hit the base of the waveguide. In this case, the curve of total AE counts had a similar form to that of the free absorption of water.

b. Drying

In this stage, in which both water evaporation and salt crystallization are occurring, no relevant AE/MS is recorded. The crystallization pressure of the sodium sulfate is considered to reach insufficient intensity to produce enough deformation on the rock and no AE/MS is generated. Figures 8 and 9 present the variation of the temperature of the surface and center of the specimen when drying (the oven was preheated to 60°C). The maximum heating rate of the surface reaches about 7°C/min and that of the center is less than 1°C/min. The thermal shock on the rock surface is considered to be not intense enough to produce AE/MS.

c. Cooling

The more important AE/MS is recorded in this stage. In each cycle, the AE/MS starts from the very beginning of the cooling, reaching the maximum about 30 minutes from the start of cooling, and progressively decreasing. After about two hours, the AE/MS is almost nil, although some isolated peaks can be monitored (Figs. 10 and 11). The shape of the AE rate curve can be explained by the dehydration of the $\text{Na}_2\text{SO}_4 \cdot 10\text{H}_2\text{O}$ (Duval, 1963) and the variation of the temperature in the specimen during cooling. When the decahydrated sodium sulfate is heated, the dehydration is not completed until 90°C. At 72°C the main composition is $\text{Na}_2\text{SO}_4 \cdot 4.75\text{H}_2\text{O}$, and below 32.4°C it is completely hydrated as $\text{Na}_2\text{SO}_4 \cdot 10\text{H}_2\text{O}$. Thus, when cooling the specimen from 60°C, the partially hydrated sodium sulfate progressively reacts with environmental water, increasing its volume and stressing the rock.

The maximum value of the AE rate (at about 30 minutes from the start of cooling) coincides with the time, when the temperature at the geometrical center of the specimen reaches 32.4°C (Fig. 12), the moment at which the salt completes its maximum hydration. The AE events registered after the maximum value are interpreted as textural modifications due to the "crack equilibrium configuration" not previously reached. Similar results have been obtained in the heating tests of a granodiorite (Ruiz de Argandoña et al., 1986). After two hours, the temperatures inside and outside the specimen become equal and the AE/MS ceases or is very low.

When the AE rates of the consecutive cycles are compared, the AE/MS increased from the first to the third cycles; in the following cycles, the AE rate decreased (Fig. 13). Such a behavior shows that the great

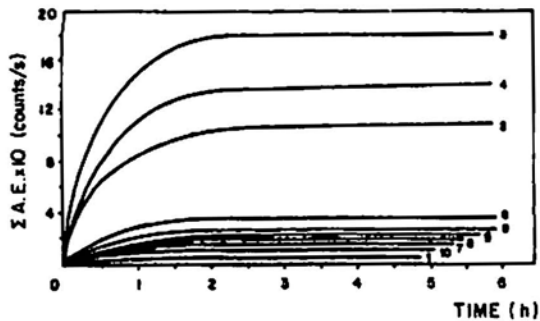


Fig. 13 Cumulative AE/MS plot for different aging cycles during cooling.

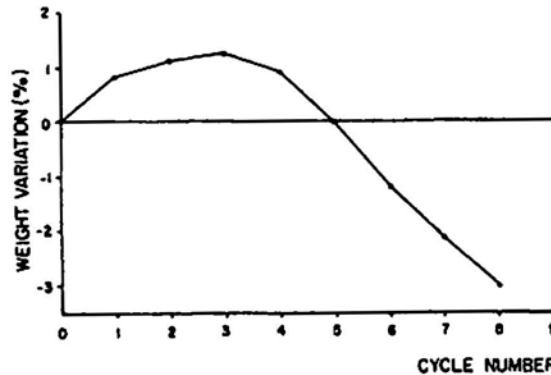


Fig. 14 Weight variation during eight salt crystallization cycles.

est damage is produced in the first few cycles and the stresses generated in the specimens decreases beyond the 3rd cycle. This behavior of the AE/MS seems to be contradictory to the weight variation of the specimen during the cycling. The specimen loses more material after the 5th cycle (Fig. 14). From the point of view of stone deterioration, it is interpreted that a higher concentration of stresses and associated microcracking occur during the first few cycles. The later disaggregation stage proceeds with a lower energy consumption.

6. Conclusions

The monitoring of the acoustic emission/microseismic activity has proved to be a valuable technique in Stone Conservation, to evaluate the damaging stresses developed inside a monumental stone (Murcia Cathedral limestone) when subjected to salt crystallization. For this stone, the most important damage is produced during the cooling stages of the firsts cycles, due to the hydration of the salts; that hydration begins at the very moment in which cooling starts. Acoustic emission is produced when the partially hydrated sodium sulfate progressively takes up environmental water, increasing its volume and stressing the rock. No significant AE/MS is detected during the drying and immersion stages.

Acknowledgements

The authors wish to acknowledge: "Consejería de Cultura" (Comunidad Autónoma de Murcia, Spain) and "Comisión Interministerial de Ciencia y Tecnología, (C.I.C.Y.T)", Spain, Project no. 485/88, for supporting this research.

References

- G. Accardo, C. Caneva, and S. Massa (1983), "Stress monitoring by temperature mapping and acoustic emission analysis: A case study of Marcus Aurelius", *Studies in Conservation*, **28**, 67-74.
- F.J. Alonso, J. Ordaz, L. Valdeón and R.M. Esbert (1987), "Revisión crítica del ensayo de cristalización de sales", *Materiales de Construcción*, **37**, 206, 53-60.
- A. Arnold and K. Zehnder (1989), "Salt weathering on monuments", 1st L'Int. Simp. La conservazione dei monumenti nel bacino del Mediterraneo (Bari), ed. F. Zezza, pp. 31-58.

- L. Calleja, V.G. Ruiz de Argandoña, L.M. Suárez del Río, and M. Montoto (1986), "Resistencia a la tracción en rocas sometidas a ciclos térmicos", *Bol. Geol. y Minero*, 97(2), 84-93.
- C. Caneva and M. Maravelli (1983), "L'emissione acustica per la diagnostica negli interventi di conservazione: il portale di S. Zeno a Verona", *First Int. Conf. on NDT in Conservation of Works of Art (Roma)*, IV/6.1-6.22.
- C. Duval (1963), *Inorganic Thermo-gravimetric Analysis, Second and Revised Edition*. Elsevier Publ., Amsterdam, 722 p.
- R.M. Eibert, C. Grossi, L.M. Suárez del Río, L. Calleja, J. Ordaz and M. Montoto (1988), "Acoustic emission generated in treated stones during loading", *Proc. VIth Int. Cong. on Deterioration and Conservation of Stone*, Torun (Poland), pp. 403-410.
- R.M. Eibert, C. Grossi, L. Valdeón, J. Ordaz, F.J. Alonso and R.M. Marcos (1990), "Estudios sobre la conservación de la piedra de la Catedral de Murcia", *Materiales de Construcción*, 40, 217, 14p.
- C.A.F. Faria Santos and Z.T. Bieniawski (1986), "Effect of artificial weathering on properties of Loyalhanna sandstone", *27th U.S. Symposium Rock Mech.*, (Alabama), pp. 147-154.
- C.A.F. Faria Santos and M. Mrugala (1989), "Variations of AE/MS activity with weathering in Loyalhanna Sandstone", *Proc. 4th Conf. on Acoustic Emission/Microseismic Activity in Geologic Structures and Materials*, Trans Tech Publications, Clausthal, Germany, pp. 15-25.
- M. Fukuda (1985), "Acoustic emissions from porous rock while freezing. Conservation and Restoration of Stone Monuments", *Scientific and Technical Study on the Conservation and Restoration of Monuments made of Stone or Related Materials*, pp. 19-22.
- E.N. Goddard, P.D. Trask, R.K. De Ford, O.N. Rove, J.T. Singewald and R.M. Querbeck (1979), "Rock-Color Chart", *The Geological Society of America*, Boulder, CO. USA.
- M. Montoto, L.M. Suárez del Río, A.W. Khair and H.R. Hardy (1984), "AE in uniaxially loaded granitic rocks in relation to their petrographic character", *Proc. 3rd. Conf. on AE/MS in Geologic Structures and Materials*, Trans Tech Publ., Clausthal, Germany, pp. 83-100.
- V.G. Ruiz de Argandoña, L. Calleja, L.M. Suárez del Río and M. Montoto (1986), "Emisión acústica/actividad microsísmica generada bajo ciclos térmicos en una roca granítica", *Bol. Geol. y Minero*, 97(1), 96-102.
- K. Zehnder and A. Arnold (1989), "Crystal growth in salt efflorescence", *J. Crystal Growth*, 97, 513-521.

Acoustic Emission Monitoring during In-situ Heater Test of Granite

T. Ishida, K. Kitano, N. Kinoshita and N. Wakabayashi

T. Ishida is affiliated with Department of Civil Engineering, Yamaguchi University, 2557 Tokiwadai, Ube, Yamaguchi 755, Japan, K. Kitano is with Central Research Institute of Electric Power Industry, 1646 Abiko, Abiko, Chiba 270-11, Japan, and N. Kinoshita and N. Wakabayashi are with Shimizu Corporation, 3-4-17 Echugima, Kohtoh, Tokyo 135, Japan.

Abstract

In order to clarify the mechanism of microcracking due to thermal attack in inhomogeneous granite, acoustic emission (AE) events were monitored during the small scale *in situ* heater test in an old quarry of Inada granite. A 2 m long electric heater was set at the depth from 3.3 m to 5.3 m in a 100 mm diameter bored hole, and the temperature of the heater was increased up to 800°C. AE events were monitored for 60 hrs with 12 sensors buried in 4 holes bored 1 m from the heater hole. 636 AE hypocenters were located. From the result, it was found that AE events started to occur in the pegmatite veins intruded into granite, and then these occurred in the pre-existing joints. These AE clusterings could result from the fact that the pegmatite veins have particles larger than those of the surrounding normal granite and the pre-existing joints have the lower frictional resistance than the surrounding normal granite.

1. Introduction

Acoustic emission (AE) monitoring is an effective method to clarify the mechanism of microcracking due to thermal attack in rock, because it can monitor at locations away from a heated region where conventional measurements are not viable. Recently, Ohtsu and Ono (1986) and Ohtsu (1988) proposed a source inversion procedure for determining crack types and crack orientations as the quantitative waveform analysis of AE based on the integral representation and the moment tensor. Moreover, Ohtsu et al. (1989) successfully applied the procedure to AE events monitored during the pull-out tests of hooked anchor-bolts from a concrete block. In light of the development, AE monitoring method has become worthy of investigating the microcracking mechanism of heated rock.

Majer et al. (1981) and Majer and McEvilly (1985) carried out large scale *in situ* AE monitoring with the increase of temperature in quartz monzonite, and compared the location and activity of AE with the temperature change in rock. To our best knowledge, however, no researcher has found the relation between the positions of clustered AE sources and the inhomogeneity of the rock including intruded veins and pre-existing joints. Thus, the mechanism of microcracking due to thermal attack in inhomogeneous granite has not been clarified yet.

We monitored AE during a small scale *in situ* heater test in an old quarry of Inada granite. In this paper, changes in the distribution of located AE sources as the temperature increases are compared with the positions of veins and pre-existing joints. The mechanism of microcracking due to thermal attack in inhomogeneous granite is discussed below.

2. In-situ Experiment

2.1 General View of Site and Experiment

The site of the experiment was on a small hill covered with 40 ~ 50 cm thick surface soil containing pieces of granite, as shown in Fig. 1. A few joints in granitic rock mass were observed at outcrops along

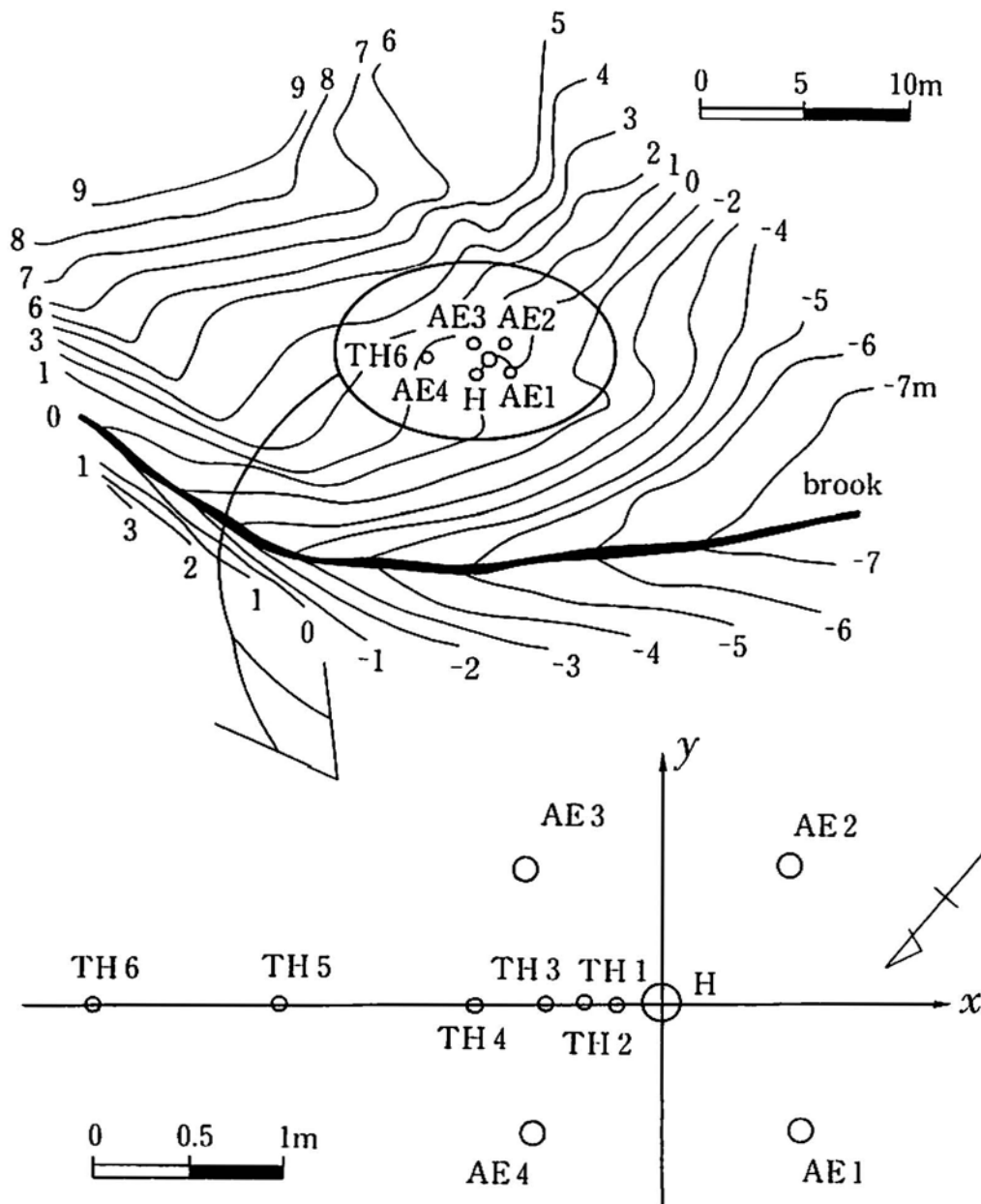


Fig. 1 Topography and locations of bored holes at the site.

the brook, about 10 m apart and 4 - 5 m down from the site. At the site, one hole (H) of 100 mm diameter and 5.65 m depth was bored to heat the rock. Four holes (AE1 - AE4) were bored surrounding the heater hole (H) at about 1 m distance to install AE sensors. These holes had 66 mm diameter and about 6.8 m depth. To measure temperature change in rock due to heating, six holes (TH1 - TH6) were bored for thermocouples along the perpendicular bisector of the line segment between the positions of AE3 and AE4 holes. These six holes of 32 mm in diameter and about 6.8 m in depth are 20, 40, 60, 100, 200 and 300 cm apart, respectively, from the heater hole as shown in Fig. 1.

Figure 2 shows the spatial arrangement of the heater and AE sensors. The heater is composed of six U-shaped electric pipe heaters covered with a stainless steel pipe for protection. The diameter, total length, and

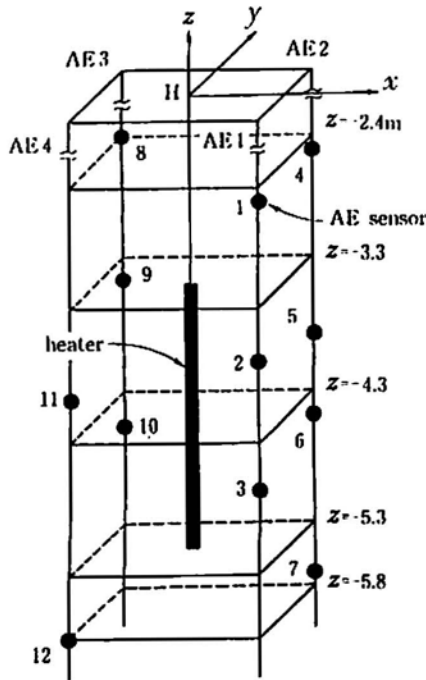


Fig. 2 Locations of the heater and AE sensors.

total maximum electric capacity of the heater are 90 mm, 2.0 m and 20 kW, respectively. The heater was embedded at the depth from 3.30 to 5.30 m below the surface in relatively homogeneous rock. The under-ground water level in the heater hole at the time of the experiment was 5.45 m below the surface. Twelve AE sensors were arranged in the four AE holes from 2.40 to 5.84 m below the surface, so as to surround the heated region three-dimensionally.

2.2 AE Monitoring Method

AE sensor is composed of a piezoelectric element and a brass case. The piezoelectric element has a disk shape of 10 mm in thickness and 30 mm in diameter, and is polarized in thickness direction. Its resonance frequency is 67 kHz. This element is attached to the bottom of the brass case, which is filled with silicone rubber for waterproofing. The outer diameter and height of the case are 40 mm and 34 mm, respectively. A pre-amplifier of 40 dB gain is also put into a brass case, and made waterproof as

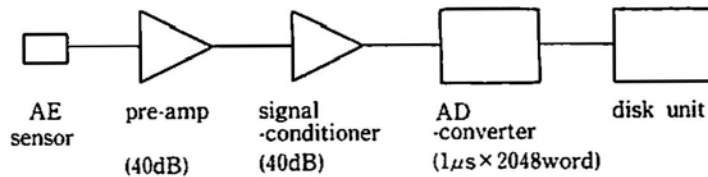


Fig. 3 Block diagram of the AE measuring system.

the AE sensor. The AE sensors and the pre-amplifier were fixed in wooden frames to coordinate them in desired positions of the bored holes and to direct the sensitive direction of each AE sensor normal to the axis of the heater hole. These wooden frames were buried in the holes with cement paste.

Figure 3 shows a block diagram of AE monitoring system. The system is composed of an AE sensor, a pre-amplifier, a signal conditioner, an A/D converter, and a disc unit. It can be equipped with twelve AE sensors at the same time. In this experiment, AE signal received at each AE sensor was amplified 80 dB (40 dB in the pre-amplifier and 40 dB in the signal conditioner). The A/D converter is of 8-bit resolution in the amplitude and of 2,048-word record length for each channel. The sampling time was one μ s and the pre-trigger point was set to be a half of the total record length. AE signals detected at No. 2 AE sensor, buried in AE1 hole, were chosen for the trigger of the A/D converter. Every time the A/D converter was triggered, twelve traces of AE signals received at twelve sensors were displayed. If P-wave arrival times were readable at more than five traces out of twelve, the data of full waveforms were transferred via GP-IB to the disc unit and stored on a floppy disc. It took about 6 s for the A/D converter to display the traces, about 18 s to transfer and store the data onto a floppy disc. Therefore, the undetectable duration corresponded to about 24 s if the data was recognized and stored onto the floppy disc, and about 6 s if the data was not stored. Because memory buffer of the floppy disc was 710 kbyte, 14 AE events (each event had 12 wave traces) could be stored in one floppy disc. Four floppy discs can be mounted in the disc unit and continuous monitoring was possible by replacing a filled disc. The frequency range of this AE monitoring system was 5 to 100 kHz.

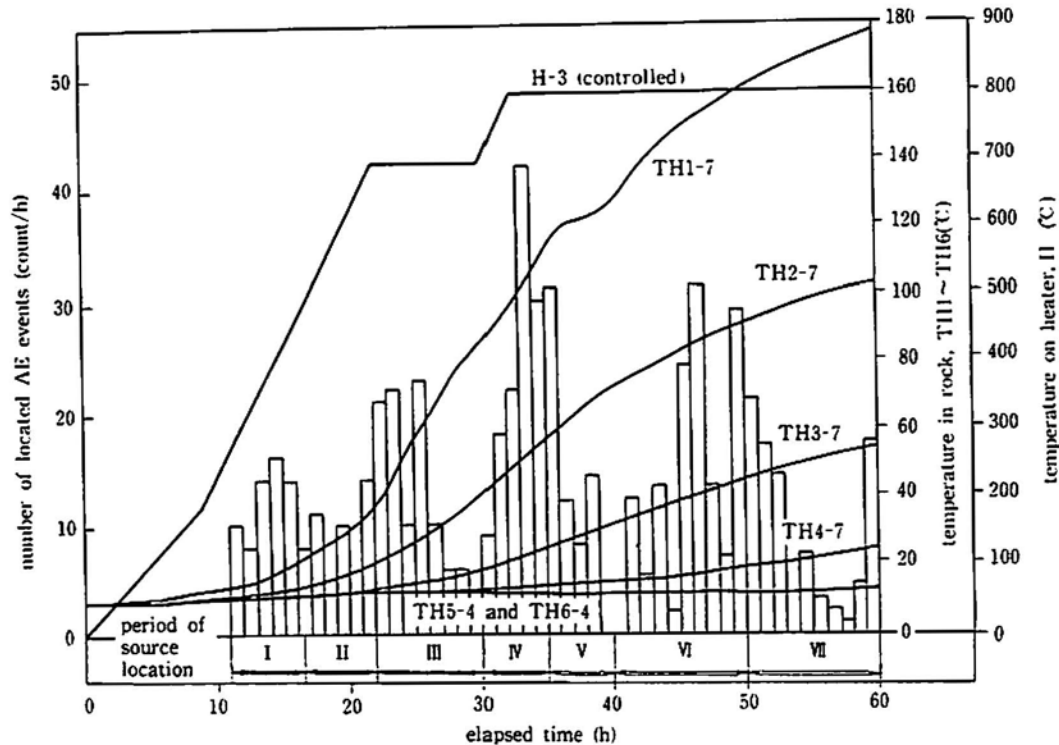


Fig. 4 Count rate of located AE events and temperatures of the rock and the heater at 4.3 m below the surface, the center of the heating range, as a function of elapsed time.

3. Results

3.1 AE Rate and Heater Temperature

Figure 4 shows AE count rate and temperatures of the heater and rock with time elapsed. The horizontal axis indicates hrs elapsed from the start of heating. The vertical axis indicates numbers of located AE events per hr and the temperatures measured on the heater and in the holes from TH1 through TH6 at 4.3 m below the surface. The scale for the heater temperature labelled by H3 is five times larger than those of rock temperatures, such as TH1-7, TH2-7 and so on. Roman numerals shown in the bottom of the graph indicate results of the source location mentioned in the next section.

The heater temperature was controlled by the following steps. The temperature was raised to 180°C over 9 hrs from the start of heating. However, AE activity was very low and the temperature was raised to 700°C over the next 13 hrs, and kept for the subsequent 8 hrs. Even at the end of this stage, AE did not occur actively. The temperature was then raised to 800°C (the heating limit of the heater) in 2-1/2 hrs and kept for the subsequent 27-1/2 hrs.

AE started to occur after 11 hrs of heating, when the heater temperature reached about 250°C. The maximum AE count rate per hr was recorded from 33 to 34 hrs, just after the heater temperature reached 800°C. After this time, AE activity decreased step by step, showing periodical increases and decreases of AE count rate.

3.2 Distribution of Located AE Sources

Figure 5 shows the distributions of located AE sources projected to the plain view (x-y plane) and two elevation views (x-z plane and y-z plane) for each period from No. I through VII indicated in the bottom of Fig. 4. In the right side of the figure, the geological section-views of the two elevation views are shown, determined from the observation of the cores taken from the heater hole and the four AE holes and from the

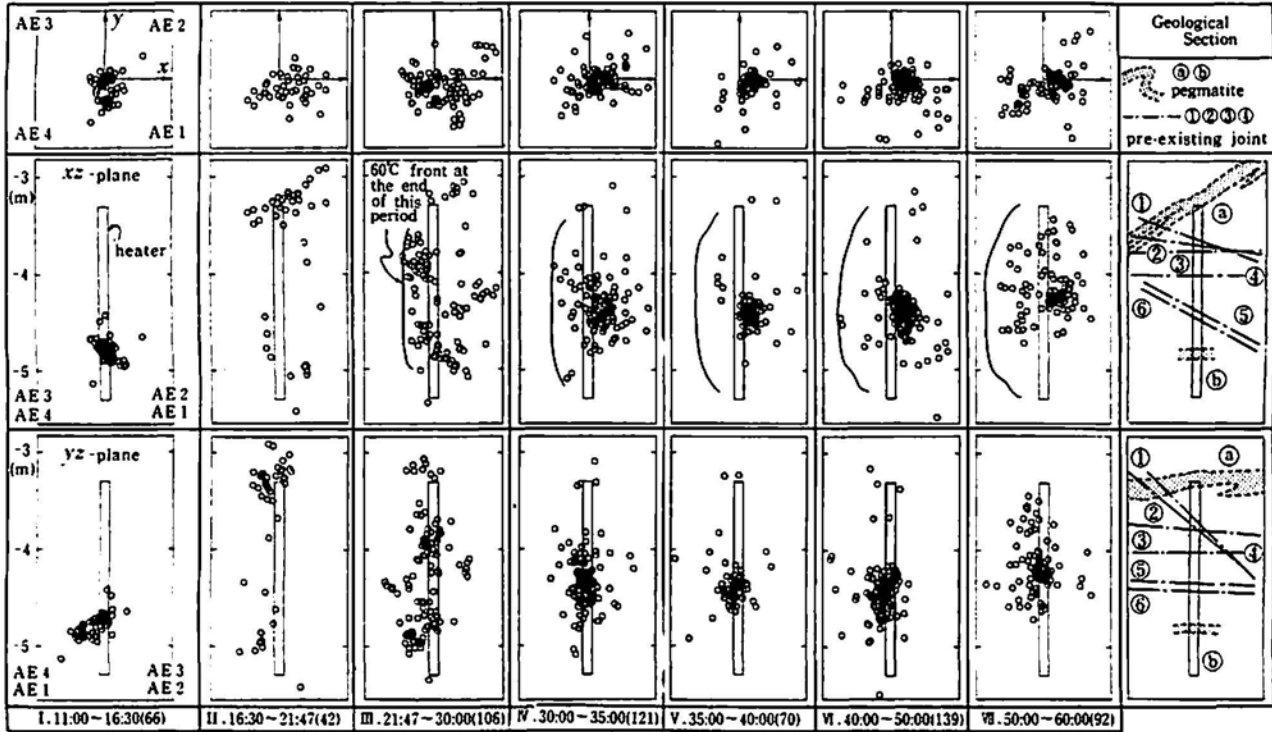


Fig. 5 AE hypocenters located in each period from I to VII and the geological view, projected to the plane view (x-y plane) and the two elevation views (x-z plane and y-z plane). In the bottom of each figure, the elapsed time and the numbers of located hypocenters are indicated.

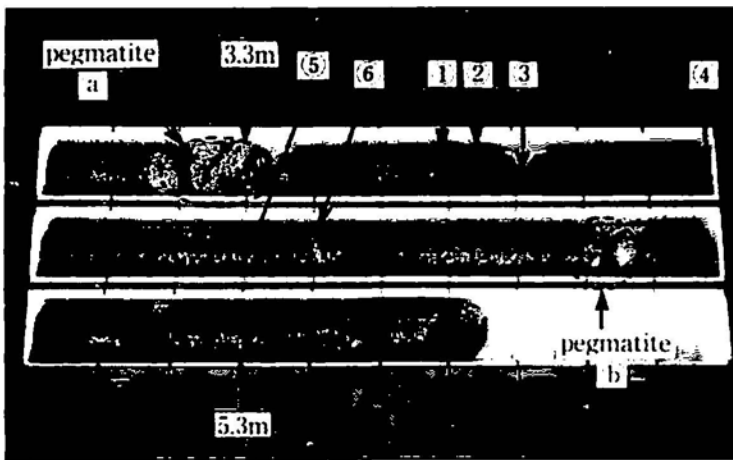


Photo 1 Core sample of the heater hole recovered from 3.0 to 5.65 m below the surface.

observation of the wall of the heater hole using a borehole television. The numerals in the bottom part of the figure indicate the elapsed time and the number of located AE events for each period. In the left side of the projection on the x-z plane for the periods from No. III through VII, 60°C temperature contour line was indicated, derived from the temperatures measured in the rock at the end of each period, which corresponds to 30, 35, 40, 50 and 60 hrs from the start of heating, respectively. The 60°C is the temperature at which AE starts to occur in granite, reported by Johnson et al. (1978), Yong and Wang (1980) and Ehara et al. (1983, 1986) in their laboratory experiments. It is noted that all AE sources are located inside the contour lines; in

other words, all AE occurred in the region whose temperature exceeds 60°C. It implies the results are consistent with the previous findings.

4. Discussion

In this experiment, AE started to occur at 11 hrs after the start of heating. At the period No. I (from 11 to 16-1/2 hrs), when AE started to occur, the located AE sources clustered around the heater hole at 4.8 m below the surface, which is the lower part of the heater. In the next period, No. II, they tended to cluster in the rock at 3.2 m below the surface near the upper end of the heater. Comparing to the geological section-views in the right side of Fig. 5, it is found that the clustered region at the period No. I corresponds to the location of the pegmatite vein (b) at 4.8 m below the surface, and that of the period No. II corresponds to mainly the location of the pegmatite vein (a) at 3.2 m.

Quartz and feldspar are main mineral compositions of granitic rock, but the coefficient of linear thermal expansion of quartz is from 1.5 to 4 times larger than that of feldspar (Skinner, 1966). As a result, with the increase of temperature, microcracks accompanying AE occur between quartz and feldspar. This is the reason why AE occurs in granitic rock with the increase of temperature.

Photo 1 shows a core sample drilled from the heater hole. The two white portions, (a) and (b), taken at 3.2 m and at 4.8 m below the surface, are the pegmatite veins. Although the pegmatite has the same mineral compositions as the surrounding normal granite, the particles are larger than those of the granite. When AE events were caused by microcracking between quartz and feldspar due to the increase of temperature, it is expected that the AE events are predominantly generated in a portion composed of large particles, or pegmatite. Among the pegmatite veins, AE events were observed in the pegmatite vein (b) earlier than in (a). This could be explained by the fact that the pegmatite vein (b) was closer to the center of the heater than that of the vein (a), and the temperature of the vein (b) increased earlier causing AE events.

In the period No. III, AE events clustered in the heater hole from 3.50 to 4.25 m (the center was at 3.90 m), and in the period No. IV, they clustered from 4.20 to 4.60 m (the center was at 4.40 m). In the period Nos. V to VII, clusters were observed in the same region as the period No. IV. In Photo 1, we can find four horizontal pre-existing joints indicated by (1) through (4), three of which are located from 3.55 m to 3.75 m and one is at 4.0 m. Two inclined pre-existing joints are indicated by (5) and (6) at 4.3 and 4.4 m and their dip angles are both about 30°. Comparing the distribution of located AE sources to the geological section view in Fig. 5, the locations of the joints from (1) through (4) correspond to the range from 3.35 to 4.25 m where the AE events clustered in the period No. III, and the locations of the joints (5) and (6) correspond to the range from 4.20 to 4.60 m where the AE events clustered in the period numbers IV to VII. These imply that AE events occurred along the pre-existing joint planes or very close to them, following the pegmatite veins. Thus, the mechanism of AE clustering along the pre-existing joint planes is as follows: Thermal stresses are released at the pre-existing joints, which have relatively low frictional resistance. This stress release causes microcracks, accompanying AE events in the rock near the pre-existing joints. In addition, pressurized water vapor emitted from the heated rock penetrates the pre-existing joints and further causes the microcracks accompanying AE events.

5. Conclusions

- (1) With the increase of rock temperature, AE started to occur in the pegmatite veins intruded into granite. Although the pegmatite has the same mineral compositions as the surrounding normal granite, the particles are larger than those of the granite. Main mineral compositions of granitic rock are quartz and feldspar. The coefficient of linear thermal expansion of quartz is from 1.5 to 4 times larger than that of feldspar. In the case that AE events were caused by microcracking between quartz and feldspar due to the increase of temperature, it is expected that AE events are predominantly generated in a portion composed of large particles. Therefore, it is reasonable that AE events began in the pegmatite, because

the particles of the pegmatite are much larger than those of the granite.

- (2) AE events occurred along the pre-existing joint planes or very close to them in the surrounding normal granite only after they occurred in the pegmatite veins. The mechanism of AE clustering along the pre-existing joint planes is predicted as follow: Thermal stresses are released at the pre-existing joints, which have relatively low frictional resistance, and the stress release causes microcracks accompanying AE events in the rock near the pre-existing joints. In addition, pressurized water vapor emitted from the heated rock penetrates the pre-existing joints and further cause microcracks accompanying AE events.

Acknowledgements

We would like to thank Messrs. T. Kanagawa and S. Sasaki of Central Research Institute of Electric Power Industry for their useful discussion throughout this investigation. We also thank Dr. Y. Kanaori of Gifu University for providing valuable comments on microfracturing mechanism of granite.

References

- S. Ehara, M. Terada, and T. Yanagidani (1983), "Thermal properties of stressed rocks", Proc. 5th Int. Cong. on Rock Mech., pp. E137-E140.
- S. Ehara, T. Yanagidani and M. Terada (1986), "AE and thermal expansion of Oshima granite during slow cyclic temperature change between 210 K and 370 K", Journal of the Society of Materials Science Japan, 35, 490-495. (in Japanese)
- B. Johnson, A. F. Gangi, and J. Handin (1978), "Thermal cracking of rock subjected to slow, uniform temperature changes", Proc. 19th U.S. Symp. on Rock Mech., No. 1, pp. 259-267.
- E.L. Majer, T.V. McEvilly and M.S. King (1981), "Monitoring an underground repository with modern seismological methods", Int. J. Rock Mech. Min. Sci. & Geomech. Abstr., 18, 517-527.
- E.L. Majer and T.V. McEvilly (1985), "Acoustic emission and wave propagation monitoring at the spent fuel test: Climax, Nevada", Int. J. Rock Mech. Min. Sci. & Geomech. Abstr., 22, 215-226.
- M. Ohtsu and K. Ono (1986), "The generalized theory and source representations of acoustic emission", J. Acoustic Emission, 5(4), 124-133.
- M. Ohtsu (1988), "Source inversion of acoustic emission waveform", Proc. of Japan Society of Civil Engineers, No. 398/I-10, pp. 71-79.
- M. Ohtsu, M. Shigeishi and H. Iwase (1989), "AE observation in the pull-out process of shallow hook anchors", Proc. of Japan Society of Civil Engineerings, No. 408/V-11, pp. 177-186.
- B.J. Skinner (1966), "Thermal expansion", in *Handbook of Physical Constants*, edited by S. P. Clark, Jr., Geological Society of America Memoir 97, p. 75.
- C. Yong and C. Wang (1980), "Thermally induced acoustic emission in Westerly granite", Geophysical Research Letters, 7, 1089-1092.

Using Acoustic Emission Testing in Seepage Investigations

Andrew R. Blystra

The authors are affiliated with A. R. Blystra and Associates, Ltd., 1481 Ring Road, Calumet City, IL 60409, USA.

Abstract

Using acoustic emission (AE) testing, we can locate the source or exit point of seepage through a dam, its foundation, or its abutments. This procedure can also be used to determine if seepage or groundwater flow is transporting soil particles. The typical AE test system used in seepage investigations consists of a sensor, an amplifier and a signal processor. The cable connecting the sensor is sealed to permit underwater usages. To obtain baseline data, laboratory testing was done to measure counts for clear flowing water and for flowing water which was transporting soil particles. A triaxial test cell was used to study flow at various velocities. Field calibration studies were made at several hydropower projects where seepage could be observed and measured. These field studies included several boils where upward groundwater flow was transporting soil particles. Based on laboratory testing and field calibration studies, it was found that 300 counts per minute represents a threshold indicating seepage. Seepage investigations have been conducted at several dams using AE testing. This method was successful in locating seepage entrance points in both earthen embankments and concrete structures. Testing also has been conducted in boreholes in earthen embankments and foundations where high seepage flows were suspected of transporting soil particles. Additional research is being conducted to provide a larger database for interpreting AE test results in seepage studies.

1. Introduction

Locating where water is seeping through a dam, its foundation, or its abutments has always been a difficult task for engineers and geologists. Once the source and the path have been identified, the seepage can be intercepted and stopped. Use of acoustic emission (AE) testing has proven to be a reliable technique for identifying the source of seepage and for evaluating whether the flow was transporting soil particles. The application of AE testing in seepage investigations is based on an understanding of the AE source and the interpretation of the data obtained in the field. Laboratory testing was conducted to provide baseline data for interpreting field information.

2. Theory and Technique

To apply AE monitoring in seepage studies, it is necessary to understand the AE source. A variety of AE sources generate a stress wave that has distinct properties. A few examples include a flowing fluid, the yielding of a material such as steel, large strains occurring in soils, and negative pressure or cavitation. The AE source in seepage is generated at the boundary layer between the flow and the concrete and soil. Another AE source can be the impacting of soil particles on the sensor if the flow is causing a piping condition whereby soil is being eroded.

A boundary layer exists in the zone of the flow in the immediate vicinity of a solid surface or boundary in which the motion of the fluid is affected by the frictional resistance of the boundary on the fluid. The boundary may be a solid such as concrete or it may be a soil such as gravel, sand, silt or clay. It has been shown that a no-slip condition exists between the fluid and the boundary at the contact surface. This requires

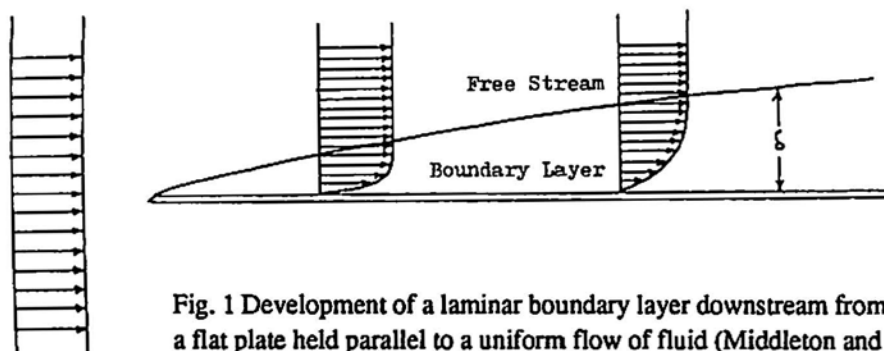


Fig. 1 Development of a laminar boundary layer downstream from the leading edge of a flat plate held parallel to a uniform flow of fluid (Middleton and Southard, 1984).

that the fluid velocity and the boundary velocity be the same at the contact. Therefore, the velocity is zero at the boundary contact. The boundary layer is the region of fluid next to the boundary across which the velocity of the fluid grades from zero at the boundary to that of the unaffected flow some distance away from the boundary.

As an example of a boundary layer that develops on the surface of a stationary flat plate is shown in Fig. 1 (Middleton and Southard, 1984). The plate in this figure is positioned in a uniformly flowing fluid. Immediately downstream from the leading edge of the plate, the boundary layer is thin and the shearing required by the transition from zero velocity to free-stream velocity is compressed into a very thin zone of strong shearing action. Near the leading edge the shear stress at the surface of the plate is relatively large. Farther downstream along the plate, the boundary layer is thicker, the shearing action is weaker, and the shear stresses at the surface of the plate is smaller. Placing the AE probe in a flowing fluid such as water is analogous to the plate in the example. However, in the case of the probe, the boundary layer not only is being developed along the probe, but it also is being developed along a concrete surface or a soil surface.

The boundary shear stress along the boundary layer provides the AE source for a flowing fluid. If the fluid, in this case water, is transporting particles, another AE source is present. The boundary shear stress is the shear stress which acts along the boundary and has a distribution as shown in Fig. 2. This figure also shows the distribution of the velocity from the boundary to the point where the velocity becomes the free stream velocity.

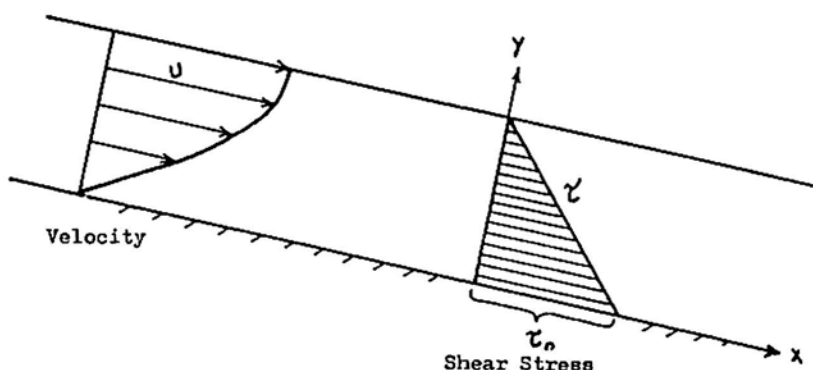


Fig. 2 Distribution of velocity and shear stress. in steady, uniform laminar flow along an inclined plane.

The basic resistance equation for steady, uniform flow along a boundary is:

$$\tau_0 = g \cdot RH \cdot \sin \phi \quad (1)$$

where τ_0 is the shear stress along the boundary, g is the weight per unit volume of the fluid, RH is the hydraulic radius and ϕ is the angle of inclination of the channel slope. Equation (1) is applicable to not only steady, uniform flows and to flows that are steady and uniform in a time-average sense, but also to flows

that show turbulent fluctuations in velocity. A shear stress also is developed as turbulent fluid flow occurs along a boundary. The resulting velocity profile for turbulent flow is different from the profile for laminar flow as shown in Figs. 3 and 4; however, both velocities cause a shear stress to develop, thereby providing an AE source.

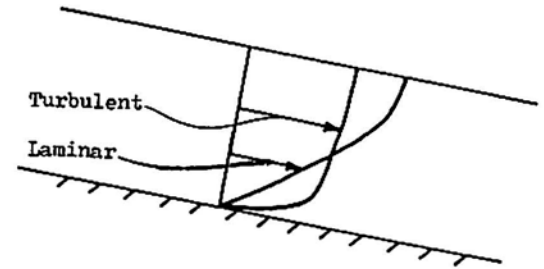


Fig. 3 Comparison of laminar and turbulent velocity profiles.

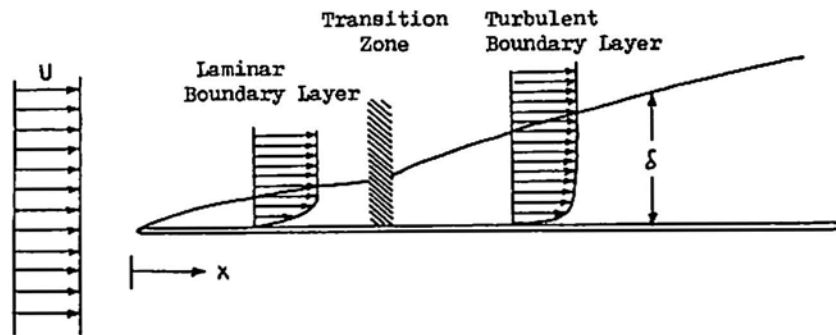


Fig. 4 Transition from laminar flow to turbulent flow in the boundary layer along a flat plate (Middleton and Southard, 1984).

At the location where water is seeping through an earth or concrete dam, the flow may be either laminar, turbulent, or a combination of the two. Regardless of the type of flow, shear stress along the flow boundary is occurring, and this stress provides an AE source. Measurements along the flow boundary with the AE sensor provides the means of locating and identifying the seepage problem. The flow boundary may result from either the sensor itself, which is analogous to placing a plate in the flow, or from the surface of concrete or soil.

To obtain as accurate record as possible of AE activity associated with seepage, other noise must be filtered out. This is especially important since the extent and severity of the seepage problem are related to the number of AE counts per unit of time. In general, the higher the counts, the more severe the seepage problem. At hydropower projects, several noise sources are present including those caused by the generating equipment and vehicular traffic. Since each type of noise source and associated stress wave has its own distinct properties, the various types can be differentiated and unwanted waves can be filtered out.

3. Equipment

The typical AE test system used in seepage investigations is composed of three elements: a sensor to detect the AE, an amplifier to boost the signal energy for transmission, and a processor to quantify the signal. All three elements are interconnected by a shielded cable. The connection between the sensor and the cable is sealed so that the sensor can be used underwater. Figure 5 shows the basic pieces of equipment that were used in these investigations.

The sensor can detect AE signals of about 30 kHz. This is the frequency found to be associated with the shear stress at the boundary layer. The amplifier boosts the signal, and the processor provides a digital read-out of the AE counts. A single channel system was used, since only one location along the boundary was being studied at a time. The length of cable varies depending on the depth of water at a particular site. The longest cable used between the sensor and the amplifier was approximately 35 m. If a longer cable is re

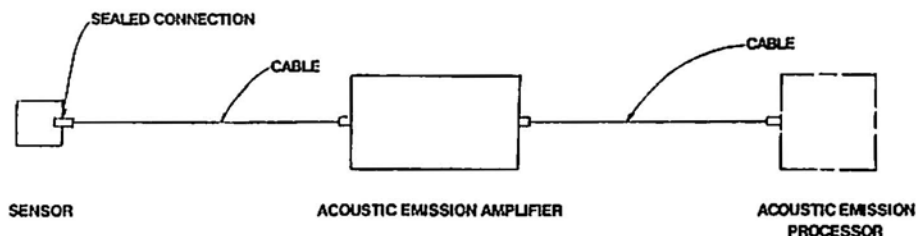


Fig. 5 The basic components used in the AE system for seepage investigations.

quired, the amplifier would have to be connected directly to the sensor to prevent the loss of a significant amount of signal.

4. Field and Laboratory Testing

To date over 100 field calibration studies have been made at approximately 20 locations where seepage could be observed and measured. AE measurements have been made on both the upstream and downstream sides of structures, at locations where water was flowing out of joints and fractures in rock formations, and at places where groundwater was flowing out of the ground. AE counts have been measured at active boils where seepage from a reservoir is flowing upward, exiting the ground, and transporting soil particles. Flow velocities at the boil locations were measured and then AE testing was conducted to obtain counts. For small boils having flow velocities of approximately 0.3 m/s, readings ranged from 500 to 900 counts/min. Very active boils having flow velocities of approximately 1 m/s yielded 3,000 to 12,000 counts/min. It was determined that the seepage velocity affected the number of counts. However, the amount of sediment being transported by the flow also affected the number of counts.

In laboratory studies, AE counts have been measured for clear flowing water and for flowing water which is transporting soil particles. For both cases, the flow rate was varied from 0.1 to 0.3 m/s. These flow studies were conducted in a triaxial test cell so that velocity could be controlled and visual observations could be made. Testing was done with the same equipment used in the field studies. The sensor was placed in the flow similar to the plate described in Middleton and Southard (1984).

After background noises were filtered in the laboratory, it was found that counts ranged from approximately 300 per minute for clear water flow at a rate of 0.1 m/s to over 10,000 counts/min for high velocity flow transporting soil particles. The transport of soil particles increases the count because soil particles impact against the sensor. The shear stress along the boundary also contributes significantly to the number of counts. The higher the velocity, the higher the shear stress along the boundary. The greater the shear stress, the higher the AE activities.

Based on the results of field calibration studies and laboratory testing, it appears that about 300 counts/min represents a threshold value indicating seepage. This value represents data obtained after background noise had been reduced or eliminated. Laboratory testing and field investigations are continuing so that additional baseline data can be used to correlate and quantify the results from individual sites.

5. Seepage Investigations

Seepage investigations have been conducted at several existing hydropower dams in the midwestern United States. The studies conducted at three projects are described to illustrate the technique and the results.

Project One

At the first project, it was necessary to prevent the fluctuation of the phreatic surface, or free water surface in the embankment. The upstream slope protection of the embankment consisted of a sloping concrete slab. This slab extended downward about 10 m where it joined vertical concrete core wall. Piezometer readings in the embankment indicated that water was seeping through this joint at various locations, resulting in higher than normal phreatic surface. The net effect of this condition was a reduction in the stability of the

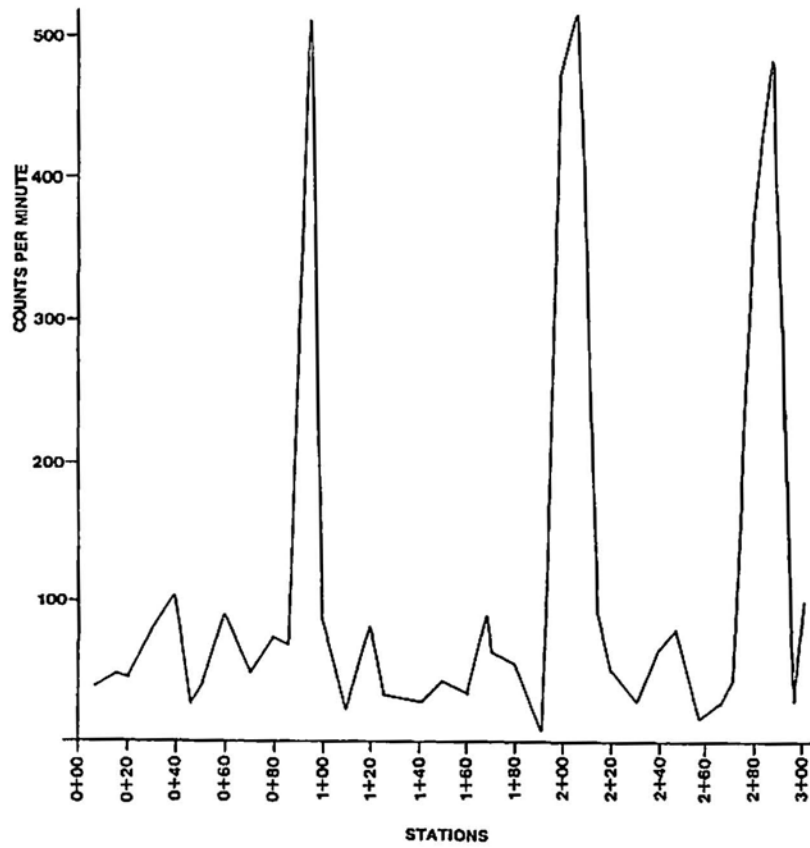


Fig. 6 Acoustic emission test results from Project One.

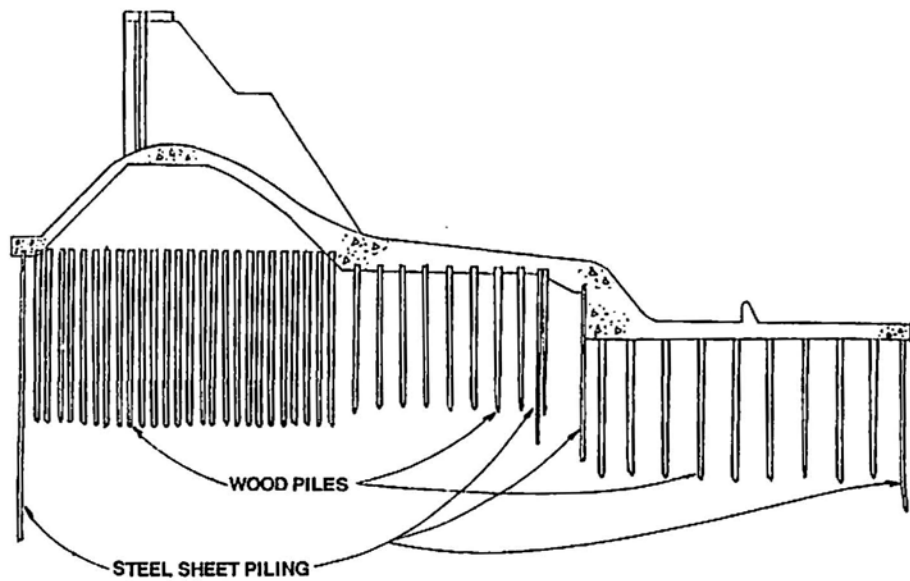


Fig. 7 Cross section of the spillway at Project Two.

embankment. As a first step in determining where seepage was occurring through this joint, AE testing was conducted along the entire length of the joint. Figure 6 shows some of the test results. The high count areas along the survey line were interpreted as probable seepage locations. Once these locations had been identified, electrical resistivity and salt tracing was used to confirm the seepage. The next step was to seal the joint where it was open and to eliminate the seepage.

Project Two

During the installation of piezometers to measure the uplift beneath the spillway at this project, it was discovered that water was flowing beneath the concrete. Additionally, voids were found beneath the spillway ranging from 4 to 10 cm. It was necessary to identify the seepage path so that the flow could be intercepted and the piping potential reduced. It was apparent that the seepage beneath the spillway had transported soil resulting in the voids. The cross section of the spillway at this project is shown in Fig. 7. The upstream and downstream sheet pile cutoff walls should have prevented flow beneath the structure. It was suspected and later confirmed using AE testing that the sheet piling on the upstream side was not completely embedded in the concrete. Acoustic emission counts were obtained along the entire length of the upstream along downstream sides of the spillway. The results showed high count areas. An underwater inspected later confirmed that the piling was not embedded along the entire upstream length and flow was coming beneath the structure at that location.

Project Three

At the third project, very loose, saturated soil was encountered in a boring adjacent to the powerhouse. During a foundation exploration program, the drill rods dropped approximately 3 m under their own weight. The loose, saturated soil was in an area where seepage had been observed for many years. Since no soil was recovered in the sampling spoon at this location, it was suspected that piping was occurring. This happens when water flowing through the embankment picks up soil particles and transports them, resulting in the development of a void. The AE sensor was lowered into the drill hole. Testing was conducted in the very loose zone where seepage and piping was suspected. In all tests, the counts were relatively low, much lower than the counts obtained during the field tests of boils. AE testing confirmed that seepage occurring, but that there was no active piping.

6. Conclusions

Acoustic emission testing can be used successfully in seepage investigations, especially to locate the origin of a seepage path and identify piping. Additional laboratory testing and field verification are needed to provide a greater database for interpreting results. To be accurate, AE investigations for seepage must eliminate as much background noise as possible. AE testing should be used in conjunction with other methods such as electrical resistivity, salt tracing, and ground penetrating radar to confirm results.

References

Gerard V. Middleton and John B. Southard (1984), "Mechanics of Sediment Movement", Lecture Notes for Short Course No. 3, Eastern Section of the Society of Economic Paleontologists and Mineralogists, Providence, Rhode Island, March.

American Society for Testing and Materials (1972), *Acoustic Emission*, STP 505, eds. R.G. Lipati et al., Philadelphia.

American Society for Testing and Materias (1975), *Monitoring Structural Integrity by Acoustic Emission*, STP 571, ed. J.C. Spanner and J W. McElroy, Philadelphia.

Acoustic Emission of Penetration Experiments to Judge Soil Condition

S. Naemura, M. Tanaka, S. Nishikawa, M. Nakamura,
K. Jo and T. Kishishita

S. Naemura and M. Tanaka are affiliated with Public Works Research Institute, Ministry of Construction, S. Nishikawa is with Chugoku Region Construction Bureau, Ministry of Construction, M. Nakamura, K. Jo and T. Kishishita are with Technical Research Institute, Fujita Corporation, Ohtana 74, Kohoku, Yokohama 223, Japan.

Abstract

This study was carried out to examine the applicability of acoustic emission (AE) to judge the ground soil condition for the boring of small-diameter holes. Four soil samples were put in a tank in compact or loose condition. A rod equipped with an AE sensor was pushed into the soil sample at a specified speed.

Results showed that AE activities and amplitudes of AE signals were markedly different according to the soil type and packing condition, compact or loose. The frequencies of AE signals from compact soil were different from those of AE observed in loose soil.

1. Introduction

When a small-diameter pipe is pushed into soil, the pushing force depends on the soil condition at the working face. However, it is normally difficult to know the soil conditions and in most cases the pushing force is controlled through engineers' experience. Therefore, we need a method to estimate the soil conditions such as those using a sonic detector or other instruments, but these are still unsatisfactory.

This report shows the results of penetration tests where frictional sounds of soil particles were detected by an acoustic emission (AE) sensor while the small-diameter pipe was being pushed. The applicability of the AE measurement is examined.

2. Outline of Test Method

Figure 1 shows a schematic view of the test device. The test device comprises of a 90 cm-cubic box, a penetrating rod with an AE sensor installed at one end, a hydraulic cylinder, a displacement gauge as a position sensor, a load cell, and a loading frame. The AE sensor detects AE while the rod is penetrating into soil. The hydraulic cylinder allows the rod to penetrate into the soil at a specified rate. In the test, soil was prepared into the box at the depth of 70 cm under two different conditions: compact and loose. Soil samples used in the test were sand, clay, gravel, and mountain sand. Table 1 shows physical properties of these samples.

The AE sensor detects weak sounds generated while the rod is pushed into the soil. Table 1 also shows the measuring condition. The amplification is set at 60 dB for all samples. The threshold is set as indicated in this table, depending on the AE activity. The sensor was installed as shown in Fig. 2. The penetrating rod comprises of a cone section, a rod section and an outer pipe. The rod section and the outer pipe form a double pipe with rubber packing-material placed between them to prevent noises from the outer pipe.

Tests were carried out after soil was packed compact or loose for each sample. The compact condition means that the maximum dry density is 85 % or more, while the loose condition implies that soil is put into the box by free fall from 1 m above the box. The penetrating speed was 10 or 20 mm/s. The rod was pushed twice in each test.

Table 1 Physical properties and measuring condition.

Soil Sample	Maximum dry density, g/cm ³	Optimum moisture content, %	Specific Gravity	Particle size at 50%, mm	Threshold, V	
					Loose	Compact
Clay	0.795	75.7	2.71	0.04	0.1	0.3
Coarse Sand	1.63	16.5	2.77	0.18	0.3	1.0
Fine Sand	1.64	0.235	2.67	0.3	1.0	1.0
Gravel	1.69	1.85	2.63	15	0.3	0.3

3. Results of Testing

The data of total AE counts and maximum signal amplitude indicates that the AE counts are higher in the case of compact soil than that of loose soil. The AE counts are smaller at penetrating speed of 20 mm/s than at 10 mm/s. When the rod is penetrating too fast, AE events overlap and the AE monitoring system cannot recognize AE signals separately. In such a case, the number of AE counts might be less than the actual number. Therefore, data obtained by the tests of 10mm/s penetrating speed will be mainly discussed.

Figure 3 shows the AE amplitudes detected in soil samples. The vertical axis shows the maximum amplitudes while the rod is penetrating into the sample. The amplitudes for gravel are the largest of all and between 1.6 and 2 V. The amplitudes for sand and mountain sand stand between 0.4 and 0.8 V. It implies that AE amplitudes depend on the particle size of the sample. Figure 4 shows the relation between total AE counts and the particle size (in the logarithmic scale), which exceeds 50 % of the sample soil. The total AE counts increase with the particle size. As the threshold level was varied for each sample, it is difficult to compare directly among different samples based on the AE counts. However, if the threshold level for gravel or sand were set as low as that for clay and mountain sand, AE counts are expected to be higher and better correlated with the particle size.

As AE events and counts are obtained with a different threshold level for each sample soil, it is difficult to judge the quality of soil only from AE counts and amplitude. Therefore, we recorded AE waveforms and carried out the spectrum analysis of the waveforms by using an FFT analyzer. Figures 5 and 6 show the frequency spectra of the AE waveforms, which were detected from sample soils. Figure 5 shows the spectra when the soil is compact and Fig. 6 shows those when the soil is loose. For compact clay, mountain sand, sand and gravel, the dominant frequency was 850 Hz, 800 Hz, 3.65 kHz and 850 Hz, respectively. For the loose case, the corresponding dominant frequencies were 100 Hz, 100 Hz, 3.30 kHz and 3.35 kHz. For compact samples, the spectra for clay and mountain sand seem to be different from those of sand and gravel. For loose samples the spectra are again different between the cases of clay and mountain sand and those of sand and gravel. In both cases, spectra around 6.0, 11.0, 15.0 and 19.0 kHz were similar. This may be attributed to the influences of characteristic frequencies for the rod in the penetrator.

4. Conclusion

We conducted tests using samples whose qualities were very different from one another. The penetration tests were carried out in two different conditions: when the sample was compact and when it was loose. From the results of these tests, we concluded that different kinds of soil show different AE counts, amplitude and spectra, which are due to the soil characteristics.

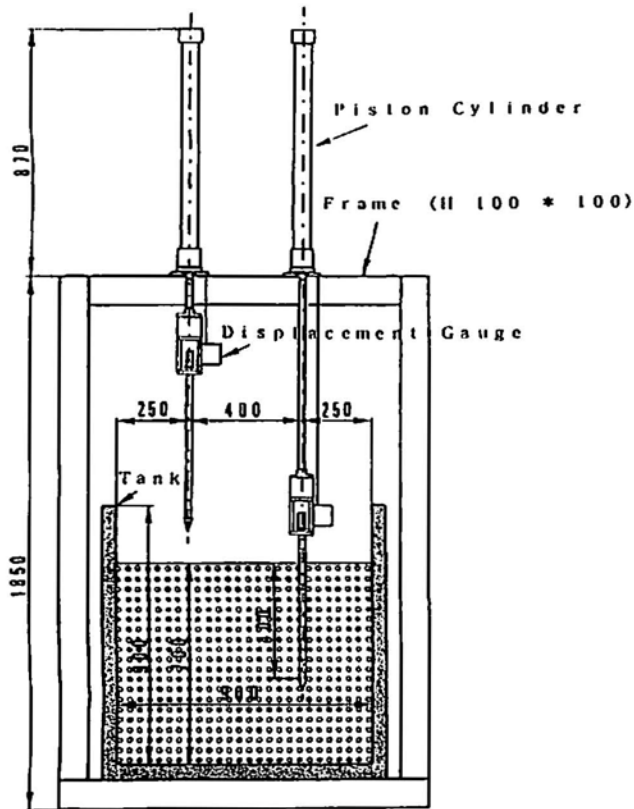


Fig. 1 Schematic view of experiment.

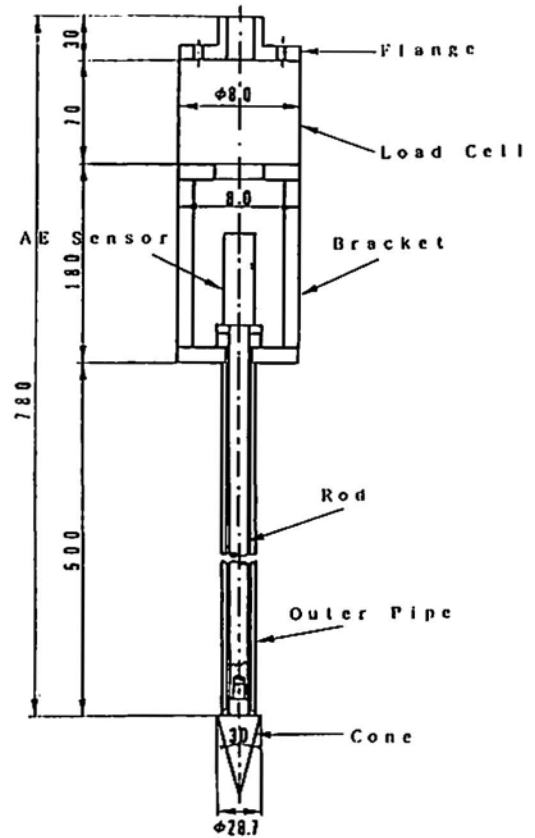


Fig. 2 Schematic view of penetration rod.

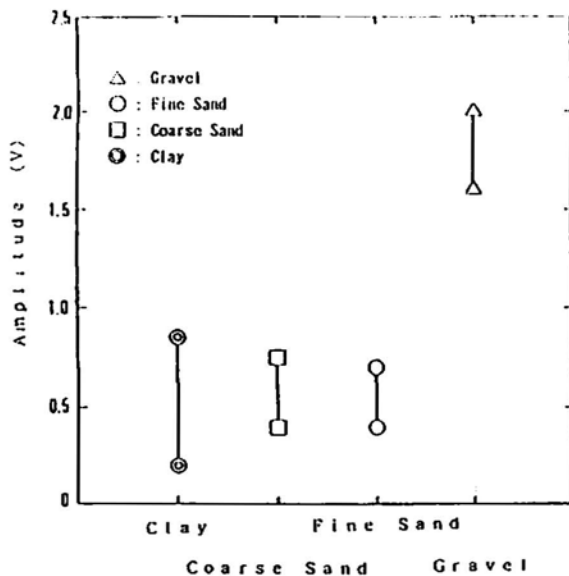


Fig. 3 The AE amplitude according to the soil samples.

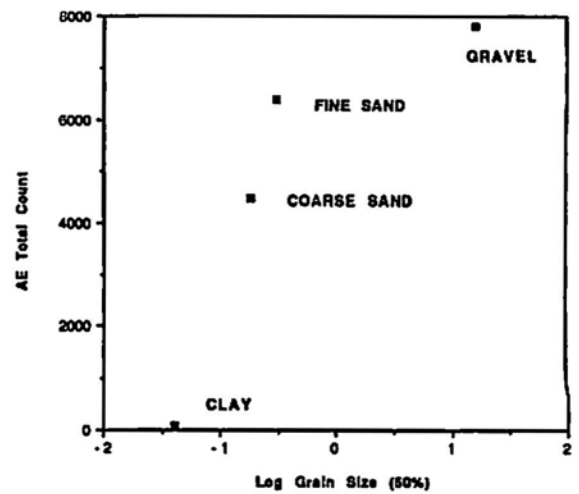
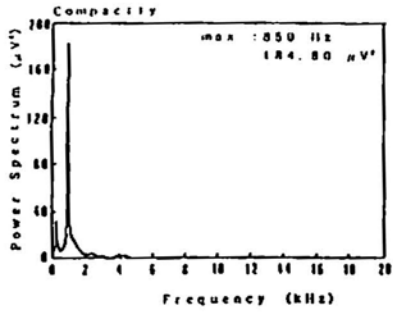
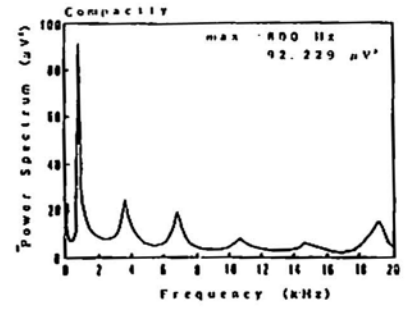


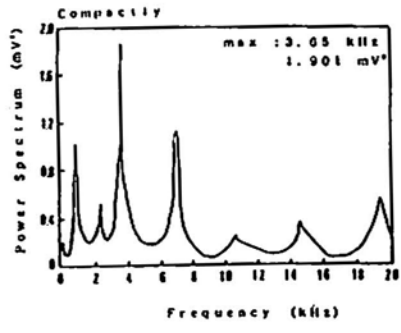
Fig. 4 The total count according to the grain size.



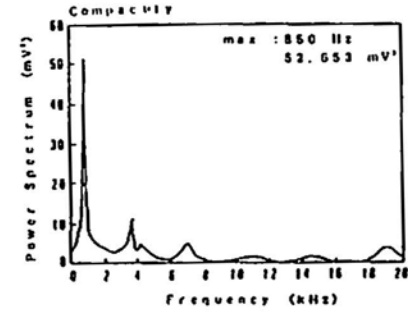
Power Spectrum (Clay)



Power Spectrum (Coarse Sand)

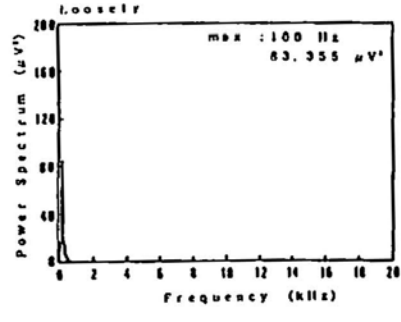


Power Spectrum (Fine Sand)

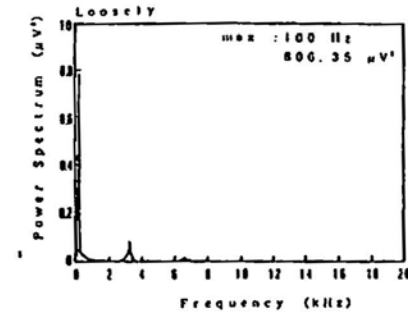


Power Spectrum (Gravel)

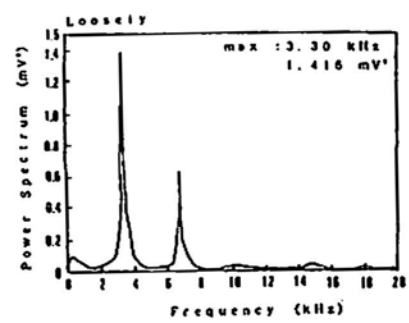
Fig. 5 Power spectra (compact).



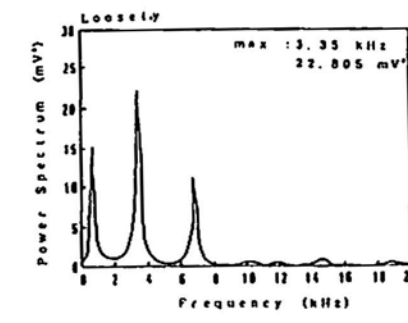
Power Spectrum (Clay)



Power Spectrum (Coarse Sand)



Power Spectrum (Fine Sand)



Power Spectrum (Gravel)

Fig. 6 Power spectra (loose).

A Laboratory Investigation of AE from Coal

R. W. Harris, B. R. A. Wood and T. Flynn

The authors are affiliated with CSIRO Division of Geomechanics, Lucas Heights Research Laboratories, PMB 7, Menai 2234, Australia.

Abstract

A laboratory investigation was carried out to study the acoustic emission (AE) generated by sized coal samples. The samples were stressed by crushing using a special mandrel in a tensile testing machine. Large sized coal samples were crushed and a specific size range was obtained using metal sieves. Some of the sized samples were then separated according to the percentage of ash using standard float/sink techniques. A predetermined mass of coal was placed in a special mandrel to which AE transducers were attached, and as the coal was crushed data was acquired. A range of AE parameters computed from the acquired data were plotted as a function of load and also as a function of ash content for given loading conditions. The graphs for AE parameters as a function of load indicated the loading region where most energy release associated with crushing was occurring. The graphs of AE parameters as a function of ash content indicated that there was a value for the percentage of ash where the maximum energy release occurred on crushing.

1. Introduction

Most investigations on AE from coal have considered the behavior of underground coal seams under stress (McCabe, 1979), but this investigation considers another aspect of the total coal mining industry, namely how the coal behaves during crushing which is important for the processing of coal to obtain a homogeneous product with a specific amount of ash (material left after combustion).

Most of the laboratory investigations on crushing of coal have been concerned with the determination of the strength of coal and the size distribution that occurs as a result of the comminution process (Bennet, 1937; Bennett et al., 1941; Brown, 1941; Pomeroy, 1957). The conclusions of most of this work as well as producing plausible distribution laws for coal sizing after breakage, are that coal is

- (i) a heterogeneous structure where the cohesive forces between grains is small compared with the forces required to fracture grains,
- (ii) the grains are quasi-homogeneous,
- (iii) fracture and cracking occurs at points where the material is weakest and all indications are that a lump of coal contains preformed cracks and fissures, and
- (iv) a particle of coal fractures to form aggregates.

There has been a laboratory investigation not specifically using coal but considering the comminution process in a cone crusher and using AE to identify the operations in the crusher (Harrington et al., 1980).

2. Experimental Arrangement and Procedures

Samples of coal having ash contents in the range 5 to 33% were obtained from different coal mines in Australia. After coarse crushing the samples were sieved so that the larger particles would not pass through a 2.4 mm mesh and the smaller particles would pass through a 1 mm mesh. The samples were then separated according to ash content using the float/sink method. This method utilizes the fact that there is a simple relationship between the percentage of ash and the density of the coal. A mass of 5 g of the samples was

placed in a mandrel comprising a shallow piston and cylinder which was placed in an Instron testing machine driven at a crosshead speed of 0.025 mm/min. The mass forms only a single layer of coal particles between the faces of the mandrel. The mandrel assembly was mechanically isolated from the tensile machine using teflon sheets.

Two different transducers (a B&K 8301 accelerometer (sensor 1) which has a resonant frequency around 25 kHz and a usable frequency range from 1 to 8,000 Hz, and a B&K 8313 AE transducer (sensor 2) which has a resonant frequency around 200 kHz) were coupled to the mandrel cylinder using silicone grease. The detected signals were amplified 40 dB in preamplifiers and a further 30 dB in main amplifiers. The signals were observed using a digital oscilloscope and also passed to the SIROEAR unit (Harris, and Wood, 1984) for the determination of peak amplitude statistics.

The first group of experiments increased the load in 1 to 2 kN steps for sized only samples of coal. The second group of experiments acquired data from coal samples having different amounts of percentage ash for a specific load increment in a sensitive region as determined from the first group of experiments.

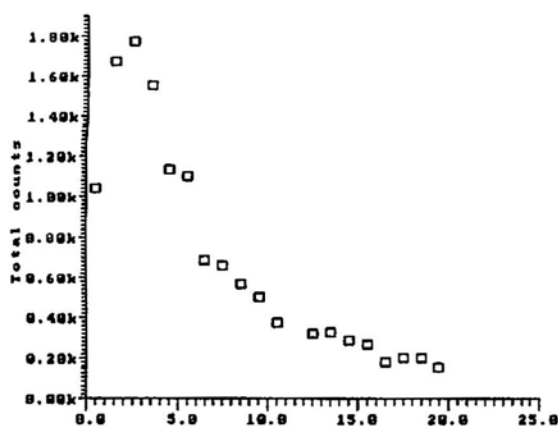


Fig. 1 AE counts/1 kN increment as a function of load for the sensor 1.

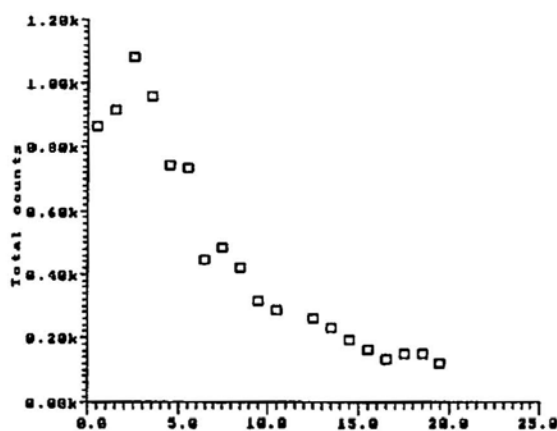


Fig. 2 AE counts /1 kN increment as a function of load for the sensor 2.

3. Results and Discussion

Various AE parameters were compared to determine those most sensitive to changes in coal characteristics and crushing regimes. The final choice of parameters were the total AE counts and three quantities derived from the SIROEAR peak distribution; namely, indicative energies 1 and 2 and the skew (Wood and Harris, 1986). These parameters are related to the zeroth, first, second and third order moments of the distribution of peak amplitudes.

Figure 1 gives the counts per 1 kN increment of load for sensor 1 and Fig. 2 for sensor 2 for a sized only sample. It is apparent that there is a peak at about 3 kN. This effect is not surprisingly most pronounced for sensor 1 since it has the best low frequency response. (In subsequent figures, only sensor 1 data will be given.) The peak at 3 kN was also apparent in the plots involving indicative energies 1 and 2 and the skew as given in Figs. 3 - 5. The effect is most pronounced for indicative energy 2 indicating an increase in the large amplitude pulses. The 3 kN peak in the AE responses corroborates the earlier finding that coal fractures along the existing cracks in a brittle manner into many small aggregates. After that initial large fracturing, there will be only smaller releases of energy since the fracturing is now associated with the smaller aggregates.

The results for AE as a function of ash content are given in Figs. 6 - 9. The count rate and indicative energy 1 were most sensitive to the effects of changing ash content. This indicates that the best discrimination occurs when the chosen parameter does not give a greater weighting to the larger amplitude pulses. Several sets of data were available for low ash contents and the plots show the scatter that may occur for

this data. The existence of a peak in the plot is considered to be associated with the structure of coal and the way that the ash is bonded into that structure so that most energy release occurs at an ash content near 10%.

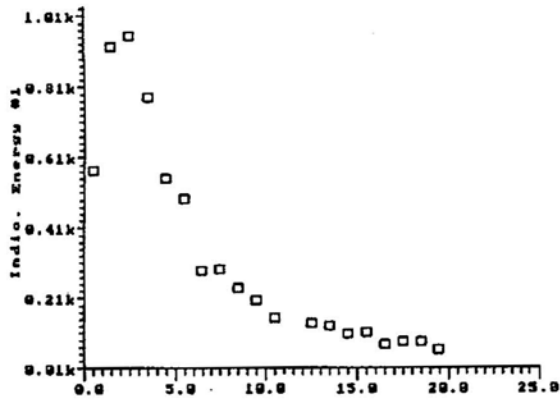


Fig. 3 Indicative energy 1/1 kN increment as a function of load.

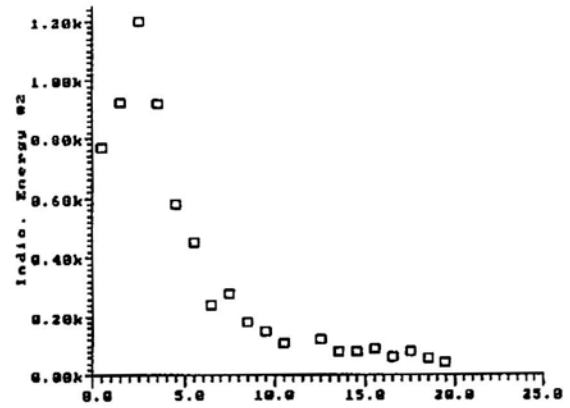


Fig. 4 Indicative energy 2/1 kN increment as a function of load.

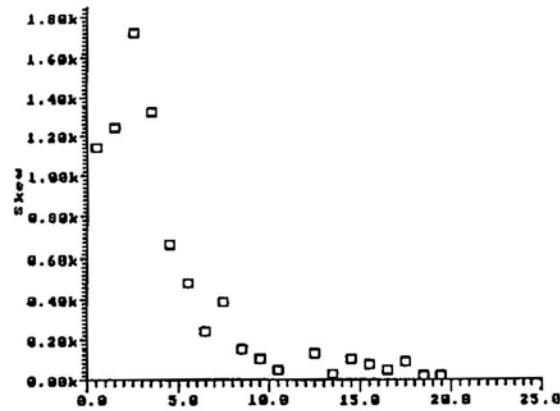


Fig. 5 Skew/1 kN increment as a function of load.

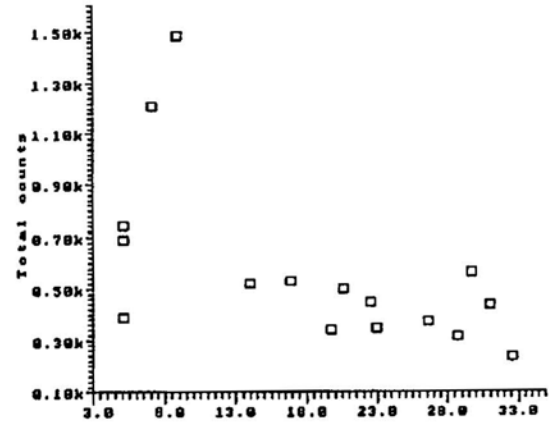


Fig. 6 AE counts as a function of % ash.

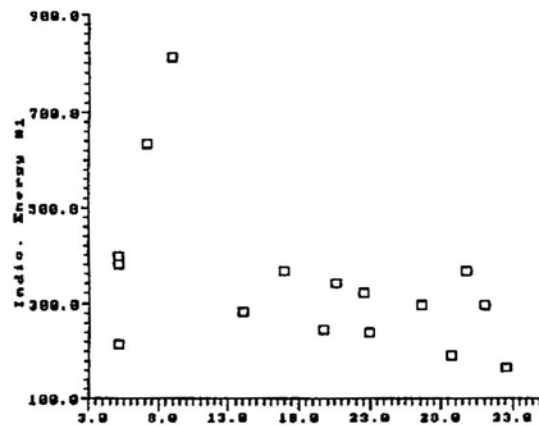


Fig. 7 Indicative energy 1 as a function of % ash.

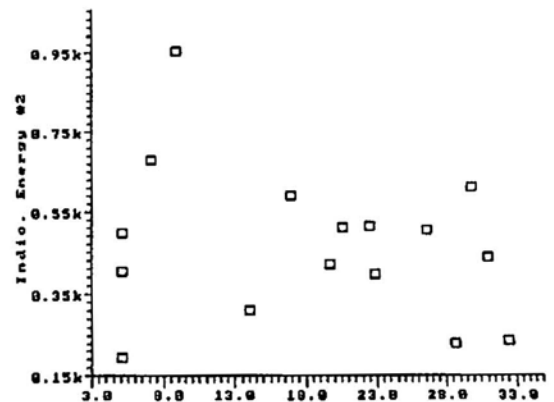


Fig. 8 Indicative energy 2 as a function of % ash.

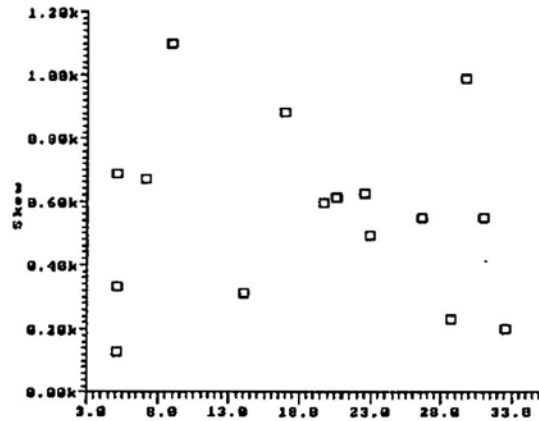


Fig. 9 Skew as a function of % ash.

4. Conclusions

AE provides information on the crushing of coal in laboratory relating to the load at which maximum fracture occurs for a given sample of coal and to the ash content associated with the maximum energy release on fracturing. The best sets of data were obtained using a sensor responding in the low frequency ranges.

References

- J.G. Bennett (1937), "Broken Coal", *J. Inst. of Fuel*, **10**, 22-39.
- J.G. Bennett, R.L. Brown, and H.G. Crone (1941), "Broken Coal II-The relation between size distribution and breakage process", *J. Inst. of Fuel*, **15**, 111-128.
- R.L. Brown (1941), "Broken Coal III - the Generalised Law of Size Distribution", *J. Inst. of Fuel*, **15**, 129-134.
- C.D. Pomeroy (1957) "A simple method for the Assessment of Coal Strength", *J. Inst. of Fuel*, **31**, 50-54.
- N.M. McCabe (1979) "Acoustic emission in coal", Ph.D. thesis, University Microfilms.
- T.P. Harrington, P.G. Doctor, and K.A. Prsbrey (1980), "Analysis of the Acoustic Emission Spectra of Particle Breakage in a Laboratory Cone Crusher", *Trans. Soc. Mining Eng. of AIME*, **270**, 1879-1883.
- R.W. Harris, and B.R.A. Wood (1984) "Acoustic Emission event counting using an Apple computer", *Progress in Acoustic Emission II*, JSNDI, Tokyo, pp. 351-358.
- B.R.A. Wood, and R.W. Harris (1986), "Acoustic Emission applied to railways", *Progress in Acoustic Emission III*, JSNDI, Tokyo, pp. 125-135.

Determination of the Initial Stresses on Rock Mass using Acoustic Emission Method

K. Michihiro, K. Hata, H. Yoshioka and T. Fujiwara

K. Michihiro is affiliated with Department of Civil Engineering, Setsunan University, K. Hata, H. Yoshioka and T. Fujiwara are with Research Laboratory, Ohbayashigumi, Shimokiyodo 4-460, Kiyose, Tokyo 204 Japan.

Abstract

Large scale underground cavern such as underground power stations and oil storages, could be designed and constructed rationally, if the initial stresses of the site are known. Authors have carried out fundamental studies on the detection of the initial stress using the Kaiser effect by which the stress history of rock could be estimated. In this study, characteristics of the Kaiser effect on the rock material have been investigated experimentally. It has been found that the (1) most rocks show that Kaiser effect phenomena; (2) stress determined from the Kaiser effect is not always identical to the maximum stress of the rock; and (3) Kaiser effect is dependent on the time period of unloading of stress.

1. Introduction

When subjected to applied stress, one part of the stored energy in the material is released in the form of the elastic waves, called acoustic emission (AE) and could be a powerful tool in assessing the mechanical change of internal characteristics in the material. Ultrasonic waves have been utilized for non-destructive testing of materials, in which waves are transmitted through the material and the characteristics of reflected waves are used to study the behavior of the material. On the other hand, AE method utilizes the waves due to the defect generated by loading. Its use is found in various fields, such as atomic reactors, pipelines, bridge structures, airplanes, etc. AE method has caught attention of civil engineers, especially, in the field of geotechnical engineering and rock mechanics. A state-of-the-report is already published on the application of AE methods in the field of geotechnology and rock mechanics (Hardy, 1981).

Once the initial stresses are determined accurately, rational design and construction of large caverns, such as underground power station and oil storages, could be accomplished. Further, the shape, location and selection of the layout can readily be determined (Hoek and Brown, 1980). By using finite elements methods (FEM), it is possible to analyze the stability of a structure. Referring to the initial stresses as one of the parameters, rational and economical design can be carried out. In addition, rock burst phenomena can be predicted. For the determination of the initial stresses, over-coring method (Sugawara et al., 1986; Kanagawa et al., 1986) and hydraulic fracturing method (Mizuta et al., 1983) have been currently in use.

Kaiser (1953) developed AE method to study material properties using tension tests of metals and found the Kaiser effect. Rusch (1959) and Goodman (1963) found the Kaiser effect in concrete and rock, respectively. Goodman's results suggested that initial stresses can be determined in rock. Kanagawa et al. (1977) first determined the initial stresses on rockmass using AE method. Kanagawa (1977) used rectangular specimens and estimated the initial stresses. Yet, many aspects of the Kaiser effect have not been clarified. Yoshikawa et al. (1981) used repeated loading on the specimen and found that there exists remarkable difference in the Kaiser effect if the specimens have different loading histories. The relation between the residual stresses and the Kaiser effect has been studied by Murayama (1984, 1985, 1986) and Michihiro (1985a, b).

In the present study, the influence of various parameters on the Kaiser effect in rock is discussed. Then, using AE method the feasibility of determining initial stresses has been examined.

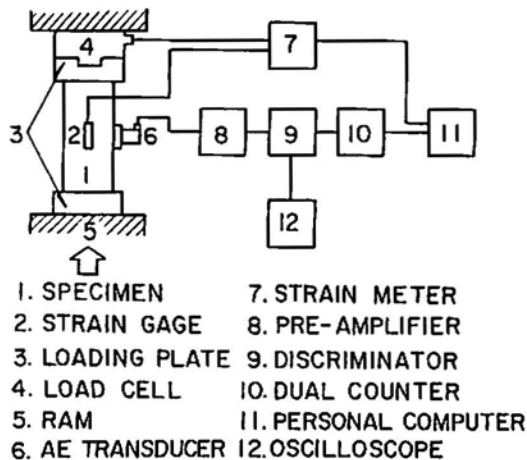


Fig. 1 Block diagram of AE measuring system.

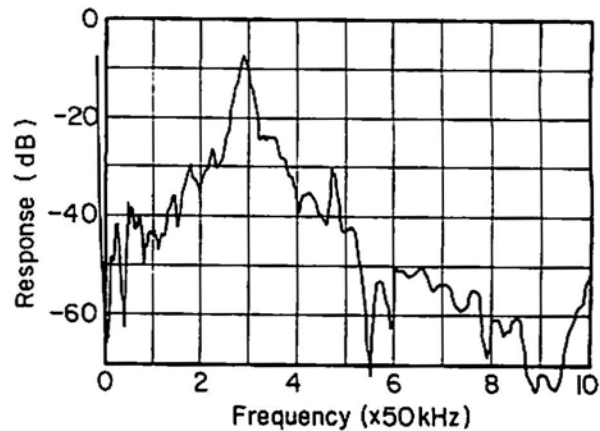


Fig. 2 Spectroscopic characteristics of transducer.

2. Experimental Equipment and Rock Samples

An outline of AE measurement system is shown in Fig. 1. AE system consists of a transducer, an amplifier, a discriminator and a counter. Resonance frequency of the PZT transducer was 140 kHz and was fixed by a silicone adhesive to the center of the specimen. In the case of a cylindrical specimen, the transducer was attached via a 3 mm thick stainless steel jig (Fig. 1). A band-pass filter (100 - 200 kHz) matched the frequency response characteristic of the transducer shown in Fig. 2. In the present study, the event counting method has been utilized to measure the AE signal occurrence. A fixed threshold level was generally used. To minimize the effect of reflected waves, two threshold levels, high and low, were also employed.

Several loading machines have been utilized. They are an Amsler-type universal tester (max. loading capacity 2 MN); a high stiffness testing apparatus (max. loading capacity 1.5 MN with 7 GN/m stiffness); a triaxial compression tester (max. axial loading 0.1 MN, confined stress 10 MPa) and a creep tester (max. loading capacity 14 kN). Accumulated AE counts and the stress-strain curves obtained from these tests were processed by a micro-computer.

One of the problems in the event counting is the discrimination of noise which results from various electronic instruments and the outside. The effect of the noise can be minimized to a greater degree by using proper grounding. Another source of the noise generation could be the gap between the loading plate and the sample. The noise due to this effect could be removed by various means. For example, Kanagawa et al. (1977) used a mixture of cement and araldite called hunch and pasted it on the top of the surface of the specimen. The use of blotting paper can also reduce the noise. Authors have used a relatively simple method to minimized the noise due to the gap, using a sponge pad with air bubbles.

Many samples were prepared. The cylindrical samples had the following dimensions; the diameter: 30 or 50 mm, the height: 60 or 100 mm. The cubic samples have the edge dimensions of 50 mm or 150 mm. Table 1 shows the various rock types used in the experiment with their original location, related project and the mean values of the unit mass and the unconfined compressive strength. Except for mud stone, all rock types (ranging from medium to hard rock) were loaded at the rate of 9.8 MPa/min, whereas, the mud stone specimens were loaded at the rate of 0.98 MPa/min. The results reported here are based on the experiments carried out at least five different times on the specimens of the same rock type.

3. Evaluation Method of the Kaiser Effect

Using mortar and rock specimens, Kanagawa et al. (1977) carried out basic experiments to study the Kaiser effect. They recognized the presence of the Kaiser effect due to the rapid increase in the AE accumulated count rate as shown in Fig. 3. When two rapid increases in the AE count are observed, it is difficult to recognize the Kaiser effect. In order to recognize the previously applied stress or Kaiser stress in such cases, we used the following observation; i.e., the AE energy (maximum amplitude) observed before the Kaiser stress is reached has a lower value than that observed above the Kaiser stress. Various combinations of sensitivity values and threshold values were used with the rock samples.

Samples with the ratio of diameter to length greater than 1:2 were used in the present experiments. Pre-loading was done under unconfined compression up to 15 kN by repetitiously loading and unloading. Once completed, samples were loaded monotonously to the higher load values than the pre-loading values with various combinations of AE sensitivity and threshold values. Typical result is plotted in Fig. 4. Table 2 shows various conditions and the results obtained. From the table, we can see that the condition (a) is the most sensitive to the Kaiser effect, whereas condition (c) shows the least. Figure 4 shows the results at the monotonous loading on load-displacement vs. AE count rates. The arrow shows the pre-loading value and the dotted line is the value of the onset of the continuous AE occurrence.

From the figure, it is found in the condition (a) that the occurrence of AE begins at 12.7 kN, but the actual loading was up to 15.0 kN. In the condition (b), pre-loading and the occurrence of AE begins almost at the same value and in the case (c) the occurrence of AE is observed at 17.2 kN which was higher than pre-loading value (15 kN). Consequently, the condition (b) is appropriate for determining pre-loading value. Under conditions (a) and (c), it is difficult to determine the preloading value. In other cases with condition (a), the occurrence of continuous AE began at 16.0 kN. Thus, we can nearly determine the preloading value. It is necessary to select appropriate sensitivity and threshold in order to determine the preloading condition using the Kaiser effect.

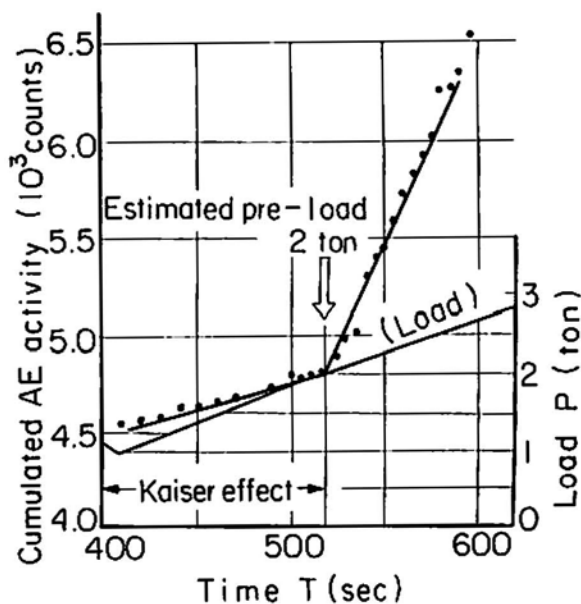


Fig. 3 Evaluation of the Kaiser effect by Kanagawa et al. (1977).

4. Experimental Method and Results

4.1 Characteristics of the Kaiser Effect Under Repeated and Constant Axial Loads

Purpose of this experiment is to investigate the effect of residual strain of the Kaiser effect when rock is subjected to repetitious loading, with the strain increasing gradually. After strain reaches the maximum value, it becomes constant as shown in Fig. 5. Here, the strain of unsaturated and of saturated conditions are defined as the states where strain continues to increase and where strain becomes constant, respectively.

Samples were first subjected to unconfined repetitious loading (sample size: dia. 30 mm, height 60 mm), triaxial loading (dia. 50 mm, height 100 mm), or constant axial loading (dia. 30 mm, height 60 mm) to prepare the samples to strain-saturated and strain-unsaturated states. The Kaiser effect was studied for both states afterward. Unconfined repetitious loading was carried out on all rock types shown in Table 1. Triaxial repetitious loading and constant axial loading were carried out on only granitic rocks and mudstones. Figures 6 - 8 show typical results obtained on granitic samples. These figures show the relation-

Table 1 Details of sample location, project, uniaxial compressive strength (σ) and unit weight (γ).

Identification		Location	Project	Mean values	
				γ (kN/m ³)	σ (MPa)
Granite	I	Ikoma	Tunnel	25.8	90
	II	Inada	Quarry	25.8	132
Granite-porphry		Akikawa	Dam	26.3	83
Porphyrite		Hyogo	Tunnel	26.5	200
Rhyolite		Minakami	Tunnel	26.4	120
Sand-stone		Aiki	Rock slope	25.9	210
Tuff		Dojo	Tunnel	24.3	84
Clay-slate		Uji	Tunnel	26.9	95
Crystal-schist		Fujioka	Quarry	28.9	71
Marble		Italy	Quarry	26.5	74
Andesite		Nagano	Tunnel	26.0	112
Mudstone	I	Machida	Tunnel	18.3	4
	II	Nagano	Tunnel	18.0	8
	III	Gifu	Tunnel	16.7	6

Table 2 Various combination of sensitivity and threshold values.

	Total amplitude (dB)	Threshold level (mV)		Pre-load (kN)	Loading value of beginning of the continuous occurrence of AE (kN)
		V _H	V _L		
(a)	80	400	380	15	12.7
(b)	80	450	430	15	15.7
(c)	80	500	480	15	17.2

ship among the axial strain, axial stress and cumulative AE count. Figures 6(a) - 8(a) show results obtained on strain-unsaturated samples and Figs. 6(b) - 8(b) show results obtained on strain-saturated samples. In these figures the arrow indicates pre-axial stress and the dotted line indicates axial stress estimated by the Kaiser effect. The application of the pre-axial stress is the same for all types of samples. It is found that the stress determined from the Kaiser effect is quite different from the pre-stress, while these stresses found to be equal for the strain-saturated samples. Other rock samples also show similar results. Therefore, it is

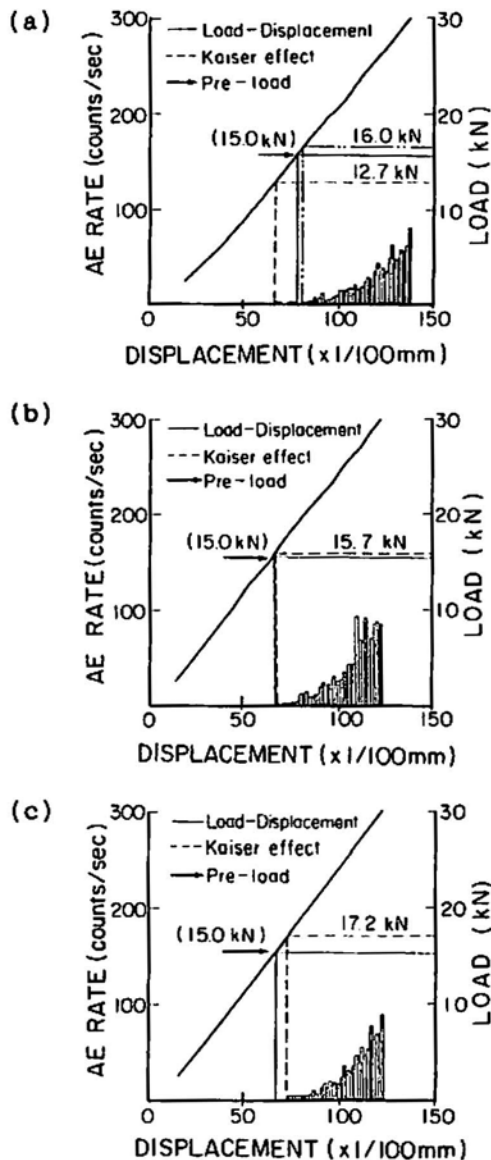


Fig. 4 Relationships among axial load, axial displacement and AE activity under various combination of sensitivity and threshold values.

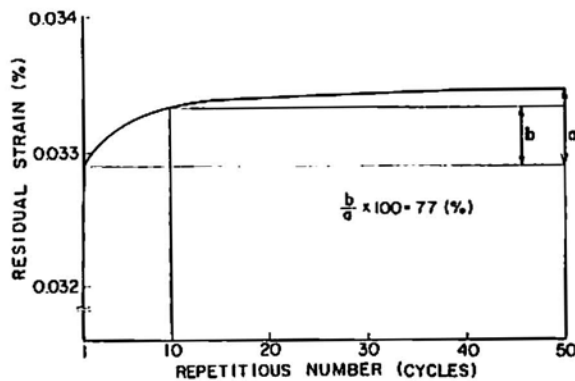


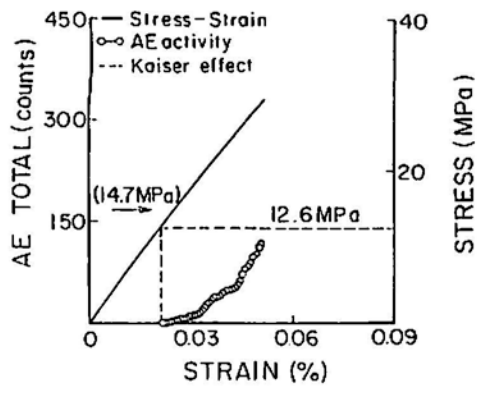
Fig. 5 Relationship between repetition numbers and residual strain.

summarized that under the strain-saturated condition, where the residual strain is left to be of high level, the applied stress level could be estimated using the Kaiser effect. This is not the case, if the rock samples are not strain-saturated. Thus, it is concluded that the axial stress estimated from the Kaiser effect is found to be dependent on the residual strain of the sample.

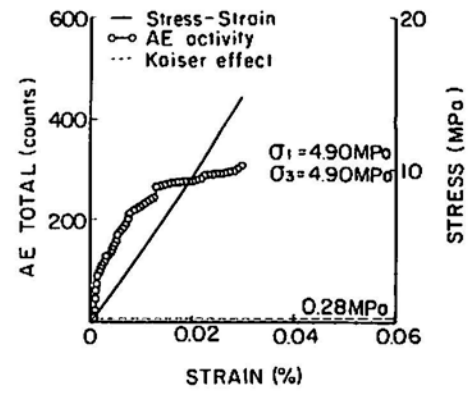
4.2 The Kaiser Effect on Three Dimensional Stress Conditions

In situ stress conditions are so complicated that they should be considered in three dimensions. Hence, it is necessary to examine the Kaiser effect on the three dimensional stress conditions. The AE characteristics were examined experimentally under three dimensional stress conditions by using cubic and cylindrical specimens. Cubic samples of dimensions 5 x 5 x 5 cm and 15 x 15 x 15 cm were prepared in strain-saturated condition by loading differently in each direction (X: 9.8 MPa, Y: 14.7 MPa and Z: 19.6 MPa). The Kaiser effect was investigated for each individual direction under the uniaxial monotonous loading condition. Three kinds of rock samples; i.e., (1) granitic rock samples, (2) sand rock samples; and (3) tuff rock samples were tested. Samples of 15 cm cube were prepared from the granitic rocks, while 5 cm cube samples were used for the sand rock and tuff rock. Results obtained on the granitic rock samples are shown in Fig. 9, showing the relationship among the uniaxial stress, uniaxial strain, cumulative AE counts under uniaxial monotonous loading for X, Y and Z directions. These results show that the pre-axial stress is estimated well by the Kaiser effect. The sand rock and tuff rock samples also showed the same tendency. Thus, it is concluded that the loading directions have no effect, i.e., the loading in Y and Z directions have no effect on the Kaiser effect obtained in X direction.

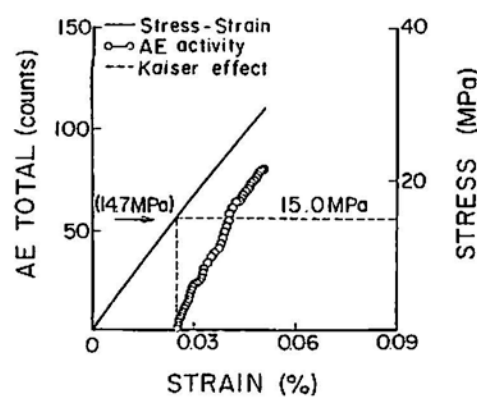
Although the apparatus employed is not capable of simultaneously loading in three directions, the present experiments could provide enough information on three dimensional loading conditions. Strain-saturated cylindrical specimen (50 mm and 100 mm height) were prepared by using triaxial tester under various repeated loading conditions by changing principal stress ratios (σ_3/σ_1). The principal stress conditions used in the experiments are



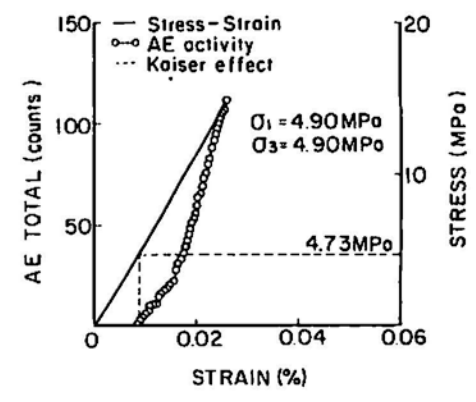
(a)



(a)



(b)



(b)

Fig. 6 Relationships among axial stress, axial strain and AE activity in a granite specimen subjected to cyclic uniaxial compressive stress (14.7 MPa). (a) strain-unsaturated. (b) strain-saturated.

Fig. 7 Relationships among axial stress, axial strain and AE activity in a granite specimen subjected to cyclic triaxial compressive stress ($\sigma_1 = 4.90$ MPa, $\sigma_3 = 4.90$ MPa). (a) strain-unsaturated. (b) strain-saturated.

summarized in Table 3. Granitic and mud-stone samples were used in these experiments. Typical results obtained from the granitic samples are shown in Fig. 10. Figures 10(b) and (c) show the results obtained when the principal stress ratios (σ_3/σ_1) were 1.0 and 0.25. From both figures, it can be seen that the axial stress estimated by the Kaiser effect is the same as that of the maximum principal stress (σ_1). Under various principal-stress ratio conditions, axial stress estimated by using the Kaiser effect are found to be same as those of pre-axial stresses. Similar results were obtained for mud-stone cylindrical samples. Therefore, it is concluded that the Kaiser effect occurring in each individual direction; e.g. X, is independent of the loading in other directions (e.g. Y and Z).

4.3 Effect of Sample Coring on the Kaiser Effect

In order to determine the initial stresses of rockmass by AE method, it is necessary to know the appropriate sample size once the samples were core-drilled from the field. When samples are taken from underground, various types of core samples are obtained by the pushing of boring drill bit. These influence on the Kaiser effect was examined. Cylindrical samples (dimensions dia. 30 mm and height 60 mm) were drilled from cubic samples (edge dimensions 15 cm) which were subjected to three dimensional stress conditions.

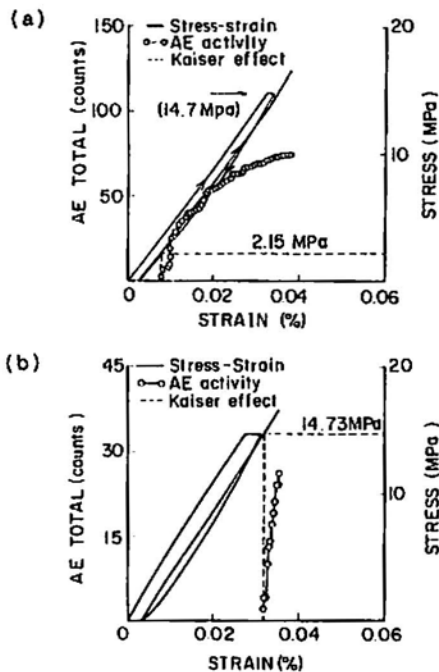


Fig. 8 Relationships among axial stress, axial strain and AE activity in a granite specimen subjected to constant uniaxial compressive stress (14.7 MPa). (a) strain-unsaturated. (b) strain-saturated.

The cubic granitic rock samples used have the same three dimensional stress conditions as described in the previous section (X:9.8 MPa, Y:14.7 MPa and Z:19.6 MPa). In all three directions, strain was saturated. Cylindrical samples were cut from the three directions as the axial direction of cylindrical specimen. Results are shown in Fig. 11. Figures 11(b-d) show the results obtained under the monotonous loading conditions for samples obtained from X-, Y- and Z-direction, respectively. From these results it can be seen that the axial stress estimated by the Kaiser effect in the individual directions are the same as pre-axial stress in the individual directions. Other rocks show similar results. Therefore, the treatment of core samples has little effect on the Kaiser effect.

4.4 Effect of Change of Loading State on the Kaiser Effect

Initial stresses of groundmass are subjected to various changes due to a variety of geological movement on the rock. These are concentration due to diastrophism and relaxation due to weathering. Thus, the stress history of rockmass changes due to various geological activities. One question is how these changes in loading conditions affect the Kaiser

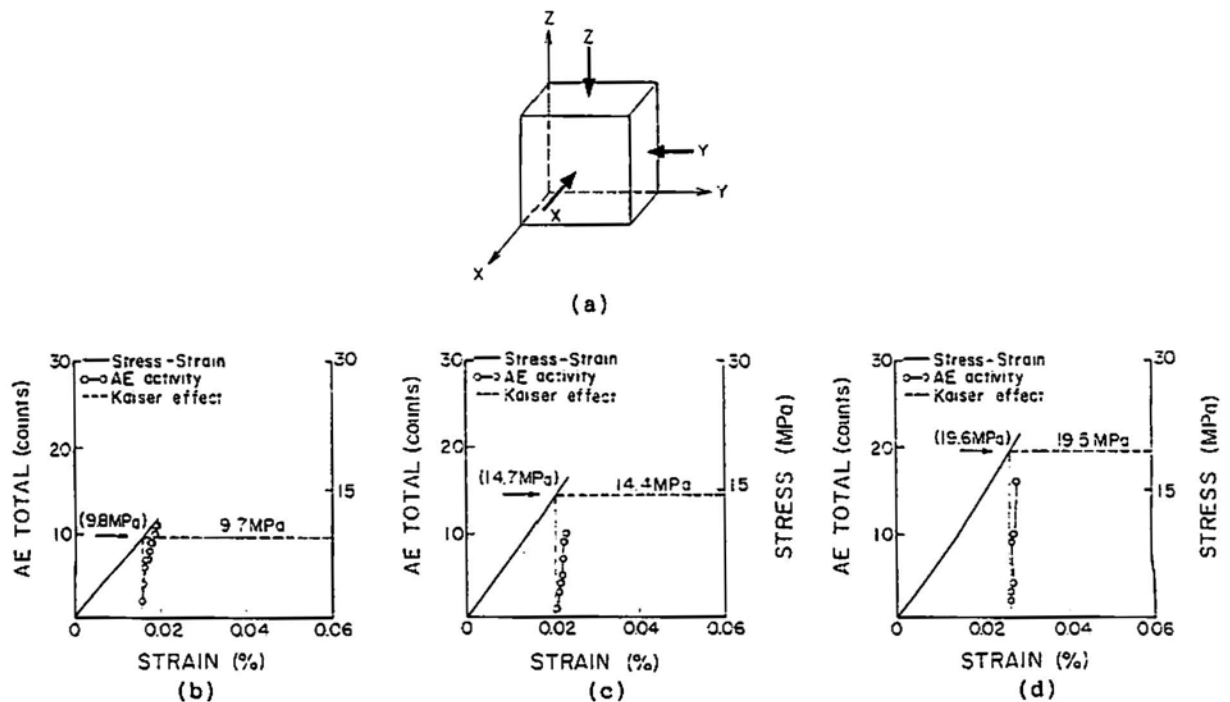


Fig. 9 Experimental results in a granite cubic specimen subjected to cyclic compressive stress of each direction. (a) Directions of stress applied. (b) Relationships among axial stress, axial strain and AE activity in X-direction. (c) Relationships in Y-direction. (d) Relationships in Z-direction.

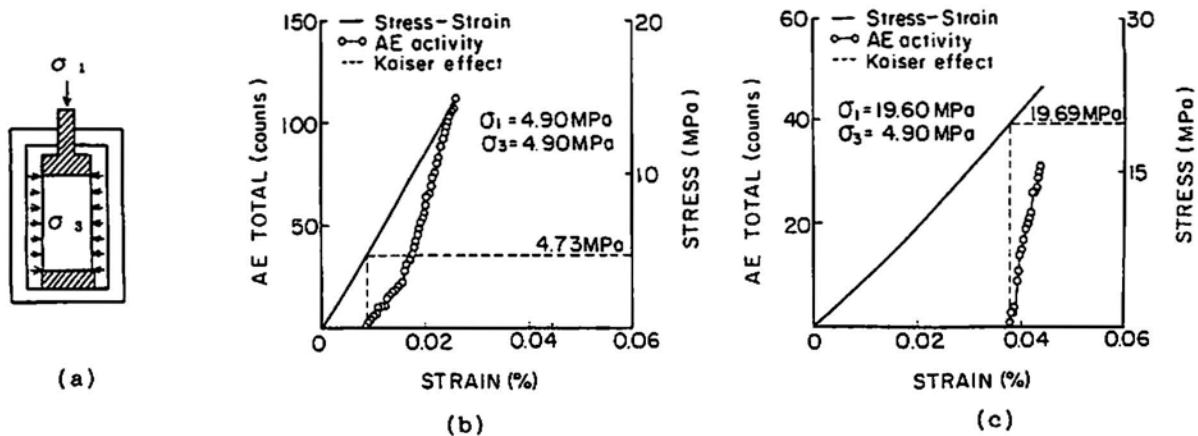


Fig. 10 Experimental result in a granite specimen subjected to triaxial cyclic compressive stress. (a) Direction of stress applied. (b) Relationships among axial stress, axial strain and AE activity ($\sigma_1 = 4.90$ MPa, $\sigma_3 = 4.90$ MPa). (c) Same as (b) ($\sigma_1 = 19.60$ MPa, $\sigma_3 = 4.90$ MPa).

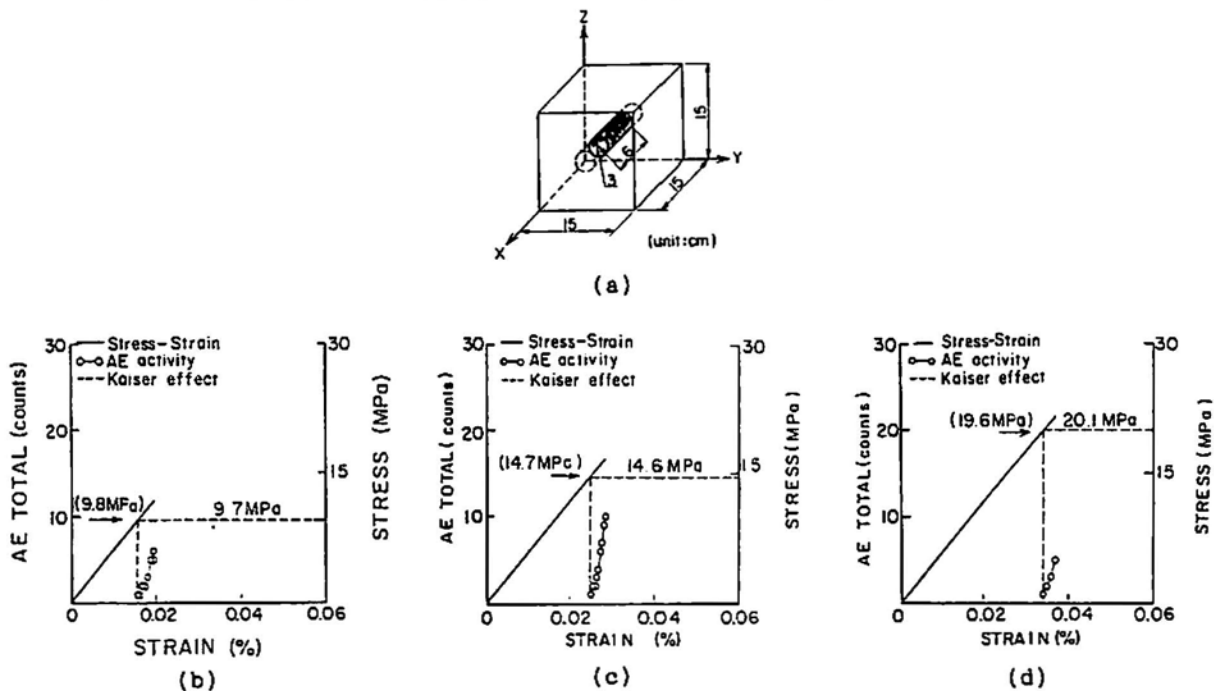


Fig. 11 Experimental result in a granite specimen cored from cubic specimen subjected to cyclic compressive stress of each directions. (a) Cylindrical specimen cored from cubic specimen. (b) Relationships among axial stress, axial strain and AE activity in specimen cored from X-direction. (c) Same in specimen cored from Y-direction. (d) Same in specimen cored from Z-direction.

Table 3 Subjected principal stress (σ_1, σ_3) in triaxial experiment.

σ_1 (MPa)	4.90	7.84	6.86	7.84	9.80	11.77	14.70	19.60
σ_3 (MPa)	4.90	7.84	4.90	4.90	4.90	4.90	4.90	4.90
σ_3/σ_1	1.00	1.0	0.71	0.63	0.50	0.42	0.33	0.25

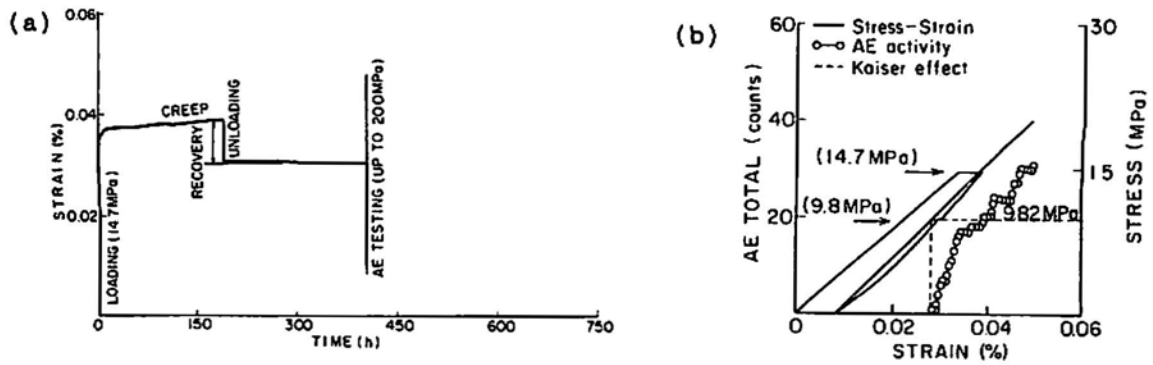


Fig. 12 Effect of a change of load on the Kaiser effect. (a) Relationships between time and axial strain. (b) Relationships among axial stress, axial strain and AE activity subjected to strain recovered after axial stress reduction.

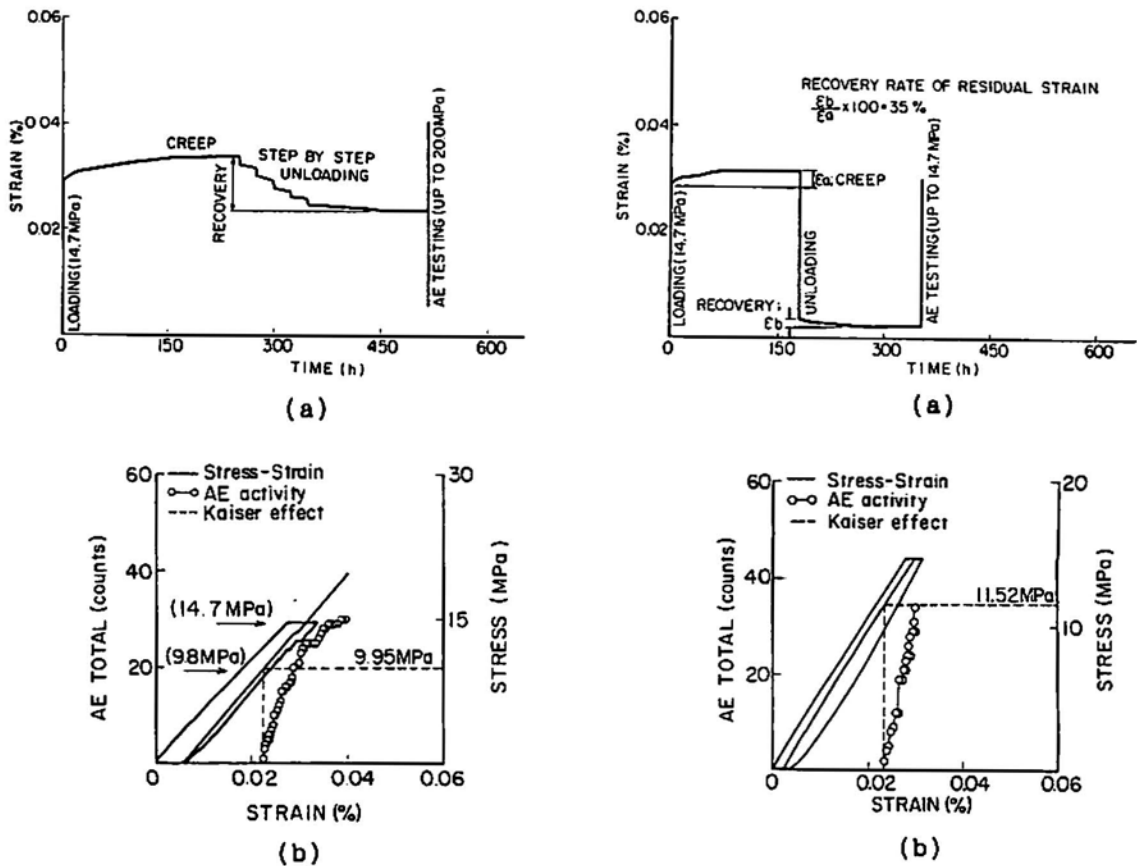


Fig. 13 Effect of five changes of load on the Kaiser effect. (a) Relationships between time and axial strain. (b) Relationships among axial stress, axial strain and AE activity subjected to strain recovered after axial stress reduction.

Fig. 14 Effect of time lapse after stress release on the Kaiser effect. (a) Relationships between time and axial strain recovery for a period of 7.5 days. (b) Relationships among axial stress, axial strain and AE activity subjected to strain recovered after axial stress reduction.

effect. To model the geological stress history on the sample prepared in the laboratory, samples were subjected to 14.7 MPa loading condition to obtain strain-saturated samples. These strain-saturated (14.7 MPa) samples were unloaded till 9.8 MPa and once again samples were strain-saturated. Then the samples

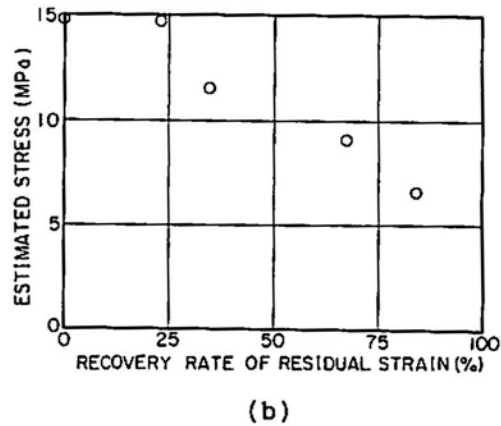
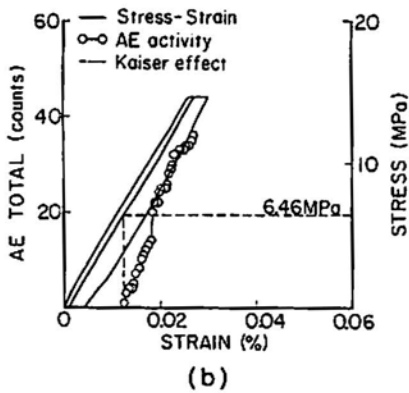
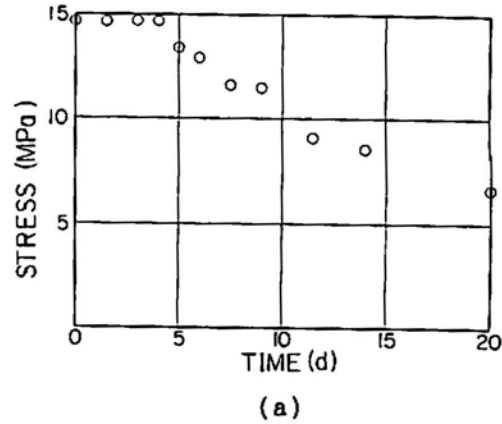
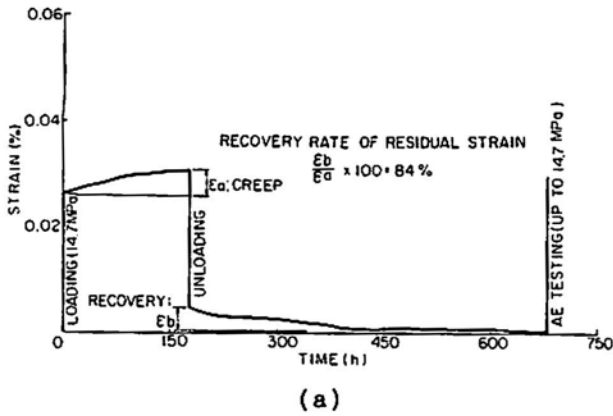


Fig. 15 Effect of time lapse after stress release on the Kaiser effect. (a) Relationships between time and axial strain recovery for a period of 20 days. (b) Relationships among axial stress, axial strain and AE activity subjected to strain recovered after axial stress reduction.

Fig. 16 Effect of times lapse after stress release on the Kaiser effect. (a) Relationships between lapse of days and estimated stress by the Kaiser effect. (b) Relationships between recovery rate of residual strain and estimated stress by the Kaiser effect.

were tested under uniaxial monotonous loading and the stresses were determined using the Kaiser effect. Figures 12(a) and 13(a) show two unloading procedures employed from 14.7 MPa to 9.8 MPa. Four different rock type samples of 30 mm diameter and 60 mm height: (1) granitic rock; (2) tuff rock; (3) sand rock; and (4) crystalline schists; were tested. Figures 12(b) and 13(b) show relationship obtained on granitic samples among axial stress, axial strain, and accumulated AE counts. These results show that the apparent axial stress determined from the Kaiser effect is not identical to that of maximum pre-axial stress (14.7 MPa), but is the same as that of stepwise decreased final axial stress (9.8 MPa). From the strain curve one may notice the recovery when the unloading was done from 14.7 to 9.8 MPa. It follows that the stress estimated using the Kaiser effect is not the maximum pre-axial stress, but is the same as final axial stress. These results show a remarkable similarity to results obtained in the previous section where the Kaiser effect was found to be dependent on the residual strain of the sample. If we compare the geological stress history on the rockmass with that of the modelled sample, results imply that we can determine the pre-stress on the rockmass at the moment and not the maximum stress to which rockmass was subjected to geologically.

4.5 Effect of the Duration following Stress Release on the Kaiser Effect

Once the sample is obtained from in-situ with the removal of the overburden pressure, samples go through the stress release process and strain recovery occurs. We have shown that the residual strain is associated with the Kaiser effect. It is important to investigate how the removal of overburden pressure

affects the estimation of stresses obtained from the Kaiser effect. Cylindrical (diameter 30 mm; height 60 mm) samples were prepared under 14.7 MPa constant axial stress conditions. Once the samples were strain-saturated, unloading was done and the samples were left for strain recovery for various durations. Then, pre-axial stress was estimated using the Kaiser effect. Granitic and mud-stone rock samples were used for the present experiments. Experimental results were obtained on the granitic samples experienced the strain recovery for 7.5 days and 20 days, respectively. Figures 14(a) and 15(a) show a strain vs. time curve. Figures 14(b) and 15(b) show relationship among axial stress, axial strain, and cumulative AE counts obtained under uniaxial monotonic loading. From the results, the stress obtained by using the Kaiser effect is not the same as that of maximum pre-axial stress (14.7 MPa). Samples left for 20 days recovery, the stress obtained by using the Kaiser effect shows less than half the value of maximum pre-axial stress. Figure 16 shows the relationship between the stress obtained by the Kaiser effect and the time elapsed for strain recovery after the stress was released. If the samples are left for more than four days (recovery of the residual strain of about 25%), the stress estimated from the Kaiser effect tend to be smaller with the increase of time period for strain recovery. From these results, we conclude that the duration for strain recovery has the significant influence on the Kaiser effect.

The duration of constant axial stress loading, for the experiments described above, was only about 10 days which is much smaller than the geological loading period of rockmass. Therefore, the Kaiser effect and time relationship was investigated for the samples which were stress-released after obtaining from the in-situ. Samples used in the experiments were porphyritic granite, mudstone and andesite. Among the rock types described, porphyritic granite was used for the detailed investigation. Porphyritic granitic rock had overburden pressure of 80 m depth and the horizontal drilling core bit of 75 mm were used to obtain the samples. Figure 17 shows the schematic diagram of the boring location. Samples obtained from the field were kept in a room with constant temperature and humidity. Cylindrical samples (dia 30 mm; height 60 mm) were obtained with various length of recovery time from various directions as shown in Fig. 18. Samples were subjected to uniaxial monotonic loading immediately after recovery and the stresses were estimated by using the Kaiser effect. Figure 19(a) shows the result obtained after one day recovery and Fig. 19(b) is the result obtained on the samples left for 10-day recovery. Figure 20 also shows a relationship among the axial stress, axial strain, and cumulative AE counts for samples obtained in Direction I of Fig. 18. All these samples were subjected to uniaxial monotonic loading. Estimated stress from the Kaiser effect was found to be 1.0 MPa for samples left for one day and 0.6 MPa for samples left for 10 days. It can be seen that the estimated stress is about half for the samples left for 10 days to that of samples left for only 1 day. Figure 20 shows the relationship between the estimated stress by the Kaiser effect and the time after the strain recovery. Triangles, squares and open circles are for the samples cut in I, II and III directions,

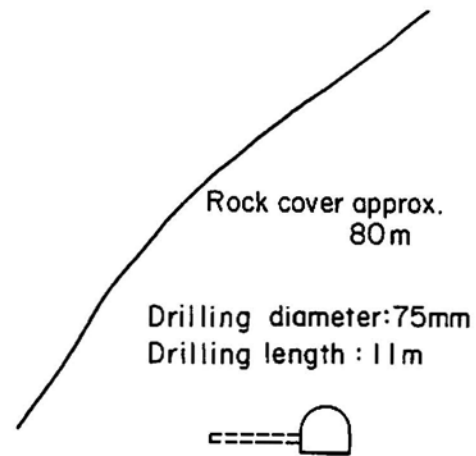


Fig. 17 Location of rock sample coring.

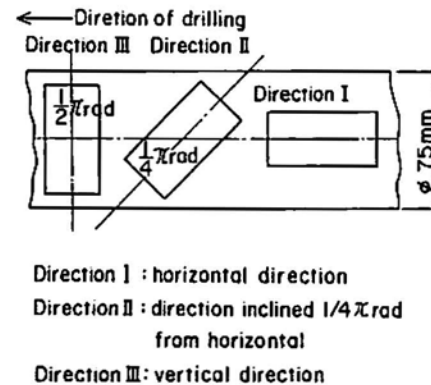


Fig. 18 Directions of shaped cylindrical specimens.

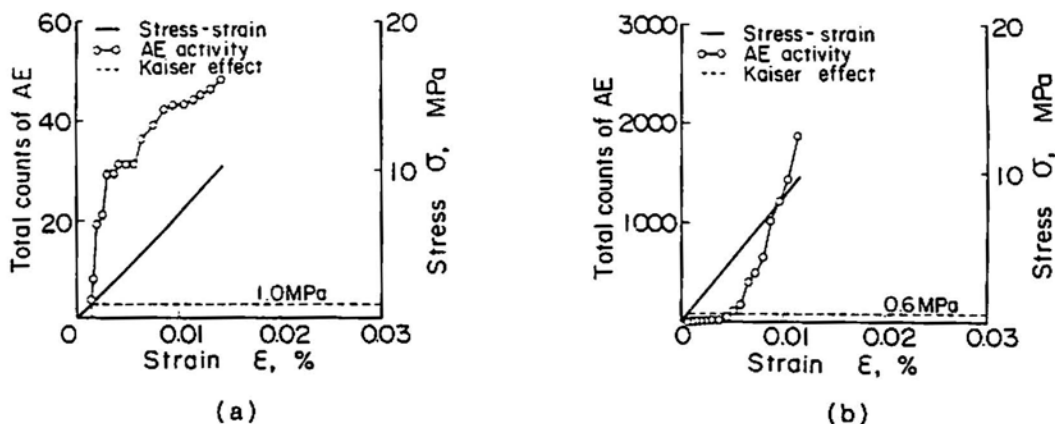


Fig. 19 Relationships among axial stress, axial strain and AE activity in a granite-porphry specimen shaped in the horizontal direction (direction I). (a) 1 day after rock sample coring. (b) 10 days after rock sample coring.

respectively (Fig. 18). For reference, results from Fig. 16 are also drawn in Fig. 20 (solid circles). Results obtained in direction III (open circle) are for the strain recovery period less than 5 days. It shows that the estimated stress from the Kaiser effect is identical for samples cut in any direction. These results show similar tendencies to those of solid circles in Fig. 21, though the magnitude is different. From the above discussions, it is clear that the estimated stresses using the Kaiser effect tend to be smaller as the duration of the stress recovery increases. Therefore, it can be said that once samples are recovered from the core, strain recovery takes place. Hence, AE testing should be done within a short period of time. If this is not the case, the estimated stress using the Kaiser effect may underestimate the pre-stress.

5. Measurement of the Initial Stresses

The Kaiser effect is applied to estimating in situ stress. Eight samples were used to calculate principal stresses. They are granite, granite porphyry, porphyrite, tuff, clay slate, mudstone (two samples), and andesite. Results obtained on granite, granite porphyry and andesite are shown in Fig. 21. Two dimensional stress calculation were done on the granitic and granite porphyritic samples whereas three dimensional calculations are carried out on andesitic samples.

6. Summary and Conclusions

For fundamental studies on the determination of the initial stresses of rockmass using the Kaiser effect, we used eleven different types of rock (more than 500 samples) and carried out various experiments to examine various parameters on the Kaiser effect. Following conclusions are drawn.

- (1) Appropriate values of sensitivity and threshold are required to monitor the continuous occurrence of AE Kaiser effect.
- (2) All rocks examined show the presence of the Kaiser effect.
- (3) The Kaiser effect mainly depends on the residual strain in rock samples.

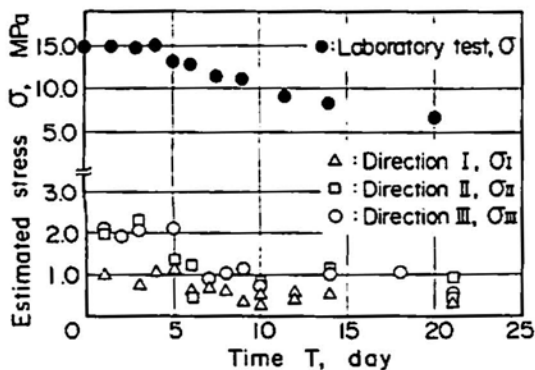


Fig. 20 Relationship between lapse of days and estimated stress by the Kaiser effect.

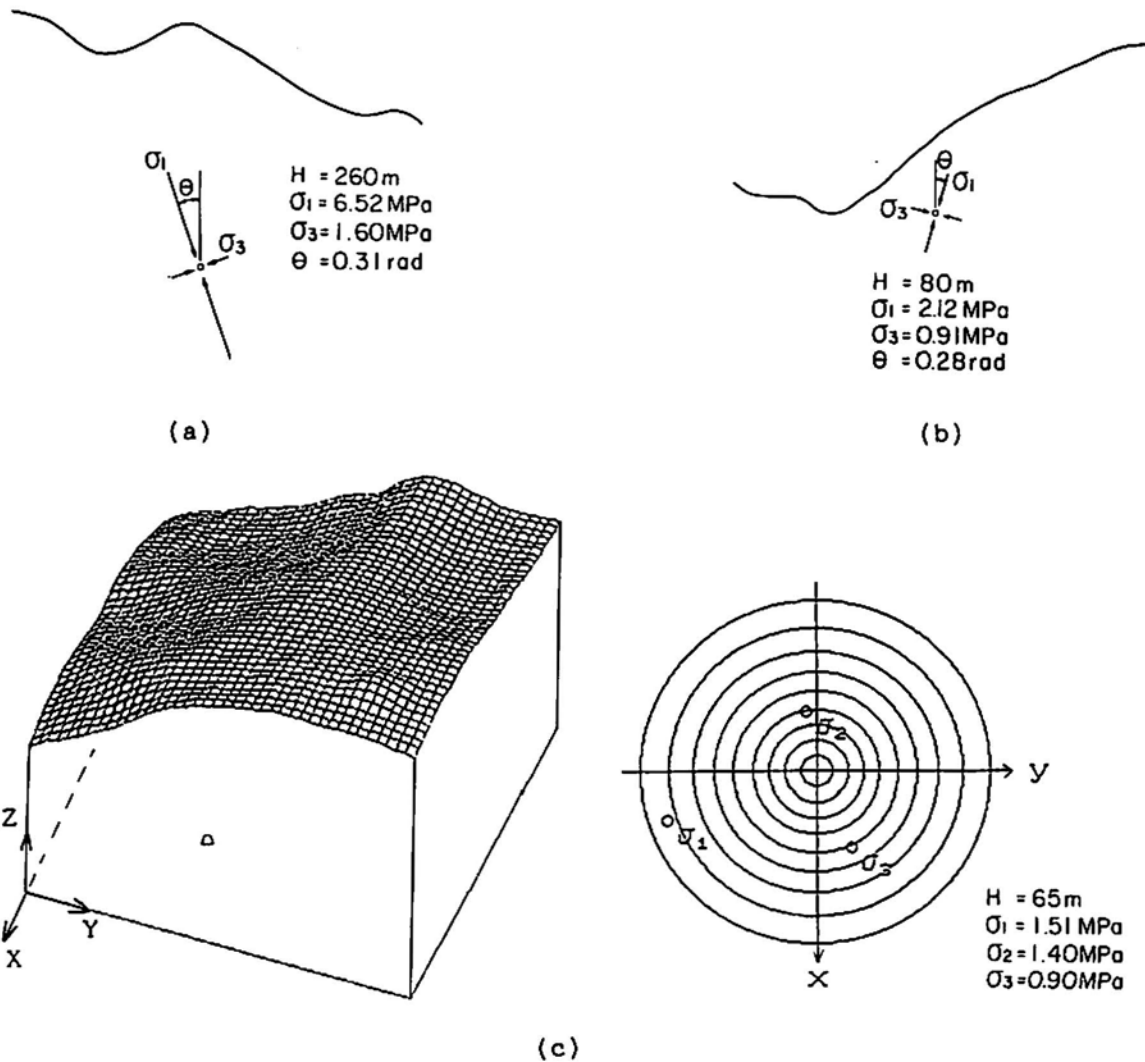


Fig. 21 Estimated principal stress by the Kaiser effect. (a) 2 dimensional principal stress (tunnel: granite I) (b) 2-dimensional principal stress (Dam: granite porphyry) (c) 3-dimensional principal stress (tunnel: andesite)

(4) Applied stresses in various directions have no effect on the stress estimated by the Kaiser effect on any certain direction.

(5) Stress determined by the Kaiser effect tend to become smaller with the passage of time.

Using AE method to estimate the initial stress, it is possible to compare the results obtained in the laboratory with field tests. Further research is required to find out how the water saturation affects the Kaiser effect. Comparing with other methods, authors hope to establish a data bank to study the effective-ness of AE method in determining the initial stresses.

References

R.E. Goodman (1963), "Subaudible noise during compression of rocks", Geological Society of America Bulletin, 74, 487-490.

H.R. Hardy, Jr. (1981), "Applications of acoustic emission techniques to rock and rock structures: A state-of-the-art review", *Acoustic emissions in geotechnical engineering practice*, ASTM-STP-750, ASTM, Philadelphia, pp. 4-92.

E. Hoek and E.T. Brown (1980), "Underground excavations in rock", *The Institution of Mining and Metallurgy*, Chapter 4.

J. Kaiser (1953), "Untersuchungen über das auftreten gerauschen beim zugversuch", *Archiv für das Eisenhüttenwesen*, 24, 43-45.

T. Kanagawa, M. Hayashi and H. Nakasa (1977), "Estimation of spatial geo-stress components in rock samples using the Kaiser effect of acoustic emission", *Proceedings of Japan Society of Civil Engineers*, No. 258, pp. 63-75. (in Japanese)

T. Kanagawa, S. Hibino, T. Ishida, M. Hayashi and Y. Kitahara (1986), "In situ stress measurement in the Japanese islands: Over-coring results from a multi-element gauge used at 23 sites", *International Journal of Rock Mechanics and Mining Science*, 23(1), 29-39.

K. Michihiro, T. Fujiwara and J. Yoshioka (1985), "Study on estimating geostresses by the Kaiser effect of AE", *The 26th U.S. symposium on Rock Mechanics*, pp. 557-564.

K. Michihiro, H. Yoshioka, K. Hata and T. Fujiwara (1985), "Strain dependence of the Kaiser effect on various rocks", *4th Conference on Acoustic Emission/Microseismic Activity in Geologic Structures and Materials*, pp. 87-95.

Y. Mizuta, S. Ogino and O. Sano (1983), "A procedure for three dimensional stress determination by hydraulic fracturing", *Proc. of the 15th Symposium on Rock Mechanics*, Japan Society of Civil Engineers, pp. 116-120. (in Japanese)

S. Murayama, K. Michihiro, J. Saito, T. Fujiwara, H. Yoshioka and K. Hata (1984), "The Kaiser effect of a granite under various loadings", *Progress in AE II*, JSNDI, Tokyo, pp. 586-593.

S. Murayama, K. Michihiro, J. Saito and H. Yoshioka (1985), "The Kaiser effect of granite caused by various loading methods", *Proceedings of Japan Society of Civil Engineers*, No. 364/III-4, pp. 107-112. (in Japanese)

S. Murayama, K. Michihiro, T. Fujiwara and K. Hata (1986), "Relationships between creep strain and Kaiser effect on granite", *Proceedings of Japan Society of Civil Engineers*, No. 370/III-5, pp. 41-46. (in Japanese)

V.H. Rüsç (1959), "Physikalische Fragen der Betomprüfung", *Zement-Kalk-Gips*, 1, 1-9.

K. Sugawara, K. Kaneko, Y. Obara and H. Okamura (1986), "Determination of the state of stress in rock by the measurement of strains on the hemispherical borehole bottom", *Proceedings of the International Symposium Large Rock Cavern*, Vol. 2, pp. 1039-1050.

S. Yoshikawa and K. Mogi (1981), "A new method for estimation of the crustal stress from cored rock samples: Laboratory study in the case of uniaxial compression", *Tectonophysics*, 74, 323-339.

U.S. Bureau of Mines Research on the Kaiser Effect for Determining Stress in Rock

Michael J. Friedel and Richard E. Thill

The authors are affiliated with Twin Cities Research Center, Bureau of Mines, Minneapolis, MN 55417.

Abstract

The state of stress in a rock mass is of utmost concern for mine design and stability analyses. Bureau of Mines researchers seeking a rapid and practical method of measuring stress in rock have investigated acoustic emission (AE) and associated Kaiser effect phenomena in six rocks: St. Cloud gray granodiorite, Barre granite, Dresser basalt, Salem limestone, Berea sandstone, and a volcanic tuff. AE signatures also were used for interpreting the rock deformation stage and for classifying modes of deformation and failure in uniaxial compression. The advantage of using the stress-volumetric strain curve as an alternative to the more conventional uniaxial curve was demonstrated for correlating AE signatures with deformation and fracture processes in rock.

The Kaiser effect was shown to be capable of indicating pre-stress levels usually to within a few % in uniaxial compression tests. Pre-stress memory was shown to be retained in the rock for periods of up to at least 5 months, the maximum period of testing. Confining stress also was shown to have a pronounced effects on the Kaiser effect, increasing it with increasing confinement. Although Kaiser effect holds promise for providing a less complex, indirect measurement of locked-in stress in rock, more research is required on the effects of confinement and other environmental factors, such as moisture and temperature, for the accurate determination of in situ stress.

1. Introduction

Numerous approaches have been developed to determine in situ stress, but none are universally applicable in rock and all suffer from deficiencies and limitations. Technology is particularly deficient for determining the stress state at depth in remote regions that are inaccessible from boreholes or mine workings, or for corrosive environments, such as may be encountered in in situ leaching or waste disposal. Continued research and development of new and improved technology is necessary for more accurate and reliable determinations of in situ stress in difficult mining situations.

A novel approach for determining in situ stress at depth or in corrosive and hostile environments is to use secondary effects of stress measurable by geophysical methods (Radcliffe et al., 1986). The National Research Council (1981) recently emphasized that geophysical methods likely will be the only tools for evaluating stress conditions at great depths where drilling is limited or precluded by costs, or where the installation of measuring devices might alter the ambient stress field. One of the more promising of these techniques relies on the so called Kaiser effect, obtained from measurements of acoustic emission (AE) in stressed rock. Kaiser (1950) observed that AE activity exhibited an irreversible effect upon unloading and reloading metal specimens tested in uniaxial tension. Upon reloading a specimen, Kaiser noted that AE activity was substantially quiet until the stress level of the previous maximum applied stress was exceeded. This phenomenon, termed the Kaiser effect, suggests that previous maximum stress levels might be detected by stressing a rock to the point where there is a marked rate of change in AE activity. Although the Kaiser effect has been well established in metals, only limited research has been conducted in a few types of rocks. Most notable is the recent work of the Japanese (Kanagawa et al., 1976; Hayashi et al., 1979; Kurita and Fujii, 1979; Mogi, 1962; Murayama, 1985), Hardy et al. (1988, 1989) and Holcomb et al. (1983, 1985, 1986) at the Sandia National Laboratories. Little research, however, has been directed toward devising

methods to apply this stress determination technique to practical mining situations and problems.

Two components of U.S. Bureau of Mines research are described in this report: (1) To compare deformation modes and AE signatures in different rock with those previously defined by Mogi (1962) or Boyce et al. (1981) for application of pattern recognition technology to rock mechanics applications, and (2) to verify the applicability of the Kaiser effect for predicting previous stress history in several types of rock common to mining. The results presented in this report represent an initial phase of research by the U.S. Bureau of Mines on utilizing the Kaiser effect for in situ stress and stress change determinations in mining applications.

2. Experimental Procedures

Experimental procedures were implemented to provide more uniform testing procedures, to permit discrimination between AE signals and electromagnetic noise, to improve the signal-to-noise ratio, and to graphically portray AE results to facilitate data interpretation. Several crystalline and sedimentary rocks were selected for the experimentation. These included St. Cloud gray granodiorite, Barre granite, Dresser basalt, Nevada volcanic tuff, Berea sandstone, and Salem limestone. Several of the rocks were included because they were part of a standardized suite of rocks for which much property and petrographic data had been determined (Krech et al., 1974).

Cylindrical cores 2.54 cm in diameter by 5.08 cm long were taken in a single direction in rock blocks to prevent variation in results due to anisotropy. Specimen dimensions and surface end finishing conformed to guidelines for uniaxial testing recommended by the American Society for Testing and Materials (1970) and the International Society of Rock Mechanics (1981). Precisely sectioning and polishing specimen ends minimized the potential for noise generation due to platen seating at the specimen interface or other frictional movements due to end-surface irregularities. Rock cylinders were then weighed for initial density determinations and, subsequently, preconditioned in a vacuum oven at moderately elevated temperature of 100°C to remove moisture and obtain a standardized dry testing environment for the uniaxial loading experiments. Specimens were stored in a desiccator until the time of testing.

3. Mechanical Testing Procedures

Unconfined uniaxial compression tests were conducted using a closed-loop, servocontrolled materials-testing machine. Specimens were pre-loaded to levels of about 7 MPa for the crystalline rocks, and 0.5 MPa for the tuff and sedimentary rocks to initially seat the platens and close the loop for automated servocontrol. Rocks were loaded at strain rates ranging between 2×10^4 and 2×10^6 per second, based on recommendations in earlier work (Boyce et al., 1981). Triaxial data are from the reanalyzed information presented in an earlier study in which test procedures were similar to those used in the uniaxial tests (Thill, 1973).

AE sensing and processing was done with a wideband (100 kHz to 1 MHz) piezoelectric transducer and an AE analyzer, modified to operate in a frequency range down to 100 kHz. Silicone grease was used between the aluminum front piece and the specimen surface to compensate for any asperities in the contact surfaces.

The schematic for the AE detection system is given in (Fig. 1). Energy released in the form of elastic waves in stressed rock is converted to an electrical signal by the transducer. This electrical signal is then transferred via coaxial cable to a 60-dB preamplifier and into the AE analyzer through an adjustable-gain, linear amplifier, which provides up to 21 dB additional gain in 3-dB increments. The analyzer is equipped with two floppy disk drives for the storage of AE data. External parametric input to the analyzer permits the simultaneous input and plotting of load (stress) or deformation (strain) data as a function of the AE response. Sampling rate for the parametric digital sampling was 1,000 samples per second. A digital oscilloscope is used for waveform capture and transfer to a computer.

The appropriate amplification level to provide the maximum amplification of AE signals, yet discriminate against transient and background noise was found to be 66 dB. To further discriminate AE signals from

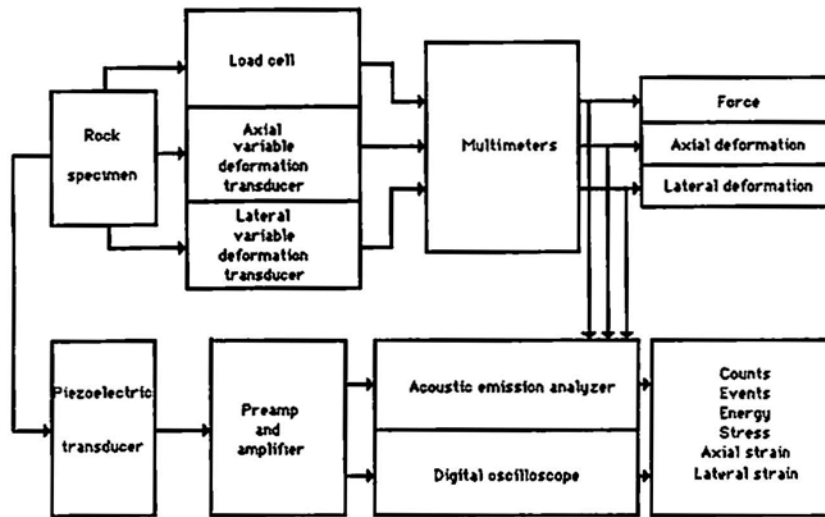


Fig. 1 Acoustic emission test system.

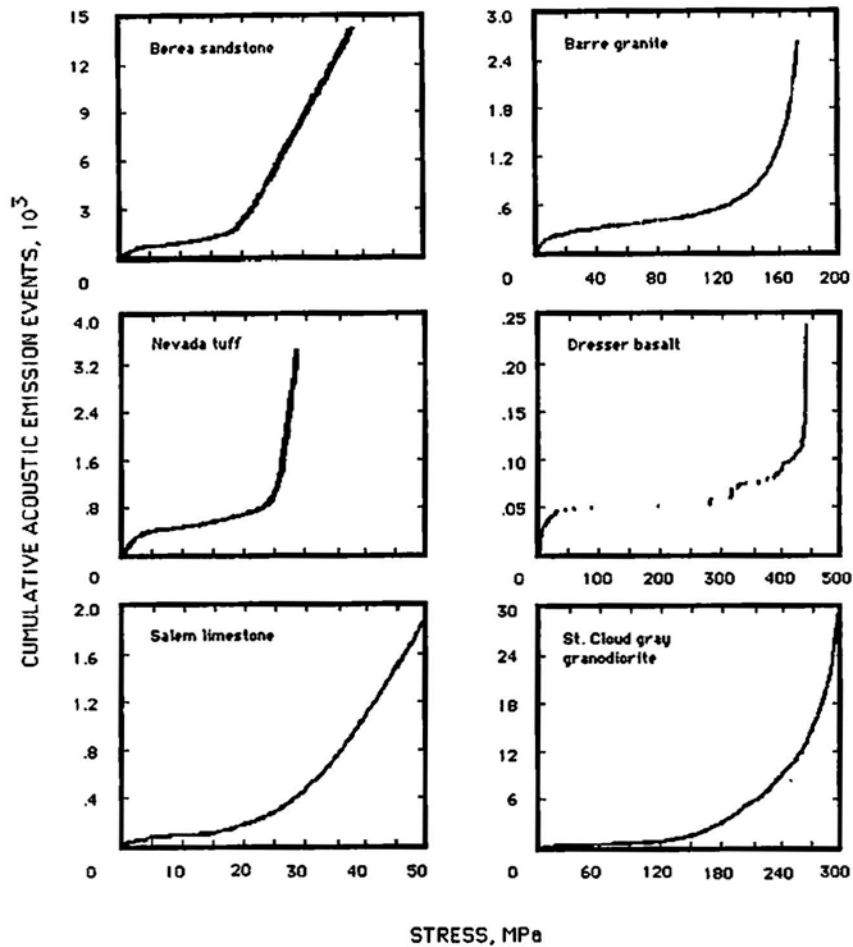


Fig. 2 Cumulative AE events as a function of stress for various sedimentary and igneous rocks loaded under uniaxial compression.

background noise during the tests, analyzer threshold trigger levels were raised slightly above the background noise level. To discriminate AE signals from spurious noise, only those AE events having 5 or

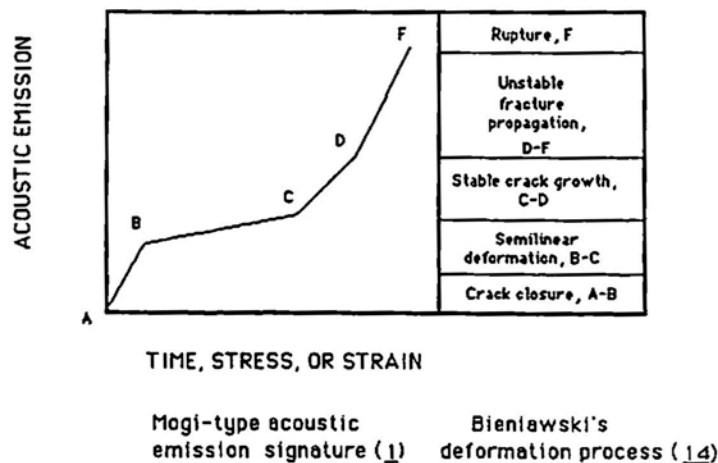


Fig. 3 AE response characteristics associated with the five regions of deformational behavior, or the fracture process.

more counts (in excess of the threshold trigger level) and exceeding 100 kHz in frequency were used in the data analysis.

4. AE Signature Patterns

Both general (primary) and specific (secondary) AE signatures were examined in the rocks tested to recognize diagnostic patterns related to rock behavior. Typical cumulative AE events in the six rock types as a function of uniaxial unconfined compressive stress are given in Fig. 2. Several signatures or patterns were recognized in the AE response curves. One type of primary-signature is referred to as the *Mogi* type of curve (Mogi, 1962), which relates the AE cumulative response to four generalized regions of deformational response for elastic-plastic materials.

The correspondence between the Mogi cumulative AE response signatures and Bieniawski classification for the deformation process leading to fracture is given in Fig. 3, following Boyce et al. (1981). In region I (A-B), crack closure and/or compaction occurs, resulting in a positive increasing slope in the cumulative AE curve. In region II (B-C), the rock undergoes elastic deformation, with a correspondingly low, nearly constant rate of AE. Hence, the cumulative AE curve in this region is nearly constant. Region III (C-D) is typified by the onset of fracturing and stable crack growth and is represented by an abrupt increase in AE activity (the Kaiser effect) with sharply increasing slope. Region IV (D-F) relates to critical energy release and unstable fracture in brittle materials. Region IV is typified by high rates of AE with steeply increasing slope.

Boyce et al. (1981) recognized variations of the Mogi pattern and re-classified signature responses for cumulative AE into four types (Fig. 4). The type I signature with four distinct slope changes was classified as the *Mogi* signature. The type II signature was designated *unstable*, relating to the absence of the C-D segment of the Mogi model. This implies that the material changes directly from linear elastic to unstable behavior, without a phase of stable crack growth. The type III signature was designated *dense* by Boyce, referring to the absence of the segment A-B of the Mogi model. The type III model implies that this type of rock is compact (dense) in the initial stages of load application. The type IV signature lacks both the first and third phases of the Mogi model and is designated *dense, unstable*, incorporating aspects of both type II and type III behavior.

In applying AE signature classification to the rock tested, the Bureau found that all segments (slope changes) of the Mogi type signature were present to some extent in each type of rock (Fig. 2). For some of the rocks, however, it appeared that certain slope segments of the Mogi type of curve were almost absent,

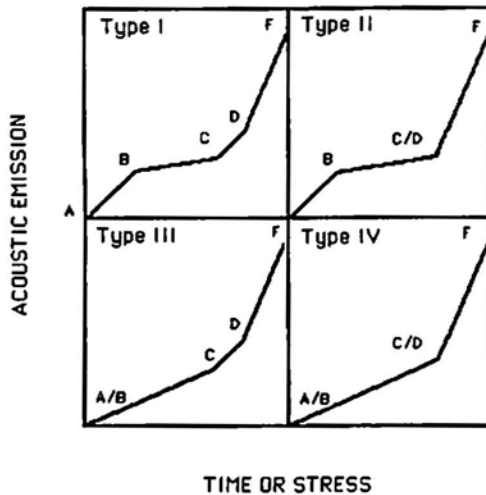


Fig. 4 Boyce signature classification based on shape of cumulative AE response curve in different types of rock (Boyce et al., 1981). Classifications: type I, Mogitype curve; type II, unstable; type III, dense; type IV, dense unstable

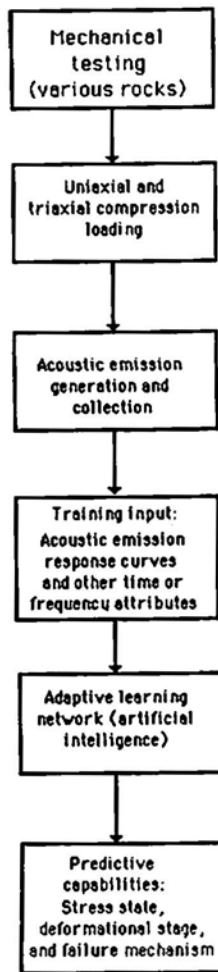


Fig. 5 AE pattern recognition.

resembling the Boyce types of signatures. The Berea sandstone curve, for example, appeared almost linear in the CD-DF segment and therefore could be classified as *type II-unstable* in Boyce's signature classification scheme. Similarly, the St. Cloud gray granodiorite curve appeared to closely resemble the *type III-dense* signature. It was hoped that such AE pattern classifications might be useful in rock mechanics applications; for example, to indicate whether or not a rock is burst-prone. Several problems were noted, however, in attempting to use the Boyce classification. Appearance of the curve shape, and therefore its signature classification, was affected by changes in the settings of the data acquisition and processing system. Setting the trigger threshold higher or lower or changing the sampling rate, e.g., could cause greater or less development of certain segments of the curve. For instance, by changing the sampling rate interval or the amplitude threshold, or by applying an initial preload to the sample, the shape of the AE curve could be changed to reduce or eliminate the A-B and C-D segments of the signature. These problems indicate there is strong need for standardization of the data acquisition and plotting parameters if AE pattern classifications are to be used in practical rock mechanics applications.

In addition to the generalized (primary) pattern of the AE response curve, which was shown to be closely related to the deformation stages of rock at different levels of stress, other diagnostic AE (secondary) signatures or patterns exist that are associated with the internal rock structure and mechanisms of failure. These patterns arise in the more detailed AE rate response within each deformation region and also from the acoustic waveform response associated with each event. Each type or family of rock appears, therefore, to have a distinct pattern of AE that distinguishes it from others. Some rocks are very *noisy* (high AE) in the early, low-stress region of deformation, whereas others may have few AE events in this region. Some have low rate of AE into the very high-stress region and then suddenly burst with high rates of AE close to the collapse stage (e.g., Dresser basalt). Other rocks (e.g., Berea sandstone or Salem limestone) may have nearly constant rates of AE over wide ranges of stress preceding failure. These individualized signatures for each type of rock are mainly diagnostic of

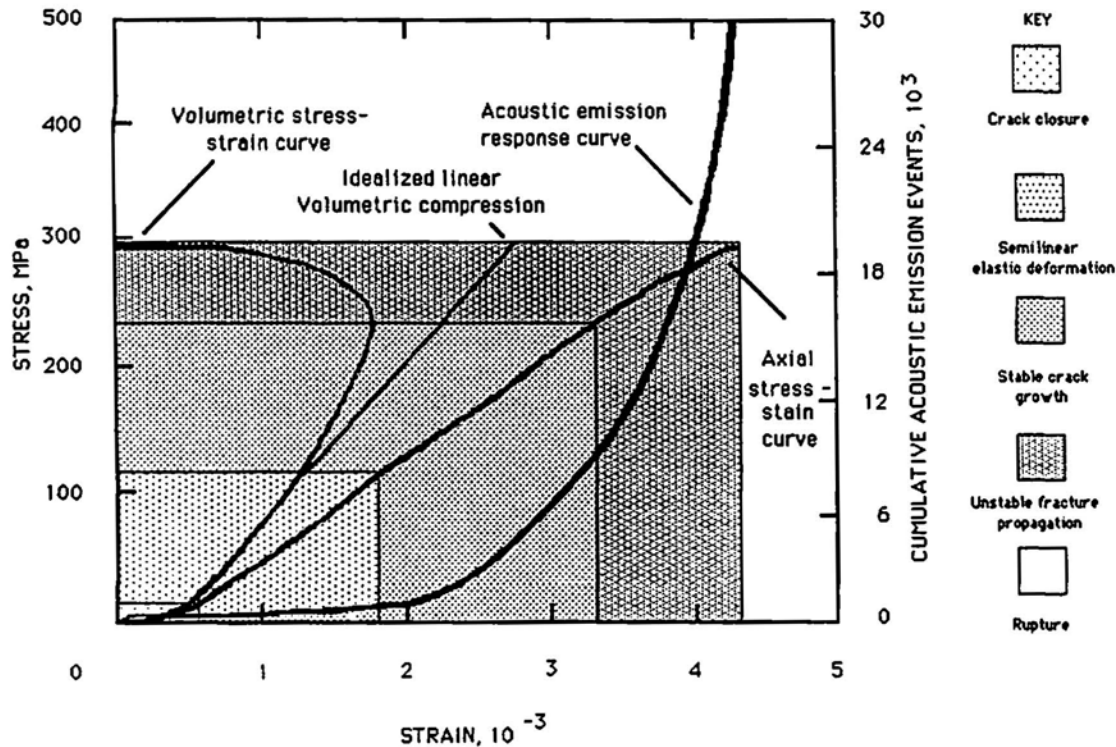


Fig. 6 Cumulative AE events as a function of both axial and volumetric stress-strain for typical St. Cloud gray granodiorite sample loaded under uniaxial compression.

the rock fabric, particularly microcracks, loading conditions, and mechanisms of failure (Thill, 1973; Scholz, 1968a, b; Brace et al., 1966; Montoto et al., 1984; Lord, Jr. and Koerner, 1983).

Since AE signatures are shown to be diagnostic of stress-strain behavior, the deformation process and mechanisms of failure in rock, computerized pattern recognition technology presents a viable approach for interpreting the stages of stress and deformation, or mechanisms of failure in stressed rock. Some mining applications of AE signature analysis and pattern recognition already have been described in Canadian research (24). Figure 5 gives a flow diagram for a conceptual pattern recognition approach recommended by the Bureau. This approach requires training input from the AE response curves or from captured AE waveforms, combined with the use of artificial intelligence to obtain predictive capabilities about the stage of stress, and the deformation or failure mechanisms in stressed rock.

Stress volumetric strain tests were conducted to correlate cumulative AE response to volumetric strain (Fig. 6). For brittle rock, initial nonlinearity in the stress-volumetric strain curve is associated with crack closure and compaction. The initial deviation of the stress-volumetric strain curve from idealized linear compression marks the onset of volume dilatation associated with crack formation. The transition from stable to unstable crack propagation occurs at the reversal of slope in the stress-volumetric strain curve. The volumetric strain categories are characterized in the cumulative AE events curve by abrupt changes in slope. This could assist in stress-strain interpretation of AE in field monitoring situations. Since the onset of dilatation and transition from stable to unstable fracture propagation are more apparent from the stress-volumetric strain than from axial stress-strain data, it is recommended that, whenever feasible, AE be plotted as a function of the stress-volumetric strain rather than the customary axial stress-strain curve.

5. Kaiser Effect Results

A typical AE rate response curve for the first cycle of uniaxial loading for Salem limestone (Fig. 7) indicates several regions of deformation: crack closure and compaction; semi-linear elastic; inelastic and

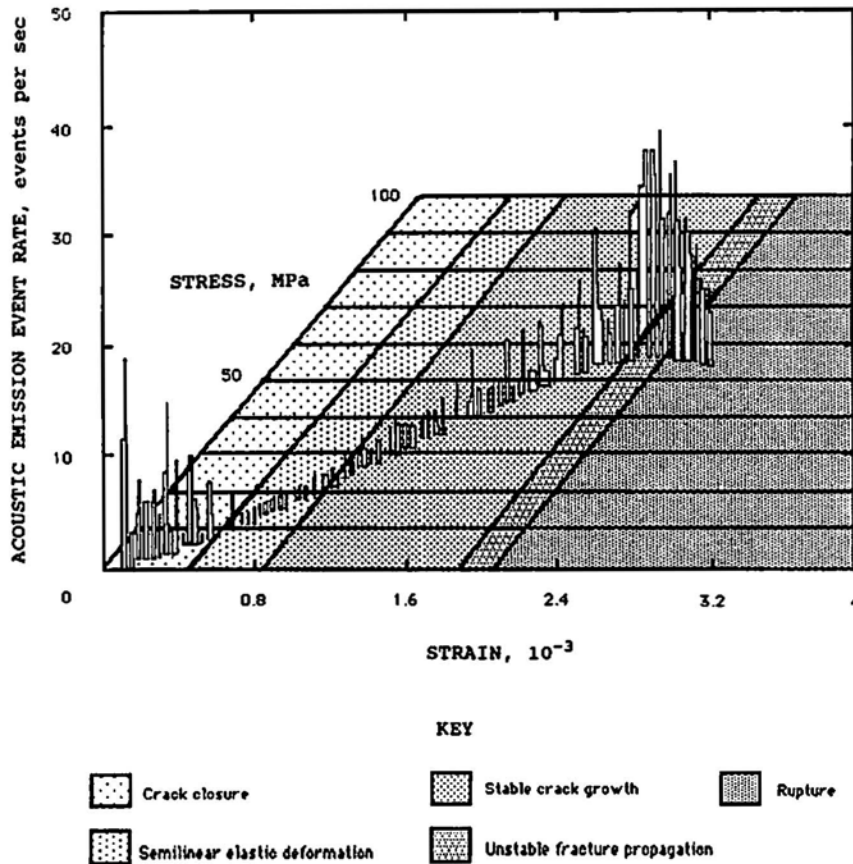


Fig. 7 AE response and its correlation to brittle deformation criteria for typical Salem limestone sample.

failure (or postpeak behavior). The Kaiser effect, in which AE rate begins to increase above the background level observed in the linear elastic region, occurs at a stress level of about 19 MPa in this case. This apparently represents the peak, locked-in stress to which the rock had been subjected. Locked-in stresses similarly determined for the six types of rocks in this study are given in Table 1.

Table 1 Peak stress history as determined by Kaiser effect

Rock Classification	Name	Previous peak stress, MPa	Difference, MPa
Sedimentary	Salem limestone	19	± 2
	Brea sandstone	31	± 1
Igneous	Nevada tuff	33	± 2
	St. Cloud gray granodiorite	115	± 5
	Barre granite	136	± 4
	Dresser basalt	263	±12

Variation was as high as 12% in the Dresser basalt, but lower than ±5% for the other rocks. These results support those of Holcomb (1983, 1985), Hardy (1985, 1988), and Kurita and Fujii (1979), who established that locked-in stresses could reasonably be determined by the Kaiser effect.

Since the Kaiser effect can sometimes be obscured by noise associated with crack closure or compaction during the first loading cycle, better resolution of the Kaiser effect can be made when such noise is sup

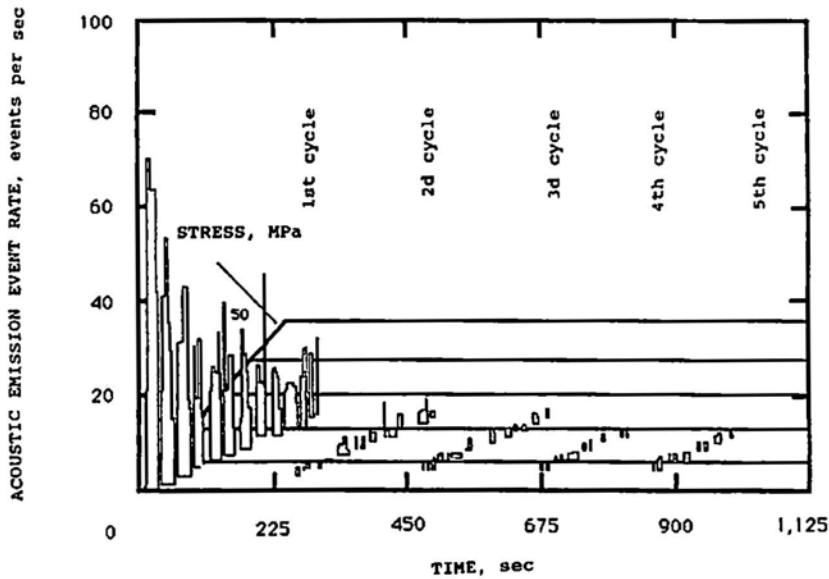


Fig. 8 Reduction of AE events associated with crack closure. Subsequent cycling shows an advantage to preloading the rock into the linear elastic range to enhance Kaiser effect.

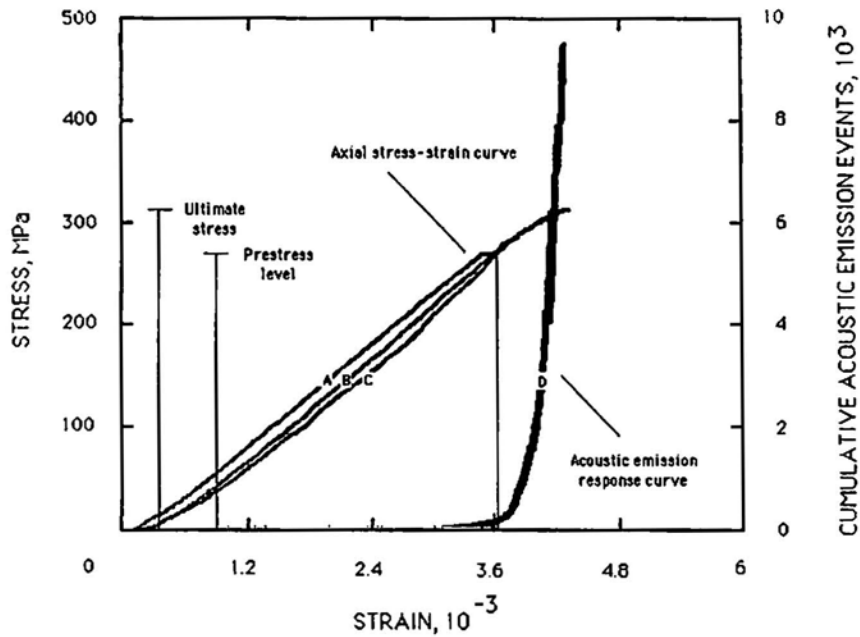


Fig. 9 Cumulative AE events as a function of stress-strain response for St. Cloud gray granodiorite under uniaxial compression. Curve A-C represents initial stress-strain path taken; curve B is subsequent stress-strain path taken to failure. Curve D depicts cumulative AE response during the subsequent stress-strain cycle.

pressed. This type of noise, fortunately, can be suppressed by subsequent unloading-reloading at stress levels within the elastic range, thereby making the Kaiser effect more pronounced. This is illustrated in Fig. 8 where it is observed that most noise is already reduced by the second loading cycle, with only minor improvement in subsequent cycles.

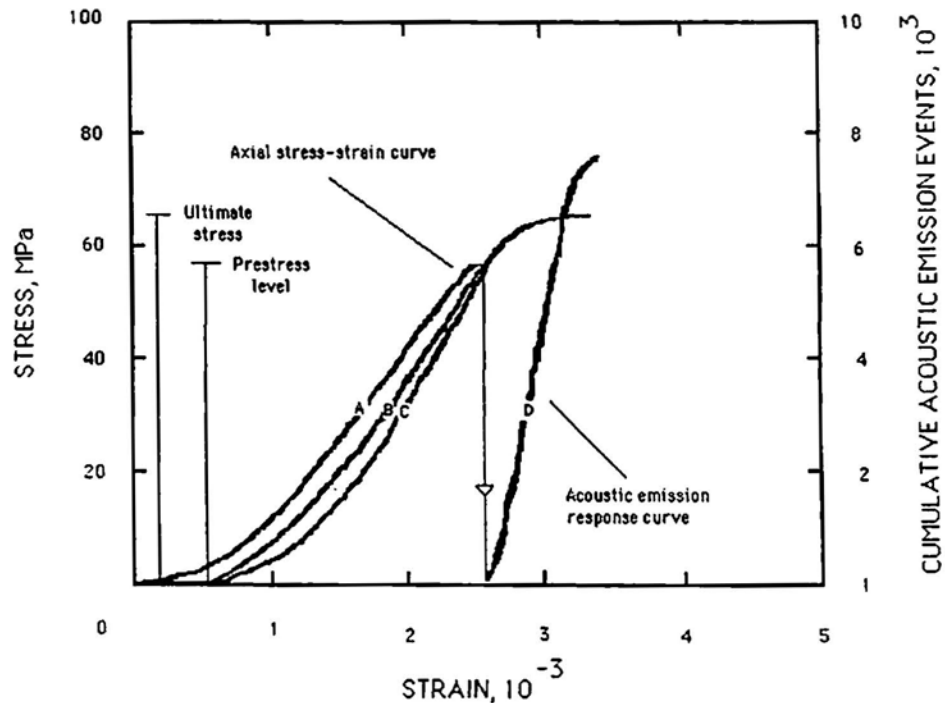


Fig. 10 Cumulative AE events as a function of stress-strain response for Salem limestone under uniaxial compression. Curve A-C represents initial stress-strain path taken; curve B is subsequent stress-strain path taken to failure. Curve D depicts cumulative emission response during the subsequent stress-strain cycle.

Examples of the sensitivity of the Kaiser effect corresponding to prestressed levels are given for St. Cloud gray granodiorite (Fig. 9) and Salem limestone (Fig. 10). In both cases, cumulative AE was plotted directly as a function of the axial stress-strain curve. The first loading cycle (A) prestressed the sample to a known stress level. The stress was held constant at this level until creep occurred. The sample was then unloaded (stress path B) and reloaded along stress path C while measuring cumulative AE (curve D). The Kaiser effect is readily obtained from the point of intercept on the stress-strain curve associated with the onset in rate change in the AE curve. Table 2 gives results for Kaiser effect determinations at several prestress levels in limestone and granodiorite. Stress levels could be reestablished to within a few % of the prestressed levels.

Table 2 Kaiser effect detection of prestress levels in Salem limestone and St. Cloud gray granodiorite

Rock	Kaiser effect stress, MPa	Previous applied stress, MPa	Difference, MPa
Salem limestone	37.5	39.0	- 1.5
	47.4	47.0	+0.4
	58.2	57.0	+1.2
St. Cloud granodiorite	132.0	136.0	- 4.0
	143.0	142.0	+1.0
	285.0	278.0	+7.0

An important question is whether the pre-stress *memory* of the rock is retained over periods of time or is only temporary. Uniaxial compression tests were conducted on several samples of Salem limestone that were all prestressed to the same level of 58 MPa. Subsequent loading cycles were performed on each sample

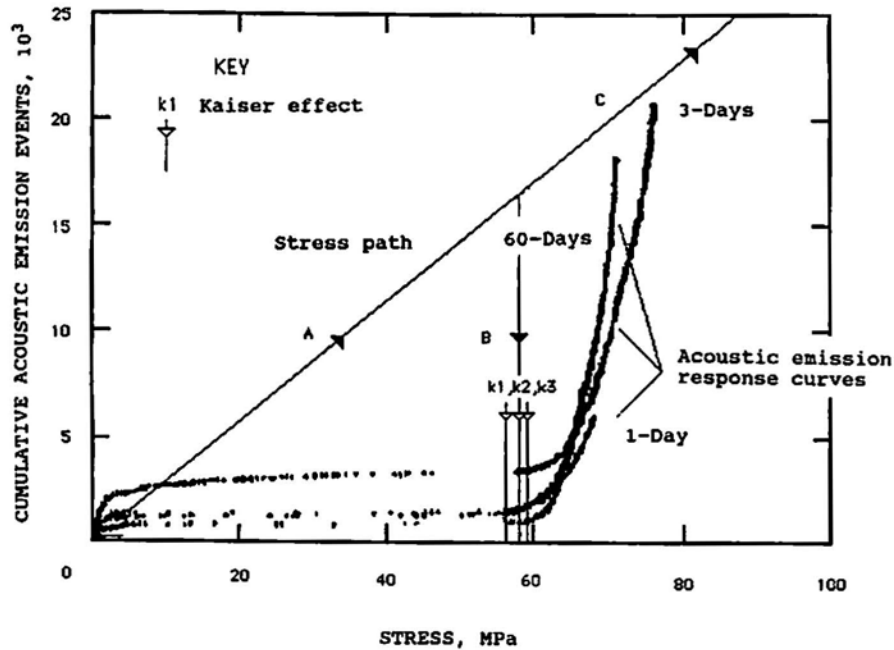


Fig. 11 Cumulative AE as a function of stress for three Salem limestone samples. Each sample was loaded to rupture under uniaxial compression at various time intervals after the initial prestress. Curve A-B represents initial stress path taken while prestress was applied. Curve A-C is stress path taken to detect Kaiser effect (for three separate samples) at time intervals of 1 (k1), 3 (k3), and 60 (k2) days following application of prestress.

to reestablish the pre-stress after periods of 1, 3 and 60 days. Results showed that after 1, 3 and 60 days, the Kaiser effect predicted the pre-stress in all three cases to within a few % (Fig. 11). Thus, even after periods of up to 2 months, the locked-in stress in the rock could accurately be predicted using the Kaiser effect. Another series of uniaxial compression tests was conducted using the St. Cloud gray granodiorite, prestressed to 130 MPa. Results showed that even after 150 days the Kaiser effect was clear, and that the locked-in stress could be estimated (at 124 MPa), within 9% of the prestressed value. For these rocks, there appears no evidence suggesting that the stress memory detected by the Kaiser effect fades within short periods of time. It remains to be established whether peak stress history is retained in rock over much longer periods of time associated with geological events.

The Kaiser effect is known to be dependent upon the confining stress, at least in some rocks. Holcomb (1983) observed that the Kaiser effect increased nearly linearly, by roughly 3.4 MPa per megapascal increase in pressure, in Westerly granite for the range of confining pressures from 5 to 69 MPa. The Kaiser effect was postulated to map a *damage* surface, similar to the Mohr-Coulomb failure envelope. Accordingly, rock under stress states bounded by the damage surface would remain stable (Holcomb and Costin, 1986). For comparison, earlier Bureau results for AE response under triaxial loading of St. Cloud gray granodiorite (Thill, 1973) were reanalyzed. Cumulative AE response was determined at atmospheric pressure and confining pressures of 23, 46, and 69 MPa in conventional triaxial compression tests. A confining pressure was applied to the desired test level, and then an axial stress was applied to the point where the Kaiser Effect could be observed from the text sample and continued through yield and failure (Fig. 12). The results plotted for comparison with those of Holcomb and Costin (1986) for the Westerly granite (Fig. 13) show that the Kaiser effect *damage surface* for the St. Cloud gray granodiorite increases roughly 7.9 MPa per megapascal increase in confinement and has somewhat of a linear trend that roughly parallels the failure surface (ultimate stress). Bureau results for the St. Cloud gray granodiorite tend to support those of Holcomb (1983) in that both the Kaiser effect and the critical stress have a similar dependence on confining pressure. Since the Kaiser effect is influenced by all principal stresses, as pointed out by Holcomb, field determina

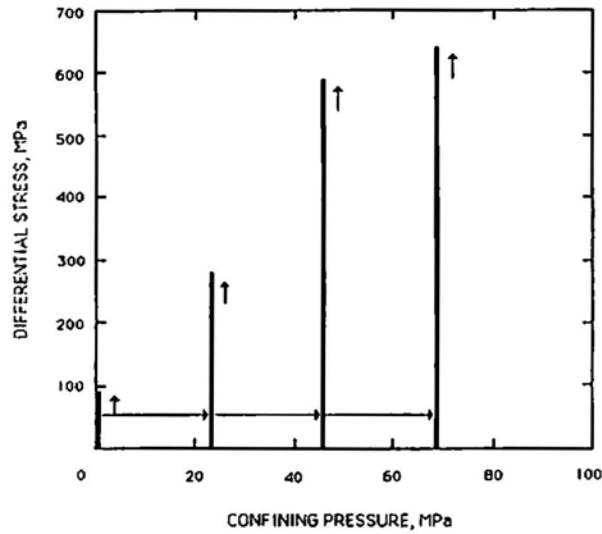


Fig. 12 Stress path used to induce damage in St. Cloud gray granodiorite sample to investigate usefulness of Kaiser effect, while sample was under triaxial compression.

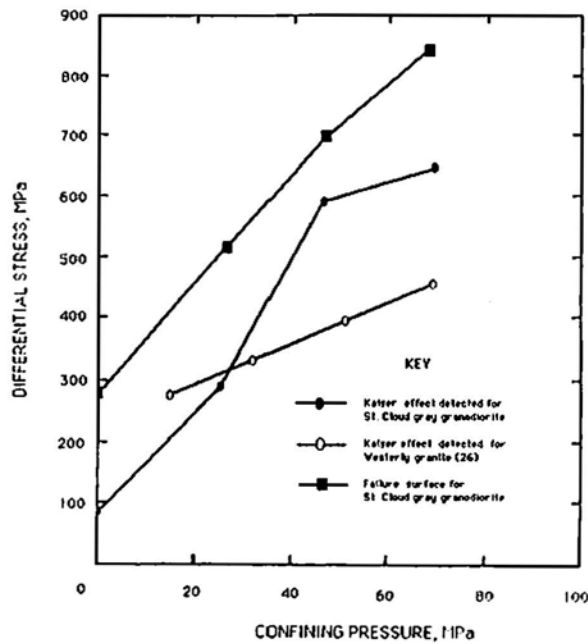


Fig. 13 Increase in ultimate stress and Kaiser effect as a function of triaxial loading for St. Cloud gray granodiorite.

tion of the state of stress using the Kaiser effect will need to separate the effects of the stress components. Hence, more research needs to be done on this topic before the Kaiser Effect can be used with confidence to determine in situ stresses.

6. Conclusions

The Kaiser effect was observed to be repeatable to within a few % for several types of brittle rock. The AE activity displayed repeatable signatures (macro-patterns) diagnostic of deformation processes in the rock,

suggesting that pattern recognition technology might be successfully employed to interpret the generalized regions of deformation and associated stress in rock. It was found, however, that the shape of the AE response curve can be sensitive to measurement settings, such as the sampling rate interval and the amplitude threshold, suggesting the need for standardized procedures when comparing AE patterns. First cycle noise was successfully suppressed to enhance the Kaiser effect by cycling at low-stress level. Stress-strain correlations for interpretation of the AE response were most comprehensive when the stress-volumetric strain curves, rather than customary axial curves, were used for comparison. The Kaiser effect was shown to retain *memory* of peak prestresses over moderate periods of time up to 5 months. Kaiser effect also was noted to be highly sensitive to confining stresses, at least in some rocks, an item that requires further research and consideration for the interpretation of in situ field stresses.

References

American Society for Testing and Materials (1970), "Special Procedures for Testing Rock for Engineering Purposes", ASTM STP 479, Philadelphia, 529 pp.

J.F. Archibald, P.N. Calder, B. Moroz, T. Semadeni, and T.K. Yeo (1988), "Applications of Microseismic Monitoring to Stress and Rockburst Precursor Assessment", *Min. Sci. and Tech.*, 7, 123-132.

G.M. Boyce, W.M. McCabe and R.M. Koerner (1981), "Acoustic Emission Signatures of Various Rock Types in Unconfined Compression", *Acoustic Emission in Geotechnical Engineering Practice*, ASTM STP 750, Philadelphia, pp. 142-154.

W.F. Brace, W.B. Paulding, Jr. and C.H. Scholz (1966), "Dilatancy in the Fracture of Brittle Rocks", *J. Geophys. Res.*, 71, 3939-3953.

E.T. Brown, ed. (1981), *Rock Characterization Testing and Monitoring-ISRM Suggested Methods*, Pergamon Press, New York, 211 pp.

M. Hayashi, T. Kanagawa, R. Hibino, S. Matojioma and V. Tahara (1979), "Detection of Anisotropic Geostresses Using Acoustic Emissions, and Nonlinear Rock Mechanics on Large Excavating Caverns", Paper in *4th International Congress for Rock Mechanics* at Montreaux, Switzerland, A. A. Balkema, Rotterdam, Netherlands, vol. 2, pp. 211-218.

H.R. Hardy, Jr. (1988), "Recent Geotechnical Applications of the Acoustic Emission/Microseismic Technique", *Proc. Conference on Nondestructive Testing and Evaluation for Manufacturing and Construction* (Univ. Ill. Urbana-Champaign, Aug. 9-12), pp. 189-201.

H.R. Hardy, Jr., D. Zhang and J. Zelanko (1989), "Recent Studies Relative to the Kaiser Effect in Geologic Materials" Proc. 4th Conference on Acoustic Emission/Microseismic Activity in Geologic Structures and Materials (Penn. State Univ., Oct. 1985), Trans. Tech. Publ., Clausthal, Federal Republic of Germany.

D.J. Holcomb (1983), "Using Acoustic Emission to Determine In Situ Stress: Problems and Promise", *Geomechanics*, 57, 11-21.

D.J. Holcomb and L.S. Costin (1986), "Damage in Brittle Materials: Experimental Methods", *Proceedings of the 10th U.S. National Congress of Applied Mechanics* (June 16-20), ASME, New York, pp. 107-113.

D.J. Holcomb and R.J. Martin III. (1985), "Peak Stress History Using Acoustic Emissions", *Research and*

Engineering Applications in Rock Masses, ed. E. Ashworth (26th U.S. Symp. on Rock Mechanics, Rapid City, SD, June 26-28), A. A. Balkema, Boston, MA, pp. 715-722.

D.J. Holcomb and L.S. Costin (1986), "Detecting Damage Surfaces in Brittle Materials Using Acoustic Emissions", *Trans. ASME, J. Appl. Mech.*, **53**, 536-544.

J. Kaiser (1950), "An Investigation Into the Occurrence of Noises in Tensile Tests or a Study of Acoustic Phenomena in Tensile Tests", Ph.D. Thesis, Tech. Hochsh. Munich, Federal Republic of Germany, 190 pp. (Engl. transl. from Lawrence Radiation Lab., Livermore, CA, Rep. UCRLTRANS-1082-L).

T. Kanagawa, M. Hayashi and H. Nakasa (1976), "Estimation of Geo-Stress Components in Rock Samples Using the Kaiser Effect", *Cent. Res. Inst. Electr. Power Ind. (Tokyo)*, Rep. 375017, 26 pp.

W.W. Krech, F.A. Henderson and K.E. Hjelmstad (1974), "A Standard Rock Suite for Rapid Excavation Research", *Bureau of Mines RI 7865*, 29 pp.

K. Kurita and N. Fujii (1979), "Stress Memory of Crystalline Rock in AE", *Geophys. Res. Lett.*, **6**, 9-12.

A.E. Lord, Jr. and R.M. Koerner (1983), "AEs in Geologic Materials", *J. Acoust. Emiss.*, **2**(1), 195-219.

K. Mogi (1962), "Study of the Elastic Shocks Caused by the Fracture of Heterogeneous Materials and Its Relation to Earthquake Phenomenon", *Bull. Earthquake Res. Inst., Univ. Tokyo*, **40**, 125-173.

M. Montoto, L.M. Suarez del Rio, A.W. Khair and H.R. Hardy, Jr. (1984), "AE in Uniaxially Loaded Granitic Rocks", 3rd Conf. on AE/Microseismic Activity in Geologic Structures and Materials, eds. H.R. Hardy and F. Leighton, *Trans Tech Publications, Clausthal, Federal Republic of Germany*, pp. 83-100.

S. Murayama (1985), "The Kaiser Effect of a Granite Under Various Loadings", *Jpn. Soc. Civ. Eng.*, 586-593.

National Research Council, Panel on Rock Mechanics Research Requirements. *Rock Mechanics Research Requirements for Resource Recovery, Construction and Earthquake Hazard Reduction*. Nat'l Acad. Press, Washington, D.C., 1981, pp. 42-66.

K.S. Radcliffe, R.E. Thill and J.A. Jessop (1986), "Use of Acoustic Velocity for Predicting Stress Under Uniaxial Compression", (Pres. at 115th Annual AIME Meeting, New Orleans, LA). *Soc. Min. Eng. AIME preprint* 86-147, 11 pp.

C.H. Scholz (1968a), "Experimental Study of the Fracturing Process in Brittle Rock", *J. Geophys. Res.*, **73**, 1447-1453.

C.H. Scholz (1968b), "Correctional to "Experimental Study of the Fracturing Process in Brittle Rock", *J. Geophys. Res.*, **73**, 4794.

R.E. Thill (1973), "Acoustic Methods for Monitoring Failure in Rock", *New Horizons in Rock Mechanics (Proc. 14th U.S. Symp. on Rock Mechanics)*, *Am. Soc. Civ. Eng.*, 649-687.

Evaluation of Joint Properties of Anti-washout Underwater Concrete by Acoustic Emission Measurement

Kazuya Miyano, Tatsuo Kita, Yuji Murakami and Takako Inaba

The authors are affiliated with Technical Research Institute, Hazama Corporation, Tsukuba, Ibaraki 305, Japan.

Abstract

Anti-washout underwater concrete, which has nonsegregating and self-leveling properties in water, has been increasingly employed in underwater massive structures in Japan. However, in such structures, it is normally required to form horizontal construction joints. In case of jointed concrete, it is difficult to elucidate the deformation behavior of the joint and to evaluate the joint properties by only rupture strength. In this study, we perform direct tensile tests of the jointed segments by using acoustic emission (AE) and the tensile strain measurement. This paper shows that AE properties are related to the joint failure behavior, and the joint failure could be located by using AE technique and strain measurement.

1. Introduction

Anti-washout underwater concrete is expected to have greater joint strengths than conventional underwater concrete, because it has high resistance against material washout and hardly breathes (CDTI, 1990). Tests on large specimens have shown that the joint strengths (direct tensile strengths) could be further raised by applying proper surface treatment to the concrete placed prior to the consecutive casting. When jointed concrete is subjected to direct tension, however, the rupture energy due to the direct tension becomes concentrated on the jointed surface, and cracks generated at one location join together resulting in rapid progress of the rupture. This makes it difficult to observe the deformation behavior during the rupture process and to evaluate the joint properties by only the rupture strength. In the present study, the joint properties are evaluated by using the acoustic emission (AE) method to track the behavior of the concrete leading to rupture, and to investigate the internal rupture behavior.

Due to the restrictions on the work underwater, good surface treatment prior to joint placement could be hindered or interrupted depending on the types of structures, construction schedule and complexity of the procedure. Investigation was made on the possibility for improving the joint properties by placement of anti-washout underwater mortar prior to the joint placement, as an alternative to the surface treatment.

Experiments were carried out in two series. Series A was implemented along with direct tensile testing and some of the results on 91-day cured core samples taken from the jointed test specimens were already reported (Miyano and Kita, 1989). The AE method was used in conjunction with the strain measurement to investigate the joint rupture behavior. In Series B, an attempt was made to locate cracks by using the AE and strain measurement. This was to evaluate the rupture behavior in the vicinity of the joints which was coated or not coated by mortar.

2. Behavior of Core Sample with Joints under Direct Tension (Series A)

2.1 Core Tests and Specimen Preparation

The surface of the large specimen used in the long-distance flow test (Kita and Fukudome, 1989) was processed by 1) no treatment, 2) deck brush treatment and 3) high-pressured water jet treatment, prior to the placement of concrete to the joint. The cement used was low-heat type cement. Mixture of crushed sand and mountain sand was used for the fine aggregate and crushed stones (maximum size: 20 mm) for the coarse

Table 1 Mix proportion.

	Series A	Series B - Concrete	Series B - Mortar
Max. aggregate size	20 mm	20 mm	---
Water/cement ratio	69 %	68.8 %	68 %
Sand/aggregate ratio	40 %	40 %	---
Unit weight (kg/m ³)			
W: Water	221	220	330
C: Cement	320	320	485
S: Sand	654	649	1213
G: Gravel	988	1012	---
Water reducing agent	0.004 x C	0.004 x C	0.004 x C
Superplasticizer	0.02 x C	0.02 x C	0.02 x C
Anti-wash agent	2.3	2.3	4.0

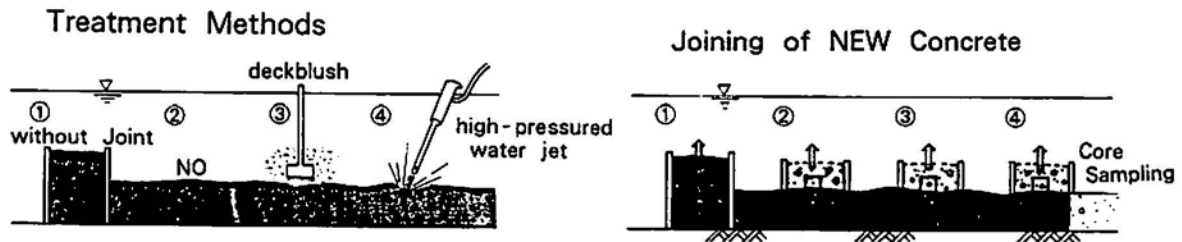


Fig. 1 Treatment methods and joint placement.

aggregate. The admixtures included air-extrated water reducing agent, superplasticizer, and anti-washout agent (cellulose-based). Mix proportion is given in Table 1. The concrete satisfied the conditions of a slump flow of 52.5 cm and air content of 4 %. Core samples were taken at 14 days after joint placement made in a cylindrical shape (15 ϕ x 30 cm), so that the joint surface was set at the center of a sample. Direct tensile test was performed after 91 days. The surface treatment methods and the placement of jointed concrete are shown in Fig. 1.

2.2 AE Measurement and Loading Method

AE measurement was carried out for tracking the behavior of internal rupture in concrete to detect slip, separation and rupture inside the core samples. Although compressive, bending and splitting tensile tests on cement paste, mortar and concrete were extensively reported (Uomoto, 1986; Kodama and Nakasone, 1986), few reports have been made on the direct tensile strength test.

In the experiment, after drying the bonded surface of the specimen, jigs were attached with epoxy bond as shown in Fig. 2. Thus, rings were attached at the top and bottom, ensuring no eccentricity and applying controlled tensile load (1 to 1.5 t/min.). For strain measurement of joint and monolithic portion, three 60 mm strain gauges were attached to each specimen at 30 mm intervals with the middle gauge covering the joint. These were numbered 1, 2 and 3 from the top to the bottom. On the joint, 2 mm gauges were also attached at 4 locations. Locations of strain gauges are shown in Fig. 2.

The AE monitoring system is illustrated in Fig. 3. AE sensors with resonance frequency of 150 kHz were attached directly to the side of the specimen at 4 locations with grease and the AE events in the central 20 cm section of the specimen were counted. For AE detection, the amplifier gain at a pre-amplifier and a main amplifier was 40 dB, and the threshold value was set at 1 V.

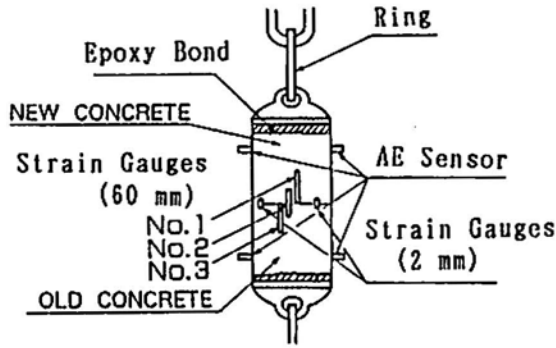


Fig. 2 Direct tensile test.

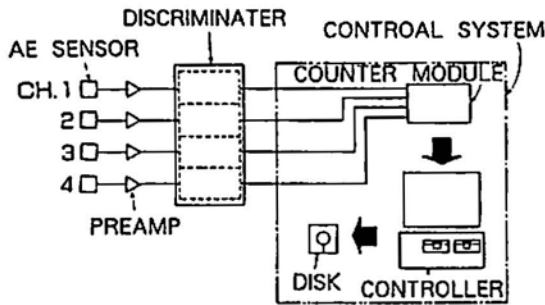


Fig. 3 AE measurement system.

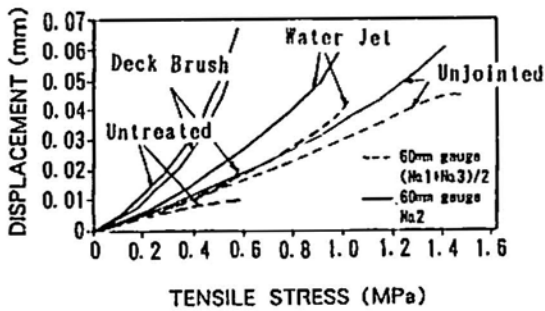


Fig. 4 Relationship between tensile stress and displacement.

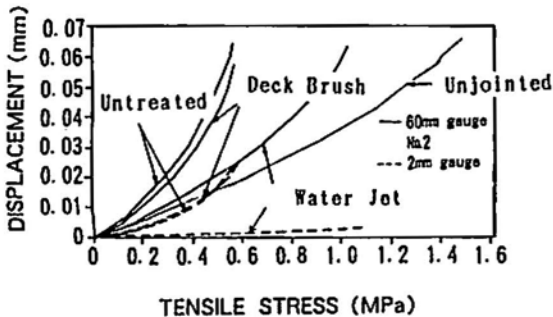


Fig. 5 Relationship between tensile stress and displacement.

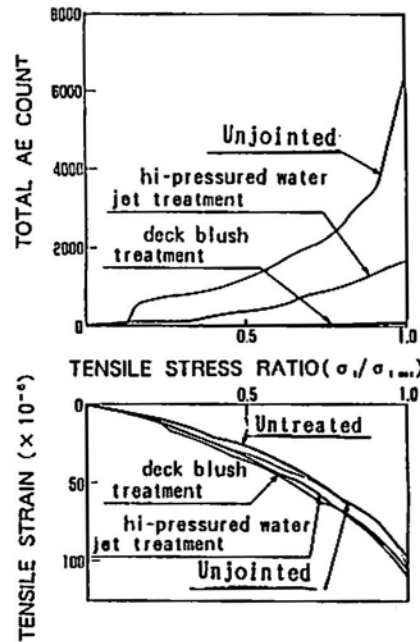


Fig. 6 Direct tensile test results.

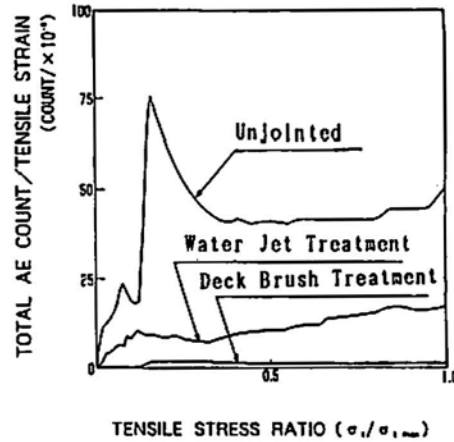


Fig. 7 Relationship between total AE count per micro-strain and tensile stress ratio.

2.3 Test Results

(1) Separation at Jointed Surface

The relationship between the tensile stress and displacement around the joint surface is shown for strain gauges attached at different locations in Fig. 4. The variation of gauge displacements is larger and their values are greater in the vicinity of the joint than those in the monolithic portions when surface treatments other than water jet were applied. The relationships between the tensile stress and displacement around the joint surface measured by a 2 mm gauge, and by the No. 2 gauge are shown in

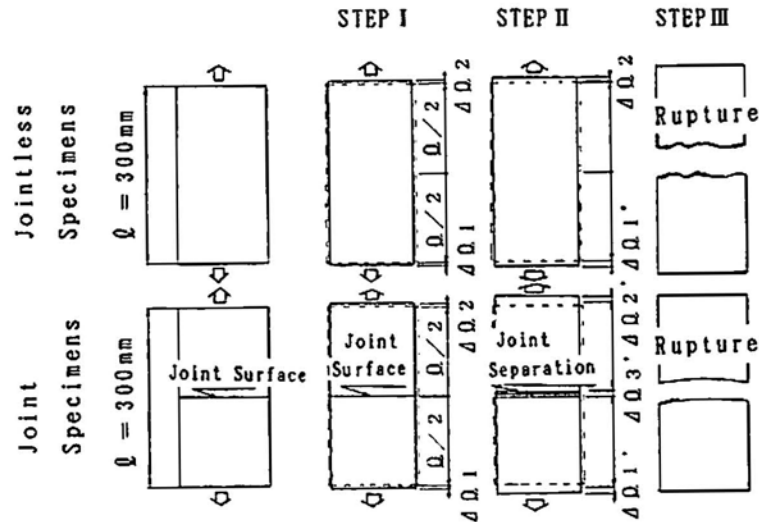


Fig. 8 Joint rupture process model.

Fig. 5. In the cases of concrete untreated and treated with deck brush prior to joint placement, the displacements on the 2 mm gauges increase up to a half of the displacement measured by the No. 2 gauge. The increase of the displacement is even smaller in the case of concrete treated with water jet. It implies that when the direct tensile strength is small, concrete in the joint surface section could deform only half the displacement inside the 60 mm section. Thus, the separation readily occur at the joint surface under direct tensile force. With water jet treatment, on the other hand, the displacement measured on the 2 mm strain gauges accounts only for about 2 % of the total displacement in the 60 mm section, indicating that the load is transferred to the whole section.

(2) AE Counts

The relationships of the total AE counts and tensile strain versus tensile stress ratio are shown in Fig. 6 where the tensile stress is normalized by the strength. Few AE events were observed in the specimen with untreated surface, while sudden emission was observed just prior to rupture in the specimens with deck brush treatment. Significant AE events were observed with water jet treatment, with AE activity gradually increasing after the tensile stress ratio of about 0.5. The monolithic concrete specimen showed a similar pattern of the AE increase to the water jet specimens, with sudden AE increase around 0.8. AE generation was also observed at low stresses. This may result from the engagement of the bonding surface, jigs and rings.

It has been reported (Ohtsu and Shimizu, 1986) that, in uniaxial compression tests, sound samples generate no AE at the initial stage of loading, but immediately prior to the ultimate failure. Opposite results were obtained in the present experiments. Under the direct tensile test, occurrence of AE was observed at the initial stage of loading in the specimens without joints, while AE activity was generally small in specimens with joints. Investigation was made on the relationship between the tensile stress ratio and the total AE count per micro-strain on the No. 2 gauge (cumulative AE/ϵ).

Results are given in Fig. 7. The total AE count per micro-strain increases with the direct tensile strength at the initial loading stage. Concrete specimens with different treatments show constant values in a certain range between 0.3 and 0.9. This implies that the tensile stress is concentrated on the joint surface when the direct tensile strength is small. As the behavior of the specimen away from the joint is similar to that of a monolithic specimen, the region resisting the tensile stress extends into the region away from the joint surface and the total AE count per micro-strain increases.

From the above results, in the direct tensile tests on jointed concrete specimens, the increase of ultimate rupture strength can be expected from the occurrence of AE at the initial loading stage. The more thoroughly the joint surface is treated, the further the region in which the tensile stress is supported extends

into the region away from the joint surface. Thus, the behavior of the specimen starts to resemble that of the jointless monolithic specimen.

(3) Separation Model of Joint Surface

From the results, the rupture process of joint surface is modeled as shown in Fig. 8. In Step I, the tensile behavior (displacement) in the jointless specimens is identical to that of the jointed specimen. In Step II, the separation starts gradually at the joint surface in the jointed specimen. The AE sources are concentrated in the joint zone. In the jointless specimen, AE is observed at the entire domain of a specimen. As a result, a higher number of the AE events is observed in the jointless specimen.

3. Joint Behaviour of Small Specimens under Direct Tension (Series B: Evaluation of AE Location)

3.1 Materials Used and Mix Proportions

Mix proportions of anti-washout underwater concrete and mortar are given in Table 1. Cement used was the same low-heat type cement as that used for the Series A test, but 4.0 kg/m^3 anti-washout agent was added to mortar.

3.2 Specimen Preparation

Four types of small jointed specimens were prepared, with different surface treatment and the placement method as test factors. Joint properties were examined by means of the direct tensile test as in Series A. In preparing specimens, concrete was placed underwater in forms of $15 \phi \times 15 \text{ cm}$ container with the water level at 20 cm. All specimens were removed from the form after 7 days. Specimens to be subjected to the surface treatment underwent the slime treatment (2 to 3 cm removed) with wire brush to prepare the surface for the treatment. The specimens of the surface treatment were placed back into forms of dimension $15 \phi \times 30 \text{ cm}$ together with the untreated specimens and cured for another 14 days. Then, the joint placement was implemented. The joint placement was carried out either by simply placing the same concrete as in Table 1 (Case C) or by placing 5 cm layer of mortar and then casting joint concrete an hour or so later (Case M).

3.3 Direct Tensile Test Method and AE Measurement

The direct tensile strength test was implemented to examine the relationship between the strain and the location of AE sources. Strain gauges are attached to the specimen as shown in Fig. 9 at the age of 56 to 60 days after joint placement. The specimens were taken out of the water tanks 5 to 10 days before the test and dried for 1 day before the jigs were attached to the top and bottom surfaces of the specimens with epoxy adhesive. The loading rate of the tensile tests was 1 to 1.5 t/min. The AE sensors, with resonance frequency of 200 kHz, were attached to the positions shown in Fig. 9, by applying grease to the sensor surfaces and fixing them down with rubber bands. AE measurement system is illustrated in Fig. 10. After increasing the amplitude by 40 dB with pre-amplifier, it was further amplified by 60 dB in the AE signal processor. The

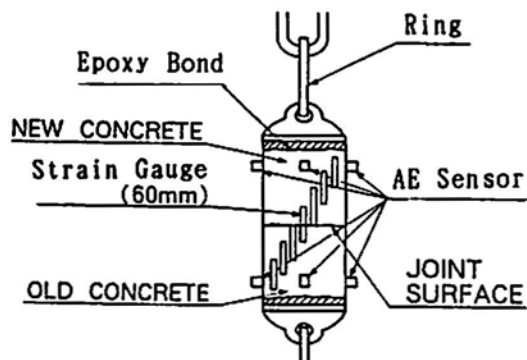


Fig. 9 Direct tensile strength test.

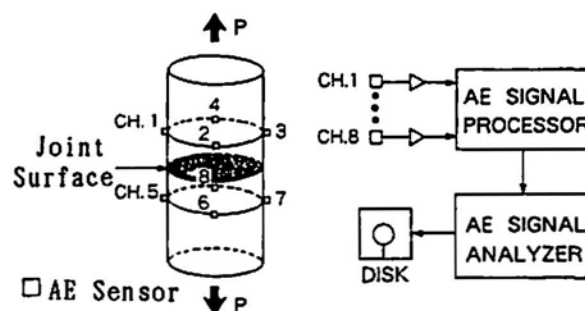


Fig. 10 AE measurement system.

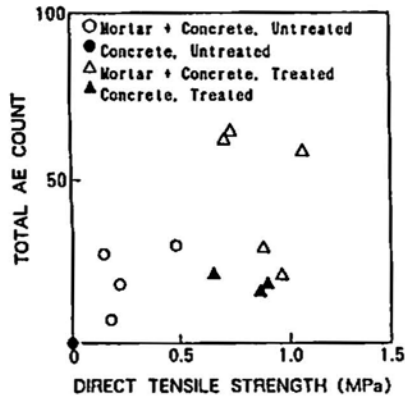


Fig. 11 Relationship between tensile strength and total AE count.

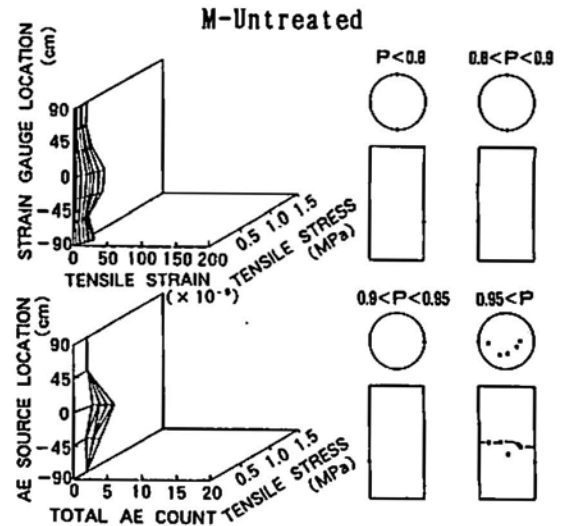


Fig. 12 Three dimensional evaluation of AE source location.

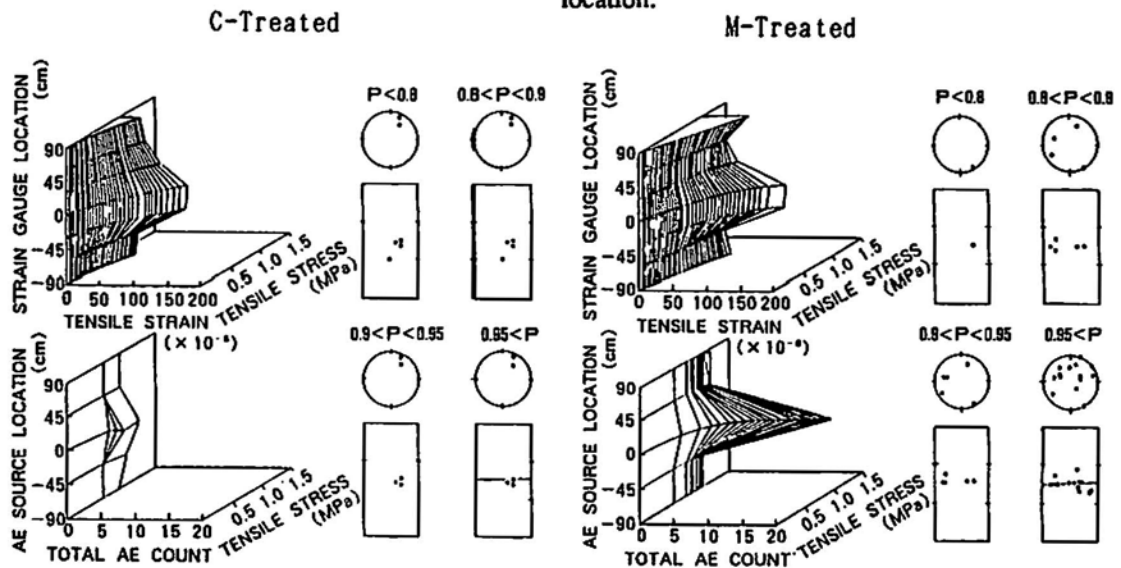


Fig. 13 Three dimensional evaluation of AE source location.

signal data exceeding the threshold value of 0.4 V were analyzed in the AE signal analyser. Although the error in evaluation of AE locations was found to reach 4.1 cm in the vertical direction outside the region surrounded by the sensors, the error in the section surrounded by the sensors was at most 1 cm. Thus, locations of AE sources were taken into account only in the section to which the sensors were attached.

3.4 Test Results

(1) Direct Tensile Strength

The relationship between the total AE counts and direct tensile strength is shown in Fig. 11. In the direct tensile tests of the untreated specimens (Case C-untreated), rupture occurred where the jigs were attached, where the rings for the tensile strength test were placed, and at the joint upon loading. In the untreated mortar-concrete joint specimens (Case M-untreated), tensile strength could be determined. Observation of the rupture surface showed that both the upper and lower rupture surfaces were slimy in Case C-untreated, while mortar could be observed in circular spots at the center of the surfaces in specimens for Case M-untreated along with some slimy parts. Although the direct tensile strengths could not be com-

pared, it was concluded that the joint properties were improved by using mortar in joint placement.

There was little difference in the direct tensile strengths between specimens for Case C- treated and Case M- treated, indicating that the use of mortar makes little difference when the surface is treated prior to joint placement.

(2) Evaluation of AE Locations

The results of the evaluation on locations of AE sources for Cases M-untreated, C-treated, and M-treated are given in Figs. 12 and 13. The counts taken in these experiments were generally low. Even in the case of M-treated which gave the largest count, AE was detected only after the stress ratio had reached 0.9, making it difficult to investigate the rupture process. In all cases, in the vicinity of the joint surface, AE could be detected from the initial stages. From the results of Series A, it is found that AE events are concentrated on the joint surface. The strain measured at various points on the specimens is closely related with the total AE counts. The specimen joined with mortar provided active AE generation on the joint surface immediately before rupture. This is because mortar resists the direct tensile stress as the bonding material between the concrete, and becomes subjected to cracking separation.

4. Conclusion

The results obtained from this study can be summarized as follow:

- 1) In the behavior of jointed specimens under direct tension, the AE count increases as the joint properties are improved by the surface treatment.
- 2) Thorough surface treatment increases direct tensile strength and result in increased AE per micro-strain. It implies that the tensile force is not concentrated on the joint surface but is resisted by the whole region around the joint surface.
- 3) In specimens without surface treatment, the joint properties can be improved by inserting mortar between the concrete. When thorough surface treatment is applied, however, the effect of the use of mortar on the direct tensile strength is small.
- 4) The joint rupture surface under the direct tensile testing can be estimated through evaluation of AE locations.

References

The Coastal Development Technology Institute (CDTI) and The Japanese Institute of Technology on Fishing Ports and Communities (1990), *Anti-washout Underwater Concrete Manual*, pp. 5-32 (in Japanese).

T. Kita and K. Fukudome (1989), "Large Scale Flowing Experiment Report of Low-heat Type Anti-washout Underwater Concrete (No. 1)," *Proceedings of the 44th Annual Conference of JSCE*, 5, pp. 258-259 (in Japanese).

K. Kodama and S. Nakasone (1986), "AE Properties of Mortar and Concrete," 006 Committee Report, No. 87, Japan Society for Nondestructive Inspection, Tokyo, pp. 1 - 6 (in Japanese).

K. Miyano and T. Kita (1989), "Joint Properties of Low-heat Type Anti-washout Underwater Concrete," *Proceedings of the 44th Annual Conference of JSCE*, 5, pp. 264-265 (in Japanese).

M. Ohtsu and E. Shimizu (1986), "Estimation of Deterioration of Core Samples by AE Properties," *Proceedings of the 41st Annual Conference of JSCE*, 5, pp. 117-118 (in Japanese).

T. Uomoto (1986), "Nondestructive Inspection Technique by AE," *Concrete Journal*, 24(3), 56-58 (in Japanese).

Automated Determination of First P-Wave Arrival and Acoustic Emission Source Location

E. Landis, C. Ouyang and S. P. Shah

The authors are affiliated with NSF Center for Science and Technology of Advanced Cement-Based Materials, Northwestern University, Evanston, Illinois, USA

Abstract

An attempt was made to improve the accuracy of AE source location analysis by improving the accuracy of the arrival time routines. The algorithm developed was coded and implemented on a microcomputer for fast data analysis. The motivation being that as less human interpretation is required for data analysis, a greater volume of data can be used and therefore hopefully more useful information can be extracted from an AE test. While it is recognized that many factors other than arrival time influence the accuracy of AE source locations, (such as P-wave velocity and isotropy, signal attenuation and reflections, and transducer size and configuration), a reduction in arrival time error leads to an immediate and substantial improvement in the processing of AE data.

1. Introduction

Measurement of acoustic emissions (AE) is becoming an increasingly popular technique to evaluate damage in quasi-brittle materials such as concrete. Recent developments in data analysis allow a much clearer picture as to how AE signals relate to different damage mechanisms. Deconvolution and moment tensor analysis can give an accurate description of source-time histories (Scruby et al., 1985; Micheals et al., 1981; Ohtsu, 1989). The location of AE sources can be related to areas of greatest damage, and could potentially trace the movement of the fracture process zone.

Obviously the usefulness of an AE source location is increased when uncertainty in its accuracy is reduced. Not only is an accurate source location in itself of interest, but quantitative measurements on crack size and orientation depend on an accurate source location. Several very good methods for determining the source location have been established and are widely being used (Budavari, 1971; Salamon and Wiebols, 1974; Ohtsu and Ono, 1988). These routines require a series of arrival time differences to deduce the source location. The location is generally found by minimizing an error term in a series of linear or nonlinear equations. An improvement in arrival time accuracy will lead to a faster convergence rate and a better estimate.

Recent advances in AE data acquisition systems have made it possible to collect very large amounts of AE data. A typical test where 500 events are detected will produce 4000 separate time histories for an eight channel system. It is quickly realized that for meaningful interpretation of data, the postprocessing of AE signals must be automated. The motivation for this study was to assemble suitable routines for the automatic analysis of AE source locations, and to serve as a platform for more advanced source characterization routines. It should be noted here that all of the following work was based on postprocessing of digitized data. The digitizing rate of the data acquisition system was 16 MHz with 8 bit resolution.

2. Time of Arrival

2.1 Determination of Arrival Time

An important but not very well documented task is the determination of the first P-wave arrival time. Estimates of AE source locations are not meaningful unless a consistent algorithm for arrival times is in

place. Visual inspection of AE signals is appropriate only for a small number of well defined events. This method, while useful as a check, is too sensitive to the subjectivity of the inspector, and is not adequate for processing large amounts of data. For both consistency and volume capacity, a computer aided method must be used.

Maji and Shah (1988) used a statistical analysis of noisy signals to estimate time of arrival. An arrival is detected when the signal exceeds a prescribed limit based on the standard deviation of the initial (noise only) part of the signal. An AE signal is not detected unless it exceeds a minimum of plus or minus three standard deviations of the mean. While the routine works quite well for signals of sufficient amplitude, problems occur when the signal does not exceed the prescribed cutoff. Also, signals with a slow rise time may not cross the threshold until well into the AE signal.

Claxton (1990) used a linear prediction (LP) filter to determine arrival times. An LP filter can be written as:

$$y_n = \sum_{j=1}^N d_j y_{n-j} + x_n$$

In this equation the value y_n is a predicted value based on the previous y_{n-j} data values. The coefficients d_j are determined by power spectrum estimation (Press et al., 1986) of an initial segment of the signal. Once these coefficients are established, they can be used to predict future values of a series based on N previous values. The x_n term represents the error between the predicted value and the actual measured value. When an AE signal arrives, the filter is no longer able to predict the future values, and the error term rises. Arrival time can then be defined as the point at which the error passes above a prescribed threshold.

While this method works quite well for determining arrival times of some types of signals, it had difficulty with signals having a slow rise time. If the signal changes gradually, the filter can respond to these changes and actually predict continued increases or decreases in signal amplitude. It was concluded that this method was not robust enough for the wide variety of signals normally encountered in AE measurements.

2.2 Proposed Filters:

For a robust arrival time algorithm to work well for a wide variety of signal types it must be able to accomplish two things: reduce the effect of noise, and enhance the signal so as to produce a well defined point which indicates the start of an AE event. An adaptive moving average filter was found to be quite effective at removing random noise, and a Laplacian filter was found to enhance a given signal for easy detection.

An analysis of the electrical noise showed not surprisingly that it is essentially a random process. The data acquisition system was triggered to record data records which contained no signal (only noise). A typical autocorrelation of one of these signals is shown in Fig. 1. The autocorrelation, $C(t, \tau)$ of any function, $f(t)$, is a measure of the influence or correlation between $f(t)$ and $f(t + \tau)$ or $f(t - \tau)$. For a stationary process

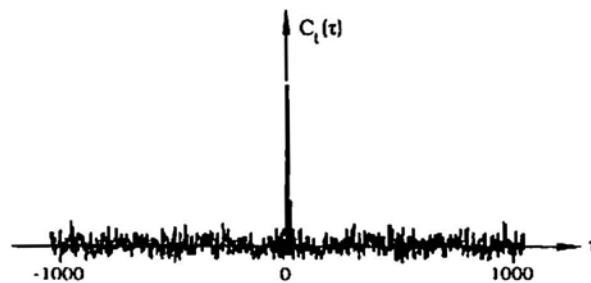


Fig. 1 Autocorrelation function for a signal with noise only.

(one in which statistical properties are invariant to a shift of the time origin), such as electrical noise, autocorrelation depends only on t , and therefore can be written $C(\tau)$. An ideal random process has an autocorrelation which approaches a Dirac delta function, $\delta(x)$. The Dirac delta function is defined as infinity at $x = 0$ and zero for all other x . The autocorrelation shown in Fig. 1 is sufficiently close to a delta function to conclude that the electrical noise is an essentially random (white noise) process.

Since the noise is a random process, simple data smoothing methods can be utilized. One such method is a moving average filter. For *each point* in the signal a new value is assigned based on the average of the surrounding points. A moving average filter can be represented as:

$$y(t) = \frac{1}{2T} \int_{-T}^T x(t - \tau) d\tau$$

where $2T$ is the width of the filter window centered at t . For the discrete time case the moving average can be written as:

$$y(t_i) = \frac{1}{2T + 1} \sum_{j=-T}^T x(t_i + j)$$

This filter effectively removes random noise by 'averaging' it out over a span of $2T$.

A fundamental problem with a moving average filter is the smearing effect it can have on the actual signal. A moving average is a form of a low-pass frequency filter. If the width of the averaging window is set too large, the useful part of the signal can be distorted. In order to minimize this smearing effect, an adaptive moving average filter was applied. In an adaptive moving average, the width of the averaging window varies according to characteristics of the signal in the neighborhood of time, t . For this study, the window width at each time point was determined by:

$$T(t_i) = \frac{1}{a + b\sigma}$$

where σ^2 is the variance of a window of fixed width centered at t_i . The constants a and b were determined by setting a maximum T of 16 points ($1 \mu s$) for a variance of zero, and a minimum T of 3 points ($0.1875 \mu s$) for a variance of two or greater. These maximum and minimum values for T were established for their desirable effect on the signal. The effect of this adaptive moving average filter is illustrated in Fig. 2.

The second stage in locating a precise arrival time is to enhance the signal so that the possible times of arrival can be reduced to a few data points. An effective method for this purpose was taken from an image analysis routine designed for edge detection in 2-dimensional video images. In this routine a new signal, $y(t)$ is generated from the old signal, $x(t)$ such that:

$$y(t) = x(t) - \nabla^2 x(t).$$

The effect of this operation is illustrated in Fig. 3. As can be seen in the figure, the leading edge of the wave front becomes sharper, and the amplitude becomes larger than the original signal. This effect allows the signal to be more easily spotted by a computer algorithm. The arrival time algorithm was coded so that the arrival time was defined as the minimum (or maximum) point before the first wave front.

The effect of this procedure was to reduce the possible arrival time to a few data points. All signals possessed the small characteristic trough (or crest) before the wave front. The width of this trough is generally small so that the arrival time can be fairly precisely defined. This operation is illustrated in Fig. 4 for an actual AE event.

The method used in this study to estimate the time of arrival can be summarized as follows.

1. The signal is "smoothed" using an adaptive moving average filter.
2. The second derivative of the smoothed signal is calculated using a second order finite difference formula. The second derivative is subtracted from the original (smoothed) signal to get the "filtered" signal.
3. The leading edge of the first peak in the filtered signal (point B in Fig. 3) is located by estab

lishing a "trigger" level for that signal, and by noting the point where the filtered signal exceeds that level.

4. The arrival time was defined as the point where the filtered signal was a minimum (or maximum) just before the peak found in 3 (point A in Fig. 3).

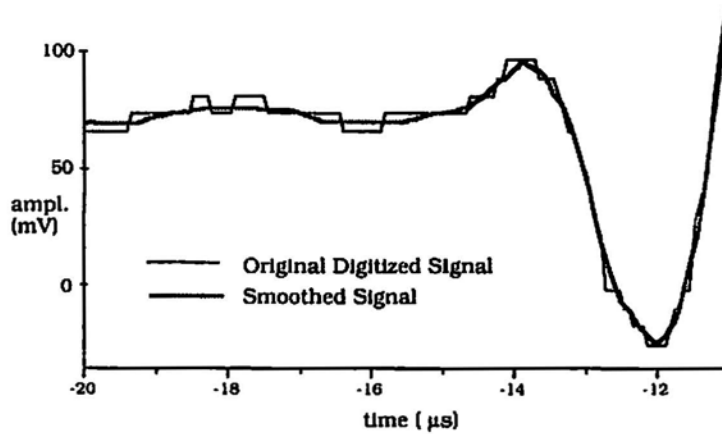


Fig. 2 Effect of adaptive moving average filter.

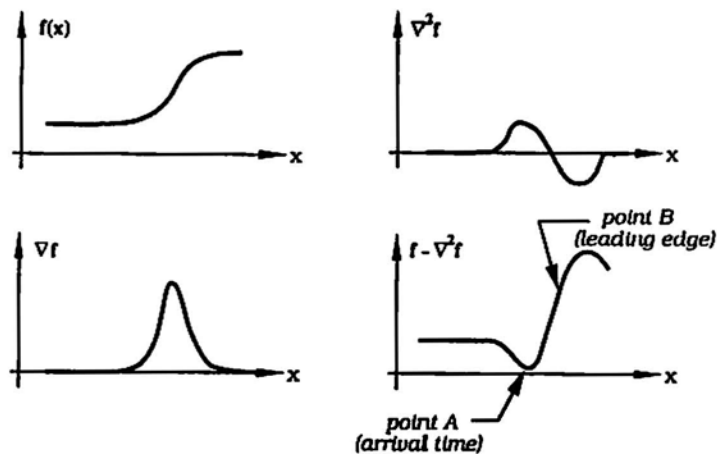


Fig. 3 Effect of a Laplacian operator applied to a smooth 1-D function.

3. Verification

3.1 Arrival Time Verification

In order to verify the accuracy of this approach, an array of AE sensors was mounted on a steel plate as shown in Fig. 5. Since the locations of the source and the receiver were known, and the velocity of a P-wave for the specimen was known, any error in measured arrival time can be attributed to error in the arrival time routine. Two different sources were used; fracture of a 0.5 mm pencil lead, and a 5 mm diameter steel ball dropped from a height of approximately 50 mm. The theoretical difference in arrival times can be computed by taking the difference in ray path lengths between the source and the receiver. These differences in theoretical arrival times were compared with the measured values to evaluate the accuracy in the method.

The pencil lead break generated a very sharp wavefront, and the difference between the theoretical and measured arrival time differences was generally zero, but in almost all cases was less than $\pm 0.125 \mu\text{s}$ (2 data points). The steel ball impact was not quite as sharp as the pencil fracture, but the error was still generally less than $\pm 0.1875 \mu\text{s}$ (3 data points).

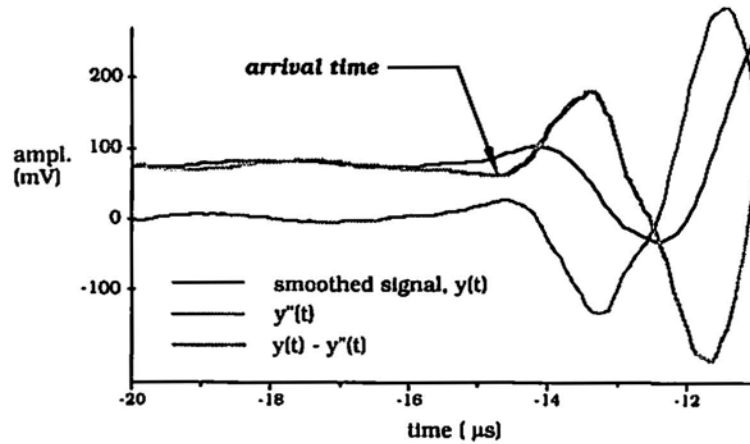
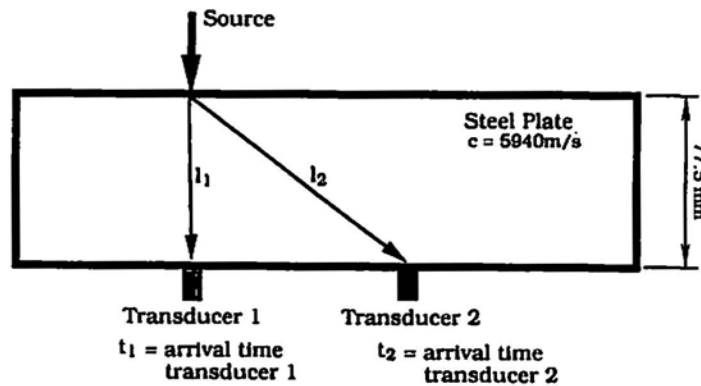


Fig. 4 Laplacian filter and arrival time.



Theoretical difference in arrival times: $\Delta t = t_1 - t_2 = \frac{l_1 - l_2}{c}$

Average error between theoretical and measured arrival time differences: 0 μs; lead pencil fracture
0.1875 μs; steel ball impact

Fig. 5 Verification of arrival time routine.

3.2 Source Location Verification

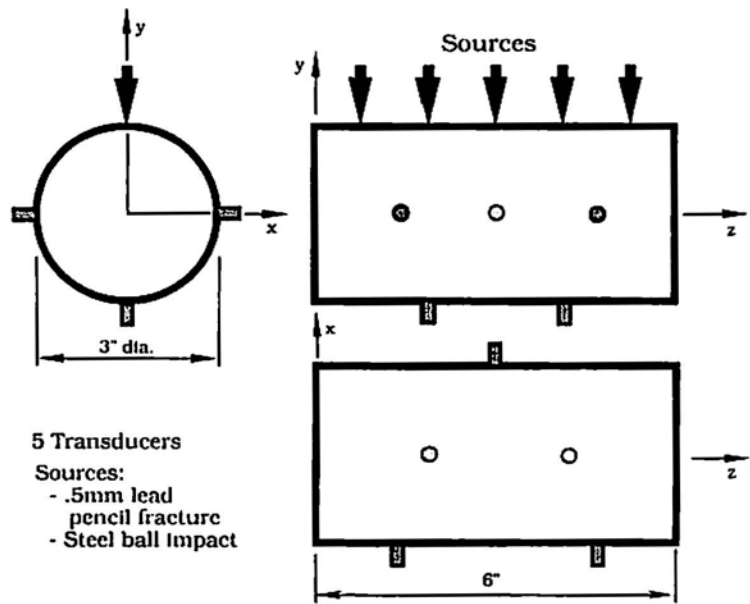
Since the ultimate goal of this study was not to determine arrival times but rather to improve on AE source location estimates, a test was run to measure the accuracy of the source location routine using the newly developed arrival time routine.

The method used to locate the source is an iterative technique which solves the following equation:

$$\Delta t_{ij} = \frac{(|r_i - r| - |r_j - r|)}{c}$$

where Δt_{ij} is the arrival time difference between the *i*-th and *j*-th transducers, *r*, *r_i*, and *r_j* are the locations of the source, *i*-th, and *j*-th transducers, respectively, and *c* is the P-wave velocity in the material (assumed isotropic). A minimum of four transducers is required to solve this equation in 3-dimensions. If more than four transducers are available, a minimum error approach can be used to solve the equation.

A normal strength concrete cylinder was fitted with an array of five AE transducers as shown in Fig. 6. The same artificial sources used on the steel plate were applied to the cylinder at the locations shown in the figure. The source location was then estimated using the above procedure. The error between the measured and actual source locations averaged less than ±1.8 mm for the lead pencil break, and less than ±3.0 mm for the steel ball impact.



Location found by minimizing: $\Delta t_y = \frac{(|r_i - d| - |r_j - d|)}{c}$

Average error between actual and measured source location:
1.8 mm lead pencil fracture
3.0 mm steel ball impact

Fig. 6 Artificial AE source locations in a concrete cylinder.

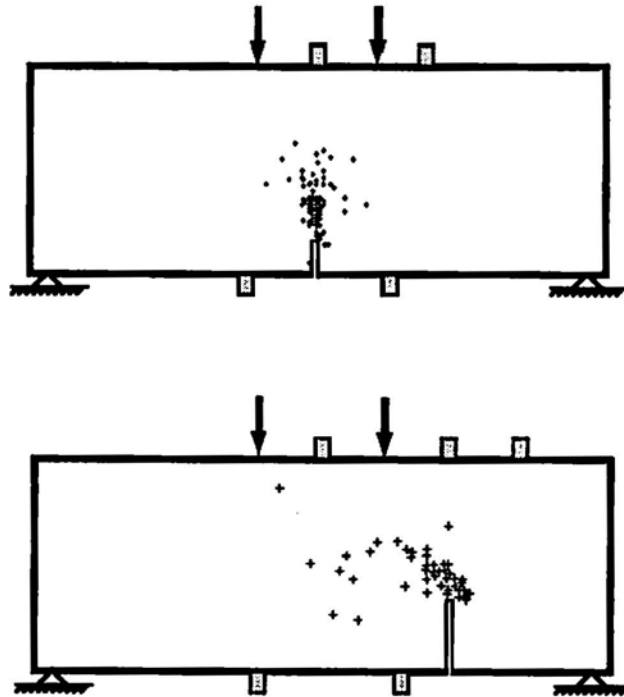


Fig. 7 2-D source locations for center and off center notched mortar beam specimens.

4. Application to Actual AE Signals

The new arrival time/source location method was used to analyze data from a previously conducted mortar beam test. A center-notched and off-center-notched standard mortar beam was subjected to four point load

ing as shown in Fig. 7. Due to equipment constraints, the test was set up for 2-dimensional AE analysis. The data was analyzed to determine the AE source locations. These locations determined are plotted in Fig. 7. This data had been analyzed earlier for source locations using the time of arrival technique of Maji and Shah (1988). While differences in individual AE source locations were noticed, the major influence of the new routine was the usefulness of more data. In the original analysis roughly 25% of all detected events had to be discarded due to either ambiguous arrival times or for failure of the source location routine to converge. For the new routine this number was reduced to about 15%.

Acknowledgements

The research reported herein was supported by a grant from the U.S. Air Force Office of Scientific Research under a program managed by Dr. Spencer T. Wu.

References

C.B. Scruby, G.R. Baldwin and K.A. Stacey (1985), "Characterisation of fatigue crack extension by quantitative acoustic emission", *International J. Fracture*, **28**, 201-222 .

J.E. Micheals, T.E. Micheals and W. Schase (1981), "Application of Deconvolution to Acoustic Emission Signal Analysis", *Materials Evaluation*, **39**, 1032-1036.

M. Ohtsu (1989), "Source kinematics of acoustic emission based on a moment tensor", *NDT International*, **22**(1), 14-20.

S. Budavari (1971), "A Mathematical Method of Determining the Anisotropic Velocity of P-Wave Propagation and for the Seismic Location of Rockbursts", *Geomechanics Journal*, **1**, 15-17.

M.D.G. Salamon and G.A. Wiebols (1974), "Digital Location of Seismic Events by an Underground Network of Seismometers Using the Arrival Times of Compressional Waves", *Rock Mechanics*, **6**, 141-166.

M. Ohtsu and K. Ono (1988), "AE source location and orientation determination of tensile cracks from surface observation", *NDT International*, **21**(3), 143-150.

A. Maji and S. P. Shah (1988), "Process Zone and Acoustic Emission Measurements in Concrete", *Experimental Mechanics*, **28**, 27-33.

R. Claxton (1990), "Characterization of Fracture in Charcol Granite Through Advanced AE Instrumentation and Deconvolution Techniques", Ph.D. Dissertation, Northwestern University, Evanston, Ill.

W.H. Press, B.P. Flannery, S.A. Teukolsky and W.T. Vetterling (1986), *Numerical Recipes*, Cambridge University Press, Cambridge.

A. Papoulis (1977), *Signal Analysis*, McGraw-Hill Book Co., New York.

W. Nieblack (1986), *An Introduction to Digital Image Processing*, Prentice Hall International, London.

H. Stang, B. Mobasher, and S.P. Shah (1990), "Quantitative Damage Characterization in Polypropylene Fiber Reinforced Concrete", *Cement and Concrete Research*, **20**, 540-558.

Application of Acoustic Emission Techniques in the Evaluation of Frost Damage in Mortar

Hisatoshi Shimada and Koji Sakai

The authors are affiliated with Materials Sec., Civil Engineering Research Institute, Hokkaido Development Bureau, 1-3 Higashi, Sapporo, Hokkaido 062, Japan.

Abstract

To characterize the deterioration of concrete due to freezing and thawing, acoustic emissions (AE) of mortar were measured and the locations of AE sources were determined. AE during ice formation and melting were examined to establish the test conditions. In addition, effects of physical and geometric factors on the accuracy of source locations were discussed in order to establish the experimental method. Results showed that AE generation due to ice formation and melting took place during both freezing and thawing cycles. Most AE events from mortar occurred during only freezing cycle and the number of AE events did not increase with the number of freezing-thawing cycles.

The result also showed that the arrival time of AE should be determined from reading waveforms and that error in the arrival time is dependent on the threshold level of the system. The physical and geometric factors were discussed to improve the accuracy of source location.

1. Introduction

In cold regions, concrete structures must be frost-resistant. Commonly, resistance to freezing and thawing is evaluated by accelerated tests based on ASTM C666. However, the relationship between the durability factor obtained from these tests and frost damage in the natural environment has not been clarified yet.

Recently, acoustic emission (AE) techniques have been found useful to detect cracking and deterioration of concrete. The purpose of this study is to describe the deterioration behavior of concrete under freezing and thawing by the AE techniques. Events, arrival time, and amplitude were measured and analyzed on plain mortar.

2. Details of Experiments

Normal portland cement and Toyoura standard sand were used. The water-cement ratio of the mortar was 0.65 and the sand-cement ratio was 2.0. Test specimens were cured in water for 7 days. A 5 mm-high frame of silicone was placed on the top edges of specimens for holding water.

Figure 1 shows a diagram of the AE measuring system. Two or four sensors (PZT type of 140 kHz nominal resonance frequency) were attached to the specimen with thermoplastic wax and silicone. Each sensor was connected to a 40 dB preamplifier with high pass filter of 50 kHz. The output from the preamplifier was fed into an AE acquisition system and a wave memory. In the AE acquisition system, the threshold was set at 55 dB and AE parameters, such as events, maximum amplitude, arrival time, and so on, were recorded. In the wave memory, one waveform was digitally recorded at 200 ns/point with 1024 points. In this paper, data obtained through the AE acquisition system and the wave memory are defined as "event data" and "wave data," respectively. All data were transferred to a computer system and stored on floppy disks.

The length of each freeze-thaw cycle was 6 or 24 hrs. Figure 2 shows these temperature histories. The range of temperatures was from 12°C to -25°C. Noise exclusion is an important consideration in AE measurements. In this study, two or four sensors were used for the source location. It was found that the noise was inconsequential when we selected only AE events which could be detected at all sensors.

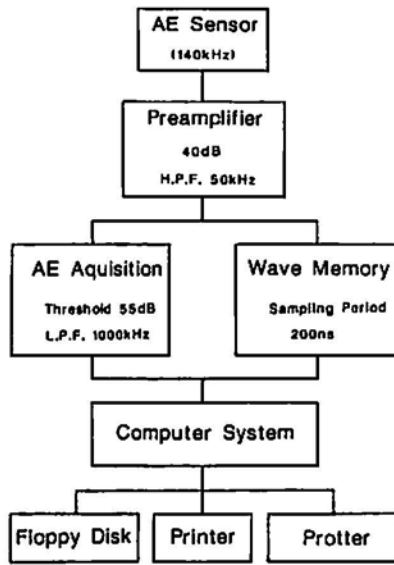


Fig. 1 Acoustic emission measurement system.

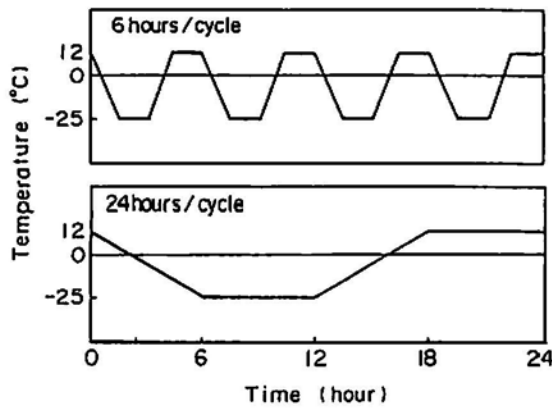


Fig. 2 Temperature history.

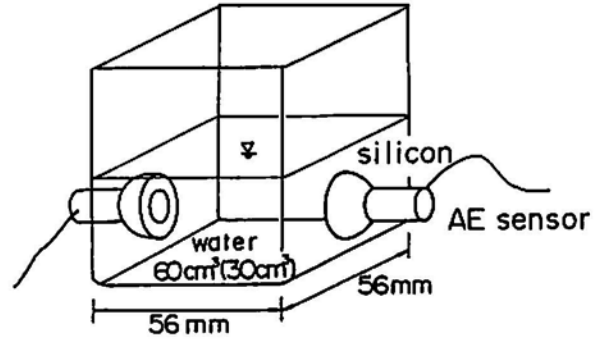


Fig. 3 AE measurement with water under freezing and thawing.

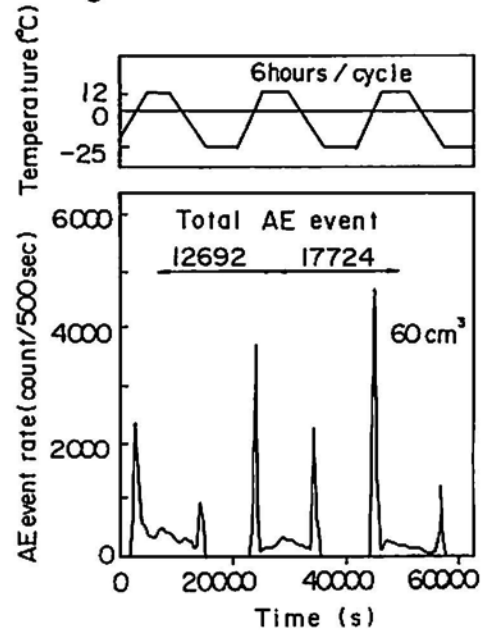


Fig. 4 Acoustic emission at ice formation and melting.

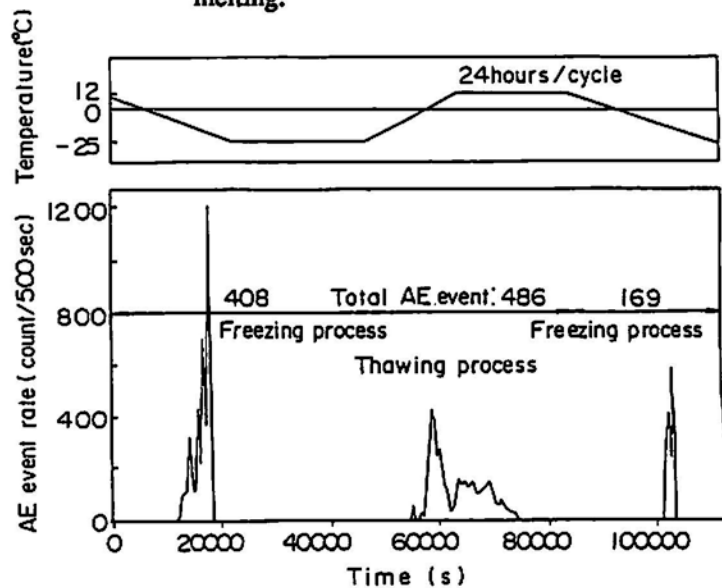


Fig. 5 Acoustic emission at ice formation and melting (24 hrs/cycle).

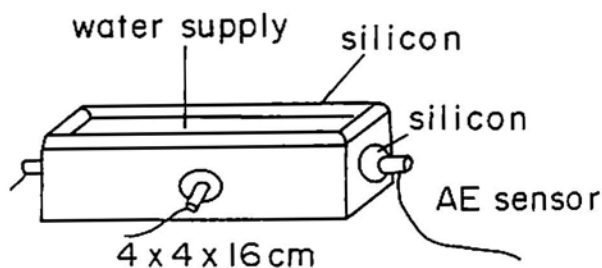


Fig. 6 Rectangular prism specimen.

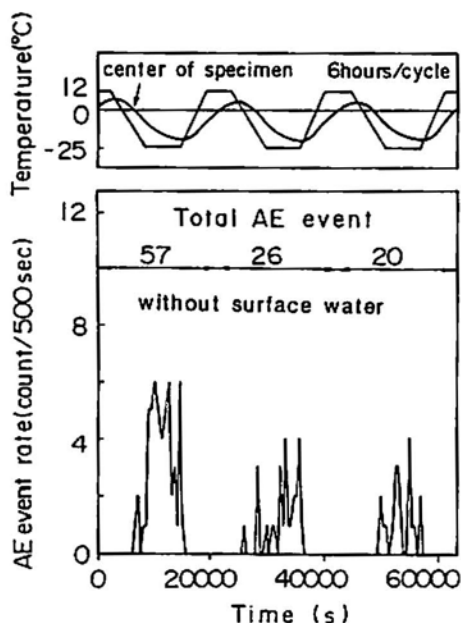


Fig. 7 Acoustic emission in mortar.

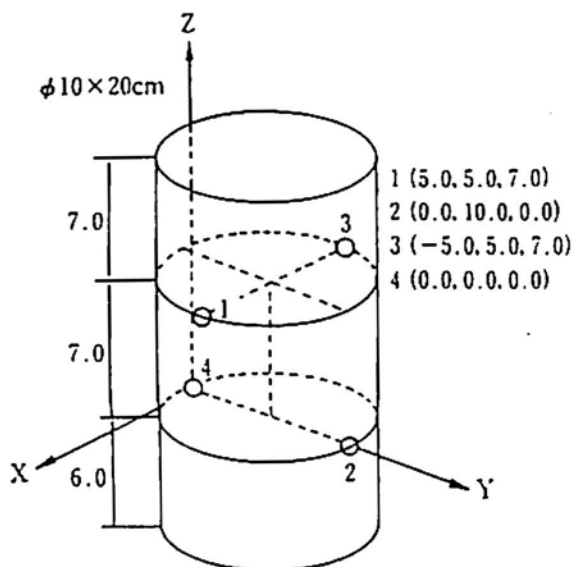


Fig. 8 Cylinder specimen.

3. AE Events due to Frost Damage in the Mortar

Prior to AE tests of mortar, AE events due to ice formation and melting were measured with 30 and 60 cm³ of water in a plastic vessel as shown in Fig. 3. Two sensors were attached to the two sides of the vessel with silicone.

Figure 4 shows the AE events due to ice formation and melting during the six-hour freeze-thaw cycle. AE events occur during thawing as well as freezing. The number of AE events tends to increase with the increase of water volume from 30 to 60 cm³. AE due to ice formation is not observed after the temperature becomes constant at -25°C, but AE due to ice melting occurs successively. This result suggests that the ice does not melt completely during this process. Figure 5 shows a result of the 24 hr freeze-thaw cycle. Under this process, AE events do not occur after ice formation or melting is complete.

Figure 6 shows a rectangular prism specimen. In this experiment, water was supplied to the top surface of the specimen. Thus, the effect of surface water on AE events was taken into account. Figure 7 shows AE events in mortar with and without surface water. AE events in mortar with surface water appears similar to that of ice formation and melting shown in Fig. 4. In contrast, AE events do not occur above 0°C with no surface water. AE events are observed with surface water. The number of AE events in the mortar with surface water is larger than that without surface water. This means that AE events are affected by surface water. The ice formed by surface water is not directly related to frost damage in the mortar. Consequently, the surface water should be removed for AE measurements due to frost damage.

As the specimen is subjected to freezing and thawing in air, water content in the specimen decreases with cycling. Therefore, as shown in Fig. 7, the number of AE tends to decrease as the number of freeze-thaw cycles increases. Although the consideration of surface water indicated that it should be removed, water supply is necessary for the frost damage in mortar. Therefore, water was supplied for about five hrs prior to AE measurements of every three freeze-thaw cycles.

As the specimen is subjected to freezing and thawing in air, water content in the specimen decreases with cycling. Therefore, as shown in Fig. 7, the number of AE tends to decrease as the number of freeze-thaw cycles increases. Although the consideration of surface water indicated that it should be removed, water supply is necessary for the frost damage in mortar. Therefore, water was supplied for about five hrs prior to AE measurements of every three freeze-thaw cycles.

The AE measurements were continued until the 100th cycles. However, there was no increase in the number of AE. This may be associated with a phenomenon like the Kaiser Effect and also with changes in propagation properties due to microcracks.

4. Source Location in Mortar

In order to clarify the deterioration process, a three-dimensional source location analysis was carried out. The shape of the rectangular prism specimen shown in Fig. 6 was found to be unsuitable for the determination of three-dimensional source location because arrival time differences were too large between the axial and lateral direction. Therefore, a cylinder specimen shown in Fig. 8 was used.

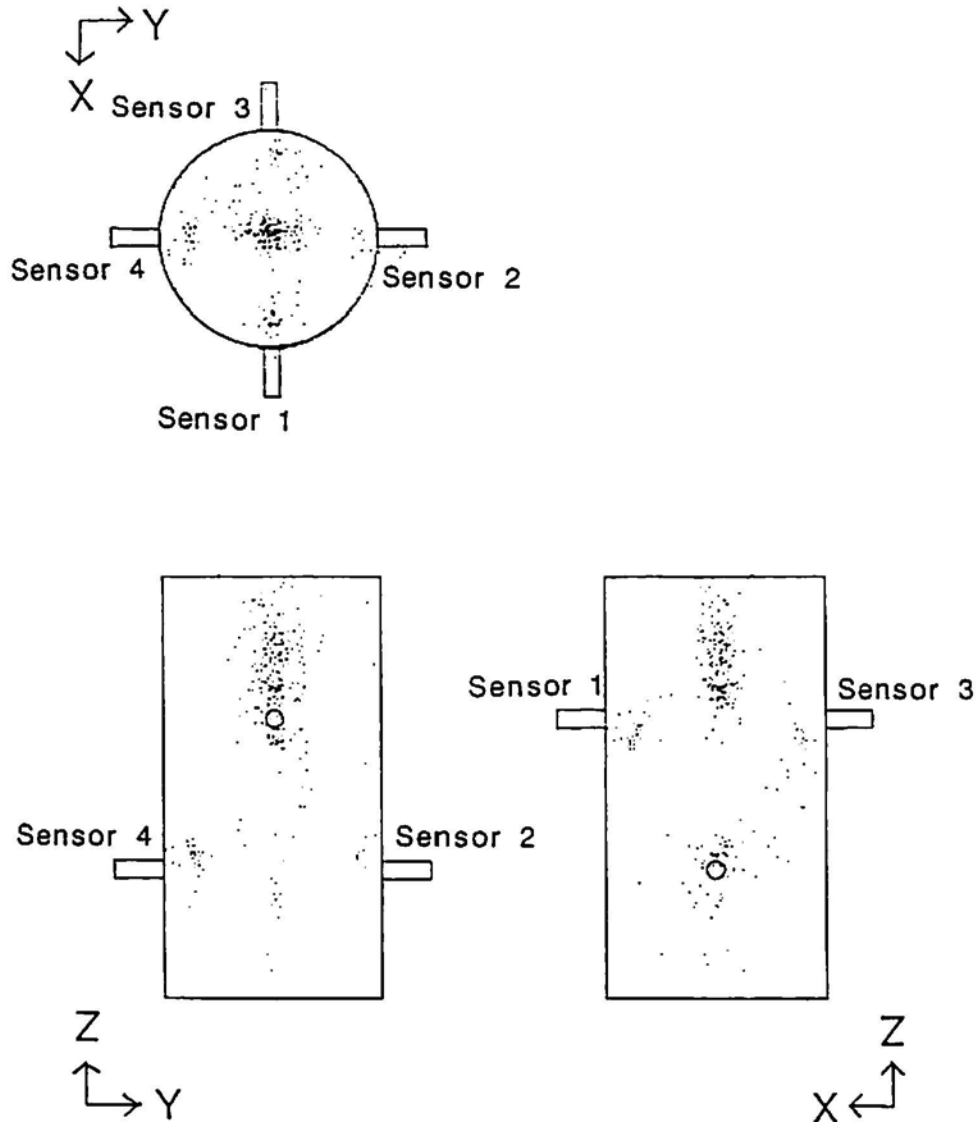


Fig. 9 AE source location.

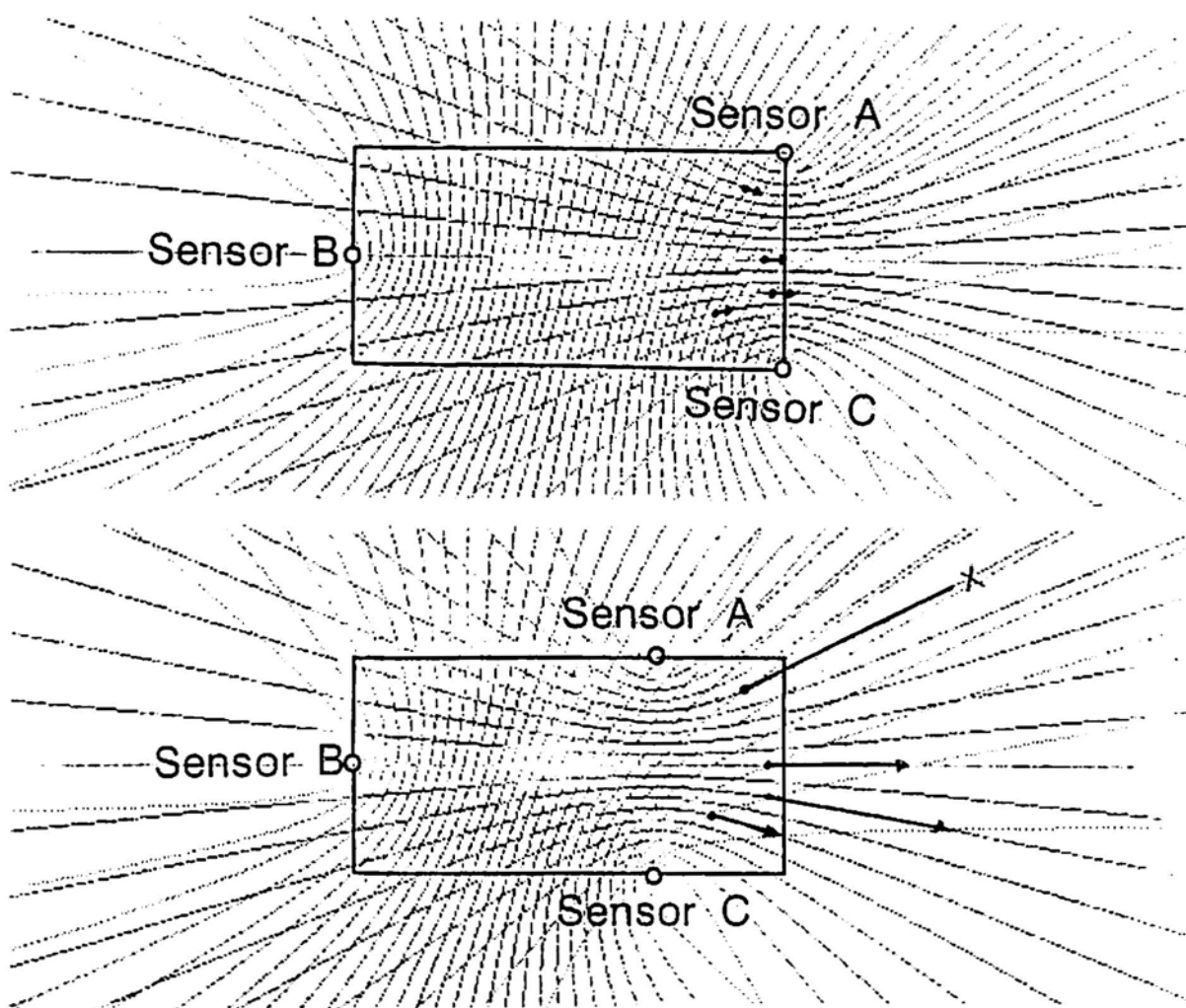


Fig. 10 Effect of geometric factors on source location.

In the analysis, two arrival times, T_e and T_w , were used. T_e is obtained from event data and is the nominal arrival time when the amplitude crosses the 55 dB threshold level for the first time. T_w is the real arrival time obtained from wave data. Based on the arrival time obtained from wave data (T_w), source locations of 64 events could be determined. Whereas based on the arrival time obtained from event data (T_e), source locations of only seven events could be determined. These results indicate that it is difficult to determine the source locations of AE due to frost damage in mortar only from the arrival time of event data (T_e).

Figure 9 shows results of the three-dimensional source location by T_w obtained from wave data. It is obvious that most of AE events occur in the upper portion of the specimen. The deterioration in the upper portion was accumulated more than that of the lower portion, because water was supplied from the top surface of the specimen.

5. Discussion of Factors to Improve the Accuracy of Source Location

In general, AE sources are located from the arrival time difference and a wave velocity. It is known that the accuracy of source location depends on such physical factors as arrival time, wave velocity, attenuation and geometric factors as sensor position and relative position of sensor and source (Rindorf, 1984). From

the present analysis, it is found that the error in arrival time can be minimized by the use of T_w . However, it seems that other factors need to be examined in order to improve the accuracy on the source location.

The wave velocity of the specimen changes depending on the freeze-thaw cycles and was measured after each three freeze-thaw cycle to evaluate the frost damage in the mortar. However, it is realized that the effect of error in the wave velocity on the accuracy of the source location is smaller than that of the arrival time difference.

The amplitude of AE decreases as the distance from the source to the sensor increases due to attenuation. AE events which occur at locations far from the sensor may not be detected. The attenuation may cause a difficulty in the determination of the arrival time as discussed above. Therefore, the distance is preferably determined by taking the effect of attenuation into consideration.

Effect of error on the arrival time was investigated. Figure 10 shows the effect of geometric factors on the two-dimensional source location on the rectangle plane of dimension 10 x 20 cm. It is assumed that the wave velocity is 4000 m/s and the error in arrival time at sensors A and C is absent and that of sensor B is 2.5 μ s. When sensors A and C are set at the corners, the effect of the error on the arrival time is small with respect to located sources. The error vector is plotted in the figure. However, in the case of the bottom figure, it is obvious that the error of located sources is very large.

6. Conclusions

1. AE is observed in ice during melting as well as freezing. The number of AE events tends to increase with the increase of water volume. AE events do not occur after ice formation or melting is complete.
2. The surface water should be removed for AE measurements due to frost damage, because AE events are affected by the surface water.
3. There are few AE events from mortar during thawing, and also there is no increase in the number of AE when the number of freeze-thaw cycles increases.
4. It becomes difficult to determine the source location with the decrease of wave amplitude. The source location could not be performed from the arrival time of event data, the maximum amplitude of which was less than 78 dB. The arrival time was best determined from wave data.
5. The relative position of the sensor and the source is quite important for the source location.

Reference

H.J. Rindorf (1984), "Location of Microseismic Activity," *Proceedings of the Third Conference on Acoustic Emission/Microseismic Activity in Geologic Structures and Materials*, Trans. Tech. Publications, Clausthal, Germany.

An Apology from the Publisher

For the past two years, I was working in Tokyo for the University of California's Education Abroad Program; overseeing the academic programs of about 100 UC students studying in Japan and helping a similar number of exchange students coming to California. My initial plan was to continue work for this Journal from Tokyo. However, the workload there was higher than anticipated since all experienced staff departed before my arrival and I had to find an assistant and train her from scratch. Thus, despite the intention, we have managed to publish only two issues through the end of volume 9 during this period. I must also apologize for not responding to many inquiries regarding papers submitted, subscriptions, publication schedules, etc. Now that I'm back in California, we'll attempt to clear the backlogs of papers and return to more regular publication schedules. Since the research environment in the US and Europe for acoustic emission work has deteriorated substantially in the last few years, we must redouble our efforts to maintain the quality of articles to be published.

This issue contains papers from The International Joint Meeting, 1st Workshop on Acoustic Emission in Civil Engineering and 2nd Workshop on AE and Rock Fracture Mechanics, held in Kumamoto, Japan, October 29 - 31, 1990. Professor Masayasu Ohtsu of Kumamoto University was the Topical Editor for this issue. He also contributed an introduction, "Current Research and Future Trend of AE Applications to Civil Engineering and Geological Technology."

Kanji Ono, Publisher

1992 MEETINGS

4th International Symposium on AE from Composite Materials

The 4th International Symposium on AE from Composite Materials, sponsored by the CARP and ASNT, will be held on July 27 - 31, 1992 at Holiday Inn Crown Plaza in Seattle, USA. Organizing Committee Chair is Dr. Burke Dykes (Boeing Commercial Airplanes) and the Program and Papers Committee is chaired by Dr. D. R. Smith, Jr. (Boeing Commercial Airplanes: FAX No. 206-393-7457). Pre-symposium seminar will be held on July 27 and the Symposium will be July 28 to 31 (3-1/2 days). Proceedings will be published by ASNT.

11th International AE Symposium

The 11th IAES, sponsored by the JSNDI, will be held on Oct. 26 - 29, 1992 at Sun Palace (convention center) in Fukuoka, Japan. Fukuoka is located on the island of Kyushu and can be reached in less than 2 hrs from Tokyo by air or in 6 hrs by trains. Paper and Program Committee Chair is Prof. K. Takahashi (Kyushu Univ.) and the Organizing Committee is chaired by Prof. T. Kishi (Tokyo Univ.) while the Secretarial Committee by Prof. M. Ohtsu (Kumamoto Univ.). For details, contact Prof. K. Takahashi, Research Institute for Applied Mechanics, Kyushu University, Kasuga, Fukuoka 816 Japan. FAX No. 81-92-582-4201 The Proceedings will be published by JSNDI.

1991/92 SUBSCRIPTION RATE for Volume 10

Base rate for one volume (four issues)	\$ 96.00
Add Postage of	
U.S. - Book rate	\$ 8.00
All others - Book rate	\$ 11.00
U.S., Canada - First class	\$ 17.00
Western Europe - Air mail rate	\$ 25.00
All others - Air mail rate	\$ 30.00
Add \$5 without payment upon order. Payment must be in U.S. dollars drawn on a U.S. bank. Bank transfer accepted to the A.E. Group account (Account No. 080-03416470) at	
Sumitomo Bank of California	
San Fernando Valley Office	
15250 Ventura Blvd	
Sherman Oaks, CA 91403-3262	

Notify us of such a transfer as the bank cannot sometimes give us the name of the payer. One volume of four issues per year. Index included in the Oct.-Dec. issue: Back issues available at \$50 per volume for Vols. 1 - 3, \$90 per volume for Vols. 4 - 9. US surface postages \$8 per volume. For Canada and overseas surface delivery, add \$11 and for air mail, add \$30 per volume (adjusted for multi-volume order). All orders should be sent to

Acoustic Emission Group
308 Westwood Blvd, Box 364
Los Angeles, CA 90024-1647

Editor-Publisher	Kanji Ono	(310) 825-5233
Send FAX to		(818) 368-8309
Editorial Assistant	Barbara Brooks	
Cover Design	Robin Weisz	
Production	UCLA Publication Services	

Publication Date of This Issue: 2 August 1992.

Notes for Contributors

1. General

The Journal will publish contributions from all parts of the world and manuscripts for publication should be submitted to the Editor. Send to:

Professor Kanji Ono, Editor - JAE
6532 Boelter Hall, MSE Dept.
University of California
Los Angeles, California 90024-1595 USA

European authors may submit manuscripts directly to:

Dr. Roger Hill, Associate Editor - Europe
Department of Physical Sciences
Trent Polytechnic
Clifton Lane
Nottingham NG11 8NS England United Kingdom

Authors of any AE related publications are encouraged to send a copy for inclusion in the AE Literature section to:

Mr. T.F. Drouillard, Associate Editor - JAE
Rockwell International
Energy Systems Group
P.O. Box 464
Golden, Colorado 80401

All the manuscripts will be reviewed upon submission to the Editor. Only papers not previously published will be accepted. However, special consideration will be given to papers published in conference proceedings of limited circulation; consult the editors.

Authors (unless stipulated otherwise by governments) must agree to transfer the copyright to the Journal and not to publish elsewhere, a paper submitted to and accepted by the Journal.

A paper is acceptable if it is a revision of a governmental or organizational report, or if it is based on a paper published in a conference proceedings volume of limited distribution.

An abstract not exceeding 200 words is needed for Research and Applications articles, while it should be shorter than 100 words for other articles.

The language of the Journal is English. All papers should be written concisely and clearly.

2. Page Charges

No page charge is levied. Fifty copies of off-prints will be supplied to the authors free of charge.

3. Manuscript for Review

Manuscripts for review need only to be typed legibly; preferably, double-spaced on only one side of the page with wide margins and submitted in duplicate.

The title should be brief. Except for short communications, descriptive heading should be used to divide the paper into its component parts. Use the International System of Units (SI).

References to published literature should be quoted in the text citing authors and the year of publication. These are to be grouped together at the end of the paper in alphabetical and chronological order.

Journal references should be arranged as below.

H.L. Dunegan, D.O. Harris, and C.A. Tatro (1968), Eng. Fract. Mech., 1, 105-122

Y. Krampfner, A. Kawamoto, K. Ono, and A.T. Green (1975), "Acoustic Emission Characteristics of Cu Alloys under Low-Cycle Fatigue Conditions" NASA CR-134766, University of California, Los Angeles and Acoustic Emission Tech. Corp., Sacramento, April.

A.E. Lord, Jr. (1975), Physical Acoustics: Principles and Methods, Vol. 11, eds. W. P. Mason and R. N. Thurston, Academic Press, New York, pp. 289-353.

Abbreviations of journal titles should follow those used in the ASM Metals Abstracts. In every case, authors' initials, appropriate volume and page numbers should be included.

Illustrations and tables should be planned to fit a single column width (85 mm or 3.3") or a double width (180 mm or 7"). For the reviewing processes, these need not be of high quality, but submit glossy prints with the final manuscript. Lines and letters should be legible (smallest character should be larger than 1 mm).

4. Review

All manuscripts will be judged by qualified reviewers. Each paper is reviewed by one of the editors and typically sent for review by members of the Editorial Board. The Board member may seek another independent review. In case of disputes, the author may request other reviewers.

5. Electronic Media

In order to reduce any chance of typographical error, the authors are encouraged to submit a floppy disk copy of the text. We can read Macintosh and IBM PC formats. Those who can connect to computer networks, such as BITNET, ARPANET, ASIANET, EARN, NETWORK, UUCP, CSNET, JANET, OZ, etc. can send to "ono@seas.ucla.edu". Note the change in this address.

6. Color Photograph

We can print color photographs needed to enhance the technical content of an article. Because of the cost, the author is asked to pay \$350 per page.

Journal of Acoustic Emission (JACEDO)

Contents

Special Issue on The International Joint Meeting, 1st Workshop on Acoustic Emission in Civil Engineering and 2nd Workshop on AE and Rock Fracture Mechanics, Kumamoto, Japan, October 29 - 31, 1990.

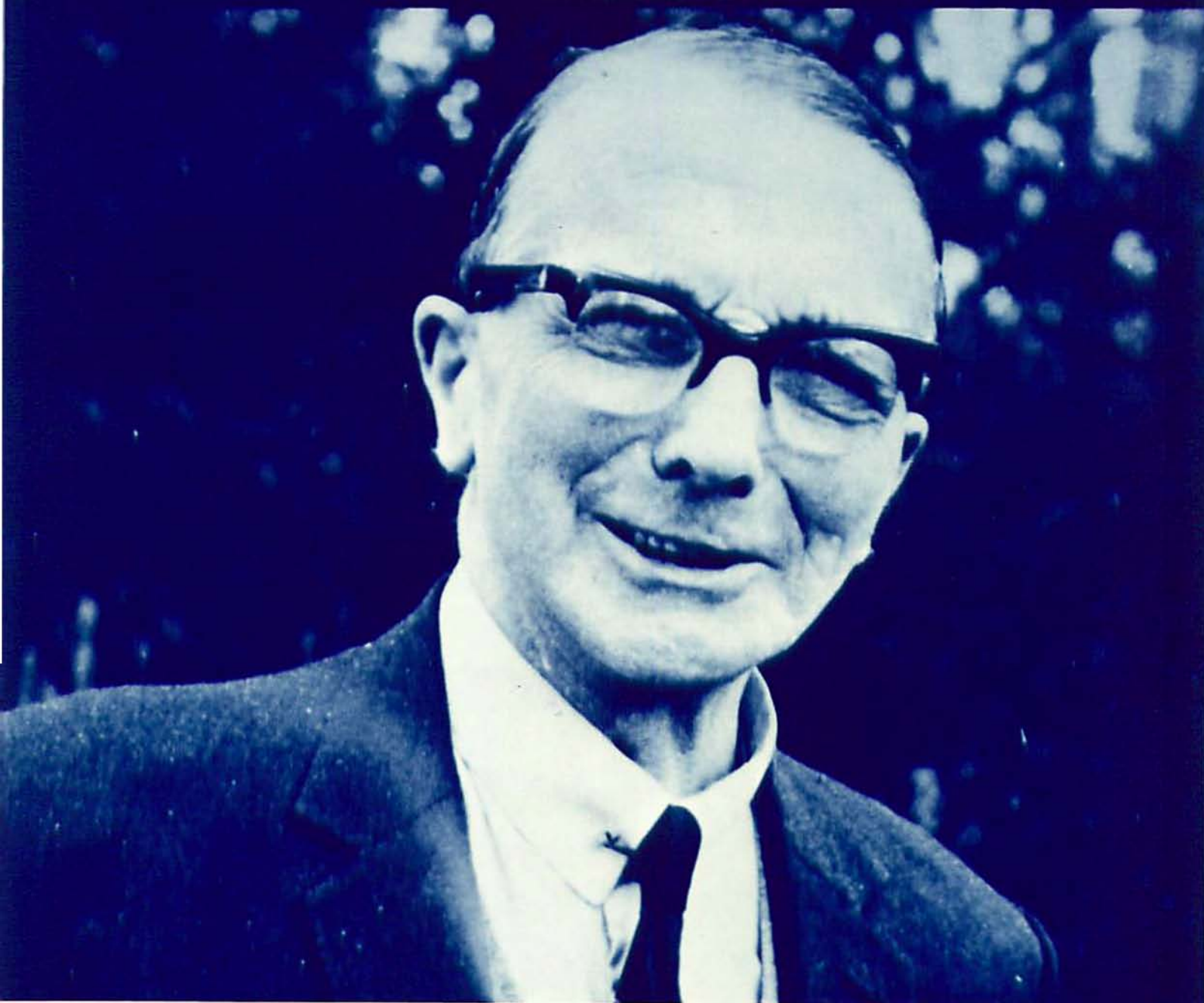
Masayasu Ohtsu, Topical Editor

Current Research and Future Trend of AE Applications to Civil Engineering and Geological Technology Masayasu Ohtsu	i
Variety of Acoustic Emission Waveforms Produced by Discrete Crack Growth in Rock Steven D. Glaser and Priscilla P. Nelson	S1-S12
Estimation of Maximum Stress in Old Railway Riveted I-Girder Bridges using Acoustic Emission Signals Hisanori Otsuka, Hiroshi Hikosaka, Hiroyuki Miyatake and Syouzou Nakamura	S13-S17
Another Look at Booming Sand Marcel F. Leach and Gottfried A. Rubin	S18-S21
Expected Acoustic Emission from Around a Shaft in Intact Rock B.J.S. Wilkins and G.L. Rigby	S22-S28
Acoustic Emission Monitoring during Microseismic Activity Caused by Mine Subsidence Brian R. A. Wood and Robert W. Harris	S29-S34
Acoustic Emission/Microseismic Activity Monitoring of Salt Crystallization for Stone Conservation M. Montoto, R.M. Esbert, L.M. Suárez del Río, V.G. Ruiz de Argandoña and C.M. Grossi	S35-S41
Acoustic Emission Monitoring during In-situ Heater Test of Granite T. Ishida, K. Kitano, N. Kinoshita and N. Wakabayashi	S42-S48
Using Acoustic Emission Testing in Seepage Investigations Andrew R. Blystra	S49-S54
Acoustic Emission of Penetration Experiments to Judge Soil Condition S. Naemura, M. Tanaka, S. Nishikawa, M. Nakamura, K. Jo and T. Kishishita	S55-S58
A Laboratory Investigation of AE from Coal R. W. Harris, B. R. A. Wood and T. Flynn	S59-S62
Determination of the Initial Stresses on Rock Mass using Acoustic Emission Method K. Michihiro, K. Hata, H. Yoshioka and T. Fujiwara	S63-S76
U.S. Bureau of Mines Research on the Kaiser Effect for Determining Stress in Rock Michael J. Friedel and Richard E. Thill	S77-S89
Evaluation of Joint Properties of Anti-washout Underwater Concrete by Acoustic Emission Measurement Kazuya Miyano, Tatsuo Kita, Yuji Murakami and Takako Inaba	S90-S96
Automated Determination of First P-Wave Arrival and Acoustic Emission Source Location E. Landis, C. Ouyang and S. P. Shah	S97-S103
Application of Acoustic Emission Techniques in the Evaluation of Frost Damage in Mortar Hisatoshi Shimada and Koji Sakai	S104-S109
An Apology from the Publisher	S110
Meetings in 1992	S110

An International
Forum For
The AE Science
and Technology

JOURNAL OF ACOUSTIC EMISSION

Vol.10,Nos.3-4, 1991/92



Dr. Raymond W. B. Stephens (1902-1990)

Endorsed by
AEWG, AEWGI
CARP and
EWGAE

Published by
Acoustic Emission Group
Los Angeles, CA

JOURNAL OF ACOUSTIC EMISSION

Editor: Kanji Ono

Associate Editors: A. G. Beattie, T. F. Drouillard, R. Hill and S. L. McBride

1. Aims and Scope of the Journal

Journal of Acoustic Emission is an international journal designed to be of broad interest and use to both researcher and practitioner of acoustic emission. It will publish original contributions of all aspects of research and significant engineering advances in the sciences and applications of acoustic emission. The journal will also publish reviews, the abstracts of papers presented at meetings, technical notes, communications and summaries of reports. Current news of interest to the acoustic emission communities, announcements of future conferences and working group meetings and new products will also be included.

Journal of Acoustic Emission includes the following classes of subject matters;

A. **Research Articles:** Manuscripts should represent completed original work embodying the results of extensive investigation. These will be judged for scientific and technical merit.

B. **Engineering Applications:** Articles must present significant advances in the engineering applications of acoustic emission. Material will be subject to reviews for adequate description of procedures, substantial database and objective interpretation.

C. **Technical Notes:** This class provides publications of works of current interest, and new or improved experimental techniques and procedures.

D. **Communications:** Short items of current interest, discussions of published articles and relevant applications.

E. **AE Literature:** This section will collect the titles and abstracts of papers published elsewhere and those presented at meetings and conferences. Reports of conferences and symposia will also be presented, together with meeting schedules.

F. **Reviews, Tutorial Articles and Special Contributions:** This class of articles will cover the subjects of general interest.

Nontechnical Section: This part will cover book reviews, significant personal and technical accomplishments, current news and new products.

2. Endorsement

Acoustic Emission Working Group (AEWG), European Working Group on Acoustic Emission (EWGAE), Committee on Acoustic Emission from Reinforced Composites (CARP), and Acoustic Emission Working Group of India have endorsed the publication of Journal of Acoustic Emission. This Journal gratefully acknowledges financial contributions from EWGAE and AEWG.

3. Governing Body

The Editor and Associate Editors will implement the editorial policies described above. The Editorial Board will advise the editors on any major change. The Editor, Professor Kanji Ono, has the general responsibility for all the matters. Associate Editors, Dr. S.L. McBride and Dr. A.G. Beattie, assist the review processes as lead reviewers and Associate Editor, Dr. R. Hill coordinates the regional review processes for Europe. Mr. T.F. Drouillard is responsible for the AE Literature section.

The members of the Editorial Board will advise and assist the editors on the publication policies and other aspects. They will promptly review the manuscript assigned and will contribute actively to the Journal. The Board presently includes the following members:

John Baron	(Canada)
F. Beall	(USA)
L. Bolin	(Sweden)
F.R. Breckenridge	(USA)
S.H. Carpenter	(USA)
H. Crostack	(FRG)
D.M. Egle	(USA)
P. Fleischmann	(France)
T.J. Fowler	(USA)
L. Golaski	(Poland)
M.A. Hamstad	(USA)
H.R. Hardy, Jr.	(USA)
T. Holroyd	(UK)
I.V. Ivanov	(Russia)
P. Jax	(FRG)
T. Kishi	(Japan)
A.E. Lord, Jr.	(USA)
K. Mogi	(Japan)
W. Morgner	(DDR)
C.R.L. Murthy	(India)
A. Nielsen	(Denmark)
M. Ohtsu	(Japan)
A.A. Pollock	(USA)
J. Rogei	(France)
I. Roman	(Israel)
C. Scruby	(UK)
C. Thaulow	(Norway)
E. Waschkies	(FRG)
K. Yamaguchi	(Japan)

4. Publication

Journal of Acoustic Emission is published quarterly in March, June, September and December by Acoustic Emission Group, 308 Westwood Blvd. - Box 364, Los Angeles, CA 90024-1647. It may also be reached at 5731 Boelter Hall, University of California, Los Angeles, California 90024-1595 (USA) telephone 310-825-5233. FAX 818-368-8309.

5. Subscription

Subscription should be sent to Acoustic Emission Group. Annual rate for 1992 and 1993 is US \$96.00. For surface delivery, add \$6 in the U.S. and \$8 for Canada and elsewhere. For air mail delivery to US and Canada, add \$15, South America and Western Europe, add \$23 and add \$28 elsewhere. Add \$5.00 for orders not prepaid and requiring invoices. Overseas orders must be paid in US currencies with a check drawn on a US bank. Inquire for individual and bookseller discounts.

6. Advertisement

No advertisement will be accepted, but announcements for books, training courses and future meetings on AE will be included without charge.

Acoustic Emission of the 45HNMFA Structural Steel during Low-Cycle Fatigue

J. Siedlaczek, S. Pilecki and F. Dusek

Abstract

This paper presents the results of the measurements of Acoustic Emission (AE) count rate during low-cycle fatigue of the variously heat treated 45HNMFA structural steel. This steel is used for the production of high-pressure chambers. The experimental technique and results are described. The most important result of this investigation is the occurrence of three stages of the AE activity during the low-cycle fatigue. These dependencies can be applied in monitoring the service life (safe operation period) of high-pressure chambers and/or other studied objects.

1. Introduction

When investigating the properties of materials in the region of low-cycle (high stress amplitude) fatigue, they are supported by the records of hysteresis loops arisen due to elastic-plastic deformations during particular loading cycles. The area enclosed by the loop is proportional to the energy dissipated by the material during this loading cycle (Szczepinski, 1984). From the practical point of view, the purpose of the investigation at low-cycle fatigue is as follows:

- a) determining the service life of a specimen or a machine part at the given loading level;
- b) estimating the allowable load for a given number of cycles to failure.

The problems in question are the accuracy in defining these and the certainty of how we can put the obtained results into practice. It is difficult to answer these questions while designing a component or structure for services at the low number of cycles to failure. Either by the influence of scattering or by an inaccurate estimation of the limiting deformation (or stress) value, a possible failure of the structure can appear.

Such a case occurs in high-pressure chamber (Unipress, 1986) subjected to conditions of low-cycle fatigue loading. The fatigue computations (Siedlaczek, 1983) based on the presumptions of Lamé do not give satisfactory results, because the problem is being solved in the region of elastic deformations (strains) and the calculated allowed loading is then (at the safety factor, $n = 1$) up to 4 times lower than that used for designing the high-pressure chamber for laboratory practice.

Received 3 September 1988, in revised form, 18 July 1991. J. Siedlaczek is affiliated with High Pressure Research Center, Polish Academy of Sciences, Sokolowska 29, 01-142 Warsaw, Poland, S. Pilecki is with Institute of Fundamental Technological Research, Polish Academy of Sciences, Swietokrzyska 21, 00-049, Warsaw, Poland, and F. Dusek is with Institute of Physical Metallurgy, Czechoslovak Academy of Sciences, Zizkova 22, 616 62 Brno, Czechoslovakia.

In this situation, a complicated system of protections from possible consequences of a breakdown of the high-pressure chamber must be used. These systems, however, do not protect the materials and equipments inside the chamber or in its close proximity. This practice does allow rational use of the material for high-pressure chambers, either.

That is why an attempt has been made to include the acoustic emission (AE) method in the research of low-cycle fatigue of 45HNMFA steel used for the production of high-pressure chambers. It was expected that the AE activity, as well as the area of hysteresis loop would be proportional to the energy dissipated by the material during one loading cycle. Besides, it was supposed that the AE activity in samples would be similar to that in working pressure chambers made of the same material. This would give a possibility to use the AE as a crack detection method for parts serving in the region of low-cycle fatigue; in our case, a possibility of the estimation of safe-service life of the high-pressure chambers.

In the present paper, the results of AE measurements on the samples of variously heat treated 45HNMFA steel during low-cycle fatigue loading are presented.

2. Experimental Details

The experimental study of AE during the low-cycle fatigue was conducted on samples of a 45HNMFA steel produced in Poland. Its chemical composition is given in Table 1.

Table 1 Chemical composition of 45HNMFA steel (in wt.%)

C	Mn	Si	Cr	Ni	Mo	V	S	P
0.45	0.50	0.30	1.00	1.70	0.25	0.15	0.027	0.026

From such a material twelve specimens were made according to Fig. 1. They were heated to 860°C for 1 hr and oil quenched. Then the specimens were randomly divided into three sets which were for 60 min. tempered at 600°, 500° and 300°C and furnace cooled to obtain three different levels of Rockwell C hardness: HRC 30, 40 and 50, respectively. The sets were marked 3, 4 and 5. Thus, each specimen number has double digit, e.g., 33, 51 etc.; the first digit is the set number, indicating its hardness, and the second one is the specimen number among this set. Each set had four samples; one of them was used for static mechanical test and the others three for low-cycle fatigue experiments. Mechanical properties obtained from static testing are presented in Table 2.

The loading of the specimens in the low-cycle fatigue region was performed with a Zwick 20T testing machine. Each

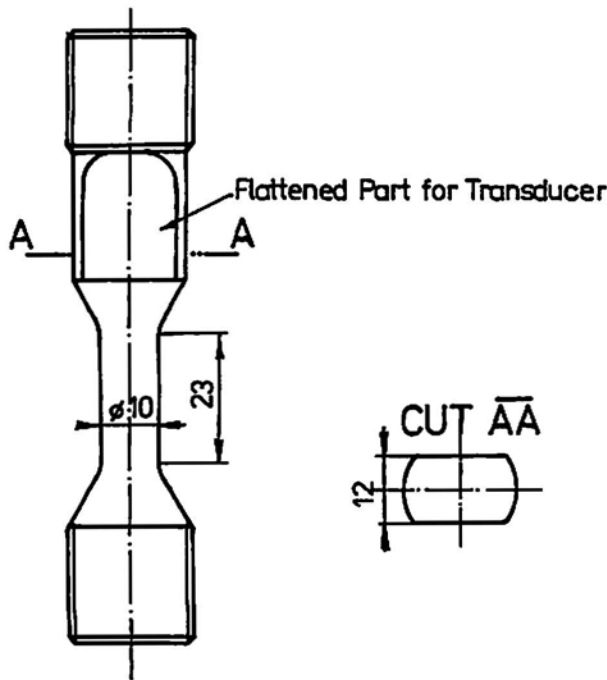


Fig. 1 Dimensions and shapes of test specimens.

specimen was loaded by cyclic force with triangular waveform from zero up to the constant maximum amplitude being the value of yield stress of this specimen (Table 3). The crosshead speed of the testing machine was chosen to be 2 mm/min.

Table 2 Mechanical properties of 45HNMFA steel

Rockwell Hardness HRC	σ_{ys} MPa	σ_u MPa	Elongation %	Necking %
30	975	1050	17	44
40	1375	1585	12	34
50	1500	1875	10	32

The AE activity was measured by the AE 10-UFM CSAV analyzer (Fig. 2), developed at the Institute of Physical Metallurgy of the Czechoslovak Academy of Sciences in Brno (Dusek et al., 1984). This analyzer has been constructed as a ten-channel device with fixed amplitude levels. The frequency range is 30 kHz to 2 MHz. The dynamic range of this amplitude analyzer is 40 dB and the separation of individual channel is 4 dB. The selected parameters of the AE analyzer were: amplification, 70 dB; bandpass, 0.1 - 0.3 MHz. It can record and analyze AE count rates and cumulative counts.

During system setup per Fig. 3, possible spurious signals caused by Zwick testing machine were examined by the AE analyzer DEMA-10 RMS, developed at the Experimental Department TECHPAN attached to the Institute of Fundamental Technological Research of the Polish Academy of Sciences, Warsaw. It was found that no extraneous signals resulted. To measure AE signals, a suitable sensor was chosen from the set of products of the Polish firm, UNIPAN, Warsaw. The measure-

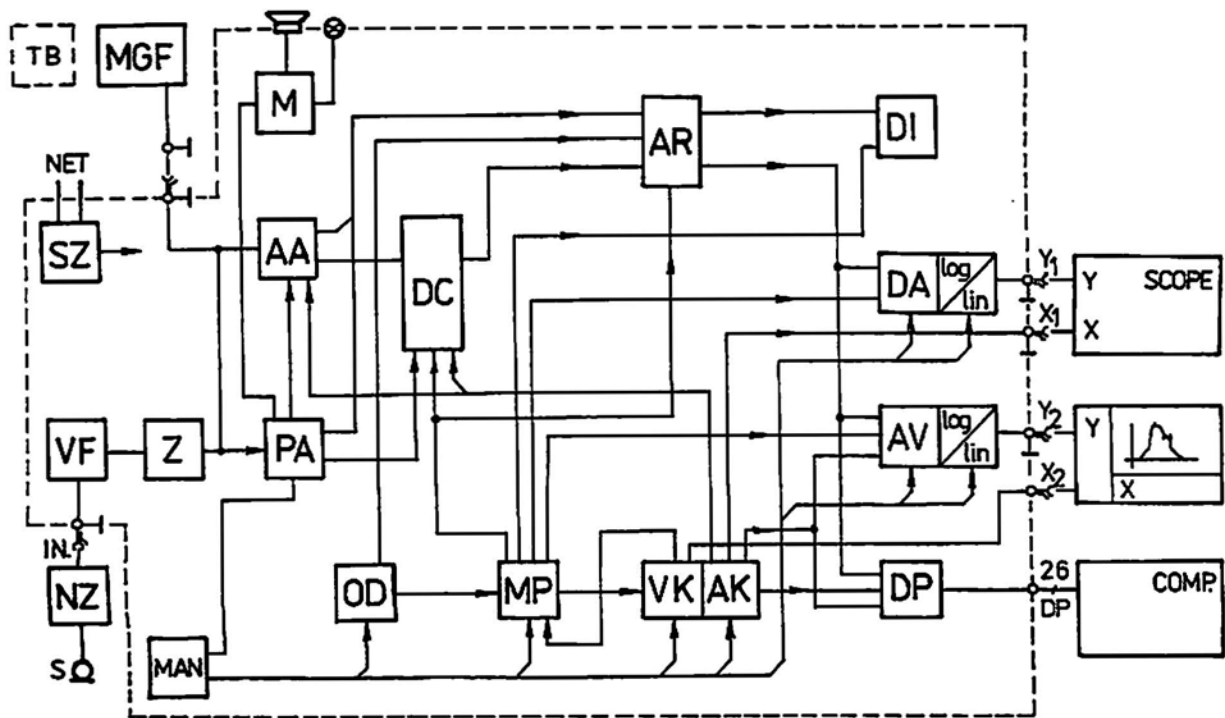


Fig. 2 Block diagram of the AE 10 Analyzer: NZ - low-noise input amplifier, VF - electronic filters, Z - linear amplifier, PA - threshold analyzer, AA - 10-channel amplitude analyzer, DC - counter, OD - control and pilot circuits, MP - multiplexer control, VK - channel selection modules, DA - D/A converter, M - acoustic and optical monitor, SZ - power supply unit.

Table 3 Summary of fatigue results of all specimens tested

Specimen No.	Max (yield) stress σ	Plastic strain ϵ_p [%]			Cycle number *		
		initial	cyclic	total	N_e	N_s	N_f
		ϵ_{pin}	ϵ_{pc}	ϵ_{pt}			
31	866	0.31	0.41	0.72	9	142	293
32	945	0.80	0.28	1.08	10	83	220
33	794	1.35	0.29	1.64	7	253	862
41	1355	0.58	0.77	1.35	8	121	206
42	1410	0.42	0.98	1.40	6	97	221
43	1320	0.65	1.13	1.78	7	157	337
51	1853	0.57	0.11	0.68	21	25	86
52	1710	0.35	0.27	0.62	22	53	153
53	1780	0.41	0.20	0.61	9	49	107

* N_e = No. of cycles to AE signal extinction. N_s = No. of cycles to 2nd AE activity appearance. N_f = No. of cycles to specimen failure.

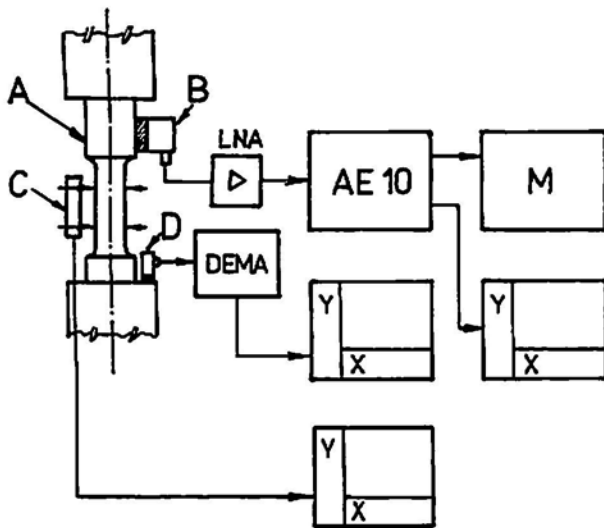


Fig. 3 Diagram of arrangement of the measuring set of AE signals during low-cycle fatigue tests. A) test specimen, B) AE transducer, C) sensor of specimen elongation, D) acoustic transducer pick-up of test machine vibration, LNA) low-noise input amplifier 40 dB, AE 10) Czechoslovak AE analyzer, M) monitor, DEMA) Polish AE analyzer, XY) XY recorder.

ments of frequency characteristics of the sensor by means of a spark calibrator were carried out at the Institute of Physical Metallurgy of the Czechoslovak Academy of Sciences (Dusek et al., 1990). The frequency characteristic is given in Fig. 4.

3. Experimental Results

3.1 Structure and Mechanical Properties

All samples of the 45HNMFA steel in the first cycle were loaded with individually chosen initial static plastic deformation, ϵ_{pin} . The deformation was achieved, as the yield stress of a particular specimen was exceeded. The chosen values of ϵ_{pin} were not depended on yield stress values; we tried to apply three quite different ϵ_{pin} for each hardness set. The specimens were

then cyclically loaded up to failure. Stresses, strains and cycle numbers are given in Table 3.

Plastically deforming a sample during the first cycle of loading was to simulate real service conditions for overloaded high pressure chambers and to examine their subsequent ability to emit warning AE signals in-service monitoring tests. It was quite obvious that exceeding the yield stress at the very onset of specimen loading cycles can reduce the AE signals via Kaiser effect till before crack appearance.

In Fig. 5a, collected results of low-cycle fatigue of the specimens Nos. 31, 32 and 33 with hardness of 30 HRC are presented in the form of dependencies of cumulative total plastic deformation on the number of cycles. Similar graphs were obtained also for all the specimens of different hardnesses. Typical stress-strain hysteresis loops of all specimens were obtained by Zwick testing machine. Two of them are shown in Fig. 5b, where it is visible that stress amplitude was practically constant; as usually is in stress controlled fatigue tests. The amounts of strain in subsequent cycles were quite different: individually chosen maximum strain, ϵ_{pin} in the first cycle, and then gradually decreasing values.

To compare the average results, the curves of cumulative strain against the number of cycles (like these shown in Fig. 5a) were normalized using the respective values of the initial static plastic strain, ϵ_{pin} , given in Table 3. These normalized curves of strain vs. the number of cycles are shown in Fig. 6. One can see a big difference between normalized strain values $\epsilon_p/\epsilon_{pin}$ in the specimens with HRC 40 and both HRC 30 and 50.

Figure 7 shows the macroscopic fracture appearances of all the specimen groups. In Figs. 8, 9 and 10, higher magnification fractographs obtained by the scanning electron microscopy are presented. The fatigue fractures of specimens with different hardness exhibit many differences in surface patterns, which indicate differences in the development of low-cycle fatigue process.

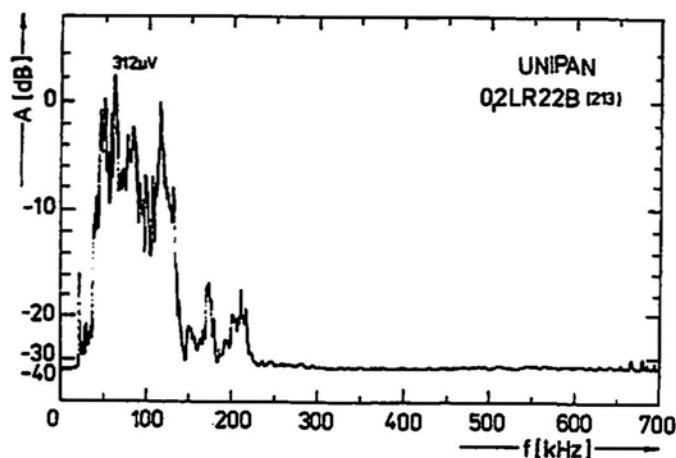
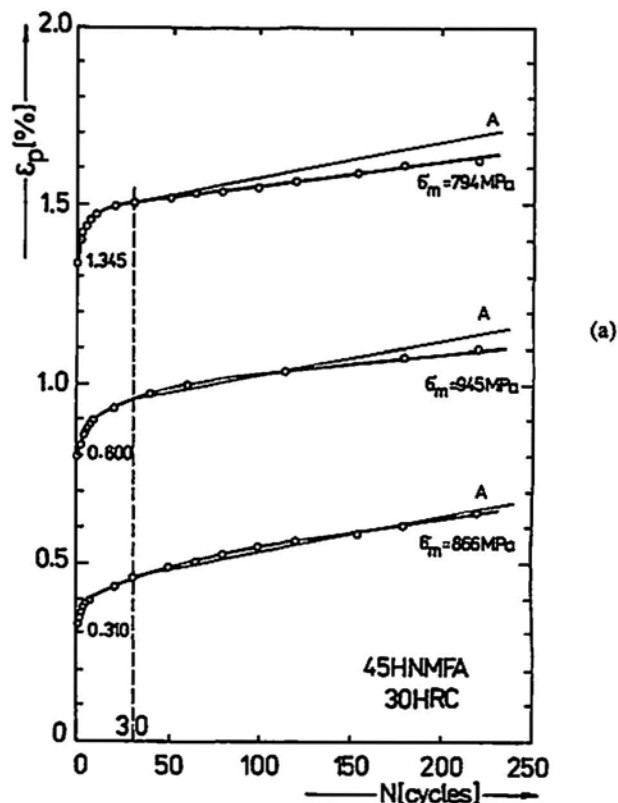
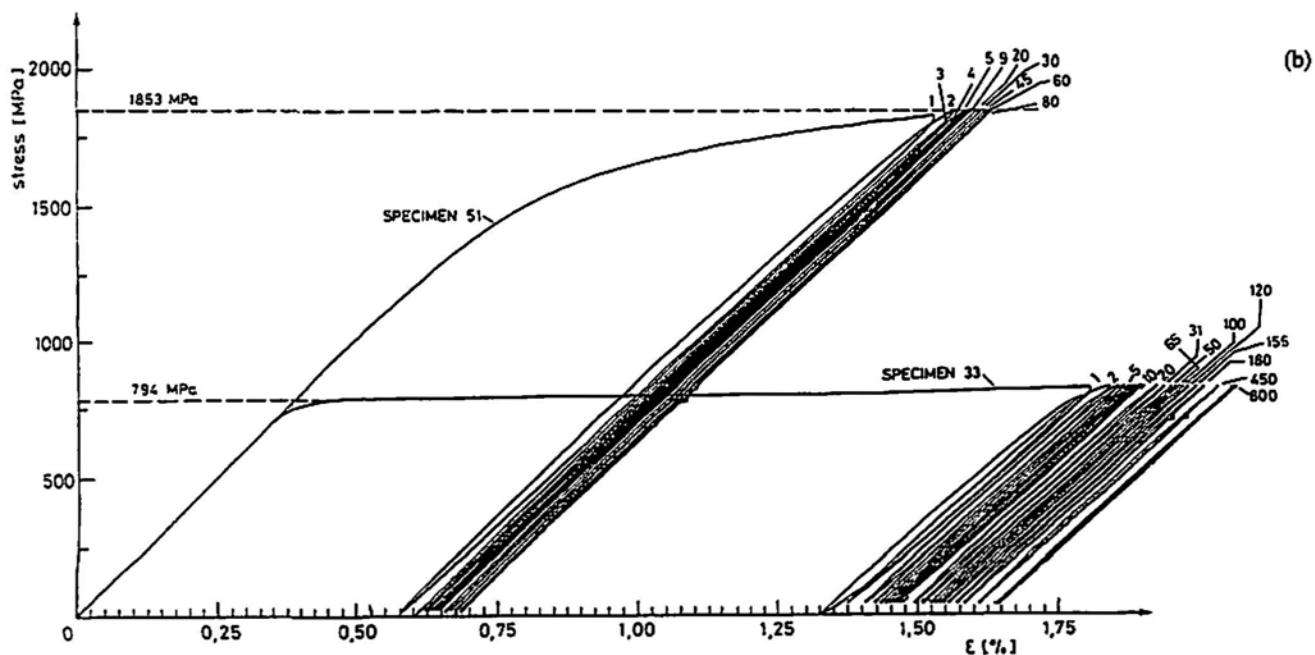


Fig. 4 Frequency characterization of the acoustic emission transducer UNIPAN-0.2LR22B, No. 213.

The 30 HRC specimen (left on Fig. 7) shows a typical cup and cone fracture, and a large necking is evident. Reduction in area, Z , was 49%. The fracture initiation area was in the middle of the specimen. The concentric fracture surface marks (see Fig. 8a) are characteristic of crack propagation in this specimen. After the crack had reached the critical dimension, a sudden failure of remaining cross section occurred, thus producing a cup and cone fracture. In Fig. 8a and b, the fatigue zone can be seen with larger magnifications. The centrally displaced faults are the evidence of the cyclic character of the process of fracture surface formed.



(a)



(b)

Fig. 5 Plastic deformation ϵ_p vs. the number of cycles N in the low-cycle fatigue affected by the different degrees of initial static deformation. a) ϵ_p vs. N for Nos. 31, 32 and 33. b) σ vs. ϵ for Nos. 33 and 51.

At 40 HRC (center on Fig. 7) a semi-brittle flat fracture with radial markings is seen. The fracture initiation region is shown at the center left of Fig. 9a, along with a very diversified fracture surface pattern. Upon fracture ($N_f = 206$), a relatively large necking ($Z = 40\%$) was observed. It is difficult to distin-

guish the fatigue and the residual zones. The characteristic features are the numerous secondary cracks displaced radially. The circumferential secondary cracks separate the origination of fracture surfaces in subsequent load cycles.

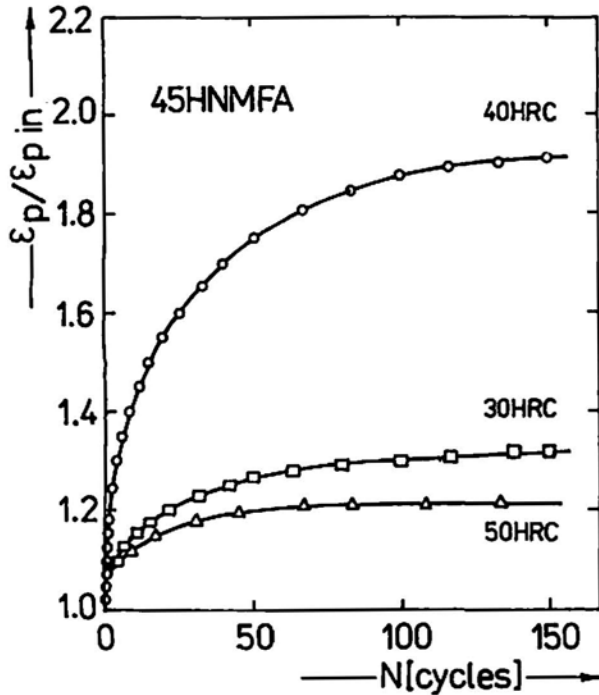


Fig. 6 Normalized changes of plastic deformation $\epsilon_p/\epsilon_{pin}$ for all three strength sets of the 45HNMFA material during low-cycle fatigue.

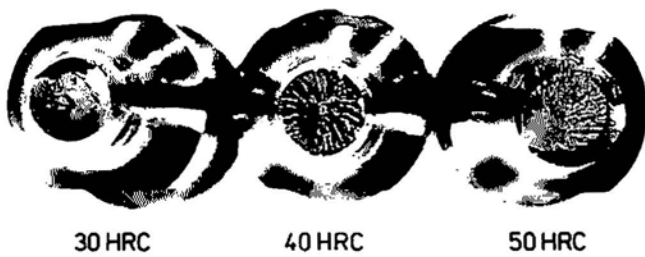


Fig. 7 Macrostructure of fractures of the 45HNMFA steel test specimens with hardness of 30, 40 and 50 HRC after low-cycle fatigue. Magnification 0.76X.

At 50 HRC, it is evident from macrophotograph (right on Fig. 7) that the fracture initiated from the surface. The initial crack then propagated over the whole cross section in the brittle fashion in very low cycles to failure ($N_f = 86$). The plastic deformation of the specimen was very small ($Z = 6\%$). There are no clear traces of cyclic fracturing of the specimen according to Fig. 10.

3.2. Acoustic Emission

During the measurement of the mechanical properties of the 45HNMFA steel in low-cycle fatigue, AE signals were recorded. The data was treated in a form of the AE count rate vs.

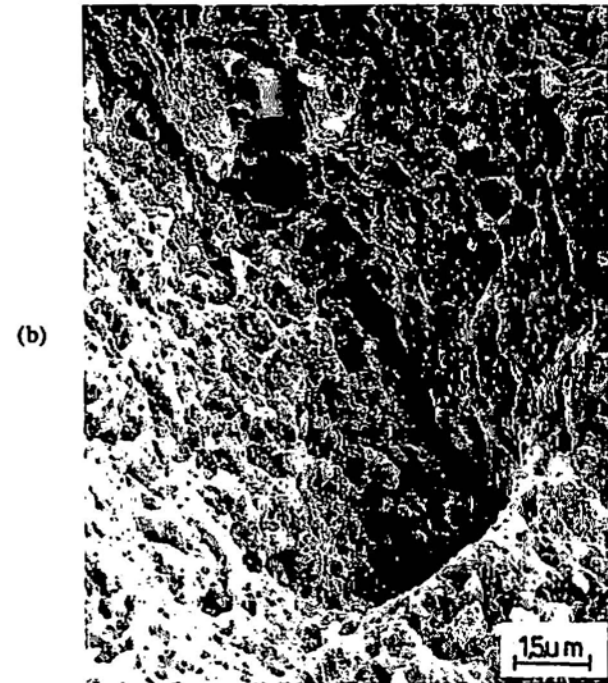
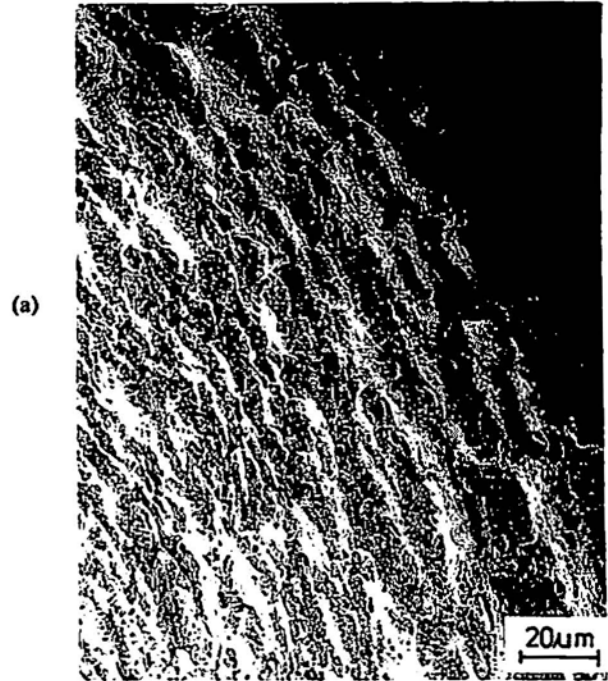


Fig. 8 Fracture surface of the specimen with hardness of 30 HRC.

the loading cycle, $AER(N)$, to see if an estimation of the service life of high-pressure chambers could be made. The amplitude distribution of AE signals was also evaluated in particular loading cycles.

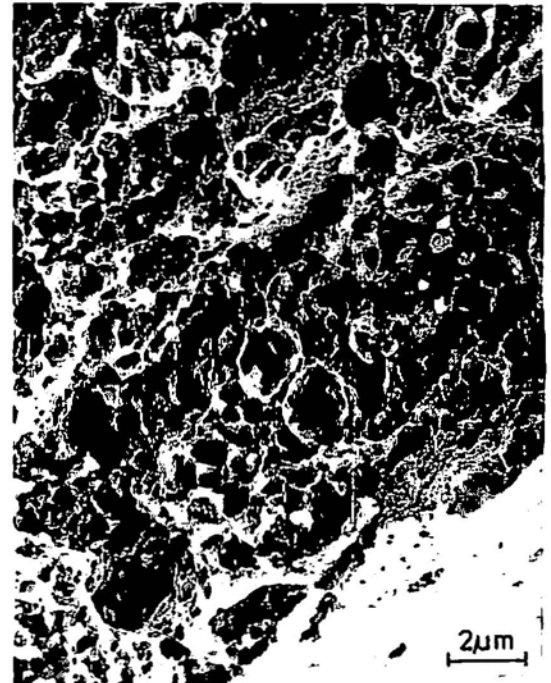
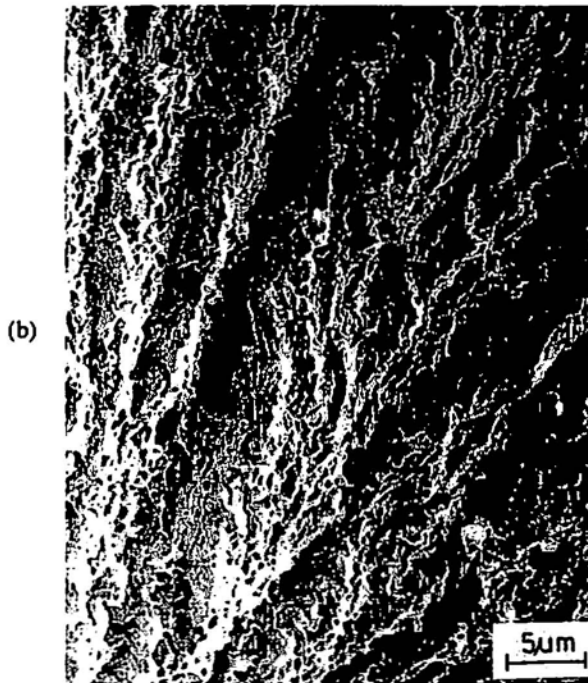
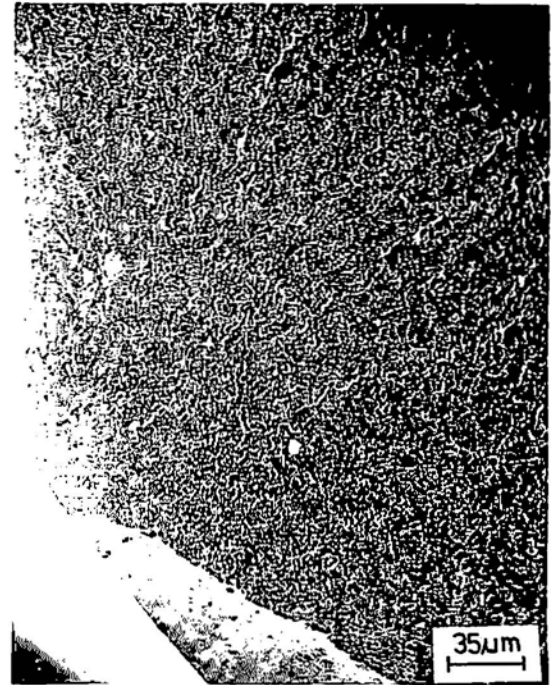
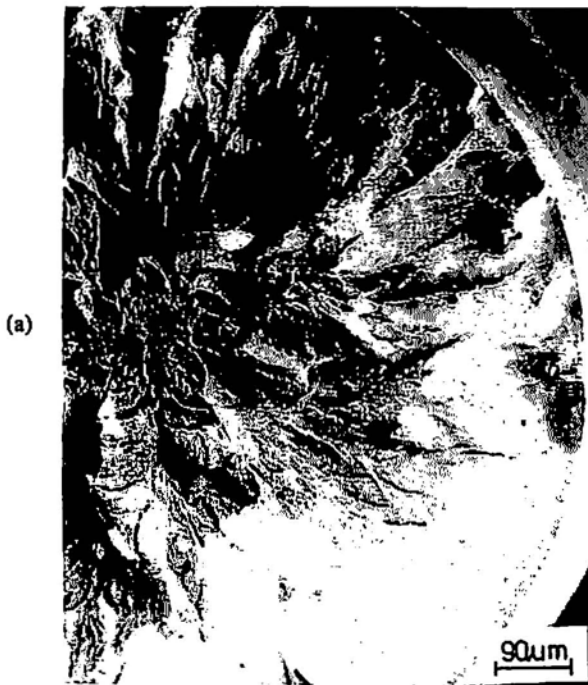


Fig. 9 Fracture surface of the specimen with hardness of 40 HRC.

Fig. 10 Fracture surface of the specimen with hardness of 50 HRC.

Such a differentiated and diversified way of fatigue fracture surface formation of the specimens with 30, 40 and 50 HRC should manifest itself as differences in the results of AE tests. Indeed, the differences concerning the AE activity itself have been found; the greatest activity was exhibited by the specimens with 50 HRC, the smallest - by the ones with 30 HRC.

However, the character of the AE activity of the specimens was similar: all of them showed maximum activity during the first cycle, decrease of activity for a few following load cycles, eventual lack of AE activity beyond several cycles to about a half of the fatigue life and then systematically increasing AE activity in the remaining fatigue life, up to failure.

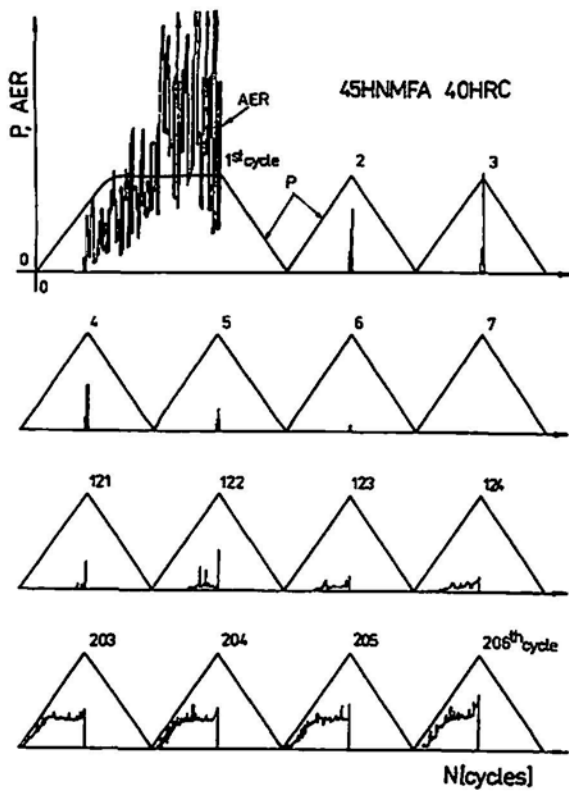


Fig. 11 Activity of the AE signals in the low-cycle fatigue process of the 45HNMFA material, hardness of 40 HRC.

In Fig. 11, a typical example of the AE count rate, $AER(N)$, for samples with 40 HRC is shown. The data is plotted against cycle number for selected cycles up to failure; for the specimen No. 41, it occurred during the 206th cycle. The results with similar character, but quantitatively different, were obtained on other samples in all the hardness sets (Table 3). It concerns especially the AE activity for the specimens with HRC 50. For example, specimen No. 51 has very short *silent* period; decrease of AE activity endured till 21st cycle and from 25th cycle there appeared secondary AE count rate increase, up to the specimen failure.

The cumulative amplitude distribution (ΣAE) of AE signals after the first loading cycle is shown in Fig. 12a. By a dashed line, the amplitude distribution of the AE signals after 136 cycles is given here. In Fig. 12b amplitude distribution for the entire 206 cycles is presented.

Cumulative amplitude distribution for all the specimens during particular loading cycles is given in Table 4. One can see that in all the specimens, amplitude distribution drifts to greater values by increasing cycle number. Besides, average AE count rate is an biggest for the specimens with 50 HRC and an smallest for those with 30 HRC. These findings seem to be consistent with crack behavior differences described in Sec. 3.1; brittle cracking which occurred in the specimens with higher hardness appears to be connected with higher AE energy.

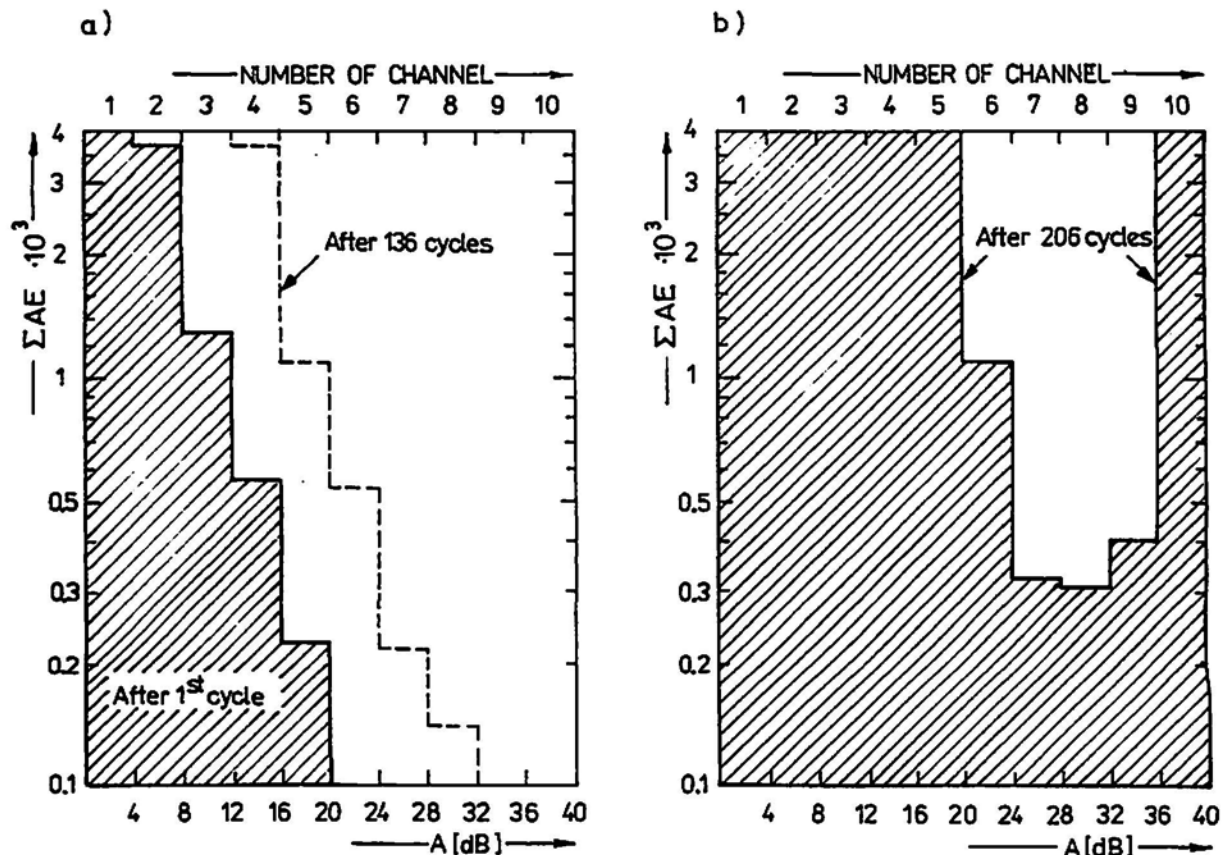


Fig. 12 Amplitude distribution of the AE signals during cyclic loading of the specimen with hardness of 40 HRC.

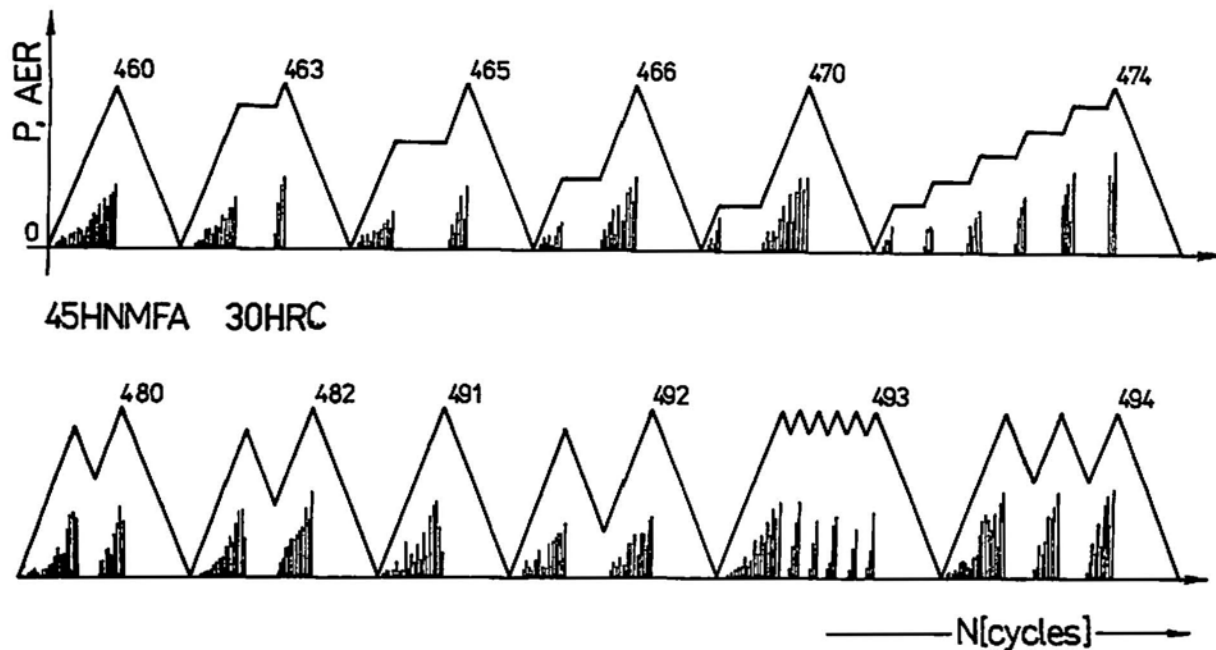


Fig. 13 AE activity in dependence on various modifications of loading schedule in the specimen with hardness of 30 HRC.

In Fig. 13, examples of AE count rate measurements in several cycles with different loading schemes for the specimen No. 33 (30 HRC) are shown. In the second half of specimen fatigue life, each increase of loading is accompanied by an increase in AE activity. This phenomenon is quite similar that shown in Fig. 11.

By means of the relationships found experimentally, three AE activity regions can be identified during low-cycle fatigue: a) high AE activity in the first cycle (with after-effects and slight showers of AE signals in the few following cycles); b) extinction of AE signals beyond several initial cycles up to about half of the number of cycles to the failure; c) rise of a second AE activity starting from the end of extinction region (b) and enduring up to the specimen failure. Now, during the few loading cycles (having triangle form - see Fig. 11) the first AE signals occur by maximum loading only. In the following cycles, AE signals appear to start at lower load levels, down to the minimum level in the last several cycles before the failure.

4. Discussion

The value of first-cycle static loading of specimens influenced the curves of strain vs. number of cycles, $\epsilon_p(N)$. The specimens with greater initial strain showed lower increase in $\epsilon_{pc}(N)$ during cyclic loading. The changes are more evident with the increasing number of cycles. For the sake of comparison, parallel lines (A) going through the points corresponding to the 30th loading cycle were plotted in Fig. 5a.

The mentioned differences in the dependence of the amount of cyclic plastic deformation on the number of cycles are not great in comparison with the differences of cyclic plastic deformations occurring in specimens with different hardness. From Fig. 6, it is clear that the cyclic plastic deformation of specimens with hardness of 40 HRC greatly exceeds the values

of cyclic plastic deformation of specimens with both 50 HRC and 30 HRC. The causes of such a conformity between the HRC 30 and 50 curves will be studied in the future.

The different mechanisms of AE occurring at the beginning of sample cycling and in its advanced stage seem to be as follows:

The changes in AE activities are the well-known results of dislocation density increase during the fatigue process of a metal. At the high deformation level, almost complete dislocation structure forms in the first few loading cycles (Grosskreutz, 1971; Grosskreutz and Mughrabi, 1975). The high AE activity corresponds to several possible processes (James and Carpenter, 1971; Heiple et al., 1981). The fundamental cause of AE is the dynamical effect of spontaneous dislocation movement, multiplication, and annihilation of parallel segments of loops, occurring especially during the high activity of Frank-Read sources (James and Carpenter, 1971; Imanaka et al., 1973; Pawelek et al., 1985), as well as sudden dislocation acceleration and/or deceleration (Pilecki, 1986). Many dislocations and Frank-Read sources take part in these processes in entire volume of the sample and AE intensity is also high. In the macroscopic elastic range, the segment length of mobile dislocation increases with increasing external stress (Imanaka et al., 1973). At small strains, the loop length and AE count rate are highest. With gradual development of plastic deformation, the length of dislocation loop gets shorter, and their number increases. Below a certain level of length of free dislocation loops (corresponding to the sufficiently high dislocation density) the detectable AE does not occur, because most of dislocation lines are immobile.

According to the Kaiser effect, no AE signals ought to occur at all during the following cycles. In our experiments, in the first few cycles, some AE signals were noted, certainly as a

Table 4 AE amplitude distribution in particular cycles

Specimen No.	Cycle No.	Amplitude Level Channel								
		2	3	4	5	6	7	8	9	10
31	1	3638	1198	432	100	30	8	0	0	0
	182	2803	459	1300	923	406	209	98	47	65
	287	7007	1149	4325	1807	1027	526	245	117	164
32	1	3535	1294	495	233	163	70	43	19	9
	86	6230	1392	348	100	64	11	0	0	0
	127	9831	2334	547	166	76	20	1	0	0
	219	12714	5469	1770	549	184	66	26	14	20
33	1	6727	1869	629	127	86	48	10	13	7
	261	4435	1275	391	110	30	25	10	15	20
	322	3564	2111	583	190	27	46	62	88	147
	526	2877	9784	2786	967	406	296	257	255	355
	862	2383	7025	2582	1711	1409	598	342	447	940
41**	1	3706	1360	558	225	90	61	30	9	11
	136	9999*	7845	3690	1040	545	220	135	50	15
	206	9999*	9999*	9999*	4216	1133	321	310	407	6374
42	1	14571	4611	1686	622	289	106	63	23	9
	100	4155	1030	322	140	53	14	11	8	11
43	56	4520	1103	283	77	17	8	0	1	4
	129	7540	302	98	32	13	24	17	11	22
	237	8578	323	104	28	14	30	28	20	32
	337	2356	3396	1834	749	735	814	736	744	2923
51	1	1411	480	169	63	27	10	2	8	95
	10	2062	594	140	49	38	29	13	10	13
	21	1623	2947	878	334	141	59	6	0	0
	60	1492	5269	1522	476	181	86	25	16	11
	269	2512	8579	6853	1539	657	311	215	195	1490
52	1	3286	687	426	121	63	20	6	10	112
	12	3273	720	227	92	51	23	9	1	3
	96	2339	3922	2651	343	175	65	28	17	3
	121	1375	3467	2179	871	348	203	183	193	223
	140	4376	6720	6343	2582	987	428	368	326	1127
53	1	4159	1272	515	224	23	44	17	5	50
	5	718	526	121	28	1	0	0	0	0
	53	689	775	168	40	11	6	2	7	9
	78	587	1067	263	43	16	8	9	6	10
	105	3794	10532	6241	2735	1419	880	456	243	1290

* off scale ** for specimen No. 41, cumulative counts Σ AE are given.

result of some dislocation rearrangements only near the maximum loading.

During many following load cycles, no AE signals appeared because of ground dislocation structure has been formed in the course of the first cycle, that resulted in a large plastic strain (see Figs. 11, 13). In the subsequent cycles, dislocation density approaches its saturation state which prevent free movement of dislocations and their significant multiplications. Though in subsequent cycles some number of dislocations may make a flip-flop movement between cell boundaries, causing some total cyclic strain increment (Grosskreutz, 1971). There is no dislocation multiplication process, but

cyclic displacements occur, giving some contribution to cumulative cyclic plastic strain growth.

After the dislocation density saturation state is reached (this is usually complete for most metals after 20 to 50 % of their life to failure), inhomogeneous plastic strains in the form of slip bands occur (Lukas and Klesnil, 1971). These bands do not begin their development until after saturation is reached (Grosskreutz, 1971). Dislocation arrangement is determined by the plastic strain amplitude which is certainly greater in the slip bands than in surrounding matrix. Because dislocation dipoles are the dominant feature of this state (Grosskreutz, 1971), it is suggested that the dislocation density saturation state could be accommodated by the equilibrium between gene-

ration process of the dislocations and the annihilation of existing ones. Since the generation of new dislocation is proportional to the mobile dislocation density and the annihilation, to the density squared, such an equilibrium state establishes only when dislocation density is sufficiently high (Pilecki, 1969, 1977; Bammann and Aifantis, 1982).

The dislocations move mainly under the action of external loading. By cyclically varying loading, dislocation velocity and displacement direction is correspondingly changed, but there occurs a net drift velocity and flux of dislocations. This is most possible in a thin surface layer from which dislocations escape to the free surface. Some dislocations, especially those in near-surface regions, can easily move to the surface by the additional influence of mirror (image) forces attracting dislocations to the surface (Hirth and Lothe, 1968; Pilecki, 1977, 1986). Thus, as a result of dislocation moving from the interior, the slip band is characterized at the surface, then accompanied by growth of roughness and finally by notch-peak geometry (Tetelman and McEvily, 1967). In the vicinity of a notch tip, the dislocation density is especially high (Yokobori et al., 1970). As a result of dislocations escaping to the notch surface, notch tip displaces, which is equivalent to crack growth. It is well known that the initiation of crack propagation causes the high AE signals. Modern understanding of this phenomenon ought to connect the AE effects with crack growth as a result of reaching the crack surface by great amount of the dislocations, moving with high velocity (Pawelek et al., 1985; Pilecki, 1986).

It appears that AE observed in the second half of fatigue life is caused by such escaping of these dislocations to the free surface in the vicinity of notch tip. In Fig. 11 we see that for $N > 120$ these AE signals appear firstly at the maximum loading only and then the beginning of the signal appearance shifts to lower and lower loads, down to zero just before failure. This means that crack growth makes the escape of dislocations more and more plentiful and thus the acceleration of crack growth must take place. When the number of applied cycles is sufficiently high, it is seen (Fig. 13) that each (even small) load increase causes a generation of new AE signals.

Second appearance of AE signals can be identified with crack initiation and gradual AE amplitude growth with crack propagation. That is, during crack growth, the AE amplitude drifts from small to large values (see Table 4). It means that fatigue cracking generates AE signals of much higher energy than plastic deformation does.

It is evident that, by means of AE signals, it is possible to describe the process of fatigue fracture nucleation, as well as both the stable and unstable crack propagation in the fatigue processes.

5. Conclusions

The data on mechanical and structure characteristics of the 45HNMFA steel in the low-cycle fatigue region was obtained. It can be applied in the construction of service-safe high pressure chambers. The most important result of these experiments is a repeated occurrence of increasing AE activity in the second half of life period of the material (Figs. 11 and 13) with in-

creasing amplitude value of AE signals (Fig. 12, Table 4). This information allows use of the AE method to estimate the safe-service life of devices working in the fatigue conditions. With regard to the AE signals, it is evidently possible (Houssny-Emam et al., 1983) to describe the output from a monitored object which consists of three stages:

1. Hardening connected with the high AE activity;
2. Dislocation density saturation characterized by extinction of AE activity;
3. Nucleation and propagation of a crack with a corresponding increase in AE activity with increasing amplitude of the AE signals up to failure.

References

- D.J. Bammann and E.C. Aifantis (1982), "On a Proposal for a Continuum with Microstructure", *Acta Mech.*, **45**, 91-121.
- F. Dusek, M. Kotoul and C. Seidl (1984), *The Acoustic Emission Analyzer AE 10*, Czechoslovakia Patent No. 231236, Prague.
- F. Dusek, C. Seidl, J. Siedlaczek and S. Pilecki (1990), "The Acoustic Emission Transducer Calibration Using Spark Technique", *Arch. Acoust.*, **15** [3-4].
- J.C. Grosskreutz (1971), "The Mechanisms of Metal Fatigue", *phys. stat. sol. (b)*, **47**, 11—31, 359—396.
- J.C. Grosskreutz and H. Mughrabi (1975), "Description of the Work Hardened Structure at Low Temperature in Cyclic Deformation", *Constitutive Equations in Plasticity*, ed. A.S. Argon, MIT Press, Cambridge, pp. 251-326.
- C.R. Heiple, S.H. Carpenter and M.J. Carr (1981), "Acoustic Emission from Dislocation Motion in Precipitation-Strengthened Alloys", *Metal Sci.*, **15**, 587.
- J.P. Hirth and J. Lothe (1968), *Theory of Dislocations*, McGraw-Hill, New York.
- M. Houssny-Emam and M.N. Bassim (1983), "Study of the Effect of Heat Treatment on Low Cycle Fatigue in AISI 4340 Steel by Acoustic Emission", *Mater. Sci. Engr.*, **61**, 79-88.
- T. Imanaka, K. Sano and M. Shimizu (1973), "Dislocation Attenuation and Acoustic Emission during Deformation in Copper Single Crystal", *Cryst. Lattice Def.*, **4**, 57-64.
- D.R. James and S.H. Carpenter (1971), "Relationship between Acoustic Emission and Dislocation Kinetics in Crystalline Solids", *J. Appl. Phys.*, **42**, 4685-4697.
- P. Lukas and M. Klesnil (1971), "Dislocation Structures in Fatigued Single Crystals of Cu-Zn System", *phys. stat. sol. (a)*, **5**, 247-258.
- A. Pawelek, W. Stryjewski, W. Bochniak and M. Dybiec (1985), "Mobile Dislocation Density Variation during Strain Rate Change Evidenced by Acoustic Emission", *phys. stat. sol. (a)*, **90**, 531-536.

A. Pawelek, W. Bochniak, H. Dybiec and W. Stryjewski (1988), "Application of the Technique of Acoustic Emission for Testing Mechanical Properties of Metals and Alloys II", *Arch. Metallurgy*, **33**, 645-661.

S. Pilecki (1969), "Proliferation, Diffusion and Vanishing of Dislocations in the Course of Process of Metal Fatigue", *Bull. L'Acad. Polon. des Sci., Ser. Sci. Techn.*, **17**, 489-496.

S. Pilecki (1977), "Dislocation-Diffusion Mechanism of Fatigue Crack Formation", *Proc. Fourth Intl. Conf. on Fracture*, Waterloo, Canada, vol. 2, pp. 687-692.

S. Pilecki (1986), "Acoustic Emission Application for Testing Mechanical Properties and Toughness of Solids (in Polish)", *Arch. Akustyki*, **21**[1], 109-134.

R.T. Sadgwick (1968), "Acoustic Emission from Single Crystals of LiF and KCl", *J. Appl. Phys.*, **39**[3], 1728-1740.

J. Siedlaczek (1983), "Acoustic Emission in the High Pressure Vessel Testing (in Polish)", XII KKBN NDT-Conference, Rydzyna.

W. Szczepinski (ed.) (1984), *Experimental Methods in Solid State Mechanics*, (in Polish), PWN, Warsaw.

A.S. Tetelman and A.J. McEvily, Jr. (1967), *Fracture of Structural Materials*, Wiley, New York, Chapter 8.

UNIPRESS (1986), "Prospect of the LC Liquid Cells", Information Leaflet of High Pressure Research Center, Warsaw

T. Yokobori, K. Sato and Y. Yamaguchi (1970), "X-Ray Micro-beam Studies on Plastic Zone at the Tip of Fatigue Crack", *Rep. Res. Inst. Strength and Fracture of Materials, Tokohu Univ.*, **6**[2], 49-67.

Progress in Acoustic Emission VI, Proceedings of The 11th International Acoustic Emission Symposium

Held at Fukuoka, Japan, October 26-29, 1992; Edited by T. Kishi, K. Takahashi and M. Ohtsu;
Published by The Japanese Society for Non-Destructive Inspection, Tokyo. 604 p.

Contents

Special Lecture

Application of Acoustic Emission Techniques in Manufacturing
D. DORNFELD

Prediction of Chaotic AE Signals by a Neural Network
I. GRABEC

Applications of Acoustic Emission Techniques for Diagnosis of Machinery in Plants and Mass Produced Goods in Factories
I. SATO

Composites 1

Determination of the Elastic Properties of Composite Materials Using Simulated AE Signals
W. SACHSE, M. VEIDT and L. NIU

The Fracture Behavior of a Model Fiber Reinforced Plastic Composite Utilizing a Displacement-Sensitive AE Monitoring System
H. SUZUKI, M. TAKEMOTO and K. ONO

Source Characterization of Acoustic Emission (AE) Wave during Tensile Test of CFRP by Analyzing Frequency Spectrum
J.-S. LEE, J.-O. LEE and S.-K. OH

Acoustic Emission Monitoring of Damage Progression of CFRP Laminates under Repeated Tensile Loading
I. KIMPARA, K. KAGEYAMA, T. SUZUKI and I. OHSAWA

Manufacturing 1

Acoustic Emission during Unlubricated Sliding Wear of Silicon Nitrides
O.-Y. KWON, D.-J. YOON, S.-K. PARK and D.-S. LIM

Origin of Acoustic Emission Produced during Wire Drawing
Y. MORI

Acoustic Emission Quality Control for Wooden Panel Production
K. SATO, K. SUGIMOTO, F. KAMIYA, T. HIRATA, K. YAMAGUCHI, N. ANDO and M. FUSHITANI

Acoustic Emission Monitoring of Incipient Failure in Journal Bearings
D.-J. YOON, O.-Y. KWON and M.-H. JUNG

Composites 2

Transient Elastic Waves Generated by Point Source in Carbon Fiber Reinforced Plastics Plate
J. K. LEE, Y. H. KIM and H. C. KIM

Monitoring of Creep Damage in Woven E-Glass Fiber/Epoxy Laminated Composites during Short Term Creep Test through Acoustic Emission
T. UENOYA

(continued to page 18)

Parameter Estimation in Acoustic Emission Signals

C. E. D'Attellis, L. V. Perez, D. Rubio and J. E. Ruzzante

Abstract

An acoustic emission signal is represented by a series of decaying bursts of the same form, random amplitudes and varying times of occurrence. The estimation of the time of occurrence and amplitude for each burst is given using Kalman filter techniques. The method is easily implementable on-line. Some simulated and experimental results are presented.

1. Introduction

By monitoring the output of a piezoelectric transducer on a oscilloscope during an acoustic emission (AE) experiment, decaying bursts stochastically spaced and with random amplitudes can be observed. The AE bursts often have similar form, so that information about material changes is largely hidden in the rate and amplitude of bursts.

Following Mitrovic et al. (1985) we can describe an AE signal by a series of wavetrains of the same form, but of different amplitudes and varying time of occurrence, by the expression

$$s(t) = \sum_i a_i h(t - t_i) \quad (1)$$

where a_i is amplitude for the i -th burst, t_i is time of occurrence for the i -th burst and $h(t)$ is the assumed waveform of a single burst, which is a damped sinusoidal oscillation which can be expressed by the function

$$h(t) = \begin{cases} \exp(-t/\tau) \sin 2\pi f_0 t & \text{if } t \geq 0 \\ 0 & \text{if } t < 0 \end{cases} \quad (2)$$

where f_0 is the resonant frequency of the transducer, and τ is the characteristic decay time. The time interval between adjacent bursts can vary by several orders of magnitude during an experiment.

As Mitrovic et al. (1985) have established, the rate and amplitude of the bursts depend on the state and rate of deformations, but for sufficiently short intervals the AE phenomenon can be treated as a Poisson impulse process for a given average rate. If the rate of bursts is very low, then the bursts are separated by more than the characteristic decay time and we get discrete acoustic emission. On the contrary, for high rates the

bursts are separated by an interval less than the decay time, so that bursts overlap and continuous AE is obtained.

The aim of this paper is the estimation of the time of occurrence and amplitude for each burst in the AE signal given by equation (1). We solve the problem using a Kalman filter as estimator (Jazwinski, 1970; Gelb, 1974). This approach provides an efficient estimator, which is easily implementable on-line.

2. Model for Representing an AE signal

In order to apply the Kalman filter theory (Jazwinski, 1970; Gelb, 1974; Mc Garty, 1974; Wong, 1971; Sage and Melsa, 1971), we ought to model the AE signal (1) using a system of differential equations (see Appendix). In the following, we will show the construction of such a system of differential equations step by step.

2.1 Differential Equation for a Single Burst

The function (2) allows us to obtain a second order differential equation corresponding to a single burst. In fact, the Laplace transform of (2) is

$$H(s) = \frac{2\pi f_0}{s^2 + \frac{2}{\tau}s + \frac{1}{\tau^2} + (2\pi f_0)^2}$$

where s is a complex variable.

The corresponding differential equation is

$$\ddot{x}(t) + \frac{2}{\tau} \dot{x}(t) + \left[\frac{1}{\tau^2} + 4\pi^2 f_0^2 \right] x(t) = (2\pi f_0) v(t)$$

with initial conditions $x(0) = 0$, $\dot{x}(0) = 0$.

Defining

$$x = \begin{bmatrix} x_1 \\ x_2 \end{bmatrix} = \begin{bmatrix} x \\ \dot{x}_1 \end{bmatrix}$$

we obtain the following system of differential equations:

$$\begin{cases} \dot{x}_1 = x_2 \\ \dot{x}_2 = - \left[\frac{1}{\tau^2} + 4\pi^2 f_0^2 \right] x_1 - \frac{2}{\tau} x_2 + (2\pi f_0) v(t) \end{cases} \quad (3)$$

The vector x is called state of the dynamical system (3). If the input $v(t)$ is a Dirac impulse applied in t_0 ,

$$v(t) = \delta(t - t_0),$$

the solution of (3) is

Received 12 November 1990, in revised form, 27 May 1992. C.E. D'Attellis, L.V. Perez and D. Rubio are affiliated with Comision Nacional de Energia Atomica, Centro de Calculo Cientifico (CAC), Avda. del Libertador 8250, 1429 Buenos Aires, Argentina, J.E. Ruzzante is with Departamento Materiales, Comision Nacional de Energia Atomica, and L.V. Perez is also with Consejo Nacional de Investigaciones Cientificas y Tecnicas. Supported by IAEA Research Contract 5987/RB.

$$x_1(t) = I(t - t_0) \exp\left[-\frac{t - t_0}{\tau}\right] \sin(2\pi f_0)(t - t_0),$$

where $I(t) = 1$ if $t \geq 0$ and $I(t) = 0$ if $t < 0$.

Thus, a single burst with t_0 as time of occurrence can be considered as the solution of equation (3) when the input function $v(t)$ is an impulse at $t = t_0$.

2.2 Differential Equation for the Time Occurrence of a Burst

A Kalman filter estimates the states of a dynamical system (see Appendix). As stated in Sec. 1, our problem is the estimation of the time occurrence for each burst in the AE signal. In order to use a Kalman filter as estimator we have to change the time-occurrence estimation problem in a state estimation problem. The following first order differential equation make it possible:

$$\dot{x}_0(t) + cx_0(t) = u(t) \quad (4)$$

with $x_0(0) = 0$ and $u(t) = a_0 \delta(t - t_0)$.

The solution of equation (4) is

$$x_0(t) = a_0 \exp[-c(t - t_0)] I(t - t_0).$$

If the constant c is large enough, the exponential function is practically equivalent to the input $u(t)$, and then the estimation of the state x_0 in equation (4) is practically equivalent to the estimation of the time occurrence to and the amplitude a_0 .

2.3 System of Differential Equations as Model of AE Signal

According to the previous discussion, connecting in cascade the dynamical systems (3) and (4) we obtain a system of differential equations for AE signals:

$$\begin{cases} \dot{x}_0(t) = -cx_0(t) + u(t) \\ \dot{x}_1 = x_2 \\ \dot{x}_2 = -\left[\frac{1}{\tau^2} + 4\pi^2 f_0^2\right] x_1 - \frac{2}{\tau} x_2 + (2\pi f_0) x_0(t). \end{cases} \quad (5)$$

Using as input $u(t)$ a sequence of impulses

$$u(t) = \sum_i a_i \delta(t - t_i) \quad (6)$$

with $\{t_i\}$ random points in time, the AE signal given by equation (1) can be considered as the output $y(t) = x_1(t)$ of the dynamical system (5). We suppose a noisy measurement so a white noise $w(t)$ with zero mean and covariance

$$E[w(t)w(\tau)] = R\delta(t - \tau) \quad (R > 0)$$

is added to the output function: $y(t) = x_1(t) + w(t)$.

Summing up, the AE signal is given by the following system of differential equations:

$$\dot{x}(t) = Fx(t) + Gu(t) \quad (7)$$

$$y(t) = Hx(t) + w(t) \quad (8)$$

where

$$x(t) = \begin{bmatrix} x_0(t) \\ x_1(t) \\ x_2(t) \end{bmatrix}$$

is the vector state,

$$F = \begin{bmatrix} -c & 0 & 0 \\ 0 & 0 & 1 \\ 2\pi f_0 & -\left[\frac{1}{\tau^2} + 4\pi^2 f_0^2\right] & -\frac{2}{\tau} \end{bmatrix},$$

$$G = \begin{bmatrix} 1 \\ 0 \\ 0 \end{bmatrix}, \quad H = [0 \ 1 \ 0]$$

and $u(t) = \sum_i a_i \delta(t - t_i)$

with $\{t_i\}$ random points in time.

2.4 Input Analysis

According to Mitrovic et al. (1985), the input (6) is a sequence of random impulses Poisson-distributed and with random amplitudes a_i , which are independent of the t_i . It can be shown (Papoulis, 1960) that this type of stochastic process has the following characteristics:

$$E[u(t)] = m\lambda \quad (9)$$

and

$$E[u(t)u(t')] = \lambda(\sigma_a^2 + m^2)\delta(t - t') + m^2\lambda^2, \quad (10)$$

where $E[a_i] = m$, $E[a_i^2] = \sigma_a^2$ and λ is the Poisson constant.

Taking the stochastic process

$$u(t) = \sum_i a_i \delta(t - t_i) - m\delta(t - t_i)$$

the expressions (9) and (10) become

$$\begin{aligned} E[u(t)] &= 0 \\ E[u(t)u(t')] &= \lambda(\sigma_a^2)\delta(t - t'), \quad a = a_i - m. \end{aligned}$$

These are the characteristics of the white noise, as Kalman filter algorithm required (see Appendix).

3. Computer Simulation

Figure 1 summarizes in a block diagram the model described in the previous section and the estimation algorithm. Figure 2 shows the AE signal corresponding to the following parameters: $i = 1, 2$ (i.e., two bursts), $t_1 = 350 \mu s$, $t_2 = 366 \mu s$, $u(t_1) = 1$ mV, $u(t_2) = 3.5$ mV, $f_0 = 0.135$ MHz, $\lambda = 0.0075$, $R = 2.02 \times 10^{-3}$, $c = 10,000$, $\tau = 172.1 \mu s$.

Figure 3 shows the estimation $\hat{x}_0(t)$ of the first state variable $x_0(t)$ given by the Kalman filter algorithm. A good estimation of time occurrence and amplitude is obtained.

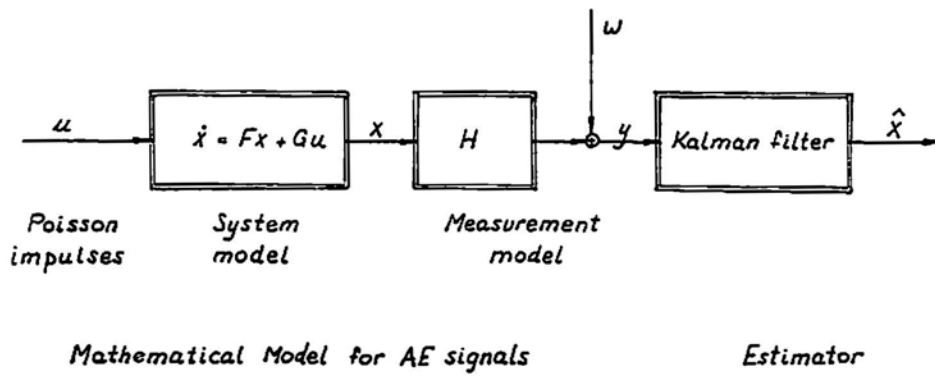


Fig. 1 Mathematical model.

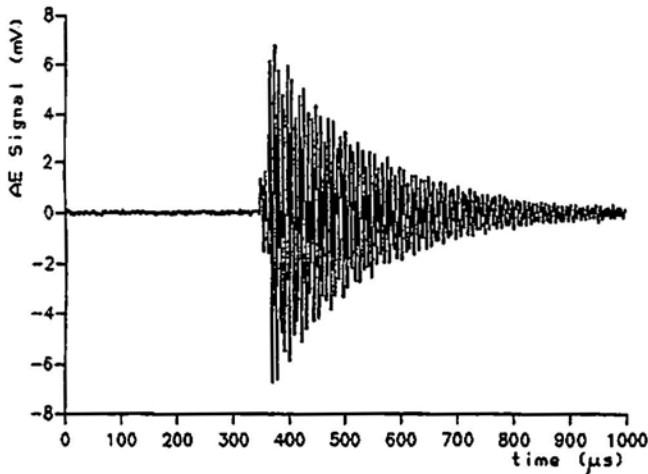


Fig. 2 Computer simulation of an AE signal composed by two bursts localized in $t_1 = 350$ and $t_2 = 366$.

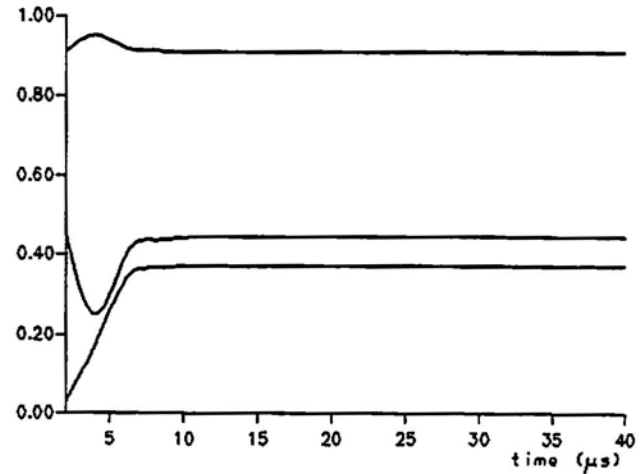


Fig. 4 Filter gain.

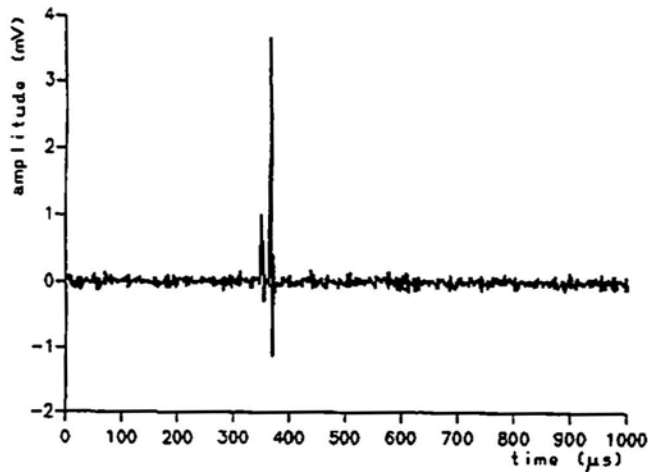


Fig. 3 Estimation of the time occurrence and amplitude given by the Kalman filter.

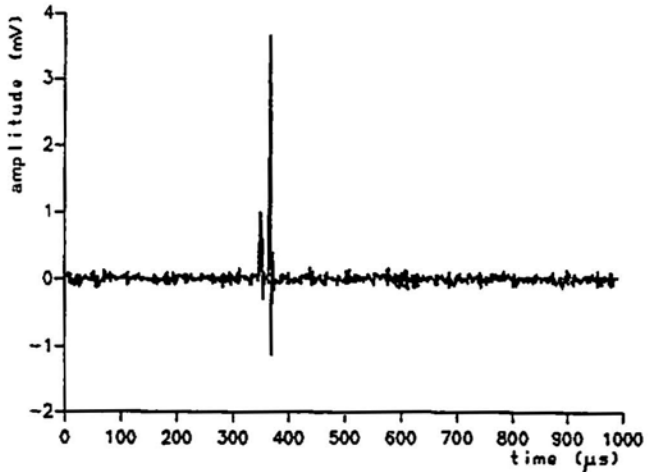


Fig. 5 Estimations given by the Kalman filter using the steady values of the gain.

As can be seen in the Appendix (see equation A1), the estimation given by the Kalman filter consists in two parts; one of them corresponds to the new information, which is weighted by a time dependent matrix $K(t)$ called "gain of the filter".

In our case this gain is a vector

$$K(t) = [k_1(t), k_2(t), k_3(t)]^T$$

and is shown in Fig. 4. As can be seen, the three entries of the matrix gain reach the steady state in a short time interval. This fact allows an easy implementation of the method, since, using

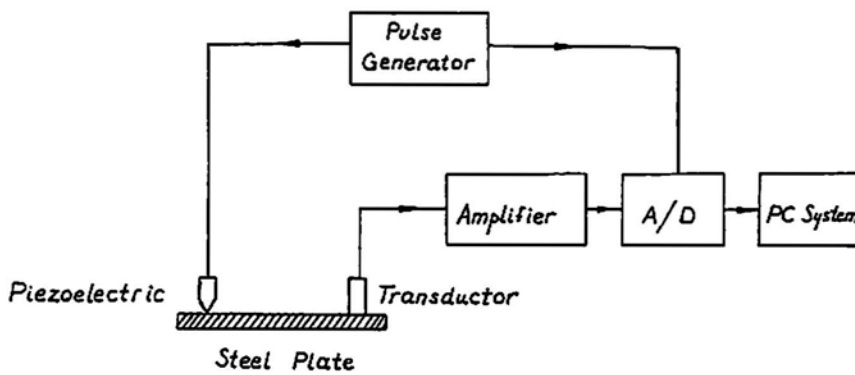


Fig. 6 Laboratory configuration for AE signal generation.

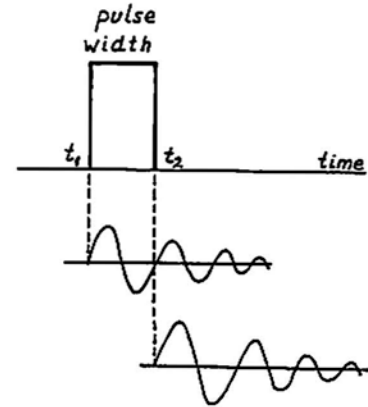


Fig. 7 Burst generator.

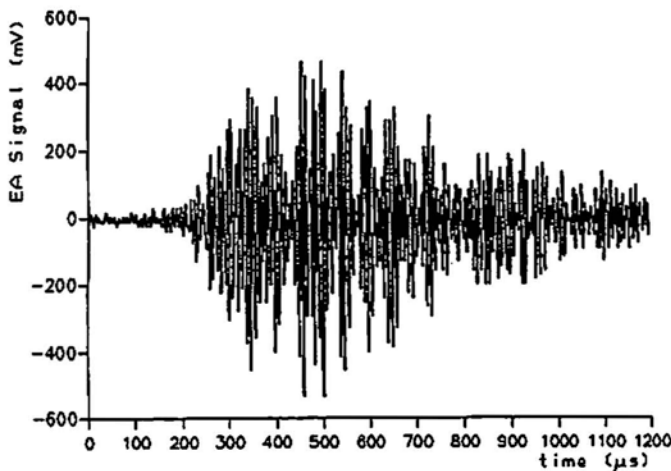


Fig. 8 Experimental AE signal.

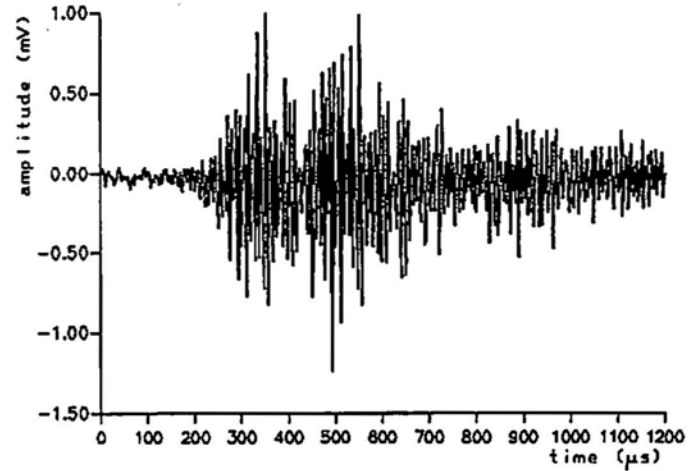


Fig. 9 Estimations given by the Kalman filter.

the constant steady state values in the filter algorithm, the estimations obtained are as good as the ones obtained using the time variable gain $K(t)$. The estimation $\hat{x}_0(t)$ corresponding to the Kalman algorithm with constant gain is shown in Fig. 5.

4. Experimental Results

Figure 6 shows the laboratory setup for the AE generation. The AE signal was obtained using a piezoelectrical crystal fed by a square wave coming from a pulse generator. Each wave front generates a burst in the steel plate, shown in Fig. 7. The pulse can vary from 1 μ s to 15 ms. The signal detection was made using a piezoelectric sensor (AEDOS-CISE) of approximately 150 kHz of resonance frequency. The signal was amplified 60 dB and digitized using an A/D converter ETUDE-TM (25 MHz, 8 bits). The analysis of the digital signal was made in a PC system.

The AE signal obtained can be seen in Fig. 8. It is composed by two bursts of the same amplitude localized in $t_1 = 350 \mu$ s and $t_2 = 500 \mu$ s.

Figure 9 shows the estimation obtained with the algorithm described in Sec. 2. We can distinguish two pulses with the

same amplitude, approximately located in 320-350 μ s and 500-550 μ s. This fact is not clear from Fig. 8; i.e., from the original AE signal, where there are similar amplitudes in 350, 400, 600 and 650 μ s.

5. Conclusion

A technique for estimating the time occurrence and amplitude of bursts in AE signals was presented. This technique is based on the model given by Mitrakovic et al. (1985) and the theory of Kalman filtering. We have shown the effectiveness of the proposed method using computer generated data and experimental data.

A possible extension of this work would be the consideration of several frequencies in the model and the analysis of the reflections of the AE signal from the boundaries of the specimen.

Appendix

Summary of continuous Kalman filter equations

System model: $dx(t)/dt = F x(t) + G u(t)$

where x is a column n -vector, u is a column m -vector, F and G are $n \times n$ and $m \times n$ matrices, respectively, and $u(t)$ is white noise with

$$E[u(t)] = 0, \\ E[u(t)u'(\tau)] = Q \delta(t - \tau) \quad (u' = \text{transpose})$$

Measurement model: $y(t) = H x(t) + w(t)$

where y is a column p -vector, H is $n \times p$ matrix and $w(t)$ is white noise with

$$E[w(t)] = 0, \\ E[w(t)w'(\tau)] = R \delta(t - \tau) \quad (R: \text{nonsingular})$$

State estimate:

$$d\hat{x}(t)/dt = F \hat{x}(t) + K(t)[y(t) - H \hat{x}(t)] \quad (A1)$$

where $K(t)$ is a $n \times p$ matrix, the gain of the filter.
Initial condition $\hat{x}(0) = \hat{x}_0(0)$.

Error Covariance Propagation:

$$dP(t)/dt = F P(t) + P(t) F' + G Q G' - K(t) R K'(t) \\ P(0) = P_0$$

Gain Matrix: $K(t) = P(t) H R^{-1}$

when $E[w(t)v'(\tau)] = 0$.

References

A. Gelb (1974), *Applied optimal estimation*, MIT Press, Cambridge.

A.H. Jazwinski (1970), *Stochastic processes and filtering theory*, Academic Press, New York.

T.P. McGarty (1974), *Stochastic systems and state estimation*, Wiley, New York.

D. Mitrakovic, I. Grabec and S. Sedmak (1985), *Ultrasonics*, 23, 227-232.

A. Papoulis (1965), *Probability random variables and stochastic processes*, McGraw-Hill, New York.

A.P. Sage and J.L. Melsa (1971), *Estimation theory with applications to communications and control*, McGraw-Hill, New York.

E. Wong (1971), *Stochastic processes in information and dynamical systems*, McGraw-Hill, New York.

Progress in Acoustic Emission VI

Relation Between AE Characteristics and Interlaminar Fracture
of Quasi-Isotropic Carbon/Epoxy Laminates
T. TANIMOTO and T. MORII

Characteristics of Acoustic Emission in Fracture Process in Static Load Tests for Notched FRP Plates
H. HYAKUTAKE and T. YAMAMOTO

Characteristics of Acoustic Emission in Notched Short Fiber Reinforced Thermoplastic
N. S. CHOI, K. TAKAHASHI and K. HOSHINO

Microfailure Mechanism and Improvement of Mechanical Properties for Sheet Molding Compound
N. SATO and T. KURAUCHI

Subsurface 1

Recent Kaiser Effect Studies on Rock
H. R. HARDY, Jr. and W. SHEN

The Estimation of Pre-Stress from AE in Cyclic Loading of Pre-Stressed Rock
M. SETO, M. UTAGAWA and K. KATSUYAMA

In Situ Stress Measurements Obtained Using Overcoring and the Kaiser Effect of Acoustic Emissions within the
Carnmenellis Granite, Cornwall, UK.
A. J. JUPE, S. P. BARR and R. J. PINE

A Study of the Time Dependency of the Kaiser Effect in the Carnmenellis Granite, Cornwall, UK.
S. P. BARR, R. J. PINE and A. J. JUPE

Systems and Analysis

The Reverberation of AE Signal in Small Specimen during Corrosion Process
B. Q. ZHANG and Y. H. LIU

A Hit Processing Procedure for Locating Acoustic Emission Events
M.-H. YANG

A SiGMA Analysis of the 2-Dimensional PMMA Model
M. SHIGEISHI and M. OHTSU

A Method of One Dimensional Source Location by Using AE Waveform Parameter
T. KISHISHITA, A. CHICHIBU and T. KIKUCHI

Acoustic Emission Waves in Heterogeneous Media and Its Application to the NDE Problems
T.-T. WU and J.-H. GONG

AE Source Waveform Analysis by Using a Neural Network
H. YUKI and K. HOMMA

Structures 1

Acoustic Emission Testing - A Mature Technology for Chemical Industry Safety
T. J. FOWLER

AE Monitoring and Studying of Signal Analysis Method for Large Spherical Tanks with Insulating Layer
G. DAI, Y. T. XU, B. Q. ZHANG and W. X. HAN

AE Monitoring and grain Measurement for Testing Pressure Vessel with Artificial Prefabricated Flaw
G. DAI, Y. T. XU and B. Q. ZHANG

(continued to page 24)

Acoustic Emission Technique at Proof Tests of Nuclear Pressure Vessels in Hungary

Peter Pellionisz and János Geréb

Abstract

One of the most successful applications of acoustic emission (AE) techniques is monitoring pressure tests. This surveillance method has been introduced in Paks Nuclear Power Plant, Hungary, where four, 440 MW pressurized-water nuclear reactors are in operation. The first application was made in 1987 at the four-year in-service inspection and proof test of the first reactor unit and it has been followed by yearly procedures of inspecting the second, third and fourth reactor units, between 1988-90. The AE investigations performed at Paks Nuclear Power Plant are presented regarding the measurement, data transmission and processing methods, the instrumentation and organization technique.

1. Introduction

Safe operation of nuclear power plants is of primary importance. One of the key components determining the overall safety of pressurized water reactors is the pressure vessel containing the highly radioactive nuclear core. In consequence of the embrittlement process of the vessel material caused by the irradiation, the safety margin decreases continuously. Periodical proof tests with enhanced pressure verify system integrity and reliability, the overloads, however, represent additional sources of potential danger. In addition to other NDT methods, acoustic emission (AE) technique is frequently used in order to detect anomalies such as microcrack formation, leakage, etc. during the hydrotests. Characteristic features of the AE technique represent benefits at these applications: the whole process can be monitored and evaluated in a relatively simple and inexpensive way. This is the reason that monitoring acoustic emissions at hydrotests of pressure retaining structures is used as an important test worldwide (Dunegan, 1989; Fowler et al., 1989; Scruby et al., 1988).

2. Proof Tests of Nuclear Reactors in Hungary

A high percentage of the electricity demand of Hungary is supplied by the country's four pressurized-water-reactor units of 440 MW each. The WWER-440 type reactors of Paks Nuclear Power Plant have been delivered by the Soviet Union and put into operation between 1983-87. The units are operating with very good reliability; their continuous operation is, however, interrupted every four years in order that in-service inspection and hydrotest of the pressure vessel be performed.

The main characteristics of the V-213-type reactor pressure vessel are as follows: diameter: 4.27 m; height: 11.8 m;

wall thickness: 140 mm; forged belt-plates welded together and inner side covered with stainless cladding of 9 mm; material: reactor steel 15Ch2MFA (C = 0.16%, Mo = 0.6%, Mn = 0.54%, Cr = 2.7%, V = 0.028%); number of water loops: 6; operating pressure: 12.3 MPa; operating temperature: 290°C.

According to the actual regulation in Hungary, proof pressure value must be 50 percent higher than the operational one. This high-value overload can cause damages in the pressure vessel material: tests can enhance the risk instead of reducing it. Acoustic emission monitoring has been introduced for this reason, for checking the most dangerous areas during the hydrotests. Communication lines have been established and data processing took place simultaneously with the measurement in order to alert control personnel and enabling them to interrupt the test if needed.

The hydrotests were applied to reactor pressure vessels, primary circuit and the water cleaning system. They were carried out before re-starting, after complete NDT testing, with reactor completely assembled and core fuel installed. The pressure was raised from 2 MPa to 19.2 MPa, with pressure hold and pressure down periods, with a total duration of several hours. The maximum rate of pressure increase was 0.6 MPa/minute and the wall temperature was at 120°C.

3. Acoustic Emission Monitoring

During the pressure tests AE sensors were applied at three regions of the structure as Fig. 1 shows. Number, application mode, and type of the AE sensors placed at regions A, B and C varied from one proof test to the other as Table 1 shows. At Unit 1 only two small, experimental AE systems were applied. This sort of surveillance proved to be a valuable method and by this reason AE monitoring has been used regularly at each of the consecutive proof tests in the Paks Nuclear Power Plant (Pellionisz et al., 1989).

Table 1 AE sensors and instrumentation for proof testing (* = High temperature sensor; ** = Sensor with waveguide)

Reactor unit	1	2	3	4
• Year of test	1987	1988	1989	1990
• Number of a.o. sensors				
- in nozzle region (A)	12	12	12	15
- on ducts (B)	---	4	4	6
- at welding 5/6 (C)	---	8	12	12
• Type of sensors				
- at (A), (C)	D9203	D9203	D9203	D9203
- at (B)	---	D9210*	D9203**	D9203
• Number of Defectophones and Expander units	3	3	3	3
• Remote check of sensors	---	---	Experim.	System Tester

Received 20 December 1990. The authors are affiliated with Central Research Institute for Physics, H-1525 Budapest, POB 49, Hungary.

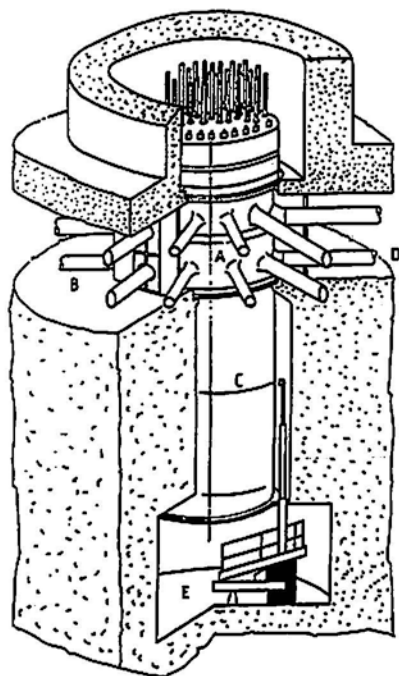


Fig. 1 WWER-440 reactor pressure vessel. Regions indicated: A = nozzle region with water inlet, outlet ducts, B = primary circuit piping, C = welding at the height of the reactor core, D = AE measuring devices for regions A and B, E = AE measuring devices for region C.

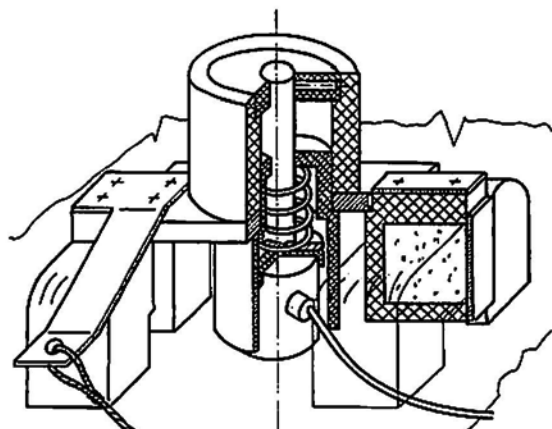


Fig. 2 Magnetic sensor holder.

At region A the AE sensors were attached manually to the vessel wall with the aid of standard magnetic holders. Access to this region from space B is by the heavy doors around the ducts. Attachment of the sensors to the pipes was made by metal straps since the pipes are of non-magnetic steel material. For placing transducers in the welding zone C inaccessible for human beings, special magnetic holders were constructed (Fig. 2) which could be taken, positioned, attached and left on the wall by the pneumatic arm of the remote controlled positioning device for ultrasonic testing.

Generally, 100-400 kHz AE sensors (Dunegan D 9203 A) were applied. After some of the tests, the sensors on the water pipes were left in place for measurements during normal operation: in these cases either high-temperature sensors (Dunegan

D9210 M1) or standard sensors with acoustic waveguide were used.

Two local AE measuring systems (Defectophone plus Expander) at places D and E were applied each one communicating with a remote computer through RS-232C serial data transmission links. Before the proof tests, sensors, instruments, communication lines, computers were checked and calibration measurements performed. By continuous surveillance of the measured AE data, on the display of the computers, acoustically active regions and periods could be identified. Since pressure was followed generally by pauses or depressurization, when acoustic activity was not detected, there was available time during the measurement for detailed analysis (plotting correlations between different parameters, making source location maps, etc.) The real-time analysis was followed by more detailed post-processing after the tests.

The AE investigations were carried out by AE researchers of KFKI (Central Research Institute for Physics, Budapest) and by those of ERÖKAR (Service Company for Power Plants) in cooperation with the NDT-staff of Paks Nuclear Station.

4. Instrumentation

The AE measurements were performed by the AE instrumentation developed and put in commercial production by the Central Research Institute for Physics, Budapest. The applied equipment was based on the multichannel AE analyzer system Defectophone NEZ-220 which is a complete family of the necessary AE instrumentation items, comprising amplifiers, frequency filters, testers, etc. An important part of the system is a powerful software package for IBM-PC and compatible computers enabling them to program and to control the measuring units as well as to receive and to analyze the AE data arriving through the RS-232-C standard asynchronous communication line. The applied systems became larger from 12 channels in 1987 to 24 channels in 1990.

AE sensors attached to the reactor wall were provided with small, impedance matching transformers, and connected by coaxial cables to logarithmic amplifiers put at an accessible place together with the programmable Defectophone System Tester. This assembly was connected to the Defectophone plus Expander units each having 16 AE plus 16 parameter input capacity and processing 4 arrays of 4 AE sensors on the first-hit principle. Defectophone plus Expander systems are 16 channel front-end processors enabling identification and digitalization of selected AE parameters of the first hit signals in any of the four-sensor arrays (elapsed time, ring-down count, peak amplitude, absolute average, rise time, event duration, parameter value), two at the same time, as well as measuring differences in arrival times at all channels in the active array. The device disposes microprocessor-based intelligence, 128 kB memory cassette for storing measured data, programmable operation modes, display, plotter, and alarm facilities, variable trigger thresholds, selectable data filtering possibilities as well as a bidirectional computer interface to IBM-PC/AT or compatible computers.

At the proof tests, each Defectophone was connected to a dedicated computer in the remote diagnostic control room of

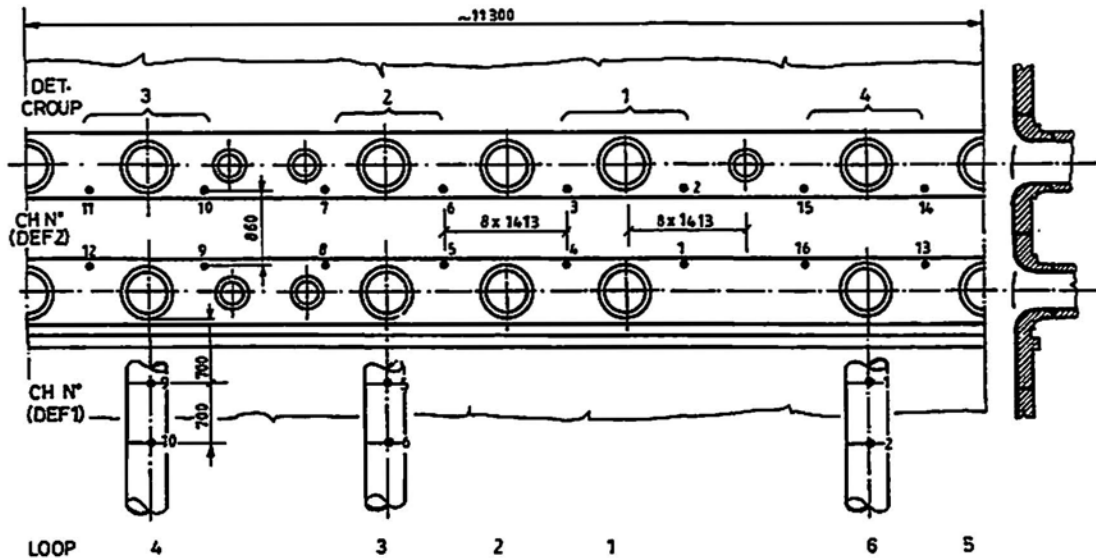


Fig. 3 Sensor arrangement at the proof test of Unit 4.

the power plant. Both instrument control and data reception as well as operating the system tester for verifying correct operation of the system were made from this control room. The system tester is controlled by digital commands from the computer through the Defectophone and stimulates the selected AE sensors by pulses up to 80 V, injecting the needed high energy for the enormous metal structure to get proper response from the sensors placed far from the stimulus.

5. Checking System Performance

Distances between adjacent sensors were selected generally between 0.8 m and 2.2 m on the wall. Additional sensors placed on the water pipes made possible cross-checking of the measured activity by comparing the signals coming from the wall and from the pipes. The sensor configuration applied at the proof test of Unit 4 (see Fig. 3) comprised two detectors at the pipes: the order of signal arrivals showed the direction of the sound waves; i.e., identified the region of sound origin.

Table 2 Summarized data for location calculations.

DEFINE LOCATING CONFIGURATION			
SETUP			
Number of groups, max:	3	Identical/different: different	
Propagation velocity m/s:	2500		
Array:	1	2	3
Type of array:	general	general	general
Origo of array (x,y) mm:	(0,0)	(4636,0)	(-3880,0)
Number of detectors:	4	4	4
Side length del1-2 mm:	2712	2712	1944
Detector positions mm:			
1 (x,y)	(1356,980)	(1356,980)	(972,980)
2 (x,y)	(-1356,980)	(-1356,980)	(-972,980)
3 (x,y)	(-1356,-420)	(-1356,-420)	(-972,-420)
4 (x,y)	(1356,-420)	(1356,-420)	(972,-420)
Border around detectors mm:	1000	1000	1000
LOCATING CALCULATIONS		DRAW CHARACTERISTIC	
Locating algorithm:	improved	Drawing algorithm:	single
First measuring section:	1	Array to draw:	2
Last measuring section:	last	Magnifying:	high

After placing the sensors in their position, correct functioning of the measuring chains were verified by mechanical stimulation and watching Defectophone display. Bidirectional communication between computers and Defectophone devices was also tested. Measuring sensitivity, background noise level, signal attenuation, optimal threshold and wave propagation velocity were made by several tests: pencil-breaking, mechanical shocks, electric pulser driven directly by the Defectophone devices and by operating the system tester unit.

It must be mentioned that Defectophone source location software is provided with a semi-automatic velocity measurement mode which instructs the user at what points should be test pulses applied, accepts or rejects the answers and calculates velocity averages in different directions. The found velocity, geometrical coordinates of the sensors, the selected location algorithm and drawing forms are summarized in location configuration tables in the computer (Table 2).

Source location ability of the AE measuring system was tested by artificial test pulses at known positions. The heating process of the reactor up to 120°C by operating the main water pumps can also be regarded as an introductory phase of the proof test. During this process, acoustic activity in the water inlet-outlet tubes was also tested: background noise originated from the pumps or showing leakage was measured and recorded.

6. Data Evaluation

Both burst data (acoustic events) and sampled values of continuous signals (acoustic averages and values of parameter signals) were displayed on the computer screen real-time. Correlation between pressure variations and burst data would have helped the AE experts to detect any anomaly, if had occurred. If change in instrument parameters was needed, one could replace the data display on the computer screen with the front panel presentation of the Defectophone, by a single keystroke and

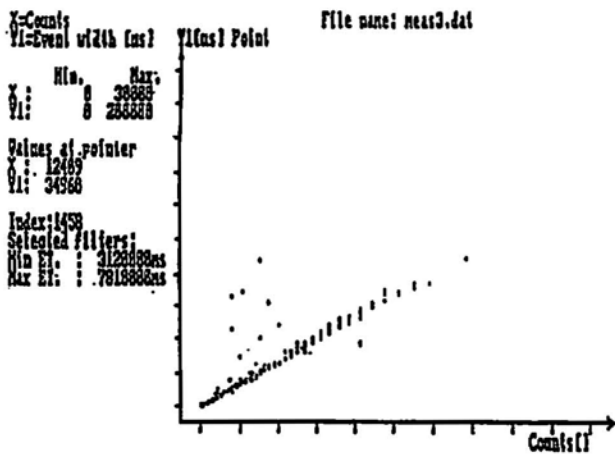


Fig. 4 Correlation plot between event duration and ring-down count.

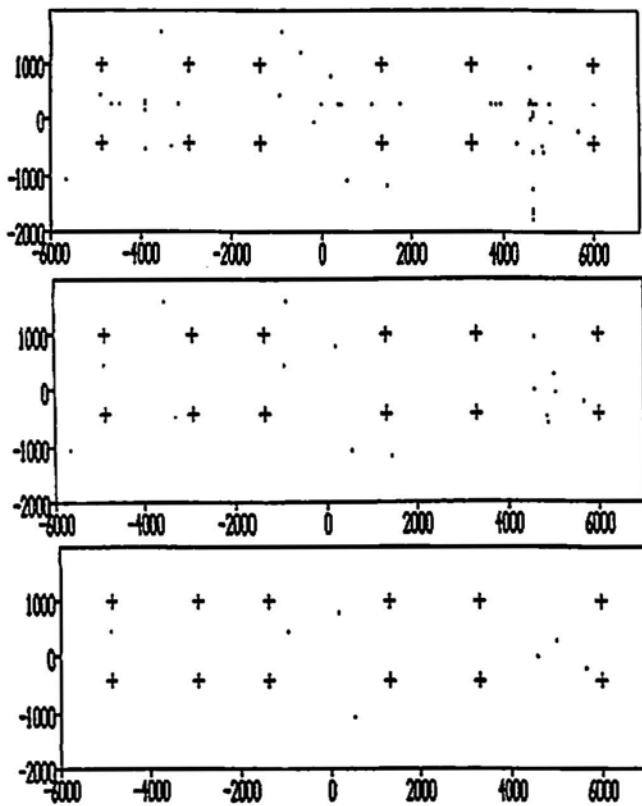


Fig. 5 Location map in the nozzle area of the reactor vessel without filtering (a), after filtering simultaneous arrivals (b), further filtering events with counts less than 1500 (c).

the required command could be sent to the measuring device, then displaying data could be continued.

Data display - real-time listing of AE parameters - offers a general overview on the acoustic activity, but details, correlations between different AE parameters, location maps, etc. are also needed to have a complete and detailed analysis. The applied Defectophone data processing software offers many options to facilitate it. A very important one is filtering, i.e.

generating new data files which exclude data satisfying user-selectable criteria (e.g., short and/or small pulses, events from certain area, etc.)

By way of illustration, some typical plots are shown. Figure 4 shows a correlation plot made by the Defectophone software between event duration and ring-down counts: events not alike can be easily separated. Figure 5 shows a series of location maps at a certain period of the proof test of Unit 2.

As a base of interpreting AE data, the corresponding ASTM standard was taken: AE sources were classified in the following groups: critically active, active and inactive. An important diagram for the overall estimation of the safety of the pressure vessel is shown in Fig. 6 from the proof test of Unit 2 in 1988. One can see that AE activity stopped during depressurization or at constant pressure, showing that no critically active AE source (see ASTM Standard, 1985) was present in the inspected zone. Another presentation mode is shown in Fig. 7, where burst amplitudes are displayed by dots together with the record of pressure and cumulated events (proof test of Unit 4).

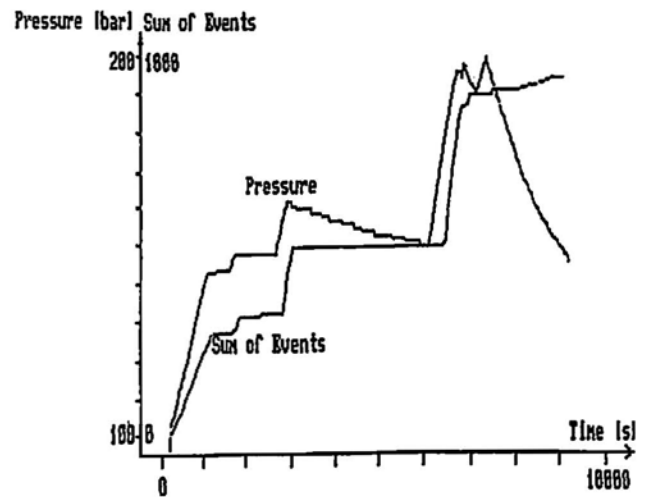


Fig. 6 Cumulated number of acoustic events and pressure during the hydrotest of Unit 2.

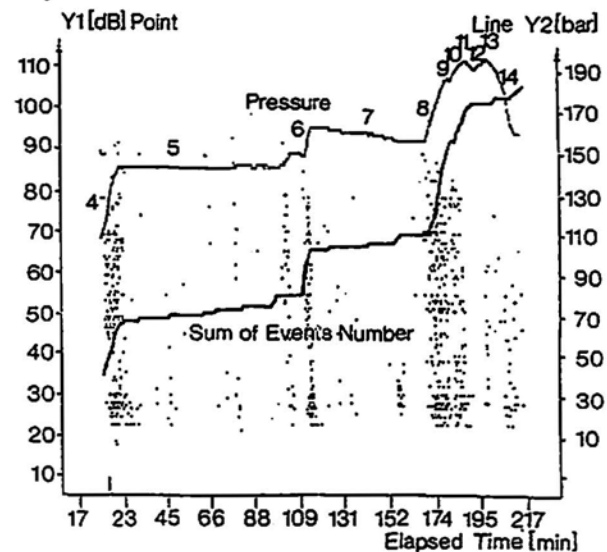


Fig. 7 AE peak amplitudes, event number and pressure in function of time at the proof test of Unit 4.

7. Conclusions

Acoustic emission monitoring proved to be an efficient method to increase safety at proof tests of nuclear reactors and to detect regions for further inspections by other NDT methods. During the proof tests of four reactor units, measuring and evaluation methodology has been perfected, instrumentation acquired, a team of experts trained: everything is prepared for routine applications. Experience gained during the proof tests has led to many improvements both in measuring hardware and software. These additions and alterations are applied at the production of the Defectophone systems from 1990.

Acknowledgment

Applied methods, measuring hardware and software are common results of a coordinated research and development work. The most important contribution was given by Messrs. G. Lafranco, T. Maróthy, A. Péter, B. Juhász, Gy. Székely. The AE monitoring measurements were performed with the participation of engineers and technicians of the KFKI as well as those of ERÖKAR (project leader: Mr. P. Szücs). The work was stimulated and highly facilitated from the side of the nuclear power plant by Mr. P. Trampus. Thanks are due to all contributors.

References

- ASTM (1985), ASTM Standard, E569-85: Standard practice for acoustic emission monitoring of structures during controlled stimulation, Philadelphia.
- H.L. Dunegan (1989), "AE - for when you absolutely cannot afford a failure", *J. Acoustic Emission*, 8(1/2), S71-S74.
- T.J. Fowler, J.A. Blessing, P.J. Conlisk and T.L. Swanson (1989), "The MONPAC system", *J. Acoustic Emission*, 8(3), 1-8.
- P. Pellionisz, P. Szücs and P. Trampus (1989), "Acoustic emission test of WWER-440 pressure vessel", *Proc. 12th World Conf. on Non-Destructive Testing*, Amsterdam, April.
- C.B. Scruby and K.A. Stacey (1988), "AE measurements on PWR weld material with inserted defects", *J. Acoustic Emission*, 7(2), 81-93.

Progress in Acoustic Emission VI

Sensors

Method for Measurement of Sensitivity Degradation of Acoustic Emission Transducer
Y. HIGO and H. INABA

Calibration of Conical Transducers in Seismic Model Tests
P.-L. LIU, T.-H. SONG and T.-T. WU

Characterization of AE-Transducers Using Davies' Bar and Laser Interferometry
A. UMEDA and K. UEDA

Data Reproducibility Improvement at Changing Contact Conditions for the Electrodynamic Sensor by Means of Using Electroacoustic Effect
YA. I. BULBIK, V. V. BULAVKIN, N. V. VASILENKO and A. G. KOZLOV

Medical

Vibration Arthrography in Degenerative Knee Joint Disorders
C.-C. JIANG, T.-T. WU, Y.-R. LIU and C.-S. LIU

The Effect of Haversian Remodeling on AE Response of Compact Bone under Quasi-Static Tension
S. TANAKA, T. HARA, T. SHIBUYA and T. KOIZUMI

Non-Destructive Evaluation of Yielding Stress of Bone during Fracture Treatment Using Acoustic Emission Technique
N. INOUE, Y. HIRASAWA, Y. WATANABE, Y. ARAI, H. TSUNEOKA and Y. HATANAKA

Nonlinear Behavior with AE of Cortical Bone Treated with Acid under Tensile Loading
T. HIRAI, T. KATAYAMA, H. YAMAMOTO, M. INADA, N. INOUE, Y. WATANABE and Y. ARAI

Structures 2

Enhanced Fatigue Crack Detection in Aging Aircraft Using Continuous Acoustic Emission Monitoring
S. L. McBRIDE, Y. HONG and M. D. POLLARD

Development and Calibration of Downhole Triaxial AE Detectors for Subsurface and Civil Engineering AE Measurements
S. NAGASHIMA, H. MORIYA and H. NIITSUMA

Characteristics of Acoustic Emission Waveform during Slope Model Test
A. CHICHIBU, T. KISHISHITA and T. KIKUCHI

Subsurface 3

A Theoretical Study of AE Traveling through a Fluid-Filled Crack with Application to Characterization of a Geothermal Reservoir Crack
K. HAYASHI and K. SATO

Subsurface AE Source Location by Multi Zone Modeling for Uncertain Velocity Structure
S. OKADA and H. NIITSUMA

Applicability of Acoustic Tomography Techniques to Evaluate the Instability of Stressed Rock
K. ITAKURA and K. SATO

Virtual Calibration Method for Neural Source Location in Subsurface AE Measurement
A. MIYAZAKI and H. NIITSUMA

(continued to page 30)

Effects of Wave Velocity Change on Magnetomechanical AE in Sintered Iron

Noboru Shinke and Yoshitugu Ohigashi

Abstract

Magnetomechanical acoustic emission (MAE) behavior shows a sensitive dependence on the change of the structure in ferromagnetic materials and can be applied for the nondestructive measurement of ferromagnetic materials. Wave propagation properties also reflect the change of the structure in the material. The purpose of this paper is to experimentally investigate MAE behavior as a function of the wave velocity in sintered iron. A correlation exists between MAE and the wave velocity in sintered iron regardless of the change of the kind, average diameter and forming condition of iron powder. That is, the intensity of MAE increases in inverse proportion to the wave velocity. Thus, this MAE phenomenon can be applied to the nondestructive evaluation of sintered iron.

1. Introduction

Machine parts made of sintered iron are used widely, because they can be manufactured economically in large quantities. As the sintered iron has a unique structure with many pores, the mechanical and other properties change greatly according to the porosity, size, form and distribution of the pores. There have been many reports on how the mechanical characteristics depend on the porosity (Sarac et al., 1974; Bard and Williams, 1984). The wave velocity is generally used as an important characteristic value to evaluate some materials, because it is sensitive to the change of the metallurgical structure and is easy to measure nondestructively. From such a viewpoint, the method of measuring the porosity of sintered materials nondestructively relied on an adequate correlation between the porosity and the velocity of ultrasonic waves (Pohl, 1969; Mihara et al., 1988). The discontinuous magnetization in the process of magnetizing ferromagnetic materials works to generate magnetomechanical acoustic emission (MAE) (Lord, 1975). It was theoretically pointed out that MAE are generated in the process of discontinuous shifts of 90° magnetic domain walls and rotation of magnetizing vector, and that the intensity of MAE increases in inverse proportion to the wave velocity in ferromagnetic materials (Ono, 1986; Shibata and Sasaki, 1986). The MAE intensity depends on the change of the metallurgical structure in ferromagnetic materials. To utilize MAE as a new method of nondestructive evaluation of sintered materials, effects of wave velocity change on MAE have been experimentally investigated in this report.

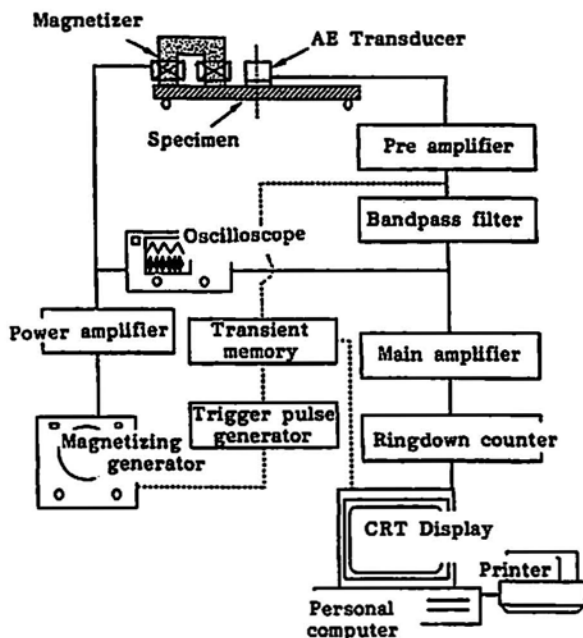


Fig. 1 Schematic diagram of experimental equipment.

2. Experimental Apparatus and Method

2.1 Analyzing Apparatus of MAE Waves

One way to estimate MAE intensity is to measure AE counts during the basic period of the magnetizing frequency, but it is also important to know the amplitude distribution of MAE. In this research, the AE counting method was adopted. The automatic MAE analyzer used to measure MAE waves produced by test-pieces is shown in Fig. 1 as previously reported (Shinke et al., 1985). The analyzer is designed to automatically set the discriminating level in the input section of the counting circuit instructed by the computer. Therefore, it operates fully-automatically after starting, and all the measurement data are recorded on the memory. These data are indicated in the form of graphs or of numerical data in hard copies. The detector used for detection of MAE signals is a PZT transducer which has a resonance frequency of 250 kHz. The transducer output is amplified by 80 dB using a pre-amplifier and main-amplifier.

2.2 Measurement of Wave Velocity

The ultrasonic flaw detector used for measuring the wave velocity of given test-pieces is made by Sonic Instruments Inc. and its transducer has a resonance frequency of 5 MHz and outside diameter of 6.35 mm, coupled to the test-piece with vacuum grease.

Received 21 January 1991, in revised form, 25 January 1992. Noboru Shinke is affiliated with Faculty of Engineering, Kansai University, Yamate 3 - 3 - 35, Suita, Osaka 564, Japan and Yoshitugu Ohigashi is with Osaka Titanium Co., Ltd., Higashihama 1, Amagasaki, Hyogo 660, Japan.

2.3 Test-Piece and Experimental Method

The test-pieces are composed of atomized iron powder or mill-scale reduced iron powder. The distribution of diameters is shown in Fig. 2. The test-pieces were formed into a rectangular shape with several pressures at room temperature, and then sintered at 1423K in an atmosphere of the decomposed ammonia gas. Test-pieces were machined to a shape with the dimensions 150(L) x 9(W) x 9(H) mm. The wave velocity and density for test-pieces used in this experiment are shown in Table 1. To magnetize the test-pieces, we used a function generator, power amplifier and magnetizer with a compact ferrite core around which a coil is wound as shown in Fig. 3. Since the magnetic field produced by the magnetizer is not fixed but changes in the form of triangular waves, the intensity of the magnetic field is shown by the peak value of the current field strength applied to the magnetizing coil.

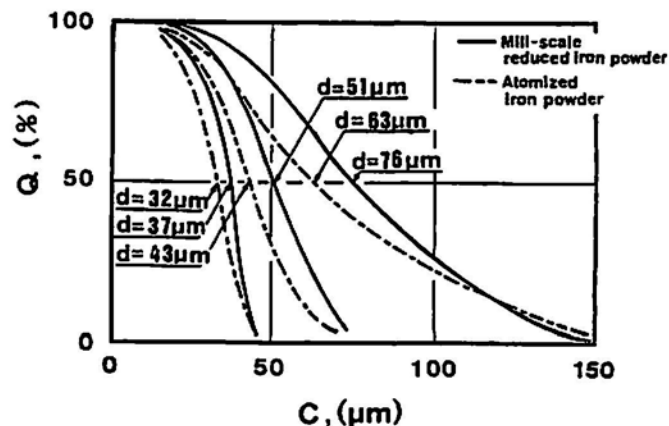


Fig. 2 Relation between the cumulative distribution percentage Q and the sieve opening C for iron powders.

Table 1 Test-Pieces

Mill-scale reduced iron powder				Atomized iron powder			
Test-piece No.	Diameter $d(\mu\text{m})$	Velocity $S(\text{m/s})$	Density $D(\text{g/cm}^3)$	Test-piece No.	Diameter $d(\mu\text{m})$	Velocity $S(\text{m/s})$	Density $D(\text{g/cm}^3)$
1	76	4140	6.09	13	63	4157	6.31
2	76	4398	6.33	14	63	4620	6.70
3	76	4730	6.61	15	63	4952	6.97
4	76	5080	6.95	16	63	5248	7.23
5	51	3992	5.94	17	43	4190	6.24
6	51	4380	6.25	18	43	4613	6.63
7	51	4800	6.66	19	43	4944	6.89
8	51	5168	6.98	20	43	5280	7.21
9	37	4080	5.94	21	32	4366	6.41
10	37	4458	6.26	22	32	4645	6.62
11	37	4835	6.67	23	32	5057	6.95
12	37	5140	6.96	24	32	5338	7.20

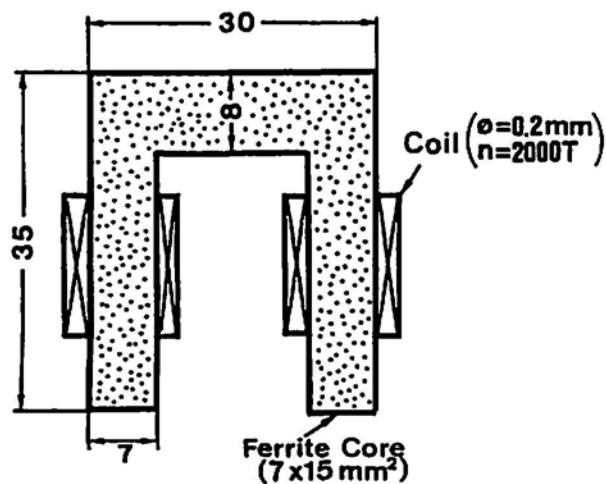


Fig. 3 Details of magnetizer.

3. Experimental Results and Discussion

Figure 4 shows examples of the total counts of MAE signals produced by magnetizing the sintered iron with differences of wave velocity. The magnetizing conditions were; frequency f

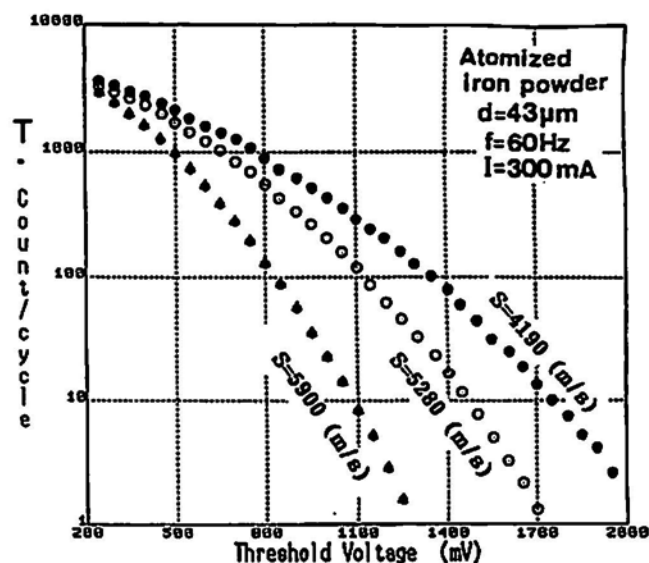


Fig. 4 Examples of the total AE counts for test-pieces with different wave velocities.

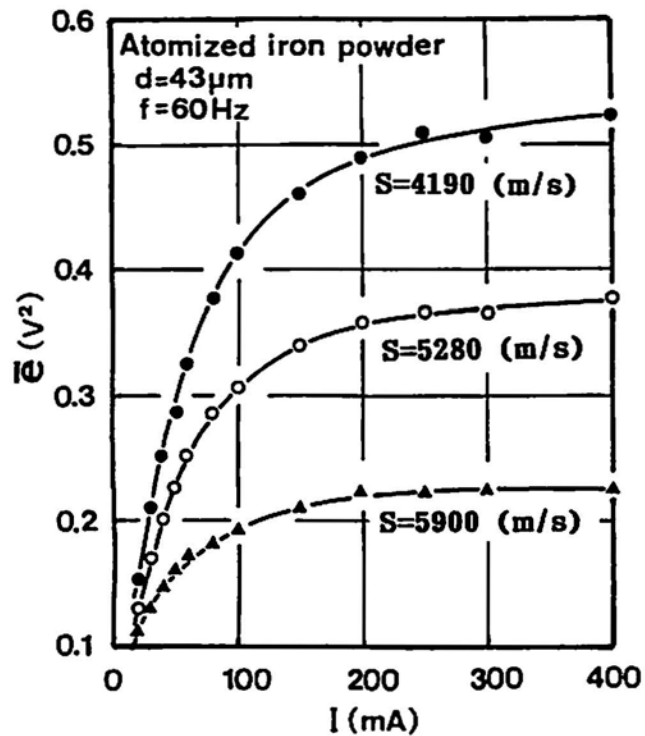
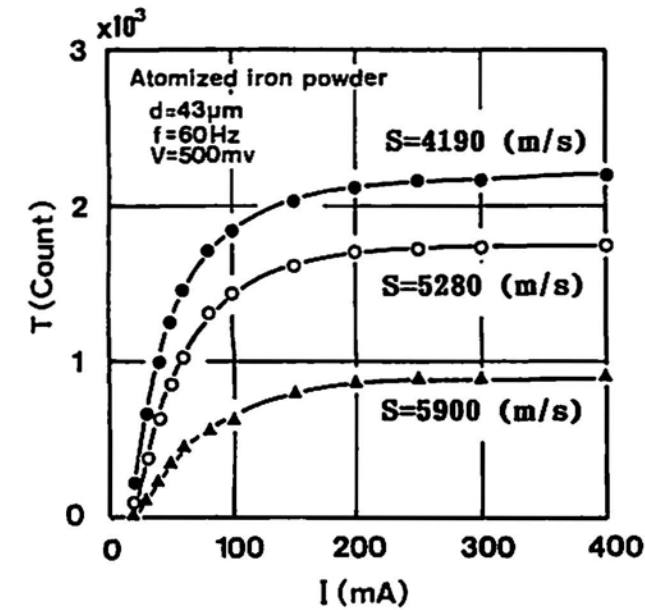


Fig. 5 AE counts per one cycle T and mean event energy \bar{E} as a function of magnetizing current I for test-pieces with different wave velocities.

= 60 Hz and magnetizing current $I = 300$ mA. In Fig. 4, T represents AE counts per one cycle of the magnetizing current. The test-piece with the wave velocity S of 5900 m/s is the pure iron (more than 99.9 % purity) which hardly contains the pores. The test-pieces of smaller wave velocity showed higher AE counts. The amplitude of MAE waves were also higher, indicating that MAE changes according to the difference of the wave velocity in sintered iron. In this paper, in order to estimate the intensity of MAE signals generated from the test-pieces, we used T (AE counts per one cycle) and \bar{E} (the mean event energy).

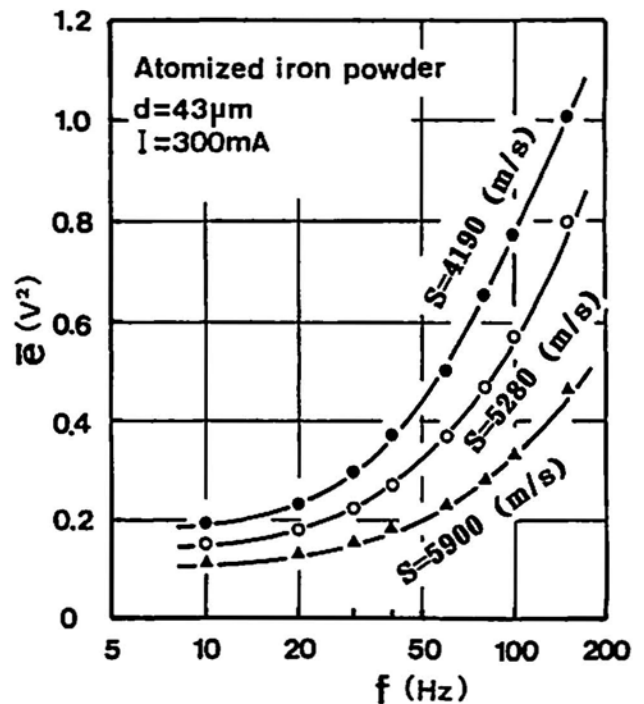
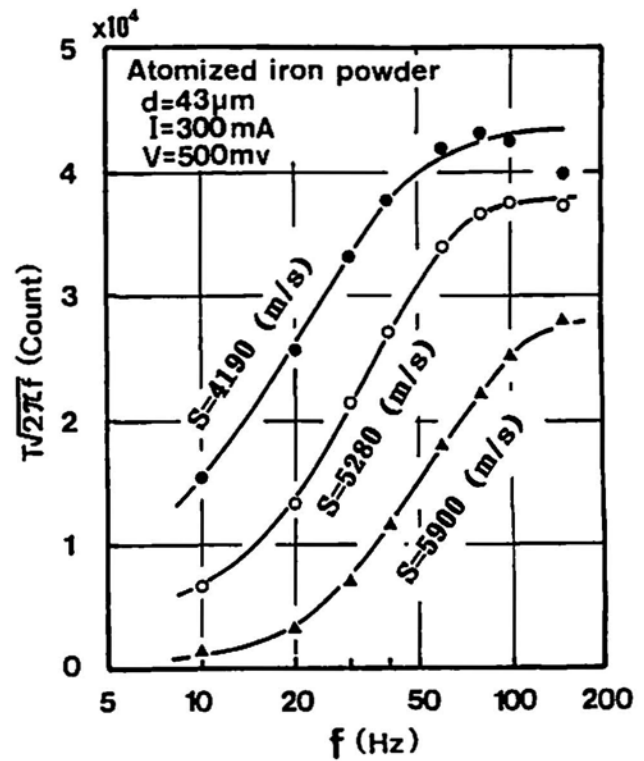


Fig. 6 Relation between $T\sqrt{2\pi f}$ and \bar{E} vs. magnetizing frequency f for test-pieces with different wave velocities.

First, we examined how the measuring conditions such as magnetic field intensity and magnetizing frequency affected MAE signals generated from test-pieces. Figure 5 shows the relation between the intensity of MAE signals generated during the magnetization of the test-pieces at 60 Hz and various magnetizing current up to 400 mA. The results showed that T and \bar{E} tend to saturate at the magnetizing current of 300 mA. This

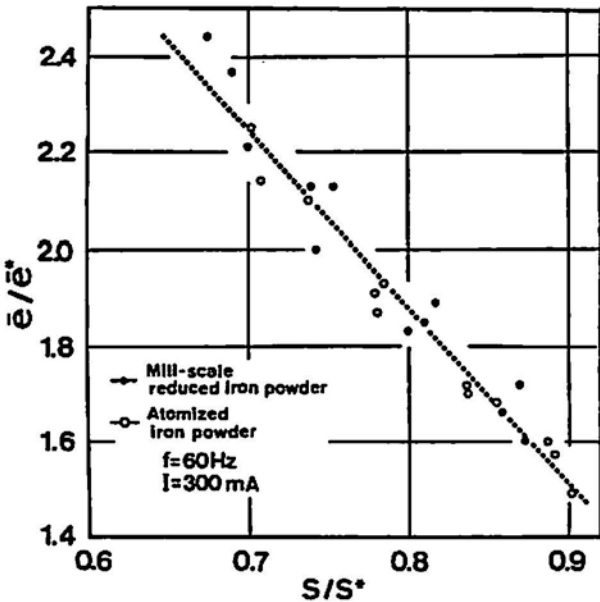
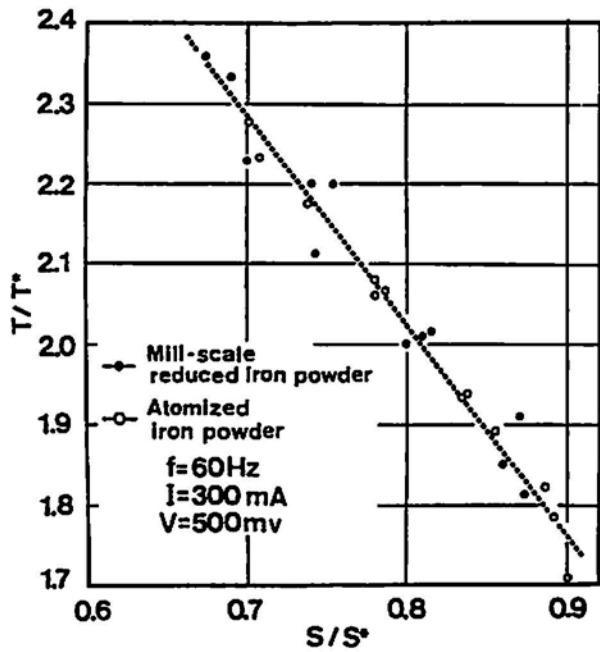


Fig. 7 Relation between the normalized AE counts T/T^* , mean event energy \bar{e}/\bar{e}^* and wave velocity S/S^* under magnetizing condition of 60 Hz and 300 mA.

behavior is commonly observed for the test-pieces having different wave velocities. When a test-piece is magnetized under the alternating fields, the eddy current is produced in the outer layer of the test-piece. The magnetizing frequency affects the skin depth of the magnetic flux and thus the source volume of MAE. Figure 6 shows the relation between $T\sqrt{2\pi f}$ and \bar{e} vs. magnetizing frequency up to 150 Hz. $T\sqrt{2\pi f}$ is the product of the square root of magnetizing frequency and AE counts. This parameter allows a comparison in terms of AE counts given by the outer layer of the test-pieces per unit thickness even at different magnetizing frequencies. When a sufficiently strong magnetic field was applied, the values of $T\sqrt{2\pi f}$ increase with a rise of magnetizing frequency, and tend to saturate at about 100

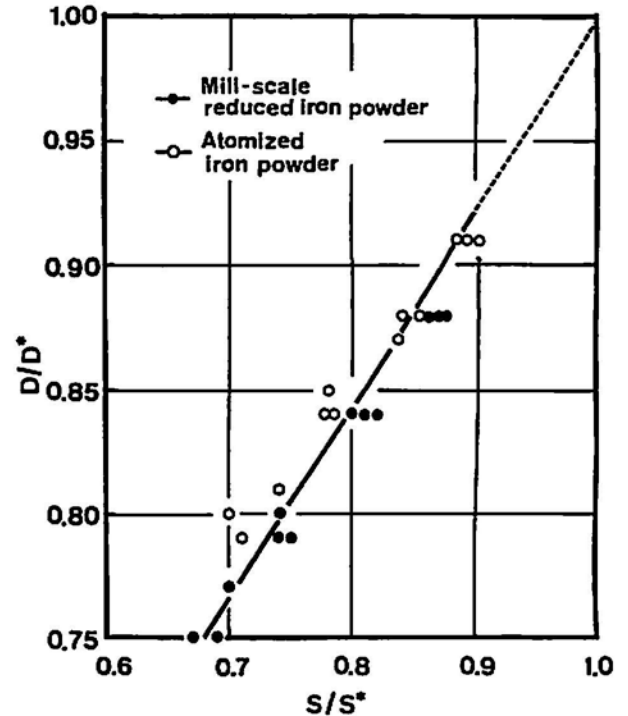


Fig. 8 Normalized density D/D^* vs. the normalized wave velocity S/S^* .

Hz. It was observed that MAE with the larger amplitude is generated according to the increase of the magnetizing frequency. The mean event energy \bar{e} based on amplitude of MAE increases with a rise of magnetizing frequency.

The effects of wave velocity up to 5338 m/s in sintered irons were examined. In order to evaluate the effects of wave velocity change on MAE, AE counts, mean event energy and wave velocity in sintered iron were normalized by their respective values for pure iron. Figure 7 shows the relation between the normalized AE counts T/T^* , mean event energy \bar{e}/\bar{e}^* and wave velocity S/S^* using a reference magnetizing condition of 60 Hz and 300 mA. In Fig. 7, T^* is AE counts, \bar{e}^* is mean event energy and S^* is wave velocity for pure iron. The normalized AE counts decreases in proportion to the increase of normalized wave velocity. The normalized mean event energy decreases linearly with the increase of the normalized wave velocity. It can be seen in Fig. 7 that the effects of wave velocity change on MAE are not influenced much by the change of the kind and average diameter of the iron powder within the range of wave velocity in this experiment. The relation between the normalized density D/D^* and the normalized wave velocity is shown in Fig. 8. Here, D^* is the density for pure iron and takes the value of 7.86 g/cm³. The normalized density tends to increase linearly with the increase of the normalized wave velocity. The skin depth due to the eddy current effect is inversely proportional to the square root of the product of the magnetizing frequency, conductivity and permeability of a sintered iron. Sintered iron has a characteristic that the conductivity and permeability become smaller with the decrease of the density (JPMA, 1987). Therefore, the source volume of MAE becomes greater with the decrease of the density of the sintered iron. The

sintered iron with the smaller density has a structure which contains many internal pores. It appears that the pores are important in consideration of wave velocity change. The pore is one of the primary factors determining the pinning source of magnetic domain walls. This increase of pinning source implies a higher MAE intensity. The experimental results of wave velocity change on MAE generated by sintered iron can be explained from the standpoint of the source volume of MAE and the pinning source of magnetic domain walls.

4. Conclusion

The dependency of wave velocity on MAE was experimentally investigated by using sintered iron with different wave velocities. The results indicated that the intensity of MAE signals varies inversely with the increase of the wave velocity in sintered iron. This suggests that MAE phenomenon can be applied to the nondestructive evaluation of sintered iron.

Acknowledgments

The authors are grateful to Japan Powder Metallurgy Co., Ltd. for providing the test-pieces and to Eishin Kagaku Co., Ltd. for measuring the wave velocity.

References

- A. Sarac, V. Miskovic, E. Dudrova and E. Rudnayova (1974), "The Dependence of Mechanical Properties of Sintered Iron Compacts upon Porosity", *Powder Metallurgy International*, 6(3), 128-132.
- K.S. Bard and J.D. Williams (1984), "Relationships Between Process Variables and Density of Explosively Compacted Iron Powder", *International J. Powder Metallurgy and Powder Technology*, 20(1), 23-32.
- D. Pohl (1969), "Ermittlung der Zugfestigkeit von Sintermetallen mit Ultraschallmessungen", *Arch. Eisenhütt.*, 40, 647-650.
- T. Mihara, M. Obata, T. Watanabe and H. Shimada (1988), "Nondestructive Evaluation of Porosity in Copper Powder Sintered Products by Ultrasonic Velocity Measurement", *J. JSNDI*, 37(5), 376-380 (in Japanese).
- A.E. Lord, Jr. (1975), "Acoustic Emission", *Physical Acoustics*, vol. XI, eds. W.P. Mason and R.N. Thurston, Academic Press, New York, pp. 290-353.
- K. Ono (1986), "Magnetomechanical Acoustic Emission - A Review", *Progress in Acoustic Emission III*, JSNDI, Tokyo, pp. 200-212.
- M. Shibata and H. Sasaki (1986), "AEM and BN Signals in Steel", *Progress in Acoustic Emission III*, JSNDI, Tokyo, pp. 213-221.
- N. Shinke, H. Maeda and Y. Usuki (1985), "Development and Application of Automatic Analyzer for AE during Magnetization", *J. JSNDI*, 34(8), 506-512 (in Japanese).
- Japan Powder Metallurgy Association (1987), "Syoketu Kikai Buhin", Gijitussyoin, Tokyo, pp. 108-114 (in Japanese).

Progress in Acoustic Emission VI

Concrete

Relation Between Acoustic Emission and Absorbed Energy of Reinforced Concrete and Fiber Reinforced Plastic
T. UOMOTO, T. YAJIMA and T. NISHIMURA

Relation Between Fracture Toughness and Widths of Fracture Process Zones in Mortar and Concrete Analyzed by Improved AE Source Location

S. NIISEKI, H. MIHASHI and N. NOMURA

AE Properties of Concrete with Corroded Reinforcement

Y. MURAKAMI, H. YAMASHITA and M. OHTSU

Rate Process Analysis of AE Activity in Core Test of Deteriorated Concrete

K. MATSUYAMA, A. ISHIBASHI and M. OHTSU

Fundamental Study of Acoustic Emission Generated in Corner Part of Reinforced Concrete Rigid Frame under Cyclic Loading

S. YUYAMA, R. TOMITA, T. OKAMOTO, S. KAJIO, M. OHTSU and M. SHIGEISHI

Metal

Evaluation of Stress-induced Martensitic Transformation Velocity in Cu-Al-Ni Shape Memory Alloy Single Crystals by Acoustic Emission Method

K. YOSHIDA, A. TAKAHASHI, K. SAKAMAKI and H. TAKAGI

The Effect of Precipitate Forming Elements in Al 4.5% Mg Alloys on the Measured Acoustic Emission and on Lüders Band Deformation

D. L. ARMENTROUT and S. H. CARPENTER

Study of the Fracture Mechanism of Hydrogen-Attacked Steel by Acoustic Emission Technique

J. TAKATSUBO and S. YAMAMOTO

Acoustic Emission from Crack Growth in 7050 Aluminum and 7075 Aluminum as a Function of Temperature and Heat Treatment

S. L. McBRIDE and Y. HONG

Analysis of Microfracture Mechanism in Al₂O₃ by Acoustic Emission

M. ENOKI and T. KISHI

Acoustic Emission Behavior during Heating/Cooling of Pd-Cu Alloys

M. YAMANAKA, K. ASAOKA, K. YOSHIDA and K. SAKAMAKI

Ceramics

Evaluation of Grade in the Grinding Wheel by Acoustic Emission

N. SHINKE and Y. ISHIDA

AE Studies on the Microfracture Process in Silicon Nitride

S. WAKAYAMA, M. IWATA and M. KAWAHARA

Nondestructive Evaluation of Ceramic Coating by Acoustic Emission and Ultrasonic Testing

M. SHIWA, H. MORI, T. KISHI, M. OHTSUKA, A. ITOH and Y. SUGITA

Composites 3

Fiber Break Characterization by Acoustic Emission in a Single SiC Fiber Aluminum Matrix Model Composite

N. CHAMBIOT-CLERC, P. FLEISCHMANN and R. FOUGERES

(continued to page 34)

Origin of Acoustic Emission in Naturally Aged Aluminum-Lithium Alloys

F. Zeides and I. Roman

Abstract

The present study identifies the origin of acoustic emission (AE) operating during plastic deformation of 2091 and Lockalite Al-Li alloys in the T3 heat treatment condition. AE intensity characterization techniques, i.e., AE rms voltage and peak amplitude distribution, were employed to compare the AE generated during tensile and compressive loading. It has been concluded that in both alloys in the naturally aged condition, AE results from plastic deformation for both uniform and jerky flow. The second potent source of AE, particles failure, is either non-operative or negligible.

1. Introduction

Aluminum-Lithium (Al-Li) alloys are under extensive investigation due to their lower density and higher elastic modulus in comparison with other aluminum base alloys used in advanced structural applications (Divecha and Karmarkar, 1986; Lavernia and Grant, 1987). However, Al-Li alloys are prone to the strain localization that impairs their deformation and fracture behavior. Better understanding of deformation and fracture mechanisms will assist in materializing of the high potential of Al-Li alloys.

It has been noted (Roman et al., 1987) that abundant acoustic emission (AE) was produced during tensile test of a Lockalite Al-Li alloy in both naturally and artificially aged heat treatment conditions. Thus, the use of AE can contribute to the characterization of Al-Li alloys, provided that AE origins are properly understood.

The present report gives an identification of AE sources during plastic deformation of Al-Li alloys and deals with alloys in the T3 heat treatment condition.

2. Experimental Procedures

Two Al-Li alloys were investigated in this study. One is a Lockheed developed alloy, Lockalite, received as a 25 mm thick plate, with a partially recrystallized pancake-grain structure elongated in the rolling direction. The other, a Pechiney 2091 Al-Li alloy, has been received in the form of a 2.5 mm thick sheet with equiaxed fully recrystallized grain structure. Chemical composition of both alloys is given in Table 1.

Tensile test employed samples in the as-received, T3, condition. Longitudinal flat tensile samples had a 6.25 x 32

Table 1 Chemical composition of principal alloying elements of the Al-Li alloys studied.

Alloy	Manufacturer	Element			
		Li	Cu	Mg	Zr
Lockalite	Lockheed	2.1	2.2	1.2	0.12
2091	Pechiney	2.0	2.4	1.7	0.10

mm gage section. Specimens machined from the 2091 alloy were of the sheet thickness. In the case of the Lockalite alloy specimens were of 2 or 5 mm thick and were taken in the rolling direction with the gage surface perpendicular to the rolling plane. Tensile tests were conducted utilizing a J.J. Lloyds machine. All samples were polished prior to testing. Compression tests were conducted in plane strain loading mode to identify AE source during plastic deformation. Acoustic emission characteristics were evaluated during mechanical testing utilizing a micro-computer based system (Model 5000, AET Corp.) comprised of 175 kHz resonant transducer (MAC175, AET), preamplifier (160, AET) with 125 to 250 kHz bandpass filter and a rms voltage processor (201, AET).

3. Results and Discussion

Significant acoustic emission was detected during tensile deformation both in the elastic and plastic regions as shown in Fig. 1. The upper portion of Fig. 1 contains a characteristic AE rms voltage vs. extension curve and shows that, initially, the AE is of a continuous nature with a maximum at the end of the elastic region, followed by a change to apparently burst-type AE activity in the plastic portion.

The peak in the rms voltage curve of the continuous AE happens shortly before general yielding. The apparently burst-type AE observed in the plastic region coincided with the Portevin-Le Chatelier serrations in the load-extension diagram. AE obtained in the tensile tests has been analyzed with a micro-computer based 5000 AET system. Cumulative distributions of AE events by peak amplitude for both continuous and apparently burst-type AE are shown in Fig. 2. The shapes of the two distributions corresponding to the two types of AE are very similar, and thus it has been concluded, that both types of AE had common AE origin. This is in accord with waveform observations using a transient recorder as well as the monitoring on an oscilloscope during testing.

Compression tests were employed in order to assist in the identification of AE sources active during the deformation of the two investigated alloys. The plane-strain mode of compression was employed. Details of the test procedure have been reported elsewhere (Zeides and Roman, 1989). Intense

Received 31 May 1991. The authors are affiliated with Graduate School of Applied Science & Technology, the Hebrew University of Jerusalem 91904, Israel.

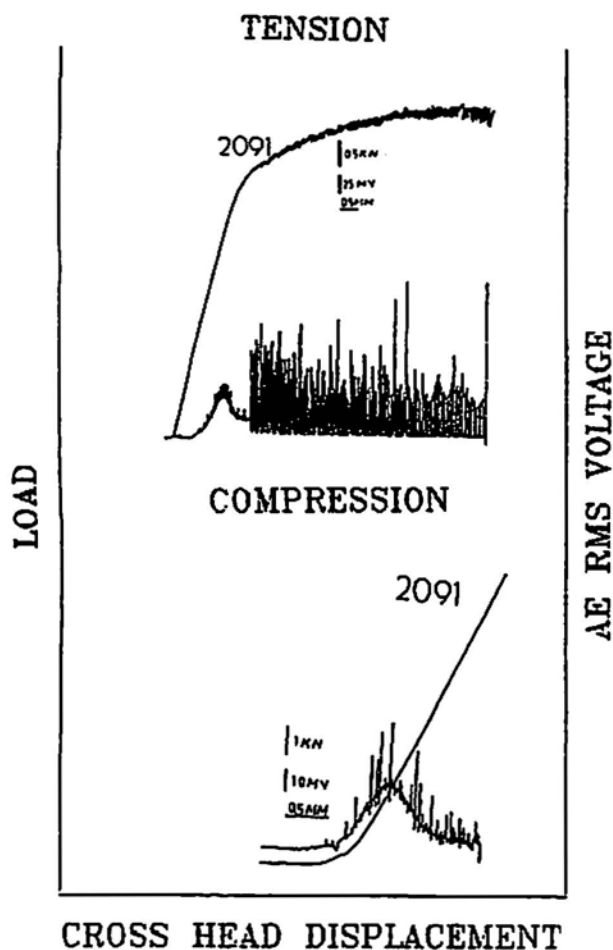


Fig. 1. Load and AE rms voltage vs. cross head displacement obtained in mechanical tests in 2091 alloy. The tensile test has been conducted at 10^{-4} sec $^{-1}$ initial strain rate.

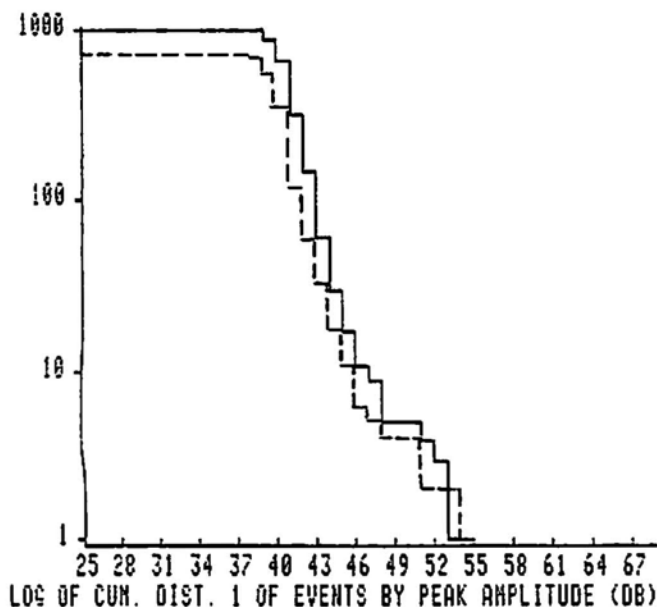


Fig. 2. Cumulative distribution of AE events by peak amplitude obtained during different stages of deformation. Dotted and solid lines relate to the continuous and apparently burst AE types correspondingly.

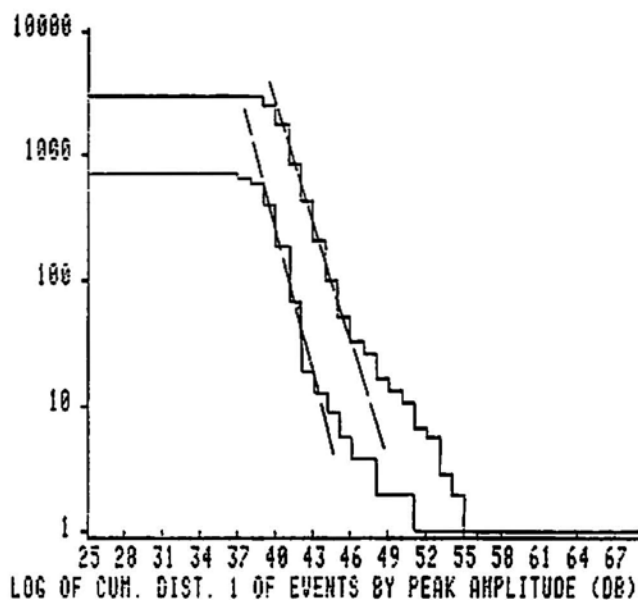


Fig. 3. Cumulative distributions of AE events by peak amplitude produced in tension and compression, the upper and lower charts correspondingly. The linear approximation is given by dotted lines.

acoustic emission was produced during compressive loading in both alloys. Load and AE rms voltage vs. cross head displacement charts are given in the lower portion of Fig. 1. Both continuous and apparently burst type AE were observed.

The shape of cumulative peak amplitude distribution of AE events produced in compression was similar to that of tension, as can be seen in Fig. 3. In both cases, the major portion of the cumulative distributions can be approximated by linear dependence with the similar slope. It follows, then, that the major AE source in plastic deformation of both alloys in T3 heat treatment condition stems from plastic deformation process and does not relate directly to the constituent particles failure.

As has been mentioned earlier, jerky plastic flow resulted in spikes of AE rms voltages. At the beginning of loading, one or two bands were produced on the surface of a sample while the load level remained constant. Striations nucleated at one of the specimen ends and propagated through the entire gage length, so that each new jump formed in front of the previous one. When the entire gage length was swept by the striations, a new Portevin-Le Chatelier band originated at that end propagated in the opposite direction. Details of AE accompanying Portevin-Le Chatelier flow will be published elsewhere. It has been found, that heat treatment affects AE in two ways. First, the peak height of continuous AE varies with an artificial aging going through a maximum. Second, constituent particles failure begins to contribute to the AE and finally becomes the predominant AE source.

4. Summary

Acoustic emission accompanying deformation process in the two Al-Li alloys in T3 heat treatment condition originates from plastic deformation during both uniform and jerky flow.

The second potent source of AE in common Al-base alloys, constituent particles failure, is either nonoperative or negligible.

Acknowledgement

The authors wish to acknowledge useful discussion with Professor K. Ono of University of California, Los Angeles, who also provided the Lockalite plate used in this study.

References

A.P. Divecha and S.D. Karmarkar (1986), *Advanced Materials & Process*, 130(4), October, 74-79.

E.J. Lavernia and N.J. Grant (1987), *J. Material Science*, 22, 1521-1529.

I. Roman, K. Ono and C.H. Johnson (1987), *J. Acoustic Emission*, 4(2/3), 111-115.

F. Zeides and I. Roman (1989), *J. Acoustic Emission*, 8(3), 47-49.

Progress in Acoustic Emission VI

Acoustic Emission Characterization of Failure Behavior of SiC Fiber/Al Composite
Z. G. JIN, X. H. PAN, C. ZHU and G. G. SONG

Acoustic Emission Behavior during Tensile Fracture of Resin-Impregnated Strands of Pitch-Based Carbon Fiber
A. NANJYO, M. MOHRI and K. ONO

Adhesion of Titanium Coated Films on Various Substrates Measured by the Scratch Tester with an Acoustic Emission Sensor
I. TAKANO, S. ISOBE, K. MATSUI, T. TAIRA and N. INOUE

Quantitative Evaluation of Bending Strength and Fracture Dynamics of Laser Fusion Produced Titanium Aluminide Coatings by AE Wave Characterization
M. TAKEMOTO and M. SHINYA

11th International AE Symposium

The 11th IAES, sponsored by the JSNDI, was held on Oct. 26 - 29, 1992 at Sun Palace Convention Center in Fukuoka, Japan. The Symposium attracted about 150 participants from 10 countries. Paper and Program Committee Chair was Prof. K. Takahashi (Kyushu Univ.) and the Organizing Committee was chaired by Prof. T. Kishi (Tokyo Univ.) while the Secretarial Committee by Prof. M. Ohtsu (Kumamoto Univ.).



During the Symposium, Prof. K. Yamaguchi, who retired from Tokyo Univ. in April 1992, received Achievement Awards from AEWG and CARP, which were conveyed by Prof. S. Carpenter and Dr. T. Fowler, respectively.

Progress in Acoustic Emission VI

Proceedings of the Eleventh International Acoustic Emission Symposium,
eds. T. Kishi, K. Takahashi and M. Ohtsu, Oct. 25-29, 1992, Fukuoka,
Japan. Publ. by JSNDI, Tokyo; xx, 604 pages.

Cost: \$150 plus shipping of
\$8 in the US and \$10 elsewhere

Send prepaid order to Acoustic Emission Group
308 Westwood Blvd, Box 364
Los Angeles, CA 90024-1647 USA
FAX 1-818-368-8309

Analysis of Artificial Acoustic Emission Waveforms Using a Neural Network

Hironobu Yuki and Kyoji Homma

Abstract

This paper deals with a method of Acoustic Emission (AE) source analysis using a neural network. Artificial AE source signals caused by pencil lead breaks were used to confirm the validity of the method. Detected waveform data were processed by the two-layer network that constituted as a software on the personal computer system. The memory of the network, corresponding to the input/output relation of the system, was formed by learning. Even though there were noises in detected waveforms, low noise source waveforms could be obtained by the network. In case of a small number of learning patterns, however, incorrect source waveforms were obtained by the network. It was demonstrated that when additional restrictions were imposed on the memory, appropriate waveforms could be obtained using the memory learned with a few pattern. Another type of network that could estimate response functions of the system from the information of the source location was also investigated.

1. Introduction

Acoustic emission (AE) source analysis is the only known method available to represent qualitatively the fracture behavior at the location of the fracture source. This is done by measuring the elastic waves emitted by the energy release due to the crack propagation of the materials (Hsu et al., 1977, 1978; Enoki and Kishi, 1988; Ohira and Pao, 1989; Homma and Ishikawa, 1989; Kim and Sachse, 1989). The analysis belongs to inverse problems (Kubo, 1988), which estimate the input information from the output, because the waveform at the AE source can be obtained from the detected waveform removing effects of the characteristics of propagation media and AE sensors.

By assuming the linear system, when either the source waveform or the response function is known and the detected waveform is provided, the other can be obtained by means of a deconvolution integral. Diverging solutions, however, could frequently result from the numerical calculations except for approximate solution (Homma and Ishikawa, 1989), e.g. least square method (Robinson and Silvia, 1978). Appropriate calculation techniques must be developed.

Recently, information processing using the neural network has been applied to problems that are difficult to solve by analytical and/or numerical treatments (Nakano, ed., 1990). In

the field of nondestructive evaluation of materials, an identification of AE source using an associative memory (Grabec and Sachse, 1989), an eddy current defect characterization using a perceptron (Udpa and Udpa, 1990), and others, have been investigated. The neural network is effective in problems where equations of the input/output relation are difficult to obtain and provides learning capability to suggest the unknown input/output relation.

This study applied the neural network to the AE source analysis by utilizing its learning capability, and investigated the validity of the method by means of an artificial AE source and the two-layer network.

2. Formulation

2.1 Input/output Relations of AE System

The detected waveform $u(t)$ as a time function can be expressed by the equation of a convolution integral using the source waveform $s(t)$ and the response function $r(t)$ under the assumption of the linear system (Hsu et al., 1977, 1978).

$$u(t) = \int_0^t r(t-\tau) \cdot s(\tau) d\tau \quad (1)$$

Hence, the source waveform $s(t)$ can be obtained by a deconvolution integral:

$$s(t) = \int_0^t h(t-\tau) \cdot u(\tau) d\tau \quad (2)$$

where, $h(t)$ is the inverse function of $r(t)$. Equation (2) could be rewritten as a discrete formula:

$$s_i = \sum_{j=0}^i h_{i-j} u_j \quad (3)$$

or in matrix form,

$$\begin{bmatrix} s_0 \\ s_1 \\ \vdots \\ s_{n-1} \end{bmatrix} = \begin{bmatrix} h_0 & 0 & 0 & 0 \\ h_1 & h_0 & 0 & 0 \\ \vdots & \vdots & \ddots & \vdots \\ h_{n-1} & h_{n-2} & \cdots & h_0 \end{bmatrix} \begin{bmatrix} u_0 \\ u_1 \\ \vdots \\ u_{n-1} \end{bmatrix} \quad (3a)$$

2.2 Neural Network

Neural networks are composed of a circuit of model neurons with idealized characteristics of multi-input vs. single output elements as shown in Fig. 1. The relation between input and output signals can be expressed as follows:

$$y = f\left(\sum_{i=1}^n w_i x_i - \theta\right) \quad (4)$$

Received 15 June 1991; in revised form, 17 December 1991. The authors are affiliated with the Department of Mechanical and Control Engineering, the University of Electro-Communications, Chofu, Tokyo, 182, Japan.

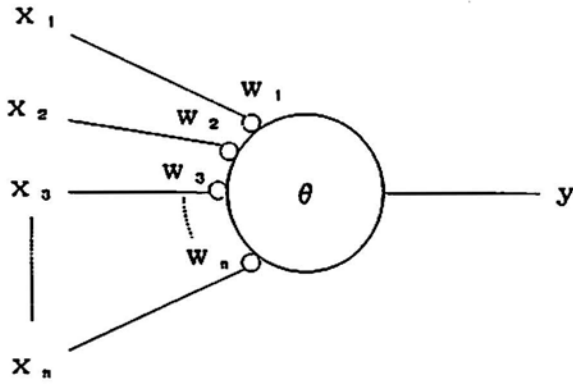


Fig. 1 Schematic of a model neuron.

where, w_i is a weighting function called a synaptic weight which expresses the bonding strength between neurons, and θ is a threshold level (Nakano, ed., 1990). The memory of the network is replaced by each synaptic weight. A perceptron is defined as the network of stratum composition of model neurons, and learning is carried out to vary synaptic weights in terms of teaching signals from the externals.

In this study, we use the two-layer network whose output signal $\{y\}$ is expressed as follows:

$$y_i = \sum_{j=0}^{n-1} w_{ij} x_j \quad (5)$$

where $\{x\}$ is the input signal and $\{w\}$ is the memory of the network. In AE source analysis, $\{x\}$, $\{y\}$ and $\{w\}$ correspond to the detected waveform $\{u\}$, the source waveform $\{s\}$ and the inverse matrix of the response function matrix $\{h\}$, respectively, so that the following equation can be deduced:

$$s_i = \sum_{j=0}^{n-1} h_{ij} u_j \quad (6)$$

or

$$\begin{bmatrix} s_0 \\ s_1 \\ \vdots \\ s_{n-1} \end{bmatrix} = \begin{bmatrix} h_{00} & h_{01} & \cdots & h_{0n-1} \\ h_{10} & h_{11} & \cdots & h_{1n-1} \\ \vdots & \vdots & \ddots & \vdots \\ h_{n-1,0} & h_{n-1,1} & \cdots & h_{n-1,n-1} \end{bmatrix} \cdot \begin{bmatrix} u_0 \\ u_1 \\ \vdots \\ u_{n-1} \end{bmatrix} \quad (6a)$$

Each weight was changed by the gradient descent method:

$$\Delta h_{ij} = -\epsilon \partial E / \partial h_{ij} \quad (\epsilon > 0) \quad (7)$$

by defining the error function E as

$$E = \frac{1}{2} \sum_{k=0}^{n-1} (s_k - \tilde{s}_k)^2 \quad (8)$$

where $\{s\}$ is the source waveform derived from equation (6), $\{\tilde{s}\}$ is the teaching source waveform corresponding to $\{u\}$, and ϵ is a coefficient of learning.

3. Calculations of Waveform

3.1 Learning Waveform

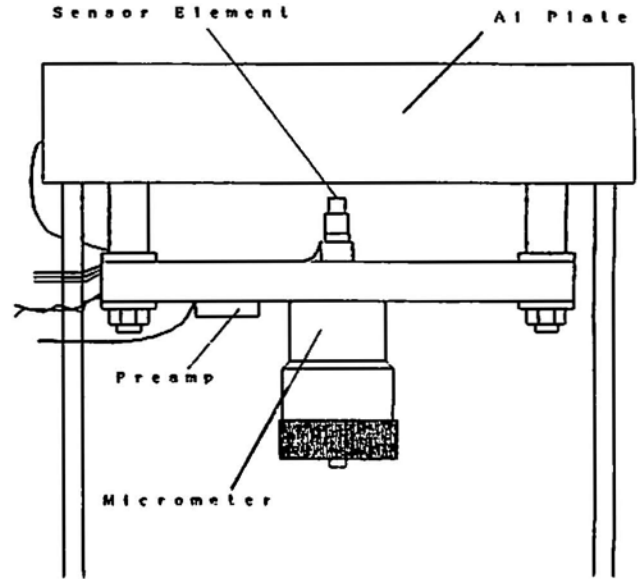


Fig. 2 Experimental apparatus.

The neural network was trained using the waveforms obtained by the experiment using an artificial AE source. The experimental apparatus is shown in Fig. 2. A mechanical pencil lead (0.5 mm dia., 2H) was broken on an aluminum alloy plate (502 x 403 x 60 mm), and epicentral displacements in the opposite side were measured by a capacitive displacement transducer (Ohisa and Kishi, 1981). A set of waveform data including various amplitudes and shapes were obtained by breaking pencil leads with different length. The waveform data contains 13 waveforms and were recorded by 50 ns sampling rates, and 80 points (4 μ s) were used for the analysis. Using an averaging technique, noise in the detected waveforms was reduced. Assuming that the plate can be regarded as infinite in association with the wave propagation, 13 teaching source waveforms were calculated from each of the 13 recorded waveforms by using the analytical solution (Knopoff, 1958).

3.2 Full Connection Network

A full connection network as shown in Fig. 3 was first investigated. The network of this type uses all points data of the detected waveform to determine one point value of the source waveform, and the learning equation is derived from equations (6-8) by considering the inertia term:

$$\Delta h_{ij}(t) = -\frac{\epsilon}{\sum_{k=0}^{n-1} u_k^2} (s_i - \tilde{s}_i) u_j + \alpha \Delta h_{ij}(t-1) \quad (\epsilon > 0, 0 < \alpha < 1) \quad (9)$$

where α and ϵ are coefficients of learning and t indicates the learning times. These were chosen as appropriate accounting for learning patterns.

For learning of the network, we randomly selected a pair of input and teaching waveforms, and presented them to the network. This learning procedure was repeated 500 times. Figure 4 shows the shape of the memory formed after the 500 iteration of this procedure. An 80 x 80 memory matrix is formed. Each of

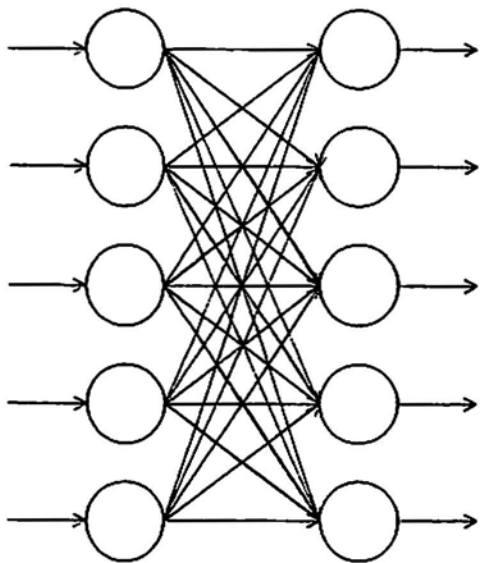


Fig. 3 Schematic of a full connection network.

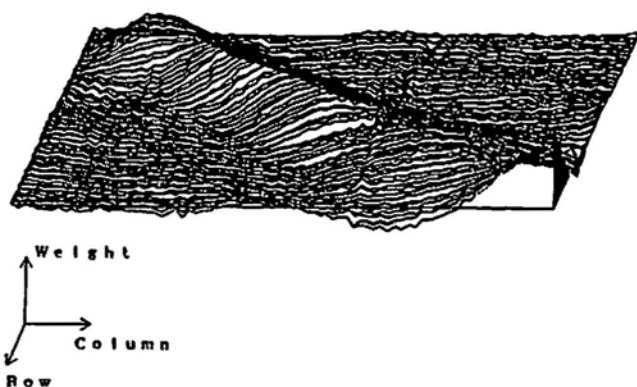
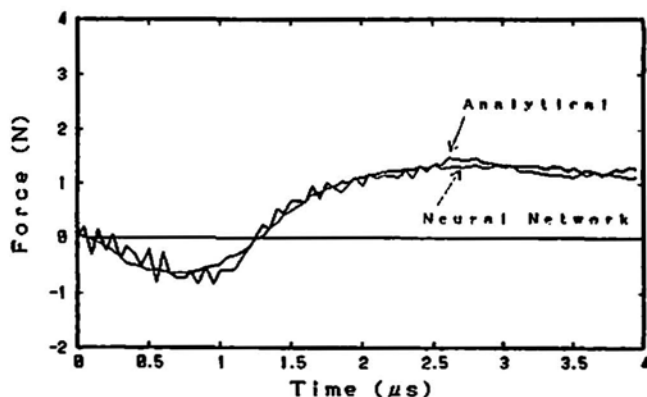


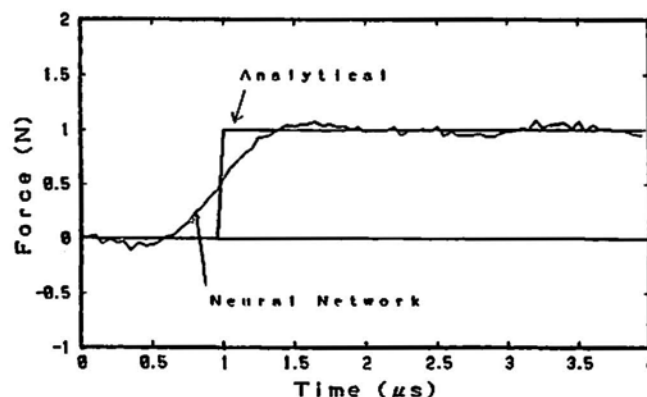
Fig. 4 The shape of the memory formed after the 500 iteration with 13-pattern waveforms.

the plane axes in Fig. 4 corresponds to the row and column of the memory matrix, and the height corresponds to the value of the matrix element. It can be observed in this figure that values on the upper right side of the memory matrix reduce to zero, and that values of the elements along the diagonal line are constant. Equation (3a) implies that to determine one-point value of the source waveform in arbitrary time only need the previous time data of the detected waveform, and that the elements along the diagonal line have identical values. In other words, to determine the source waveform, the matrix $[h]$ in equation (6a) can be written as a triangular matrix. The shape of memory matrix shown in Fig. 4 is consistent with this characteristics. It implies that learning of the convolution integral would be successful.

Using the memory matrix shown in Fig. 4, source waveforms can be obtained by feeding recorded waveforms into the network. Results are shown in Fig. 5. Figure 5(a) shows the source waveform which was calculated from the recorded wave-



(a)



(b)

Fig. 5 Source waveform obtained by memory formed with 13-pattern waveforms. (a) artificial waveforms. (b) simulated waveform with step function.

form due to pencil-lead break without the averaging technique for noise reduction. This figure shows that the source waveform obtained by using the network coincides with the analytical form. Further, the noise in the source waveform can be reduced without eliminating noise in recorded waveforms. Figure 5(b) shows the source waveform calculated from the simulated waveform at the epicenter when the ideal step function with the amplitude of 1 N was provided. Discrepancy in step rising between the ideal step function waveform and the waveform obtained by the network would be revealed in Fig. 5(b), which should attribute the rising time of the waveform used for learning. Improvements of this aspect may be expected when higher gradient waveforms by other artificial AE source could be used for learning.

The number of recorded waveforms was altered to know how many learning patterns might be required. When we used 6 recorded waveforms (6-pattern) for learning, the memory shape coincides with the 13-pattern case, and an appropriate source waveform was also obtained. However, in case of only one pattern for learning, the memory shape disagrees with the 13-pattern case, and the source waveform was not appropriate (see Figs. 6 and 7). Therefore, in case of full connection network, multiple waveforms for learning are needed to obtain appropriate source waveforms. This is also obvious from the memory

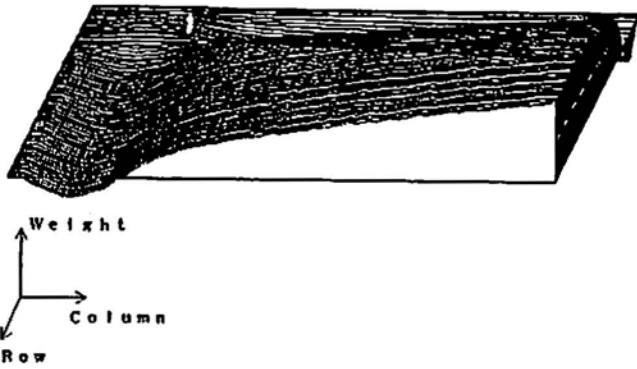
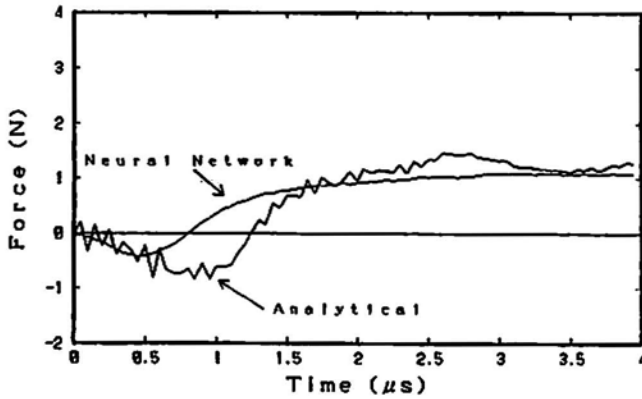
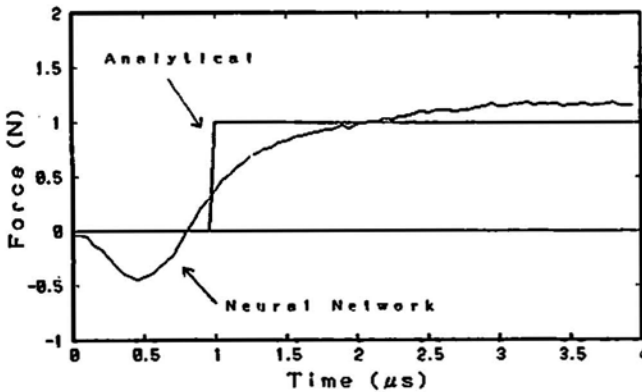


Fig. 6 Shape of the memory learned with 1-pattern waveform.



(a)



(b)

Fig. 7 Source waveforms obtained by the memory learned with 1-pattern waveform. (a) artificial waveforms. (b) simulated waveform with step function.

shape formed by 1-pattern learning shown in Fig. 6, without having the characteristics mentioned above.

3.3 Convolution Network

Next, we investigated convolution form network as shown in Fig. 8. By combining equations 3, 7 and 8, the learning equation is obtained as follows:

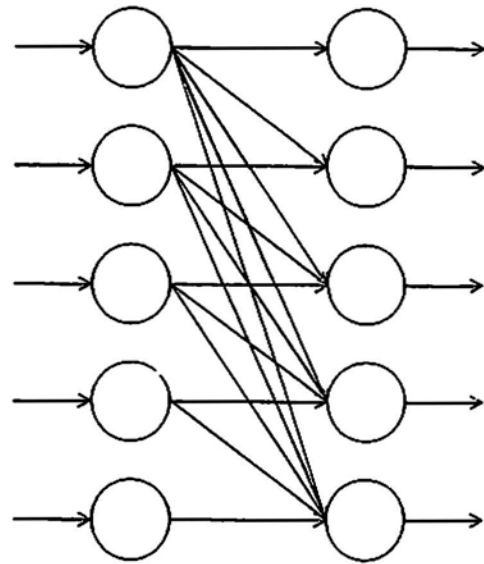
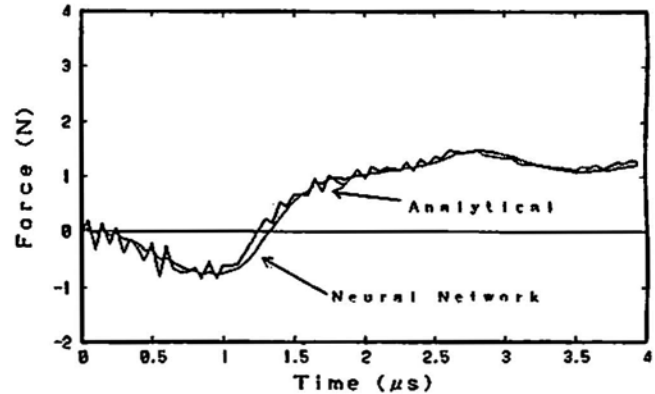
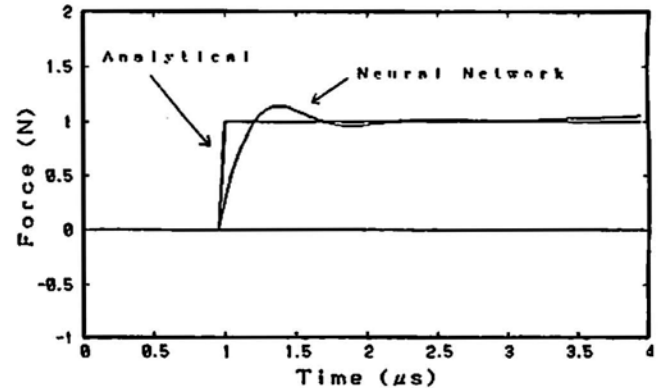


Fig. 8 Schematic of a convolution form network.



(a)



(b)

Fig. 9 Source waveforms obtained by the memory learned with 1-pattern memory in convolution form. (a) artificial waveforms. (b) simulated waveform with step function.

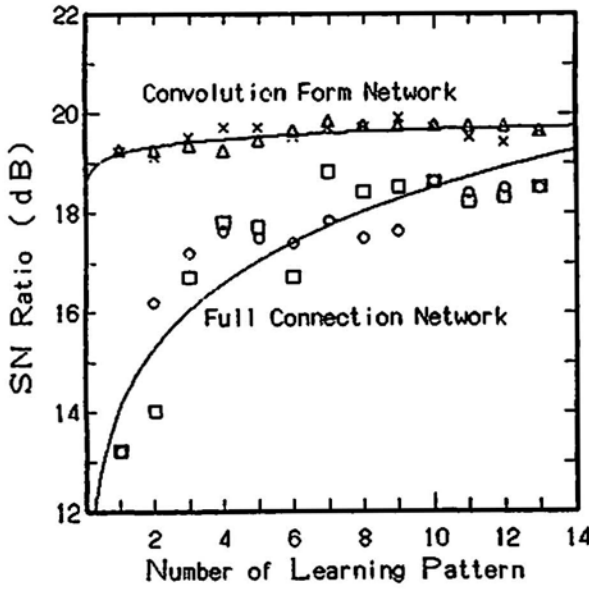


Fig. 10 Relation between the number of learning pattern and the signal to noise (S/N) ratio.

$$\Delta h_i(t) = -\frac{\varepsilon}{\sum_{k=0}^{n-1} u_k^2} \sum_{j=0}^{n-i-1} (s_{i+j} - \tilde{s}_{i+j}) u_j + \alpha \Delta h_i(t-1) \quad (\varepsilon > 0, 0 < \alpha < 1) \quad (10)$$

Using the same waveforms as in Sec. 3.2, 500 iteration learnings were conducted. In the case of 13- and 6-patterns, appropriate source waveforms could be obtained. We tried whether 1-pattern would be available. Figure 9 shows the source waveform obtained by using 1-pattern learning memory matrix. These results show that appropriate source waveforms can be obtained irrespective of the number of patterns needed for learning. It is expected that each weight was learned repeatedly in the same waveform in terms of the restriction of the matrix mentioned above. This restriction is of great advantage in the calculation to save the memory capacity of the matrix, from $n \times n$ to n . Disagreements at the step rising still remained to resolve.

3.4 Effects of Parameters on Network Calculations

Figure 10 shows the relation between the number of learning pattern and the signal to noise (S/N) ratio defined as the reciprocal value of the variance of the error of the source waveform. It is demonstrated in this figure that in case of the full connection network, the S/N ratio is improved as the number of learning pattern is increased. In case of convolution form network, however, the S/N ratio hardly changes. Therefore, it is found that the output of the network is independent of the number of learning pattern in the convolution form network, while the full connection network depends on the number of learning pattern.

Effects of frequency component of the source waveform were also investigated. We supplied a $4 \mu\text{s}$ long wave train comprised of 80 points at 50 ns interval. The wave is of a sine function of various frequencies. Results demonstrate, regardless

of network types that satisfactory waveforms can be obtained in frequencies below several hundreds kHz, but at high frequencies above 1 MHz, source waveforms cannot be recovered. This is due to the same reason as the discrepancy in the rising phase of the step input waveform. Hence, it is necessary to improve the frequency response in high frequency range.

4. Estimation of Response Function

4.1 Calculation of Response Function by Using a Network

A deconvolution integral is the procedure to determine $p(t)$ by providing $f(t)$ and $g(t)$ in the following equation:

$$g(t) = \int_0^t p(t-\tau)f(\tau) d\tau = p(t) * f(t) \quad (11)$$

Therefore, the formation of a network memory is equivalent to the deconvolution integral. Representing the memory and the response function by an $n \times n$ matrix and a vector, respectively, the response functions could be obtained by providing the delta function data into the network. For the discrete formula, the following function is used.

$$f_i = \begin{cases} 1 & (i=0) \\ 0 & (i>0) \end{cases} \quad (12)$$

By taking the source waveform as the input and the displacement waveform as the teaching, the memory matrix could be formed. This corresponds to the response function of *force-to-displacement*. On the other hand, when one takes the inverse relationship between the displacement and the source, the response function of *displacement-to-force* could be obtained. In order to obtain the source waveform, the latter only requires the convolution integral, while the former needs the deconvolution integral. This deconvolution integral is liable to diverge. The neural network, however, allows the calculation of the deconvolution integral, once the memory matrix is obtained.

4.2 Estimation of Response Function

To learn the network considered above, the source location has to be specified. In the case of AE associated with fracture, learning of the network is not possible after AE has been measured, since the geometry of the propagation media has already been changed. The source location, however, cannot be specified precisely before fracture. Therefore, network constitutions are discussed to estimate the response function from the information of the source location.

For learning of the network, pencil leads were broken at 8 points with an interval of 0.2H (0.0H, 0.2H, ..., 1.4H; H is the thickness of the plate) on the opposite side of the plate where the sensor was attached. Then, response functions of *displacement-to-force* were obtained by the deconvolution integral using the network as mentioned above. These response functions were used as teaching signals. Input signals were encoded to be the source location vector.

Figure 11 shows shapes of memory matrices that are used to estimate the response function by providing the source loca-

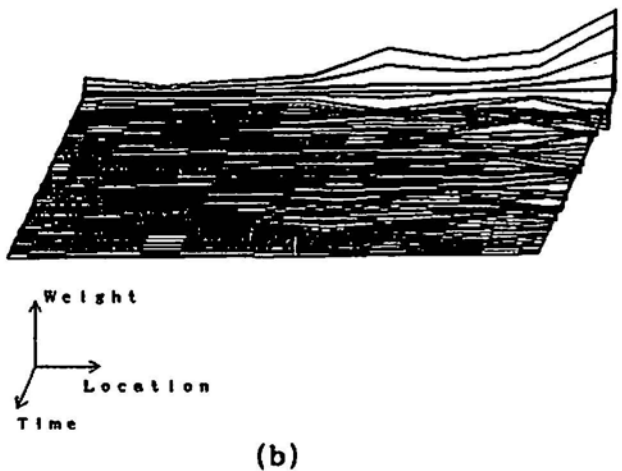
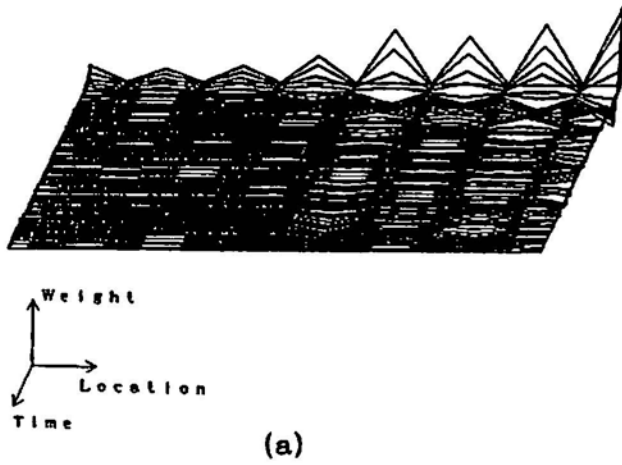


Fig. 11 Shapes of memory matrices that estimate the response function. (a) without weight, (b) with the weight of $\pm 0.1H$.

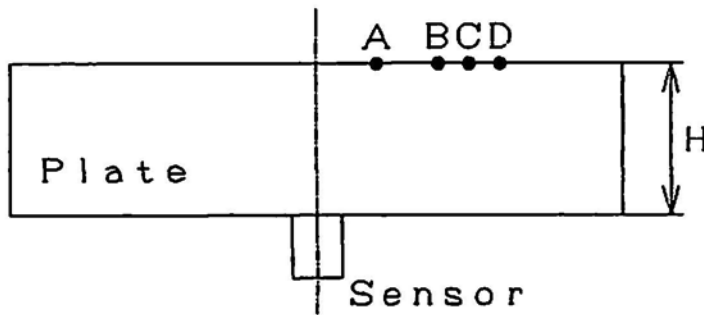


Fig. 12 Relative locations between the AE source and the sensor. (Response functions at points A and D are known, and those at points B and C are unknown and to be estimated.)

tion data to the network. In the figures, the column and the row indicate the source location and the time of the response function, respectively. These memory matrices are formed by using known source locations and response functions. When input signals are encoded to learn, the weight represented by the non-zero width in the vector has to be considered. Figure 11(a)

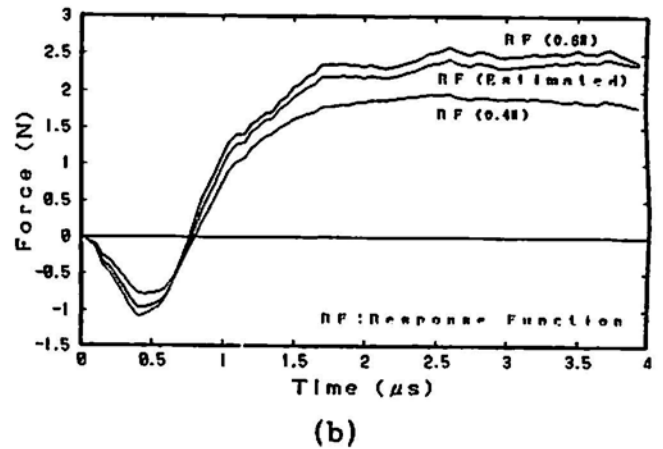
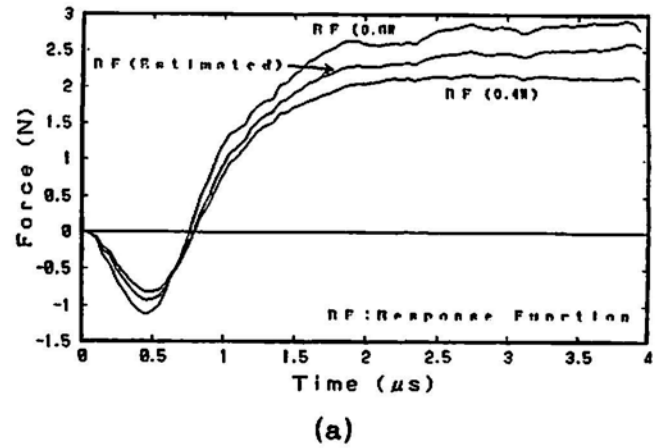


Fig. 13 Source waveforms obtained by using estimated response functions; (a) at the location of $0.5H$. (b) at the location of $0.55H$.

shows the shape of the memory matrix formed by learning without weight, and Fig. 11(b) is the case with the weight of $\pm 0.1H$. Figure 11 demonstrates that in case of no weight, no suitable response function could be estimated, because the values at the location without learning have not been changed. On the other hand, larger non-zero width makes ill-convergence, so that the appropriate width must be considered.

After the learning procedure, response functions can be obtained by providing source location data to the network. Then, source waveforms can be obtained by the convolution integral, using above response functions. Figure 12 shows locations where response functions are known (points A and D), and unknown (points B and C). Each point A, B, C and D is $0.4H$, $0.5H$, $0.55H$ and $0.6H$ distances from the opposite side where the sensor was attached. We determined source waveforms on intermediate points B and C. Figure 13(a) demonstrates that the source waveform in terms of the estimated response function lies between the waveforms by the known response function. Figure 13(b) shows the source waveforms at the location of $0.55H$ with encoding step of $0.05H$. In the latter figure, the waveform in terms of the estimated function lies in the range between $0.4H$ and $0.6H$, and that it is close to $0.6H$ line rather than intermediate. These results suggest that the

method of the network is useful for the estimation of the response function.

5. Conclusions

Analyses of AE source waveform using the neural network were carried out and following conclusions were obtained;

(1) Low noise source waveforms were obtained by using the neural network from detected waveforms.

(2) In case of small number of learning patterns, it is efficient to obtain appropriate source waveforms imposing additional restrictions on the memory matrix.

(3) By applying learning capability of the network, a deconvolution integral could be carried out without tendency of divergence.

(4) Providing AE source locations to the input, response functions could be obtained as the output of the network.

References

- M. Enoki and T. Kishi (1988), "Theory and analysis of deformation moment tensor due to microcracking", *Int. J. Fract.*, **38**, 295-310.
- I. Grabec and W. Sachse (1989), "Application of an intelligent signal processing system to acoustic emission analysis", *J. Acoust. Soc. Am.*, **85**(3), 1226-1235.
- K. Homma and H. Ishikawa (1989), "AE Source Analysis of fracture in Ceramics" (in Japanese), *Trans. Jpn. Soc. Mech. Eng.*, **55**(515), A, 1607-1612.
- N.N. Hsu, J.A. Simmons and S.C. Hardy (1977), "An Approach to Acoustic Emission Signal Analysis - Theory and Experiment", *Mat. Eval.*, **35**, 100-106.
- N.N. Hsu and S.C. Hardy (1978), "Experiments in Acoustic Emission Waveform Analysis for Characterization of AE Sources, Sensors and Structures", *Elastic Waves and Non-Destructive Testing of Materials*, AMD-Vol. 29, ed. Y.H. Pao, ASME, New York, pp. 85-106.
- K.Y. Kim and W. Sachse (1989), "Study of brittle fracture by acoustic emission from indentation cracks", *J. Appl. Phys.*, **65**(11), 4234-4244.
- L. Knopoff (1958), "Surface Motions of a Thick Plate", *J. Appl. Phys.*, **29**(4), 661-670.
- S. Kubo (1988), "Inverse Problems Related to the Mechanics and Fracture of Solids and Structures", *JSME Int. J., Ser. I*, **31**(2), 157-166.
- K. Nakano, ed. (1990), *An Introduction to Neurocomputing* (in Japanese), Corona Publishing, Tokyo.
- T. Ohira and Y-H. Pao (1989), "Quantitative Characterization of Microcracking in A533B Steel by Acoustic Emission", *Metall. Trans.*, **20A**, 1105-1114.
- N. Ohisa and T. Kishi (1981), "Characterization of Piezoelectric Transducers by Using a Capacitive Transducer for Acoustic Emission Source Wave Analysis" (in Japanese), 1981 National Conference on Acoustic Emission, JSNDI, Tokyo, pp. 57-62.
- E.A. Robinson and M.T. Silvia (1978), *Digital Signal Processing and Time Series Analysis*, Holden-Day Inc., San Francisco.
- L. Udpa and S.S. Udpa (1990), "Eddy Current Defect Characterization Using Neural Networks", *Mat. Eval.*, **48**, 342-347.

Papers to be presented at the 36th Meeting of Acoustic Emission Working Group, March 17-19, 1993, Denver, CO

C.M. Fortunko, M.A. Hamstad and D.W. Fitting

Sensitivity Considerations for Wide-Band Acoustic Emission Sensor/Preamplifier Subsystems

A computer model has been used to evaluate the suitability of five piezoelectric materials for use in broadband (10 kHz-2 MHz) acoustic emission (AE) "point" sensors. The computer model accounts for the effects of the electrical loading of the piezoelectric material by the input impedance of the preamplifier and the mechanical loading by the specimen and backing materials. The model predictions are compared with results of measurements, which are normalized using the NIST Standard Reference Material (SRM) "conical" transducer. The effects of selecting different piezoelectric materials (PZT-5A, lead metaniobate, X-cut LiNbO₃, and PVDF) and transducer configurations ("pinducer" vs. "conical") are evaluated experimentally and analytically. It is shown that materials exhibiting the highest dielectric constant, ϵ_{33}^s , are best suited for high-performance AE sensor applications. In addition, it is concluded that field-effect transistors exhibiting very small noise currents, less than 1.9 fA/ $\sqrt{\text{Hz}}$, are required to maximize the low-frequency signal-to-noise performance of PZT-5A sensors.

Marcel F. Leach

Method for Controlling Frequencies from Booming Sand

Acoustic emissions from booming sand, when shaken by hand in the laboratory, are characterized by a rhythmic thrum of a few hundred Hz like the rubbing of fingers on a washboard, producing noticeable vibrations in the hand. Typical signals of these emissions display very distinct intense beat-like patterns with great regularity. This is consistent with observations of the enigmatic phenomenon of booming in the field and agrees with the effects of some of the factors, such as grain shape, degree of sorting and coherent motion which are agents considered responsible for the behavior of booming sand. Measurements of beat and carrier periods of the beat patterns recorded in the laboratory seem to agree with observations and results obtained in the field on AE from booming sands. The present study provides further insight into the peculiar phenomenon of booming sand and may also help to shed more light on other odd phenomena such as the observation of very intense moonquakes recorded by lunar probes, as suggested by some space scientists.

H. Kwun, J.J. Hanley and C.M. Teller

Performance Comparison of a Noncontact Magnetostrictive AE Sensor with a Conventional Piezoelectric Sensor on a Steel Rod

A noncontact sensor for detecting acoustic emission (AE) signals in ferrous materials is described. The sensor is based on the inverse magnetostrictive or Villari effect; that is, it senses changes in magnetic induction caused by stress waves associated with AE signals. The frequency response characteristics and sensitivity of the sensor were measured experimentally using 0.5-mm pencil lead break on a 3.6-m-long, 6.4-mm-diameter cold-rolled steel rod and were compared with those of a conventional piezoelectric AE sensor. The advantages and potential applications of this magnetostrictive AE sensor are discussed.

K. Yoshida, H. Takagi and K. Sakamaki

Evaluation of Stress-Induced Martensitic Transformation Velocity in Cu-Al-Ni Shape Memory Alloy Single Crystals by Acoustic Emission Method

In order to clarify the dynamic behavior of the phase transformation, the acoustic emission behavior during stress-induced martensitic transformation in Cu-Al-Ni shape memory alloy single crystals has been determined in the previous report (10th IAES). It was revealed that there was the asymmetry of the acoustic emission activity in the process of loading and unloading because of the stored strain energy due to the forward and backward phase transformations, and the five types of acoustic emission waveforms were observed. In this study, the martensitic transformation velocity was evaluated using the acoustic emission waveform analysis by Takashima and co-workers.

(Continued to page 66)

Source Force Waveforms: The Use of a Calibrated Transducer in Obtaining an Accurate Waveform of a Source

Thomas M. Proctor, Jr. and Franklin R. Breckenridge

Abstract

Experiments in which a point source and a receiver are placed opposite each other on an elastic plate of known Green's function have been applied to the absolute calibration of both sources and receivers. With this technique, a transducer was calibrated using a glass-break source, and then this transducer was used to measure dynamic force waveforms from elastic sphere collisions with the plate. Calculations, from Hertz's theory, of predicted force waveforms agree closely with the measured waveforms.

1. Introduction

One of the major goals of acoustic emission work is to be able to determine the force waveforms from acoustic emission events, but presently we fall far short of being able to do this in general. In the typical experiment, emission events taking place in a solid elastic medium produce voltage waveforms at the terminals of a transducer placed on the surface of the medium. In most cases there is no known way to derive the source waveform from the transducer data. However, it has been demonstrated that, for elastic bodies of certain particular geometries, force waveforms of source events initiated on the surface of the medium can be recovered from the output voltage data from a transducer placed at some location on the medium remote from the source. (Hsu and Hardy, 1978; Hsu and Eitzen, 1979; Hsu and Eitzen, 1982; Hsu and Eitzen, submitted 1988) In the work described in this paper, we have carried out the force waveform recovery with somewhat more accuracy than in previous work, have placed bounds on the accuracy of the work, and have demonstrated, using principles of mechanics and elasticity theory, that the results fall within the claimed accuracy bounds. The accuracy of the present technique depends on an in situ calibration of the receiving transducer. Our results indirectly corroborate the displacement measurements implicit in the National Institute of Standards & Technology (NIST) primary transducer calibration procedure (Breckenridge, 1982) and agree with other recent dynamic force measurements (Breckenridge et al., 1990). We have shown that dynamic force waveforms can be determined in detail.

2. Experimental Arrangement

The apparatus (Fig. 1) consists of a horizontal circular plate of optical glass having diameter 420 mm and thickness 89 mm with a device for dropping balls onto the upper surface and an NBS conical transducer mounted on the lower surface

opposite the ball impact location. The transducer is connected to a 10-bit, 20 megasample/s recorder via a unity gain buffer amplifier mounted close to the transducer. For calibration of the transducer, the ball-dropping apparatus is replaced by a capillary-loading-screw device similar to that used in the NIST primary transducer calibration system (Breckenridge, 1982). In addition, a camera, light source, and rotating mirror allow for measurements of ball rebound heights.

Optical glass was chosen as the material for the transfer plate because, in the experience of the authors, it is the most homogeneous readily available material. Sound-speed measurements in aluminum, fused quartz, and other materials have shown large variation with location within the sample (Proctor, 1971). Longitudinal and shear sound speeds, density, and plate thickness were measured in the glass disk and, from these measurements, the shear modulus was calculated, and the Green's function was obtained (Hsu, 1985).

The source events used for the experiment were the collisions of small ball bearings dropped upon the upper surface of the plate from a height of 30 mm (bottom of ball to plate surface). Balls of ten different sizes, ranging from 1.59 mm (1/16 inch) to 9.53 mm (3/8 inch) were used. A special vacuum device was used for holding the balls and releasing them from the specified height with zero initial velocity.

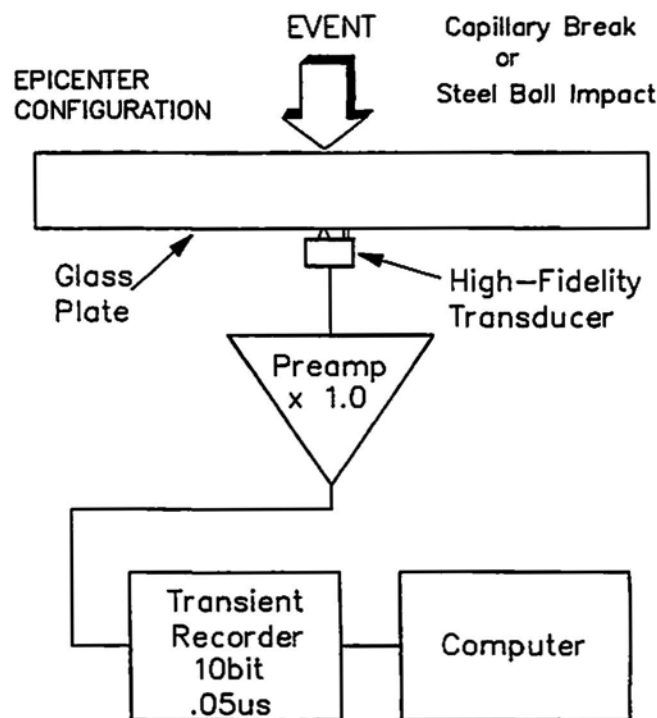


Fig. 1 Experimental setup.

Received 24 June 1991. The authors are affiliated with Automated Production Technology Division, National Institute of Standards and Technology, Gaithersburg, MD 20899.

The NBS conical transducer (Proctor, 1982, 1986), used as the receiver, was held upward against the bottom of the plate by a spring which had been adjusted to apply, at the conical transducer tip, a contact force equal to the normal gravity load. A strip of 12 μm thick aluminum foil coupled to the glass plate formed the ground electrode for the transducer.

3. Theory of the Experiment

The physical experiment can be represented:

$$F * G * T = V, \quad (1)$$

where F is the dynamic force of the source, G is the transfer function (Green's function) of the plate, T is the impulse response of the receiving transducer, V is the voltage output of the receiving transducer, and "*" denotes convolution, and all of the variables are functions of time. If G and T can be found and inverted with respect to convolution, then

$$F = V * G^{-1} * T^{-1}. \quad (2)$$

The possibility of recovering F depends on two conditions:

- (1) G must be known, either from theory (Pao et al., 1979; Hsu, 1985) or from experiment, and it must be capable of being inverted with respect to convolution;
- (2) T must be measurable, and must be capable of being inverted.

The problem of inverting either G or T is not solvable in general (Carasso and Hsu, 1985). As a practical matter, however, the invertibility of a function depends on how fast the function breaks away from the base line. The fact that it is possible to invert the theoretical Green's function for the plate medium with source and receiver opposite each other (the

epicenter arrangement) makes the experiment possible and was a deciding factor in its design. The impulse response of the NBS conical transducer is sufficiently similar to the ideal delta function that, with negligible modification, it can also be inverted. The inverses of G and T were found by direct time-domain deconvolution (Hsu and Eitzen, 1979).

For the purpose of finding T , or calibrating the receiving transducer, a separate experiment was performed in which a glass capillary was broken at the source location, and the force of the glass-break was measured by a calibrated sensor in the loading screw. We assumed the glass-break event produced a step force, F_c . This assumption can be justified by experimental evidence, but we defer this to a later point in the paper. Inversion of the step function is easy. (This operation is equivalent to introducing a differentiation of any one of the time functions with which F_c^{-1} is convolved.) Inversion of G is possible, so

$$T = V_c * G^{-1} * F_c^{-1}, \quad (3)$$

where V_c is the captured voltage waveform of the calibration.

Effects of error in the Green's function used in our calculations were investigated by a computer experiment. An altered Green's function was constructed using sound speeds which differed from the measured ones, and this altered Green's function, G_1 , was used to calculate a transducer response, T_1 , which was found to exhibit spurious pulses independently known to be absent in the T function of the conical transducer (Fig. 2). These pulses occur in the T_1 waveform at times corresponding to the arrival of energy traveling with the shear speed (S waves) and with the longitudinal speed having been reflected from both surfaces (PPP waves).

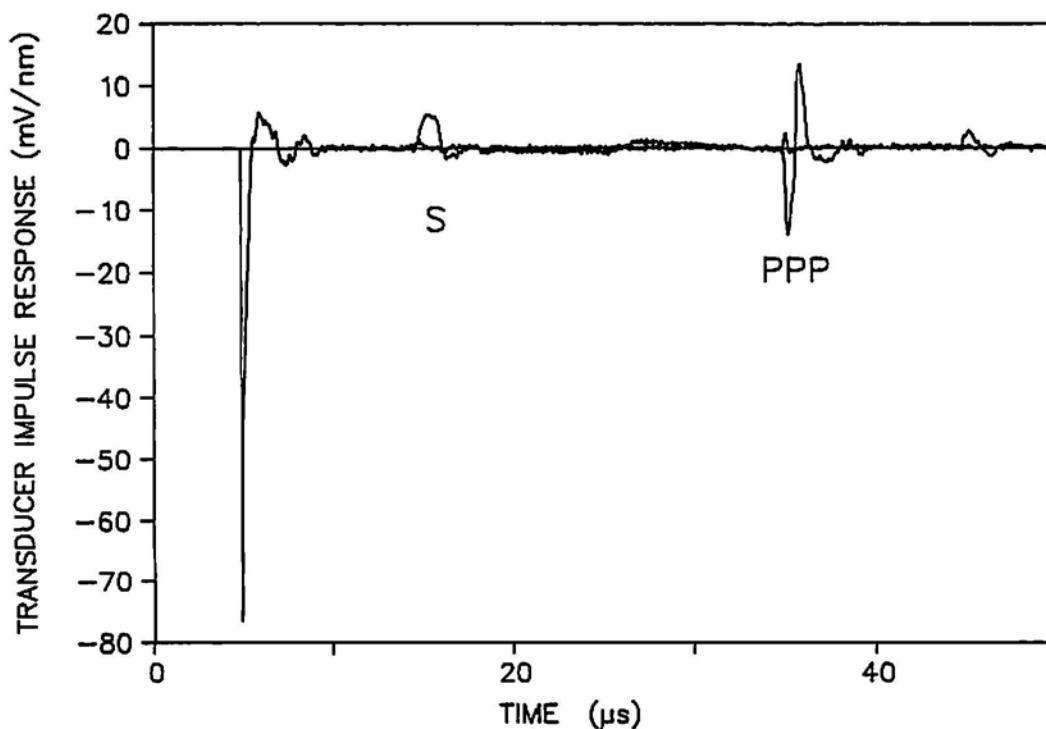


Fig. 2 Transducer impulse response function from the calculation of equation (3). The curve with the quiet tail was obtained from the Green's function based on sound speed measurements in the glass plate; the curve with the extra pulses was obtained from a Green's function based on slightly altered sound speeds.

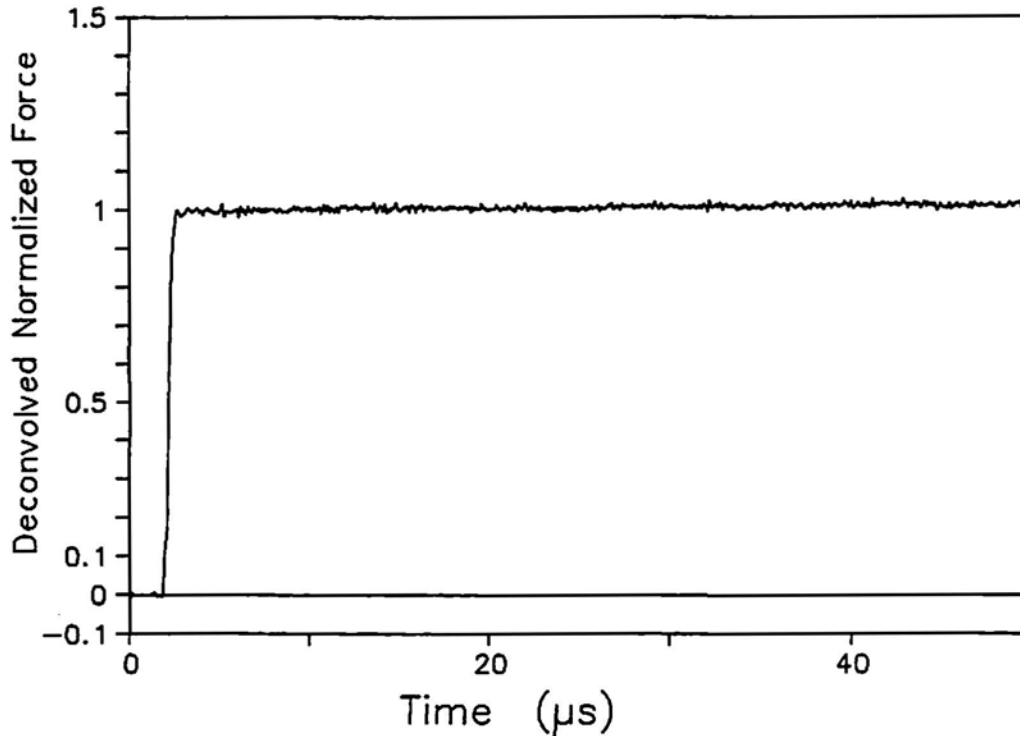


Fig. 3 Force waveform from a capillary break as obtained by the calculation of equation (2) and normalized by the loading screw measurement.

Their presence in the T_1 waveform is a consequence of arrival-time errors for these waves in the G_1 waveform, and clearly indicates that the altered sound speeds are incorrect. The deconvolution of the G and T functions, therefore, serves not only to determine T , but also to verify the correctness of G , provided T is known to be free of late-arriving pulses.

Although G and T were determined separately, it is their convolution that figures in the equation that relates F and V . Physically, $G*T$ describes the response of the plate-transducer system to a force. The final force-measurement results would have been no different if we had found $(G*T)^{-1}$ from the same calibration event that was used to find T^{-1} . The properties of G and T that make their inversion possible carry over to their convolution, $G*T$. From equation (1),

$$G*T = V_c * F_c^{-1}, \quad (4)$$

from which it follows that

$$F = (V_c^{-1} * F_c) * V. \quad (5)$$

A characterization of the transfer function of the combined plate-transducer system would have sufficed for the purposes of determining the source force waveforms. In other words, the G and T functions need not be present in the equation relating measured voltage waveform, V , and force, F . In the computer experiment described above, alteration of the G function brought about no significant change in the calculated source force waveform.

Elasticity theory has been developed for the force produced by the collision of elastic spheres (Hertz, 1881; Goldsmith, 1960). Using measured values for the weights of the balls, and a handbook value (Metals Handbook, 1978) for Young's modu-

lus, the force waveforms for each size of ball were calculated. Originally, our calculations used a well known half-sine approximation to the force-vs.-time function, but it became apparent that errors involved in this approximation caused disagreement with our experimental data. We therefore performed more exact calculations of the force waveforms based on numerical integration of an elliptic integral (Goldsmith, 1960). It is these more exact calculations that were used as the basis of comparison for the measured force waveforms in this paper.

4. Experimental Results

As a check on the effectiveness of the computational systems used in this experiment to accurately determine the force waveforms of sources, we used the system to determine waveforms of capillary-break events other than the calibration events (Fig. 3). Since the assumption that such events produce step waveforms was made at the outset, it would, of course, have been disastrous if the resulting waveforms had not represented experimentally realized steps. The results of this test showed that the numerical convolutions and inversions perform properly and produce a result consistent with the assumptions of the experiment.

By means of the experimental and computational system described, source waveforms were obtained for one hundred ball-impact events: ten each for ten sizes of ball. Force waveforms were calculated for all events. For one ball of each size, the waveform, normalized in magnitude by division by the square of the ball radius and normalized in time by division by the radius, is displayed in Fig. 4 along with the corresponding waveform calculated from Hertz's theory. Here, the outlier is the

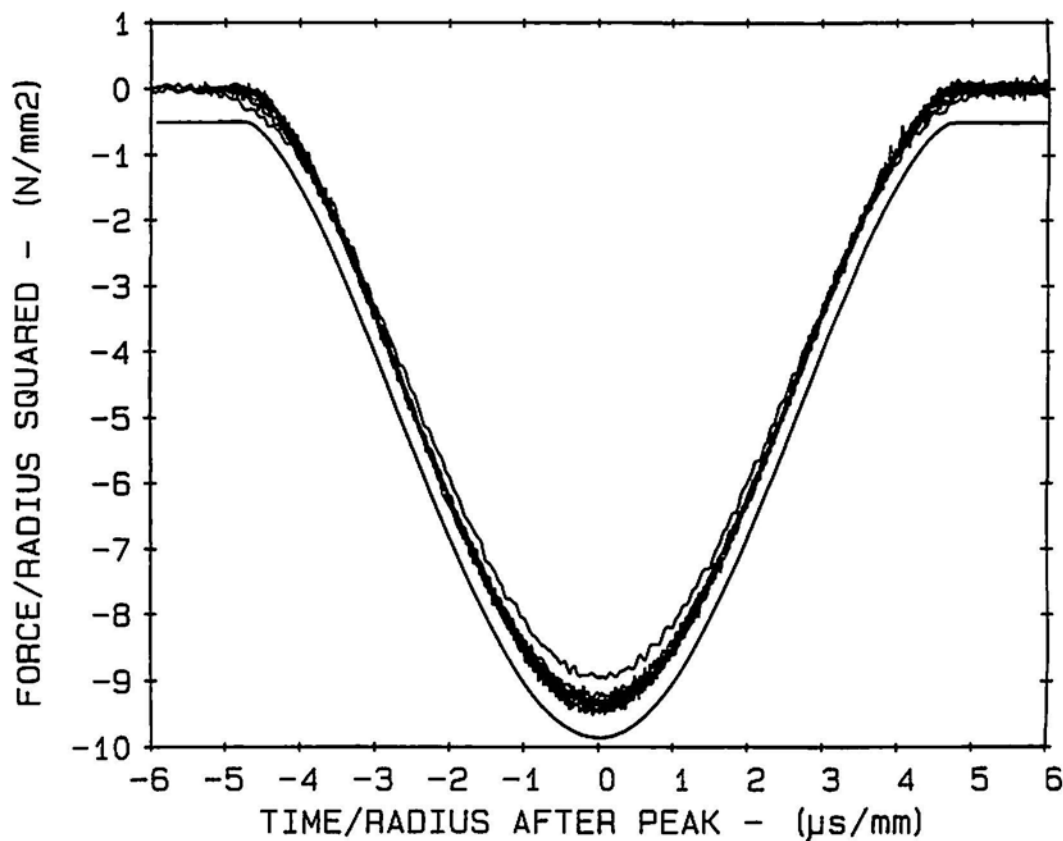


Fig. 4 Dynamic impact force waveforms for ten sizes of ball. Each waveform represents one event using a particular size of ball. The waveforms were obtained from the calculation of equation (2) and normalized in magnitude by $1/r^2$, and in time by $1/r$. The smooth curve, offset by $1/2$ division, is calculated from Hertz's theory.

curve for the 3.18 mm ball, and the smooth curve is the theoretical one, which has been displaced vertically for clarity. The overlapping of ten lines of data illustrates the consistency of the normalized values of dynamic force. For each size of ball except the smallest, the variation of the magnitude of the force function from event to event was less than 2%.

The Hertz theory applies only to loss-free elastic media, and also does not take into account radiative losses. Without the radiation of sound into the medium the experiment would be impossible. It may be expected that the various loss mechanisms would prevent the ball from returning from the collision with the same energy it had on impingement. To determine the extent of such losses, careful photographic measurements were made to determine the successive rebound heights of the trajectories. It was found in the course of these experiments that surface pitting and contamination of the balls and the plate were associated with increased losses. Certain balls performed more poorly than others, and microscopic examination revealed that the 3.18 mm balls had larger surface imperfections than the others. After discarding the worst balls of each size and by carefully cleaning the balls and the plate, we were able to obtain rebound heights that were 99.0% of the drop height. A systematic error of 0.3% in the values of F owing to rebound losses has been ignored in our calculations.

Based on the values of density and Young's modulus for the steel balls and the glass plate, and the controlled drop height of 30 mm, Hertz's theory predicts the following size-independent physical parameters:

$$F_p/r^2 = 9.736 \text{ (9.260) N/mm}^2,$$

$$t_h/r = 5.179 \text{ (5.124) } \mu\text{s/mm},$$

$$I/r^3 = 49.883 \text{ (47.15) N } \mu\text{s/mm}^3,$$

where F_p is the peak force, t_h is the pulse width at half the peak force, I is the impulse ($I = \text{change in momentum}$), r is the ball radius. The experimentally determined values are shown in parentheses. Figure 5(a,b,c) shows the experimental values of these parameters as a function of ball size. In general, the experimental errors do not significantly depend on ball size, although the error in t_h is greatest for the smallest ball size.

A worst case error analysis was performed based on estimated uncertainties of the input parameters (the measured sound speeds in the glass, the measured densities of the glass and steel, the handbook value for the Young's modulus of the steel, and the drop height). This analysis indicates that the uncertainty in F_p , t_h , and I were 0.7%, 0.5%, and 0.6%, respectively. The fact that the experimental values of F_p and I are low in magnitude by 5% and 6%, respectively, is attributable mainly to errors in calibration of our apparatus by the glass capillary-

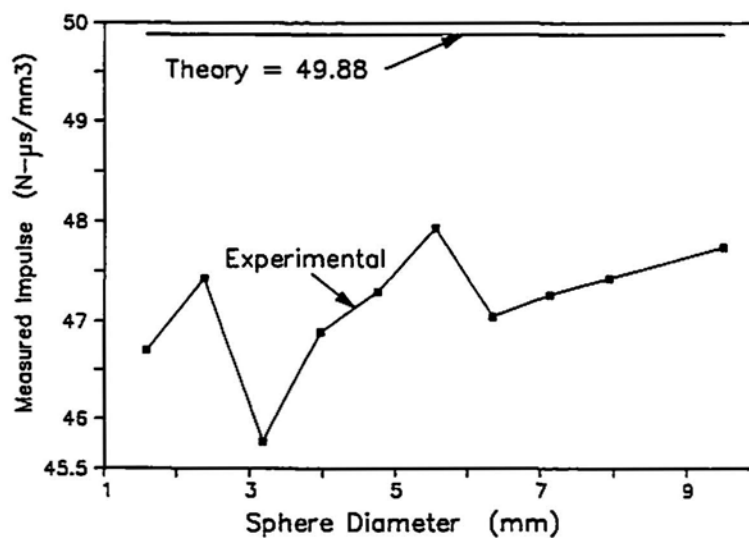
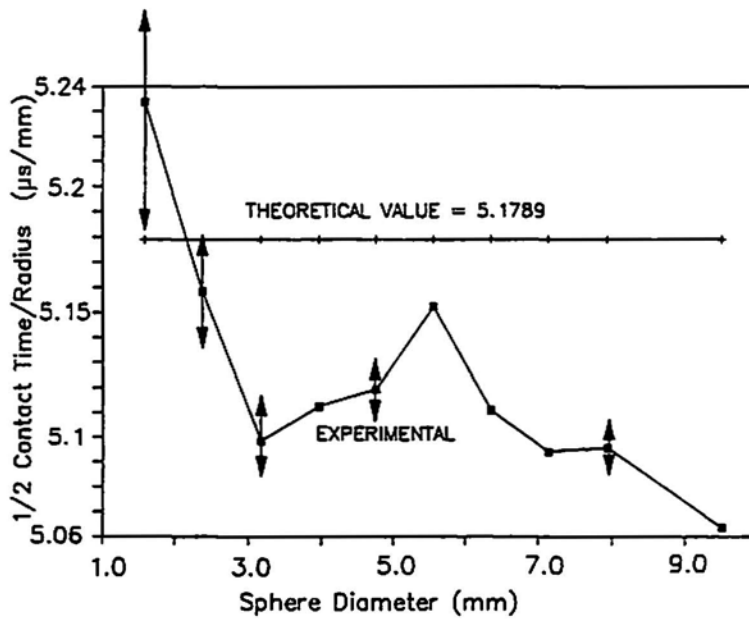
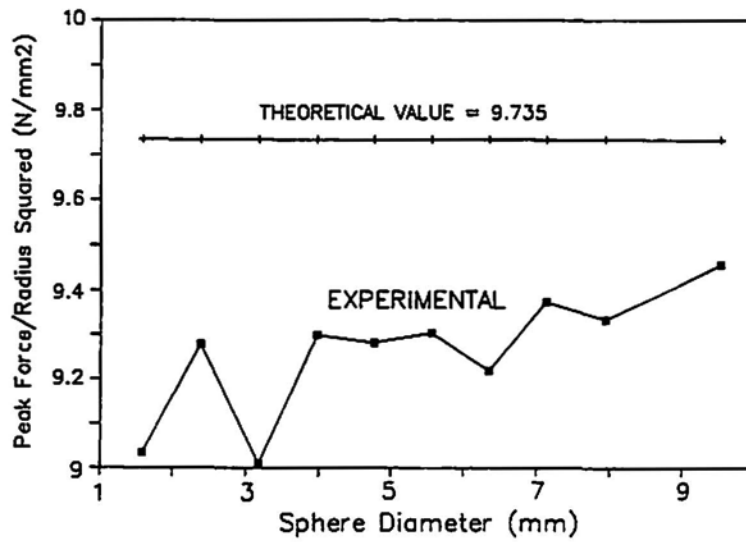


Fig. 5 Measured physical parameters as a function of ball size: a) F_p/r^2 ; b) t_c/r ; c) I/r^3 .

break technique. From previous experience, we feel that the uncertainty of the glass capillary-break calibration scheme is about 6 to 7 %, which is consistent with the present results.

A careful examination of many glass capillary-breaking experiment reveals considerable variation in the details of capillary collapse. At least two different processes can be observed. About half of the glass capillary-breaks exhibit a relatively clean single step, but the other half exhibit collapse in multiple steps, i.e., not all the initial force is relieved in the first break. This phenomenon can be seen in the deconvolved force-vs.-time waveforms and also in the waveforms from the load cell of the glass capillary breaking apparatus. By monitoring these waveforms, data from glass capillary-breaks having multiple steps could be discarded during the calibration process.

5. Conclusion

It is shown that unknown dynamic forces can be accurately measured. Agreement between measured force waveforms and those predicted by Hertz's theory establishes the correctness of the method and implicitly corroborates the results of the NIST primary transducer calibration measurements and recent force measurement results.

It is shown that the relation between the measuring system output and the unknown force is described by the transfer function of the entire system (plate and transducer in this case), and need not be separated into convolutional factors representing the individual components. Furthermore, it is shown that incorrectness of the plate Green's function manifests itself as spurious pulses visible in the derived transducer response waveforms provided that the transducer response is free of late-arriving pulses.

Acknowledgment

This work was supported by the National Institute of Standards and Technology and the Office of Naval Research.

References

ASM (1978), *Metals Handbook, Ninth Edition, vol. 1 Properties and Selections: Iron and Steel*, American Soc. Metals, Metals Park, OH, p. 680.

F.R. Breckenridge (1982), "Acoustic Emission Transducer Calibration by Means of the Seismic Surface Pulse", *J. Acoustic Emission*, 1(2), 87-94.

F.R. Breckenridge, T.M. Proctor, N.N. Hsu, S.E. Fick and D.G. Eitzen (1990), "Transient Sources for Acoustic Emission Work", *Progress in Acoustic Emission V*, eds. K. Yamaguchi et al., Japanese Soc. for Nondestructive Inspection, Tokyo, Japan, pp. 20-37.

A.S. Carasso and N.N. Hsu (1985), "Probe Waveforms and Deconvolution in the Experimental Determination of Elastic Green's Functions", *SIAM J. of Applied Mathematics*, 45(3), 369-382.

W. Goldsmith (1960), *Impact*, E. Arnold Ltd., London, Chapter 4.

H. Hertz (1881), *Gesammelte Werke*, J. Reine Angew. Math 92, reprinted in 1986 as *Miscellaneous Papers*, Macmillan, London, p. 156.

N.N. Hsu (1985), "Dynamic Green's Functions of an Infinite Plate - A Computer Program", National Bureau of Standards, NBSIR 85-3234.

N.N. Hsu and D.G. Eitzen (1980), "Acoustic Emission Source Characterization Through Direct Time-Domain Deconvolution", *Proc. ARPA/AFML Rev. Quantitative NDE*, AFWAL-TR-80-4078, pp. 81-84.

N.N. Hsu and D.G. Eitzen (1982), "The Inverse Problem of Acoustic Emission--Explicit Determination of Acoustic Emission Source Time-Functions", *Review of Progress in Quantitative Nondestructive Evaluation*, Vol. 1, Ed by D.O. Thompson and D.E. Chimenti, Plenum Publishing Corp., New York, pp. 405-412.

N.N. Hsu and D.G. Eitzen (submitted 1988), "Experimental Determination of Point Impact Force-Time Function", *Experimental Mechanics*.

N.N. Hsu and S.C. Hardy (1978), "Experiments in Acoustic Emission Waveform Analysis for Characterization of AE Sources, Sensors, and Structures", *Elastic Waves and Non-Destructive Testing of Materials*, AMD - vol. 29, ed. Y. H. Pao, ASME, New York.

Y.H. Pao, R.R. Gajewski, and A.N. Ceranoglu (1979), "Acoustic Emission and Transient Waves in and Elastic Plate", *J. Acoust. Soc. America*, 65(1), 96-105.

T.M. Proctor (1971), "Sound Speed Measurements in Solids: Absolute Accuracy of an Improved Transient Pulse Method", *NBS J. of Research*, 75C(1), 33-39.

T.M. Proctor (1982), "An Improved Piezoelectric Acoustic Emission Transducer", *J. Acoustical Soc. America*, 71(5), 1163-1168.

T.M. Proctor (1986), "More Recent Improvements on the NBS Conical Transducer", *J. Acoustic Emission*, 5(4), 134-142.

Acoustic Emission Monitoring of a Fatigue Test of an F/A-18 Bulkhead

C. M. Scala, J. F. McCardle and S. J. Bowles

Abstract

This paper describes the application of acoustic emission (AE) to identify cracking in several fatigue-critical regions on the port and starboard sides of an F/A-18 aircraft bulkhead undergoing fatigue testing. AE data acquisition was carried out using an array of three sensors on each side of the bulkhead. AE features stored by each array included relative arrival times of AE events at the three sensors, event rise time at the first-hit sensor, and the load level and the position on the load cycle of event occurrence. AE data processing involved a comparison between the features of those AE events stored during the fatigue testing and predicted features for cracking in the complex-shaped bulkhead. Feature prediction was based on wave propagation characteristics obtained by Pentel-lead calibration, and the known load cycle dependence of crack-related AE events. The AE processing was completed following failure of the bulkhead, and gave the correct locations of all cracks, greater than about 1 mm in depth, present in the bulkhead during the fatigue testing. The study shows that AE associated with cracking can be distinguished, even when many extraneous sources are present, and demonstrates that AE is a promising technique for nondestructive evaluation of a complex structure such as the F/A-18 bulkhead.

1. Introduction

Assuring the airworthiness of high-performance military aircraft such as the F/A-18 by nondestructive evaluation (NDE) presents special challenges. In particular, for an F/A-18 structural component such as a wing-attachment bulkhead, access for nondestructive inspection is limited. Also, the large size and complex shape of the bulkhead lead to a reduction in the reliability of application of conventional NDE techniques. However, in the bulkhead the need exists to detect defects which lie on the detectability limits of conventional techniques under idealized conditions. The alternative to airworthiness based on a damage-tolerant NDE approach is to establish not only a safe life for the component but also precision manufacturing and maintenance procedures to guard against the presence of "rogue" flaws. However, even then, the high capital cost of the F/A-18 aircraft makes operation of the aircraft beyond the bulkhead's safe life an attractive option. Thus, improved NDE capabilities are required.

DSTO Aeronautical Research Laboratory (ARL) has been developing acoustic emission (AE) as a possible NDE technique for in-situ monitoring of aircraft components. Emphasis has

been placed on monitoring complex-shaped components not readily inspected by more conventional techniques. Promising results were obtained in early AE studies on a Macchi aircraft, from which the feasibility of in-flight AE measurements was established (Scott, 1981; Scala et al., 1989). Following the Macchi study, all significant cracks were located in the main wing-spar of a Mirage jet-fighter during full-scale fatigue testing (Scala and Coyle, 1987; Scala et al., 1989). The Mirage study was arguably one of the most difficult AE aircraft applications likely to be encountered, requiring crack identification in numerous bolt holes amid a wide range of spurious AE sources. Hence, an important outcome of the Mirage study was the development of AE processing which should be useful for crack detection in a wide range of aircraft applications. The processing involves identifying possible cracking by a comparison between AE features obtained from a fatigue-critical region during aircraft loading and predicted features for cracking in the region. Feature prediction is based on (i) wave propagation characteristics for cracking in the region obtained from Pentel-lead calibration in fatigue-critical regions (Scala and Coyle, 1983 and 1987), and (ii) source-related characteristics from background studies of AE events (Scala et al., 1989).

Considerable background information on source-related features is available to distinguish between AE sources, particularly in laboratory applications where a wide range of features has been obtained (Graham and Elsley, 1983; Hutton, 1985; Scala and Coyle, 1983; Scala et al., 1989) including fundamental characteristics such as the directivity patterns of different sources (Buttle and Scruby, 1989 and 1990a). Some of the features applicable under idealized laboratory conditions are also useful for distinguishing between crack-related and extraneous sources detected in the far field in complex-shaped aircraft components (Buttle and Scruby, 1990b; Scala et al., 1989). For example, electromagnetic interference is typified by a shorter rise time than other sources detected under such conditions; also, hydraulic noise has a relatively long duration, long rise time and low frequency compared to crack-related AE (Graham and Elsley, 1983; Hutton, 1985; Scala and Coyle, 1983; Scala et al., 1989). The position on the load cycle of AE event occurrence is another useful feature on which to eliminate AE from some extraneous sources (Buttle and Scruby, 1990b; Scala et al., 1989). In particular, various extraneous sources, such as electromagnetic interference and hydraulic noise, can occur on all parts of the load cycle. Also, AE from fretting of a bolt in a hole has been observed on negative load gradients during cycling of bolted plates (Graham and Elsley, 1983) and at a range of load-cycle positions for misaligned specimens. AE due to crack propagation in aircraft aluminum alloys occurs on a load maximum for constant amplitude load cycling; the source also occurs on a positive load gradient during application of an overload (Lindley et al., 1978; McBride and MacIachlan, 1984;

Received 15 January 1992. The authors are affiliated with Airframes and Engines Division, DSTO Aeronautical Research Laboratory, 506 Lorimer St., Fishermens Bend, 3207 Australia.

Scala and Cousland, 1985). Although detailed overload type studies on the features of AE due to a crack-face rubbing source are lacking, AE due to rubbing has been observed predominantly on a positive load gradient, usually below the mean load but occasionally rising above this level, in several systematic studies involving constant amplitude loading (Graham and Elsley, 1983; Kim and Weertman, 1984; Lindley et al., 1978; Mori and Obata, 1988). Hence, the occurrence of AE events exclusively on a positive load gradient and load maximum is consistent with the characteristics of a crack-related source, i.e., crack propagation or crack-face rubbing, but may not be consistent with an extraneous source (Scala et al., 1989; Weatherly et al., 1984).

In this paper, the feasibility of using AE to monitor possible cracking in several fatigue critical regions during a fa

tigue test of the aluminum alloy bulkhead of an F/A-18 aircraft is investigated, using some of the procedures developed in the Mirage AE study described above. Section 2 of the paper gives brief details on the bulkhead fatigue test and outlines the procedures for Pentel-lead break calibration and AE data acquisition during fatigue testing; a description of the AE data processing is also given. Section 3 compares features of the AE obtained during fatigue testing with predicted features in order to determine the location and source of any AE-based cracking indications in the bulkhead. Also, the AE results are compared with fractographic results obtained from the bulkhead. Section 4 discusses the significance of the AE results, particularly in terms of the reliability of AE for bulkhead monitoring, and recommends some improvements in AE data acquisition procedures for future F/A-18 bulkhead tests. Finally, Sec. 5 summarizes the major conclusions of the present study.

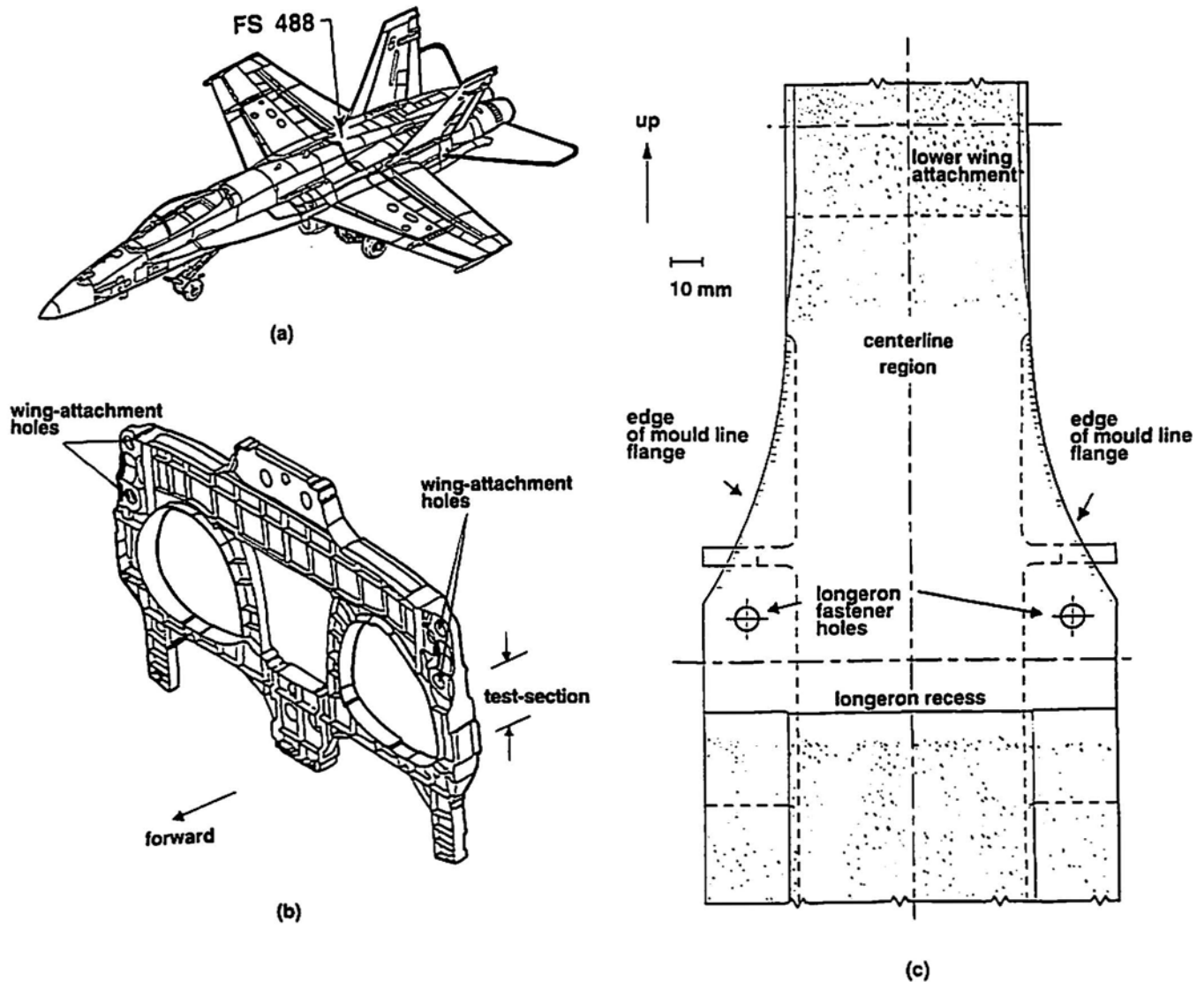


Fig. 1 (a) F/A-18 aircraft showing FS 488 wing-attachment bulkhead. (b) View of bulkhead with port fatigue test-section indicated. (c) Bulkhead with 6-inch (15.2-cm) mold-line flange, showing as unshaded the approximate extent of the section for which AE monitoring of crack propagation was undertaken. Fatigue-critical regions indicated are: (i) edges of mold-line flanges (hatched); (ii) longeron recess; (iii) longeron fastener holes; (iv) outer face of bulkhead below lower wing attachment towards the centerline (denoted centerline region).

2. Experimental Details and Procedure

2.1 AE Data Acquisition

As part of a feasibility study of suitable NDE techniques to apply to the F/A-18 fuselage station (FS) 488 wing-attachment bulkhead (Fig. 1a), AE monitoring of a bulkhead undergoing fatigue testing at ARL was investigated. The ARL fatigue test formed part of an international program to establish a safe life for the bulkhead (Anderson and Revell, 1990). The fatigue testing caused the bulkhead (made from thick plate aluminum alloy 7050-T7451) to be subjected to a repeated loading program. Each loading program comprised a sequence of loads, variable in both amplitude and frequency, and simulated 300 flight hours of an F/A-18 aircraft. The loading was designed to test sections which were mirror images on the port and starboard sides of the aircraft (Fig. 1b). Each test section included several fatigue-critical regions which had been established prior to the commencement of the test. The regions comprised the longeron recess, the longeron fastener holes and the curved parts of the forward and aft edges of the mold-line flanges (Figs. 1b and c). Each port and starboard designated test-section also included other regions higher up towards the wing-attachment area which U.S. tests identified as fatigue-critical after the ARL fatigue testing (and AE monitoring) was well-advanced. These additional regions comprised the centerline region below the lower wing-attachment lugs on each outer face of the bulkhead and the edges of the mold-line flanges right up to the level of the centerline region (Fig. 1c).

The objective in applying AE to the bulkhead fatigue test was to monitor known fatigue-critical regions within the designated test-sections on the port and starboard sides of the bulkhead. The bulkhead test was simpler than the Mirage-spar AE application described in Sec. 1, involving fewer possible spurious AE sources. Therefore, a simpler AE data acquisition system (than the twenty-five sensor, waveform-based Mirage system) was used for the bulkhead test, given the need for more efficient storage and processing of data than in the Mirage test (Scala et al., 1989). The acquisition system used was a six-channel Dunegan DART system linked to an IBM PC-AT. Small-diameter, point-contact sensors (Valpey-Fisher pinducers) were used with the system for AE detection, as space for sensor attachment was extremely limited due to the presence of numerous strain gauges associated with the safe-life study of the bulkhead. The AE sensors were also selected because of their wideband characteristics and their consequent suitability for feature extraction studies (Scala et al., 1989). The DART system was limited to the use of up to six AE sensors so an array of three sensors was assigned to each of the port and starboard sides of the bulkhead. Each 2D array had to perform dual roles in rejecting extraneous sources in a 3D structure and locating crack-related sources in fatigue-critical regions in the bulkhead. As location accuracy is, in principle, better for source locations close to an array, the sensor arrays were set up in close proximity to the regions identified as fatigue-critical at the start of the ARL fatigue testing. Therefore, the arrays were some distance from the additional critical regions identified after testing had commenced (see above). Due to the space limitations, the sensor array placements were similar but not identical on the port and starboard sides of the bulkhead.

Following array attachment, the next step was to set up the DART for event detection at each array sensor for a threshold level just above the DART electrical noise level with no external input applied. Then, the DART was configured to allow storage of the following features of AE events detected by each array: (i) record number, (ii) array hit, (iii) the relative AE event arrival-times at the three sensors in an array, (iv) event rise time at the first-hit sensor, (v) event duration at the first-hit sensor, (vi) event amplitude at the first-hit sensor, (vii) event counts at the first-hit sensor, (viii) load level of event occurrence during fatigue testing, and (ix) occurrence either on a positive load gradient/load maximum or negative load gradient/minimum.

The DART system was used to acquire data in calibration studies, using the fracture of 2H 0.3 mm diameter Pentel lead to obtain wave propagation features for crack-related AE from the bulkhead. The Pentel lead, which gives a high-amplitude, short-rise-time source, has been successfully used to predict a limiting range of wave propagation features in various large, complex-shaped aircraft components (McBride et al., 1991; Scala et al., 1989). In such components, these wave-propagation features are usually the far-field characteristics, complicated by various wave reflections and mode conversions. In keeping with the simplified approach adopted in the present study, emphasis was placed on fewer Pentel-lead features than used previously (Scala et al., 1989), viz., the relative event arrival-times at the three sensors in an array and also the maximum possible rise time at the first-hit sensor for AE events from a given source location. Data were obtained by breaking Pentel leads at 10 mm intervals in the critical regions. For each simulated source location, data corresponding to five separate Pentel-lead fracture events were recorded in order to establish a limiting range of features for the location and to ensure reproducibility of results. These calibration measurements also allowed the likely limitations in the AE location accuracy to be assessed for the fatigue-critical regions more distant from the arrays. The Pentel-lead source was also applied adjacent to each array sensor to verify that each of the six sensors was operating at the same sensitivity.

To assist in the elimination of sources extraneous to the fatigue-critical sections, some additional calibration measurements were undertaken at locations outside the fatigue test sections (Fig. 1c), especially at likely locations for extraneous sources such as at the wing attachment holes. From this additional set of calibration data, a value for extraneous sources of the minimum relative arrival-time between first-hit and last-hit sensors (ΔT_2) was obtained (this value being greater than that for events within the test-sections). During data acquisition, events having ΔT_2 greater than or equal to this minimum value were flagged by the DART as extraneous; detailed features for such events were not calculated to maximize the data acquisition rate.

During the entire bulkhead fatigue testing, AE data acquisition was carried out with only minor loss of data due to occasional equipment failures. Small changes in AE sensor placements were necessary at 7500 simulated flight hours, following remachining of the edges of the bulkhead mold-line flanges from a standard F143 configuration to a 6-inch (15.2-cm) radius

configuration (Anderson and Revell, 1990). Other minor changes in AE sensor placements were also necessary on a regular basis throughout the test due to external factors associated with the safe-life study, e.g., due to repositioning of strain gauges and temperature sensors. Recalibration was undertaken regularly throughout the test to allow for these minor changes in the sensor placement and test re-configuration. The recalibration was also necessary to ensure long-term reproducibility of sensor characteristics and detection levels in the AE acquisition system and to verify the correct operation of the ΔT_2 arrival-time criterion.

2.2 AE Data Processing

The data processing used for this study was similar to, but less sophisticated than, that described in detail for AE monitoring of the Mirage aircraft during full-scale fatigue testing (Scala and Coyle, 1987). The processing involved comparing measured and predicted features of crack-related AE during the bulkhead testing, with fewer features being examined than in the Mirage test. Feature prediction for crack-related AE in the aluminum alloy bulkhead was based on a combination of (i) the wave propagation data obtained from the Pentel-lead calibration (see Sec. 2.1), and (ii) background information which in this application was limited to the load cycle dependence of crack related AE sources (see Sec. 1). Our previous work involved the use of background features from AE from crack propagation exclusively (Scala and Coyle, 1987; Scala et al., 1989). However, in the present study, the probability of detecting any cracking in the bulkhead was maximized by combining the load dependencies for both AE from fatigue-crack propagation and AE from crack-face rubbing in the feature prediction. An additional reason for including AE from crack-face rubbing was that the likely AE activity from fatigue propagation was unknown at the start of the test, due to a lack of either microstructural information or laboratory AE studies on the bulkhead material.

The data processing was carried out in four successive stages using a standard data-base program (Fox-base) operating on an IBM PC-AT:

I. AE events located within fatigue-critical regions

AE events which occurred within the fatigue-critical regions were located on the basis of a comparison between predicted and measured event relative arrival-times and rise-times. In particular, firstly a stored AE event was assigned a location if the event relative arrival-times matched Pentel-lead criteria for any of the fatigue-critical locations. Then, rise-time criteria were applied to a located event: an event was accepted as correctly located if its rise time was in the range greater than $1 \mu s$ (i.e., to reject AE events due to electrical and electromagnetic interference) up to the value obtained in the Pentel-lead calibration for the assigned location.

II. Crack-related AE validated

Next, load-cycle dependence criteria were applied to validate as crack-related AE events located within a specific fatigue-critical region: Those AE events with characteristics meeting stage I were accepted as crack-related, provided that the characteristics for a specific location were observable only on positive load gradient or load maximum.

III. Crack-related AE compared with loading history

Finally, detailed features of those AE events meeting stage

II at a specific location within a fatigue-critical region were determined as a function of loading history for comparison with fractographic data. In particular, event rate, position on the load cycle of event occurrence and event amplitude were all obtained as a function of load program number.

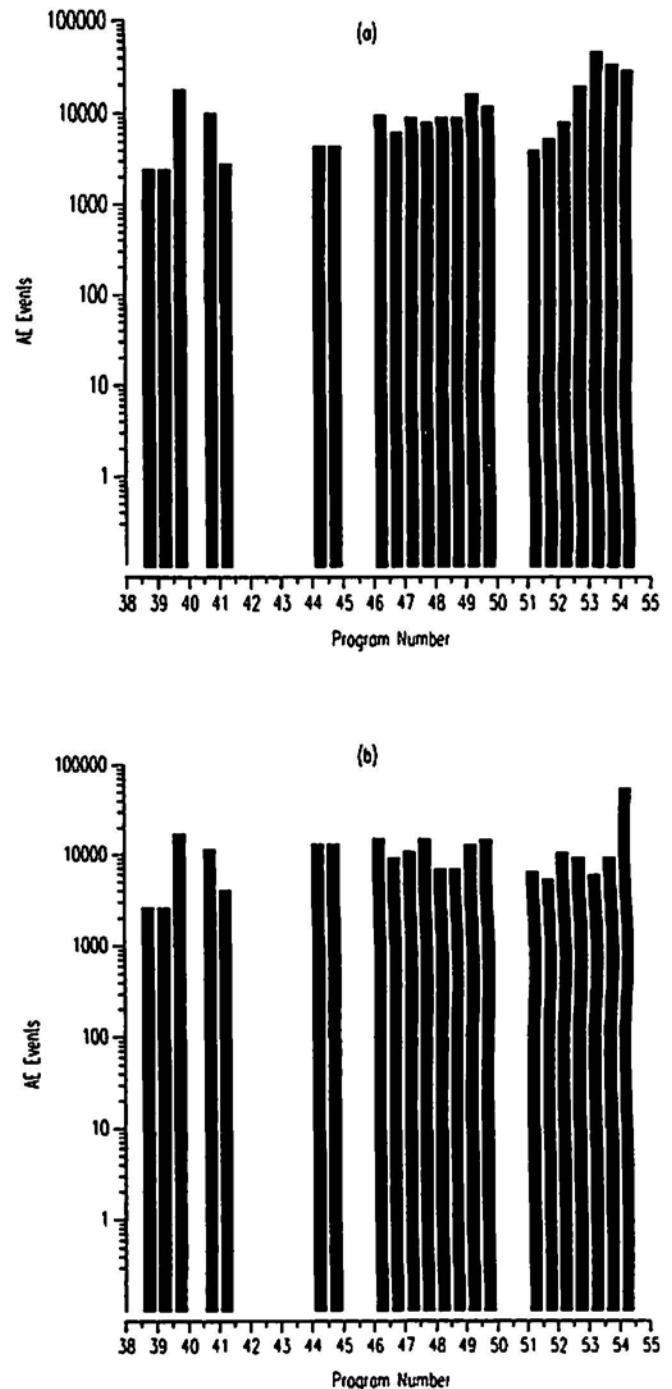


Fig. 2 The dependence on loading program number (from program 38 up to failure) of the unprocessed AE event rate per half load program for AE acquired on (a) port and (b) starboard sides of the bulkhead. (Note that, due to equipment malfunction, AE data were not stored for those half programs for which no events are plotted.)

The AE processing was undertaken at weekly intervals, corresponding to data from about one load program for the first 7500 simulated flight hours ranging up to five loading programs per week following the radius remachining. This weekly processing schedule meant that AE data from the first forty-nine load programs were processed prior to bulkhead failure in the 54th program of testing on the port side from the forward mold-line flange; AE events from the remaining programs were processed after failure.

3. Results

3.1 Limitations in Source Location from Calibration Data

Pentel-lead calibration measurements, undertaken following the real-time implementation of the ΔT_2 arrival-time criterion to flag extraneous sources (see Sec. 2.1), demonstrated the validity of the system for AE source location close to the AE sensor arrays. These measurements also showed the limitations in AE location accuracy for simulated source locations more distant from the arrays, e.g., some ambiguities in source location were found in the vicinity of the centerline region shown in Fig 1c. Furthermore, the Pentel-lead calibration measurements demonstrated that isolated AE events would be flagged as extraneous if they occurred above the centerline region or below the longeron recess level shown in Fig. 1c.

3.2 AE during Fatigue Testing

3.2.1 Overview of AE data

As the fatigue test progressed, no systematic variation was observed between load-program number and the unprocessed AE event rate for either the port or starboard sensor array (Fig. 2a and b). For the port array, the event rates obtained in program 53 and the final program 54 were somewhat higher than had been observed previously from this array during testing, and some data were lost due to the occurrence of overflows. However, the port array event rate actually decreased from the start of program number 53 up to failure (Fig. 2a). The highest event rate for the fatigue test was obtained on the starboard side of the bulkhead in the final load program (Fig. 2b).

Application of arrival-time criteria in processing stage I resulted in the rejection of most of the data throughout the test as due to extraneous sources outside the test-sections (Table 1 and Fig. 2). This extraneous source activity varied from program to program, presumably associated with the changes which occurred in the loading train. For example, a significant increase in extraneous events early in the fatigue testing (before the remachining of the bulkhead mold-line radius) corresponded to problems with a loading strap below the longeron region. Also, the likelihood of fretting of the pins at the wing attachment points varied as these pins were removed and regreased each half load-program.

The arrival-time processing showed that, up to program 45, the only AE events which could be assigned a location within the test-section corresponded to the location of a temperature sensor on the starboard section. These events passed criterion I, having the correct rise time for the temperature sensor location, but failed criterion II, occurring on a negative

Table 1 On the basis of arrival-time criteria for the port and starboard fatigue-critical regions in the bulkhead, the percentage of extraneous AE events is given for each half-program (from 38.5 onwards) for which data were stored.

LOAD PROGRAM	EXTRANEIOUS SOURCES (% of total events)
38.5-39.0	100.0
39.0-39.5	100.0
39.5-40.0	99.4
40.5-41.0	100.0
41.0-41.5	100.0
44.0-44.5	100.0
44.5-45.0	100.0
46.0-46.5	100.0
46.5-47.0	100.0
47.0-47.5	100.0
47.5-48.0	100.0
49.0-49.5	99.8
49.5-50.0	99.8
51.5-52.0	96.2
52.0-52.5	97.7
52.5-53.0	99.7
53.0-53.5	99.9
53.5-54.0	99.0
54.0-failure	98.6

load gradient. Shortly after these AE indications were obtained in program 39, the temperature sensor disbonded.

From program 46 till bulkhead failure in program 54, a small number of events on port and starboard met stage I in processing; some of these events also passed stage II (see Secs. 3.2.2 and 3.2.3).

3.2.2 Processed port AE data from program 46

Application of arrival-time criteria resulted in 528 events being assigned locations within the port test-section on the port flange. 14 of these events were distributed randomly through the section and failed stage I in processing, having a rise time of 1 μ s (these events occurred on both positive and negative load gradient below 50% of the peak applied load). The other 514 events were assigned the location, denoted AE cracking indication 1, shown in Fig. 3; these events also met the range of rise-time criteria for the location and therefore passed stage I in processing.

While the 514 events from indication 1 met the Pentel lead criteria on the forward edge of the mold-line flange at the level shown in Fig. 3, 25% of these events also met stage I acceptance criteria for locations at the same level but 10 mm, 20 mm and 30 mm across on the outer face towards the aft flange. This partial overlap in crack location resulted from an overlap in the Pentel-lead criteria for sources distant from the arrays (see Sec. 3.1).

The AE events corresponding to indication 1 occurred fairly late in the test - this indication was first detected in program 46, further activity was observed in program 52, and then the activity increased rapidly up to failure (Table 2 and Fig. 4).

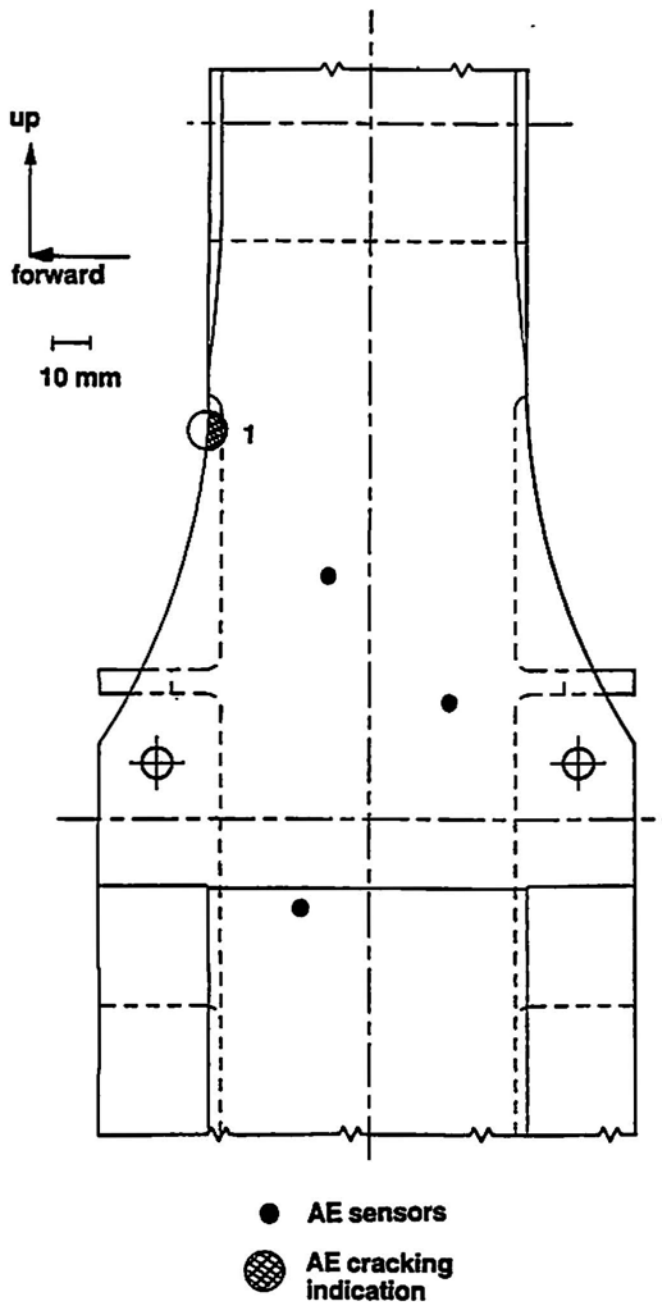


Fig. 3 2D sketch of port side of the bulkhead on which failure occurred: The placement of AE sensors at bulkhead failure and the approximate location of AE cracking indication 1 are shown.

The AE events corresponding to indication 1 all occurred on a positive load gradient and therefore also passed stage II in processing. From stage III, these events occurred over a small range of relatively low loads through several loading programs (Fig. 5), and exhibited a narrow band of amplitudes separated from the minimum detection level (Fig. 6).

3.2.3 Processed starboard AE data from program 46
 Starboard AE events meeting arrival-time and rise-time cri-

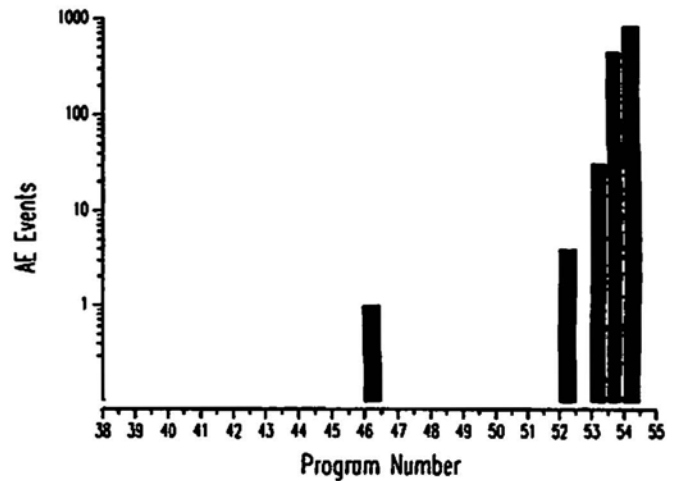


Fig. 4 The dependence on loading program number (from program 38 up to failure) of the AE event rate (per half load program) corresponding to the port indication 1.

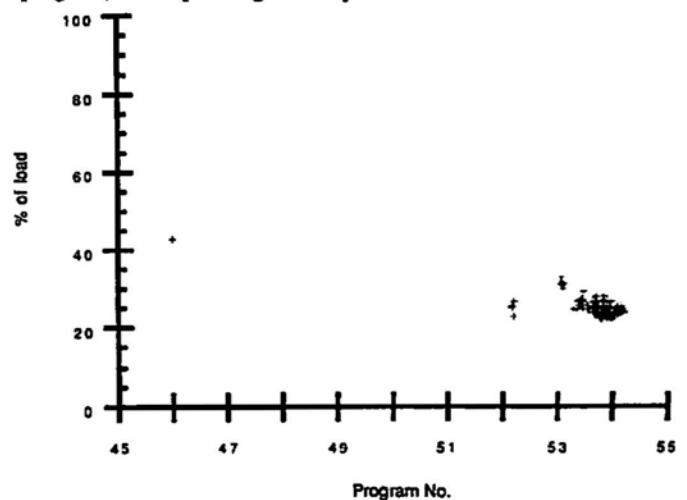


Fig. 5 The position of occurrence on a loading cycle (as a percent of the peak load applied in the fatigue test) of the AE events corresponding to the port indication 1 as a function of loading program number from program 45 up to failure.

Table 2 For events passing stage I in AE processing, the number of AE events detected from each cracking indication are given, together with the stage in fatigue testing at which each AE cracking indication was first detected.

AE CRACK INDICATION	NO. EVENTS	AE FIRST DETECTED (PROGRAM No. - Flight)
1	514	46 - 1
2	238	51 - 124
3	1236	49 - 1
4	3	53 - 124

teria for stage I in processing gave the AE cracking indications denoted 2, 3 and 4 (Table 2). The AE indication 2 comprised 238 events with source locations in the centerline fatigue-critical region in the approximate range 10 to 30 mm across the

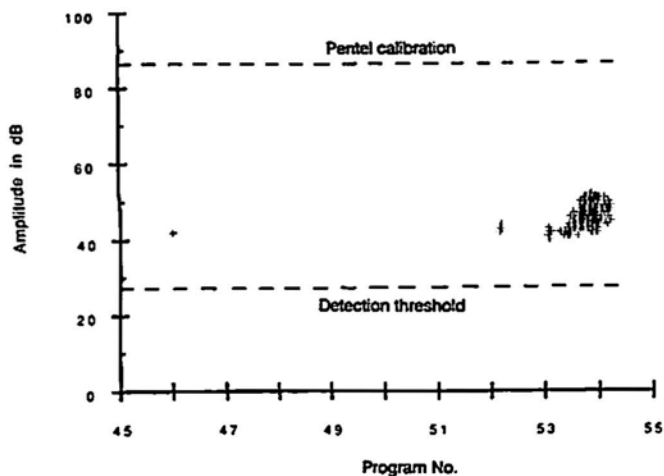


Fig. 6 The amplitude of AE events corresponding to the port indication 1 as a function of loading program number from program 45 up to failure. (Also shown are (i) the minimum amplitude detectable by the data acquisition system and (ii) the amplitude of Pentel-lead fracture events on the outer face of the bulkhead about 10 mm from each sensor.)

outer face from edge of the forward side of the starboard flange towards the aft flange (Fig. 7). The AE indication 3 comprised 1236 events at the edge of the forward flange with locations ranging from approximately 110 to 120 mm above the starboard longeron recess fillet (Fig. 7). The 3 AE events for AE indication 4 could have arisen from either of the two locations (4a and 4b) given in Fig. 7 (due to limitations in source location accuracy for sources distant from the array; see Sec. 3.1). Other events meeting arrival-time criteria for the starboard section but failing stage I based on rise-time criteria were: (i) 30 events which were located by arrival times at the forward edge of the mold-line flange at the corner of the radius (these events all occurred on a negative load gradient), (ii) 5 events located by arrival times at the forward edge of the mold-line flange 80 mm above the starboard recess fillet (these events occurred on both positive and negative load gradients), and (iii) 10 events distributed randomly through the section with a rise time of 1 μ s (these events occurred on both positive and negative load gradient below 50% of the peak applied load).

All events from cracking indications 2, 3 and 4 also passed stage II in processing. However, the events corresponding to (i), (ii) and (iii) above which failed stage I in processing also failed stage II.

As for the port side of the bulkhead, all starboard AE cracking indications were obtained relatively late in the fatigue test (Table 2 and Fig. 8). Indication 3 gave the greatest AE with considerable activity for several load programs; then, the activity gradually decreased as the bulkhead neared failure. The AE behavior for AE cracking indication 2 was similar to indication 3 but with fewer cumulative AE events detected. The small AE activity from indication 4 only commenced in the final loading program.

Application of stage III in processing showed that the AE events comprising indications 2 and 3 exhibited similar load and amplitude characteristics to crack 1 (Figs. 5 and 6) but for higher ranges of load (45-55 % of peak load) and amplitude (57-

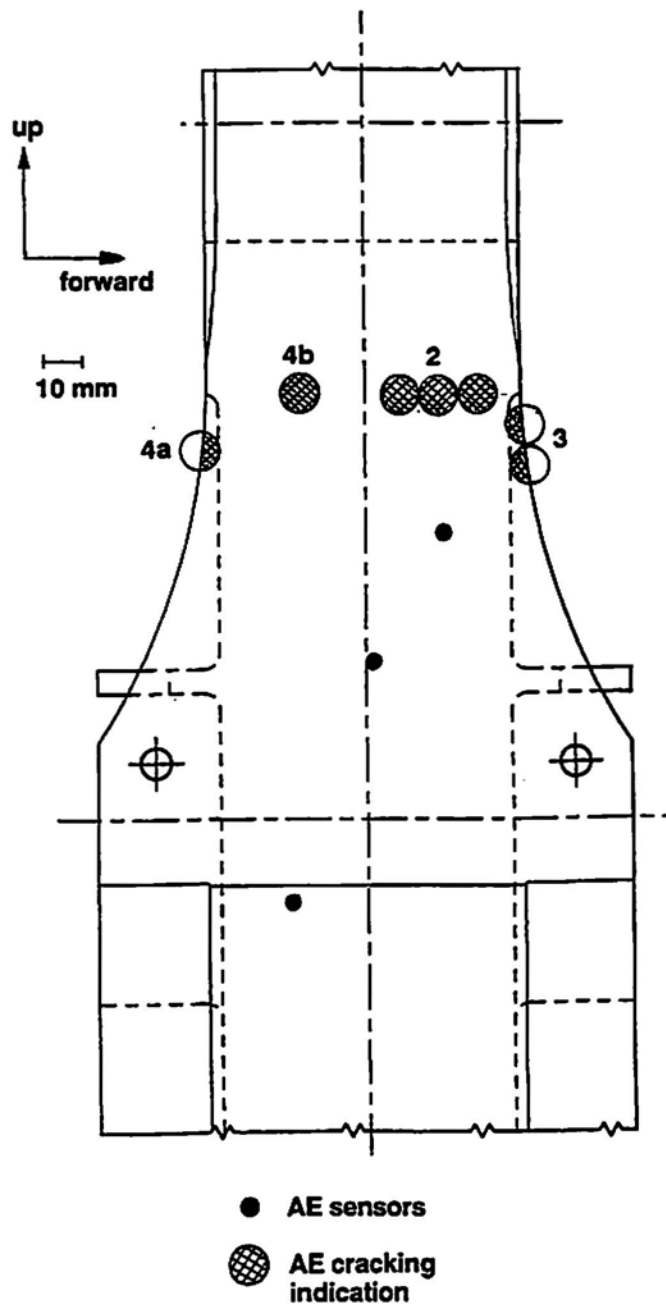


Fig. 7 2D sketch of starboard side of the bulkhead showing AE sensor placements at bulkhead failure and approximate locations of starboard AE cracking indications numbered 2, 3 and 4 - for the small number of AE events corresponding to the crack 4 indication, there are two possible locations (4a and 4b) due to limitations in the data acquisition system discussed in Sec. 2.1.

63 dB). Cracking indication 4 only comprised a few events and therefore was not amenable to stage III processing.

3.3 Comparison between AE Data and Fractography

The AE cracking indication 1 on the edge of the port forward mold-line flange (Fig. 3) corresponded to the initiation

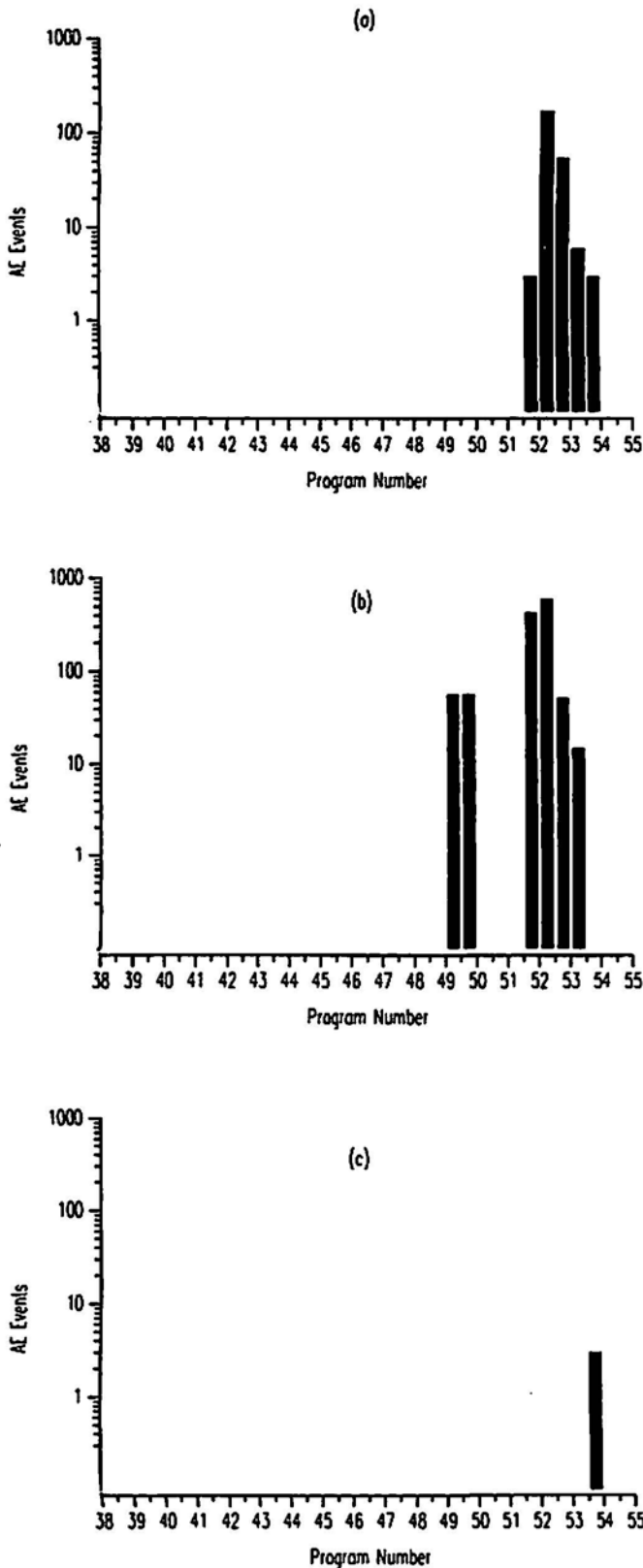


Fig. 8 The dependence on loading program number (from program 38 up to failure) of the starboard AE event rates (per half load program) corresponding to (a) indication 2, (b) indication 3 and (c) indication 4. (Note that data for the several half-programs were not stored due to equipment malfunction - see Table 1 and Fig. 2).

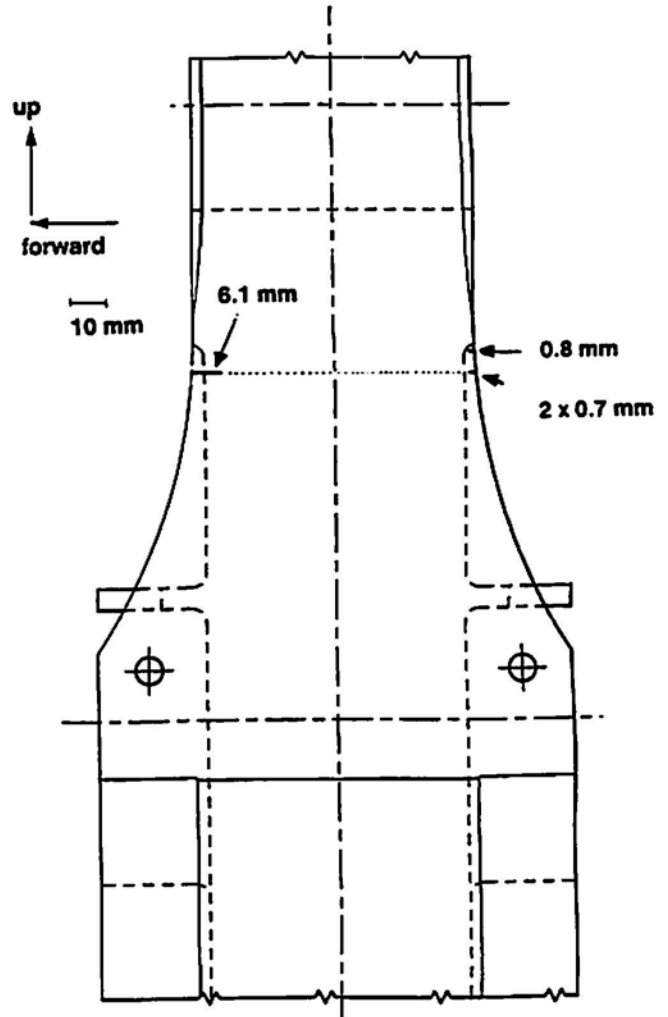


Fig. 9 2D sketch of port side of the bulkhead on which failure occurred from a crack originating above the cured section of the forward port mold-line flange: Depths of those cracks greater than 0.5 mm measured by fractography after bulkhead failure along the dotted line are shown.

site of the crack causing the bulkhead's failure (Fig. 9) (Barter et al., 1991). Fractographic examination showed that this fatigue crack was (i) about 0.5 mm deep at program 46 when the AE processing first gave indication 1, (ii) 2 mm deep at program 52 when further AE was obtained corresponding to indication 1, (iii) 3 mm deep at program 53 when the rapid increase in indication 1 AE commenced, and (iv) 6.1 mm in depth just before bulkhead failure.

On the starboard side of the bulkhead, fractographic examination showed that the AE cracking indication 2 (Fig. 7) corresponded to a group of centerline cracks on the starboard outer face of the bulkhead (Fig. 10). The maximum depth of these cracks was 0.8 mm when AE indication 2 was first obtained and ranged up to a depth of 3 mm at bulkhead failure. AE indication 3 corresponded to the deepest crack in the starboard section - the crack was 0.6 mm deep when first detected by AE and 4.4 mm deep at bulkhead failure. For the few AE events from cracking indication 4 (Fig. 7), a small crack of depth 0.6 mm and a large group of cracks to a maximum depth of 0.8 mm were pre-

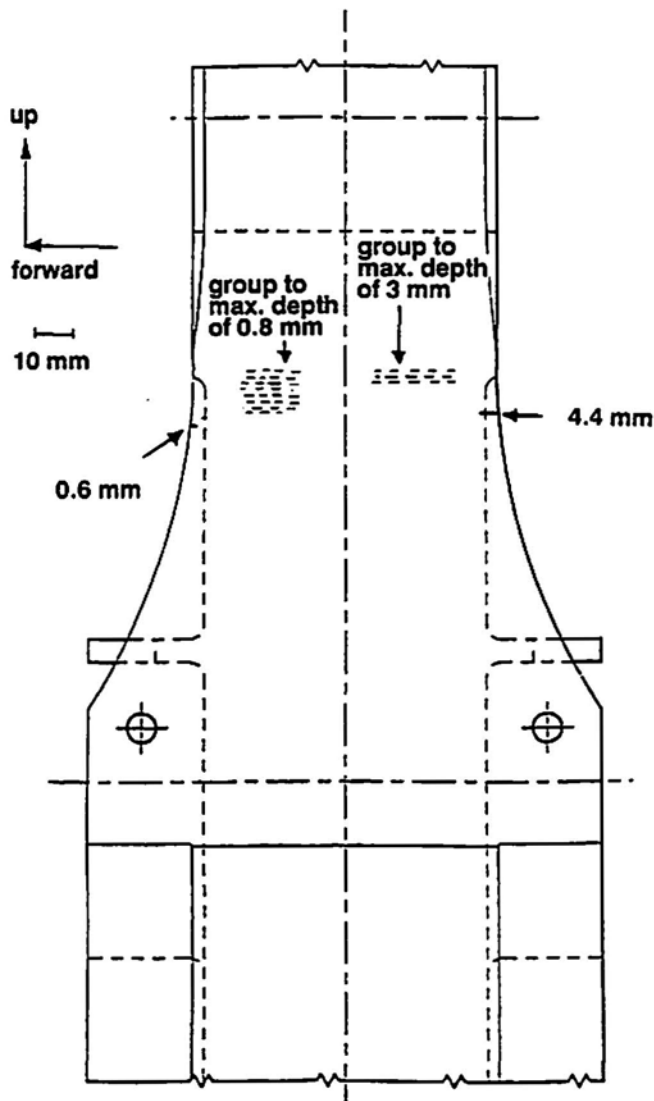


Fig. 10 2D sketch of starboard side of the bulkhead showing depths of those cracks greater than 0.5 mm measured by fractography after bulkhead failure - for each group of center-line cracks, the arrow corresponds to the coordinate in the forward direction of maximum crack depth.

sent at the two possible AE source locations 4a and 4b, respectively (Fig. 10).

Extensive visual, metallographic and nondestructive inspection indicated that no other cracks greater than 1 mm in depth were present in the port or starboard sections at bulkhead failure (Barter et al., 1991). However, numerous tightly-closed cracks smaller than 1 mm in depth were present, including several greater than 0.5 mm in depth which were broken open for fractographic examination, viz., (i) two 0.7 mm deep cracks on the port aft edge of the failure plane, and (ii) an 0.8 mm deep crack on the port aft edge above the fracture plane (Fig. 9).

Examination of the fracture surfaces of the 6.1 mm deep port crack (Barter et al., 1991) showed that a rapid increase in crack propagation rate had occurred from program 45 onwards.

This increase was associated with (i) increased out-of-plane crack deviation, (ii) evidence of multi-site crack reinitiation and branching, and (iii) isolated pockets of overload-type tearing behavior. All of these contributed to an increase in fracture surface roughness from program 45 onwards. A further, more substantial, increase in roughness occurred from program 51 up to failure, corresponding to the consolidation of the overload failure areas into discrete tear bands. Thus, from a crack depth of about 1 mm the crack advanced in large, rapid jumps involving significant ductile tearing. As with the port crack, the starboard cracks greater than about 1 mm in depth exhibited substantial ductile tearing, together with increasing surface roughness for the remainder of the test.

Examination of the microstructure of the bulkhead aluminum alloy showed the presence of inclusions which varied up to 100 μm in length and 5 μm in thickness. Inspection of crack fracture surfaces after failure of the bulkhead showed the occurrence of some fractured inclusions only at crack depths greater than about 1 mm.

4. Discussion

The AE monitoring of the F/A-18 bulkhead was successful in that all major cracks, including the port crack which caused failure of the bulkhead, were identified in the AE data processing following completion of the fatigue test. The crack depth at which AE was first detectable was about 1 mm for all cracks occurring in the bulkhead, although substantial emission from the port crack which caused failure was only obtained after the crack reached a depth of 2 mm. As in previous AE monitoring of fatigue tests of aircraft components (Scala and Coyle, 1987; Scala et al., 1989), the AE activity from extraneous sources in the bulkhead test was extremely high. Nevertheless, this study provides further evidence that AE associated with cracking can be distinguished, even when a complex structure is monitored and many extraneous sources are present.

In the bulkhead test, the likelihood of detecting cracks by AE was maximized by identifying crack-related AE on the basis of the combined features of AE associated with crack propagation and crack-face rubbing. Whilst an understanding of which of these possible sources gave the crack-related AE is not essential here, consideration of the results of stage III in AE processing and the morphology of the fracture surface should give some insight into the AE generation mechanism. In particular, during steady fatigue crack propagation in aluminum alloys, the detectability of AE has been linked indirectly to the presence of fractured inclusions (Buttle and Scruby, 1990a and b; McBride and Harvey, 1987; Scala et al., 1989) - fractured inclusions were observed on fracture surfaces from the bulkhead from a crack depth of about 1 mm when AE cracking indications were first obtained. Also, from this crack depth there was a consolidation of isolated overload failure areas into ductile tear bands - this cracking process is known to be acoustically "noisy", at least in some steels (Clark, 1977). Various fracture surface features which have been correlated previously with substantial AE from crack-face rubbing were also observed from a crack depth of about 1 mm, viz., significant surface roughness and multiple crack branching (Martin, 1984; Mori and Obata, 1988). Hence, the fractographic results provide inconclusive evidence as to the crack-related AE source detected in

the bulkhead test. More insight into this AE source can be gained by a comparison between the detailed features of the AE from the bulkhead obtained in stage III in processing and the expected features for AE due to crack propagation (whether related to steady propagation or ductile tearing) and due to crack-face rubbing. In particular, at least some of the AE events due to crack propagation should occur on high loads towards the maxima in load cycling, based on our previous laboratory studies during the application of a single overload amidst otherwise constant amplitude load cycling (Scala and Cousland, 1985) and also aircraft studies of overload-related cracking (McBride and Maclachlan, 1984; Scala and Coyle, 1987). Also, AE events due to crack propagation should have a wide range of amplitudes (McBride and Maclachlan, 1984). Therefore, the fact that, for all the cracks detected in the bulkhead, the crack-related AE occurred over a narrow range of amplitudes and only at relatively low loads is inconsistent with crack propagation as the source. However, such observations are consistent with AE obtained from crack-face rubbing for relatively long cracks, both during constant amplitude testing (Graham and Elsley, 1983; Kim and Weertman, 1984; Lindley et al., 1978; Mori and Obata, 1988) and during our series of single overload studies. Clearly, confirmation that crack-face rubbing was the source detected in the bulkhead would require further studies to establish whether the features for rubbing AE under simple loading conditions are also observed under simulated flight loading. Whether such studies would be cost-effective could be questioned, provided that the source detected is a reliable crack indicator (see below).

The hypothesis, that AE from crack propagation (whether associated with steady fatigue crack growth or ductile tearing) was not detected in the present test, requires some consideration, as this source has been detected in other aircraft aluminum alloys, both in laboratory studies (Buttle and Scruby, 1990a; McBride and Harvey, 1987; Scala and Cousland, 1985; Scala et al., 1989) and also during monitoring of other aircraft components (McBride et al., 1991; Scala and Coyle, 1987). Various factors are likely to affect the detectability of AE due to crack propagation in an aircraft aluminum alloy in a given test, particularly (i) the inclusion size distribution, (ii) the matrix condition, (iii) loading conditions, (iv) crack length and propagation rate, including the extent of any overload, (v) the source-sensor separation, and (vi) the sensitivity of the AE sensor. The effects of factors (i)-(iv) are difficult to assess. In particular, while long, thin, fractured inclusions were found on fracture surfaces from the bulkhead (see Sec. 3.3), the inclusion size distribution has yet to be determined for representative bulkhead material. Also, specific loading conditions and alloy heat treatment affect greatly the detectability of AE due to crack propagation (McBride and Harvey, 1987; Scala and Cousland 1985; Scala et al., 1989). Hence, fundamental studies on overload-related AE in representative bulkhead material would be needed to assess adequately the effects of factors (i)-(iv). A consideration of factor (v) shows that, in retrospect, the placement of sensors in the bulkhead test was far from ideal due to the lack of knowledge of all fatigue-critical regions at the start of testing (see Sec. 2.1). Hence, sensitivity was reduced compared to our previous testing because the sensors were not only up to a factor of 25 further away from the cracks in the bulkhead than from cracks monitored in our laboratory studies but also more distant than from cracks detected in our previous aircraft moni-

toring. The use of a sensor with a small contact area was necessary in the bulkhead test due to the existence of several constraints, viz. space limitations, the need for meaningful feature extraction to reject numerous extraneous events, and also the requirement for accurate time-of-flight event location (see Sec. 2.1). However, the type of sensor necessary for the bulkhead test was much less sensitive than that used in our previous laboratory studies on aluminum alloys in which sensor selection could be made without the constraints discussed above. Thus, our hypothesis that AE due to fatigue crack propagation was not detected in the present test but had been in some previous studies is consistent with some reduction in detection capability due a combination of factors (v) and (vi) above, and could also be affected by factors (i)-(iv). Clearly, the effects of factors (v) and (vi) could be modified in future bulkhead tests to improve the likelihood of detecting AE associated with crack propagation as well as crack-face rubbing.

In the present F/A-18 bulkhead test, the AE source detected was very reliable, allowing identification of all cracks at a similar depth. However, the hypothesis that the detected AE was associated with crack-face rubbing rather than crack propagation needs consideration in terms of the possible reliability of AE for future bulkhead monitoring. In particular, rubbing is by its nature an erratic process. Hence, AE from rubbing has usually been characterized by erratic features such as occurrence for many cycles at one position on the positive gradient of the load cycle before ceasing completely or starting up at a different position on the positive gradient (Graham and Elsley, 1983; Kim and Weertman, 1984; Lindley et al., 1978; Mori and Obata, 1988). The erratic behavior of crack-face rubbing could account for the decrease in AE activity from cracks 2 and 3 just before bulkhead failure (Fig. 8), although this decrease could also have been due to loss of data in the AE data overflows towards the end of the test. While reliability of crack detection could be questioned for a rubbing AE source, some differences in the reliability of a possible crack propagation source would also be expected in the anisotropic bulkhead material for crack propagation along different directions. Hence, all of the above suggest that AE monitoring of additional bulkhead tests is required to establish the reliability of the AE technique for F/A-18 monitoring. Additional monitoring is also required of a painted bulkhead, as bulkheads fitted to operational aircraft are painted, unlike the free-standing bulkhead in the ARL test, and paint disbonding is one of the many spurious AE sources which are likely to cause complications.

Another reliability factor which should be considered in future bulkhead tests is the establishment of confidence limits on the number of AE events required for reliable crack prediction. In the present test, each bulkhead crack was detectable from a crack depth of about 1 mm, with a large number of AE events being obtained for AE cracking indications 2 and 3 from this depth. However, while AE cracking indication 1 was first obtained at a crack depth of about 1 mm, substantial activity was only obtained when the crack reached a depth of 2 mm (Fig. 4 and Sec. 3.3). Hence, prediction of crack 1 at a relatively small depth would have required confidence in the validity of only a small number of AE events.

Several modifications to data acquisition are required if optimal advantage is to be gained from AE monitoring of fur

ther bulkhead tests. Improved discrimination between crack-related AE and extraneous sources could be achieved by the use of (i) additional sensors to extend the present 2D analysis to a more realistic 3D analysis, and (ii) guard sensors which are invaluable for eliminating extraneous sources. Moreover, increased AE sensitivity to cracking and also improved location accuracy could be gained by attaching sensors close to all the fatigue-critical regions (rather than near the limited number of regions identified at the start of the ARL fatigue test). Then, problems of overlapping criteria, such as obtained for cracks 1 and 4, could be significantly reduced. While location accuracy could be improved for a free-standing bulkhead test, consideration also needs to be given to likely limitations in space availability for array attachment in an aircraft application. Ideally, future bulkhead fatigue tests would result in evaluation of both optimal ground and in-flight array configurations.

Re-evaluation of possible AE sensor types would also be of value for future bulkhead monitoring. In particular, while the type of sensor used in the present study was ideal for accurate source location and pattern recognition analysis, both the sensor's length and susceptibility to disbonding if knocked sufficiently hard would make the sensor unsuitable for flight applications. Also increased sensor sensitivity could lead to improvements in the detectability of cracking. Currently available alternatives include the point-contact sensor (Buttle and Scruby, 1989, 1990a, b) which would have similar limitations to the type of sensor used in the present work and more resonant sensors whose use would lead to a degraded capability for eliminating extraneous sources. Hence, some sensor development research could facilitate possible in-flight applications.

Consideration also needs to be given to overcoming the problems of the data overflows experienced late in the present bulkhead test. The development of a more dedicated AE data acquisition system which allowed faster data acquisition would prove useful for this purpose. In the present study, catastrophic failure occurred only one program after the crack causing failure gave substantially increasing AE (Fig. 4). However, even half a loading program would be sufficient to identify such cracking in a component, provided that some real-time processing was incorporated in the data acquisition system. Certainly, the development of real-time processing would be required if AE monitoring of an operational F/A-18 aircraft were to become a reality.

5. Conclusions

AE processing following completion of the fatigue test of the F/A-18 FS 488 bulkhead was successful in that all major cracks, including the port crack which caused failure of the bulkhead, were identified. The crack depth at which AE was detectable was about 1 mm for all cracks occurring in the bulkhead, although substantial emission from the port crack causing failure was only obtained when the crack reached about 2 mm in depth. The data processing suggested that the crack-related AE events in the bulkhead were attributable to crack-face rubbing rather than crack propagation, although background studies of AE from the bulkhead material under random loading conditions would be required to confirm this suggestion. The study shows that AE associated with cracking can be distinguished, even when many extraneous sources are present and a

complex structure is monitored. The study also demonstrates that AE is worth pursuing further as a possible technique for future nondestructive evaluation of the F/A-18 bulkhead.

AE monitoring of additional bulkhead fatigue testing is required to establish confidence limits in terms of the number of AE events required for reliable crack prediction in bulkheads in operational F/A-18 aircraft. For such future fatigue testing, the present study has allowed recommendations to be made for the development of AE equipment to improve the AE detectability of cracking (for AE sources associated with both crack-face rubbing and crack propagation). The promising results obtained in the present bulkhead AE study should provide the impetus for such equipment development.

Acknowledgments

Numerous ARL staff have made considerable contributions during the two years of AE monitoring of the F/A-18 bulkhead test. B.C. Bishop carried out AE sensor attachment throughout the test, and also provided useful advice on NDE for the bulkhead. P. Bates assisted with AE data storage. L. Sponder designed and constructed the load interface to the DART. S.A. Barter provided all the fractographic information used in the paper, and he and Dr. G. Clark provided useful insight into failure mechanisms in the bulkhead. Finally, Dr. S.K. Burke provided valuable advice and encouragement throughout the bulkhead monitoring.

References

- I. Anderson and G. Revell (1990), "F/A-18 fuselage station 488 free-standing bulkhead fatigue test", DSTO Aeronautical Research Laboratory Aircraft Structure Tech. Memo AR-006-111.
- S.A. Barter, B.C. Bishop and G. Clark (1991), "Assessment of defects in F/A-18 488 bulkhead test article," DSTO Aeronautical Research Laboratory Aircraft Materials Report AR-006-618.
- D.J. Buttle and C.B. Scruby (1989), *NDT Internat.*, **22**, 81-96.
- D.J. Buttle and C.B. Scruby (1990a), *J. Acoustic Emission*, **9**, 243-254.
- D.J. Buttle and C.B. Scruby (1990b), *J. Acoustic Emission*, **9**, 255-269.
- G. Clark (1977), *Metals Science*, **11**, 531-537.
- L.J. Graham and R.K. Elsley (1983), *J. Acoustic Emission*, **2**, 47-55.
- P.H. Hutton (1985), "Develop in-flight acoustic emission monitoring of aircraft to detect fatigue crack growth - Volume I," NADC Report 85012-60.
- C.J. Kim and J. Weertman (1984), *Microstructural Characterization of Materials by Nonmicroscopical Techniques*, ed. N. Hessel Anderson et al., RISO National Laboratory, Denmark, pp. 349-353.

T.C. Lindley, I.G. Palmer and C.E. Richards (1978), *Mater. Sci. Engng.*, **32**, 1-15.

S.L. McBride and J.W. Maclachlan (1984), *J. Acoustic Emission*, **3**, 1-9.

S.L. McBride and J.L. Harvey (1987), *Review of Progress in Quantitative Nondestructive Evaluation 6A*, ed. D.O. Thompson and D.E. Chimenti, Plenum, NY, pp. 353-360.

S.L. McBride, M.R. Viner and M.D. Pollard (1991), *Review of Progress in Quantitative Nondestructive Evaluation 11*, ed. D.O. Thompson and D.E. Chimenti, Plenum, NY (in press).

G.G. Martin (1984), "Acoustic emission from 4340 steel during fatigue", Ph.D. Thesis, Monash University, Australia.

Y. Mori and Y. Obata (1988), *Nondestructive Testing Commun.*, **4**, 11-21.

C.M. Scala and S. McK. Cousland (1985), *Mater. Sci. Engng.*, **76**, 83-88.

C.M. Scala and R.A. Coyle (1983), *NDT Internat.*, **16**, 339-343.

C.M. Scala and R.A. Coyle (1987), *J. Acoustic Emission*, **6**, 249-256.

C.M. Scala, S.J. Bowles and I.G. Scott (1989), *Internat. Advances in Nondestructive Testing*, **14**, ed. W.J. McGonagle, Gordon and Breach, New York, pp. 219-258.

I.G. Scott (1981), *Proc. 13th Symposium on Nondestructive Evaluation*, ed. B.E. Leonard, NTIAC, pp. 210-219.

G. Weatherly, J.M. Titchmarsh and C.B. Scruby (1986), *Mater. Sci. Technol.*, **2**, 374-385.

Maximum Curvature Method: A Technique to Estimate Kaiser-Effect Load from Acoustic Emission Data

M. Momayez, F. P. Hassani and H. R. Hardy, Jr.

Abstract

This paper presents an objective technique to estimate previous stress level from a Kaiser effect experiment. The maximum curvature method can be easily implemented as a computer program, thus allowing a large amount of data to be processed automatically. It is shown that this technique is more efficient than another objective method, method of tangents, in terms of accuracy and speed of execution. The only disadvantage in using the maximum curvature method is the fact that its performance may be hampered if few acoustic emission data recorded at a low sampling rate are available.

1. Introduction

For many years, the only method to estimate the Kaiser-effect load from acoustic emission (AE) data was to plot time or load versus cumulative AE count and to determine the previous level by eyeballing the deflection point in the curve (Kanagawa et al., 1976). Although this method produces good results if high resolution data is available, it requires some experience in detecting the exact point where the change in the slope occurs. More recently, objective techniques such as the method of tangents have been proposed (Boyce, 1981). These methods call for some level of judgement in the analysis of data and the results may not be particularly consistent or accurate.

The present paper discusses the details of an improved technique first applied by Momayez et al. (1990). The method estimates the curvature at each point along the Kaiser-effect curve and provides the exact location of the deflection point, which can then be used to determine the previous load level. The method can be implemented easily as an algorithm on a computer. It is shown that if the number of data points are large enough, the maximum curvature method provides consistent and precise estimate of the Kaiser-effect load.

2. Methods of Estimating Kaiser Effect

In order to obtain the previous stress level in a sample under load, it is customary to plot time or load readings versus the cumulative number of AE events recorded during a test. The point where the curve changes its slope is usually used to estimate the Kaiser effect.

This technique was first used by Kanagawa et al. (1976) to estimate stresses in rocks. Their slope change method to determine the geo-stress in an underground power plant in Japan was demonstrated using tuff samples. The in-situ stresses estimated by the AE method were then compared with the values obtained from the overcoring method. Because the average geo-stress component estimated by the AE (slope change) method was higher than the one using the overcoring method, they speculated that the stresses obtained by the Kaiser-effect technique correspond to the maximum stress imposed on the rock mass during the long geological age rather than the existing in-situ stress.

There are some cases where the Kaiser effect cannot be observed clearly by plotting the data using the slope change method. Yoshikawa and Mogi (1981) presented another method to remedy this situation. Their difference method consisted of loading the sample once and plotting the data as load or stress versus cumulative AE counts. If one reloads the sample after unloading, it can be seen that the AE activity for the second loading cycle is very different from the first cycle. Since the difference begins to increase markedly at the known previous maximum, they used this difference to estimate the stress.

Hayashi (1979) suggested a difference method based on the sum of AE rate and the sum of AE rate squared. This technique was employed to successfully determine the anisotropic stress state in a deep excavation near a nuclear power plant in Japan. This technique requires one load cycle and AE data must be expressed as AE rate for the sample tested.

A somewhat objective procedure for determining the previous maximum stress has been employed by Boyce (1981). Here, tangents were drawn to the quiet as well as the more active portions of the stress versus AE data. The intersection of these tangents were then used to define the required stress value. Hardy et al. (1985) applied statistical methods to the reload stress versus incremental and total count data, in order to estimate the applied load.

Hughson and Crawford (1988) used the felicity ratio to improve the estimates of stress using the Kaiser-effect method. The felicity ratio is defined as the ratio of the stress estimated using acoustic emissions divided by the known previous maximum stress. By determining the felicity ratio for a given material at different stress levels, a felicity ratio profile is generated by joining the points plotted on a graph of recalled stress versus felicity ratio. This profile is then used to improve the Kaiser-effect load obtained from an experiment through a series of iterations.

All the methods used to determine the Kaiser-effect load are based to various degree on the judgement of the person per

Received 18 January 1992. M. Momayez and F.P. Hassani are affiliated with Department of Mining and Metallurgical Engineering, McGill University, Montreal, Canada H3A 2A7 and H.R. Hardy, Jr. is with Department of Mineral Engineering, The Pennsylvania State University, University Park, PA 16802.

forming the analysis. The statistical approach used by Hardy et al. (1985) is the first attempt at automating the process of analyzing AE data in the search for previous stress. The problem with this technique is that if one takes the best fit tangents (using linear regression) to the stress or time versus cumulative AE counts, it is not guaranteed that the intersection of the two lines would produce acceptable values for the Kaiser-effect load. In such cases, some degree of personal judgement must be exerted to adjust the slope of either or both tangent lines in order to get more accurate values.

A totally objective method for determining the Kaiser-effect point is valuable in the sense that it could be implemented as an algorithm, therefore accelerating the process of data analysis and allowing stress values to be estimated using the same set of rules. In addition, in cases where the change in the slope of the stress or time versus cumulative acoustic emission data is not sufficiently sharp to guarantee the correct detection of the Kaiser-effect point, an objective method would provide the most accurate estimate of the previous load.

3 Maximum Curvature Method

Consider a typical Kaiser-effect curve. The change of slope is indicative of the effect of the previous load applied to the specimen. This manifestation of the effect of past load may occur at a slightly higher or lower load level than the one applied previously, depending on the specimen state and test conditions.

The Maximum Curvature Method (MCM) implements the idea of detecting the change in the slope of the Cumulative Acoustic Emission (CAE) data by calculating the amount of curvature along this curve. The maximum value for the curvature corresponds to the deflection point (i.e., the graph of time versus CAE is most "curved" around the Kaiser-effect point) which is used to obtain the Kaiser-effect load or stress.

There are different approaches available to calculate the curvature; e.g., see Pang (1975). The method that provides the best results with the data obtained from a Kaiser-effect experiment was found to be the one that computes the rate of change of the angle. This idea can be most simply described as follows: the time or load versus CAE curve has an "exponential" shape, that is, it has the greatest curvature where the change in the slope occurs, while the remaining portions can be approximated by straight lines. If one calculates the angle θ between this curve and the horizontal x-axis and differentiates the resulting series, a measure of the curvature along the entire length of the curve may be obtained. Denoting the curvature by K and the angle by θ , we have:

$$\theta = \arctan(\text{CAE}/\text{time})$$

$$K = d\theta/dt$$

Assuming that the AE data is sampled at an interval of one second and the angle θ is expressed in radians, then the curvature K will be in radians per second.

3.1 Measuring the Maximum Curvature of the Exponential Function.

The analytical formula for the curvature K of a function, f , at the point (a,b) is given by Pang (1975):

$$K = \left| \frac{f''(a)}{(1 + [f'(a)]^2)^{3/2}} \right|$$

where $f'(a)$ and $f''(a)$ are the first and second derivatives of the function f at the point a . Let us now calculate the maximum curvature of the exponential function $f(x) = e^x$. Since $f(x) = e^x = f'(x)$, the formula for the curvature becomes:

$$K = \frac{e^x}{(1 + e^{2x})^{3/2}}$$

Differentiating K with respect to x and setting $dK/dx = 0$, we obtain the critical value for x :

$$x = -\ln \sqrt{2} = -0.347.$$

Therefore the exponential function has its maximum curvature at $x = -0.347$. Figure 1 presents the graph of the exponential function over the interval $[-5, 4]$ as well as its calculated curvatures using the analytical formula and the Maximum Curvature Method. In addition, the plot of the exponential function shows a curvature around the point $x = 2$ which can be seen by the eye. The analytical formula for the curvature cannot discriminate this fact and therefore it does not show up in the graph.

However, the estimated curvature using the Maximum Curvature Method described above has its minimum and maximum value at $x = -0.343$ and $x = 2.074$ respectively. These values correspond to the maximum curvature determined analytically ($x = -0.347$) and the one that appears in the graph of the exponential function around the point $x = 2$.

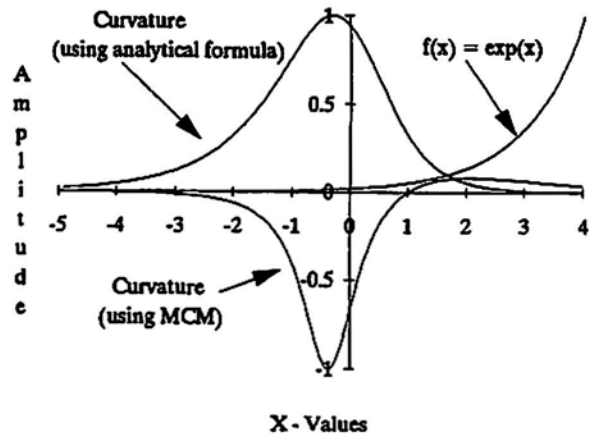


Fig. 1 Graph of exponential function and its curvatures.

3.2 Application of Maximum Curvature Method to Acoustic Emission Data

In order to compute the curvature of the cumulative AE data, the Kaiser-effect curve must be smoothed before the MCM technique is applied. The amount of smoothing that one

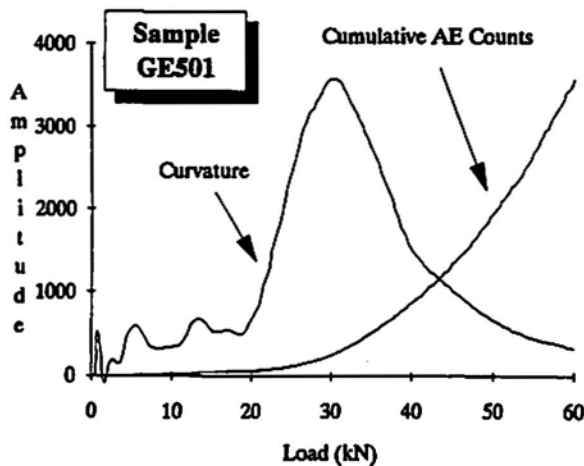


Fig. 2 Kaiser-effect curve and related curvature using raw CAE data.

applies directly affects the position of the deflection point in the time or load versus CAE curve. Depending on the quality and quantity of AE data, a number of criteria can be developed to stop the smoothing process. For example, the chi-square test can be run to find out the degree of departure from the original CAE data. A maximum deviation of 0.5% is usually sufficient to produce the desired results. In general, the smoothing process may be stopped as soon as a degree of departure equal to 0.1% to 0.3% with respect to the original series is achieved.

To test the Maximum Curvature Method on experimental data, 4-cm diameter Stanstead Granite cores were loaded to a maximum level of 30 kN under displacement control and held there for 5 minutes. The second load cycle was applied few hours later and the maximum level was allowed to reach 60 kN. For the second loading stage, the AE data was collected at a sampling interval of one second. A 250 kHz resonant frequency transducer was used, while the monitoring system amplification and threshold were set at 54 dB and 5 mV, respectively.

Table 1 Results of estimating Kaiser effect using MCM and the method of tangents.

Sample (number)	First Load (kN)	Estimated Load Maximum Curvature (kN)	Estimated Load Method of Tangents (kN)
GES01	30.4	29.634	34.249
GES02	30.6	29.391	34.735
GES03	30.5	33.763	39.107
GES04	30.2	30.848	35.463
GES05	30.8	30.484	37.407
GES06	30.3	31.091	36.799
GES07	30.2	32.053	39.471
GES08	30.6	30.848	39.107
		average = 30.818	average = 37.042
		variance = 1.250	variance = 4.320
		time = 190.370 sec	time = 2715.63 sec

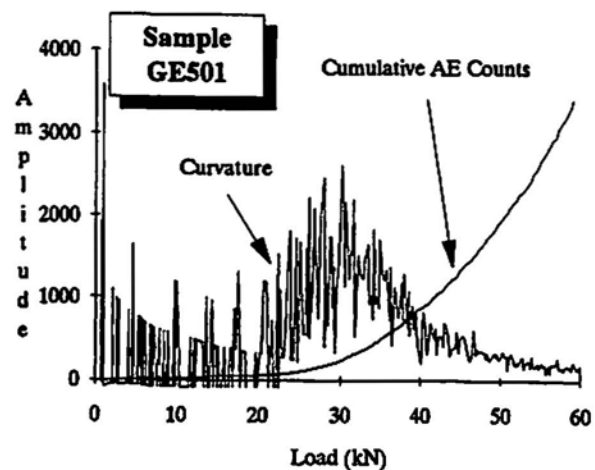


Fig. 3 Kaiser-effect curve and related curvature using smoothed CAE data.

Figures 2 and 3 present the curvature as a function of load (kN) for the sample GE501. In Fig. 2, the raw CAE data was used to calculate the curvature. In this case, the Kaiser-effect load was calculated to be 33.9 kN. Figure 3 shows the curvature for processed CAE data using a 5-point averaging filter. It can be seen that smoothing CAE data affects greatly the shape of the curvature graph and the previous load using smoothed data was calculated to be 29.6 kN. Table 1 presents the results for 8 Stanstead Granite samples by applying the Maximum Curvature Method and the Method of Tangents.

4. Discussion

Although Figures 2 and 3 show the Kaiser-effect curve and its calculated curvature as a function of load, it was found that plotting the data as a function of time produces much sharper and smoother curves. Figure 4 shows the same data as in Fig. 3 plotted as a function of time. The reason for the increased sharpness is that the time-based data is sampled at a constant rate; that is, the independent series (x-axis) increases evenly. For the same reason, when the curvature is computed, the CAE data is differentiated with respect to time instead of load or stress.

In addition, another computer program was developed to estimate Kaiser-effect loads using the Method of Tangents. The program was provided with two search algorithms namely, (1) fast search and (2) complete search. Both algorithms fit two straight lines to the quiet and active portions of the CAE curve in the least-squares sense. The complete search algorithm looks for the set of all straight lines fitting the CAE curve through a series of iterations by applying the chi-square test until the best two lines are found. The complete search algorithm was selected in this study and the goodness of fit for all the samples analyzed was better than 99%. The intersection of the two straight lines was used to estimate the Kaiser-effect load. As shown in Table 1, the Maximum Curvature Method processes the data in a much shorter time and more accurately than the Method of Tangents. The reported execution time (in seconds) is the time it took to analyze all eight data files on a

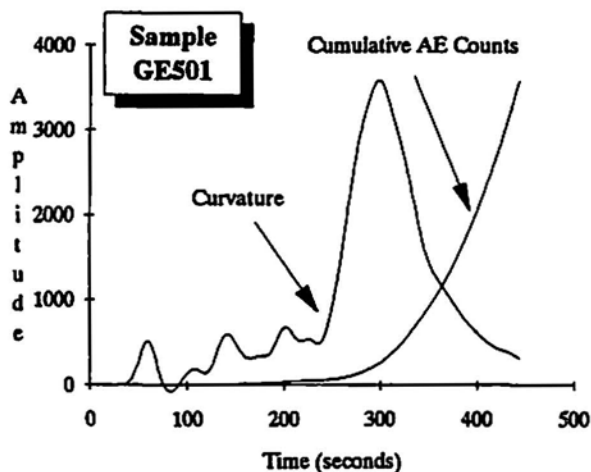


Fig. 4 Kaiser-effect curve and related curvature using smoothed CAE data as a function of time.

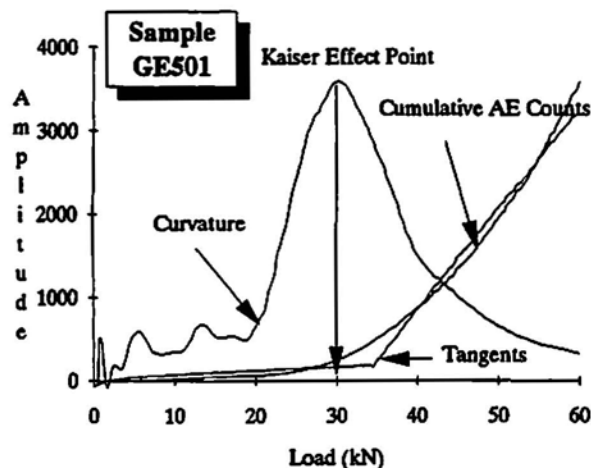


Fig. 5 Previous load estimates using MCM and method of tangents.

microcomputer (with 25-MHz 80386 processor) using the GAUSS Mathematical and Statistical System. Figure 5 presents the results for sample GE501 using both methods.

The Maximum Curvature Method was also used to analyze a large amount of AE data. It was found that the accuracy of values produced by using this technique depends on two important factors. The first is data quality, that is the CAE data must clearly show a deflection point in the vicinity of the Kaiser-effect load. The second concerns the number of data points collected during the experiment. When more data is available for a given test, the CAE curve will have better resolution and the Maximum Curvature Method will provide more accurate values.

Let us consider the situation where few data points (less than 100) are available. The amount of smoothing applied (using a 5-point averaging filter) to the data will affect to a great extent the shape of the Kaiser-effect curve. For example, when the 5-point averaging filter was applied 7 times to 66 data points sampled at an interval of 10 seconds from a limestone specimen, the difference between the two curves was found by applying the chi-square test to be about 1.783%.

However, the 444 data points from specimen GE501 sampled every one second produced a degree of departure equal to 0.214% of the raw data when the averaging filter was applied 51 times. Figure 6 shows the curvature along with the raw and smoothed CAE curves for the limestone sample. The original CAE curve displays a very sharp Kaiser-effect point at 34.8 MPa while the maximum curvature calculated using the smoothed CAE curve provides a stress value of 33.1 MPa. The agreement between these two estimates can be attributed to the quality of AE data; i.e., the Kaiser-effect curve possesses a very sharp deflection point at the previous stress level.

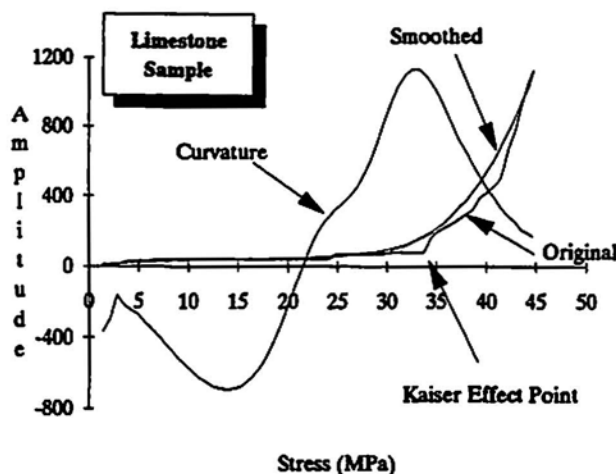


Fig. 6 Application of MCM to short but well-defined Kaiser-effect data.

In general, if one wishes to use the Maximum Curvature Method it would be more appropriate to sample the data at a high rate for the whole duration of the experiment. As far as smoothing the data is concerned, the treated data should not deviate more than 0.3% from the original set depending on its quality and quantity, in order to keep the location of the deflection point within the correct range. Further tests are being carried out to investigate thoroughly the performance of the Maximum Curvature Method on poor quality data.

5. Conclusion

Studies have shown that a computer-based Maximum Curvature Method can be used to analyze Kaiser-effect data obtained from various rock samples. The method produces accurate results if conditions such as (1) the quality of data, in terms of the presence of a well defined deflection point at the previous maximum and (2) the amount of data, in terms of a relatively high sampling rate are met. Another point to take into account when using this method is the degree of smoothing applied to the original data. Studies have shown that if smoothing is applied indiscriminantly, the location of the deflection point will change and the correct Kaiser-effect load may not be obtained.

References

G.L. Boyce (1981), "A Study of the Acoustic Emission Response of Various Rock Types", Master of Science thesis, Drexel University, Philadelphia.

H.R. Hardy, D. Zhang and J.C. Zelanko (1985), "Recent Studies of the Kaiser Effect in Geological Materials", *Proc. Fourth Conference of AE/MS Activity in Geological Structures and Materials*, TransTech Publ., Clausthal-Zellerfeld, Germany, pp. 27-55.

M. Hayashi (1979), "Acoustic Emission to Detect the Geostress", *Proc. 4th International Congress, Rock Mechanics Symposium*, Montreux, Switzerland.

D.R. Hughson and A.M. Crawford (1988), "Felicity Ratio: A Significant Factor in the Determination of Previous Stress through Kaiser Effect Gauging." *Proc. 15th Canadian Rock Mechanics Symposium*, Toronto, Canada, ed. J.H. Curran, pp. 147-154.

T. Kanagawa, M. Hayashi and H. Nakasa (1976), "Estimation of Spatial Geostress Components in Rock Samples using the Kaiser Effect of Acoustic Emission", *Proc. 3rd Acoustic Emission Symposium*, Tokyo, Japan.

M. Momayez, F.P. Hassani and H.R. Hardy (1990), "Stress Memory Measurement in Geological Materials using the Kaiser Effect of Acoustic Emission" *Proc. 10th International Acoustic Emission Symposium*, JSNDI, Tokyo, Japan, pp. 476-482.

L.C.F. Pang (1975), "A Method for Measuring the Curvature of a Boundary on a 2-Dimensional Quantized Grid", Master of Science thesis, McGill University, Montreal.

S. Yoshikawa and K. Mogi (1981), "A New Method for Estimation of the Crustal Stress from Cored Rock Samples: Laboratory Study in the Case of Uniaxial Compression", *Tectonophysics*, 74, 323-339.

AEWG 36th Meeting

One difference between the transformation behaviors of $\beta_1 \rightarrow \beta'_1$ and $\beta_1 \rightarrow \gamma'_1$ was discussed from this point of view, and the effect of fatigue damage on the change of this velocity, was examined. AE measurements were made using two wide band AE transducers (M5W). AE signals were amplified at a constant gain of 60 dB through a bandpass filter of 100 kHz to 1 MHz. Detected AE waveforms were analyzed by off-line FFT.

Results obtained are as follows: (1) In the γ'_1 transformation which has larger hysteresis, a large number of AE events and higher amplitude AE were observed in the loading process. (2) The risetime of AE source, which is related to the transformation velocity in the γ'_1 transformation, was shorter than in the β'_1 transformation. (3) With increase of surface fatigue damage due to plane strain bending, the risetime became shorter in the β'_1 transformation because of the easiness of the transformation. From that result, it is considered that the risetime measurement would enable a new method of fatigue damage evaluation in these types of alloys.

Kanji Ono

Acoustic Emission Behavior of Composites: Cooperative Studies

While stationed in Japan for the past two years, I have worked with two groups on composite AE research. I will report on these results. One is AE monitoring during tensile fracture testing of resin-impregnated strands of high-strength, high-modulus pitch-based carbon fibers. This was done at Nippon Oil Co. with A. Nanjyo and M. Mohri. The influence of the degree of surface treatment and the Weibull coefficient of filament strength on AE behavior was also investigated. Resin-impregnated strands were made from pitch-based carbon fibers of a single lot with varying degrees of surface treatment. When the degree of surface treatment of the carbon fiber was low, many filament pull-outs were observed, accompanied by many long-duration ($>75 \mu\text{s}$) AE signals having high peak amplitudes. With high degree of surface treatment, almost no filament pull-outs and few long-duration AE signals were detected. Resin-impregnated strands were made with different filament strengths having Weibull coefficients between 5.7 and 13. When the Weibull coefficient of filament strength was high, AE signals were observed close to the fracture stress. When the Weibull coefficient was low, AE signals occurred over a wide range, beginning at low stress. Short-duration AE signals also exhibited a Weibull distribution, suggesting their origins of fiber fracture. Because of multiple fractures of a single fiber, however, the Weibull coefficients were greater than those measured for the filament tensile strength. These results indicated that the short-duration, low amplitude AE signals were caused by the fracture of individual carbon fibers. Comparison studies were also made with glass and PAN-carbon fibers.

The second group was at Aoyama Gakuin University with M. Takemoto and H. Suzuki. Displacement signals were detected from model composites (quartz fibers in polyester) and signal characteristics were compared with simulated emissions. Fiber fracture, delamination and debonding have each distinct signal behavior. Fibers treated with silane gave different results in terms of rise time and amplitude of P-waves.

Ed Lowenhar

Towards a Practical AE System using DSP

Digital signal process (DSP) is becoming more and more common place in today's world. This popularity has come about due to advances in high speed, high density digital integrated circuits, and the constantly declining cost of digital processing as a result of the high volumes and use in the military, industrial and commercial marketplace. The ability to convert an analog signal into a digital equivalent for the evaluation of AE signals has been an area of high interest in the NDT community as users are trying to find out as much about the received AE transient (frequency and time features) as possible. This presentation discusses the relative merits of digital signal processing of AE account in the design of a practical AE system.

Kusuo Yamaguchi

A View of Instrumentation and Signal Processing for AE Monitoring and Future Directions

Frank C. Beall

AE From Creep of Wood-Based Composites

Harold L. Dunegan

Quantitative Crack Growth Measurements by Use of AE

Acoustic Emission techniques have been used routinely for many years for the detection and location of growing

(Continued to page 90)

Acoustic Emission Measurements on Bridges

H. Hick, H. Willer, E. Winter and F. Simacek

Abstract

A short experimental program was carried out to investigate the suitability of acoustic emission analysis for the structural monitoring and checking of bridges. On a prestressed concrete bridge we could recognize typical sounds, which were interpreted as friction noises generated by loose rebars. Some flat Teflon supports were found to emit strong ultrasonic signals due to metallic contact after exhaustion of the radial gap. On a concrete box girder bridge a crack was investigated and diagnosed as still acoustically active, despite a previous repair attempt by injection.

1. Introduction

During the past ten years, we have concentrated on acoustic emission (AE) analysis as applied to the safety monitoring of large engineering structures of rock and concrete, like hydroelectric dams, deep mines and civil engineering structures. For such large structures AE analysis differs from seismology mainly by its smaller geometric scale and its higher signal frequencies (which are in the audible range) (Hick, 1982). Significant emission phenomena are fracture, friction and turbulent flow. Progressive material damage is accompanied by cracking noises, which should not be ignored, as the noises give advance warning of imminent structural failure.

Parallel to AE analysis in the context of rock burst research in a deep lead mine (Grube Stefanie der Bleiberg Bergwerksunion AG) and the permanent monitoring of a large hydroelectric dam (Kölnbreinsperre, Maltatal), we performed laboratory experiments on rock and concrete samples, prestressed concrete railway sleepers and a 10 m long prestressed concrete beam during 1978 - 1983 (Hick, 1986).

In all these investigations AE analysis proved to be a reliable indicator of progressive microstructural damage in advance of macroscopic fracture, except when high noise levels from some nearby mechanical equipment masked the AE signals. We were therefore not optimistic whether the traffic noise would allow any useful observations on a bridge during normal use. On the other hand, earlier laboratory experiments had shown that prestressed railway sleepers with deliberately cut prestressing cables produced characteristic audible ("ringing" and "ticking") sounds during bending deformation with increasing or decreasing loads, while intact samples produced only high frequency fracture noises (Hick et al., 1983). These char-

acteristic sounds were interpreted as due to a mechanical resonance of the partially loose rebar, excited by friction and/or progressive debonding fractures between rebar and concrete. We hoped therefore, that this could become the basis for a non-destructive inspection method for the detection of loose or broken prestressing cables in concrete bridges. However we were not sure that deformations due to normal traffic loads would be sufficient to produce these sounds and we were pessimistic with regard to the detectability of these characteristic sounds in the presence of strong background noise levels.

2. Experimental Equipment

Piezoelectric accelerometers (B&K 4370, AET AC30L, AET AC175L) were coupled via magnets to steel discs which had been glued to concrete surfaces. Signals were filtered (1-25 kHz, 15-45 kHz and 125-250 kHz), amplified by 80-100 dB and analysed in the field by an FFT-analyzer and also monitored by headphones. Further analysis in the laboratory was based on analog tape recordings and digital disk files from the FFT-analyzer.

3. Measurements on a Large Prestressed Concrete Bridge

The bridge, with an individual field span width of approximately 50 m, was known to have a number of prestressing cables, which had been inadequately injected. To optimize the signal-to-noise ratio, the transducers were mounted as close as possible to the suspected cables and as far away as possible from the road vehicle noise (at approximately half height of the I-beams at the underside of the bridge).

Traffic noise, as measured with the accelerometers, was concentrated in the 3 - 7 kHz range, with a mean level of approximately 500 μ -g. However, the noise varied strongly with individual passing vehicles. It became immediately obvious that the human auditory system was for that frequency range much better at identifying the various noise sources, than any signal analysis with the FFT-analyzer.

Each individual passing road vehicle produced a "hissing" sound, very similar to the familiar noise of a passing car on a wet road surface. This sound in the 5 - 15 kHz range is probably produced by the abrasive action of sand particles between the elastically deforming tires and the road surface. Some vehicles produced a periodic "rattling" sound, similar to the sound of a vehicle with snow chains on a hard road surface. Figure 1 shows that the signal consists of individual sharp peaks with an irregular pattern, which repeats itself with a period corresponding to a tire revolution at a typical vehicle speed of 66 km/h. The irregularity rules out ignition spark interference as a possible explanation. We concluded, therefore, that this noise was gen-

Received 15 April 1990. H. Hick, H. Willer are affiliated with Austrian Research Centre Seibersdorf, Forschungszentrum, A-2444 Seibersdorf, Austria and E. Winter and F. Simacek are with Community Department, Magistrat der Stadt Wien.

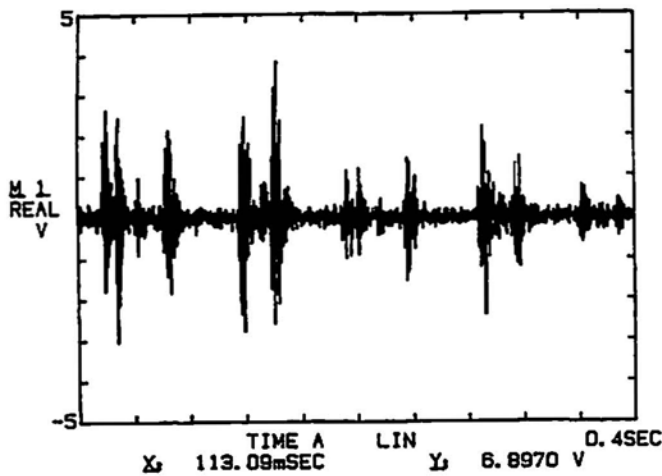


Fig. 1 "Rattling" noise due to tires with pebbles.

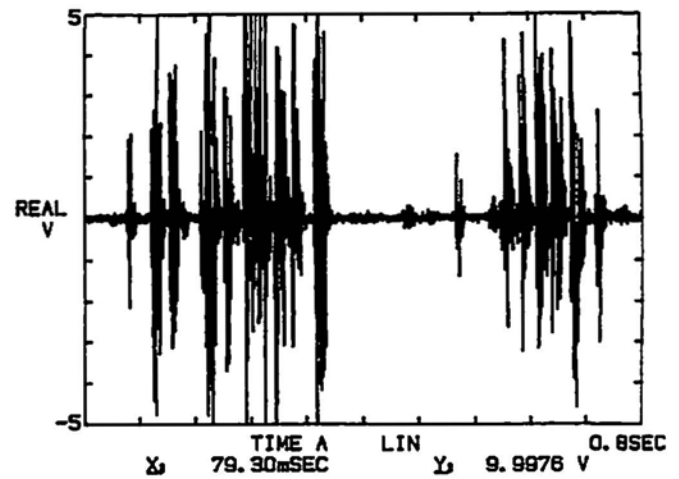


Fig. 3 "Creaking" signal near prestressing cables (mainly 8 - 12 kHz).

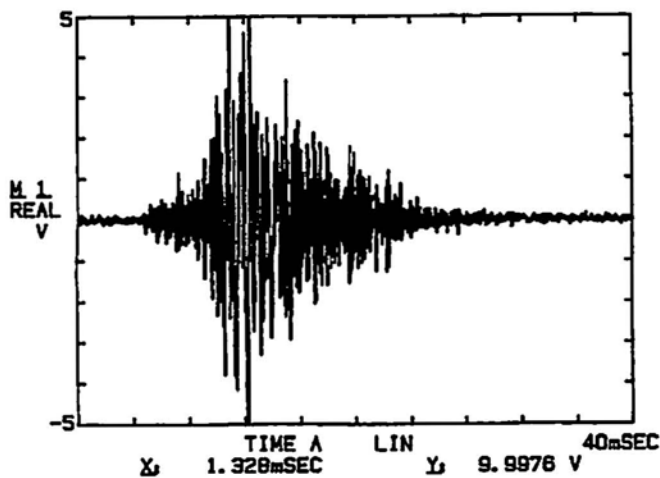


Fig. 2 "Fracture" signal near prestressing cables (mainly 8 - 14 kHz).

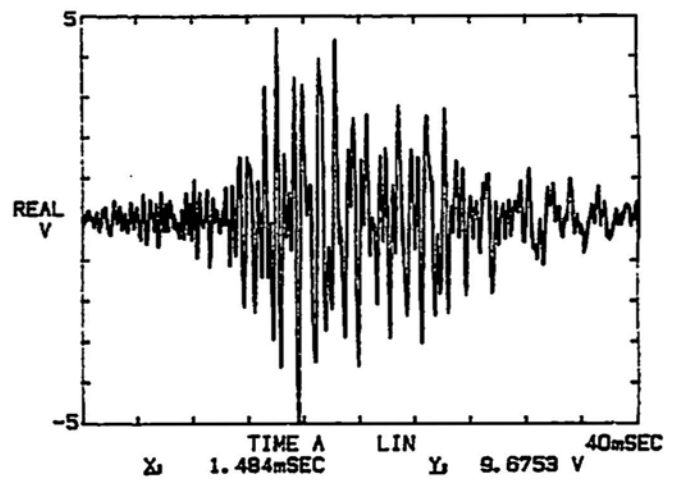


Fig. 4 "Ringing" signal near prestressing cables (mainly 0.3 - 2 kHz).

erated by pebbles locked within the tire-profile grooves of lorries, which came from a nearby building site.

Figure 2 shows a typical time signal of events, which were frequently observed during the passage of a vehicle but also occasionally during the relatively quiet pauses between vehicles. These events appeared like fracture noises, as observed in laboratory tests on concrete samples. During the passage of a vehicle they might have been caused by the crushing of some small pebbles on the road surface. However, their occasional observation during quiet periods indicates, that some structural damage process in the bridge itself must be their cause. Also, mainly during the quiet pauses immediately after a very heavy vehicle, we observed sometimes events as shown in Fig. 3, which could be described as "creaking" and Fig. 4 which could be described as "ringing". From their audible characteristics and their similarity to the sounds observed in the laboratory from a railway sleeper with a cut rebar, we believe that these events are generated by prestressing cables upon deformation due to friction and/or debonding fracture. A search for other sound generation sources such as a steel inspection gallery mounted at the underside of the bridge provided no alternative

explanation. All these events could be detected across the whole bridge section, but were more frequent and louder under the city-bound lane of the bridge.

With a two channel system (with its sensors installed at opposite ends of a 50 m long bridge section), we could also demonstrate that it was possible to locate such a source by propagation-time-difference measurement. For hydroelectric dams and mines, with a relatively quiet background situation, this can be done automatically by a seismoacoustic location and monitoring system which we have developed (Hick, 1986). Due to the strong interference from traffic noise this was however not applicable in the present case. We had to perform cross-correlation averaging of selected events from a 2-channel tape recording with the FFT-analyzer.

During later repair work, a systematic endoscopic examination via boreholes confirmed that the city-bound lane of the bridge contained a higher number of inadequately injected prestressing cables, than the other lane, as well as some concrete damage.

20kHz A: AC/ 5V B: AC/ 50V INST 0/16 ChA 2k

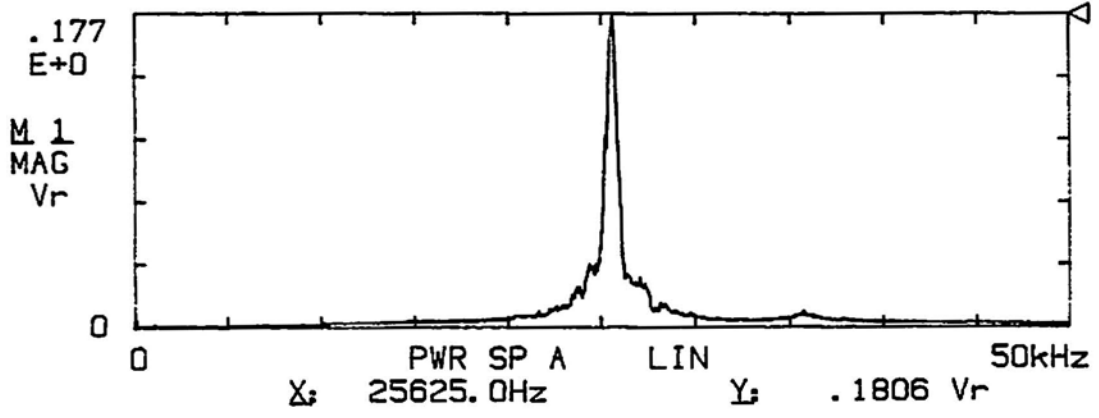
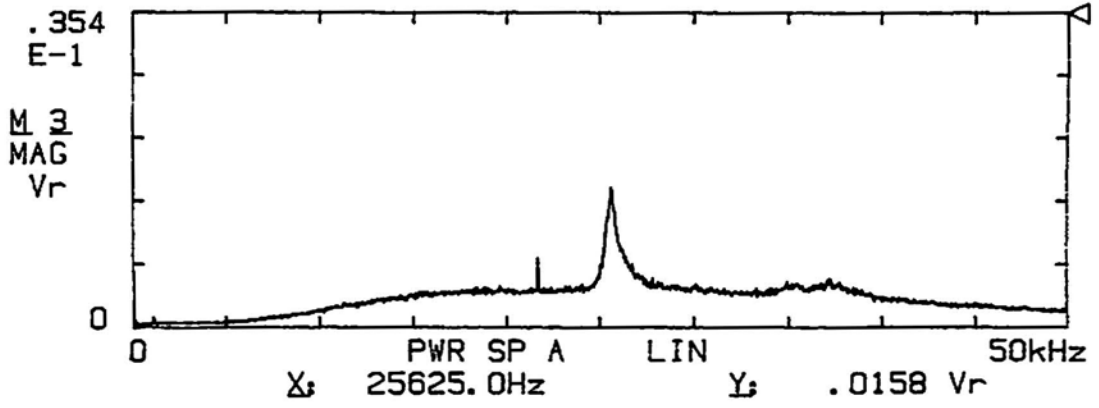


Fig. 5 "Friction" noise spectra of "good" and "bad" bearing.

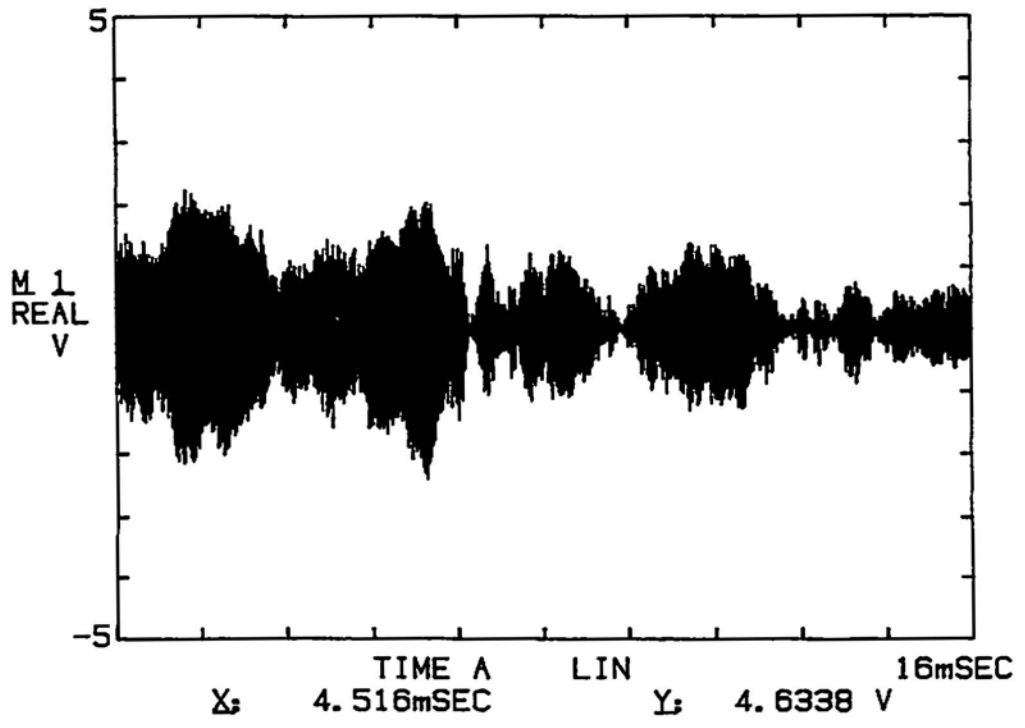


Fig. 6 "Friction" noise signal of "bad" bearing.

4. Measurements on Flat Teflon Support Bearings

It is well known that dry metal-metal friction can produce strong acoustic emission at ultrasound frequencies. For a curved section of a city-motorway, mounted on pylons, it was known from accurate field survey measurements, that some of the flat Teflon support bearings had exhausted their radial gap due to an excentric displacement and were in metal-metal contact with their stop-rim. By a quick coupling method (using a small magnet and a steel waveguide of 3 mm diameter and 300 mm length) it was relatively quick and easy to reach into the narrow horizontal gap between the bridge section and the pylons and to check a number of bearings for the emission of ultrasound due to the small dynamic deformations of the bridge during its normal traffic load.

Figure 5 shows the signal spectra (measured with a 25 kHz resonant transducer) for a "good" and a "bad" bearing, as known from the surveying measurements (note the difference in scales). Figure 6 shows time signals for a bearing due to friction with maximum amplitudes of approximately 9 V peak-to-peak, while for a bearing without friction, only a noise band of approximately 0.7 V peak-to-peak was observed. A surveying measurement requires approximately 45 minutes per bearing, while an AE analysis takes approximately 5 minutes.

5. Measurements on a Crack in a Box-Girder Bridge

By chance, one of the maintenance workers had observed the actual occurrence of a crack on a box-girder bridge as a loud, thundering noise. The crack had a length of several meters and a width of less than 1 mm. With a micrometer, it had also been possible to measure a dynamic variation of crack width with traffic load. A repair attempt by injection of plastic cement had been made some time ago.

The aim of our measurements was to find out, if this crack was still acoustically active. Transducer locations were selected in close proximity (10 cm) to the crack center with respect to the crack tip as well as some 10 m away from the crack, but always at the inside of the box, and just 1 m below the traffic lane surface. Low frequency noise from passing road vehicles was very intense. Therefore, a transducer AC175L with 100 dB amplification and 125 - 250 kHz filtering was used. As access to the inside of the box was difficult, only lightweight, transportable instruments could be used.

In view of the high signal frequencies, ring-down count rates were observed on a ratemeter during the passage of heavy road vehicles. The following peak readings were observed at the three transducer locations (but not simultaneously) for a succession of several typical events

Transducer Location	Counts per minute > 1 V threshold
10 cm from crack center	110, 660, 380, 420, 690
10 cm from crack tip	540, 930, 3330, 3720, 2320
10 m from crack	10, 60, 30, 70, 80

These large differences show that the background count rate due to traffic noise is relatively low (10 - 80 cpm), while the crack produces strong signals, mainly at the crack tip. The strong signals created at the crack tip may be due to new fracture as well as due to friction between relatively fresh and rough crack faces. We know from laboratory experiments that older cracks produce less intense friction noises, probably because of grinding wear and loss of contact between the crack faces (Hick et al., 1983).

These observations proved, that the repair attempt had not been successful. This bridge has since been rebuilt.

6. Conclusions

The AE signals observable on a prestressed concrete bridge during normal use are a complex mixture of various noise sources. Within the audible frequency range, their interpretation requires careful observation and evaluation. A routine observation of these signals could give valuable information about unusual prestressing cable conditions. AE signals in the ultrasonic range can be used for rapid and easy identification of metallic friction contact in support bearings. Ultrasonic AE signals can also be used to detect further propagation of cracks in concrete.

References

- H. Hick (1982), "Anwendbarkeit der Schallemissionsanalyse auf sicherheitstechnische Probleme der Felsmechanik" OEFZS-Bericht A0335-PH-347/82.
- H. Hick (1986), "Praktische Anwendungen der Schallemissionsanalyse in der Bergschlagforschung und zur Staudammüberwachung" OEFZS-Bericht A0821-PH-428/86.
- H. Hick, T. Schmeskal, R. Schwara, S. Zagiczek, C. Werbik, J. Nemet et al. (1983), "Untersuchung zur sicherheitstechnischen Überwachung sowie zur Fehlerauffindung mittels Schallemissionsanalyse für Bauwerke aus Spannbeton" OEFZS-Bericht A0404-PH-365/83.

Acoustic Emission Monitoring of the Sensitivity of Chemicals to Impact

Timothy G. Crowther, Adrian P. Wade and Nancy Brown

Abstract

Acoustic emission monitoring has been used to improve the method that industry uses to determine the sensitivity of compounds to impact. This method is particularly important in measuring the safety of handling explosive compounds in transport, and in storage. The apparatus used presently involves the dropping of a weight from a height onto a small sample, which is confined in a specially designed enclosure. A positive result only occurs when enough energy is supplied to cause an explosion. Whether a result is positive or negative is somewhat open to the interpretation of the operator. Signs of a positive result include smoke, piercing of a diaphragm, or the formation of a dark residue within the sample enclosure. The amount of potential energy (height x weight) required to cause a positive result in at least 50% of tests is termed the sensitivity value. Used in this conventional fashion, the instrument produces a single YES/NO decision per experiment. Many experiments are required to characterize each sample, in what is a very tedious procedure. In this present work it is shown that acoustic emission can be used to effectively monitor controlled explosive reactions occurring within the drop-weight tester sample cavity. The acoustic emission resulting from the impact was captured using a broadband transducer mounted on a clip, which rested on the sample holder. Frequencies from 100 kHz to 1 MHz were captured. This has resulted in an automatic method for distinguishing between a positive and a negative result in calibration and solid sample tests. Spectrogram (time vs. frequency of emission) analysis suggests that acoustic emission may be used to probe the mechanism of the explosion within the sample container. The high non-repeatability of results for the nitromethane samples was due to the piercing of the "O-ring" surrounding the sample, rather than the expected rupture of the diaphragm situated above it. The results show that better design of the present drop weight apparatus must be undertaken to improve the reproducibility. Acoustic emission will provide a useful means to quantify that improvement.

1. Introduction

There is an urgent need for an alternative method for evaluating the sensitivity of explosive compounds to impact. The resistance of a material to impact-induced explosion is one of its most valuable quantitative characteristics, as it gives assurance of safety in handling, transportation and use. The present method involves repetitive use of a drop-weight tester. Small

amounts of sample materials (mg) are subjected to impact. The indication of a positive result (an explosion) is very subjective and operator dependent; therefore acoustic emission was considered as an alternative method for determining if the result was positive, and hence improve the reliability of the sensitivity values obtained for explosives and propellants.

1.1 Explosives

An explosion is a rapid combustion in homogeneous fuel/air mixtures with the flame front passing through the mixture from the source. The result of an explosion is the production of a considerable quantity of heat and a large volume of gas. The design and application of explosives are a science and explosives are as capable of being controlled as are other products of industry. Steel can be hardened by explosives. The intricate patterns that are created by fireworks are dependent on the correct mixture of compounds, and a detailed knowledge of their burning rates and flame colors.

An explosive can be classified as being either a deflagrating explosive (propellant), a high explosive (secondary explosive), or an initiating explosive (primary explosive). A propellant is an explosive that burns at a steady speed and can be detonated only under extreme conditions. An initiator (e.g., mercury fulminate) is an explosive that is extremely sensitive to shock. High explosives normally burn without undue violence when ignited in an open space, but can be detonated by a sufficiently large sudden mechanical or explosive shock. The most important properties of explosives are the velocity of burning or detonation, the explosion temperature, the sensitivity to impact and the power. Sensitivity and power are measured on a relative scale.

Originally for sensitivity, picric acid was used as a standard compound, with an assigned value of 100 (Anon., 1965). Nowadays, each machine used for sensitivity testing has its own method of calibration. The present drop-weight method for sensitivity testing yields very imprecise values. This is partly because the interpretation of results from the test is very subjective; for instance, the sign of smoke, the smell of a gas, or the visual observation of a dark residue in the sample holder have all been used to adjudicate a positive result. Therefore a more sophisticated method for sensitivity testing is necessary. Acoustic emission (AE) is a possible alternative for the testing of explosives, since obvious amounts of audible AE result from explosions. We decided to monitor AE resulting from the existing shock sensitivity testing procedure, and evaluate the efficacy of both AE monitoring and the present procedure for determining the sensitivity of liquid and solid explosives and calibration compounds.

Received 24 June 1991. Timothy G. Crowther and Adrian P. Wade are affiliated with Laboratory for Automated Chemical Analysis, Chemistry Department, University of British Columbia, 2036 Main Mall, Vancouver, B.C. V6T 1Z1, Canada, and Nancy Brown is affiliated with Dow Chemical Canada Inc, South Vidal Street, Sarnia, Ontario, N7T 7M1.

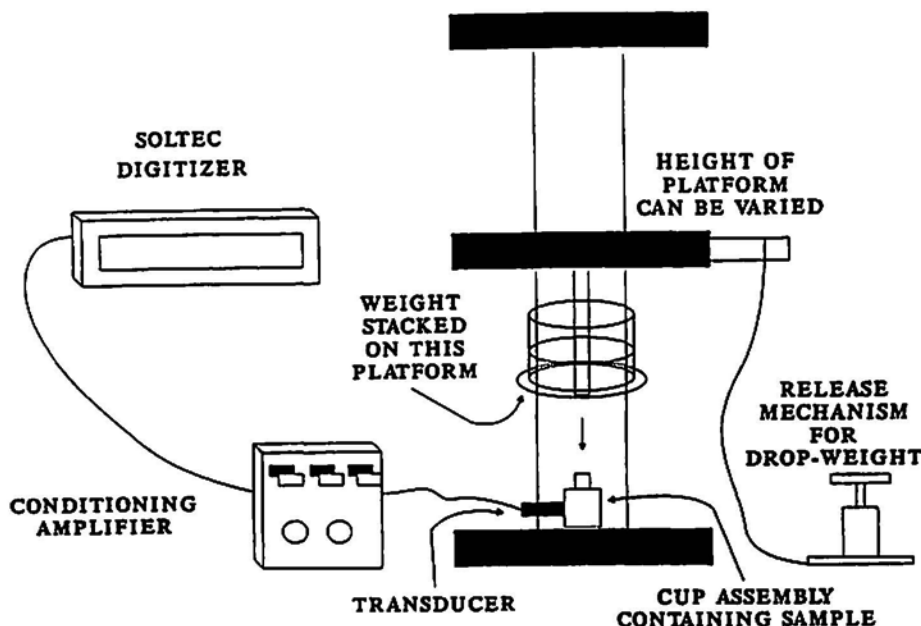


Fig. 1 Drop-weight testing apparatus.

1.2 Drop-weight Testing

In the early 1930s, the Bureau of Mines Explosives Experiment Station introduced drop-weight testing for testing the sensitivity of explosives used in the mines. There were two machines designed. One was a small impact machine, which was used for testing fine-grained or finely pulverized homogeneous explosive compounds. The size and design of the apparatus was similar to the Olin-Mathieson drop-weight tester used in our work (Fig. 1), and the same sample volumes were used. With this machine a weight of 6 kg can be dropped from a height of 50 cm onto a sample of 20 mg. The other machine was a large impact machine, which was used to test coarse-grained material (e.g., compounded explosives such as dynamite). With this machine a 200 kg weight could be dropped from 7.5 m onto 80 g samples. World War II caused a considerable need for a more detailed study of the fundamentals involved in the impact test, but little headway was made; however, the apparatus and testing procedures used were improved. In 1959 the Joint Army-Navy-Air Force Panel on Liquid Propellant Test Methods accepted the Olin-Mathieson drop-weight tester as the standard method for determining the impact sensitivity of liquids. Apart from drop-weight testing, there is no other quick and simple way to evaluate solid and liquid propellants for their explosive sensitivity.

The impact sensitivity for a given sample may be defined as the potential energy value (height x weight) at which explosion occurs in 50% of tests. In liquid propellant testing the explosion is initiated by the adiabatic compression of the gas volume present in the sample. This process is extremely complex, and prevents the fundamental significance of the test from being established. The same is true for the testing of solid propellants, although the governing factors are different. There is, however, no standard impact test for solids at the present time.

The determination of the relative safety of handling haz-

ardous chemicals is the principal function of the impact test. For this reason, materials are compared with known materials on a relative basis, rather than on a standard numerical scale (Barbour, 1981; Bowden and Yoffe, 1952; Fordham, 1966). Many different types of drop weight testers have been designed and consequently many different values for the same explosives materials have been reported. Even two machines of the same design can give contrasting values.

Bowden and Yoffe (1952) showed that "hot spots" are the reason for initiation on impact, and not uniform heating. These "hot spots" can be caused by friction between crystal particles, the compression of small gas pockets in the solids and even by heating of the solid by viscous flow. The "hot spot" theory has also been confirmed by Cook (1958). The importance of cross-sectional area, thickness of the sample, drop-distance, and drop-weight used in impact testing were all verified by Africano (1959). Most machines have very good agreement for sensitive explosives but vary considerably for less sensitive materials, probably due to the difference in striker area.

The thermodynamic and physical properties of a propellant or explosive can be measured on an absolute basis. However, as will be discussed below, the chemical-kinetic properties (burning rate, spontaneous ignition temperature, ignition delay, compression ignition sensitivity, detonation sensitivity, and thermal stability) are not fundamental properties, and therefore cannot be determined on an absolute basis. These chemical-kinetic properties are dependent on the temperature and reaction-velocity relationship of a system and its heat of reaction, and are the critical factors on which the practicability of a propellant or explosive must be judged. They are, in turn, functions of the physical conditions governing the rate of transfer of heat between the system and surroundings, and between the reactants and products. This explains the effect of pressure on ignition and burning rate, and the critical diameter effect in detonation and deflagration propagation (Griffin; 1961).

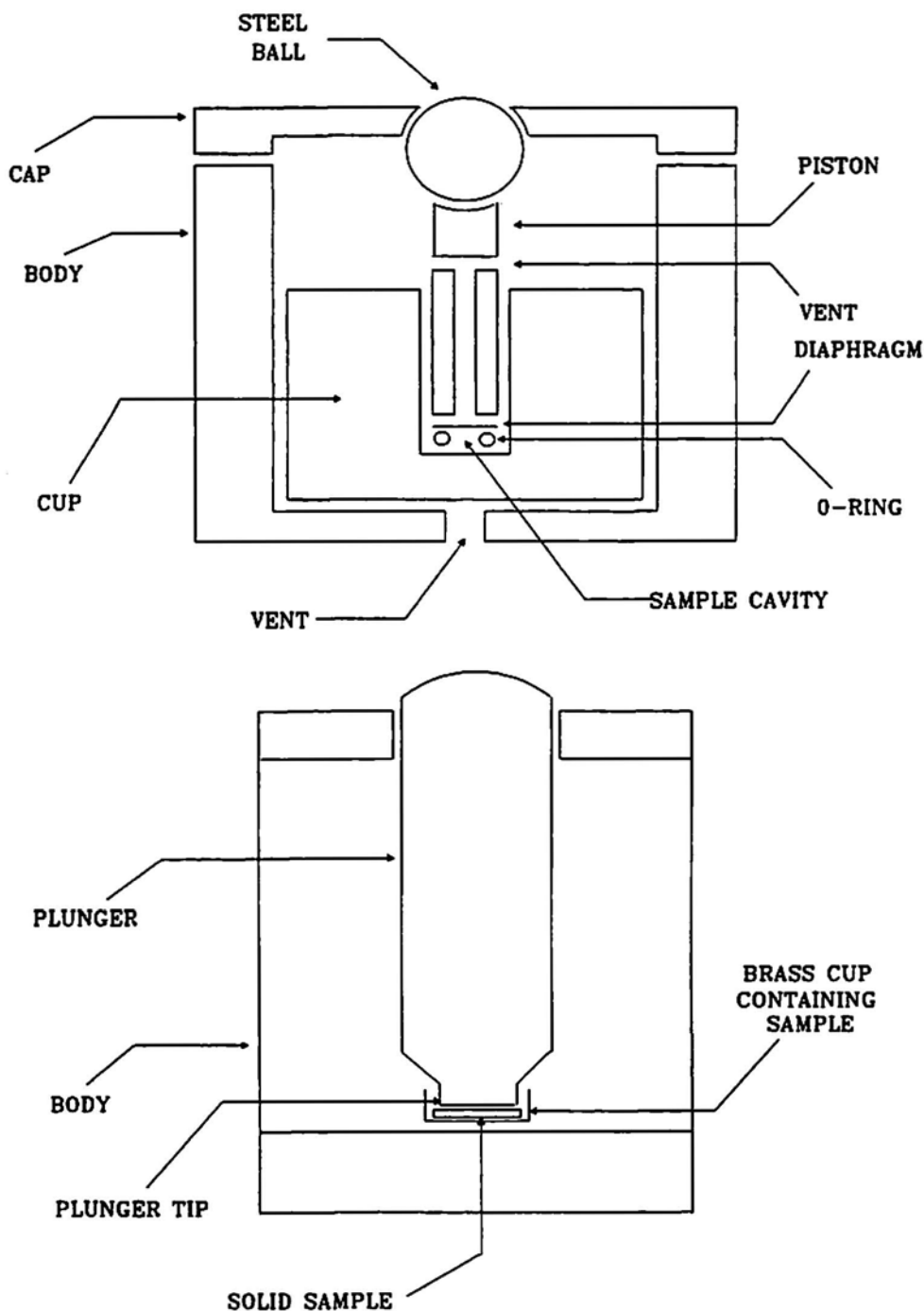


Fig. 2 a) Sample holder for liquid samples (top). b) Sample holder for solid samples (bottom).

When a weight falls, the transfer of energy from the falling weight to the sample is a function of many factors: namely; the mass and velocity of the weight; the mass and surface hardness of the striker and anvil; and the cross-sectional area, thickness, physical composition, and degree of confinement of the sample. The last of these factors is often dependent on the constant thickness of the diaphragm used to confine the liquid sample. This thickness proved inconsistent throughout the experiments detailed in this paper. In fact, many of these variables are difficult to control, even though the test conditions are arbitrary.

The Olin-Mathieson drop-weight test was designed to provide an accurate sample volume, a controlled bubble volume (air pocket within the cavity), and complete sealing of the sample cavity to prevent leakage during the impact and explosion. The prevention of leakage resulted in a large reduction in the impact energy required for initiation of explosion, so that the method has been able to differentiate between materials covering the full range, from insensitive fuels to highly sensitive explosives.

Compression ignition (Griffin; 1961) can be a complicated process when there is both liquid and vapor present in the

sample cavity. For the simple case, where just vapor compression is involved, adiabatic conditions can be assumed and the temperature increase during compression can be expressed as a function of the compression ratio and specific heat ratio of the gas or vapor. However, when both liquid and vapor are present the adiabatic assumption can no longer be true, since there can be a transfer of heat from the vapor to the liquid. The size of the bubble is very important, since the rate of transfer of heat from the bubble to the surrounding liquid is inversely dependent on the size of the bubble. Consequently for very small bubbles adiabatic conditions cannot occur. Sample volume and temperature are therefore very important properties for accurate sensitivity measurements.

Radiometric and spectroscopic methods (Buntain et al., 1988a, b) have been used to investigate the decomposition of explosives on the drop-weight machine, and the initial radiometric results revealed consistent, sequential emissions for specific impacted explosives. To our knowledge, this work (Crowther, 1991) is the first application of (ultrasonic) acoustic emission to this process.

2. Experimental

2.1 Reagents

Water (distilled and deionized, Chemistry Department, University of British Columbia).

Dichloromethane (AnalaR grade, BDH Chemicals, Toronto, Ont.).

Ammonium Dichromate (AnalaR grade, Fischer Scientific, Fair Lawn, NJ).

Nitromethane (AnalaR grade, Aldrich Chemical Co. Inc., Milwaukee, WI).

2.2 Equipment

All experiments involved the Olin-Mathieson drop-weight tester (Technoproducts Division, Quantic Industries Inc., San Carlos, CA). All the equipment was provided by the manufacturers of the drop-weight, unless otherwise stated. The height and weight of the dropping weight could be altered. Different sample holders were used for solid and liquid measurements.

Liquid samples: The sample holder for the calibration test and other tests on liquid samples was as shown in Fig. 2a. A steel cup (25.4 mm diameter, 15.9 mm depth), with a cylinder (9.5 mm diameter, 12.7 mm depth) cut out, was positioned in the body of the sample holder. A rubber O-ring (Type AN-62275, 6.1 mm ID. and 7.1 mm OD.) was placed in the bottom of the cup and pushed down firmly using the piston (9.2 mm diameter and 19.1 mm height). The sample solution (0.03 ml) was injected into the cavity created using a fixed-stroke syringe (No. 4250, Nimetrics Corporation, Anaheim, CA), and a stainless steel diaphragm (0.38 mm thick and 9.2 mm diameter) was dropped flat onto the O-ring. The piston was placed onto the diaphragm, and was designed with a vent hole which is blocked by the diaphragm. A steel ball (21.0 mm diameter) was placed on the piston to prevent it from moving upwards after the explosion. The last stage in assembly was the addition of the cap to the body of the sample holder. This cap was screwed onto the body and tightened to a torque of 0.08 kg·m (7 lb·in)

using a torquemeter. Finally, the sample holder was situated in the base of the drop-weight tester.

Solid Samples: The sample holder for solids is depicted in Fig. 2b. A solid sample of mass 20 mg was weighed out on an analytical balance, and deposited in a brass cup (8.0 mm ID, 3.1 mm depth, and 0.31 mm thickness). The plunger tip (7.7 mm diameter) was then carefully lowered into the cup. The sample holder was then placed onto the base of the drop-weight tester.

Acoustic Emission Detection: The broadband transducer (Model FAC500, Acoustic Emission Technologies Inc., Sacramento, CA) used for all measurements was mounted using insulating tape onto one end of a flexible strip of stainless steel (2 mm thick, 2.5 cm width and 20 cm length), which, in turn, rested on the sample holder. Petroleum grease was used to improve the coupling between the transducer and the strip, and between the strip and the sample holder. The output of the transducer was connected to a conditioning amplifier (Type 2638, Bruel & Kjaer, Naerum, Denmark). This provided a switch-selectable gain of 0 to 60 dB in 1 dB steps, and several bandpass filter ranges. The ac output of this amplifier was connected to a digitizer (Model SDA 2000, Soltec Inc., San Fernando, CA). The digitizer transferred the data via an IEEE488 interface to the hard drive of a PC/XT class personal computer for later processing. The digitizer was controlled using the software provided by the digitizer's manufacturer.

2.3 Method

Initial Experiments: Improvements to the stability of the tester were made by bolting the tester to a rectangular steel plate of 19.1 mm thickness, 914 mm length, and 610 mm width, which in turn was mounted in a wooden frame. A trigger mechanism was also added to facilitate a more reproducible release of the dropping weight. These improvements greatly increased the reproducibility of the experiment.

Water Calibration: The purpose of the calibration procedure was to determine the sensitivity value at which hydraulic pressure from the sample causes a puncture of the diaphragm. The sensitivity value for the water calibration sets the maximum sensitivity value. The sensitivity value for nitromethane must lie below the water sensitivity value in order to eliminate the possibility that the diaphragm has ruptured because of hydraulic pressure.

Calculation of Sensitivity Value: The sensitivity value for liquid or solid samples is this potential energy value (height x weight) at which the probability of explosion is 50%. The 50% point (E50) was determined by a statistical method known as the "Up and Down" method (Dixon and Massey, Jr., 1957). The sample cavity was filled with 0.03 ml of distilled water. After every test the diaphragm and O-ring were changed, and all parts of the sample holder for liquids (Fig. 2a) were cleaned with a cloth soaked in dichloromethane. The conditioning amplifier gain was set to 30 dB, and a 50 kHz-2 MHz bandpass filter was used. A sampling interval of 7 μ s, and a record length of 65536 (64 k) data points was used, initially, to measure the time of the bounce of the dropped weight. These conditions provided a time window of 389.9 ms (with 70 ms pre-trigger).

Table 1 Procedure for calculating sensitivity value.

E/Kg cm	NUMBER OF TRIALS																				TOTAL		% POSSIBILITY
	1	2	3	4	5	6	7	8	9	10	11	12	13	14	15	16	17	18	19	20	+	-	
140.0	+		+		+				+				+		+					+	7	0	100
133.0		-		-		+		-		+		-		-		+		-		-	3	7	30
126.0								-				-									0	3	0

Once this was established, the sample size was then increased to 128 k samples and the sampling interval changed to 200 ns, so as to satisfy Nyquist frequency conditions, and create a time window of 26 ms.

A weight of 4 kg was dropped from a height of 35 cm. If the diaphragm punctured, or stuck to the piston, then a positive result was deemed to have occurred, and the weight was sequentially reduced in steps of 200 g until a negative result was obtained (no puncture of the diaphragm). From this point, another 20 trials were carried out. During these, whenever a positive result was obtained, the weight was reduced by 200 g, and if a negative result was obtained, 200 g was added. Once a minimum of 20 tests was completed, the total positive and negative tests were marked down, as well as their respective probabilities (Table 1). The mean value, E50, was then estimated by linear interpolation between the percentages either side of the 50% point (E50 = 135.0 kg.cm for the data of Table 1). The mean may also be taken from the arithmetic mean of all the tests (positive and negative). The sensitivity value was always presented to the nearest 1/10 kg cm.

Liquid Propellant Test: The digitizer conditions were similar to those used for the water calibration except that a smaller record length (16384 samples) was used to make data storage easier. The conditions provided a time window of 3.244 ms, which avoided the inclusion of a bounce, if it occurred. The sample cavity was filled with 0.03 ml of nitromethane. Initially, a 6 kg weight was dropped from 20 cm; if puncture of the diaphragm occurred, the weight was decreased to 1 kg. If the latter test appeared positive then the height was reduced until a negative result was obtained. The weight or height was gradually reduced, or increased, until a change in sign (positive or negative) was obtained with a change of approximately 5% of the total weight. Once these conditions were attained, 20 more tests were carried out. If the sensitivity value exceeded the energy required to rupture the diaphragm by hydraulic pressure (i.e. the value obtained from the water calibration), then the test was aborted. Again the diaphragm was changed every time a test was completed, irrespective of whether the test was positive or negative.

Solid Explosive Test: The same digitizer conditions were applied as used for tests on liquid samples. A brass cup was filled with 0.02 g of ammonium dichromate and placed in the solid sample holder (Fig. 2b). The conditioning amplifier gain was set to 40 dB, with a filter setting of 50 kHz-2 MHz. The filter

setting was changed to 400 kHz-2 MHz when it was realized that most of the acoustic emission observed was at 400 kHz and beyond. A 6 kg weight was first released from a height of 50 cm. If this test was negative, then the sample could not be tested. If the test was positive (as indicated by deformation of the brass cap, signs of gas evolution, or discoloration of the sample) then the weight was reduced to 1 kg. Thereafter, for a positive test the new weight (3 kg) would be half the previous weight (6 kg). The procedure was continued by adding or decreasing the test by half the previous weight until a change in sign has occurred for a change of weight of approximately 5% of the total weight (e.g., for a 2 kg weight the test would finish once the change in weight had reached 0.1 kg). Once this condition was achieved, the results of a further 20 trials were acquired. After every test the brass cap was changed and the plunger tip was wiped clean using dichloromethane.

3. Results and Discussion

3.1 Initial Modification of the Drop-weight Tester

Bouncing of the dropping weight initially provided a serious problem; since the bounce occurred at 360 ms (Fig. 3), it was thought this could interfere with a long-lasting acoustic

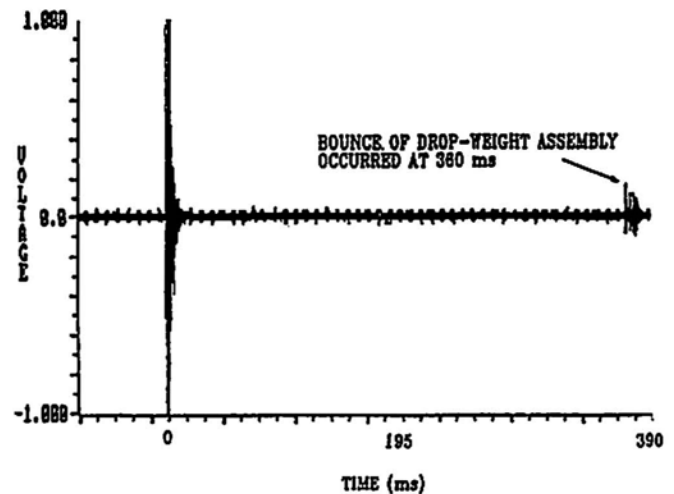


Fig. 3 This trace indicates that the bounce occurs at 360 ms. This enabled the window to be reduced for further experiments, eliminating the noise associated with the bounce.

signal. To avoid all possibility of such interference the sampling time was restricted to less than 50 ms. Furthermore, the improvements to the apparatus (i.e. bolting of the drop-weight tester to the steel plate) completely removed the occurrence of a bounce for the water calibration (but not for other samples). Under such conditions all tests which appeared positive from their root-mean-square (rms) voltage values, also resulted in the perforation of the diaphragm. The modified apparatus therefore facilitated a fast YES/NO answer to the impact procedure, and reliable determination of a positive result for the water calibration. Before the modifications, the results were extremely inconsistent for all experiments, and a sensitivity value for the water calibration could not be obtained.

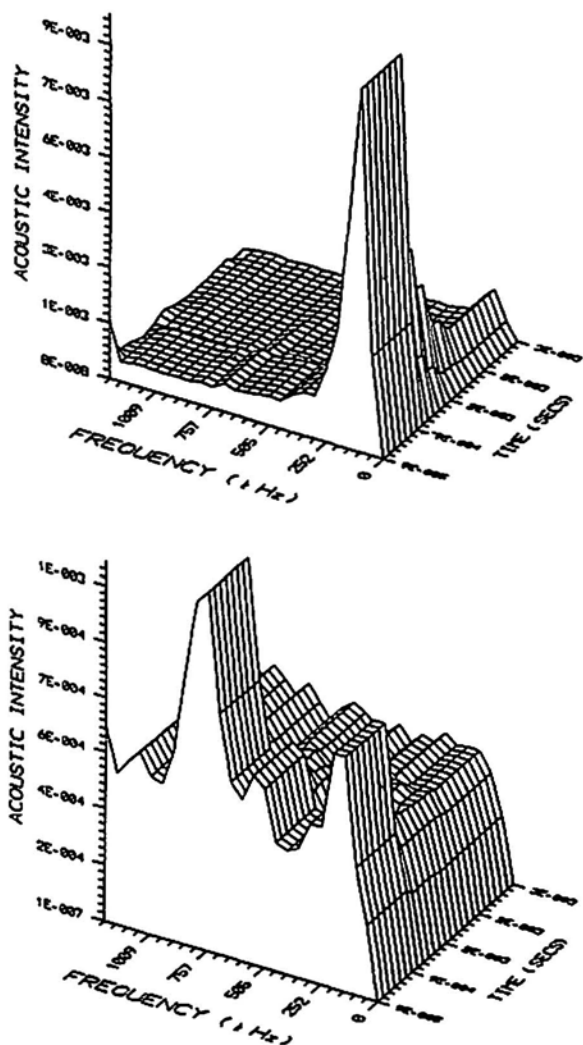


Fig. 4 a) Spectrogram for the blank liquid sample holder with no sample present (top). b) Spectrogram for the blank solid sample holder with no sample present (bottom).

3.2 Frequency-time Spectra for Liquid and Solid Sample Holders (Empty)

We sought to visualize and understand the change in frequency spectrum present over the time period of the experiment by use of spectrograms. A computer program, TRAPS (Lee et al., 1990), was applied to the signals obtained from the impact, to obtain time-resolved averaged (frequency) power spec-

tra for the duration of experiment, in the hope of being able to associate the frequencies observed with the various stages of impact and reaction. The spectrograms for the liquid and solid sample tests with no sample present (blanks) are shown in Figs. 4a, b, respectively. The liquid sample holder spectrogram shows a distinct peak at 300 kHz, which is vastly different to the broad band of frequencies shown in the spectrogram for the solid sample holder. The variation is caused by the different way in which the striker interacts with parts of the sample holder cup assembly. For instance, the liquid sample holder contains a rubber O-ring, which would be expected to have relatively low resonant frequencies, and prevents the collision of the two metal surfaces (the steel diaphragm with the base of the sample cup); however, direct collision between two metal surfaces (the plunger with the brass cup) occurs within the solid sample holder, and thus would be expected to produce higher frequency emission.

3.3 Water Calibration

The modified apparatus was calibrated using distilled water. It was found that a positive result could be obtained, and that this result could be verified not only by puncture of the diaphragm, but also by the lack of a bounce after the initial

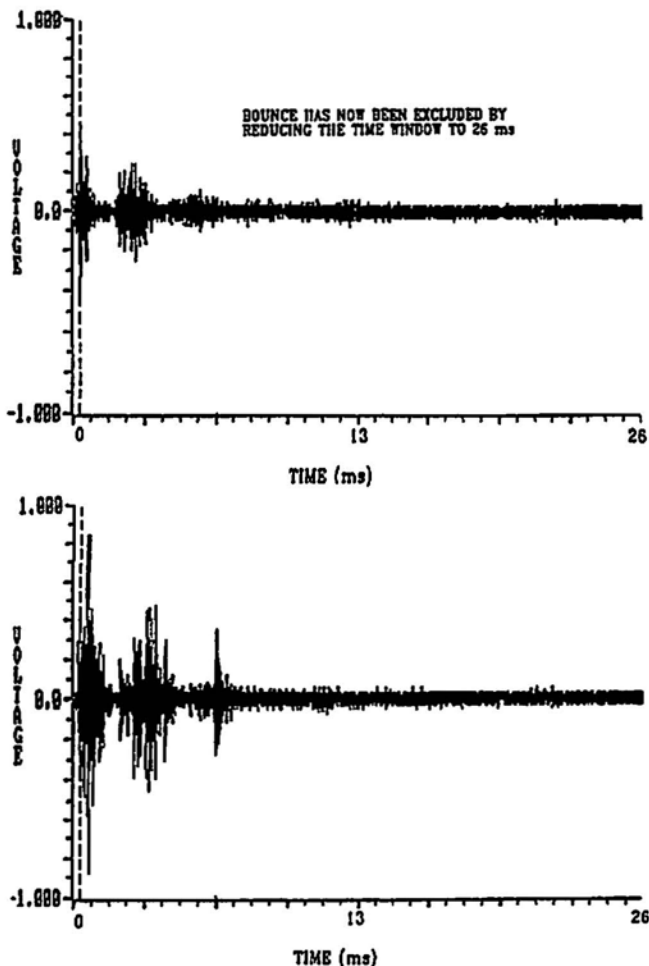


Fig. 5 Time-domain signal for the calibration of the apparatus using water. a) Trace from a negative result (top). A bounce occurred at 360 ms (not shown). b) Trace from a positive result. No bounce was seen at 360 ms (bottom)

striking of the sample holder. The time domain signal for an experiment in which a bounce occurred (Fig. 5a) was considerably different to that from a positive result (Fig. 5b) and therefore the two could readily be distinguished. The rms voltage of the signal over a frequency range of 50 kHz-2 MHz was used to predict the result of the impact on the sample. The rms voltage values for the positive tests were always considerably less than that for the negative tests, in which a bounce was always observed. Table 2 shows that, when the bounce was removed from consideration by using a smaller time window, the positive result had a higher rms voltage values (7.2 ± 1.9 mV) than the negative result (4.8 ± 1.0 mV) at the 90 % confidence level. Furthermore, the release of the explosion products (the water calibration experiments produced water vapor) at high pressure will undoubtedly lead to the generation of sound waves. Generally, if the rms voltage value is more than 6.0 mV, then the test is positive and rupture of the diaphragm has occurred. The sensitivity value for water was calculated to be 133.1 kg cm (Table 1), with an arithmetic mean of 134.4 kg cm. This E50 was consistent with values from previous tests conducted elsewhere (5). Attainment of this value allowed the testing of the liquid propellant (nitromethane) to be carried out, knowing the potential energy required to rupture the diaphragm by hydraulic pressure alone.

3.4 Spectrogram of Water

The acoustic intensity obtained from calibration tests (Fig. 6) was considerably greater than that obtained from a blank test, in which the sample compartment contained no distilled water (Fig. 4a). This observation confirmed the existence

of acoustic emission other than that produced by the initial impact. The spectrum indicates that rupture of the diaphragm occurs approximately 1.6 ms after the initial impact. This is in agreement with previous values (Anon., 1965) obtained elsewhere. The increase in intensity of the frequency band centered about 300 kHz after approximately 1.6 ms (Fig. 6a) is associated with the rupture of the diaphragm by hydraulic pressure. Where no rupture has occurred this increase is absent, as seen in Fig. 6b. The boiling of water is known to give similar spectra with the majority of emission at frequencies below 300 kHz. The peak around 1 MHz is believed to be the movement of the sample holder parts in the initial impact, and the friction thereby produced.

3.5 Liquid Sample Testing of Nitromethane

The test for nitromethane proved difficult because the explosion of the sample refused to pierce the diaphragm, but instead favored cutting through the O-ring, and scoring the side of the piston. Because of this, the time domain signal obtained was found to vary considerably. The higher magnitude of rms voltage values, relative to those from the water calibration, is in part due to the different time window considered. A typical negative result is shown in Fig. 7. It proved impossible to calculate the sensitivity value (E50) for nitromethane because no value had a 50% chance of exploding (Table 3). None of the positive tests mentioned in Table 3 resulted in rupture of the diaphragm; therefore, a positive result was assigned when the O-ring and piston had been scored. The maximum weight of 6.05 kg could not be exceeded since the sensitivity value would

Table 2 Correlation of rms voltage values with positive and negative results for water calibration.

TEST NO.	HEIGHT/cm	WEIGHT/Kg	E/Kg cm	POS	NEG	REMARKS	RMS/mV
1	35	4.0	140.0	+			9.069
2	35	3.8	133.0		-	BOUNCED	4.159
3	35	4.0	140.0	+			8.384
4	35	3.8	133.0		-	BOUNCED	5.836
5	35	4.0	140.0	+			7.562
6	35	3.8	133.0	+			7.631
7	35	3.6	126.0		-	BOUNCED	4.750
8	35	3.8	133.0		-	BOUNCED	4.555
9	35	4.0	140.0	+			7.214
10	35	3.8	133.0	+			6.350
11	35	3.6	126.0		-	BOUNCED	5.702
12	35	3.8	133.0		-	BOUNCED	4.736
13	35	4.0	140.0	+			8.126
14	35	3.8	133.0		-	BOUNCED	4.071
15	35	4.0	140.0	+			7.379
16	35	3.8	133.0	+			5.437
17	35	3.6	126.0		-	BOUNCED	4.650
18	35	3.8	133.0		-	BOUNCED	3.841
19	35	4.0	140.0	+			4.649
20	35	3.8	133.0		-	BOUNCED	5.624

Table 3 Lack of correlation between rms voltage values and positive and negative results for nitromethane.

TEST NO.	HEIGHT/cm	WEIGHT/Kg	E/Kg cm	POS	NEG	REMARKS	RMS/mV
1	20	6.00	120.0	+	-		75.8
2	20	5.95	119.0		-		147.1
3	20	6.00	120.0	+	-		45.07
4	20	5.95	119.0		-		181.2
5	20	6.00	120.0		-		108.9
6	20	6.05	121.0		-		255.0
7	20	6.05	121.0		-		148.8
8	20	6.05	121.0		-		180.9
9	20	6.05	121.0		-		258.3
10	20	6.05	121.0	+	-		79.7
11	20	6.00	120.0		-		343.7
12	20	6.05	121.0		-		236.4
13	20	6.05	121.0		-		98.9
14	20	6.05	121.0	+	-		61.1
15	20	6.00	120.0		-		73.9
16	20	6.05	121.0		-		310.1
17	20	6.05	121.0		-		71.6
18	20	6.05	121.0		-		161.3
19	20	6.05	121.0		-		196.2
20	20	6.05	121.0	+	-		58.9

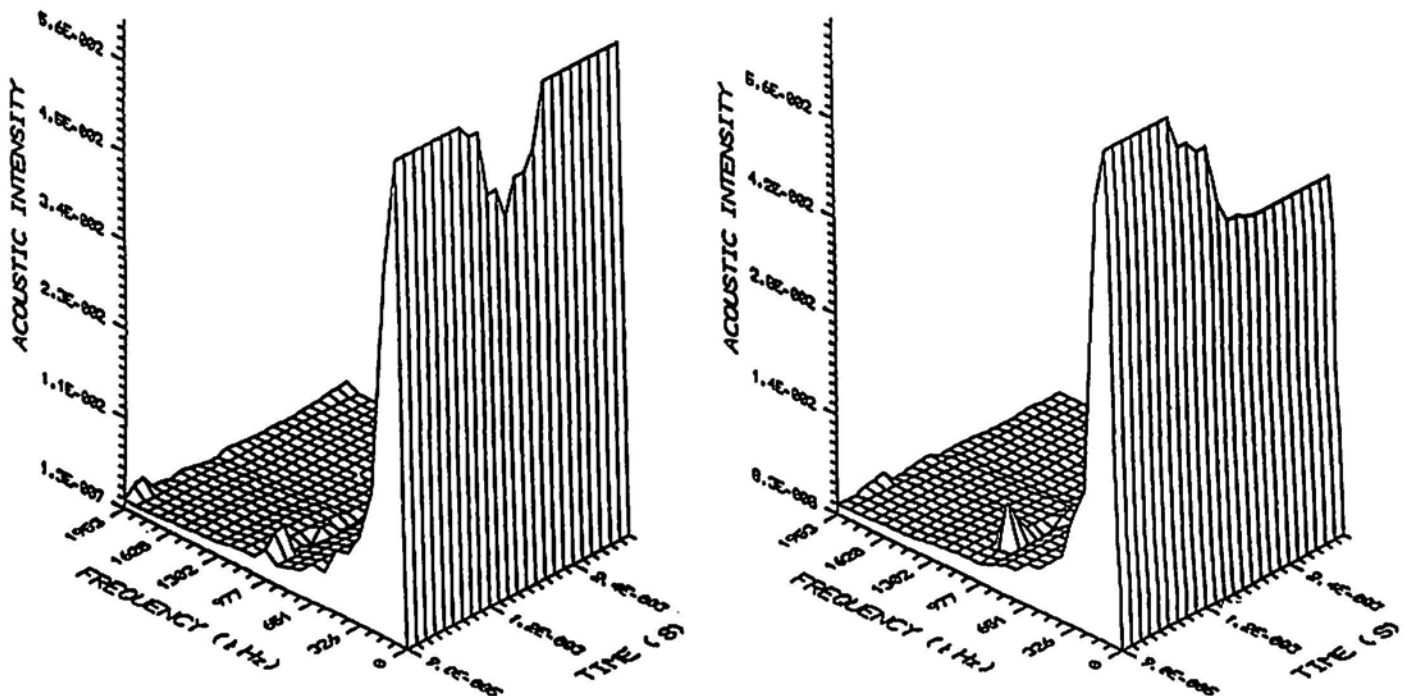


Fig. 6 Time-frequency domain traces for water calibration experiments. a) A positive result (left): the 300 kHz (impact) peak decreases in intensity after 1.2 ms. This is followed by an increase in the peak intensity due to rupture of the diaphragm and subsequent release of water vapor. b) A negative result (right): the 300 kHz (impact) peak again decrease in intensity of the after 1.2 ms, but the diaphragm does not rupture, and so the 300 kHz emission does not increase thereafter.

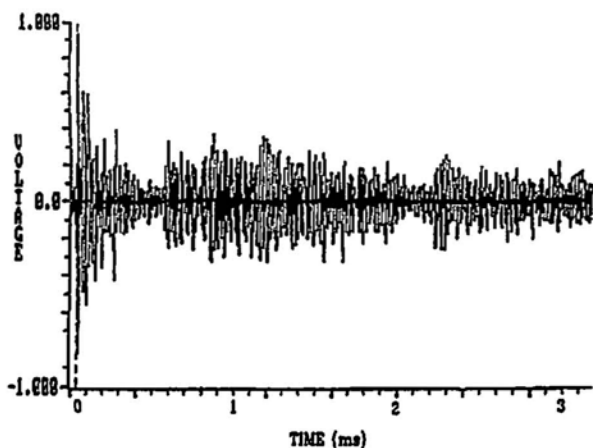


Fig. 7 Time-domain signal for a typical negative result from nitromethane.

be too close to that for hydraulic rupture, and the maximum amount of weight that could be added was 6.05 kg. This restriction limited the test to a maximum value of 121 kg cm and therefore if the test proved negative at this value (which it frequently did) then the value could not be further increased. This factor, along with the absence of puncture of the diaphragm, cutting and or melting of the diaphragm, and the random alternative escape route of the reaction products up the sides of the piston, resulted in acoustic rms voltage values that did not follow any particular pattern. However, Table 3 indicates that a higher rms voltage is generally associated with a negative result.

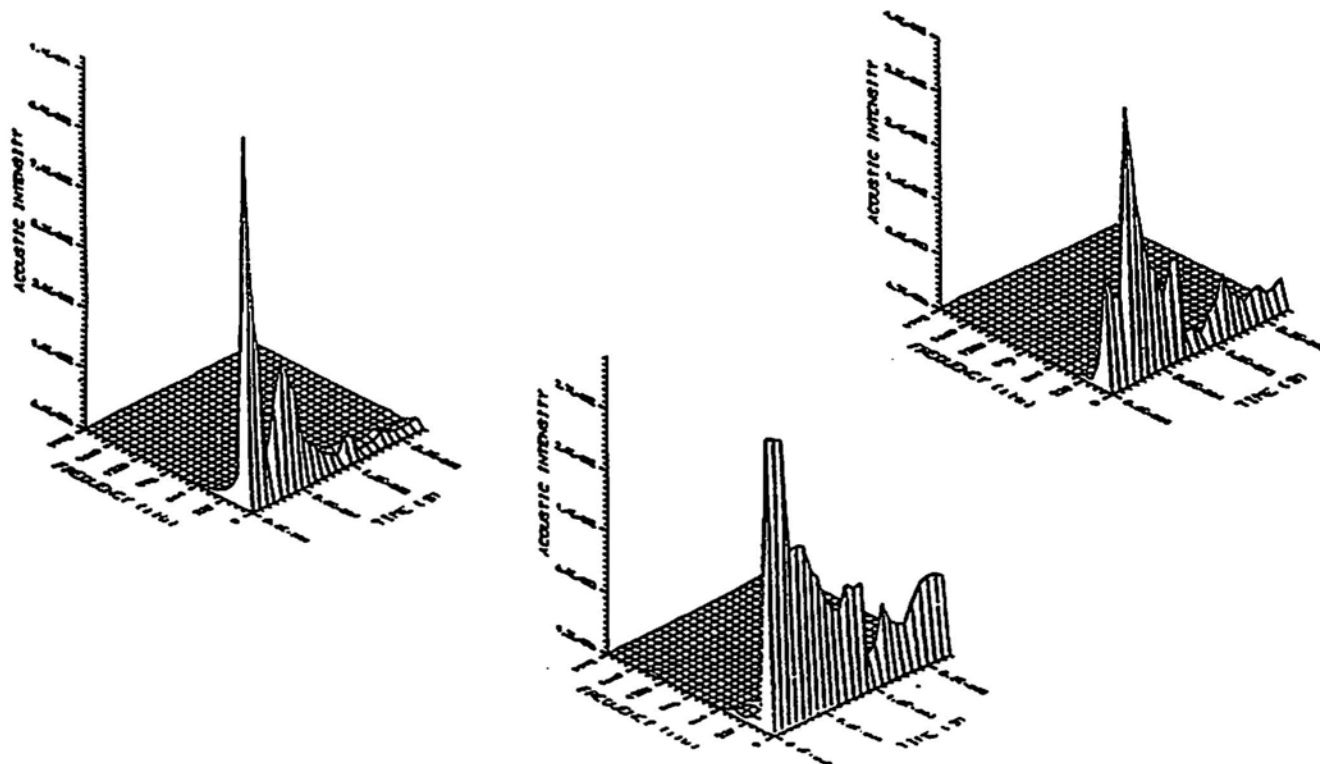


Fig. 8 Spectrograms showing the inconsistency of negative results for nitromethane samples. The variability in the spectra is due largely to the liquid sample holder. The diaphragm did not rupture, but rather the sample scored the O-ring and escaped through the side.

3.6 Spectrogram of Nitromethane

The inconsistency of the frequency spectra for negative results for nitromethane are shown in Fig. 8. The positive results provided equally inconsistent frequency spectra. There seems much randomness in the intensities of the 3D surfaces generated and, while the surfaces exhibit the same general frequencies as found for the liquid sample holder, no distinct spectral features exist which distinguish a positive from a negative result.

3.7 Solid Sample Testing of Ammonium Dichromate

For the solid samples, again much variation was seen in the way the explosive deforms the brass cap, and the degree to which the sample actually explodes. One reason for this variability is almost certainly due to the grain size of the solid explosive sample (Bowden and Yoffe, 1952). If samples were ground to the same particle size distribution then the results would be improved. However, grinding of explosive materials bears its own hazards. A typical time domain signal can be seen in Fig. 9. The time domain signal always consisted of several intense bursts of acoustic emission followed by a decay after 2.5 ms. The calculation of the sensitivity value was straightforward and a value of 180.1 kg cm was obtained. A high rms voltage value indicated a positive result, whereas a low rms voltage value indicated no detonation (Table 4). The acoustic detection of detonation proved to be very dependent on where, and how well the transducer was coupled to the metal strip resting on the sample holder, and where the strip was placed on the

Table 4 Correlation of rms voltage values with positive and negative results for ammonium dichromate.

TEST NO.	HEIGHT/cm	WEIGHT/Kg	E/Kg cm	POS	NEG	REMARKS	RMS/mV
1	50	3.65	182.5	+			26.98
2	50	3.60	180.0	+			39.76
3	50	3.55	177.5		-		9.77
4	50	3.60	180.0		-		24.87
5	50	3.65	182.5		-		15.42
6	50	3.70	185.0	+			38.00
7	50	3.85	182.5	+			65.55
8	50	3.60	180.0		-		20.79
9	50	3.65	182.5	+			42.59
10	50	3.60	180.0		-		26.01
11	50	3.65	182.5		-		
12	50	3.70	185.0		-		24.38
13	50	3.75	187.5		-		
14	50	3.80	190.0	+			58.39
15	50	3.75	187.5	+			42.30
16	50	3.70	185.0	+			31.10
17	50	3.65	182.5		-		14.97
18	50	3.70	185.0	+			48.61
19	50	3.65	182.5	+			46.07
20	50	3.70	185.0	+			

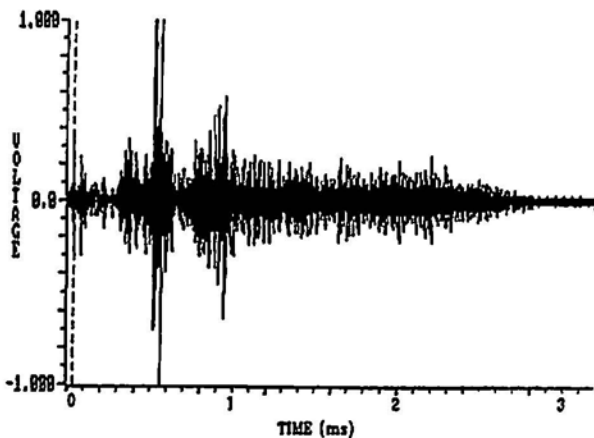


Fig. 9 Typical time-domain signal for the ammonium dichromate solid sample.

sample holder. The reason for this is probably due to the ease with which the released explosion products create sound waves which are intense enough to reach the transducer, through the thick steel of the sample holder.

Experiments to increase the intensity of sound released due to an explosion resulted in a procedure which was too noisy (audibly) for the laboratory. These experiments used stainless steel cups (12.7 mm diameter, 6.1 mm depth, and 2.5 mm thickness). The intention was to increase the amount and reproducibility of the acoustic energy by (i) improving the confinement of the reaction gases within a stronger cup, and (ii) removing any effects caused by the variability in fracture of the brass cups. The original brass cups resulted in less audible

noise, and some of the acoustic emission detected was from their deformation and cracking.

3.8 Spectrogram of Ammonium Dichromate

Again it was observed that the acoustic intensity for the spectrogram of ammonium dichromate was significantly greater than the acoustic intensity observed for a blank test (no sample present). We were expecting to hear the fracture processes involved in the crushing of the solid sample, and the sounds of subsequent reaction. The initial spectra for ammonium dichromate indicated that there might be acoustic activity at frequencies beyond 400 kHz, and therefore a higher frequency band filter (400 kHz-2 MHz) was used. The acoustic emission above 400 kHz provided a fairly reproducible frequency spectrum. The difference between a detonation (Fig. 10a) and no detonation (Fig. 10b) was readily seen (as expected from the rms voltage values) in the intensity of the emission spectrum. Likely reasons for the increase in intensity of the emission spectrum include crystal fracture, release of explosion products, and the high frequency emission associated with the deformation and cracking of the brass cup after the sample detonated.

4. Conclusions

Acoustic emission has been successfully applied to the dropweight tester method for measuring the sensitivity of explosives and propellants. Modifications made to the dropweight apparatus eliminated problems in calibration caused by bounce of the dropweight and generally increased the reproducibility of operation of the impact procedure. Once these improvements were made, acoustic emission successfully monitored a reliable series of instrument calibration experiments.

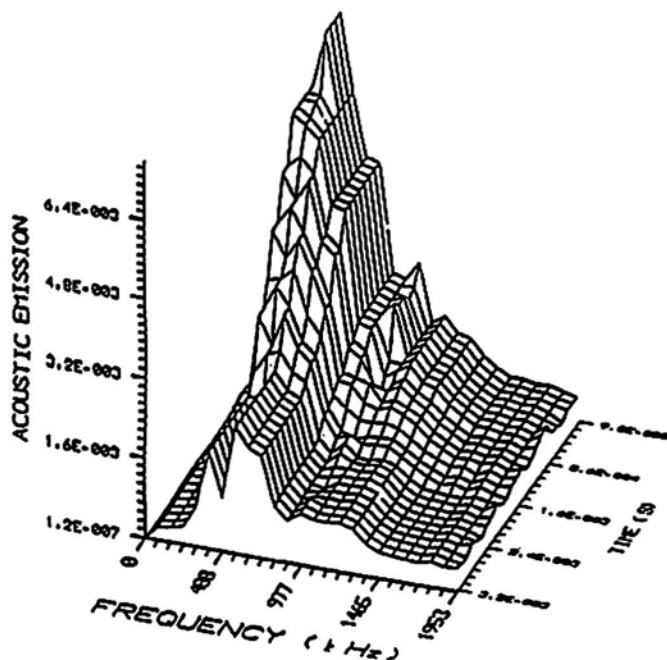
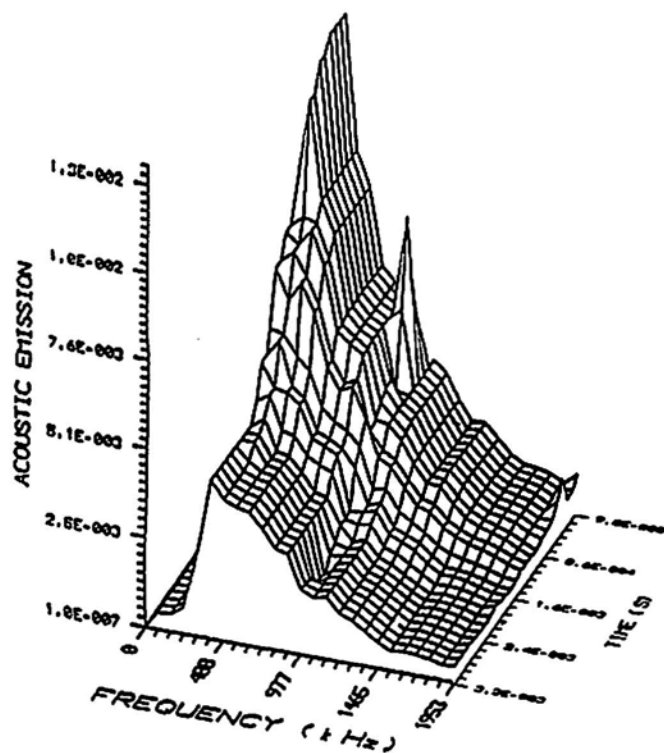


Fig. 10 Time-frequency spectra for impact sensitivity testing of ammonium dichromate at 182.5 kg cm. a) Detonation occurred (top). This is a positive result, as indicated by the intense peak around 900 kHz. The intensity of a positive result is greater than a negative result. b) No detonation occurred (bottom). The peak around 900 kHz is not so pronounced for this negative result.

and determined the presence or absence of reaction within the sample chamber for solid samples. In both cases the acoustic

rms voltage provided a numerical basis for assigning a positive result, and was more reliable than the previously uncertain YES/NO assignment of the result by the operator. Problems with the (standard) design of the liquid sample cavity resulted in the failure to quantify the sensitivity of liquid propellant samples.

This work suggests that acoustic emission should prove to be a useful tool for redesign of parts of the apparatus which are presently the major sources of non-repeatability. The sample holders must be designed to respond in a more reproducible way when an explosion has occurred. The diaphragms provided by the manufacturer were too thick for successful application to the liquid propellant tested, and should be redesigned. Since the temperatures and pressures generated in the nitromethane experiments were too high for the rubber O-ring to withstand, alternative Oring materials and designs should be evaluated. The strength of the brass caps used for solid samples should be increased.

The ability to measure acoustic frequency spectra at intervals of 0.15 ms or less throughout the brief course of the drop-weight experiment has transformed this instrument from a device which provided a simple YES/NO decision per experiment into one which yields numerical information in two dimensions. Currently, the time taken to perform the necessary computations on large data sets can be significant, but near real-time spectral analysis will be possible with a digital signal processor. Spectrogram analysis indicates that acoustic emission may provide an alternative means to determine sample explosion rates.

Acknowledgments

Special thanks are due to Richard Ironmonger for his assistance with modifications to the apparatus and his knowledge of explosives. The authors also thank Brin Powell and Brian Snapkauskas for their engineering assistance. This work was made possible by Grant 550886 from the Institute for Chemical Science and Technology, and matching Grant 580389 from the Cooperative Research and Development Program of the Natural Sciences and Engineering Research Council of Canada.

References

- A. Africano (1959), "Maximum Rate Theory of Impact Sensitivity", presented at the Cryogenic Engineering Conference, University of California, Berkeley.
- Anon. (1965), Data Bulletin #66830, Technoproducts Division, Quantic Industries Inc., San Carlos, CA, p. 1.
- R.T. Barbour (1981), *Pyrotechnics in Industry*, McGraw Hill, New York.
- J.P. Bowden and A. D. Yoffe (1952), *Initiation and Growth of Explosion in Liquids and Solids*, University Press, Cambridge.
- G.A. Buntain, T.L. McKinney, T. Rivera, and G.W. Taylor (1988a), 19th Annual Conference for ICT, Federal Republic of Germany.

G.A. Buntain, T.L. McKinney, T. Rivera, and G. W. Taylor (1988b), 9th International Symposium on Detonation, Silver Spring, MD.

M.A. Cook (1958), *The Science of High Explosives*, Reinhold Publishing Corp., New York.

T.G. Crowther (1991), M.Sc. Thesis, University of British Columbia, April.

W.J. Dixon and F.J. Massey, Jr. (1957), *An Introduction to Statistical Analysis*, 2nd Edition, McGraw Hill, New York.

S. Fordham (1966), *High Explosives and Propellants*, Pergamon Press, London.

D.N. Griffin (1961), "The Initiation of Liquid Propellants and Explosives by Impact", presented at Propellants, Combustion and Liquid Rockets Conf., Palm Beach, FL, Apr. 26-28, American Rocket Society, paper No. 1706-61 (Source: International Aerospace Abstracts, 1961).

O. Lee, Y. Koga, and A.P. Wade (1990), *Talanta*, 37, 861.

S.F. Sarner (1966), *Propellant Chemistry*, Reinhold Publishing Corp., New York, (1966).

Study of Acoustic Emission Generation in Sliding Motion

Musa K. Jouaneh, Richard Lemaster and Frank C. Beall

Abstract

Increasing interest in automation requires the development of a variety of sensors for monitoring and feedback purposes. One such area is tactile sensing where there is a need for sensors to characterize the interaction between a probe and the surface. Acoustic Emission (AE) is sensitive to plastic deformations that occur in a material due to dynamic contact. This paper investigates AE signal generation during sliding motion when a probe moves over a surface. The objective is to understand how geometrical properties of the surface affect the characteristics of the resulting signal. An AE sensor, connected to a probe through a waveguide, picks up the AE signal as the probe is moved over the surface. A needle, bar, and a rod were used as contact probes. The AE generation mechanism is assumed to be primarily due to the following two sources: impact of the moving probe with surface asperities, and deformation of asperities due to sliding motion. Coated abrasives ranging from 600 to 36 grit size were used as testing surfaces.

Experimental results using various feed speeds and the three different probes have shown that the AE event count is the most sensitive to variations in grit sizes while the rms voltage and mean peak amplitude per event of the AE signal are only sensitive for low grit sizes. In addition, the needle and bar are more sensitive than the rod probe. For hard materials, such as co71-81vng probe with asperities is the more dominant source of AE. This work suggests that, with further study, AE might be able to be used to measure average surface roughness characteristics.

1. Introduction

Increasing interest in tactile sensing as a means of providing feedback on surface texture requires the development of sensory techniques to capture this information. Humans perceive texture through dynamic sensing in which some form of contact motion is involved (Hollerbach, 1984; Schiff and Foulke, eds., 1982). Dynamic sensing is needed to understand friction and wear in contacting surfaces, and to detect and control slip in robotic grasping operations. A review of dynamic sensing techniques is given in Cutkosky and Howe (1988). An essential part of the sensing process is to understand the interaction between the sensor and the surface. One possible method for assessing contact characteristics is acoustic emission (AE) sensing.

Received 15 May 1991. M.K. Jouaneh is affiliated with Department of Mechanical Engineering & Applied Mechanics, University of Rhode Island, Kingston, RI 02881, and R. Lemaster and F.C. Beall are with Forest Products Laboratory, University of California, Richmond, CA 94804.

AE signal analysis has been used in several contact studies (Rangwala et al., 1988; Dornfeld and Cai, 1984) in the past and the results obtained showed that AE was sensitive to parameters such as the contact separation distance and the initiation of slip. Our objective in studying sliding motion is to understand how the geometrical properties of a surface affect the characteristics of the AE signal that is used to monitor this interaction. A possible configuration for the AE method is to attach the AE transducer to a probe that is dragged over the surface. Due to the contact nature of the proposed technique, it is speculated that it will be sensitive to rough surfaces. AE technique offers several attractive features. The AE signal produced is a function of the distribution of surface asperities. It is a low cost technique that can be used at moderately high speeds, and can operate in real-time.

Since surface characteristics directly affect the interaction process in sliding motion, it is of interest to describe the current techniques used to measure surface characteristics. The mechanical stylus and the optical profilometer are the most widely used techniques (Sherrington and Smith, 1988a), with the mechanical stylus technique being one of the oldest for recording surface profiles. The stylus, a pointed needle with a round diamond tip, is held from a supporting fulcrum through a lever arrangement. In operation, the stylus is dragged over the surface at a constant speed, and a record of the vertical motion of the tip is kept. Amplification of the profile features is provided by the lever ratios in the connecting linkages. A transducer, such as a Linear Variable Differential Transformer (LVDT), transforms the mechanical motion of the stylus into electrical signals.

Usually, two configurations of the stylus technique have been used: the true datum stylus, and the surface datum stylus (Maxey, 1964). The true datum stylus gives a true profile of the surface, since the vertical motion of the stylus is with respect to an accurately flat or curved shape which corresponds to the nominal shape of the specimen. The surface datum will hide (2nd order) irregularities since the stylus records only differences between the surface and a skid or shoe that rides on the surface. Since in areas of gentle curvature, the plane of the skid is close to the surface, the tracing will appear as a horizontal line corresponding to the initial zero-set position. This high pass filtering of surface wavelengths larger than the skid size is a shortcoming of surface datum stylus. While the true datum stylus configuration can record all variations from the nominal shape, it is a more time consuming method than the surface datum one, and requires extensive setting up procedure to align the specimen and datum (Sherrington and Smith, 1988a).

Although, current stylus designs can offer high vertical resolution, they have some limitations. The dynamics of motion prevents rapid transverse movement (<7.6 cm/min), and

since it is a fragile device, it requires a clean environment and thus is not applicable to on-line production conditions. In addition, the width of the stylus tip must be small compared to the lateral size of the surface irregularities.

The other commonly used technique, optical profilometry, generates a profile of the surface using a laser beam that replaces the diamond tip in the mechanical stylus technique. Different configurations of profilometers have been developed, but all are made primarily of two parts: a light source with a lens focusing system, and a detector to monitor the intensity of the reflected light. While optical techniques have desirable properties (Sherrington and Smith, 1988b) such as they are non-contacting and thus do not damage the surface, they are adaptable to operate in an on-line fashion, and they do not require special specimens to be prepared, they have some limitations (Stedman, 1989). The horizontal resolution is dependent on the wavelength of the incident light and the numerical aperture of the focusing lens. Also, errors might occur in non-homogenous specimens due to variable phase changes on reflection. Furthermore, there is a limit on profile angle or slope that can be measured by this technique.

This paper is divided into several sections: in the next section a review of previous studies of AE in contact motion is given; Sec. 3 discusses the assumed mechanism of AE generation in sliding motion; Secs. 4 and 5 discuss the experimental approach used to test the ideas; and Sec. 6 presents and discusses the data obtained. The last section presents our conclusions for this study.

2. Previous AE Studies in Contact Motion

Several investigators have examined the use of AE in contact studies. Much of the discussion below follows from Rangwala et al. (1988). In one of the first attempts, Dornfeld and Cai (1984) conducted grinding experiments in which the rms voltage level of AE was monitored during the process of wheel sparkout. Sparkout is defined as the end of material removal as indicated by the end of spark generation. They showed that the AE energy level is very sensitive to sparkout. As the level of engagement between the grinding wheel and the workpiece gradually decreases, so does the AE level. Sparkout is then marked as the point where the AE energy level drops to the background noise. The above authors have also shown that the AE energy level can be used to indicate the instant of first contact by monitoring the AE level as the gap between the grinding wheel and the workpiece is decreased. A sharp increase in the signal is observed as the gap goes to zero. By using a suitable threshold, the instant of first contact can then be monitored.

In another investigation, Fleischaker (1986) investigated the sensitivity of the AE rms voltage to sparkout in grinding. Using a grinding wheel that was mounted on a milling table, several runs were made in which the workpiece was moved in both directions with a preset depth of cut. The above tests have shown a similar trend to the experiments discussed in the previous paragraph. In an investigation of sliding contact and wear, Jiaa (1989) has studied the influence of process variables such as loading condition, sliding speed, and distances on the AE generated from the sliding contact of metal-metal pairs

using a pin-on-disk experimental setup. In wear sliding tests, the AE rms voltage signal was characterized into three distinct regions depending on the time elapsed from the start of the test. In the velocity and load tests, the mean level of AE was shown to be an increasing linear function of sliding speed under different loads.

The above experimental studies have shown that AE is sensitive to contact when the relative velocity between contact surfaces is high. AE has also been shown to be sensitive to slipping motion of a workpiece. Dornfeld and Handy (1987) have investigated the influence of normal load, material combination, surface finish, and relative velocity on the rms voltage level during slipping motion. Their experimental setup consisted of an aluminum block mounted on a dynamometer on which specimen blocks of various materials and surface finish were placed. The tangential force and the rms voltage of AE were recorded at the inception of slip as the blocks were moved along the aluminum plate at different speeds. For the case of steel on aluminum, an interesting dependence of AE spike amplitude on normal load, surface finish, and velocity was observed. At high velocities, the AE amplitude increases with the normal load for rough surfaces and shows the opposite trend for smooth surfaces.

In a study of slip detection for cylindrical workpieces, Rangwala et al. (1988) discuss the generation mechanism of AE during slip motion. Using a two-finger gripper with rectangular fingers attached to an industrial robot, they examined the rotational and translational slip modes. They showed that rotational slip, which involves a transition from line to point contact, generates a high frequency, attenuating type of AE signal. For translational slip, which does not involve a change of contact mode, the AE signal is a periodic signal with superimposed, high frequency activity. It is speculated that AE generation during sliding is produced by surface asperity deformation, formation of microcracks, and separation of asperities from the surface due to fatigue and microcutting. It is seen that the above studies have only concentrated on detection of slip or tool-workpiece engagement, but not on a study of surface geometry effect on AE generation in sliding motion. For identifying texture, it is important to understand the characteristics of AE signals as a probe is moved over a surface.

3. Sources of AE in Sliding Motion

Previous studies on friction and wear mechanisms (Czichos, 1978; Suh, 1981) show that materials can exhibit two basic responses to surface traction: deformation of the surface and subsurface, and fracture of solids. Both have been demonstrated as potential sources of AE (Ono, ed., 1979). In sliding contact, additional sources of AE from friction and wear include impulsive shock due to asperity collision and debris (Sayles and Poon, 1981), and microvibration excited by stick-slip at the interface (Dornfeld and Handy, 1987). In using AE for studying sliding motion, our technique will use a probe that is moved over the surface. In this configuration, the AE generation mechanism will be assumed to be primarily due to the two following sources: 1) Impact of the moving probe with surface asperities, 2) Deformation of asperities due to sliding motion.

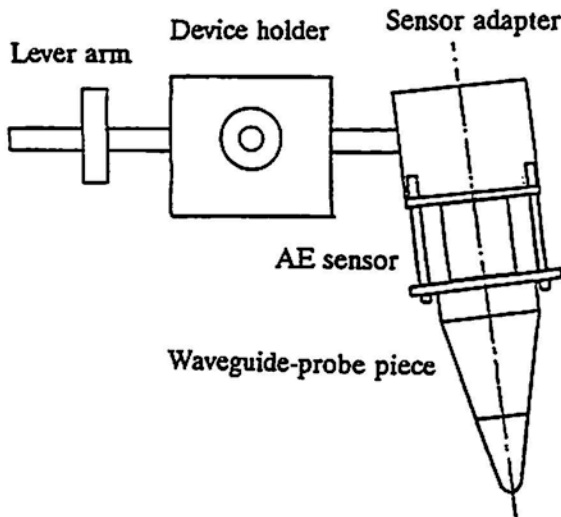
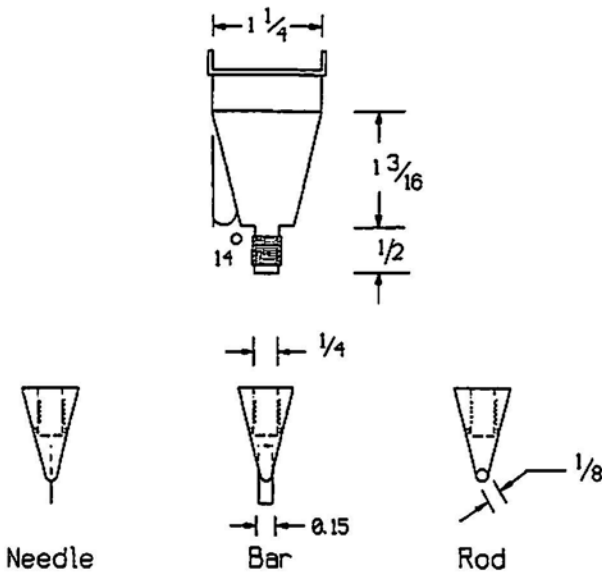


Fig. 1 A schematic of experimental setup.



Note: All Dimensions are in Inches.

Fig. 2 A cross section of the waveguide-probe piece.

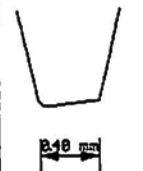
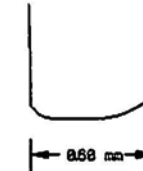
The assumption is that these two components occur at the same time with the relative contribution of each depending on the hardness of the surface. The probe material should be made of hardened material that has good wear resistance and is a good transmitter of AE signals. The normal load effect can be investigated by designing a setup which can apply a variable effective load at the probe. Since the probe is intended to study sliding motion, its design should allow for maintaining contact with the surface at all times. The dynamics of moving the probe at high velocities over the surface calls for a design which minimizes vibrations. These considerations were taken into account in designing the experimental setup discussed in the next section.

4. Experimental Setup

The experimental setup consists of five parts: a device holder, a sensor lever arm, a sensor adapter, an AE sensor, and a waveguide-probe piece. Figure 1 shows these parts. The sensor assembly, which was mounted on the lever arm, was attached to a Cincinnati milling machine. The lever arm position can be adjusted to apply a given effective load at the probe end. In addition, lead counterweights mounted on the lever arm are used to change the effective load. The sensor adapter, an angle-shaped piece which holds the AE sensor and the waveguide-probe piece, can be adjusted to change the orientation of the waveguide-probe about two axes. The waveguide-probe is a nylon-66 cone-shaped part made of two pieces that are screwed together (see Fig. 2). The AE sensor rests on the base of the upper part and probes of different geometry are attached to the lower part. The probe piece has small holes in its side which provide an outlet for the excess AE couplant between the probe piece and the waveguide. This design allows for different probe pieces to be attached to the sensor without changing the sensor position while also insuring good coupling. In addition, the arrangement offers a convenient way for replacing probes due to wear.

A needle, a thin rectangular bar (edge), and a rod (roller) are the three different probes that we used in this study. Table 1 shows a profile of each probe with its dimensions and material properties. Due to the different contact areas of the three probes, the counterweights in the above set were adjusted differently for each probe to obtain a particular effective probe load. The loads were 0.020, 0.060, and 0.19 kg for the needle, bar and rod probes respectively.

Table 1 Probe data.

	Rod Probe	Needle Probe	Bar Probe
Material	Hardened Carbon Steel	Hardened Spring Steel	Hardened Carbon Steel
Profile Section			

The workpiece consists of ten 203 mm x 38 mm strips of 3M silicon carbide coated abrasives that were glued to a rectangular piece of fiberboard. Coated abrasives were selected since they are readily available and they represent random surfaces (Pandit et al., 1977; Phadke et al., 1975), typical of the primary texture components of ground or lapped surfaces (Peklenik and Kubo, 1968). The strips were equally spaced 19 mm from each other using Avery self-adhesive white labels. The labels provide a smooth transition between the different coated abrasives. The coated abrasives samples were made of closed coat grits on dry/wet cloth with grit sizes ranging from 600 to 120. Table 2 lists the relevant data on the coated abrasives used, and the appendix provides a brief description of coated

Table 2 Coated abrasives workpiece data.

Abrasive Index	Size (μm)	Coat	Backing
600	14.5	Closed	Dry/wet
500	18.2		
400	22.1		
360	27.3		
320	34.3		
240	51.8		
220	66.0		
180	80.0		
150	95.0		
120	116.0		

abrasives structure. The coated abrasives workpiece was held on to the milling table using screws. The vertical position of the table was adjusted so that the sensor lever arm was oriented horizontally with the probe touching the workpiece. At this position, the axis of the conical waveguide was oriented at 10° with respect to the vertical direction. The output of the AE sensor is connected to a filter and a 40 dB preamplifier. The output of the preamplifier is then fed into an AET 5500 acoustic emission system where the signal is amplified by an additional 40 dB gain before being processed.

5. Experimental Procedure

Since many combinations of filters and AE transducers can be used, several tests were performed to determine the best transducer-filter combination. The tests were performed by moving an earlier version of the needle probe over a finely finished hardwood workpiece at a speed of 6.7 mm/s. The wood surface represents a weak surface interaction situation, and hence suitable for measuring sensitivity. Using an AET (Acoustic Emission Technology Corporation) AC30-L, AC75-L, AC175-L, and AC375-L resonance transducers with five different filters: 15-45 kHz, 45-90 kHz, 625 Hz-125 kHz, 0.125-0.25 MHz, and 0.25-1.0 MHz, the rms voltage level of the AE signal was monitored. The AC175-L and the AC375-L transducers showed the most sensitivity in terms of higher magnitude mean rms values for most of the filters used, with the AC375-L performing better for the higher filter ranges. The AC375-L transducer was then selected and similar runs were made using 625 Hz-0.125 MHz and 0.125-1 MHz filters. In this case, the frequency content of the amplified signal was analyzed. The data shows that most AE activity was in the frequency range 100-400 kHz. The tests showed that a 375 kHz transducer with a 0.125-1 MHz filter would be the most sensitive in our application, and subsequently all runs were made using this combination.

AE data was collected for the three different probe geometries at three different speeds. The speeds were 0.35 cm/s which for simplicity is referred to later as 0.35 cm/s, 0.68 cm/s, and 1.27 cm/s. The speed ratios are approximately in geometric proportion, and the 1.27 cm/s speed is the maximum table speed for the milling machine. In each run, a different segment of the coated abrasives is traced.

Since the event count and duration are dependent on the specification of a threshold level, a threshold level needs to be specified. A 0.5 V value was used for the different probe geometries and speeds used so that a comparison of the sensitivity of each probe could be made. The 0.5 V level was selected by

moving the rod probe (low sensitivity) at a speed of 0.68 cm/s. The AE events for four threshold levels ranging from 0.25 to 1.0 V were monitored. While the 0.25 V threshold level gives greater signal amplitude, the 0.5 V level shows a better discrimination between the different coated abrasive surfaces.

6. Results and Discussion

Several parameters that are available on the AET 5500 were initially considered. After much data analysis, only three parameters were kept. They include the event count, the mean peak amplitude per event, and the rms voltage. These parameters were chosen since they describe different but complementary components of the AE signal. The above parameters were computed for every 1.27 mm displacement so that the effect of speed variation could be compared. The time interval between separate events was set to 256 μs on the AET 5500. For illustration purposes, the average of each parameter over the coated abrasive sample length (38 mm) is displayed.

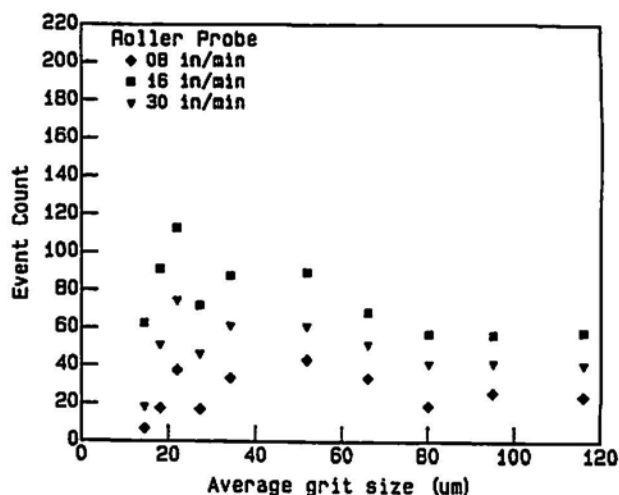


Fig. 3 Average event count vs. average mineral particle diameter (rod probe)

Figures 3-5 show plots of the average event count for the three probes used. The data is plotted against the average mineral particle diameter size (Anon., 1984; see Table 2 for conversion to abrasive index). Since this parameter is understood to be a crude approximation of coated abrasive geometry, more quantitative representation of coated abrasives geometry using parameters such as the ones obtained from a broad probe profilometer (Gagliardi et al., 1985) is underway. Several trends are observed in the data. The first is the needle and bar probe are more sensitive to variations in grit size and show more noticeable patterns than the rod probe. The rod probe shows a decreasing event pattern only for particle diameter sizes larger than 50 μm . This can be attributed to the fact that the geometries of needle and bar probes cause more impact with the asperities. The second trend is that the events decrease as the grit size diameter increases, since fewer asperities per unit length will come into contact with the probe. While the intensity of impact increases as the grit size increases, the event count is insensitive to the signal amplitude as long as the signal exceeds the threshold level.

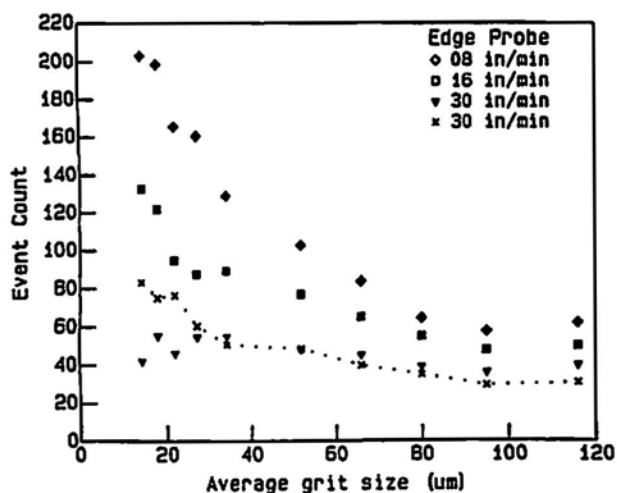


Fig. 4 Average event count vs. average mineral particle diameter (bar probe)

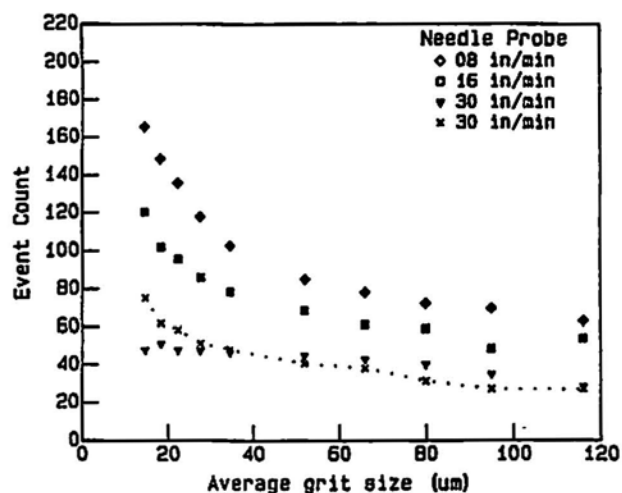


Fig. 5 Average event count vs. average mineral particle diameter (needle probe)

The third trend is that increasing the travel speed results in a decrease in the event count. This can be attributed to the fact that at higher speeds less contact occurs with the grit due to the dynamics of the probe. The dotted curve for the needle and the edge probe data illustrates the effect of changing the threshold from 0.5 to 1.5 V for the 12.7 mm/s run. The noise level is reduced in this case and a smoother relationship is obtained. However, the threshold level should not be set very high since in that case very few events are detected resulting in a reduction in sensitivity. A signal-dependent threshold level similar to that used by Pan and Dornfeld (1985) will eliminate the problem of specifying the threshold level. Figure 6 shows plots of the event count for the three different speeds. The figure shows the variation in this parameter value, which is similarly exhibited by the other parameters considered, and when using other probes. Due to these fluctuations, the measured parameters can be related to surface geometry only in an average fashion. In what follows, only data plots for the needle probe will be shown due to space considerations.

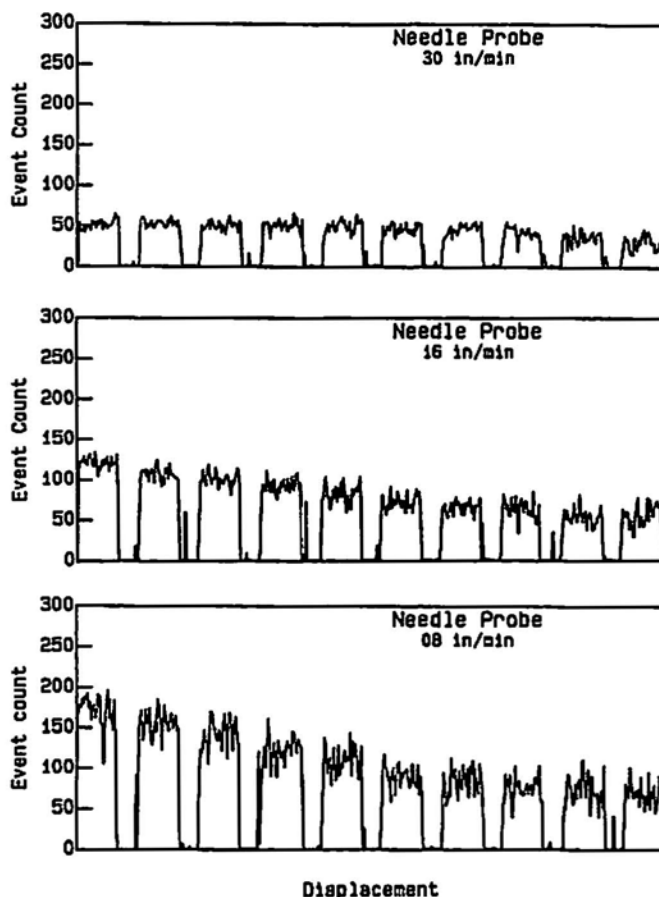


Fig. 6 Event count data for needle probe.

The rms voltage is plotted in Fig. 7. Unlike the event count parameter, the voltage increases as the speed increases for the three probes used. This occurs since the intensity of impact increases with increasing speed. While fewer events are generated at higher speed, the change in momentum is higher resulting in an increase in the rms value. As for the data trend, the average rms increases up to a particle diameter size of 52 μm and then slightly decreases as the particle size increases. This occurs because as the interval between events increases, the increased signal intensity due to the grit size increase stops overriding the decrease in the number of impacts around a grit size of 50 μm . The rms voltage is not sensitive to changes in threshold level, unlike the event count. The rms voltages from the needle and bar probes have a higher sensitivity than the rod probe, similar to the trend in the event count data.

The mean peak amplitude parameter is plotted in Fig. 8. The mean peak amplitude increases up to a particle diameter size of 52 μm , and then either slowly increases or remain flat. This parameter shows a similar trend to the rms voltage for low particle sizes. The mean peak amplitude does not depend on a measurement time interval and therefore does not decrease as the spacing between grits increases. The anomaly in this parameter for the 12.7 mm/s run is due to the decreased sensitivity at the 0.5 V threshold level. A smoother and less variable trend is obtained when the threshold is set to 1.5 V as shown in the dotted curve in the figure. While fewer events are generated at higher speeds, the signal amplitude is higher at higher speeds

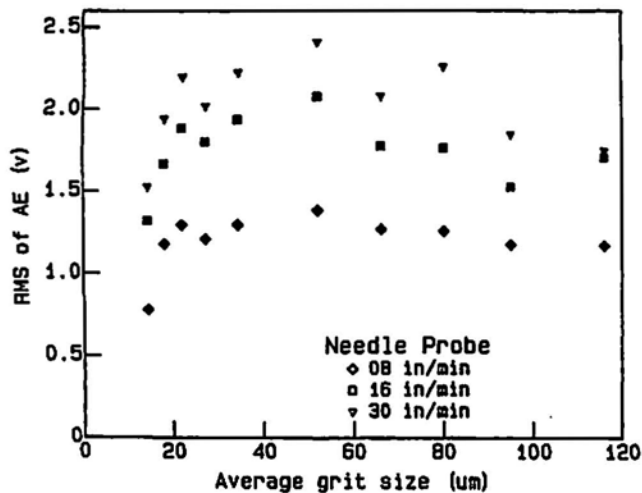


Fig. 7 Average rms voltage vs. mineral particle size (needle probe).

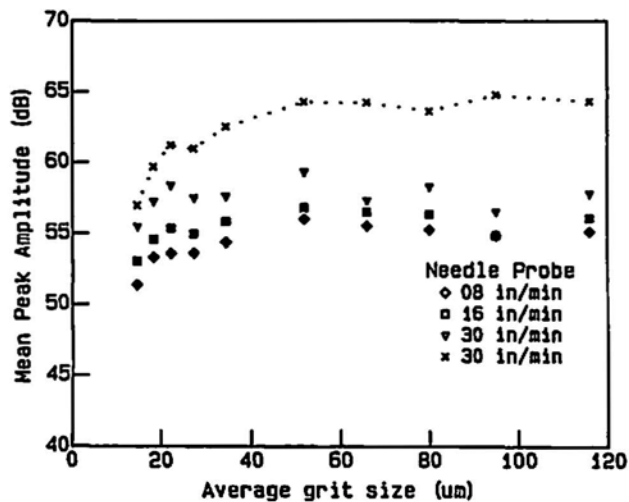


Fig. 8 Average mean peak amplitude per event vs. mineral particle size (needle probe).

due to the increased intensity of impact resulting in a higher mean peak amplitude.

7. Conclusions

This paper investigated AE generation mechanism in sliding motion. Using the surface interaction between probes of different geometries and coated abrasives as a source of AE, the study investigated the effect of speed, contact geometry, and surface grit sizes on the AE signal obtained. Since coated abrasives are made of very hard grits (9.6 Mohs) that are rigidly attached to their backing, some of the conclusions stated below may not be applicable to soft materials where other modes of AE generation mechanisms are more predominant. The study conclusions are:

1. The impact between a probe and asperities of a hard surface is a more dominant source of AE than deformation of asperities.
2. A flexible probe with small contact area such as the needle is

more sensitive to surface interactions than a more rigid probe with wider area such as the rod.

3. The event count is the AE parameter most sensitive to variation in grit sizes. However, it is threshold dependent. The rms voltage and the mean peak amplitude per event are sensitive for low particle size diameters. Since all the parameters show a non-negligible fluctuation, AE can only be used to indicate properties averaged over a length of the sample.

4. Increasing the speed results in a decrease in the event count because less contact is occurring with the grits due to the dynamics of the probe. It also results in an increase in the rms voltage due to a net increase in momentum transfer, and an increase in the mean peak amplitude due to an increase in the intensity of impacts.

5. Increasing the grit size results in a smooth decrease in the event count since less contact with asperities is occurring per unit length. There is a limited increase and then a gradual decrease in the rms voltage since the increased signal intensity does not override the increase in the time interval between events and a gradual increase in the mean peak amplitude occurs since the intensity of impact increases.

For future work, as part of developing a general relationship between surface geometry and AE signal characteristics, a different characterization of coated abrasives is needed for more descriptive representation of their geometrical features. Also, it would be of interest to study sliding motion for general surfaces other than coated abrasives.

Acknowledgement

Thanks to Dr. E. Duwell of 3M Company for providing information about coated abrasives, to Kevin Strauss for his helpful discussions on designing the experimental setup, and to T. Breiner for providing some of the analysis programs.

References

- Anon. (1984), "American National Standard for Grading of Certain Abrasive Grain on Coated Abrasive Material", ANSI/ASC B74.18.
- M. Cutkosky and R. Howe (1988), "Dynamic Tactile Sensing", ROMANSY 88: 7th CISM- IFToMM Symp. on the Theory and Practice of Robots and Manipulators, Udine, Italy.
- H. Czichos (1978), *Tribology*, Elsevier, Amsterdam.
- D. Dornfeld and C. Handy (1987), "Slip Detection using Acoustic Emission Signal Analysis," Proceedings of the 1987 IEEE International Conference on Robotics and Automation, Raleigh, NC, pp. 1668-1675.
- D. Dornfeld and H. Cai (1984), "An investigation of Grinding and Wheel Loading using Acoustic Emission," Trans. ASME, Journal of Engineering for Industry, 106(1), 28-33.
- D. Dornfeld and C. Pan (1985), "Determination of Chip Forming States using Linear Discriminant Function Technique

with Acoustic Emission", 13th NAMRC Conf., SME, Berkeley, CA, pp. 299-303.

T. Fleischaker (1986), Analysis of Grinding Process Using Acoustic Emission Signal Analysis, M.S. Report, Department of Mechanical Engineering, University of California at Berkeley.

J. Gagliardi, I. Hong and E. Duwell (1985), "Analysis of Coated Abrasive Surfaces with a "broad probe" profilometer", 13th NAMRC Conf., SME, pp. 321-325.

J. Hollerbach (1984), "Tactile Sensors and the Interpretation of Contact Features", Workshop on Intelligent Robots: Issues and Achievements, SRI International, Menlo Park, CA, November, pp. 143-152.

C. Jiaa (1989), Intelligent Acoustic Emission Sensing in Machining for Tool Condition Monitoring, Ph.D. dissertation, Department of Mechanical Engineering, University of California at Berkeley.

C. Maxey (1964), "Measuring Texture and Contact Area of End-Wood Surfaces," Materials Research and Standards, 4(6), 279-285.

K. Ono, ed. (1979), *Fundamentals of Acoustic Emission*, UCLA, Los Angeles, CA.

S. Pandit, F. Nassirpour and S. Wu (1977), "Stochastic Geometry of Anisotropic Random Surfaces with Application to Coated Abrasives," Trans. ASME, J. Engineering for Industry, 99, 218-224.

J. Peklenik and M. Kubo (1968), "A Basic Study of a Three-Dimensional Assessment of the Surface Generated in a Manufacturing Process", Annals of the CIRP, 16, 257-265.

M. Phadke, F. Burney and S. Wu (1975), "Evaluation of Coated Abrasive Grain Geometry and Wear via Continuous Time Series Models," Wear, 31, 29-38.

S. Rangwala, F. Forouhar and D. Dornfeld (1988), "Application of Acoustic Emission Sensing to Slip Detection in Robot Grippers," Int. J. Mach. Tools Manufact., 28(3), 207-215.

R. Sayles and S. Poon (1981), "Surface Topography and Rolling Element Vibration", Precision Engineering, 3, 137-144.

W. Schiff and E. Foulke, eds. (1982), *Tactual Perception: A Sourcebook*, Cambridge University Press, Cambridge.

I. Sherrington and E. Smith (1988a), "Modern Measurement Techniques in Surface Metrology: Part I; Stylus Instruments, Electron Microscopy and Non-Optical Comparators," Wear, 125(3), 271-288.

I. Sherrington and E. Smith (1988b), "Modern Measurement Techniques in Surface Metrology: Part II; Optical Measurements," Wear, 125(3), 289-308.

M. Stedman (1989), "Limits of Surface Measurement by Optical Probes," *Surface Measurement and Characterization*, Jean M. Bennet, ed., Proc. SPIE 1009, pp. 62-67.

N. Suh (1981), *Tribophysics*, Prentice-Hall, Englewood Cliffs, NJ.

Appendix: Background on Coated Abrasives

This appendix follows from reference (Anon., 1984). Coated abrasives are multiple point cutting tools that are available in a variety of geometric configurations. A typical coated abrasive is produced from three basic raw materials: a mineral, an adhesive "bond", and a backing. Figure A1 shows a cross section of a typical coated abrasive. The backing serves as the base upon which a coating of adhesive known as the "make" coat is uniformly applied to anchor a single layer of mineral particles. Individual mineral particles are applied to the make coat and oriented in an electrostatic fashion or with a mechanical process to maximize the probability that a particle will be positioned with its long axis perpendicular to the backing. After the make coat is cured, a second coat of adhesive, known as the "size" coat, is applied over the surface to further support the particle and give rigid support to the backing. Coated abrasives are commonly available in "closed" and "open" coat product variation. The close coated abrasive is one whose backing is fully covered with mineral particles to maximize the number of cutting points available. The open coat construction widens the area between particles and produces a self-cleaning action during grinding. The weight designation A, C, .., etc. refers to the weight of a given number of coated abrasive sheets.

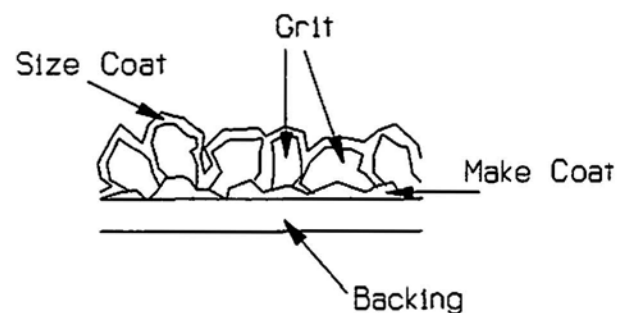


Fig. A1 Cross section of a typical coated abrasive.

AEWG 36th Meeting

cracks in engineering materials and structures. Although it is an excellent technique for detecting and locating cracks, it has not been an effective method to use for objectively determining the amount of crack growth occurring. This is due to the "color" introduced by plate-like structures on the transient elastic waves and the "color" introduced by the transducer and electronics. Attenuation as well as dispersion of the stress waves also plays an important role in changing the characteristics of the AE signal as a function of distance from the source.

This report shows the results of research presently in progress to remove the effects of "color" introduced by a structure, transducers, electronics, and attenuation on AE signals from a growing crack during an Acoustic Emission test in order to estimate the amount of crack area generated during the test. This is accomplished by the use of controlled hydrogen embrittlement cracking of a high strength bolt. Acoustic Emission signals generated from cracking of the bolt are injected via waveguide into the structure at a known crack location. Following failure of the bolt, the amount of crack area generated due to crack growth prior to failure of the bolt is measured. The total number of AE counts from each channel is recorded for this amount of crack area and is then used as a calibration criteria for each channel for estimating the amount of new crack area generated by the known crack in the structure. The fixture holding the bolt, as well as the bolt and waveguide also contribute "color" to the AE signal from the cracking bolt. Therefore, it is necessary to measure these effects in order to more accurately calculate the crack area from the structural crack. The approach being used to measure these characteristics will also be discussed in this report.

Jerry W. Whittaker

Characterization of the ASL Parameter

Electron beam (EB) welding of uranium produces large amounts of acoustic emission (AE) having a broad range of amplitudes. The Average Signal Level (ASL) parameter has been used to summarize and quantify such emission. The parameter's ability to average the effects of numerous signals and its large dynamic range make it particularly useful. We performed experiments to provide a better understanding of the response of the ASL circuitry to AE produced under various conditions. The effects of emission type (continuous, burst and mixed), signal amplitude and frequency, and recording instrument were evaluated.

Baxter H. Armstrong

Low Strain Level AE due to Seismic Waves and Tidal/Thermoelastic Strains Observed at the San Francisco Presidio

Oh-Yang Kwon and Dong-Jin Yoon

Monitoring of Lubrication Quality in a Simulated Journal Bearing System by AE

A simulated journal bearing system was built and used for developing a rotating machinery diagnosis scheme with acoustic emission monitoring. Since the quality of lubrication is thought to be the most critical condition for sound operation of a journal bearing system its acoustic emission behavior has been studied under various lubrication conditions deliberately contaminated with alumina and iron powders. To change lubrication conditions, 0.1 to 0.5% in volume of alumina powders whose particle size are 1, 8 and 38 μm were added to the lubricant. The minimum clearance between the journal and the bearing was kept as 15 μm by selecting the load and rotating speed.

Results showed that AE activity increased considerably with increasing speed of rotation whereas it increased moderately with increasing volume fraction of contaminants. The erosive action of alumina particles can account for this result. On the other hand, AE activity was virtually not affected by increasing particle size from 1 to 8 μm , then was drastically increased with 38 μm particles. This implies that the AE source mechanism is different when the particle size is larger than the minimum clearance (15 μm). The bearing surface could have been under plowing action of alumina particles and was found severely worn after about 10 minutes of operation.

The objective of this study is early detection of abnormal operation conditions in rotating machinery with journal bearings. Various parameters and conditions which affect the AE activity at the boundary layer of journal bearings are to be systematically investigated.

Yakichi Higo

The Method for Measurement of Sensitivity Degradation of AE Transducer

Clinton Heiple, S.H. Carpenter and D.L. Armentrout

Comments on the Origin of AE in Fatigue Testing of Aluminum Alloys

(Continued to page 96)

The Role of Acoustic Monitoring as a Diagnostic Tools in Nuclear Reactors

Shahla Keyvan and Ron King

Abstract

This paper presents the results of a survey on acoustic monitoring applications in light water reactors and an assessment of application of acoustic monitoring technology in Experimental Breeder Reactor II (EBR-II), the only power producing liquid metal fast breeder reactor in the United States. The main objective of this paper was to obtain information on various applications of acoustic techniques in light water reactors (both boiling water reactors and pressurized water reactors) and to assess applications for EBR-II from its past experiences.

1. Introduction

Among the phenomena found usable in detection of incipient equipment failure are the acoustic emission (AE) phenomenon, and the resonant frequency phenomenon. The acoustic emission phenomenon is most applicable to material faults. The resonant frequency phenomenon applies to rotating machinery, since the relative motion rather than material itself is the source of the sound. In rotational equipment, such as pumps or generators, a form of acoustic energy exists when a failure mechanism is in process or has created a very small defect. This is the resonance frequency phenomenon and is created by shock excitation of a rotational mass spring over a defect, as a ball in a ball bearing rolling over a spall. All components of the mechanical equipment resonate when shock excited, thus creating a wide range of frequencies.

In the decade of the 1960's, engineers became interested in utilization of the AE phenomenon in studies under the category of nondestructive testing (NDT). AE is defined as transient elastic wave generated from release of energy in material; e.g., as a result of plastic deformation. AE sensors respond to pressure waves over a wide range of frequencies. Hence any events creating detectable pressure waves such as pressure boundary leaks, or loose parts can also be detected by AE sensors, thus broadening the application of AE techniques. This paper presents an evaluation of acoustic monitoring applications in light water reactors (LWRs) and liquid metal reactors (LMRs), and specifically addresses applications of acoustic monitoring technology in Experimental Breeder Reactor II (EBR-II), a liquid metal reactor.

Received 18 June 1991. S. Keyvan is affiliated with Department of Nuclear Engineering, School of Mines and Metallurgy, University of Missouri, 222 Fulton Hall, Rolla, MO 65401-4748 and R. King is with Argonne National Laboratory, Argonne West, EBR-II Division, P.O. Box 2528, Idaho Falls, ID 83403-2528. This work was supported by the U.S. Department of Energy, Reactor Systems Development and Technology, under Contract W-31-109-ENG-38.

The purpose of this paper is:

- To address the role of AE monitoring as a diagnostic tool for nuclear plant surveillance.
- To identify current areas of application of AE for diagnostics in nuclear power plants.
- To identify current and potential areas of application in LMRs/EBR-II.
- To provide information to encourage acceptance of the technique by evaluation of its application at LWRs.

A representative sample of thirteen nuclear plants (LWRs) were selected on the basis of:

- Plant type (boiling water reactors or BWR and pressurized water reactors or PWR).
- Commercial operation.
- Geographical location.

Table 1 gives the list and brief information about these nuclear power plants. This assessment is primarily based on the information directly provided by each plant on the subject of acoustic monitoring applications (Keyvan, 1989). Applications of acoustic technology in nuclear reactors for surveillance and diagnostics are increasing. Currently, this technique is utilized in the following areas:

- Loose parts monitoring.
- Leak detection monitoring.
- Valve position monitoring.
- Sodium boiling detection (in LMRs).

Table 2 provides information on the current areas where acoustic techniques are utilized, and the task or function of the corresponding monitoring system in the LWRs in the United States.

1.1 Loose Parts Monitoring in Light Water Reactors

According to the US Nuclear Regulatory Commission (NRC) Regulatory Guide 1.133, any reactor licensed since 1978 must have systems to detect loose parts and components within reactor vessels and primary coolant systems. Early detection of loose parts in LWRs is important from a safety point of view, since the loose parts could either be part of a safety related system or could damage a safety related system by their interference with the reactor coolant system (RCS). In addition, early detection of loose parts can prevent extended outages, reduce downtime for repair of damage caused by undetected parts, and could provide an indication of degradation of reactor internals.

Loose Part Monitoring Systems (LPMS) are applied to both PWRs and BWRs. However, PWRs have experienced more damage due to loose parts than BWRs. Although LPMS are similar for both BWRs and PWRs, requirements for the number of sensors and sensor locations are different in these two types of LWRs. Background noise in a BWR is also different from a PWR because of BWR's relative low flow in the lower reactor vessel, steam flow noise in the upper vessel, and the recircula

TABLE 1 List of LWRs in the Survey of Acoustic Monitoring Program.

UTILITY	PLANT NAME	MW _e	TYPE	COMMERCIAL OPERATION
Philadelphia Electric Co.	Peach Bottom 2 & 3	1065	BWR	1974
Philadelphia Electric Co.	Limerick 1 & 2	1055	BWR	1986, 1989
Gulf State Utilities Co.	River Bend 1	936	BWR	1986
System Energy Resources, Inc.	Grand Gulf 1	1250	BWR	1985
Carolina Power & Light Co.	Brunswick 1 & 2	790	BWR	1977, 1975
Toledo Edison Co.	Davis-Besse 1	866	PWR	1977
Louisiana Power & Light Co.	Waterford 3	1104	PWR	1985
Tennessee Valley Authority	Watts Bar	1177	PWR	Indefinite
Arkansas Power & Light Co.	ANO 1 & 2	836, 858	PWR	1974, 1980

Table 2 Areas of utilization of AE technique and its function.

AE APPLICATION	FUNCTION/TASK
Steam relieve valve position monitoring	Monitoring for open valves
Continuous vibration monitoring	Monitoring critical rotating equipment
Steam leak detection	Monitoring valves for seat leakage
Check valve testing	Monitoring of check valves to determine valve condition
Portable AE system	Detection of valve leaks
Loose part monitoring system	Detection of loose parts in the reactor
Sodium boiling detection	Detection of boiling in sodium
Transformer partial discharge detection	Monitoring transformers for internal corona
Drywell valve packing leak detection	Detection and identification of leaking valves
Safety relief valve pilot leakage detection	Monitoring second stage pilot valve for leakage

tion flow noise in the middle region of the vessel. PWRs appear to have a higher operating noise level than BWRs.

Although LPMS are generally used to detect structure-borne sound resulting from the impact of loose parts, BWR's experiences indicate that they can also be used as a means for monitoring of internal structural integrity. LPMS in BWRs have been able to detect problems other than loose parts, such as valve mechanical problems, steam dryer problems and metal impact signals associated with cracked sparger brackets (Mayo et al., 1988).

Proper loose part monitoring in PWRs requires a minimum of six sensors in the reactor vessel: three for upper vessel head; three for lower vessel head; and seven sensors for monitoring the steam generator. A U-tube steam generator requires a minimum of two sensors in the primary inlet region. One sensor is necessary on the primary coolant outlet, one near the top of the tube bundle, two sensors at the upper tube sheet, and one sensor at the lower tube sheet.

Proper loose part monitoring in BWRs requires a minimum of twelve sensors in the reactor vessel distributed three each at lower vessel head, core support plate, feedwater inlet, and steam outlet. To install the sensors on the surface of a component, four different mounting methods can be used. The best is the drill-and-tap method. A strapped or clamped sensor is also acceptable. The third choice is magnetic sensor mounting with epoxy, and the last choice would be magnetic attachment. After

installation, sensors must be checked (without removal) for system response verification. Two methods of impact calibration are recommended (Mayo et al., 1988); namely, pendulum impact, and an instrumented hammer. Each method has its own advantages. The pendulum impact involves simple data acquisition and analysis; while the instrumented hammer requires fewer tests.

Loose part signal characteristics must be used in order to minimize false alarms and responses to events with sources other than loose parts. Alarm set points are typically set about five times the background noise level (Mayo et al., 1988). Bandpass filters are also necessary to reject low frequency noise associated with flow and pump noise, and high frequency sensor resonance response. Typical loose part signal characteristics are determined from relationships between amplitude and frequency as a function of mass, energy, distance and shape of loose parts. In addition, relationships between parameters such as wave velocity, frequency and thickness of the transmitting structure can be used to validate a loose part related signal.

1.2 Acoustic Leak Monitoring System (ALMS)

The physical principle behind acoustic leak detection is that fluid flowing out of a component, (i.e., a pipe) generates high frequency continuous noise. The frequency depends on the size of the leak, and the fluid pressure. Generally, the smaller the leak size or the higher the pressure, the higher the frequency. A unique characteristic associated with leaks is that a

leak-related signal is a continuous signal. In detection of leakage via the AE technique, signals are first amplified and filtered to discriminate against the environmental noise, and then the rms voltage of the signal (which is the most applicable method for continuous signal) is measured. Basically, there are two types of leakage: one associated with components susceptible to leakage such as pump seal and valves; the other is leakage associated with a pipe crack or break. Successful application of the AE technique for detection of a pipe crack or break depends on the information and knowledge of the characteristics of leak and background noise, attenuation characteristics of the leak noise with distance, as well as the relationship between AE noise and leak rate. Generally, the acoustic level (rms voltage) increases as the leak increases until the point where the differential pressure across the leakage point decreases, which causes the acoustic level to drop.

Performance of a leak detection system are evaluated based on the following three criteria: (1) sensitivity, (2) location and (3) quantification. None of the presently acceptable leak detection methods qualify in all three criteria. Acoustic methods have good sensitivity and ability to determine leak locations, and moderate quantification capability. AE leak detection capabilities are comparable to other leak detection methods prescribed in national standards (McElroy, 1982).

2. Acoustic Emission Technology for LMRs

This section provides a review of the areas of application of acoustic techniques in LMRs in foreign countries. The advantages and difficulties in applying the acoustic techniques in each area is also discussed. General areas of monitoring via acoustic techniques in LMRs consist of:

- Sodium boiling detection.
- Leak detection.
- Cavitation detection.
- Loose part detection.

In the area of application of acoustic techniques in detection of boiling in LMRs, major efforts have been undertaken in the past decade. In sodium boiling, the collapse of vapor bubbles is the source of acoustic noise, which in highly subcooled conditions gives rise to sharp high-amplitude pressure pulses and generates noise with frequency components extending well beyond 100 kHz (Burton, 1977). Detection of this noise requires:

- Discrimination against background noise.
- Knowledge of the transmission of acoustic waves in reactor pools, structures and effects of gas bubbles.

An acoustic signal from boiling is highly impulsive. Hence, to take advantage of this characteristic, the detection method can consist of either detecting the impulses in the time domain, or detecting a high frequency signals in the frequency domain. Achieving high sensitivity and early warning requires sophisticated data processing, although simple signal processing is sufficient to provide trip protection.

Two major advantages in boiling detection via acoustic techniques are: 1) a single detector can monitor a large volume of core due to acoustic signal transmission in the medium, and 2) there is no need to mount a detector within the fuel element.

Leak detection in LMR is another active area in application of acoustic technology. The acoustic monitoring program in Super Phenix (a French liquid metal fast breeder reactor) involves water leak detection in the steam generator. The principle of the acoustic leak detection in the steam generator is based on the generation of acoustic waves from the following phenomena:

- Vibration of the supporting structure.
- Stress wave generation due to rapid temperature increase of surrounding structure.
- Generation of pressure wave in sodium due to bubbling of water and gaseous product (hydrogen) from water-sodium reaction and due to turbulence of the jet.

These phenomena are the secondary effect arising from the failure of water circuit tightness within a steam generator causing water (or steam) to be injected into the surrounding sodium. These leak-related acoustic waves propagate to the external shell of the steam generator where they are detected by the transducers.

In addition, an acoustic technique was used to detect the sodium leak in the "barillet" of Super Phenix. The barillet is a large double-walled cylindrical sodium tank located close to the primary tank. It is used for transfer of fresh fuel to the core and temporary storage of spent fuel for decay. Among the several methods used (i.e., helium detection, ^{133}Xe (xenon) detection method, thermography and an acoustic technique), the acoustic technique was a successful method and provided the earliest indication of the leak location.

Another application of the acoustic technology in French reactors is the use of a pattern recognition instrument for monitoring acoustic signals in the Phenix reactor core. Phenix is another smaller French LMR. This pattern recognition instrument utilizes "fuzzy-logic" classification and a self-training procedure, and is based on acoustic signals measured in the core of the Phenix reactor. The instrument is also used as a test bench for further applications such as acoustic surveillance of the steam generators of the Super Phenix. Successful application of this tool to detect a known anomaly, i.e., the incipience of cavitation, has confirmed the sensitivity of the instrument.

3. Application of AE Technique in EBR-II

EBR-II is a US Department of Energy liquid metal fast breeder power generating reactor. The reactor started operation in August, 1964. EBR-II has a full power output capacity of 62.5 MW. Reactor coolant is liquid sodium. EBR-II is a pool-type reactor with the core, reactor vessel, and primary system components all submerged in 86,000 gallons of sodium at 371°C which are contained in the primary tank (see Fig. 1).

Acoustic monitoring techniques have been applied to EBR-II as part of the acoustic surveillance program and acoustic monitor development program for the purpose of:

- Diagnosis of primary sodium pump anomaly
- Development of correlations between mechanical (control rod motion) and neutron noise.
- Noise investigation within the Intermediate Heat Exchanger (IHX).

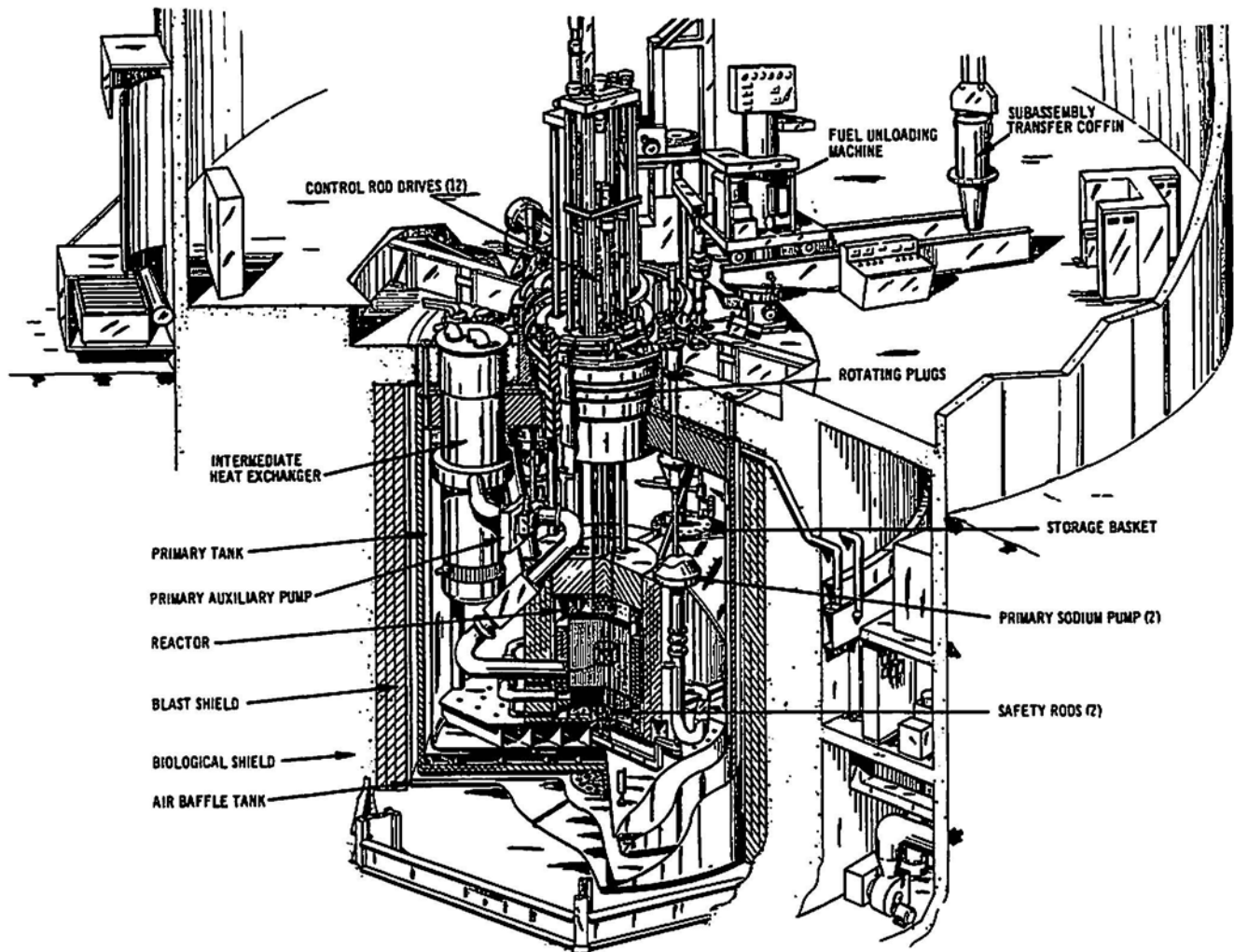


Fig. 1 Schematic diagram of Experimental Breeder Reactor II (EBR-II).

The acoustic monitoring program at EBR-II also included the vibration signature analysis from accelerometers mounted on plant components such as primary pumps and sensors on the IHX. The vibration signature analysis of pump No. 1 (which had experienced a disturbance on September 29, 1970) indicated a variation in vibrations at harmonics of the pump rotational speed. Subsequent disassembly of the pump revealed an uneven build up of sodium oxide on the pump shaft causing the shaft to bind (Anderson et al., 1972).

Another experience with the application of an acoustic technique in EBR-II relates to the incident involving the loud banging noise heard on the night of November 14, 1970 in the vicinity of the IHX. Noise signature analysis was utilized to confirm that: a) an evacuation tube was a likely suspect, b) the noise source was eliminated after complete removal of the tube (Anderson et al., 1972).

Additional acoustic monitoring capability was added to EBR-II in 1973 by installing and utilizing a microphone and an acoustic waveguide located in the acoustic monitor shield plug at nozzle G-1 in the primary tank cover. The position of these two detectors was about 1/3 m below the sodium surface in the

primary tank beside the fuel handling mechanism, 2.6 m from the tank centerline, equispaced between the two primary pumps and diametrically opposite the IHX. The microphone and waveguide were inside a perforated basket (60% open area) at the bottom of the 3.3 m long shield plug. The main objectives for installation of this equipment were to test long-term performance of high-temperature acoustic devices in sodium, to develop correlations with other signals, and to obtain information on acoustic background noise as a function of sodium flow rate and reactor power level.

The result of tests with this equipment showed that significant information can be obtained from the high temperature acoustic devices, particularly in assessing the relative contribution of primary flow noise and reactor power noise to total background noise (Anderson et al., 1974).

The G-1 plug probe has recently been upgraded. The waveguide and the microphone are replaced with three new microphones for monitoring the fuel handling system.

The upper plenum acoustic emission experiment was performed in 1976-1977. The main purpose of this experiment

was to obtain information on the acoustic background noise in the upper plenum region. The result of this experiment indicated that the acoustic data were stationary in the broad sense (or weakly stationary). It was concluded that the high frequency acoustic noise source was the global flow noise produced by the fuel subassemblies and local hydrodynamic effects. The low frequency noise data were attributed mainly to vibro-acoustic effects (Carey et al., 1977).

Another acoustic experiment at EBR-II was performed for the purpose of obtaining acoustic background noise (Anderson et al., 1972). The sensor locations used for this experiment were: Three reactor cover hold downs; the top of the valve stem in a primary system throttle valve; and the upper motor flange of each primary pump system. The result of this test also indicated a flow dependent background noise. In addition, tests were performed on the core component test loop (CCTL) to perform an independent check on the flow dependency of the background noise at EBR-II. The CCTL reduced flow tests indicated flow dependent background noise similar to the accelerometers signals in the EBR-II (Anderson et al., 1972).

4. Conclusion

The utilization of AE technology for diagnostics in light water reactors in the US has been supported by NRC in the area of loose part monitoring. Vessel integrity testing in LWRs, however, is not performed by an acoustic technique, rather via techniques specified in ASME code and approved by NRC. It should also be pointed out that although the areas of application of acoustic monitoring cover quite a wide range, not every power plant is utilizing this technique in all of the areas specified in Table 2. This clearly suggests that AE technology is not utilized to its fullest potential. Some plants apply this technique based on the NRC requirement, hence only for loose part monitoring. Therefore, not all utilities are benefiting from the full potential and capabilities of this diagnostic tool. The successful application and tests of AE technology in LMRs also suggests that it will be put to use for diagnostics in next generation advanced reactors.

References

T.T. Anderson, A.P. Gavin and J.P. Bobis (1974), unpublished information, Argonne National Laboratory.

T.T. Anderson, A.P. Gavin, J.R. Karvinen and K.J. Reimann (1972), "Detecting Acoustic Emission in Large Metal Cooled Fast Breeder Reactors", *Acoustic Emission*, ASTM STP 505, American Society for Testing and Materials, Philadelphia, pp. 250-269.

H.L. Balderston (1972), "The Broad Range Detection of Incipient Failure Using the Acoustic Emission Phenomena", *Acoustic Emission*, ASTM STP 505, American Society for Testing and Materials, Philadelphia, pp. 297-317.

E.J. Burton, P.G. Bentley, I.D. Macleod and J.A. McKnight (1977), "The Development of Techniques for the Surveillance of LMFBR", *Progress in Nuclear Energy*, vol. 1, Pergamon Press, London, pp. 393-408.

W.M. Carey, A.P. Gavin, J.P. Bobis, S.H. Sheen, T.T. Anderson, R.D. Doolittle and R.W. Albrecht (1977), "The Detection of Sodium Vapor Bubble Collapse in a Liquid Metal Fast Breeder Reactor"; *Progress in Nuclear Energy*, vol. 1, Pergamon Press, London, pp. 437-468.

P. Jax and V. Streicher (1989), "AE Application and Recent Results in Nuclear Components", *J. Acoustic Emission*, 8(1/2), S53-S56.

S. Keyvan (1989), "Survey of Acoustic Monitoring Applications in Nuclear Reactors and Assessment of Applications for EBR-II", *Enterprise Energy & Research*, ANL Report, EER-89-02, July.

G. LeGuillou, R. Berger and M. Brunet (1977), "Boiling Detection in Fast Reactors by Noise Analysis Studies Performed in France". *Progress in Nuclear Energy*, vol. 1, Pergamon Press, London, pp. 409-426.

I.D. MacLeod, E. Catling and C.G. Taylor (1977), "Acoustic Detection of Boiling in LMFBRs: An Estimate of Sensitivity Derived From Experiments During the Commissioning of PFR", *Progress in Nuclear Energy*, vol. 1, Pergamon Press, London, pp. 469-485.

J.W. McElroy (1982), "Acoustic Emission Leak Detection Methods for Light Water Reactor Application", Philadelphia Electric Company, DOE Report COO-35208-3, August.

C.W. Mayo, D.P. Bozarth, G.N. Lagerberg and C.L. Mason (1988), "Loose-parts Monitoring System Improvements", Electric Power Research Institute, EPRI NP-5743, March.

H.B. Patel and A.W. Cook (1989), "Acoustic Emission Leak Monitoring in Pressurized Piping", *J. Acoustic Emission*, 8(1/2), S101-S104.

C. Sklarczyk and E. Waschkies (1989), "Detectability of Defects in Reactor Pressure Components by Location and Interpretation of AE Sources", *J. Acoustic Emission*, 8(1/2), S93-S96.

J.A. Thie (1982), "The Third Specialists Meeting on Reactor Noise", *Nuclear Safety*, 23(5).

D. Williams (1984), "Acoustic Emission Testing of Reactor Coolant Pump Motor Flywheels", *Power Engineering*, Pennwell Publishing Co., October.

AEWG 36th Meeting

The size of acoustic emission (AE) signals expected from inclusion fracture during fatigue testing of 7075 aluminum has been estimated on the basis of previous measurements of AE produced by the fracture of boron particles incorporated into 2219 aluminum. The AE signal size expected from deformation in the plastic zone ahead of the fatigue crack was estimated from the results of tensile tests on 7075 aluminum. The signals predicted from both processes are near or below the noise level in the fatigue experiments and are therefore far too small to account for the signals actually observed. Nearly simultaneous fracture of multiple inclusions could produce signals as large as those observed in fatigue tests of 7075 aluminum, however, fatigue tests of 7050 aluminum produced signals as large or larger than in 7075. Since 7050 has substantially fewer inclusions than 7075, the simultaneous failure of multiple inclusions is unlikely to be a major AE source in fatigue testing of either aluminum alloy. Thus, the most probable source of acoustic emission during fatigue testing of 7075 and 7050 aluminum is the crack advance itself. The measured crack advance per cycle is large enough to release sufficient elastic energy to account for the AE signals observed.

William H. Prosser and M.R. Gorman
Plate Mode Acoustic Emission Signals Produced by Impact

Previous research has demonstrated that acoustic emission signals propagate as the extensional and flexural plate modes in thin plates. In this research, plate mode signals generated by impact sources on aluminum plates are presented. The effect of variations in impactor velocity on the amplitude and frequency content of the plate mode signals is demonstrated. Theoretical predictions of the flexural mode displacement based on a normal mode solution to the classical plate theory equations of motion have been made. The input forcing functions for the theoretical calculations were varied to simulate variations in impactor velocity. Qualitative agreement with the experimental signals was obtained.

Qixin Huang and Kanji Ono
AE Characterization of Carbon/Epoxy Quasi-isotropic Composites with Pattern Recognition

The structure failure of carbon fiber reinforced epoxy composites is a complicated process consisting several micro failure mechanisms, especially, certain areas within a structure system will develop local instabilities long before the structure fails. Besides, the structure made of such composite may be subject to catastrophic failure without any apparent indication. Therefore, to ensure the structural reliability and to reveal its failure characteristics are major tasks for practical applications of such composites. Fiber fracture, matrix cracking, splitting (matrix cracking along fibers) and delamination are common micro-fracture modes occurred in the failure process of the composite. These micro-fractures are typical acoustic emission (AE) sources in composites, and can be detected by AE detecting systems.

Characteristics of AE signals generated in the failure process of quasi-isotropic carbon fiber reinforced epoxy composites are investigated by pattern recognition analysis in this study. The AE signals are recorded in the form of digitized data and analyzed by employing a trained K-nearest neighbor classifier which can classify signal types of unknown waveforms. The identified signal types are then correlated to different failure modes so that the entire failure process can be more precisely described by distributions of various signal types or failure modes in the loading stress range. Features of AE signals from the failure process of a $\pm 45^\circ$ angle-ply and simulated plate waves propagating in the specimen were also investigated to help discriminate features of various signal types and correlate identified signal types to sources.

S.H. Carpenter, C.R. Heiple, D.L. Armentrout, F.M. Kustus and J.S. Schartzberg
Acoustic Emission Produced by Sliding Friction and its Relationship to AE from Machining

Acoustic emission (AE) was measured during block-on-ring sliding friction tests as a function of various experimental variables. A major goal of the investigation was to determine if the characteristics of AE generated by friction correspond to those of AE produced by single-point machining. An excellent correlation was observed between AE and friction force at constant sliding speed for both general features and detailed behavior. The AE in friction tests increased sharply with sliding speed and only slightly with increasing load. This result corresponds to the observation in machining that AE increases strongly with cutting speed and is usually only modestly dependent on feed speed and depth of cut. Furthermore, AE in friction testing was much lower for a low-friction couple; corresponding to low AE when machining low-friction materials. Thus, the friction test results support the hypothesis that

(Continued to page 102)

Acoustic Emission Produced by Sliding Friction and its Relationship to AE from Machining

S. H. Carpenter, C. R. Heiple, D. L. Armentrout, F. M. Kustas
and J. S. Schwartzberg

Abstract

Acoustic emission (AE) was measured during block-on-ring sliding friction tests to determine if the characteristics of AE generated by friction correspond to those of AE produced by single-point machining. An excellent correlation was observed between AE and friction force at constant sliding speed for both general features and detailed behavior. The AE in friction tests increased sharply with sliding speed and only slightly with increasing load. This result corresponds to the observation in machining that AE increases strongly with cutting speed and is usually only modestly dependent on feed speed and depth of cut. Furthermore, AE in friction testing was much lower for a low-friction couple; corresponding to low AE when machining low-friction materials. Thus, the friction test results support the hypothesis that rubbing friction is generally the primary source of acoustic emission during single-point machining.

1. Introduction

Heiple et al. (1991) have recently measured acoustic emission (AE) produced during single-point machining of a variety of materials. These measurements were undertaken as part of a program to evaluate AE for monitoring tool wear. The results indicated that the major source of AE during single-point machining is rubbing friction between the nose/flank of the tool and the freshly machined surface. This hypothesis is consistent with the results of a limited number of measurements of AE generated during friction testing (Jiaa and Dornfeld, 1990; Kita et al., 1980) in situations where large numbers of wear particles were not likely to be present.

Acoustic emission measurements were undertaken during additional sliding friction tests to determine if the characteristics of AE generated by friction correspond to those of AE produced by single-point machining. Both AE and friction force were monitored as a function of applied load and sliding speed. Friction testing used a block resting on a rotating ring in order to minimize the buildup of wear particles during the test. The presence of wear particles, as occurs in standard pin-on-disk tests, is known to greatly increase the level of AE (Jiaa and Dornfeld, 1990).

The material combinations investigated were chosen to be similar to metal combinations used in previous single-point machining experiments (Heiple et al., 1991). Analysis of the

data clearly indicates a close correlation between AE and friction force and establishes that rubbing friction is the major source of AE in the friction tests. The results also support the hypothesis that rubbing friction is generally the primary source of AE in single-point machining.

2. Experimental

A commercial block-on-rotating ring friction testing machine (Favielle Le Valley, model LFW 1) was used during the investigation. All of the friction tests were performed dry without any type of lubrication. Blocks with a face width of 6.35 mm were placed in contact with a rotating ring of face width 8.9 mm and radius 17.5 mm. The normal force between the block and the ring, as well as the angular speed (or sliding speed) of the ring could be easily changed over a wide range of values. An additional and convenient feature of the testing apparatus used was the ability to continuously monitor the friction force and AE during the entire test.

The AE was detected with a commercial resonant piezoelectric sensor (Physical Acoustics, model $\mu 30$) which has a resonant frequency of approximately 170 kHz. The sensor was mounted on the housing holding the test block. The output of the sensor was amplified 40 dB by a Panametrics model 5050B preamplifier. The output of the preamplifier was then fed into a Hewlett Packard 3400A rms voltmeter. The measured value of the rms voltage was used to characterize the AE. The output of the rms voltmeter was connected to both a strip chart and a digital transient recorder. The analog output for the friction force was also fed into the transient recorder. The transient recorder provided an accurate measurement and correlation of the AE and the friction force. It was set to measure both the rms voltage and the friction force every 50 ms, yielding a 410-s record for a 8,192-point trace. The data were then saved on a hard disk and a new collection started. Values plotted subsequently for friction force and rms voltage are an average of many individual points measured by the transient recorder. All of the AE rms voltage values have been corrected for noise and are referenced to the output of the transducer. A schematic diagram of the experimental arrangement used is provided in Fig. 1.

The primary materials tested were a carbide block on either a 440C steel or a 6061-T6 aluminum alloy ring. The carbide block was chosen to simulate a carbide cutting tool. The rings used, 440C steel and 6061-T6 aluminum, are similar to materials used in previous single-point machining experiments (Heiple et al., 1991). An additional experiment was also carried out using a O1 tool steel block with a diamond like carbon (DLC) film against a 440C steel ring. Two basic types of experiments were carried out: (1) a constant load was maintained while the sliding speed of the ring was increased in a step-wise

Received 30 March 1992. S.H. Carpenter, C.R. Heiple and D.L. Armentrout are affiliated with Plutonium Technology, EG&G Rocky Flats, P.O. Box 464, Golden, CO 80402 and F.M. Kustas and J.S. Schwartzberg are with Martin Marietta Corp., Astronautics Group, Denver, CO 80201.

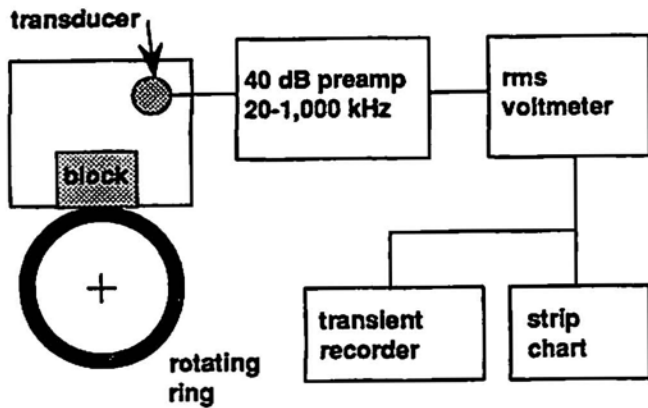


Fig. 1 Acoustic emission measuring system.

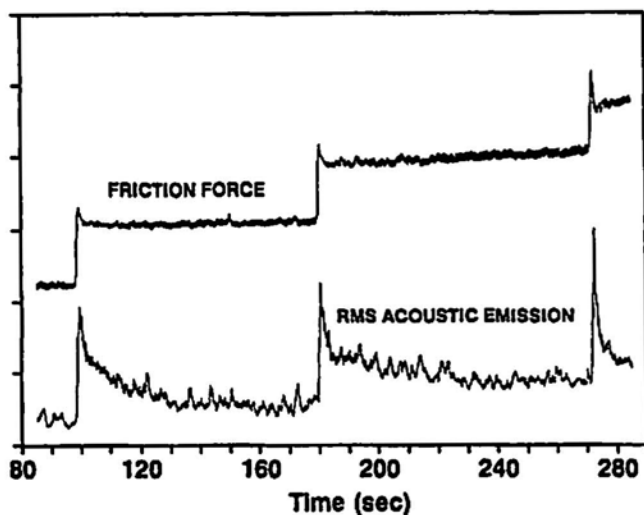


Fig. 2 Example of variation with time of friction force and AE resulting from sliding friction between the carbide block and 440C steel ring as the load is increased in a stepwise fashion.

manner, and (2) a constant sliding speed was maintained while the load was increased in a step-wise manner.

3. Results

A portion of a data trace from the strip-chart recorder, showing both AE rms voltage and friction force, is shown in Fig. 2. In this particular trace, both the AE and friction force data are fairly well behaved. This was not always the case; in some instances, significant variation of both rms voltage and friction force was observed with time for constant experimental test conditions. Average values of the rms voltage and friction force are used in all the following figures. Each point is an average of 1700 to 2000 values acquired by the transient recorder.

As expected, the friction force increased in a linear manner with increasing applied load at constant sliding speed; see Fig. 3. The friction force was less sensitive to increases in sliding speed at constant load, as shown in Fig. 4.

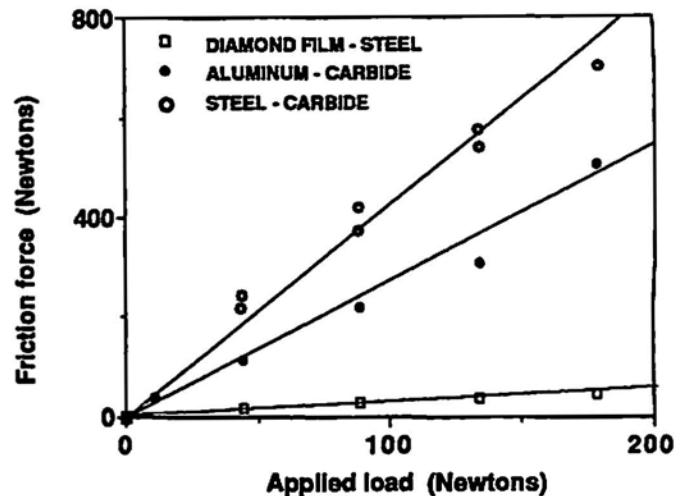


Fig. 3 Friction force versus applied load at a constant sliding speed of 0.18 m/s.

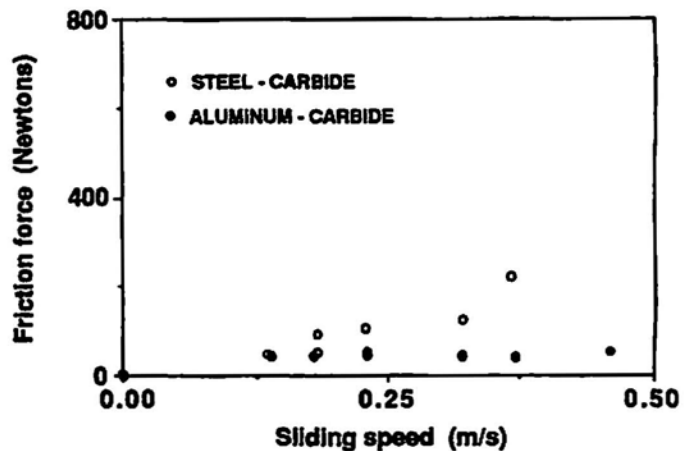


Fig. 4 Friction force versus sliding speed at constant applied load. (Steel-carbide load 44.5 N, aluminum-carbide load 11.1 N)

The AE rms voltage increased markedly as sliding speed increased (Fig. 5). The cause of the sharp increase in acoustic emission at the highest speed tested for each material has not been determined. However, it is probably related to heating of the ring and block and oxidation of the ring. When sliding speed was constant and applied load increased, only a slight increase in rms voltage with increasing applied load was detected, Fig. 6. The increase in rms voltage for increasing load is clearly much less than that observed for increases in sliding speed.

The acoustic emission generated during block-on-ring friction tests correlated very well with earlier results from single-point machining investigations. As in the friction tests, rms voltage increased rapidly with increases in cutting speed during single-point machining. AE signal level versus cutting speed is shown for a variety of materials in Fig. 7. It is less apparent how to relate increasing load at a constant sliding speed during

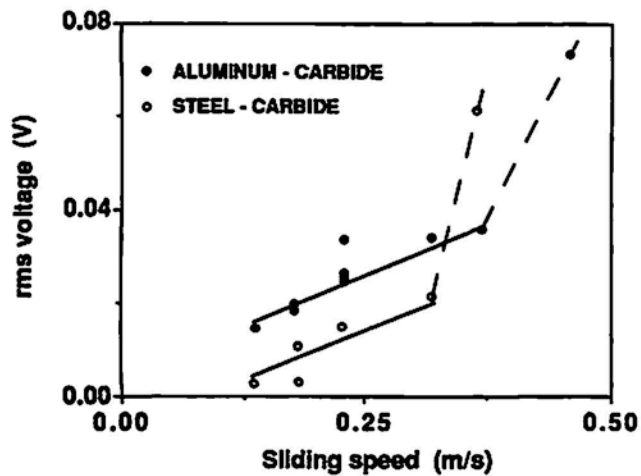


Fig. 5 Acoustic emission rms voltage versus sliding speed at constant applied load. (Steel-carbide load 44.5 N, aluminum-carbide load 11.1 N)

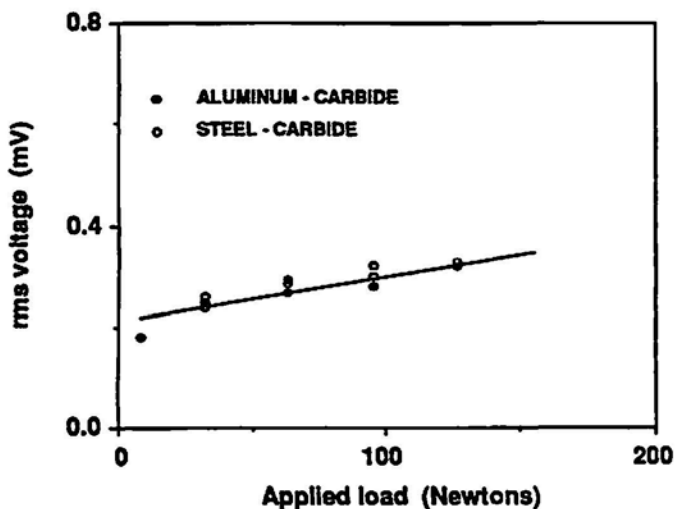


Fig. 6 Acoustic emission rms voltage versus applied load at a constant sliding speed of 0.18 m/s.

friction testing to single-point machining. During single-point machining operations at a constant cutting speed, it is possible to either increase the depth of cut or to increase the feed speed. As shown in Figs. 8 and 9, only a modest increase in the rms voltage is observed in either case. Thus, in either single-point machining or block-on-ring friction testing, the AE generated is primarily dependent upon relative velocity; i.e. cutting speed or sliding speed.

An excellent correlation between rms voltage and friction force at constant sliding speed was observed for both short-term and long-term behavior. Figure 10 shows long-time data for rms voltage and friction force plotted against each other.

Data for both 440C steel and 6061-T6 aluminum alloy rings are shown. Each data point in Fig. 10 represents the average value over 85 - 100 seconds of friction force and rms voltage from the transient recorder. Individual points represent

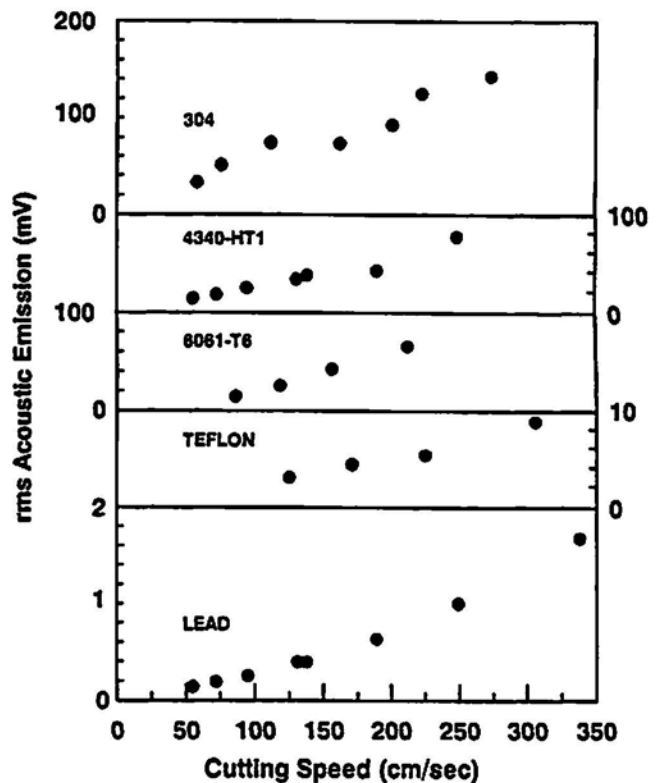


Fig. 7 Acoustic emission produced during machining various materials as a function of cutting speed. Depth of cut 0.25 mm (except 0.13 mm for 4340-HT1 steel); feed speed 0.046 mm/revolution. The data for 304 stainless steel were taken using different bits. (Heiple et al., 1991)

different applied loads at a constant sliding speed of 0.18 m/s (sliding distance of 15 - 18 m). A single straight line gives a good fit to both sets of data. It is not known if the single straight line fit is a general result or if it is a result of the carbide test block.

As mentioned earlier, rms voltage and friction force were not always as well behaved as shown in Fig. 2. For example, Fig. 11 shows data from the transient recorder for a portion of the friction test of a carbide block on a 440C steel ring. A significant variation in both rms voltage and friction force was observed, although test conditions were held constant.

A good correlation of major features of the two data traces is obvious. However, a good correlation can also be shown to exist even on very minor features by evaluating the ratio of friction force and rms voltage on a point by point basis (50 ms per data point). Figure 12 is the ratio of friction force and rms voltage traces for the data presented in Fig. 11. An almost constant value of the ratio is obtained. The results of Figs. 10 and 12 clearly indicate the excellent correlation of the friction force and the rms voltage for both short-term and long-term behavior. Identification of the detailed micro-mechanical processes responsible for the friction forces and AE is beyond the scope of this work. Nevertheless, it is clear that friction between the block and ring is the source of AE in these experiments.

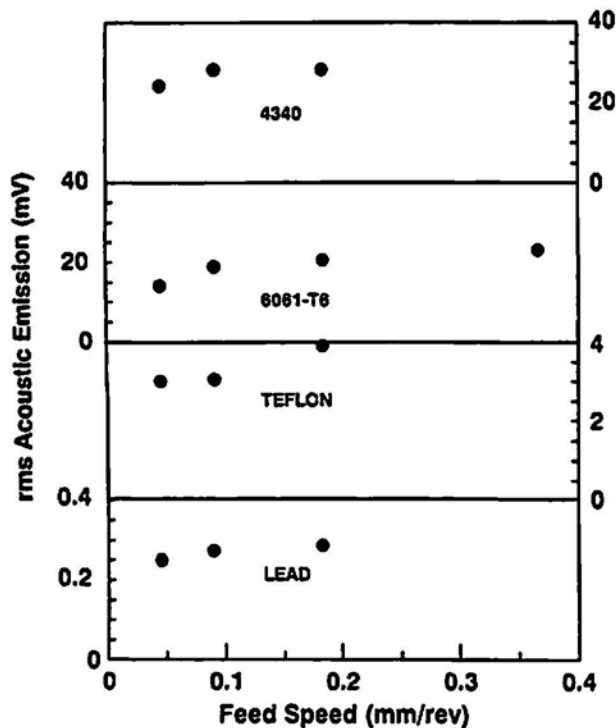


Fig. 8 Acoustic emission produced during machining various materials as a function of feed speed. Cutting speeds varied for the different materials, but were near 100 cm/sec; depth of cut 0.25 mm (except 0.13 mm for 4340-HT1 steel). (Heiple et al., 1991)

4. Conclusions

The primary source of AE during single-point machining has been proposed to be rubbing friction between the nose and/or flank of the tool and the freshly machined surface. Acoustic emission (as measured by rms voltage) and friction force were continuously monitored during block-on-ring sliding friction experiments to determine if the characteristics of AE produced by friction corresponded to those of AE produced by machining. The block-on-ring technique was chosen to minimize complications in the AE data from the presence of wear particles. Materials investigated were chosen to be similar to those previously investigated in single-point machining experiments. Analysis of the data allows the following conclusions.

An excellent one-to-one correlation between AE and friction force was obtained for both general features and detailed behavior. Any changes in friction force, at a constant sliding speed, were accompanied by corresponding changes in rms voltage. The data clearly demonstrate that the source of AE in sliding friction tests is rubbing friction between the block and ring.

Acoustic emission behavior observed in sliding friction experiments is completely consistent with AE behavior in earlier single-point machining experiments. The AE (rms voltage) in friction tests was observed to be strongly dependent upon

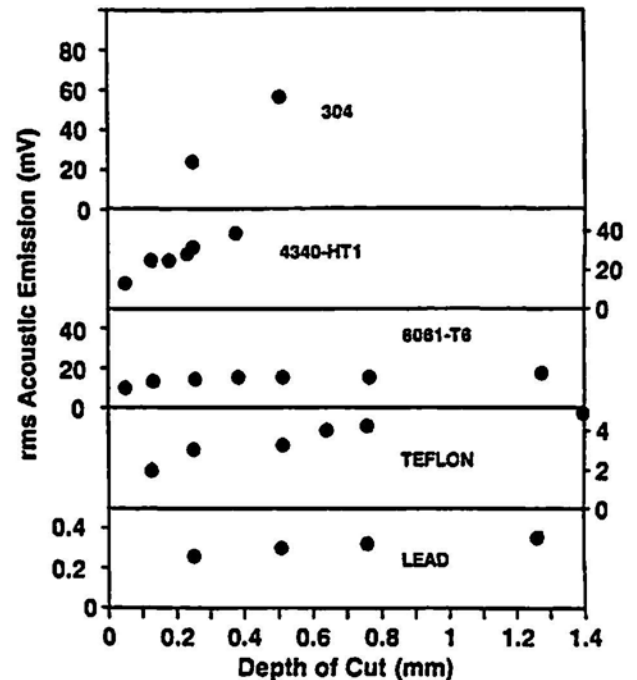


Fig. 9 Acoustic emission produced during machining various materials as a function of depth of cut. Cutting speeds varied for the different materials, but were near 100 cm/sec; feed speed 0.046 mm/revolution.

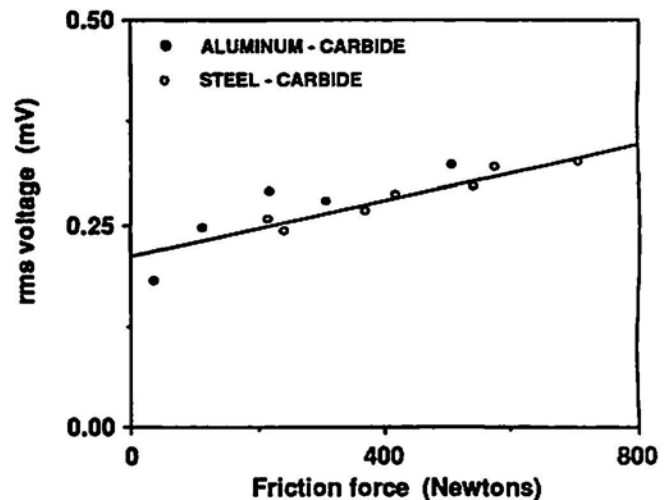


Fig. 10 Acoustic emission rms voltage versus friction force at constant sliding speed.

sliding speed and only slightly dependent upon load. In machining, AE was strongly dependent on cutting speed and only modestly dependent on feed speed and depth of cut. The AE in friction tests was dramatically lower for the low-friction couple of tool steel rubbing on a diamond-like carbon coating. In machining tests, AE produced was dramatically lower when the low-friction materials lead and teflon were cut. The friction test results therefore support the hypothesis that rubbing friction is

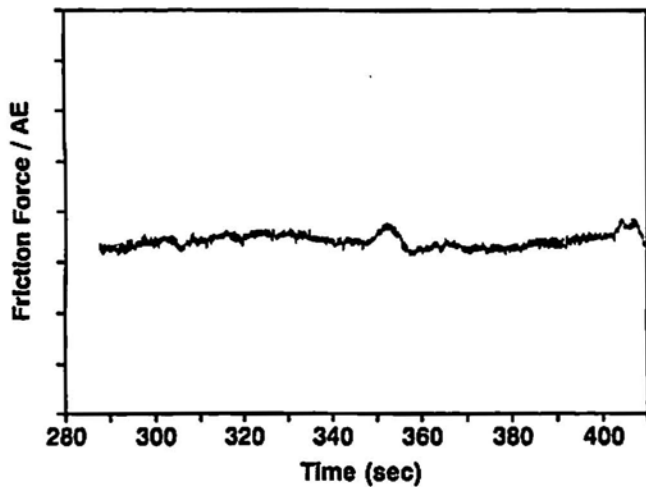


Fig. 11 Example of short-term variations in friction force and acoustic emission rms voltage at constant applied load and sliding speed for carbide on 440C steel.

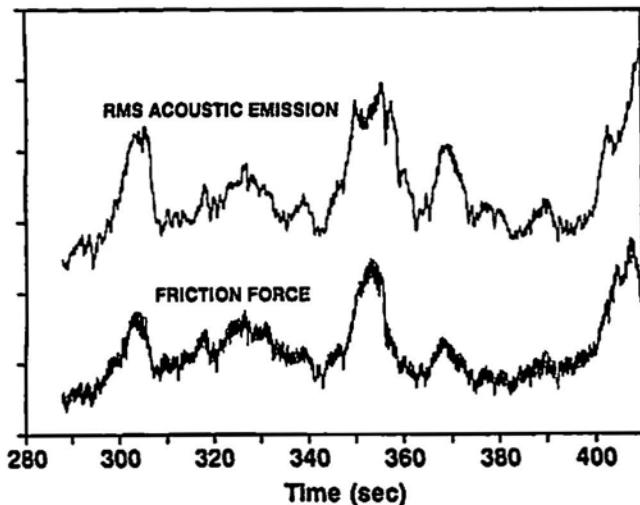


Fig. 12 Friction force trace in Fig. 11 divided by the acoustic emission trace on a point-by-point basis. The nearly constant value obtained demonstrates a high correlation between variations in friction force and acoustic emission.

generally the primary source of AE during single-point machining. Since friction is the primary AE source, changes in AE characteristics with tool wear are expected to be strongly dependent on the material being machined, as observed. Tool wear monitoring is possible with AE because AE characteristics change with tool wear, but the magnitude and even direction of the changes are material dependent.

Acknowledgment

This work was supported by the Department of Energy, Albuquerque Operations Office. Their support is gratefully acknowledged.

References

- C.R. Heiple, S.H. Carpenter and D.L. Armentrout (1991), Proceedings of the 4th World Meeting on Acoustic Emission and 1st International Conference on Acoustic Emission in Manufacturing, ed. S.J. Vahaviolos, ASNT, Columbus, OH, pp. 463-470.
- C.L. Jiaa and D.A. Dornfeld (1990), *Wear*, 139, 403-424.
- T. Kita, K. Kogure, Y. Mitsuya and T. Nakanishi (1980), *IEEE Trans. on Magnetics*, MAG 16, 873-875.

AEWG 36th Meeting

rubbing friction is generally the primary source of acoustic emission during single-point machining. Preliminary tests were also conducted to determine if AE could be used to detect failure of thin coating or films during sliding friction.

D.L. Armentrout and S.H. Carpenter

The Effect of Precipitate Forming Elements in Al-4.5% Mg Alloys on the Measured Acoustic Emission and on Lüders Band Deformation

Acoustic emission (AE) measured in Al-4.5% Mg alloys with varying amounts of additional elements which form precipitates in this system. During tensile testing, the samples deformed inhomogeneously with multiple yield points - often called Lüders bands. Calculated strain rates during Lüders deformation were greater than 10 s^{-1} . Three distinct regions could be observed in close examination of the drop in stress associated with the yield points. The AE signal peak was found to occur during the region of steepest decrease in the stress. The magnitude of the stress drops which is proportional to the amount of plastic deformation in the individual yield points correlated well with the height of the corresponding rms voltage bursts.

James R. Mitchell

A Standard Test for Stress Corrosion Cracking with AE

Thomas F. Drouillard

Acoustic Emission/Restrained Bend Test to Detect Embrittled Braze Joints

The braze joint between Monel tubes and beryllium parts must be adequate to provide structural integrity throughout the life of the structure. The joint must withstand all of the stresses imposed during manufacture and handling without cracking or forming a leak path. In response to a number of production joints that were found cracked, an acoustic emission/restrained bend test was developed and implemented in production as a nondestructive testing method to detect braze joints that many already have existing cracks or embrittled braze joints that might be susceptible to cracking. This was a proof test in which the joint was stressed while being monitored for acoustic emission from brittle fracture. This paper summarizes the results of using the AE/restrained bend test to effectively sort out good and bad braze joints, and to define good and bad braze joints. The paper presents data showing a direct correlation between acoustic emission test results and typical microstructures for both good and bad braze joints, and identifies the relationship between cracking and the formation of a brittle intermetallic which was caused by overheating of the joint. Results for both induction brazed and furnace brazed joints are given.

A.G. Beattie

Development of an Acoustic Sand Detector

Robert Krauz

AE Interests at US Bureau of Mines

Comments on the Origin of Acoustic Emission in Fatigue Testing of Aluminum Alloys

C. R. Heiple, S. H. Carpenter and D. L. Armentrout

Abstract

The size of acoustic emission (AE) signals expected from inclusion fracture during fatigue testing of 7075 aluminum has been estimated on the basis of previous measurements of AE produced by the fracture of boron particles incorporated into 2219 aluminum. The AE signal size expected from deformation in the plastic zone ahead of the fatigue crack was estimated from the results of tensile tests on 7075 aluminum. The signals predicted from both processes are near or below the noise level in the fatigue experiments and are therefore far too small to account for the signals actually observed. Nearly simultaneous fracture of multiple inclusions could produce signals as large as those observed in fatigue tests of 7075 aluminum, however, fatigue tests of 7050 aluminum produced signals as large or larger than in 7075. Since 7050 has substantially fewer inclusions than 7075, the simultaneous failure of multiple inclusions is unlikely to be a major AE source in fatigue testing of either aluminum alloy. Thus, the most probable source of acoustic emission during fatigue testing of 7075 and 7050 aluminum is the crack advance itself. The measured crack advance per cycle is large enough to release sufficient elastic energy to account for the AE signals observed.

1. Introduction

Recent work by McBride et al. (1988) and Buttle and Scruby (1990) has revived questions on the origin of acoustic emission (AE) during deformation and fatigue of aluminum alloys. McBride and MacLachlan (1983) originally proposed that the source of AE during fatigue crack growth in 7075 aluminum was fracture of Mg-Si inclusions by the advancing fatigue crack. This conclusion was based primarily on a remarkable agreement between the number and area-size distribution of the inclusions in a section parallel to the fatigue-crack plane and the number and amplitude distribution of the observed AE signals. More recently, McBride et al. (1988) found large numbers of fractured inclusions in the plastic zone of the fatigue crack in 7075; indeed, there were about 100 fractured inclusions for each AE event. They have also performed similar tests on 7050 aluminum (McBride, 1991). This alloy is similar to 7075, but has a much lower inclusion content. In spite of the much lower inclusion content, about half as many signals were generated in 7050 as 7075, and the signals were somewhat larger than in 7075. Their observations led them (McBride et al., 1988) to propose that the source of AE during fatigue crack growth was intense plastic flow ahead of the growing crack. Their observations also rekindled the long-

dormant controversy over the origin of the second AE peak in 7075 during tensile deformation.

Buttle and Scruby (1990) have just reported the results of an elegant series of experiments in which the source location and signal-radiation characteristics were measured with high accuracy during fatigue tests of 7075 aluminum. They concluded that the signal sources were crack advancement, because the signals came from locations close to the crack plane and crack tip, and because the signal-radiation pattern was in best agreement with that of a microcrack source.

Heiple et al. (1990) measured the AE signals produced by the fracture of boron particles in an aluminum alloy matrix during tensile deformation, and compared the signals to the energy released by particle fracture. We can use these results to estimate the size of signals to be expected from inclusion fracture in 7075. The results of measurements of acoustic emission produced by tensile deformation can also be used to estimate the amount of acoustic emission expected from deformation in the plastic zone ahead of the growing crack tip. Here, we compare these estimates to experimental results during fatigue testing of 7075 aluminum.

2. Results and Discussion

There are four plausible mechanisms for the origin of acoustic emission during fatigue crack growth in 7075 and other aluminum alloys. These possible AE sources are:

- (1) Fracture/decohesion of individual inclusions by the advancing fatigue crack.
- (2) Nearly simultaneous fracture/decohesion of multiple inclusions in the plastic zone as the fatigue crack advances.
- (3) Dislocation motion (plastic flow) in the plastic zone.
- (4) Crack advance.

Evidence bearing on these mechanisms is presented below.

Heiple et al. (1990) measured the acoustic emission produced by the fracture of boron particles in 2219 aluminum tensile bars during deformation. The energy released by fracture of the particles was calculated from an expression due to Kant (1979) (equation 1), using fracture sizes obtained from detailed metallographic observations.

$$\Delta E = 4/3(1 - \nu)(\sigma^2)^3/E)R \quad (1)$$

In equation 1, ΔE is the energy released, ν is Poisson's ratio for the matrix, σ is the applied tensile stress, and E is Young's modulus for the matrix. R is a function of the ratios of the shear moduli and Poisson's ratios for the matrix and inclusion, and has a value of about 0.5 for boron in aluminum. A linear relation was found between the calculated particle fracture energy

Received 30 March 1992. The authors are affiliated with Plutonium Technology, EG&G Rocky Flats, P.O. Box 464, Golden, CO 80402.

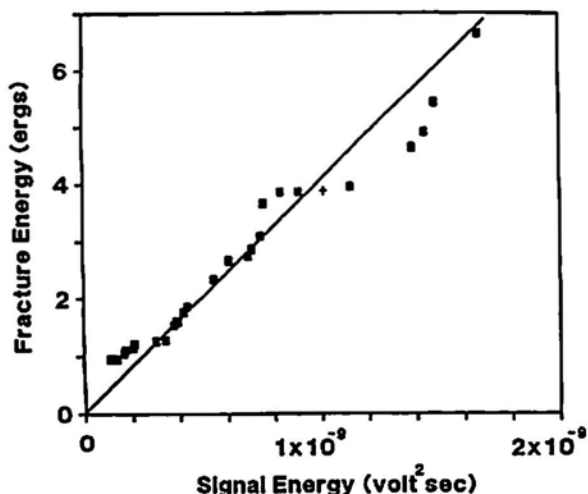


Fig. 1 Boron particle fracture energy vs. AE signal energy, referred to transducer output. The point plotted with a "+" is from a particle with a branching crack. (Heiple et al., 1990)

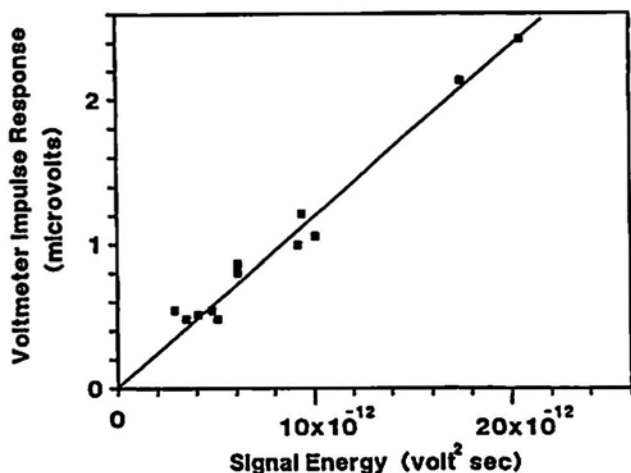


Fig. 2 Impulse response of the rms voltmeter vs. AE signal energy from the fracture of small boron particles. Values referred to transducer output. (Heiple et al., 1990)

ΔE and the energy S of the resulting AE signal, Fig. 1. The signal energy S was taken to be the integral of the signal voltage squared (referred to the transducer output). The relation is

$$\Delta E = 4.1 \times 10^9 S, \quad (2)$$

with ΔE in erg and S in $V^2 \cdot s$. The response of an rms voltmeter to a single AE burst signal is a voltage spike. The height of this spike or pulse above noise (P_{rms}) is referred to here as the impulse response of the voltmeter. Heiple et al. (1990) demonstrated that the impulse response of an rms voltmeter to both individual AE signals from particle fracture and individual artificial signals from an AE simulator was linearly proportional to signal energy, S (see Fig. 2). The relation is

$$P_{rms} = 1.2 \times 10^{11} S \quad (3)$$

with P_{rms} in μV referred to the transducer output and S in $V^2 \cdot s$.

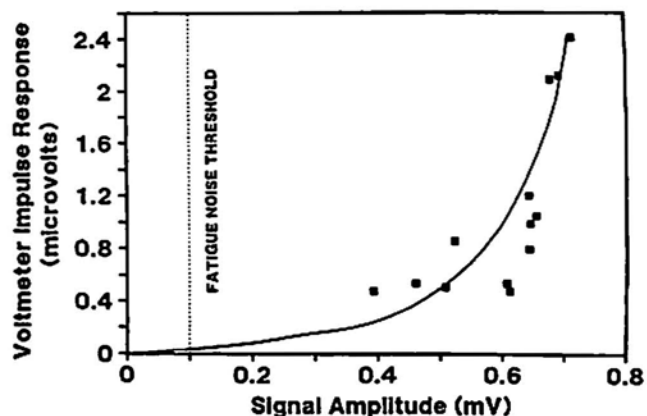


Fig. 3 Impulse response of the rms voltmeter vs. AE signal amplitude from the fracture of small boron particles. Values referred to transducer output.

The impulse response of the rms voltmeter is a non-linear, more scattered function of peak signal amplitude than of signal energy for real AE signals. For AE signals from the smallest boron particle fractures, the relation between the impulse response of the rms voltmeter and signal amplitude (both referred to the transducer output) is plotted in Fig. 3.

We will use these results to estimate the minimum particle fracture size required to produce the AE signals observed by McBride and Harvey (1985) in fatigue tests on 7075 aluminum. This estimate is subject to a number of uncertainties. First, the mechanical properties of Mg-Si inclusions are not known. These properties affect the value of R in equation 1. However, it is unlikely that they differ substantially from those of boron, and in any event R is a slowly varying function of inclusion mechanical properties (Heiple and Carpenter, 1987b). Thus, a value of 0.5 will be assumed for R . Second, sample geometry significantly affects the measured signal energy from the same event. The boron particle measurements were performed on small, round tensile bars with a Dunegan-Endevco S140 transducer directly on the gauge length. On the other hand, the Bruel and Kjaer 8313 transducer in the fatigue experiments was 38 cm away from the fatigue crack, and the samples were thin strips (McBride et al., 1988). The signal sensitivity was therefore less in the fatigue experiments. However, the extent of this difference is not known. Thus, larger fractures than estimated (on the basis of the boron particle experiments) are required to produce the signals actually observed in the fatigue experiments.

For aluminum, $\nu = 0.33$, $E = 74$ GPa, and R is taken to be 0.5 (Heiple et al., 1990). The yield stress for 7075-T6 is 430 MPa, and the ultimate tensile strength is 570 MPa. Taking the stress near the crack tip to be about 570 MPa, equation 1 for fracture of an inclusion of radius r becomes (r in mm, ΔE in ergs)

$$\Delta E = 2 \times 10^4 r^3. \quad (4)$$

Since $\Delta E = 4.1 \times 10^9 S$, and $P_{rms} = 1.2 \times 10^{11} S$,

$$r^3 = 1.7 \times 10^{12} P_{rms} \quad (5)$$

where r is in mm and P_{rms} in μV . In the boron particle experiment, the smallest particle-fracture signals which could reli

ably be detected with the rms voltmeter produced a voltmeter impulse response of about 0.4 μV (Fig. 2). This corresponds to a fracture radius of 9 μm , or a fracture area of 250 μm^2 . The largest inclusions observed in the fatigue experiments had areas less than 100 μm^2 , and only 0.5% were larger than 50 μm^2 (McBride and Harvey, 1985).

Because signal amplitudes (rather than the impulse response of the rms voltmeter) were used for signal detection in the fatigue experiments, smaller signals could be detected. The noise threshold was set at 0.1 mV in the fatigue experiments (McBride et al., 1988), which would correspond approximately to 0.04 μV rms-voltmeter impulse response (Fig. 3), if that response could be observed. (An impulse response of 0.04 μV corresponds to less than 25 μm deflection on a 20 cm strip chart when the scale is such that the system noise level is over half full-scale.) A P_{rms} of 0.04 μV would result from a fracture radius of 4 μm , or an area of 50 μm^2 . Thus, less than 0.5% of the inclusions observed in 7075 fatigue tests are capable of producing signals as large as the noise threshold used, and the largest signals observed would require particle fracture areas exceeding 600 μm^2 .

Therefore, the AE signals observed in fatigue tests of 7075 and other similar alloys cannot arise from the fracture of single inclusions, in agreement with the later conclusions of McBride et al. (1988). In principle, the advancing fatigue crack could fracture many inclusions nearly simultaneously and produce detectable signals. In McBride and Harvey (1985), the median inclusion area was 2.7 μm^2 (0.93 μm radius) and the median signal amplitude (for signals above a 0.1 mV threshold level) was 0.2 mV. A 0.2 mV signal corresponds approximately to 0.08 μV rms-voltmeter impulse response (Fig. 3). The estimated energy release which would produce a signal of this size is 2.7×10^{-3} ergs. It would require the simultaneous failure of about 170 of the median-sized inclusions to release this much energy at once. Experimentally, only about 100 fractured inclusions were found for each AE event (McBride et al., 1988). Thus, it appears unlikely that simultaneous fracture of multiple inclusions is a major source of acoustic emission during fatigue testing of 7075 aluminum. This conclusion is verified by observations on 7050 aluminum (McBride, 1991). This alloy has substantially lower inclusion content than 7075, yet the AE signals produced during fatigue of 7050 are as large or larger than those produced in 7075 aluminum.

The third possible AE source is dislocation motion in the plastic zone ahead of the fatigue crack. Heiple et al. (1981) have measured acoustic emission produced by deformation of 7075 aluminum and other alloys. The acoustic emission was characterized by a peak near yield (the first AE peak) which has been shown to arise from dislocation motion. The maximum rms-voltage value of the quasi-continuous AE signal near yield in 7075 for any heat treatment attempted was about 0.2 μV . The rms-voltage value of the continuous or nearly continuous signal produced by dislocation motion is known to be proportional to the square root of strain rate and deforming volume (Heiple and Carpenter, 1987a). If the volume and strain rate of the plastic zone in fatigue tests can be approximated, then the rms-voltage of AE signals can be estimated from tensile tests.

The plastic zone radius r is given approximately by

$$r = (K/\sigma)^2/2\pi \quad (6)$$

where K is the stress intensity at the crack and σ lies about midway between the yield and ultimate strength. For 7075-T6, $(K/\sigma)^2 \approx 2.5$ mm, so $r = 0.4$ mm. (Buttle and Scruby (1990) estimated r between 0.15 and 0.45 mm in their fatigue experiments on 7075 Al.) McBride et al. (1988) gives the crack advance as 0.1 to 0.2 $\mu\text{m}/\text{cycle}$. Sample thickness was 4.7 mm, so the maximum deforming volume/cycle is about 7.6×10^{-4} mm^3 .

A value for the strain rate is more difficult to estimate, but an order of magnitude approximation can be made. The frequency of the fatigue test was 0.5 Hz, with an approximately triangular stress-time history. Crack propagation was assumed to occur in the top 20% of the rising load cycle; i.e., over 0.2 s. If the total strain is assumed to be 0.11 in the plastic zone each cycle (0.11 is the strain to failure for 7075-T6), then the strain rate is 0.55/s. For the tensile tests, the deforming volume was 250 mm^3 at a strain rate of $5.6 \times 10^{-5}/\text{s}$. Thus the rms-voltage peak height from the plastic zone ahead of the fatigue crack can be estimated in the following manner:

$$(0.2 \mu\text{V}) \sqrt{\frac{7.6 \times 10^{-7} \text{ cm}^3 \cdot 0.55 / \text{s}}{0.25 \text{ cm}^3 \cdot 5.6 \times 10^{-5} / \text{s}}} = 0.03 \mu\text{V}$$

This value assumes that the rms voltmeter sees the peak value over a time comparable to the voltmeter time constant, as in a tensile test. However, the actual signal occurs over 0.2 s (or less). The signal energy for a continuous sinusoidal signal of 0.03 μV rms for 0.2 s is 2.4×10^{-16} $\text{V}^2\text{-s}$, giving a predicted impulse response of the rms voltmeter of 3×10^{-5} μV (equation 3), if the signal is treated as an impulse. The actual value will lie between the continuous signal estimate (0.03 μV) and the impulse estimate (0.03 nV). Since the noise threshold in the fatigue tests corresponds to 0.04 μV rms voltmeter impulse response, signals from deformation are below the noise level, and in any event are far too small to account for the larger signals observed in fatigue.

The final possible mechanism is elastic energy released by the crack advance itself. The area of crack advance (0.1 to 0.2 μm across a thickness of 4.7 mm) is 470 to 940 μm^2 . This area is consistent with the 600 μm^2 crack area calculated above which would be required to produce the larger signals observed in fatigue testing. Signal amplitudes are expected to decrease with increasing temperature, both because the yield stress decreases ($\Delta E \propto \sigma^2$ in equation 1) and because the sudden crack jumps probably become smaller. A sharp decrease in signal amplitude with temperature was observed by McBride and Harvey (1985). The number and size of AE events during fatigue is only indirectly related to inclusion content, as observed in 7075 and 7050 aluminum. Thus, experimental observations and signal size estimates demonstrate that the AE source in fatigue of aluminum alloys is the crack advance itself, as proposed by Buttle and Scruby (1990).

The results derived above are also consistent with the accepted mechanism of inclusion fracture and decohesion as the

source of the second AE peak (typically occurring beyond 1% plastic strain) observed in tensile deformation of 7075 and other aluminum alloys. There are large numbers of inclusions present in 7075 and some other aluminum alloys. The fracture and decohesion of many of these inclusions at nearly the same time produces the almost continuous AE signal often observed.

Cousland and Scala (1981) have measured the acoustic emission from both 7075 and 7050 aluminum in tension. They also made detailed measurements of the size distribution of inclusions in both materials. The second peak was substantially larger in 7075 than 7050, and the 7075 had substantially more inclusions in every size range than the 7050. The 7075 had a substantial number of inclusions in the 100 to 1000 μm^2 range. The inclusions in the materials tested by Cousland and Scala were both larger and more numerous than those in the materials tested by McBride and Harvey. Fracture of the big inclusions is expected to produce large individual bursts and a "spiky" rms-voltage curve, as observed. The 7050 had relatively few of these large inclusions, and exhibited a much smoother rms-voltage trace. Neither material produced acoustic emission in compression. These results are not consistent with dislocation mechanisms, and are completely consistent with the AE source being the fracture and decohesion of inclusions.

3. Conclusions

The size of AE signals expected from inclusion fracture and plastic flow in fatigue tests of 7075 aluminum has been estimated. The estimates are based on measurements of acoustic emission from the fracture of boron particles in a 2219 aluminum matrix and from tensile tests of 7075 aluminum. Failure of the inclusions observed in 7075 fatigue tests is predicted to produce signals far too small to account for AE signals actually observed. Simultaneous or nearly simultaneous fracture of multiple inclusions also is not likely to be a major source in view of the observation that signals similar to those detected in 7075 are produced during fatigue of 7050 aluminum. The latter alloy has substantially fewer inclusions than 7075. The AE signal produced by deformation in the plastic zone ahead of the growing fatigue crack is also too small to account for the observed signal.

Thus, the AE signals are produced by the crack advance itself. The elastic energy released by crack advance is consistent with the size of AE signals produced. Calculated and observed results are also consistent with inclusion fracture and decohesion being the source of the second AE peak observed in tensile deformation of 7075 and other aluminum alloys.

Acknowledgment

This work was supported by the Department of Energy, Albuquerque Operations Office. Their support is gratefully acknowledged.

References

- D.J. Buttle and C.B. Scruby (1990), *J. Acoust. Emiss.*, 9, 243-254.
- C.R. Heiple and S.H. Carpenter (1987a), *J. Acoust. Emiss.*, 6, 177-204.
- C.R. Heiple and S.H. Carpenter (1987b), *J. Acoust. Emiss.*, 6, 215-237.
- C.R. Heiple, S.H. Carpenter and M.J. Carr (1981), *Met. Sci.*, 15, 587-598.
- C.R. Heiple, S.H. Carpenter and S.S. Christiansen (1990), *Acta Metall. Mater.*, 38, 611-618.
- R. Kant (1979), "The Elastostatic Axisymmetric Problem of Cracked Sphere Embedded in a Dissimilar Matrix," Doctoral Thesis, University of California, Berkeley, CA.
- S.L. McBride (1991), Unpublished research.
- S.L. McBride, P. Bowman and K.L. McRae (1988), *Progress in Acoustic Emission IV*, eds. K. Yamaguchi et al., The Japanese Society for Nondestructive Inspection, Tokyo, Japan, pp. 528-535.
- S.L. McBride and J. Harvey (1985), *J. Acoust. Emiss.*, 4, S220-S223.
- S.L. McBride and J.W. Maclachlan (1983), *J. Acoust. Emiss.*, 2, 179-185.
- S. McK. Cousland and C.M. Scala (1981), *Met. Sci.*, 15, 609-614.

Acoustic Emission of Wood during Swelling in Water

Stefan Poliszko, Waldemar Molinski and Jan Raczowski

Abstract

In order to characterize acoustic emission (AE) generated in wood swelling in water, the total event counts, the amplitude distribution of AE signals and rate of their generation were determined. The kinetics of the increase in total number of AE signals was compared to that of wood swelling in the same conditions. A rapid increase in the number of AE signals generated in time unit was observed when volumetric swelling of a sample reached about 20% of the maximum swelling. Together with the measurements of AE effects in swelling wood, the measurements of critical strains of wood tensile-tested in radial direction for different moisture contents have been performed. The values of wood swelling in water, which generate AE signals, are comparable to mechanical deformations of wood tissue upon its failure. The obtained results indicate that the main source of AE in swelling wood are microcracks induced by non-homogenous distribution of hygrostress, locally exceeding the strength of the investigated material. It was found that the intensity of acoustic effects in the swelling wood is proportional to the microcracks area on the longitudinal-radial and longitudinal-tangential plane of the wood. The results of temperature measurements indicate that the activation energy of bond dissociation within the microcracks takes a value about 12.5 kJ/mole. A temperature dependence of AE total event counts exhibits a rapid decrease at 55°C, which may be taken as the glass-transition temperature for the amorphous components of wood.

1. Introduction

Investigations of wood properties by means of acoustic emission (AE) method have been carried out for several years. This method is most often applied to get a better insight into the process of wood destruction due to mechanical effects (Porter et al., 1972; Morgner et al., 1980; Sato et al., 1984; Noguchi et al., 1986). Recently, this method has become useful in investigations of cracks formation in wood during its drying (Noguchi et al., 1980, 1982, 1983, 1985; Becker, 1982; Honeycutt et al., 1985; Wassipaul et al., 1986). From the above papers, the source of AE signals generated in wood are microcracks appearing mostly in the radial plane. In case of wood with clear structural nonhomogeneity the source of AE can also be microcracks on the boundary of annual increments. The appearance of this kind of structural defects at relatively low stress (much below the proportionality limit) is directly related to irreversible changes in the examined material.

Received in August 1989, in revised form, 1 July 1990. The authors are affiliated with Department of Physics and Chair of Wood Science, Agricultural University of Poznan, Wojska Polskiego 38/42, PL 60-637 Poznan, Poland.

Particularly pronounced permanent changes in wood are observed in the case of the simultaneous action of two or more variables (e.g., mechanical stress and moisture), which can be seen as the so-called, mechano-sorptive effect. Raczowski (1969), concerned with mechano-sorptive effects in wood, has presented a thesis about the superposition of a creeping process resulting from changing orientation of definite bounds on the substructural level with the simultaneous destruction process. The latest analyses of the creeping process by AE method (Morgner et al., 1980; Beall, 1986; Niemz and Hansel, 1987) seem to have fully confirmed this thesis. However, as far as we know, the literature does not provide any data on the appearance of structural defects in wood during moistening. Thus assuming that better recognition of this problem can contribute to more accurate determination of the causes of the mechano-sorptive effect, a project was undertaken to explain acoustic effect phenomena in moistened wood.

2. Experimental Procedures

Because of the characteristic high sorptive stress, beech wood (*Fagus sylvatica* L.) has been chosen for investigations of acoustic emission in wood on its moistening in water. The experiments were carried out on sample, in the shape of rectangular prisms of 1 to 5 cm in height (along the fibres) and square cross-sections with the edges of 2, 3, 4 and 5 cm. The samples were made of one block 2 m long in such a way that the cross-section of the smallest samples covered the same yearly increments as the central part of the samples with the largest cross-section. The samples prepared in this way were gradually dried in laboratory dryer to the oven-dry state. The density of wood in the oven-dry state was within the limits of 680 to 712 kg/m³.

The measurements of acoustic emission during moistening of the samples were performed on DEMA-20 apparatus (Technipan-Warsaw) equipped with a resonant piezoelectric transducer (500 kHz). The sensor was always mounted in the middle of the sample cross-section (Fig. 1).

In each experiment the same amplification level of 85 dB was used. The discrimination threshold was selected in such a way that the release of air bubbles was not registered. During the moistening of the samples the changes in effective rms voltage of the AE signal as well as the AE total event counts were also registered. A block diagram of the measuring system is given in Fig. 1.

3. Results and Discussion

In the first stage of the investigations of acoustic emission in swelling wood, the kinetics of the increase in the total

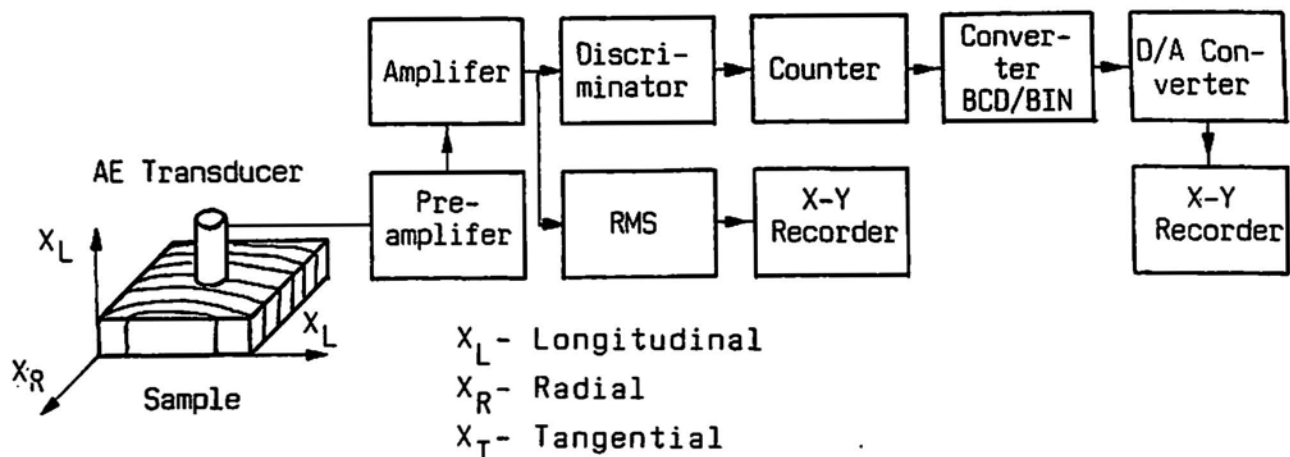


Fig. 1 Block diagram of the equipment for AE measurements.

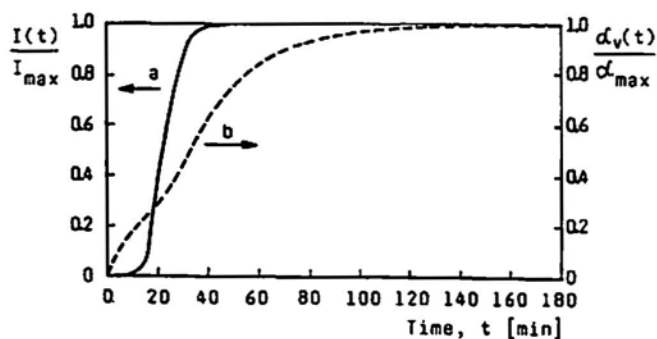


Fig. 2 Kinetic curves of acoustic emission (a) and volumetric swelling (b) of beech wood in water.

number of AE events was compared with the kinetics of the increase of volumetric wood swelling (α_v), measured in the same conditions. As follows from the exemplary kinetic curves presented in Fig. 2, in the first stage of water penetration in wood the changes in volume precede the acoustic effect which can be clearly observed only after some dead time. This dead time has been determined to be the time within which the volumetric swelling of the sample has reached 20% of its maximum value. At that time, the number of AE signals generated per time unit increases rapidly, and from then the swelling is considerably delayed relative to the AE effect.

The AE measurements in the swelling wood were accompanied by those of strain at failure of wood samples stretched in the radial direction for different wood moisture content. The value of moisture caused deformation, which is equal to the strain at failure of wood sample in tension across the grain, can be determined as critical strain. The connection between a relative number of AE signals and the relative wood moisture testifies to an unambiguous relationship between the critical strains in wood and the appropriate moisture caused strains (Fig. 3), which may become the sources of acoustic emission. The above results can be interpreted assuming that in nonstationary conditions for investigating the acoustic emission induced by swelling, the water penetration of wood occurs in such a way that a sharp line may be drawn between the fully penetrated and

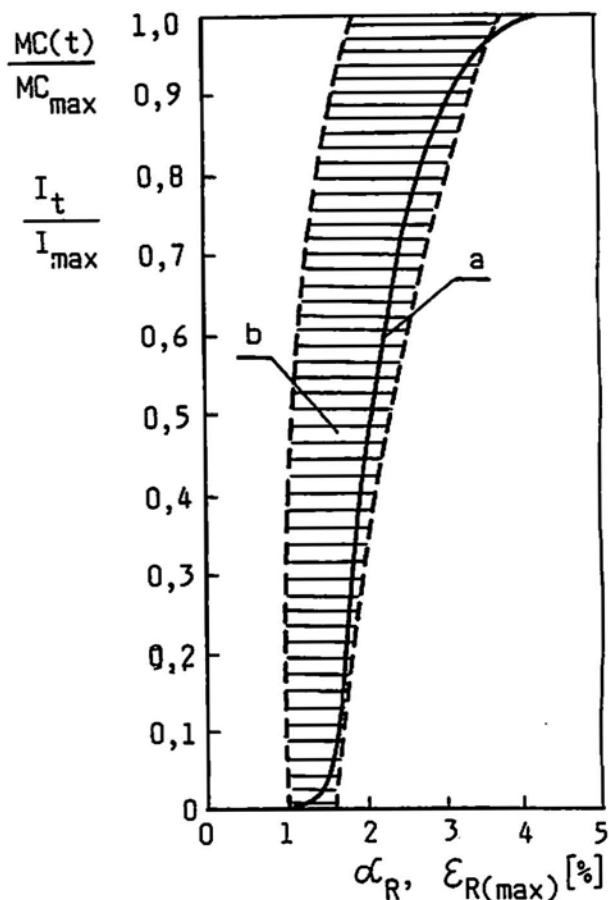


Fig. 3 The relative number of AE total event counts (I_t/I_{max}) versus the degree (α_r) of wood swelling (a) and the relative moisture content (MC/MC_{max}) as a function of critical strains (ϵ_{max}) in radial direction (b).

unpenetrated regions (Helinska-Raczowska et al., 1988). The swelling of the penetrated regions brings about the deformation in the neighbouring unpenetrated regions. This may produce the stress which can locally exceed the strength of material and become a source of AE signals recorded on the wood swelling.

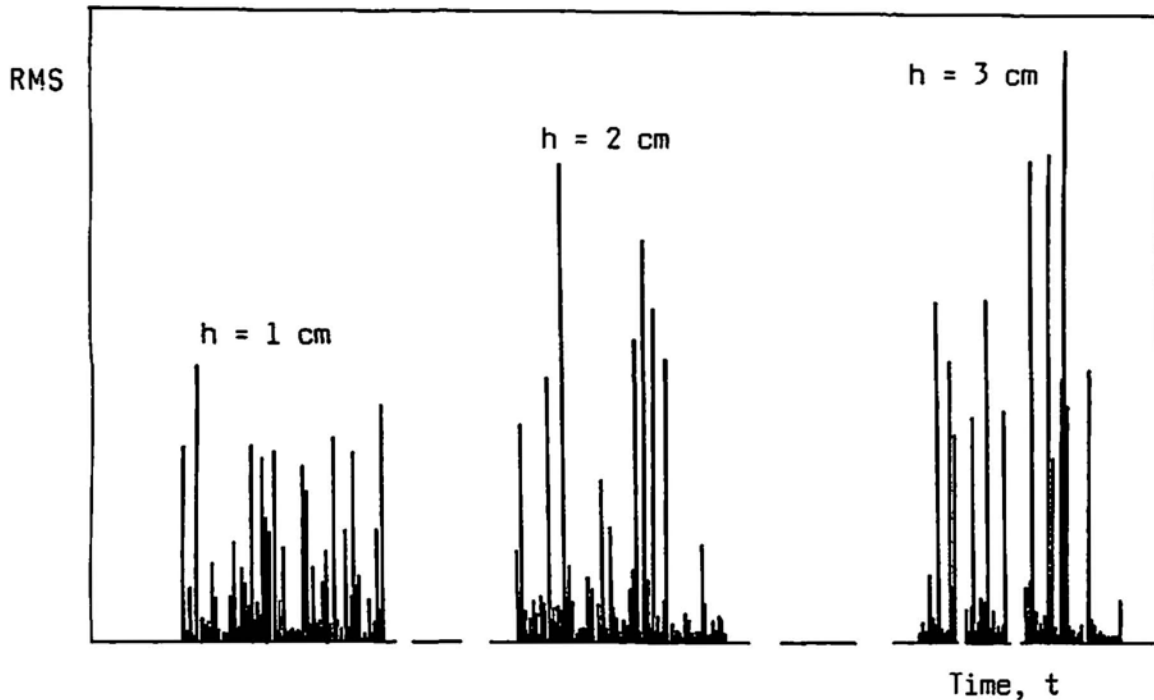


Fig. 4 Distribution of energy of AE signals (relative units) generated by swelling in water of wood samples of different height (h) and the same area of square cross-section (3×3) cm^2 .

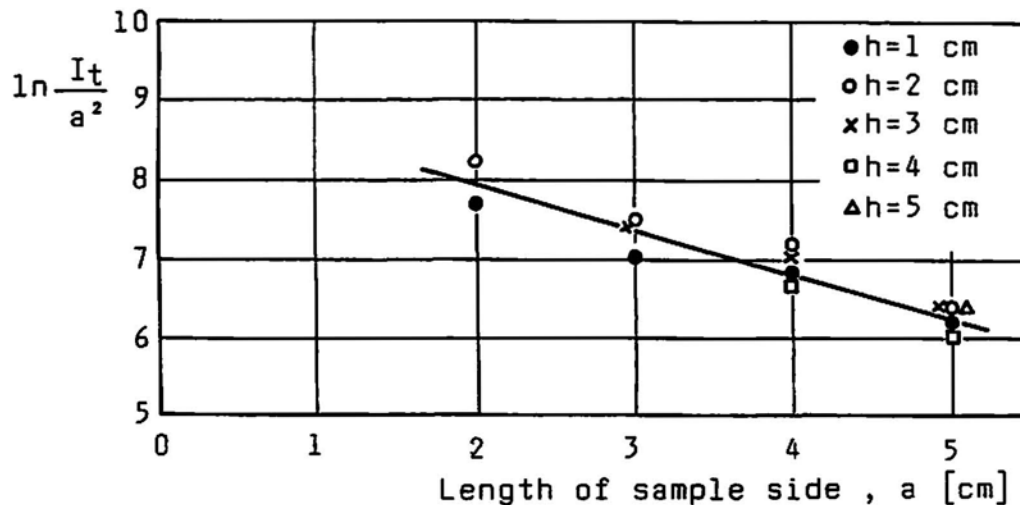


Fig. 5 Diagram of dependence of the total AE event counts per unit area of cross-section of samples on the length of the sample edges.

In order to give a quantitative description of acoustic emission in the swelling wood, the AE measurements were performed for wood samples of different size. It was interesting to find that there is no significant relationship between the AE total event counts per a unit area of the sample cross-section and the height of the samples (Fig. 5). However, as follows from Fig. 4, the average energy of the generated AE signals increases proportionally to their height. With the increasing height of the samples, the area of cracks, proportional to the AE signal energy, increases. This may indicate that the cracks spread all over the height of the samples. This conclusion is consistent with an earlier relationship between the impact resistance and

the frequency of the emitted waves per unit area destroyed (Suzuki and Schniewind, 1987). In the light of the above and taking into account the anatomical wood structure, we may assume a model in which a net of mutually crossing lines of cracks covers the cross-section area of the swollen wood. The crossing points of the lines determine the width of elementary microcracks, which are the elementary sources of acoustic emission in swelling wood.

According to the model, the number dN of elementary microcracks in $dS (= dX_1 dX_2)$ area of the cross-sectional (X_1, X_2) surface can be described by:

$$dN \cong 2 \frac{dX_r dX_t}{l_r l_t} \quad (1)$$

where l_r and l_t are the microcracks mean dimensions in the radial and tangential directions.

Among all AE signals emitted by microcracks, the transducer records only the signals of the intensities exceeding the threshold of the measuring equipment. This means that the AE signals from small microcracks and those whose intensity falls below the threshold due to the attenuation are not recorded. The decrease in the AE signal amplitude for a distance X from the source is described by an exponential relation (Skudrzyk, 1971) of the type:

$$s = s_0 \exp(-\delta X), \quad (2)$$

where the coefficient δ is a measure of losses of acoustic energy in the medium. Therefore, taking (1) and (2) into account, the total number of recorded AE signals registered due to swelling of wood is described by the equation:

$$I_t \cong \int_s \frac{2k}{l_r l_t} \exp[-\delta(X_r^2 + X_t^2)^{1/2}] dX_r dX_t \quad (3a)$$

where k is a coefficient related to the sensitivity of the measuring system. For samples of the square cross-section, when $a_r = a_t = a$ and the transducer is located in the center of the samples, integration of equation (3a) leads to the relation:

$$I_t \cong \frac{2k a^2}{l_r l_t} \exp[-\delta a/2] \quad (3b)$$

The diagram of the dependence of $\ln(I_t/a^2)$ on the length of the edges of the tested samples, given in Fig. 5, indicates a good agreement between the experimental data and relation (3b).

The appearance of a crack in the material is a random effect of thermo-fluctuational dissociation of the bonds initiated by the stress (Regel et al., 1974). Thus, formation of a crack of the area (h) requires a certain number of bonds, proportional to the area of the crack, to dissociate. The probability (p) of appearance of such a crack on the cross-sectional surface of the sample of the area (h) is determined by a ratio of the number of the dissociated bonds to the number of all bonds; i.e., the ratio of (h) to (h). Therefore, $p = 1/a$ and according to the Boltzmann's law:

$$p = 1/a = \exp[-\Delta E/RT] \quad (4)$$

where $l = (l_r l_t)^{1/2}$ is the mean length of a microcrack on the $X_r X_t$ -plane, ΔE is the activation energy of dissociation of one mole of bonds, R is gas constant and T is the absolute temperature.

According to our considerations the temperature dependence of the total number of AE signals generated by swelling wood should be as follows:

$$I_t = 2k \exp[2\Delta E/RT] \exp(-\delta a/2) \quad (5)$$

Consistent with theoretical predictions, the results of temperature measurements presented in Fig. 6, reveal a linear character of $\ln(I_t)$ dependence on $1/T$, for temperatures ranging from 0°C to about 50°C. The activation energy ΔE of bond dissociation within microcracks determined from the line slope assumes the value of the order of 12.5 kJ/mol.

Above 55°C, a rapid decrease is observed in this dependence. It is probably a consequence of the fact that the glass-transition temperature of some amorphous components of

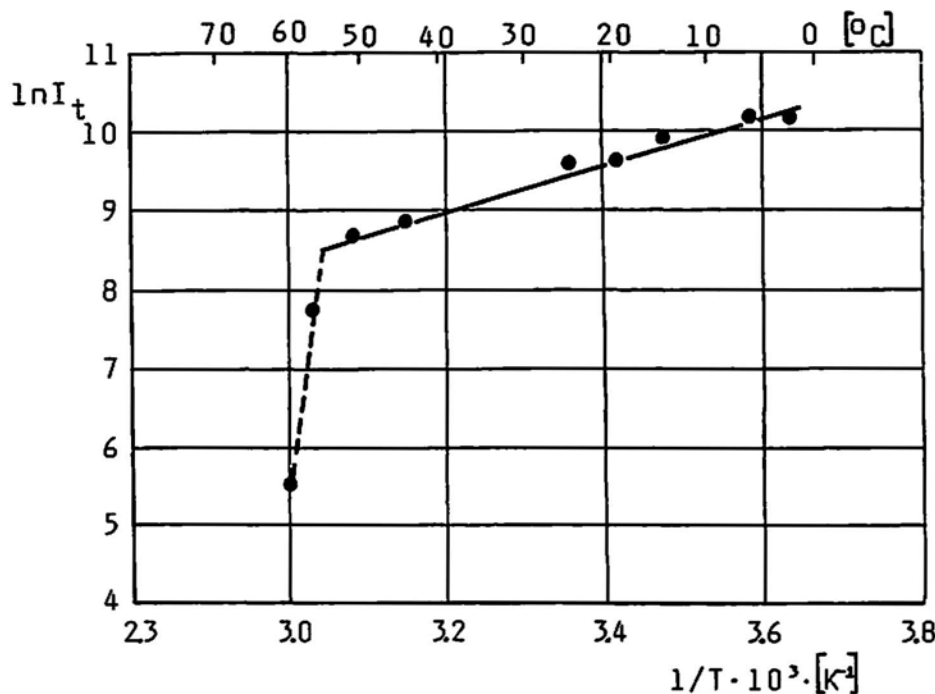


Fig. 6 Temperature dependence of the total number of AE signals recorded during swelling of wood in water.

wood cell walls has been reached (Dawidson, 1962; Irvine, 1984; Iida, 1986). This, in turn, would imply a rapid increase in acoustic wave damping coefficient (δ) in the medium as well as a decrease of the probability of brittle cracks formation.

4. Conclusions

1. The investigations of AE in swelling wood indicate the existence of less recognized adsorptive cracks besides the commonly known desorptive microcracks.

2. The values of wood swelling in water that generates AE signals are comparable with mechanical deformations of wood tissue upon its failure.

3. The intensity of AE effects in the swelling wood is proportional to the microcrack area on the cross-sectional surface of wood.

4. The activation energy ΔE of bond dissociation within the microcracks takes the values comparable to the energy of hydrogen bonds that is of about 12.5 kJ/mol.

5. A temperature dependence of AE total event counts exhibits a rapid decrease above 55°C, which may be taken as the glass-transition temperature of amorphous components of wood.

Acknowledgments

The authors would like to express their thanks to Prof. J. Ranachowski and Mr. Z. Ranachowski from the IPPT of the Polish Academy of Sciences for their valuable help in our investigations.

References

F.C. Beall (1986), "Effect of moisture conditioning on acoustic emission from particleboard", *J. Acoustic Emiss.*, 5(2), 71-76.

H.F. Becker (1982), "Schallemissionen während der Holz Trocknung", *Holz als Roh- u. Werkstoff*, 40, 345-350.

R.W. Davidson (1962), "The influence of temperature on creep in wood", *Forest Prod. J.*, 12, 377-381.

L. Helinska-Raczkowska, S. Poliszko and J. Raczkowski (1988), "Stress relaxation in wood under unsteady penetration of physically active liquids", *Progress and Trends in Rheology II, Supl. to Rheologica Acta*, eds. H. Gieskus and P. Mitschka, 26, 236-238.

R.M. Honeycutt, Ch. Skaar and W.T. Simpson (1985), "Use of acoustic emission to control drying rate of red oak", *Forest Prod. J.*, 35(1), 48-50.

I. Iida (1986), "The thermal softening of green wood evaluated by its Young's modulus in bending", *Mokuzai Gakk.*, 32(6), 472-477.

G.M. Irvine (1984), "The glass transition of lignin and hemicellulose and their measurement by differential thermal analysis", *Tappi J.*, 67(5), 118-121.

W. Morgner, P. Niemz and K. Theis (1980), "Anwendung der Schallemissionsanalyse zur Untersuchung von Bruch- und Kriechvorgängen in Werkstoffen aus Holz", *Holztechnologie*, 22(2), 77-82.

P. Niemz and A. Hansel (1987), "Zur Anwendung der Schallemissionsanlage in der Holzforschung", *Holztechnologie*, 28(6), 293-297.

M. Noguchi, Y. Kagawa and J. Katagiri (1980), "Detection of acoustic emissions during hardwoods drying", *Mokuzai Gakk.*, 26(9), 637-638.

M. Noguchi, Y. Kagawa and J. Katagiri (1983), "Acoustic emission generation in the process of drying hardwoods", *Mokuzai Gakk.*, 29(1), 20-23.

M. Noguchi, S. Okumura and S. Kawamoto (1985), "Characteristics of acoustic emissions during wood drying", *Mokuzai Gakk.*, 31(3), 171-175.

M. Noguchi, K. Nishimoto, Y. Imamura, Y. Fujii, S. Okumura and T. Miyauchi (1986), "Detection of very early stages of decay in western hemlock wood using acoustic emissions", *Forest Prod. J.*, 36(4), 35-36.

A.W. Porter, M.L. El-Osta and D.J. Kusec (1972), "Prediction of failure of finger joints using acoustic emissions", *Forest Prod. J.*, 22(9), 74-82.

J. Raczkowski (1969), "Der Einfluss von Feuchtigkeitsänderungen auf Kriechverhalten des Holzes", *Holz als Roh- u. Werkstoff*, 27(6), 232-237.

W.R. Regel, A.I. Slucker and E.J. Tomaszewskij (1974), *Kineticskaja priroda prochnosti tverdykh tel*, Nauka, Moskva.

K. Sato, N. Kamei, M. Fushitani and M. Noguchi (1984), "Discussion of tensile fracture of wood using acoustic emissions. A statistical analysis of the relationships between the characteristics of AE and fracture stress", *Mokuzai Gakk.*, 30(8), 653-659.

E. Skudrzyk (1971), *The foundations of acoustics*, Springer-Verlag, Wien-New York.

M. Suzuki and A.P. Schniewind (1987), "Relationship between fracture toughness and acoustic emission during cleavage failure in adhesive joints", *Wood Sci. Technol.*, 21(2), 121-130.

F. Wassipaul, M. Vanek and A. Mayerhoffer (1986), "Klima und Schallemissionen bei Holz Trocknung", *Holzforsch. u. Holzverwert.*, 38(4), 73-79.

Characterization of the ASL Parameter

J. W. Whittaker

Abstract

Electron beam (EB) welding of uranium produces large amounts of acoustic emission (AE) having a broad range of amplitudes. The Average Signal Level (ASL) parameter has been used to summarize and quantify such emission. The parameter's ability to average the effects of numerous signals and its large dynamic range make it particularly useful. We performed experiments to provide a better understanding of the response of the ASL circuitry to AE produced under various conditions. The effects of emission type (continuous, burst and mixed), signal amplitude and frequency, and recording instrument were evaluated.

1. Introduction

Electron beam welding of uranium (Whittaker and Murphy, 1991) produces continuous AE interspersed with large numbers of high amplitude bursts. Continuous emission is representative of weld formation. Large amplitude bursts (many as high as 95 dB in reference to 80 dB = 1 V) are produced by weld expulsion (and possibly other sources) and smaller amplitude ones (<60 dB) are related to some, as yet unidentified, cooling phenomena. Since emission is produced by welding processes, it has the potential to provide some indication of the quality of the weld that is being formed. Measurement of weld penetration, for example, in real time would be beneficial in that a post-weld ultrasonic examination could be eliminated and the cost of the weldment reduced. An experimental program is underway to establish AE monitoring as a viable technique for real-time penetration measurement of a variety of materials.

Early experiments were designed to evaluate the ability of various signal conditioning techniques to provide an adequate representation of the welding process from an AE viewpoint. The most commonly used averaging measurement, root-mean-squared voltage, was discarded because it is typically limited to a linear dynamic range of only 20 - 25 dB. The ASL parameter, as measured by a Physical Acoustics Corporation (PAC) Model 3102 AE analyzer (100 kHz high-pass filtered), was found to adequately average the time-varying weld AE signals and had a useful dynamic range of ~ 70 dB. The ASL has been successfully used to measure AE signatures of welds with a broad range of penetration. (See Fig. 1 for a typical signature.) A search of the literature revealed that the ASL parameter is very seldom utilized. Only one paper mentioning the ASL (Falchi, 1986) is known to the author. Since little was known about how the ASL

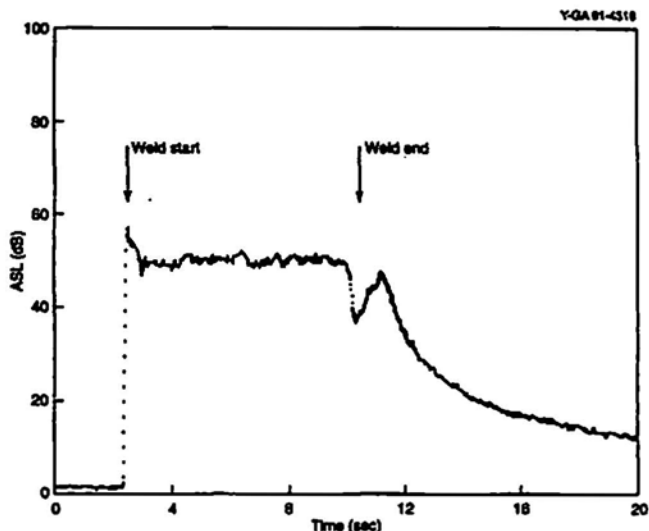


Fig. 1 Typical acoustic emission signature from electron beam welding.

circuitry would respond under different AE conditions, experiments were performed to elucidate the effects of emission type (i.e., continuous, burst and mixed), frequency response, burst parameters (rate, amplitude and duration), and recording instrument.

2. Experimental Work

2.1 Apparatus

According to the manufacturer, the quantity known as ASL results when the logarithmic amplitude of the preamplified and filtered AE waveform is continuously measured and the resultant voltage passed through a resistance/capacitance circuit for averaging. It is generally utilized to measure the average level of continuous emission such as that resulting from fluid leaks and is relatively insensitive to burst-type emission. However, if bursts occur at a very rapid rate or have very long duration, they can affect ASL measurement.

The apparatus in Fig. 2 was used to subject the ASL circuitry of a PAC 3104 AE analyzer to electronically-generated signals designed to simulate continuous, burst and mixed (continuous and burst) emission. (A 3104 was used because of its availability. The ASL circuitry of the 3104 is identical to that of the 3102.) Continuous emission was simulated by the oscillator (Krohn-Hite Model 4200A) which generated steady-state sine waves of selected frequency and amplitude. The AE simulator (Acoustic Emission Associates Model AES-1) was used to simulate either burst-type emission or (through mixing its burst and carrier wave signals) mixed continuous/burst emis-

Received 5 May 1992. The author is affiliated with Development Division, Oak Ridge Y-12 Plant, PO Box 2009, Oak Ridge, TN 37831. Oak Ridge Y-12 Plant is managed by Martin Marietta Energy Systems, Inc. for the U. S. Department of Energy under Contract DE-AC05-84OR21400.

Journal of Acoustic Emission
Volume 10, Number 3/4

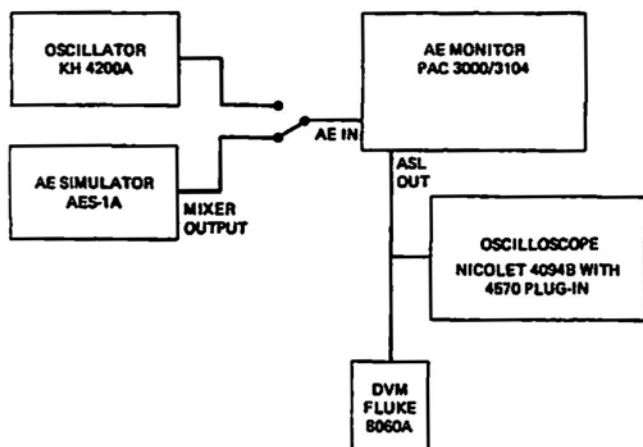


Fig. 2 Experimental apparatus.

sion. A digital oscilloscope (Nicolet 4094B with a 4570 plug-in amplifier) was used to observe the signals and make peak voltage measurements. The digital voltmeter (Fluke 8060A) was used to measure the dc voltage resulting from ASL measurement of continuous signals. The PAC Model 3000 computer attached to the 3104 recorded data.

As the project progressed, a new AE analyzer (PAC Model LOCAN-AT) was introduced. It utilized a 100 - 300 kHz pass-band. The signal conditioning features (including the ASL circuitry) of the instrument are essentially the same as a 3102 or 3104. It differs, though, in that it internally samples the ASL signal and records it. The 3102 and the 3104 measure the ASL directly but have no provision to digitally sample it as they do other more standard AE parameters measured (i.e., AE counts, amplitude, etc.). Instead, the ASL signal is routed to an external parametric input where it passes through a low-pass filter and is then digitized and recorded. To enable comparison of the ASL recording capability of the LOCAN-AT and the 3000/3102, the input signal generated during a typical weld was simultaneously recorded by both instruments.

2.2 Procedure

Oscillator frequency was varied over the 100 kHz to 1 MHz range and signal amplitude varied from 0.01 to 8.0 V peak-to-peak. The pulsed output of the AE simulator was mixed with a low level (60 mV) sine wave from the simulator's carrier output to produce a signal which simulated continuous emission mixed with high amplitude bursts. Pulses with a 95 dB peak amplitude were produced at a rate of 240/s. Pulses of this amplitude and rate have been observed during high expulsion portions of some welds. Pulse durations (above an arbitrary 0.1 V threshold) of 100 and 1000 μ s were also used to assess potential pulse duration effects on ASL measurement.

The signal output generated during a welding run was routed simultaneously to the 3102 and LOCAN-AT. The ASL signal was sampled by each instrument at its maximum rate, 100/s for the 3000/3102 and 10/s for the LOCAN-AT.

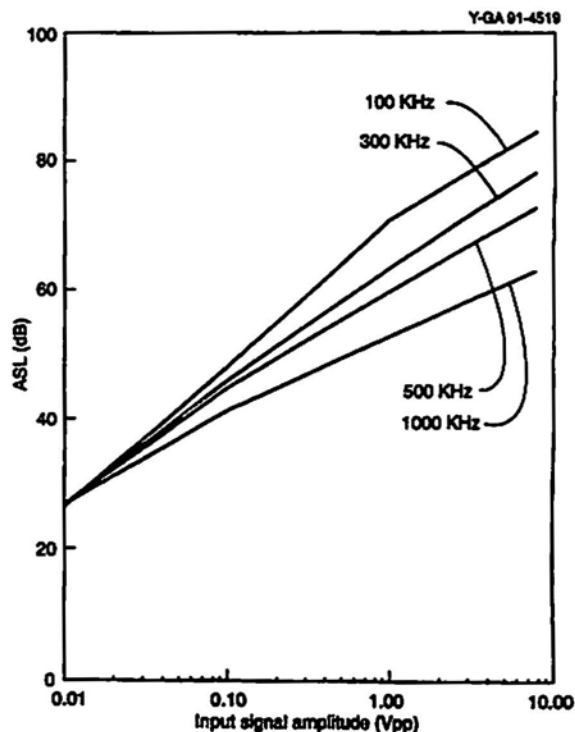


Fig. 3 Behavior of the ASL parameter as functions of signal amplitude and frequency.

3. Results

In Fig. 3, the recorded ASL value is plotted as a function of frequency and amplitude. The ASL increased approximately linearly as a function of the logarithmic signal level. Linearity was best for 300 kHz and 500 kHz. Additionally, for a given signal amplitude, the ASL value decreased with higher frequency. Due to the linear ASL behavior at 300 kHz, the expectation is that the ASL value of signals derived from welding (in which a 300 kHz resonant sensor is used) should vary linearly with the logarithm of the input signal amplitude, as desired.

The ASL values for various simulator output conditions are summarized in Table 1. The normal noise level of the ASL circuitry is 1 - 2 dB. Sine wave input is significantly greater (38 - 39 dB). Short duration pulses added only 2 dB while long pulses added 7 dB to the overall ASL level. Thus, if weld expulsion occurs simultaneously with the continuous emission produced by volumetric weld processes, the expulsion-related AE will contribute only a modest amount to the peak ASL value rather than constitute the main portion of it. Consequently, even in expulsion-prone weld portions, such as at initiation, the largest majority of the ASL is due to welding. This clarifies some of the AE behavior of weld observed previously.

Table 1. ASL value as a function of simulator output conditions.

	Sine Wave Only	+ Short Pulses	+ Long Pulses
ASL (dB)	40	42	47

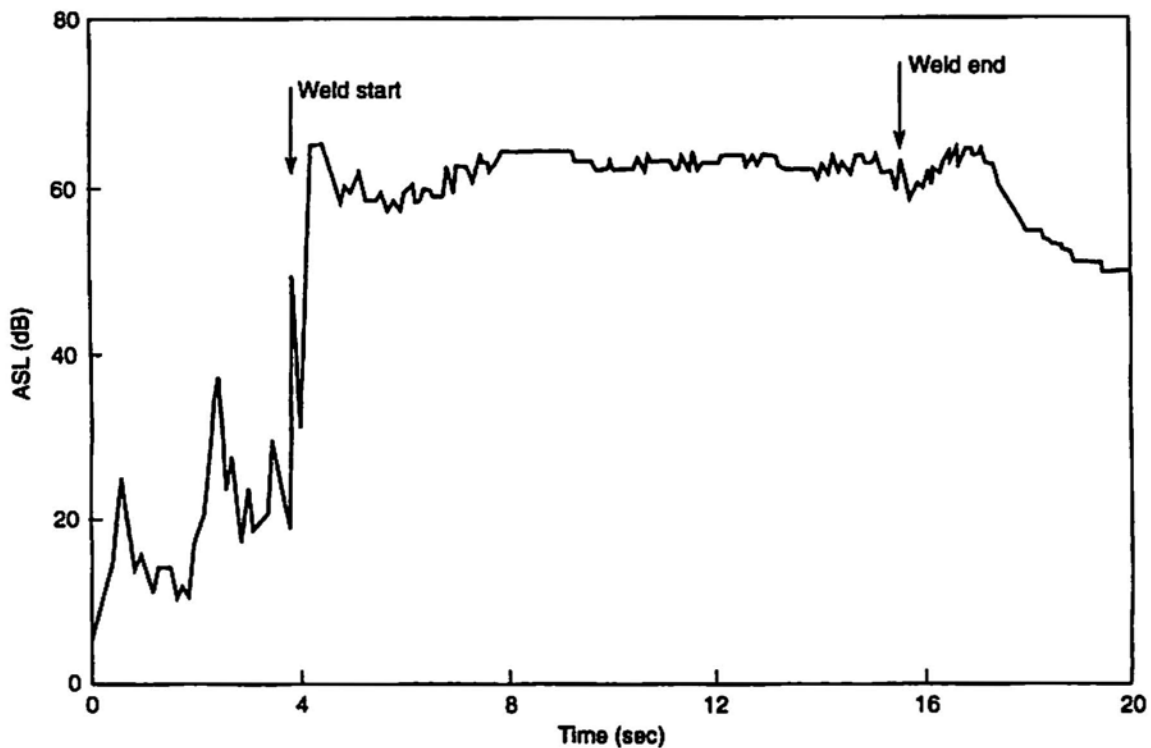
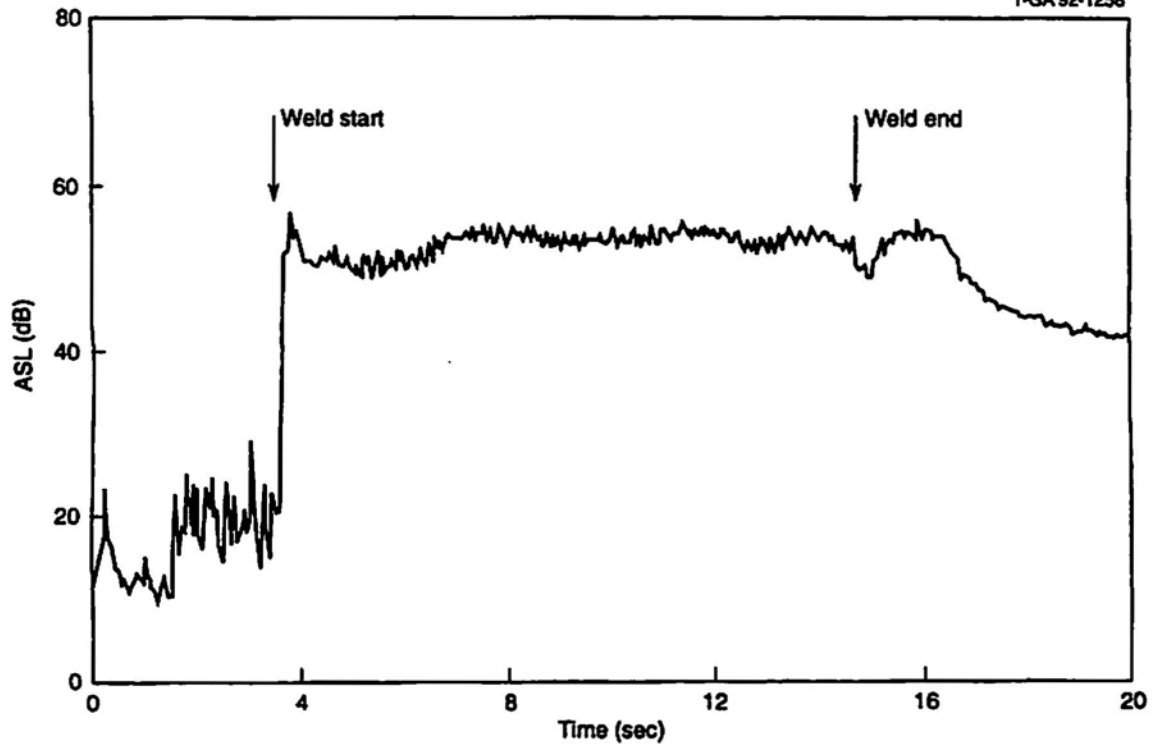


Fig. 4 Comparison of ASL signatures recorded by different AE analyzers during welding of a step joint in uranium. a. PAC 3000/3102 (top); b. PAC LOCAN-AT (bottom).

The AE signatures of the weld recorded simultaneously by the 3000/3102 and LOCAN-AT are compared in Fig. 4. All features present in the 3000/3102 signature are also present in the LOCAN-AT signature. The LOCAN-AT signature is smoother

due to the lower sampling rate. The key difference between the signatures is that the features of the LOCAN-AT signature are higher in amplitude (~ 9 dB). Since both instruments processed the same signal input with essentially the same circuitry (the

only difference is the 100 to 300 kHz filtering used in the LOCAN-AT which should *attenuate* the signal rather than amplify it) the difference arises elsewhere. Investigation revealed that filtering of the parametric input of the 3000/3102 is responsible for the difference. The increased ASL value of the LOCAN-AT signature should not in any way affect measurements required to correlate ASL value with weld penetration, similar to those made with the 3000/3102 data.

4. Conclusion

The ASL parameter, as implemented in PAC instrumentation, exhibits essentially linear response with logarithmic amplitude over frequencies typically used in AE experiments. It has a large dynamic range, which makes its use in certain applications more attractive than the more traditional root-mean-squared voltage measurement. It is relatively insensitive to pulsed emission. Care must be taken in selection of the method of recording the ASL since low-pass filtering can attenuate its dc-voltage representation.

References

J.W. Whittaker and J.L. Murphy (1991), "Real-Time Measurement of Electron Beam Weld Penetration in Uranium by Acoustic Emission Monitoring," Proceedings of the 4th World Meeting on Acoustic Emission and 1st International Conference on Acoustic Emission in Manufacturing, 16-19 September, Boston, MA, ASNT, Columbus, OH. pp. 447-452.

Acoustic Emission from Bubbles in a Water Column

Mark A. Friesel and Jack F. Dawson

Abstract

The unique remote monitoring capability of acoustic emission methods shows a potential for quantitatively monitoring multi-phase flow in pipes. Using a simple experimental apparatus where gas bubbles are injected into a tube filled with standing water, an ability to obtain a quantitative relationship between acoustic emission and void fraction during a very simple two-phase flow simulation is demonstrated. Models for the source and the attenuation/sensor sensitivity function are proposed, and are shown to accurately describe experimental results.

1. Introduction

Acoustic emission (AE) is a passive NDT method commonly used for process control and to identify and monitor damage in structural materials. An ultrasonic receiver coupled to the surface of a structural component can identify remote microscopic damage by detecting acoustic radiation produced as the damage occurs. Acoustic emissions may also be produced by sources unrelated to material damage, some of which are or may be useful for process control; i. e., to diagnose operation of mechanical, hydraulic, or electrical systems. One such application is monitoring reactor coolant to determine the void fraction during two-phase flow. In recent reactor models, such coolant may be liquid metal, where "void" fraction is a measure of the amount of coolant in vapor form. This application may involve temperatures in excess of 1200°C, making standard methods of flow monitoring unfeasible (Lahey and Moody, 1977). Acoustic emission technology has been successfully adapted to extreme environments, including high ambient radiation levels and temperatures (Hutton et al., 1987). Although AE sensor components can be made fairly radiation resistant, a waveguide sensor must be used to protect sensor components from the heat (Friesel, 1986).

Work reported here is a demonstration of the potential of AE techniques to monitor and quantify two-phase liquid coolant flow, which builds on and complements earlier work. It has been shown that cavitation in coolant channels and boiling produces detectable acoustic emission. Examination of cavitation noise was performed by Saxe and Lau (1968) using primarily spectral analysis at frequencies below 30 kHz. Relevant to current research was an apparent linear relationship between small bubble population in the flow, and measured acoustic signal amplitudes. An experimental loop facility was used by Leemans et al. (1981) to study flow quality and flow rate with

AE at higher frequencies. These authors reported successful use of a pattern recognition technique with data vectors composed of spectra in various frequency bands along with other parameters related to the spectral and signal amplitude distributions. Beattie (1982) developed a model to describe the response at a sensor to boiling-related sources in a solar receiver. The model is based on the integral of a distributed source function and an attenuation function similar to the method used below.

2. Experimental Apparatus and Setup

A simple apparatus was designed and built to allow a simulated two-phase condition to be created in a vertical fluid column. Materials used in the experiment are as follows:

Glass tube 91.5 x 4.7 cm (O.D.) with 0.46 cm wall thickness,

Compressed He gas with regulator,
0.43 mm I.D. syringe needle,

Cylindrical rod waveguide sensor,
Broadband amplifiers (nominally 20 dB and 40 dB,
respectively),

AE data acquisition instrument (30 dB internal gain),
Rubber plug, ring stand, miscellaneous hardware.

The apparatus consists of a water-filled tube (Fig. 1), open at the top and with a rubber stopper in the bottom. Pressurized helium was allowed to flow through a rubber hose connected to a needle, which was inserted either through the rubber stopper or down through the top of the glass tube. The insertion point could be changed by positioning the needle tip at different depths in the tube, producing a slight change in quiet fluid level. The void fraction is related to the gas flow rate, and was varied by increasing the gas pressure. The steel waveguide AE sensor was spring-mounted to the tube about 36 cm below the water surface level using the apparatus illustrated in Fig. 2. Sensor response was fed through the amplifiers into the data acquisition instrument, yielding nominally 90 dB of gain from the sensor output. A Dunegan 1032 AE instrument and a machine designed and built at Battelle for the Nuclear Regulatory Commission were used at different times during the test. These instruments derived various AE parameters such as signal amplitude, risetime, event time, etc., and stored the data for analysis.

During setup and calibration, a significant number of emissions were detected from bubbles bursting at the upper surface of the water column. Since a high background rate could interfere with measurements, an acoustic barrier was constructed using a 2-cm wide band of putty on the outside of the tube about 10 cm below the quiet water level, supplemented by a rolled thin plastic sheet inserted inside the water tube, extending from the putty level to above the tube top.

Received 1 March 1991. The authors are affiliated with Automation and Measurement Sciences Department, Pacific Northwest Laboratory, Richland, WA 99352.

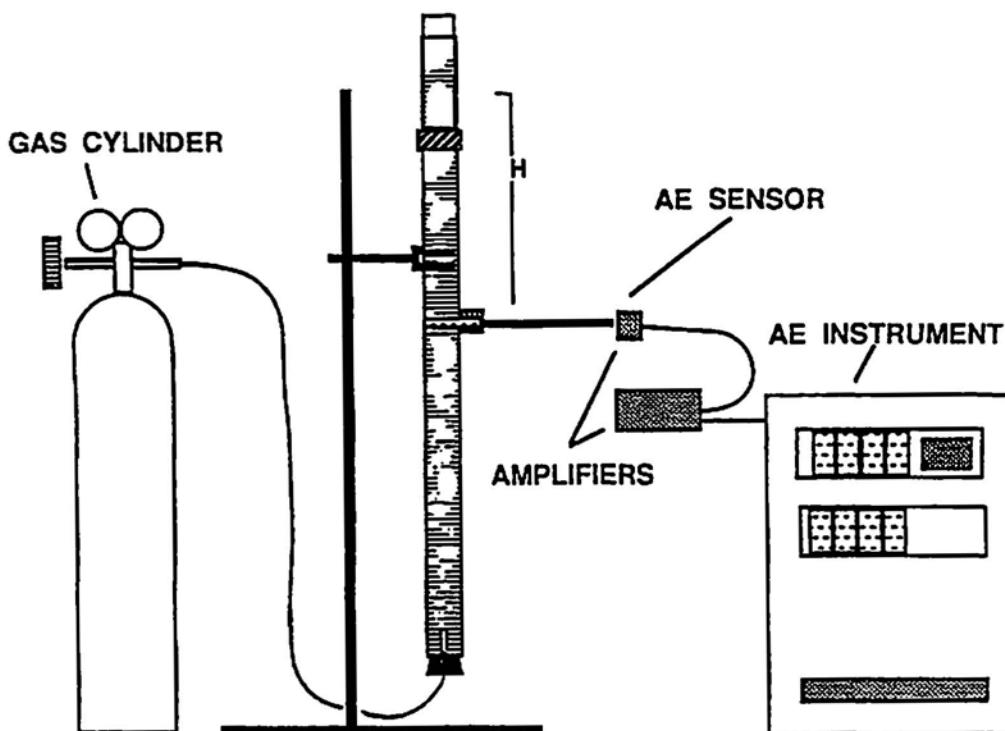


Fig. 1 Schematic of the test apparatus. H is approximately 36 cm.

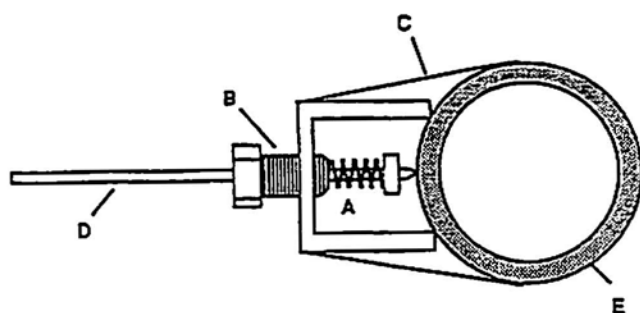


Fig. 2 Waveguide and mounting apparatus. A: spring, B: bolt, C: metal strap, D: waveguide, E: glass tube.

3. Experimental Results

Experiments were performed to examine the effect of void fraction and relative injection point/sensor distance on the measured acoustic emission. The contribution of surface-breaking bubbles on the AE and the effectiveness of putty and plastic sheeting in reducing emissions from this source were examined.

3.1 General Observations

Observable bubble activity was in the form of expansion and oscillation of individual bubbles, collisions among bubbles, collisions between bubbles and the tube wall, and bubble coalescence. At higher gas pressures and as the bubbles rose, increasingly large bubbles formed through coalescence and expansion, culminating in a form of plug flow. Determination

of the height of the fluid in the tube in the presence of large bubbles was rendered somewhat difficult by fluctuating levels. The behavior of the bubbles suggests that void fraction in these experiments is depth dependent, hence the void fraction estimates are values averaged over the entire fluid volume.

3.1.1 Experiment 1: With an acoustic barrier of putty and plastic sheet installed near the quiet fluid level, the needle was inserted through the rubber stopper and the gas flow increased stepwise. Each flow rate was maintained for 20 minutes and AE events recorded, while the maximum and minimum fluid levels were determined to obtain void fraction estimates. Void fraction was defined as $f = \Delta h / (h + \Delta h)$, where h is the quiet fluid level, and Δh is the change in level caused by gas injection. The AE event rate is plotted against estimated void fraction in Fig. 3.

The fluid level at a given gas pressure would vary depending upon how close large bubbles were to the surface. The bubbles also appeared to expand with decreasing depth; hence in this case, void fraction calculated by volume ratio is not a depth-independent quantity. Because of these conditions, the relation between AE rate and void fraction has some additional inherent uncertainty, but the general trend suggests that the AE rate and void fraction are closely correlated over the range examined.

3.1.2 Experiment 2: For this experiment, the gas pressure was held constant while the insertion point was raised from an initial position just above the rubber stopper. Again emissions were monitored for 20-minute intervals at each needle location with the acoustic barrier in place. The results shown in Fig. 4 illustrate a rising event rate as the needle approaches the sensor

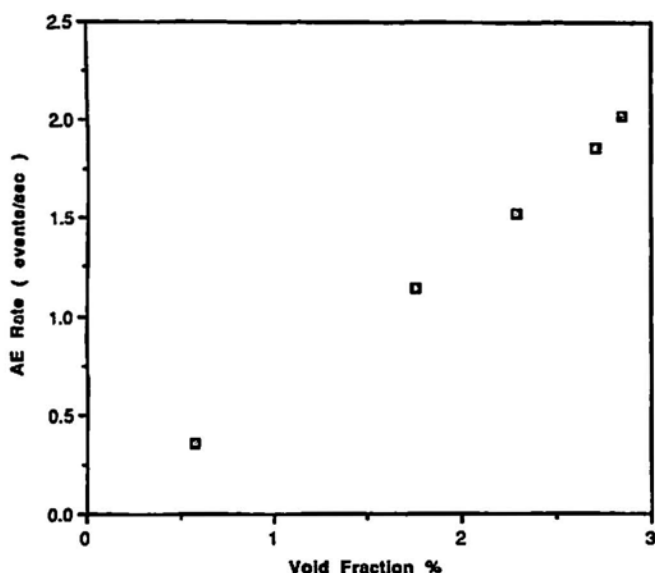


Fig. 3. AE rate vs. mean void fraction.

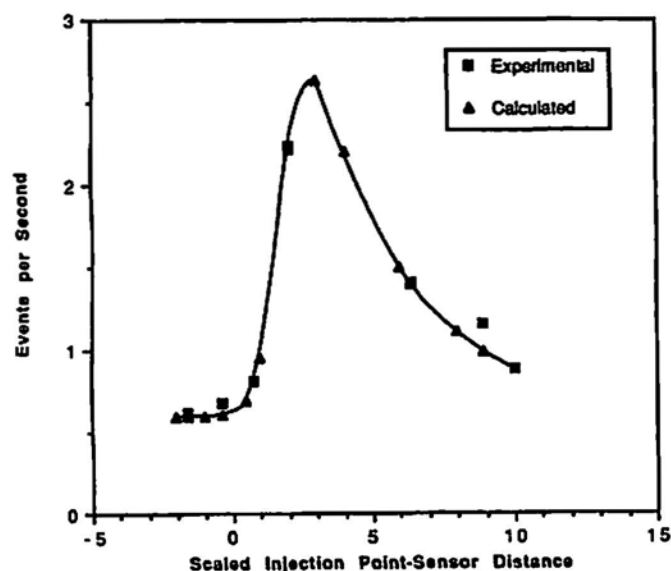


Fig. 4 Calculated and experimental event rates vs. needle tip-sensor distance. Distance scale factor is about 4.45:1.

position from below (positive r value), a sharp drop in the rate *before* the needle tip reaches the sensor, and a low emission rate dropping towards background level as the injection point passes the sensor position and moves upward. Although the emergence of bubbles from the needle tip was originally considered a potential AE source, from the results of this experiment, such cannot be the case if the sensor response is symmetric. The drop in AE rate as the needle tip passes the sensor position also suggests that the sensor sensitivity drops off rather sharply with distance. The observed behavior can then be qualitatively explained if a) only emissions from bubbles in the vicinity of the sensor are detected, and b) if smaller, more densely packed bubbles occurring closer to the injection point produce more emissions per unit volume than larger bubbles at greater distance from the needle tip.

3.1.3 Experiment 3: In order to verify the results of experiment 2 and the effectiveness of the acoustic barrier, AE was monitored a) with or without the barrier with the needle tip placed 3 cm below the water surface, and b) with the barrier set up to block emissions except in the vicinity of the sensor.

In part a), the putty ring and plastic were placed as for Experiment 1 to insulate the tube from the bubbles. Results of this experiment are shown in Table 1, where the emission rates with no barrier, putty only, and both putty and plastic are shown along with the background rate obtained without gas flow. The AE event rate of 0.55 events/s is seen to be reduced 85% by the putty and plastic, to a value of about three times the background rate. In part b), the needle was inserted through the bottom plug, and gas flow held constant for all measurements. Table 2 shows the effects of putty and plastic placed so as to block emission from outside a region extending from about 5 cm below to 5 cm above the sensor location. Two plastic sheets were employed, one extending from the upper putty ring to the end of the tube and the other from the lower ring to the rubber stopper. As shown, the use of putty and plastic reduces emission only by about 20%, or 0.7 events/s.

Table 1 Acoustic barrier effects on near-surface AE

Condition	Events/Second
Bare Glass	0.53
Putty	0.12
Putty + Plastic	0.08
Background	0.03

Table 2 Acoustic barrier effects on AE

Condition	Events/Second
Bare Glass	3.15
Putty (Top)	3.06
Putty (Top & Bottom)	2.72
Putty + Plastic	2.45
Background	0.03

The greatest drop in event rate in b) was obtained when the lower putty strip was applied, indicating that most of the detectable emission was produced below the sensor position where the bubble size is smaller, and the density of bubbles greater. If the result from a) yields a good estimate of the barrier effectiveness (e.g. about 85%), then over half of the emissions detected in b) originate within 5 cm of the sensor, and most of these originate below the sensor position.

4. Analysis

The results of Experiment 1 illustrate the potential of AE to monitor void fraction. To analyze the uncertainties in the data of Fig. 3, an estimate for the variance σ_r^2 in the void fraction may be obtained in the usual way by averaging over a Taylor expansion and neglecting higher order terms, giving

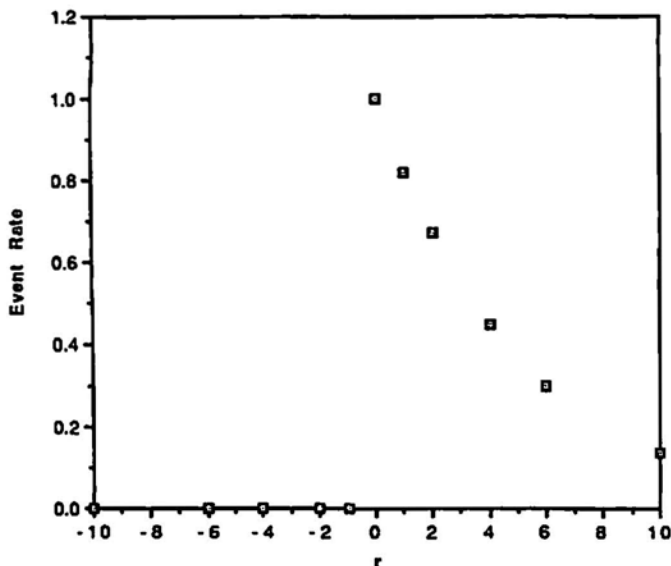


Fig. 5 AE event rates for a delta function sensor response and exponentially decaying source function.

$$\sigma_r^2 = (df/dh)^2 \sigma_h^2 + (df/d\Delta h)^2 \sigma_{\Delta h}^2 \quad (1)$$

where the fluid level h and the change in fluid level Δh are treated as independent variables. Values for Δh ranged from about 0.5 to 10 cm, with uncertainties ranging from near zero to ~3 cm. Uncertainty in the void fraction is therefore about one to two percent at larger void fraction.

To describe the results of Experiment 2, it is necessary to postulate both a source model $s(x)$ and a sensor response and attenuation model $p(x)$. The sensor response is defined as the fraction of events detected from a constant rate point source located a distance x from the sensor. The event rate can then be written as the sum of the contributions from each volume increment in the fluid tube, plus the background rate:

$$\frac{dE}{dt} = \int_0^H s(x)p(x-r)dx + \dot{E}_0 \quad (2)$$

Here $x = 0$ corresponds to the position of the needle tip where the gas is injected, H is the fluid surface level, and r is the position of the sensor. Since the sensor was fixed, the distance between it and the fluid surface level was approximately constant $h = H - r$.

It seems reasonable to assume that the sensor response is symmetric and decreases at greater source/sensor distances. In the extreme, $p(x-r) \rightarrow \delta(x-r)$, which can be substituted into equation (2). By defining $s(x)$ as an exponentially decaying function with an appropriate constant, the curve obtained from equation (2) bears qualitative resemblance to the experimental data (see Fig. 5). A reasonable starting point for the system model thus appears to be

$$\frac{dE}{dt} = \frac{n_0}{\sigma\sqrt{2\pi}} \int_0^H \exp(-\alpha x) \exp[-(x-r)^2/2\sigma^2] dx + \dot{E}_0 \quad (3)$$

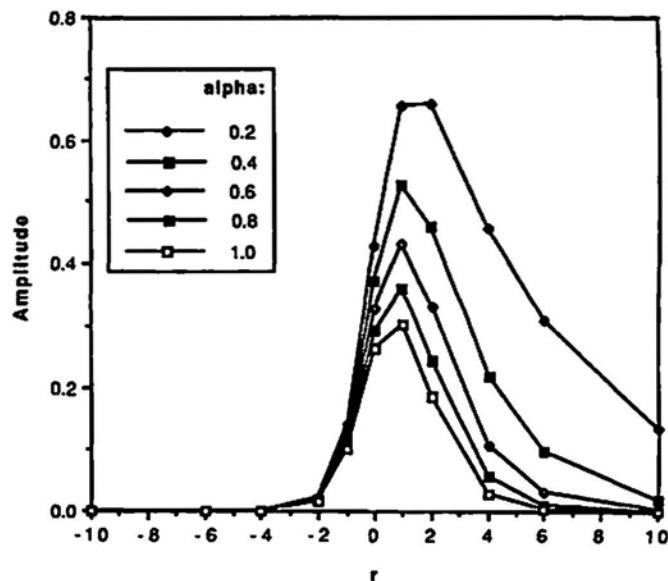


Fig. 6 a) Effect of α on dE/dt with $\sigma = 1.0$.

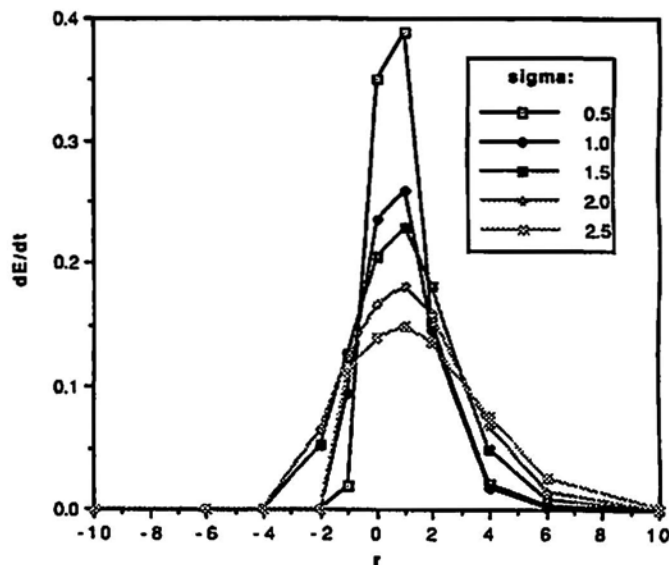


Fig. 6 b) Calculated dE/dt for various σ values with $\alpha = 1.0$.

By completing the square, equation (3) becomes

$$\frac{dE}{dt} = n_0 [\exp(-\alpha\sigma)^2/2 - \alpha\sigma] x [Q(\alpha\sigma - r/\sigma) - Q(\alpha\sigma + h/\sigma)] + \dot{E}_0 \quad (4)$$

where

$$\frac{dE}{dt} = \frac{1}{\sqrt{2\pi}} \int_a^{\infty} \exp(-z^2/2) dz \quad (5)$$

Figures 6a and 6b illustrate the behavior of the family of curves obtained by varying α and σ in equation (4), using $n_0 = 1$, $\dot{E}_0 = 0$, with r on the interval $\{-10, 10\}$. The r values can be linearly scaled to the experimental data. Letting $r' = kr$, and other quantities in the new scale denoted by the primes,

$$\alpha'\sigma' - r'/\sigma' = \alpha\sigma - r/\sigma \quad (6a)$$

and

$$(\alpha'\sigma)^2/2 - \alpha'r = (\alpha\sigma)^2/2 - \alpha r \quad (6b)$$

from which

$$\alpha' = \alpha/k \quad (6c)$$

$$\sigma' = k\sigma.$$

Comparing the behavior of these curves indicates that it may be necessary to provide an ordinate transformation. Since r is the position of the sensor relative to the needle tip, the zero source-sensor distance from experiment should correspond to $r = 0$ in the theoretical curve. One cannot, therefore, simply shift the axis by redefining r as $(r + \text{constant})$ in equation (4) in order to improve the fit. However, it is easy enough to show that adding a term to the argument of Q is equivalent to shifting the origin of the scale on the tube, and therefore the event rate distribution. In equation (4), $r - \beta$ is substituted for r in the argument of Q and by working backwards, equation (3) is recovered if x is redefined as $x + \beta$. By again representing $p(x - r)$ as a delta function and integrating equation (3), the position which produces the highest event rate along the gas bubble train is found to be b above the needle tip.

An iterative estimation procedure was written to solve equation (4) by comparing experimental data with values calculated using incremented values of α , σ and β . Values for Q were calculated using a slight modification of a series expansion for $P(x)$ given in Abramowitz and Stegun (1965). The experimental data was linearly scaled to fit in the interval $\{-10,10\}$ using a factor of 4.45. An approximate background was subtracted from the data, and no estimated by dividing the largest experimental data point by the calculated value at the same position. After vertically scaling the remaining data, the difference between calculated and experimental values was found, and the sum of the absolute differences compared to find the lowest value. A comparison of the experimental data and the curve calculated for $\alpha = 0.29$, $\sigma = 0.68$, $\beta = 1.76$, $\dot{E}_0 = 0.60$, and $n_0 = 5.02$ is shown in Fig. 4. It should be noted that good fits were not obtained for values too far from the ones used above. The source and sensitivity functions can now be estimated:

$$s(x) = 5.02 \exp[-0.058x] \quad (7a)$$

$$p(x) = \exp[-(x - r)^2/18.31] \quad (7b)$$

In the experiment, position was measured from the needle tip where the gas was injected. By rescaling β , the analytic result indicates that the rate of maximum event production is roughly 8 cm above the needle tip, where from observation the bubbles begin to interact directly with the tube wall. In Experiment 3, it was noted that the acoustic barrier reduced surface AE to about 0.8 events/s, only slightly more than the background used above. There is a tacit assumption that the upper surface contribution is roughly constant despite insertion depth.

5. Discussion

It is encouraging that the analytic results provide a good fit to the data, since the initial choices for $s(z)$ and $p(z)$ were made on the basis of fairly limited observations. Steps which would enable the model to be verified or expanded upon are to obtain a dense data set, and to obtain or write a least-squares routine for finding the best fit of the variables.

The form of the event rate equation is similar to that used by Beattie (1982) although in the present case the rate of occurrence of discrete events rather than the signal amplitude is measured, and only one sensor is used. A Gaussian function was used here for the sensitivity function since it provided the necessary symmetry. An advantage offered by the present experiment over most acoustic emission experiments was that the behavior of the sources could be observed, and predictions of the model verified directly.

The sources of detected emission appear to be the interaction of the bubbles with the tube wall or turbulence caused by passage of the bubbles, and bubble rupture on the free surface of the water. Some process associated with the production of bubbles, initially considered the prime candidate for the emission source, was not detectable to any appreciable degree with the present experimental setup. The degree of localization of the sensor response was somewhat surprising, since s in the scale of the experiment is only about 3.5 cm. This result was supported by Experiment 3, however. The results of Experiment 3 also indicate that detected AE is transmitted via the tube walls rather than through the fluid.

Acknowledgment

The authors would like to thank Zen Antoniak of PNL and the U.S. Department of Energy for providing funding to obtain the experimental data. Pacific Northwest Laboratory is operated for the U.S. Department of Energy under Contract DE-AC06-76RLO 1830.

References

- M. Abramowitz and I.A. Stegun, eds. (1965), *Handbook for Mathematical Functions*, Dover Press, New York.
- A.G. Beattie (1982), "An Acoustic Measurement of Boiling Instabilities in a Solar Receiver," *J. Acoustic Emission*, 1(1), 21-28.
- M.A. Friesel (1986), "Acoustic Emission Source Identification Using Long-Waveguide Sensors," *NDT Int.*, 3(19), 203-206.
- P.H. Hutton, M.A. Friesel, and J.F. Dawson (1987), "Detection of Cracking in Vitrified Nuclear Waste Using Acoustic Emission Methods." Report prepared for Kernforschungszentrum Karlsruhe GmbH Karlsruhe, FDR. Pacific Northwest Laboratory, Richland, Washington.
- R.T. Lahey, Jr. and S.J. Moody (1977), *The Thermo-Hydraulics of a Boiling Water Reactor*, American Nuclear Society, La Grange Park, Illinois.
- D.V. Leemans, J.A. Baron and O.A. Kupics (1981), *Advances in Acoustic Emission*, ed. H.L. Dunegan and W.F. Hartman, Dunhart Publishers, Knoxville, pp. 323-329.
- R.F. Saxe and L.W. Lau (1968), "Cavitation Noise in Nuclear Reactors," *Nuc. Eng. and Des.*, 8, 229-240.

In Memoriam

Dr. RAYMOND W. B. STEPHENS **(1902-1990)**

We are sorry to report the death in London of Dr. R. W. B. Stephens at the age of 88. Longtime Reader in Acoustics at Imperial College, London, Dr. Stephens was the leading light of acoustics in England and was well known all over the world.

In his long and distinguished career Dr. Stephens trained a prodigious number (>110 Ph.Ds) of postgraduate students from many countries, who have made their mark in acoustics all over the world. The full scope of these activities has been reported more completely by Dr. E. A. Shaw in the *Journal of the Acoustical Society of America*.

In acoustic emission, Dr. Stephens' Ph.D. students included Adrian Pollock (1964-68), Roger Hill (1968-72), and R. S. Geng. He also supervised the Ph.D. project of Brian Woodward (1965-69) who later undertook the first acoustic emission work in Australia. The first project in acoustic emission was sponsored by Roy Sharpe's nondestructive testing group at the Atomic Energy Research Establishment, Harwell stimulated by Roy's contacts with Battelle Northwest. Dr. Stephens secured the grant and Adrian Pollock, newly graduated from Cambridge, joined the Acoustics Group to perform the work. Graham Curtis, another of Dr. Stephens' students, took the knowledge of this project back to Harwell and initiated there the work in AE that was eventually taken up by Wadley, Scruby et al. Meanwhile at Imperial College, Roger Hill moved in after Adrian Pollock's graduation, and started under Dr. Stephens the train of work that he later carried to Robert Gordon's Institute of Technology and Nottingham Polytechnic.

From the beginning, Dr. Stephens was intrigued with acoustic emission as he was with all aspects of acoustics; in particular he recognized from the start the relationship between AE and earthquakes, and the possibility of locating AE sources based on time difference measurements. (AAP)

Adrian Pollock recalls:

Students from all over the world were crammed into a large upstairs laboratory and an even larger, very tall basement laboratory in which he had his resident technician build a mezzanine floor out of Dexion scaffolding to double the working space. His workload was enormous and his desk was legendary. About twelve feet long, it was completely covered in papers to a depth of about twelve inches. He

would rummage in the piles and unerringly extract something relevant to the discussion in hand. Meanwhile, outside the offices, the other students and overseas visitors were always tapping on the door. "I'm a little pressed today," he would gently excuse himself when one of his students was trying to get his thesis read. "Perhaps we could do it on Sunday at, say, three o'clock?"

While he left us to our own devices as far as the technicalities of our projects were concerned, Steve always pushed us to attend technical society meetings, to speak at them and to publish. All his students had to give a presentation to their peers quite early in their research programs, a nerve-racking prospect for an inexperienced student but an invaluable icebreaker for later public speaking. Steve was very active in the Institute of Physics and pushed me into organizing, with the Institute, the first conference in Europe on acoustic emission which was held in 1972. It was their most successful topical conference of the year, attended by over 180 people. Out of that conference the European Working Group on Acoustic Emission was born. Long after he retired, Steve was still asking people to write papers, give presentations or organize sessions for the conferences and journals and professional associations he was involved with - Acustica, Ultrasonics, the International Congress of Acoustics, the Institute of Acoustics and many more.

Steve did not hesitate to seek publicity for the work of his group, and cheerfully turned a blind eye to the protests that the publicity aroused. The major disaster of 1968 was "Ronan Point", the collapse of a large apartment block in the London suburbs. The newspapers made passing mention of the fact that residents of the block had been "hearing strange noises" for weeks before the collapse. "We should call *The Times*," said Steve, and we did. An article duly appeared extolling the potential of AE to prevent such failures. Of course, this article brought in several valuable enquiries for more information. However, we soon received a stiff reprimand from our government sponsor, AERE Harwell, who took the brunt of complaints from other ministries who were embarrassed by the implications of our report. I was summoned to appear before George Brodie, our contract administrator, who dutifully rapped me over the knuckles but also let me know that personally, he had no complaints about our action.

All of his students and many others will remember Steve with affection for his warm and gentle nature, the tremen-

dous breadth of his knowledge, his total commitment to acoustics and its people, and the special influences he had on their lives.

Sadly we report also the death, a little earlier, of Dr. Stephens' wife Ellie, a lady of exceptional intelligence and charm to whom he was totally devoted. Many workers in the field of acoustics will remember the warm hospitality of their home in East Putney. Their son survives them.

Robert Chivers writes:

Raymond Stephens was a classical physicist in every sense. Apart from a brief period in India during his pre-school days, all of his life was lived in South West London - a vantage point which enabled him to maintain an extraordinary level of activity in professional organisations and in hospitality to dozens of overseas visitors. After attending Emmanuel School, he studied Physics at Imperial College from 1921 - 24, before Heisenberg's uncertainty principle was enunciated! This was followed by 45 years' service to Imperial College as Demonstrator, Lecturer, Reader and Senior Tutor. Retiring at the age of 68, he worked for another 15 years at Chelsea College as a Visiting Research Fellow. Raymond's concern for his students - and indeed for all with whom he came into contact - was well recognised in many quarters, not least by the students of Imperial College who elected him to Honorary Membership of the Union (only the second staff member to be honoured in this way).

The first few scientific papers published (mainly in the *Philosophical Magazine* in the 1930's) give some clue to the career that was to flower later. While concerned mainly with the measurement of thermal properties of materials, they range widely, and have a key element - that of a dedication to the teaching of experimental physics. For 19 years Raymond was Chief Examiner in the Practical Physics Examinations for London University. In addition to being Chief Examiner in A level Physics for the University of London, he was also the Physics Examiner for the Institute of Plastics, the Royal Aeronautical Society, the British Optical Association, and External examiner at the Universities of Ibadan (Nigeria), Malawi, Kumasi and Khartoum (Sudan). In his 'spare' time he held part-time evening lectureships in a number of colleges and polytechnics in the London area. However, Raymond clearly saw a broader range of professional involvement as essential. He served on the Council, the Education Committee, the Technical Papers Committee, the Library Committee and the Non-destructive Testing Group of the Physical Society. He was a Fellow of the Institute of Physics, and sometime Secretary and Chairman of the Acoustics Group of the Institute.

Remarkably, Raymond's interest in Acoustics, for which he is pre-eminently well-known, was a relatively late development. If dates can be identified for such evolutionary processes, it would probably be 1947 which marked the start of his keen activity in Acoustics, (a date which also marks the formation of the Acoustics Group of the Physical Society).

The sheer statistics of his work are extraordinary. Raymond had a relatively modest publication list - some nine books (the last was published when he was 84 years old) and 60 - 70 papers which belies the reality. Much of the work of his early postgraduate students did not bear his name (save in the acknowledgments). Indeed, it is these students that begin to reveal the nature of the man. He supervised almost 100 postgraduate theses at the University of London, and examined over 120 doctoral theses from all over the world. Not only have many of these students held eminent positions in a wide variety of acoustics, but it is reputed to be hard to find a country of the world where at least one of this ex-students does not reside.

The growth in activity in acoustics in the UK after the Second World War gave Raymond the opportunities which only someone of his breadth of interest, depth of human understanding, and clear vision, could fully exploit. A former member of the Acoustics Group of the Physical Society, Raymond became Committee member in October 1950 and Joint Honorary Secretary in March 1952, a post which he filled actively (to judge from the Minutes) for a number of years. He was a prime mover in the founding of the British Acoustical Society and the British Society of Audiology in the 1960's. In the early 1970's he was one of the principal architects of the forging of the Institute of Acoustics out of the conjunction of the British Acoustical Society and the Acoustics Group of the Institute of Physics. This was achieved just in time to host the ICA in London in 1974, Raymond serving as Chairman of the Organising Committee (as well as being Founding President of the Institute).

Raymond enthusiastically supported the formation of the Federation of the Acoustical Societies of Europe, and was closely involved with the formation of *Espanola de Acustica* and the *Grupo de Acusticos Latino-Americanos*. For thirty years he served as English Editor of *Ultrasonics* and one the Advisory Board of the *Journal of Sound and Vibration*. He was a consultant to the Admiralty Underwater Establishment for eighteen years prior to his retirement from Imperial College, and for fourteen years was an Honorary Physicist at the Institute of Laryngology and Otology at London.

With this intense activity with organisations in different countries, it is perhaps surprising that Raymond's research activities still flourished. In addition to working in most of the main areas of acoustics (architectural, noise control, etc.) Raymond's major work was in Physical Acoustics and ultrasonics - but even so, the list of areas researched under his guidance is extraordinary. It includes: sound propagation in tubes, rods, plates, sheets, anisotropic solids, liquid metals, porous media and liquid crystals; finite amplitude waves in gases, liquids and solids, sonoluminescences, hypersonic waves in liquids, infrasonics, ultrasonic imaging, surface waves, acoustic emission in stressed solids, modal regeneration, vibration isolation, viscoelasticity and photoacoustics.

Recognition of Raymond's achievements was wide. He was elected a Fellow of the Acoustical Society of America in 1967 and in 1977 was the first British scientist to receive

their Gold Medal. The British Acoustical Society awarded him the Rayleigh Gold Medal in 1971, the French Acoustical Society (Gala) their Silver Medal in 1973, he was made a Doctor Honoris Causa of the University of Cordoba in Argentina in 1972, and was elected a Honorary member of the British Society of Rheology, the British Society of Audiology, the Institute of Acoustics (UK), the Sociedad Espanola de Acustica, the Grupo de Acusticos Latino-Americanos, the Polish Acoustical Society, and the Ultrasonics Society of India. One of the most surprising features of Raymond's career was the relative lack of recognition accorded him by the British establishment. This may have been due in part to his modesty and gentility, but it is sad that we in England did not better honour the man, who was almost certainly the most eminent British acoustician since Lord Rayleigh.

No tribute to Ray Stephens would be complete without mention of the activity of which he was as passionately fond as his physics, namely Association Football. In addition to being a lifelong supporter of Fulham Football Club, Ray was a keen participant at different times and in different ways in the Association Football Club of Imperial College, of which he was President and a life Vice-President. He was also a Vice-President of the University of London Football Club, and of Ulysses (the University of London Old Students' Football Club).

In all his endeavours, Raymond was fully supported by his charming wife, Ellie, who predeceased him by a few months. Raymond was in very sense one of that rare breed, a gentleman and a scholar, but first and last a friend.

Roger Hill, Associate Editor Europe, *Journal of Acoustic Emission* writes:

Raymond Stephens was one of the pioneers in acoustic emission in the world and one of the first to study the phenomenon in the UK -but this was only one aspect of a wide interest in the field of acoustics. As Dr. Chivers states, he was a classical physicist: he studied acoustic phenomena of which AE was just one and the projects within his laboratory at Imperial College covered topics such as low frequency vibration work, acousto-optic phenomena, room acoustics, underwater ultrasound, acoustic emission and attenuation studies of high frequency ultrasound. His projects spanned the frequency spectrum and crossed the boundaries into other areas of physics.

He was not essentially an NDT physicist but he was one of the earliest to recognise the potential of AE, before the ready availability of commercial instrumentation and saw its potential as a method of materials evaluation and NDT. He was possibly the first to use amplitude analysis of AE signals, the first to see the need to model AE sources and the first to detect the Felicity Effect. He predicted the acoustic equivalent of magnetic Barkhausen noise before it was reported in the literature although his idea was not tested, presumably due to lack of funding. He also realised the

potential of AE for testing a wide range of materials.

Raymond Stephens was a quiet man who succeeded by the friendships he made with all he met. He was not one to offend others and took offense when faced with what he regarded as bad manners in others. His quiet manner was, no doubt, not well regarded in some quarters, and this accounts for his lack of recognition in his own country. Ironically, for those friends from abroad who expected an Englishman to be a gentleman he was always that. For those interested in acoustics rather than science politics his contribution was regarded with respect.

He made an impact on generations of students and his impact in the field of acoustic emission is evident in that his research students in AE are all still active in the technology over twenty years on. His longevity meant that he brought to the latter part of the twentieth century scientific values from before the first world war and an earlier age. His personality has marked the lives of many and in a world of increasing materialism and aggression we can perhaps remember the importance of a milder and more gentlemanly way of conducting our affairs.

Footnote by Roger Hill

I recently obtained a copy of Imperial College "Calendar" for 1935-36, which gives information on forthcoming activities at the college during the following academic year. At this time Physics courses were still dominated by Classical Physics and listed are the courses to be taught by RWBS, just at the beginning of his long academic career. The courses to be taught were, magnetism and current electricity and a problem solving class, but no indication of the wide ranging acoustic work to follow after the second world war. However, within the pages of the Calendar we do see foreshadowed, an indication of what was to come. The Physics department had an academic staff complement of twenty, with four professors (UK style), of whom the most famous was perhaps G. P. Thomson, who was responsible for confirming the wave nature of electrons and shared a Nobel Prize with Davisson in 1937. Perhaps more relevant to the later work of RWBS was Emeritus Professor within the department, The Lord Rayleigh M.A., Sc.D., FRS. This man was the son (?) of the 3rd Baron Strutt, Lord Rayleigh whose book published in 1878 did so much to provide the theoretical foundations of acoustics. Rayleigh (the son) had written a biography of his father and no doubt visited the college from time to time and had an influence on the future direction and work of RWBS, but it was not until after the war that his interest began to take shape, in what was no doubt a restructure college.

Cover photograph: courtesy of Roger Hill.

INDEX to Volume 10, 1991/92

Author Index

D. L. Armentrout	97, 103	Yuji Murakami	S90
Frank C. Beall	83	S. Naemura	S55
Andrew R. Blystra	S49	M. Nakamura	S55
S. J. Bowles	49	Syouzou Nakamura	S13
Franklin R. Breckenridge	43	Priscilla P. Nelson	S1
Nancy Brown	71	S. Nishikawa	S55
S. H. Carpenter	97, 103	Yoshitugu Ohigashi	25
Timothy G. Crowther	71	Masayasu Ohtsu	i (1/2)
C. E. D'Attellis	13	Hisanori Otsuka	S13
Jack F. Dawson	117	C. Ouyang	S97
V. G. Ruiz de Argandoña	S35	Peter Pellionisz	19
L. M. Suárez del Río	S35	L. V. Perez	13
F. Dusek	1	S. Pilecki	1
R. M. Esbert	S35	Stefan Poliszko	107
T. Flynn	S59	Thomas M. Proctor, Jr.	43
Michael J. Friedel	S77	Jan Raczkowski	107
Mark A. Friesel	117	G. L. Rigby	S22
T. Fujiwara	S63	I. Roman	31
János Geréb	19	Gottfried A. Rubin	S18
Steven D. Glaser	S1	D. Rubio	13
C. M. Grossi	S35	J. E. Ruzzante	13
H. R. Hardy, Jr.	61	Koji Sakai	S104
R. W. Harris	S29, S59	C. M. Scala	49
F. P. Hassani	61	J. S. Schwartzberg	97
K. Hata	S63	S. P. Shah	S97
C. R. Heiple	97, 103	Hisatoshi Shimada	S104
H. Hick	67	Noboru Shinke	25
Hiroshi Hikosaka	S13	J. Siedlaczek	1
Kyoji Homma	35	F. Simacek	67
Takako Inaba	S90	M. Tanaka	S55
T. Ishida	S42	Richard E. Thill	S77
K. Jo	S55	Adrian P. Wade	71
Musa K. Jouaneh	83	N. Wakabayashi	S42
Shahla Keyvan	91	J. W. Whittaker	113
Ron King	91	B. J. S. Wilkins	S22
N. Kinoshita	S42	H. Willer	67
T. Kishishita	S55	E. Winter	67
Tatsuo Kita	S90	B. R. A. Wood	S29, S59
K. Kitano	S42	H. Yoshioka	S63
F. M. Kustas	97	Hironobu Yuki	35
E. Landis	S97	F. Zeides	31
Marcel F. Leach	S18		
Richard Lemaster	83		
J. F. McCardle	49		
K. Michihiro	S63		
Kazuya Miyano	S90		
Hiroyuki Miyatake	S13		
Waldemar Molinski	107		
M. Momayez	61		
M. Montoto	S35		

Contents

Number 1/2

Current Research and Future Trend of AE Applications to Civil Engineering and Geological Technology Masayasu Ohtsu, Topical Editor	i
Variety of Acoustic Emission Waveforms Produced by Discrete Crack Growth in Rock Steven D. Glaser and Priscilla P. Nelson	S1-S12
Estimation of Maximum Stress in Old Railway Riveted I-Girder Bridges using Acoustic Emission Signals Hisanori Otsuka, Hiroshi Hikosaka, Hiroyuki Miyatake and Syouzou Nakamura	S13-S17
Another Look at Booming Sand Marcel F. Leach and Gottfried A. Rubin	S18-S21
Expected Acoustic Emission from Around a Shaft in Intact Rock B.J.S. Wilkins and G.L. Rigby	S22-S28
Acoustic Emission Monitoring during Microseismic Activity Caused by Mine Subsidence Brian R. A. Wood and Robert W. Harris	S29-S34
Acoustic Emission/Microseismic Activity Monitoring of Salt Crystallization for Stone Conservation M. Montoto, R.M. Esbert, L.M. Suárez del Río, V.G. Ruiz de Argandoña and C.M. Grossi	S35-S41
Acoustic Emission Monitoring during In-situ Heater Test of Granite T. Ishida, K. Kitano, N. Kinoshita and N. Wakabayashi	S42-S48
Using Acoustic Emission Testing in Seepage Investigations Andrew R. Blystra	S49-S54
Acoustic Emission of Penetration Experiments to Judge Soil Condition S. Naemura, M. Tanaka, S. Nishikawa, M. Nakamura, K. Jo and T. Kishishita	S55-S58
A Laboratory Investigation of AE from Coal R. W. Harris, B. R. A. Wood and T. Flynn	S59-S62
Determination of the Initial Stresses on Rock Mass using Acoustic Emission Method K. Michihiro, K. Hata, H. Yoshioka and T. Fujiwara	S63-S76
U.S. Bureau of Mines Research on the Kaiser Effect for Determining Stress in Rock Michael J. Friedel and Richard E. Thill	S77-S89
Evaluation of Joint Properties of Anti-washout Underwater Concrete by Acoustic Emission Measurement Kazuya Miyano, Tatsuo Kita, Yuji Murakami and Takako Inaba	S90-S96
Automated Determination of First P-Wave Arrival and Acoustic Emission Source Location E. Landis, C. Ouyang and S. P. Shah	S97-S103
Application of Acoustic Emission Techniques in the Evaluation of Frost Damage in Mortar Hisatoshi Shimada and Koji Sakai	S104-S109

Number 3/4

Acoustic Emission of the 45HNMFA Structural Steel during Low-Cycle Fatigue J. Siedlaczek, S. Pilecki and F. Dusek	1-11
Parameter Estimation in Acoustic Emission Signals C. E. D'Attellis, L. V. Perez, D. Rubio and J. E. Ruzzante	13-17
Acoustic Emission Technique at Proof Tests of Nuclear Pressure Vessels in Hungary Peter Pellionisz and János Geréb	19-23
Effects of Wave Velocity Change on Magnetomechanical AE in Sintered Iron Noboru Shinke and Yoshitugu Ohigashi	25-29
Origin of Acoustic Emission in Naturally Aged Aluminum-Lithium Alloys F. Zeides and I. Roman	31-33
Analysis of Artificial Acoustic Emission Waveforms Using a Neural Network Hironobu Yuki and Kyoji Homma	35-41
Source Force Waveforms: The Use of a Calibrated Transducer in Obtaining an Accurate Waveform of a Source Thomas M. Proctor, Jr. and Franklin R. Breckenridge	43-48

C. M. Scala, J. F. McCardle and S. J. Bowles	49-60
Maximum Curvature Method: A Technique to Estimate Kaiser-Effect Load from Acoustic Emission Data	
M. Momayez, F. P. Hassani and H. R. Hardy, Jr.	61-65
Acoustic Emission Measurements on Bridges	
H. Hick, H. Willer, E. Winter and F. Simacek	67-70
Acoustic Emission Monitoring of the Sensitivity of Chemicals to Impact	
Timothy G. Crowther, Adrian P. Wade and Nancy Brown	71-82
Study of Acoustic Emission Generation in Sliding Motion	
Musa K. Jouaneh, Richard Lemaster and Frank C. Beall	83-89
The Role of Acoustic Monitoring as a Diagnostic Tools in Nuclear Reactors	
Shahla Keyvan and Ron King	91-95
Acoustic Emission Produced by Sliding Friction and its Relationship to AE from Machining	
S. H. Carpenter, C. R. Heiple, D. L. Armentrout, F. M. Kustas and J. S. Schwartzberg	97-101
Comments on the Origin of Acoustic Emission in Fatigue Testing of Aluminum Alloys	
C. R. Heiple, S. H. Carpenter and D. L. Armentrout	103-106
Acoustic Emission of Wood during Swelling in Water	
Stefan Poliszko, Waldemar Molinski and Jan Raczkowski	107-111
Characterization of the ASL Parameter	
J. W. Whittaker	113-116
Acoustic Emission from Bubbles in a Water Column	
Mark A. Friesel and Jack F. Dawson	117-121
In Memoriam, Dr. Raymond W. B. Stephens (1902-1990)	122-124
Conferences and Symposia	
Progress in Acoustic Emission VI, Proceedings of The 11th International AE Symposium	12, 18, 24, 30, 34
36th Meeting of Acoustic Emission Working Group	42, 66, 90, 96, 102

Fourth International Symposium on Acoustic Emission from Composite Materials, July 27-31, 1992, Seattle, WA

Fourth International Symposium on Acoustic Emission from Composite Materials (AECM-4) was held at Holiday Inn Crowne Plaza in downtown Seattle with about 80 participants from 13 countries and areas. AECM-4 was organized by CARP with Dr. Burke Dykes of Boeing Commercial Airplanes as Chairman, Dr. D.R. Smith as Paper and Program Chairman. A one-day, pre-symposium educational seminar was also conducted. The Symposium opened with a sad news that Dr. Daniel Valentine of Ecole des Mines de Paris, who served as the Paper and Program Chairman for AECM-3 in Paris, France, in 1989 passed away earlier in the year. He has actively studied AE behavior in connection with the failure mechanisms/criteria of fiber-reinforced composite materials. Two keynote addresses by Prof. T. Kishi (Microfracture analysis with AE) and by Dr. P. Fleischmann (AE and rheological behavior) as well as nearly 50 papers presented contributed to further advances of this field. Proceedings volume is available from ASNT (Catalogue No. 1335).

1993 SUBSCRIPTION RATE for Volume 11

Base rate for one year (four issues, Mar. - Dec.)	\$ 96.00
Add Postage of	
U.S. - Book rate	\$ 8.00
All others - Book rate	\$ 11.00
U.S., Canada - First class	\$ 17.00
Western Europe - Air mail rate	\$ 25.00
All others - Air mail rate	\$ 30.00
Add \$5 without payment upon order. Payment must be in U.S. dollars drawn on a U.S. bank. Bank transfer accepted to the A.E. Group account (Account No. 080-03416470) at	
Sumitomo Bank of California	
San Fernando Valley Office	
15250 Ventura Blvd	
Sherman Oaks, CA 91403-3262	

Notify us of such a transfer as the bank cannot sometimes give us the name of the payer. One volume of four issues per year. Index included in the Oct.-Dec. issue. Back issues available at \$50 per volume for Vols. 1-3, \$90 per volume for Vols. 4-8, \$96 per volume for Vols. 9-10. US surface postages \$8 per volume. For Canada and overseas surface delivery, add \$11 and for air mail, add \$30 per volume (adjusted for multi-volume order). All orders should be sent to

Acoustic Emission Group
308 Westwood Blvd., Box 364
Los Angeles, CA 90024-1647 USA

Editor-Publisher	Kanji Ono (310) 825-5233
Editorial Assistant	Barbara Brooks
Cover Design	Robin Weisz
Production	Pace Publications

Publication Date of This Issue: 15 March 1993.

AVAILABLE BOOKS ON ACOUSTIC EMISSION

- Progress in Acoustic Emission IV (1988)** The Proceedings of the 9th International AE Symposium.
Progress in Acoustic Emission V (1990) The Proceedings of the 10th International AE Symposium.
Progress in Acoustic Emission VI (1992) The Proceedings of the 11th International AE Symposium.
These volumes are \$ 150 plus shipping. Earlier Proceedings volumes also available. Inquire below.
Proc. Second International Conference on AE (1985) October 1985. about 350 pages \$ 50
Proc. World Meeting on AE (1989) March 1989. about 350 pages \$ 50
Acoustic Emission - A Bibliography with Abstracts (1979) T.F. Drouillard 806 pages. Published by Plenum Press. \$ 135 post paid (surface).
Fundamentals of Acoustic Emission (1979) Ed. K. Ono - microfiche version only 360 pages. \$ 10.
Journal of Acoustic Emission, Vol. 1 - 3 (1982 - 84) \$ 50 per volume (plus shipping)
Journal of Acoustic Emission, Vol. 4 - 8 (1985 - 89) \$ 90 per volume (plus shipping)
Journal of Acoustic Emission, Vol. 9 - 11 (1990, 91/92, 93) \$ 96 per volume (plus shipping)

Above are available from

Acoustic Emission Group
308 Westwood Blvd, Box 364
Los Angeles, CA 90024-1647
FAX 1-818-368-8309

- NDT HANDBOOK (2nd Edition), Vol. 5, Acoustic Emission Testing (1988)**
Eds. R.K. Miller and P. McIntire. 650 pages. \$110.25
Third International Symposium on AE from Composite Materials (1989) Cat. No. 770.
Fourth International Symposium on AE from Composite Materials (1992) Cat. No. 1335.
Proc. Fourth World Meeting on AE (1991) Sep. 1991. Cat. No. 1332.
Advances in Acoustic Emission (1981) eds. Dunegan & Hartman 385 pages - \$ 68.
Available from Book Dept., ASNT, P.O.Box 28518, Columbus, OH 43228. Also call (800) 222-2768.

- First International Symposium on AE from Reinforced Plastics (1983)**
Proceedings of the San Francisco Symposium, July 1983. about 400 pages - \$ 50 + shipping.
Second International Symposium on AE from Reinforced Plastics (1986)
Proceedings of the Montreal Symposium, July 1986. about 225 pages - \$ 65 + shipping.
Available from Publication Sales, SPI, 355 Lexington Ave., New York, NY.

- Acoustic Emission (1983)** J.R. Mathews 167 pages.
Basic Acoustic Emission (1991) Ian G. Scott, 246 pages. Available from Gordon & Breach, New York.

- Third Conf. on AE/Microseismic Activity in Geologic Structures and Materials (1982)**
Fourth Conf. on AE/Microseismic Activity in Geologic Structures and Materials (1989)
Eds. Hardy & Leighton. Available from Trans Tech Publications, 16 Bearskin Neck, MA 01966.

- Acoustic Emission (1980)** tr. A.R. Nicoll 385 pages - \$ 63.
Available from DGM Metallurgy Information, 150 E. 27th St., New York, NY 10016

- Acoustic Emission (1980)** R.V. Williams 140 pages - \$ 29.
Available from A. Hilger Ltd, Bristol, UK or Heyden & Sons, Philadelphia.

- ASTM-STP's: Acoustic Emission (1972), STP-505.**
Monitoring Structural Integrity by Acoustic Emission (1975), STP-571.
Acoustic Emission Monitoring of Pressurized Systems (1979), STP-697.
Acoustic Emission in Geotechnical Engineering Practice (1982), STP-750.
Acoustic Emission, Current Practices and Future Directions (1991), STP-1077.
Acoustic Emission Testing of Aerial Devices and Associated Equipment used in the Utility Industries (1992), STP-1139.
Available from ASTM, 1916 Race St, Philadelphia, PA 19103.

Notes for Contributors

1. General

The Journal will publish contributions from all parts of the world and manuscripts for publication should be submitted to the Editor. Send to:

Professor Kanji Ono, Editor - JAE
5731 Boelter Hall, MSE Dept.
University of California
Los Angeles, California 90024-1595 USA
FAX (1) 818-368-8309
e-mail: ono@seas.ucla.edu

European authors may submit manuscripts directly to:

Dr. Roger Hill, Associate Editor - Europe
Department of Chemistry and Physics
The Nottingham Trent University
Clifton Lane
Nottingham NG11 8NS UK
FAX (44) 602-45-6002

Authors of any AE related publications are encouraged to send a copy for inclusion in the AE Literature section to:

Mr. T.F. Drouillard, Associate Editor - JAE
EG&G Rocky Flats
P.O. Box 464
Golden, Colorado 80402 USA

Note some changes in the addresses.

All the manuscripts will be reviewed upon submission to the Editor. Only papers not previously published will be accepted. Authors must agree to transfer the copyright to the Journal and not to publish elsewhere, a paper submitted to and accepted by the Journal.

A paper is acceptable if it is a revision of a governmental or organizational report, or if it is based on a paper published in a conference proceedings volume of limited distribution.

An abstract of about 200 words is needed for Research and Applications articles, while it should be shorter than 100 words for other articles.

The language of the Journal is English. All papers should be written concisely and clearly.

2. Page Charges

No page charge is levied. Fifty copies of off-prints will be supplied to the authors free of charge.

3. Manuscript for Review

Manuscripts for review need only to be typed legibly; preferably, double-spaced on only one side of the page with wide margins and submitted in duplicate.

The title should be brief. Except for short communications, descriptive heading should be used to divide the paper into its component parts. Use the International System of Units (SI).

References to published literature should be quoted in the text citing authors and the year of publication. These are to be grouped together at the end of the paper in alphabetical and chronological order.

Journal references should be arranged as below. Titles for journal or book articles are helpful for readers, but may be omitted.

H.L. Dunegan, D.O. Harris and C.A. Tatro (1968), *Eng. Fract. Mech.*, 1, 105-122.

Y. Krampfner, A. Kawamoto, K. Ono and A.T. Green (1975), "Acoustic Emission Characteristics of Cu Alloys under Low-Cycle Fatigue Conditions," NASA CR-134766, University of California, Los Angeles and Acoustic Emission Tech. Corp., Sacramento, April.

A.E. Lord, Jr. (1975), *Physical Acoustics: Principles and Methods*, vol. 11, eds. W. P. Mason and R. N. Thurston, Academic Press, New York, pp. 289-353.

Abbreviations of journal titles should follow those used in the ASM Metals Abstracts. In every case, authors' initials, appropriate volume and page numbers should be included.

Illustrations and tables should be planned to fit a single column width (87 mm or 3.3") or a double width (178 mm or 7"). For the reviewing processes, these need not be of high quality, but submit glossy prints with the final manuscript. Lines and letters should be legible.

4. Review

All manuscripts will be judged by qualified reviewer(s). Each paper is reviewed by one of the editors and typically sent for review by members of the Editorial Board. The Board member may seek another independent review. In case of disputes, the author may request other reviewers.

5. Electronic Media

In order to reduce any chance of typographical error, the authors are encouraged to submit a floppy disk copy of the text. We can read Macintosh and IBM PC formats. Those who can connect to computer networks, such as BITNET, ARPANET, ASIANET, EARN, NETWORK, UUCP, CSNET, JANET, OZ, etc. can send to "ono@seas.ucla.edu".

6. Color Photograph

We can print color photographs needed to enhance the technical content of an article. Because of the cost, the author is asked to pay \$350 per page.

Journal of Acoustic Emission (JACEDO)

Contents

1-11	Acoustic Emission of the 45HNMFA Structural Steel during Low-Cycle Fatigue <i>J. Siedlaczek, S. Pilecki and F. Dusek</i>
13-17	Parameter Estimation in Acoustic Emission Signals <i>C. E. D'Attellis, L. V. Perez, D. Rubio and J. E. Ruzzante</i>
19-23	Acoustic Emission Technique at Proof Tests of Nuclear Pressure Vessels in Hungary <i>Peter Pellionisz and János Geréb</i>
25-29	Effects of Wave Velocity Change on Magnetomechanical AE in Sintered Iron <i>Noboru Shinke and Yoshitugu Ohigashi</i>
31-33	Origin of Acoustic Emission in Naturally Aged Aluminum-Lithium Alloys <i>F. Zeides and I. Roman</i>
35-41	Analysis of Artificial Acoustic Emission Waveforms Using a Neural Network <i>Hironobu Yuki and Kyoji Homma</i>
43-48	Source Force Waveforms: The Use of a Calibrated Transducer in Obtaining an Accurate Waveform of a Source <i>Thomas M. Proctor, Jr. and Franklin R. Breckenridge</i>
49-60	Acoustic Emission Monitoring of a Fatigue Test of an F/A-18 Bulkhead <i>C. M. Scala, J. F. McCardle and S. J. Bowles</i>
61-65	Maximum Curvature Method: A Technique to Estimate Kaiser-Effect Load from Acoustic Emission Data <i>M. Momayez, F. P. Hassani and H. R. Hardy, Jr.</i>
67-70	Acoustic Emission Measurements on Bridges <i>H. Hick, H. Willer, E. Winter and F. Simacek</i>
71-82	Acoustic Emission Monitoring of the Sensitivity of Chemicals to Impact <i>Timothy G. Crowther, Adrian P. Wade and Nancy Brown</i>
83-89	Study of Acoustic Emission Generation in Sliding Motion <i>Musa K. Jouaneh, Richard Lemaster and Frank C. Beall</i>
91-95	The Role of Acoustic Monitoring as a Diagnostic Tools in Nuclear Reactors <i>Shahla Keyvan and Ron King</i>
97-101	Acoustic Emission Produced by Sliding Friction and its Relationship to AE from Machining <i>S. H. Carpenter, C. R. Heiple, D. L. Armentrout, F. M. Kustas and J. S. Schwartzberg</i>
103-106	Comments on the Origin of Acoustic Emission in Fatigue Testing of Aluminum Alloys <i>C. R. Heiple, S. H. Carpenter and D. L. Armentrout</i>
107-111	Acoustic Emission of Wood during Swelling in Water <i>Stefan Poliszko, Waldemar Molinski and Jan Raczkowski</i>
113-116	Characterization of the ASL Parameter <i>J. W. Whittaker</i>
117-121	Acoustic Emission from Bubbles in a Water Column <i>Mark A. Friesel and Jack F. Dawson</i>
122-124	In Memoriam, Dr. Raymond W. B. Stephens (1902-1990) Conferences and Symposia
12....34	Progress in Acoustic Emission VI, Proceedings of the 11th International AE Symposium
42....102	36th Meeting of Acoustic Emission Working Group
I-4	Available Books on AE
I-1 - I-3	Index to Volume 10, 1991/92